

Proceedings of NEWRAD 2021

Edited by

Mikhail Korpusenko, Aalto University

Petri Kärhä, Aalto University

John Lehman, NIST

Erkki Ikonen, Aalto University / VTT MIKES

FOREWORD

These Proceedings contain the extended abstracts of the NEWRAD 2021 Conference arranged online by NIST, Boulder, USA, June 21 - 24, 2021. The presentations are listed in the conference program at <https://www.nist.gov/news-events/events/2021/06/14th-international-conference-new-developments-and-applications-optical>

The extended abstracts of these Proceedings are organized according to the assigned codes under the following categories:

INV – Invited talks

DBS – Detector-based radiometry: scale realisations

DBA – Detector-based radiometry: applications

SBR – Source-based radiometry

QOT – Quantum optics technologies

PM – Photonic momentum

EAO – Earth observation

SSR – Solar / stellar radiometry

OPM – Optical properties of materials / components

OT – Other topics

List of contents

Invited Talks

INV_001, Jarle Gran, Three-dimensional modelling of photodiode responsivity.....	1
INV_002, Kuniaki Amemiya, Novel perfect blackbody sheet having nano-precision surface microtextures for a planar standard radiator.....	3
INV_003, Odele Coddington, TSIS Solar Spectral Irradiance Measurements.....	5

DBS – Detector-based radiometry: scale realisations

DBS_OR_002, Anna K. Vaskuri, Planar Absolute Radiometer Operating at Room Temperature for Replacing NIST's Legacy Laser Calorimeter.....	7
DBS_OR_0010, Kinza Maham, Optical power scale realization using the predictable quantum efficient detector.....	9
DBS_OR_012, Meelis-Mait Sildoja, High efficiency five-element trap detector with low optical losses.....	11
DBS_OR_014, Terubumi Saito, Calorimetric Measurements for Conversion Efficiency of Optical Devices.....	13
DBS_OR_015, Uwe Arp, Ultraviolet Scale Realization based on a Laser-driven Light Source.....	15
DBS_OR_017, Matthew Spidell, A Bilateral Comparison of NIST And PTB Laser Power Standards for Increased Calibration Confidence at LIGO.....	17
DBS_OR_018, Jan Lalek, Implementation of the Spectral Irradiance Standard based on a high-temperature black body.....	19
DBS_OR_019, Florian Stuker, Towards 1 W, High Accuracy, Absolute Radiometer.....	21
DBS_OR_000, Mikhail Korpusenko, Double laser radiometry for study of detector linearity.....	23
DBS_OR_021, Mikhail Korpusenko, Quantum efficiency of Predictable Quantum Efficient Detector in the ultraviolet region.....	25
DBS_OR_022, Philipp Schneider, Calibration of a modular trap detector system towards a new realization of the luminous intensity unit.....	27
DBS_OR_004, Marit Ulset Nordsveen, Simultaneous optical and electrical heating in dual-mode photodiode operation.....	29
DBS_OR_026, Brian G. Alberding, Development of a pyroelectric detector-based method for low uncertainty irradiance and radiance calibrations in the short-wave infrared.....	31
DBS_OR_028, J.E. Neira, Electrical-Substitution Fourier Transform Spectrometry for Absolute Calibration of Detector Responsivity.....	33
DBS_OR_029, Ping-Shine Shaw, NIST's primary optical power responsivity scale realized using a supercontinuum source with automation from 480 nm to 1650 nm.....	35

DBS_OR_030, Damian Twerenbold, Novel Integrating Sphere Based Attenuation Method for Single Photon Detector Calibrations.....	37
DBS_OR_031, Yuqin Zong, Recent Progress on Calibration of Spectroradiometers using Tunable Lasers.....	39
DBS_OR_002, Xu Nan, Near Infrared Spectral Responsivity Realization based on Cryogenic Radiometer.....	41
DBS_PO_001, Minoru Tanabe, Absolute irradiance responsivity calibration system using diode lasers for tricolour laser applications.....	43
DBS_PO_003, Tobias Pohl, Realization and Dissemination of the Spectral Responsivity of Thermal Detectors in the Mid-Infrared Spectral Range at the PTB.....	45
DBS_PO_004, CM Tsui, Interpolation of Spectral Responsivity of Trap Detectors and Evaluation of Measurement Uncertainties Using Monte Carlo Method.....	47
DBS_PO_007, Jeongwan Jin, Establishment of single photon detection efficiency calibration system at NRC.....	49
DBS_PO_008, Alexander Gottwald, Recent status of VUV/EUV photodiodes for radiometric scale comparison.....	51
DBS_PO_011, A. Gamouras, Advancements in NRC's Primary Spectral Irradiance Scale Realisation.....	53
DBS_PO_013, Eivind Bardalen, Packaging of silicon photodiodes for use as cryogenic electrical substitution radiometer.....	55
DBS_PO_023, Ozhan Koybasi, Investigation of surface passivation thin film materials for improved predictable quantum efficiency detectors.....	57
DBS_PO_005, Seval Meric, Spectral Radiance Scale Traceability Chain by Using Monte Carlo Application.....	59
DBS_PO_027, Nicole L George, Improving the spectral radiance and irradiance facility at NPL.....	61
DBS_PO_033, Stefan Källberg, Upgrade of cryogenic radiometer control electronics and software.....	63
DBA – Detector-based radiometry: applications	
DBA_OR_001, Haifeng Meng, Measurements of monolithic GaInP2/InGaAs/Ge triple-junction solar cells.....	65
DBA_OR_002, Jeanne M. Houston, UV spectral irradiance responsivity calibrations using a scanning method in a monochromator-based facility.....	67
DBA_OR_003, Howard W. Yoon, Nonlinearity corrections of spectrographs using combinatorial methods.....	69
DBA_OR_005, Sucheta Sharma, Cantilever-based photoacoustic detection of electromagnetic radiation.....	71
DBA_OR_006, Petri Kärhä, Differential spectral responsivity measurements of large bifacial solar cells.....	73

DBA_OR_007, Saulius Nevas, Application of a Tuneable Pulsed Laser for Spectral Responsivity Measurements of UV Radiometers Based on Wide-Bandgap Photodiodes.....	75
DBA_OR_008, Christopher Yung, Broadband absolute radiometers for far infrared sensing.....	77
DBA_OR_009, M G White, The Nature of Fibre Beam-Splitters for Absolute Radiometric Measurements.....	79
DBA_OR_010, C. Cameron Miller, Development of UVC Measurement Tools at NIST to Combat Healthcare-Associated Infections (HAIs).....	81
DBA_OR_011, Thada Keawprasert , Absolute Calibration Setup for Spectral Responsivity of a NIR radiation thermometer.....	83
DBA_OR_012, Janne Askola, Increased response of trap detectors with apertures due to nitrogen flow.....	85
DBA_OR_016, Maritoni Litorja, Radiometric calibration method for dim sources.....	87
DBA_OR_018, Ping-Shine Shaw , A fast AC mode measurement system for detector response and spatial uniformity characterization.....	89
DBA_PO_004, Dong-Joo Shin, Power and wavelength-meter in one for lasers and other narrow-band light sources based on the dual-photodiode radiometer concept.....	91
DBA_PO_015, A. Yu. Dunaev, Stable spectrally tunable source based on supercontinuum laser and monochromator for detectors radiometric calibration.....	93
DBA_PO_017, B. Carol Johnson, Thermal Characterization of Fiber-Coupled Spectrographs.....	95
SBR – Source-based radiometry	
SBR_OR_004, Zhao Weiqiang, Experimental Correction of Temperature Dependence for LED Filament Lamps.....	97
SBR_OR_005, Ingmar Mueller, A Lens-free InGaAs-Radiation Thermometer with improved Detectivity at 1.6 μm to cover the Temperature Range from 80 °C to 962 °C.....	99
SBR_OR_006, Tobias Pohl, Absolute Calibration of the Spectral Responsivity of Thermal Detectors at a High-Temperature Blackbody at the PTB.....	101
SBR_OR_007, Moritz Feierabend, A Blackbody for Calibration of Hemispherical Infrared Detectors.....	103
SBR_OR_008, Wu Zhifeng, Low Light Level Realization at Near Correlated Color Temperature.....	105
SBR_OR_009, Mai Huong Valin, New spectral irradiance traceability scale at LNE-CNAM.....	107
SBR_OR_010, Irina Santourian, Development, implementation and validation of a high-power LED-based radiation source for goniometric spectral radiance factor measurements	109
SBR_OR_013, Robert E. Vest, New Facility for Deuterium Lamp Calibrations at SURF III.....	111

SBR_OR_015, Peter Sperfeld, Spectral Mismatch Correction for the Calibration of UVA Radiometers.....	113
SBR_OR_018, T. Gerloff, Novel LED standard source for absolute radiometry in the visible wavelength range.....	115
SBR_OR_019, Yanfei Wang, Spectral Irradiance Measurement Based on Large-area WC-C Fixed Point Blackbody.....	117
SBR_OR_020, Eric L. Shirley, High-temperature behavior of diffraction effects in blackbody calibrations: higher-order effects.....	119
SBR_OR_022, J. Dubard, Characterisation of high irradiance level 254 nm UV sources for UVmeter calibration.....	120
SBR_PO_001, Thiago Ferreira da Silva, Intercomparison of indoor and outdoor spectral irradiance measurements between INTI and INMETRO.....	122
SBR_PO_002, Kenji Godo, Development of illuminance meter calibration system with LED spectrally tunable light source.....	124
SBR_PO_003, Yuri Nakazawa, Comparison of Two Methods for Total Luminous Flux Measurement of White LEDs.....	126
SBR_PO_011, Iu. A. Sild, Enhancement of the state primary standard of the unit of total radiance.....	128
SBR_PO_016, Vladislav Zemlyanoy, Simulation of Thermal Processes in High-Temperature Blackbodies and Fixed-Point Cells for Improving their Characteristics...	130
SBR_PO_017, Boris Khlevnoy, High-Temperature Fixed-Point Blackbody with Temperature of about 2856 K Based on Melting Phase Transition of $\delta(\text{MoC})\text{-C}$	132
SBR_PO_023, S.V. Nikanenko, Reference UVC LED Source.....	134
SBR_PO_024, S.V. Nikanenko, NATIONAL STANDARD OF BELARUS OF THE UNITS OF RADIANT INTENSITY, SPECTRAL RADIANCE AND IRRADIANCE IN THE SPECTRAL RANGE FROM 0.2 μm TO 3.0 μm	136
QOT – Quantum optics technologies	
QOT_OR_001, Hristina Georgieva, Calibration of silicon single-photon avalanche diode detectors using a narrow-bandwidth quantum emitter.....	138
QOT_OR_004, Thomas Gerrits, Calibration of free-space and fiber-coupled single-photon detectors.....	140
QOT_OR_005, Stefan Kück, Molecule-based single photon source for quantum radiometry.....	142
QOT_OR_007, Marco López, Pilot study on the detection efficiency measurement of InGaAs/InP single-photon detectors.....	144
QOT_OR_011, Thiago Ferreira da Silva, Optical frequency metrology based on photon counting.....	146
QOT_OR_012, Robin L. Williams, Nanowire-based Sources of Non-classical Light....	148
QOT_PO_002, Beatrice Rodiek, Core-shell CdSe/CdS quantum dot based single-photon emitter for SPAD calibration at room temperature.....	150

QOT_PO_003, Robin Eßling, Calibration of InGaAs/InP single-photon avalanche detectors.....	152
QOT_PO_006, Stefan Kück, The SIQUST-project – towards single-photon sources as new quantum standards.....	154
QOT_PO_008, In-Ho Bae, Performance evaluation of a thermoelectrically-cooled SiC single photon avalanche photodiode.....	156
QOT_PO_009, Justus Christinck, Comparison of back focal plane imaging of nitrogen vacancy centers in nanodiamond and core-shell CdSe/CdS quantum dots.....	158
QOT_PO_010, Trinh Tran, Simulated internal quantum deficiency of induced junction photodiodes.....	160
PM – Photonic momentum	
PM_OR_001, Alexandra Artusio-Glimpse, HALO – High Amplification Laser-pressure Optic.....	162
PM_OR_002, Gordon A. Shaw, SI traceable electrostatic balance to measure laser power.....	164
PM_OR_003, Gordon A. Shaw, Use of photon pressure in small mass and force calibration.....	166
PM_OR_008, Suren Vasilyan, Optical power measurements via photon momentum and its comparison with SI-traceable reference methods.....	168
PM_PO_004, Alexandra Artusio-Glimpse, Validation of a compact radiation pressure power meter at hundreds of watts.....	170
PM_PO_005, Jonathan Cripe, Design and calibration of a radiation-pressure based laser power meter and force sensor.....	172
EAO – Earth observation	
EAO_OR_009, Ling Li, A Simple Method of UV Stray Light Correction for Field Spectrometers in Ground Validation Sites.....	174
EAO_OR_012, Nigel Fox, Traceable Radiometry Underpinning Terrestrial- and Helio-Studies (TRUTHS): Enabling a Space-based Climate and Calibration Observatory - An ESA Earth Watch mission.....	176
EAO_OR_013, Steven van den Berg, CubeSat spectroradiometer calibration with a laser-based tunable radiance source.....	178
EAO_OR_0016, C. Monte, THE REDUCED BACKGROUND CALIBRATION FACILITY 2 FOR INFRARED DETECTORS, CAMERAS AND SOURCES.....	180
EAO_OR_017, Valeriy Gavrilov, VNIIOFI's developments in measurement assurance of Earth remote sensing.....	182
EAO_OR_018, M. Smid, Design and Development of a Tuneable Portable Radiation Source for In Situ Characterisation of Dobson Spectrometers.....	184
EAO_OR_019, Dmitri Lanevski, Gonireflectometric properties of the sand from RadCalNet Gobabeb test sit.....	186

EAO_OR_020, Max Reiniger, Experience with the radiometric traceability concept for the Network for Detection of Mesospheric Change (NDMC).....	188
EAO_OR_021, Steven W. Brown, Measurements of absolute, SI traceable lunar irradiance with the airborne Lunar Spectral Irradiance (air-LUSI) Mission.....	190
EAO_OR_022, Paul D Green, The STAR-CC-OGSE system for pre-flight sensor calibration.....	192
EAO_OR_025, Greg Kopp, The HyperSpectral Imager for Climate Science (HySICS) on the CLARREO Pathfinder Mission.....	194
EAO_PO_005, Andrei Burdakin, New fixed point on the basis of In-Bi eutectic system for perspective space borne standard low temperature fixed point blackbodies.....	196
EAO_PO_006, Steven W. Brown, Development of a laser-based satellite sensor illumination system to advance the capabilities of Earth observing systems.....	198
EAO_PO_008, Annett Barboutis, Recent developments in the VUV transfer source calibration based on calculable synchrotron radiation.....	200
EAO_PO_010, Jinwha Gene, Primary and working standards for spectral total reflectance in Mid-IR region in KRISS.....	202
EAO_PO_014, Emma Woolliams, The European metrology network for climate and ocean observation: a review of Earth observation needs for metrology.....	204
EAO_PO_023, Emma Woolliams, SI Traceability, Uncertainty Analysis and Comparison for RadCalNet.....	206
SSR – Solar / stellar radiometry	
SSR_OR_003, Natalia Kouremeti, Stray-Light Correction Methodology for the Precision Solar Spectroradiometer.....	208
SSR_OR_004, Natalia Kouremeti, Traceability of Solar and Lunar Direct Irradiances Measured with Precision Filter Radiometers.....	210
SSR_OR_005, Khaled Mahmoud, New Laser-Driven Light Source (LDLS)-based DSR measurement facility for calibration of reference solar cells.....	212
SSR_OR_006, Dave Harber, Compact total irradiance monitor flight demonstration...	214
SSR_OR_011, John T. Woodward, Spectroradiometric Calibration of Bright Stars, Vega and Sirius.....	216
SSR_PO_002, Gregor Hülsen, JTSIM-DARA Pointing Measurements.....	218
OPM – Optical properties of materials / components	
OPM_OR_001, Tatjana Quast, Polarization effects in diffuse reflection measurements at the transition between the UVA and VIS spectral range.....	220
OPM_OR_003, Alejandro Ferrero, Recommendation for finite intervals in BRDF measurements of glossy samples.....	221
OPM_OR_004, Pablo Santafé, A facility for measuring the BSSRDF.....	223

OPM_OR_006, Charles Stark, Improving multiphoton spectroscopy standards through the creation of an accurate, high-throughput spectrometer facility.....	225
OPM_OR_007, Wen-Chun Liu, Transmittance Haze Measurement by DIN 5036 Part 3.....	227
OPM_OR_009, Ma Yuxuan, Design and Evaluation of Extremely Low-Reflectance Measurement Device.....	229
OPM_OR_011, Heather J. Patrick, ROSI: the new NIST reference facility for UV-SWIR specular and diffuse reflectance calibrations.....	231
OPM_OR_012, M G White, Fresnel Reflection for Fibre-Coupled Cryogenic Radiometric Measurements.....	233
OPM_OR_013, Robin Ångerman, CCPR-K5.2019 Key Comparison of Spectral Diffuse Reflectance.....	235
OPM_OR_014, Dmitri Lanevski, Determining the shape of reflectance reference samples for curved surface reflectors.....	237
OPM_OR_016, Pierre Chavel, Advocating a statistical definition for the BRDF.....	239
OPM_OR_018, Hiroshi Shitomi, A novel optical diffuser with potentially higher spectral flatness in the near infrared region.....	241
OPM_OR_019, Dmitry Vorobiev, Measurement of far-ultraviolet transmission in hollow-core optical fibers.....	243
OPM_OR_020, Catherine C. Cooksey, Improvements to the Ultraviolet Measurement Capabilities of RTS.....	245
OPM_OR_022, Ellie Molloy, Effects of rotation errors on goniometric measurements.....	247
OPM_OR_025, Ramin Lalezari , Production and Characterization of Optics and Coatings with Extremely Low Losses and High Reflectivity.....	249
OPM_PO_002, Alexander Gottwald, Determining Optical Constants in the VUV Range: Combining Ellipsometry and Angle-Resolved Reflectometry.....	250
OPM_PO_005, Shau-Wei Hsu, On-Site Measurements of Reflection Characteristics of a Dry Asphalt Road.....	251
OPM_PO_008, Martin Dury, Temperature and Pressure Dependence of the Reflectivity of Vertically Aligned NanoTube Arrays.....	253
OPM_PO_015, Lutz Werner, Quantum Yield in Induced Junction Silicon Photodiodes at Wavelengths around 400 nm.....	255
OPM_PO_017, Jinhwa Gene, Systematic errors that depend on diffusivity and absorptance of sample in IEC method for absolute photoluminescence quantum efficiency.....	257
OPM_PO_021, Li-Lin Ta, Spectroscopic Analysis of Black-Carbon Emissions from Aviation Sources.....	259
OPM_PO_023, David C. Deisenroth, Simultaneous Time-Resolved Measurements of Reflected Laser Power, Emittance and Radiance Temperature in Laser Powder Bed Fusion.....	260

OPM_PO_024, Georgi T. Georgiev, CHARACTERIZATION OF BIDIRECTIONAL TRANSMISSIVE AND REFLECTIVE PROPERTIES OF BLACK SILICON.....	262
--	-----

OT – Other topics

OT_OR_001, Constantine Lukashin, ARCSTONE: Calibration of Lunar Spectral Reflectance from Space.....	264
OT_OR_002, Qing Sun, High Precision Measurement of Terahertz Frequency Based on Frequency Comb.....	266
OT_OR_003, M. Huriev, Reference lamp and directional radiation source with LED spectrum.....	268
OT_OR_005, R. Savage, Displacement fiducials for gravitational-wave detectors with sub-percent accuracy using laser power sensors calibrated at NIST.....	270
OT_OR_006, Markus Katona, System analysis of ILMD-based LID measurement systems using Monte Carlo simulation.....	272
OT_OR_008, Kanokwan Nontapot, Design and development of laser power transfer standard in telecommunication wavelengths under scientific collaboration MOU between NIMT and PTB.....	274
OT_OR_010, Yoshi Ohno, Global Interlaboratory Comparison of 41 Goniophotometers Measuring Solid- State Lighting Products.....	276
OT_OR_013, J. S. Kissel, Calibrating Gravitational Wave Interferometers: A Review with Astrophysical Implications.....	278
OT_PO_009, Jae-Keun Yoo, Performance Evaluation of a Mid-infrared Spectrometer for Remote Sensing Applications.....	282

Three-dimensional modelling of photodiode responsivity

Jarle Gran¹, Trinh Tran¹ and Timo Donsberg²

¹*Justervesenet, Kjeller, Norway*

²*Aalto University, Espoo, Finland*

Corresponding e-mail address: jag@justervesenet.no

The responsivity of silicon trap detectors commonly used as calibration standards today is to 99.5 % defined by the values of fundamental constants when accounting for calculable reflectance losses. With predictable quantum efficient detectors (PQEDs) the percentage contribution from fundamental constants to the responsivity increases to 99.99%. The simple structure of the PQEDs makes them well suited for three-dimensional modelling and opens a new path of traceability where the spectral response over a wide spectral range can be extracted from a model fit of current – voltage (I-V) characterisations done at one wavelength only.

INTRODUCTION

Through the silicon technology developments in the latter half of the 20th century two important benefits were achieved:

- I. “impurity free” manufacturing of silicon photodiodes and
- II. computational resources became widely available at a low cost.

The computational resources have continued to develop into this century and are expected to increasingly do so also in the future when quantum computers becomes available. However, the radiometric community has so far exploited the beneficial computational technology developments in the calibration of detectors and optical measurement systems to a limited extent.

Some measurement systems are not easily available once they are installed in a possibly remote and unattended location where the metrological quality relies on the initial pre-installed calibration. New experimental techniques capable of performing calibrations of integrated measurement systems in possibly remote operation will increase confidence and add value to the measurement data.

In the following sections a presentation of the principles and possible methods to exploit photodiodes as independent primary standard detectors is given.

BASIC PRINCIPLE

The responsivity of a silicon photodiode can be modelled as

$$R(\lambda) = \frac{e\lambda}{hc} (1 - \rho(\lambda)) \cdot (1 - \delta(\lambda)), \quad (1)$$

where the electron charge e , plancks constant h , speed of light in vacuum c and radiation wavelength in vacuum λ define the ideal responsivity term where one photon generates exactly one electron hole pair. An independent spectral response scale realisation with photodiodes is converted into a problem of quantifying the spectrally dependent reflectance $\rho(\lambda)$ and internal quantum deficiency (IQD) $\delta(\lambda)$. Reflectance losses can be predicted over a wide spectral range from well known material parameters and the oxide thickness or made arbitrarily small by mounting two or more photodiodes in a trap structure.

Different strategies and techniques have been used to independently predict the IQD. One method is to develop experimental techniques to measure and estimate the spectrally dependent losses as done in the past [1-4]. Another way is to construct photodiodes with negligible IQD (~100 ppm) as made with the predictable quantum efficient detector (PQED) [5-8] and use the photodiode trap structure as an ideal photodiode possibly corrected for IQD depending on needed measurement accuracy.

PREDICTABLE RESPONSE

The PQED photodiode is a simple structure consisting of a low-doped wafer with fixed charges in the oxide structure. Once a high quality PQED photodiode is manufactured its structure is defined. This means that when the photodiode is irradiated with a beam the charge carriers inside the photodiode will move in a predictable way depending primarily on the fixed charge density Q_f , surface recombination velocity SRV , bulk lifetime τ_B in addition to experimental parameters such as beam shape, wavelength and bias voltage. With new simulation tools it is possible to model the simple structure of the

PQED photodiodes and hence predict the expected responsivity of the photodiodes.

Measured relative change in photocurrent with bias voltage of a 7 – reflection p-type PQED at 4 different power levels (100 μW to 560 μW) is shown in Fig.1. The curves are normalised to the maximum value of the photocurrent in the experiment. The experiment is made at 488 nm with a gaussian like, slightly elliptical shaped beam with $1/e^2$ axis of 1223 μm by 806 μm .

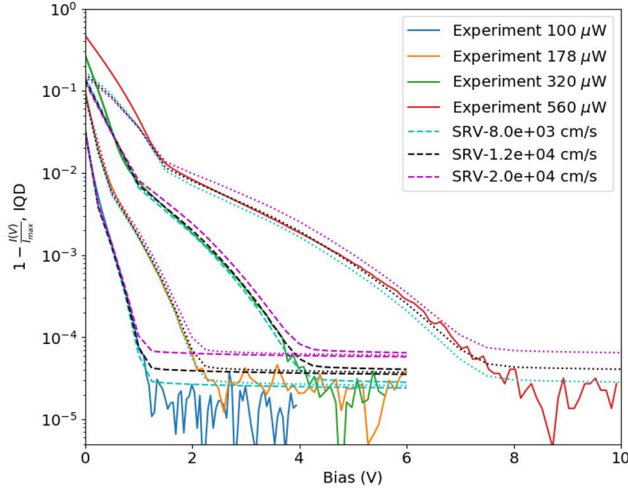


Figure 1. Measured relative change in photocurrent as a function of applied bias voltage plotted against its maximum value in solid lines. Simulated IQD with 3 different values of SRV is shown as dashed lines.

When simulating a PQED instead of a single photodiode several approximations has to be made. At 488 nm p-polarization, 87 % of the optical power is absorbed in the first photodiode, which is hit at a 45 degree angle of incidence. The projected beam profile is modified with the 45 degree angle of incidence to an elliptical beam with axis of 1367 μm by 1067 μm . By fitting various model parameters to the experimental curves an independent prediction of the responsivity can be achieved. In order to limit the number of fitting parameters as much as possible we assumed that experimental curves were defined by the absorbed power in the first photodiode (87 % of the total irradiance) and that the beam size is a flat top approximation of the elliptical beam size of 1367 μm by 1067 μm . It should be noted that the fitted IQD is very sensitive to beam size and charge carrier concentration.

As seen from Fig. 1 a surprisingly good fit is achieved with the approximations given above with the Cogenda Genius Device Simulator. By adjusting the fitting parameters to values enveloping the

experimental curves, uncertainty bands of the various parameters can be obtained as demonstrated with the SRV in Fig. 1.

Table 1. Fitted parameters used in the simulations

Fixed oxide charge, Q_f	$6.5 \cdot 10^{11} \text{ cm}^{-2}$
SRV	$1.2 \cdot 10^4 \text{ cm/s}$
Bulk lifetime τ_B	2.9 ms
Bulk doping	$1.4 \cdot 10^{12} \text{ cm}^{-3}$

DISCUSSION

Fitting 3D model parameters to simple I-V measurements of a PQED at multiple power levels is a promising primary technique to extract the photodiode parameters necessary to independently predict the PQED response. The first demonstration here must be validated and possibly improved, which is the task of the on-going European project 18SIB10 *chipS-CALe* (2019 – 2022) [9]. One of the benefits of the technique is the ability of independently predicting the IQD of a PQED over a wide spectral range from the measurement at one wavelength only.

ACKNOWLEDGMENT

This work has received funding from the EMPIR programme co-financed by the Participating States and from the European Union's Horizon 2020 research and innovation programme.

REFERENCES

1. E.F. Zalewski and J. Geist, Silicon photodiode absolute spectral response self-calibration, *Appl. Opt.*, 19, 1214-16, 1980.
2. J. Gran and A.S. Sudbø, Absolute calibration of silicon photodiodes by purely relative measurements, *Metrologia*, 41, 204-12, 2004.
3. J. Gran, Accurate and independent spectral response scale based on silicon trap detectors and spectrally invariant detectors, Dissertation for the Degree of Doctor Scientiarum, ISSN 1501-7710 No 434, University of Oslo, 2005.
4. M. U. Nordsveen et. al., Demonstration of dual-mode Si detector as a self-calibrating device at room temperature, *Opt. Express*, 25, 8459-69, 2017.
5. J. Geist, G. Brida and M.L. Rastello, Prospects for improving the accuracy of silicon photodiode self-calibration with custom cryogenic photodiodes, *Metrologia*, 40, S132-35, 2003.
6. M. Sildoja et.al., Predictable quantum efficient detector: I. Photodiodes and predicted responsivity, *Metrologia* 50, 385-94, 2013.
7. Muller et. al.: Predictable quantum efficient detector: II. Characterization and confirmed responsivity, *Metrologia*, 51, 197-202, 2013.
8. T. Dönsberg et. al.: Predictable quantum efficient detector based on n-type silicon photodiodes, *Metrologia*, 54, 821-36, 2017.
9. J. Gran, Publishable Summary for 18SIB10 *chipS-CALe*. Zenodo Jun.2019. <http://doi.org/10.5281/zenodo.354567>.

Novel perfect blackbody sheet having nano-precision surface microtextures for a planar standard radiator

Kuniaki Amemiya¹, Yuhei Shimizu¹, Hiroshi Koshikawa², Masatoshi Imbe¹,
Tetsuya Yamaki², and Hiroshi Shitomi¹

¹National Metrology Institute of Japan (NMIJ), AIST, Tsukuba, Japan,

²National Institutes for Quantum and Radiological Science and Technology (QST), Takasaki, Japan

Corresponding e-mail address: k.amemiya@aist.go.jp

We present a novel perfect blackbody sheet from an elastomer. Nano-precision microtextures embossed on a PDMS sheet exhibit an extremely low reflectance of ≤ 0.001 (an absorptance of ≥ 0.999) over the entire thermal infrared wavelengths (typically $8\ \mu\text{m} - 15\ \mu\text{m}$). In addition, this sheet maintains its high resilience to direct contact, tape-pulling, repeated bending, and scratching. Our tough planar blackbodies offer unprecedented applications including perfect standard radiators/absorbers, particularly with respect to thermal infrared detector/imager calibration.

INTRODUCTION

Low reflectance absorber materials have various applications including stray light suppression, light energy harvesting or management. Vertically aligned carbon nanotubes exhibit a very low reflectance of < 0.001 [1–3]. Despite their excellent optical performance, they are too fragile to be used in an open environment.

We have developed a novel perfect blackbody sheet from polydimethylsiloxane (PDMS) having a microtextured surface, fabricated via high-energy heavy-ion manufacturing and replica molding [4]. The PDMS blackbody sheet exhibits an extremely low reflectance of ≤ 0.001 across the entire thermal infrared wavelengths (typically $8\ \mu\text{m} - 15\ \mu\text{m}$). This blackbody sheet is highly durable for field use, whereas other porous nano-phonic absorbers are usually susceptible to mechanical contact.

This blackbody sheet is based on a micro-cavity strategy [4–6], in which incident light experiences multiple bounces, resulting in reduced reflectance. According to the finite differential time-domain (FDTD) simulation, the cavity aspect ratio (h/r , h : depth, r : radius) should be > 3 , and the cavity opening diameter should be on par with or greater than the longest wavelength of interest when targeting < 0.001 total hemispherical reflectance [4–6]. We used the high-energy heavy-ion beam to fabricate such high-

aspect-ratio micro-cavities on a substrate [4,5]. The microfabricated substrate can be used for replica molding, which more than compensates for the availability of a heavy ion beam facility. Therefore, we can scalably fabricate planar perfect blackbody replicas for the large-area application, including perfect standard radiators/absorbers, particularly with respect to thermal infrared detector/imager calibration.

EXPERIMENTS AND RESULTS

Fig. 1 shows the fabrication process of a perfect blackbody sheet from a microtextured elastomer. CR-39 plastic substrates were irradiated by swift heavy ion beam of Ne 200 MeV from a cyclotron accelerator of Takasaki Ion Accelerators for Advanced Radiation Application (TIARA) at ion exposure density of $\sim 10^6\ \text{cm}^{-2}$. After that, the irradiated substrates were etched in 6.4 N NaOH solution at $70\ ^\circ\text{C}$ for $\sim 10\ \text{h}$ to fabricate micro-cavities (etch pits) on their surface. Fig. 2 (left) shows the fabricated micro-cavity mold of a large area ($80\ \text{mm} \times 100\ \text{mm}$). By using this CR-39 master mold, we replicated large-area microtextured sheets from PDMS with carbon black filler. The resultant sheet is shown in Fig. 2 (right). The mid-infrared ($8\ \mu\text{m} - 15\ \mu\text{m}$ in wavelengths) hemispherical reflectance was extremely low (≤ 0.001), confirmed by FT-IR spectrometry with an integrating sphere (Fig. 3). Good reproducibility was confirmed as well.

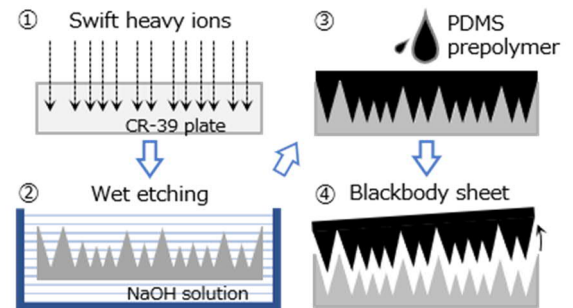


Figure 1. Fabrication process of a perfect blackbody sheet from a microtextured elastomer.

©AIST.

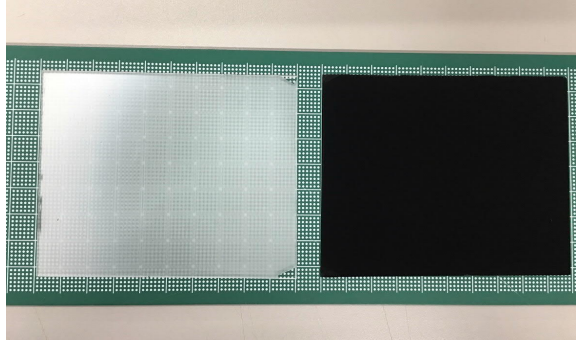


Figure 2 (left) Microtextured mold via swift heavy ion manufacturing, and (right) its replica from PDMS with carbon black filler.

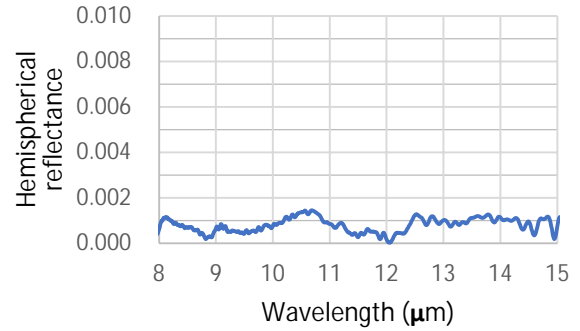


Figure 3 Spectral hemispherical reflectance of the PDMS blackbody sheet.

The appearance of the PDMS blackbody sheet seemed to be uniform over the entire area. The uniformity of the hemispherical reflectance is now under quantitative investigation.

Our PDMS blackbody sheets would serve as a planar standard radiator to calibrate thermography cameras. The advantage is that the emissivity correction can be extremely small ($\Delta\epsilon/\epsilon \sim 0.001$), equivalent to the temperature uncertainty $\Delta T < 50$ mK at room temperature (~ 23 °C). More practically, we can use the microtextured PDMS sheets as blackbody tapes, which would enable the accurate radiation thermometry of an arbitrary surface. It should be noted that the thermal conductivity of blackbody sheets is also a key issue for these precision applications.

SUMMARY

We have developed a novel perfect blackbody sheet from microtextured PDMS. They exhibit an extremely low reflectance of $\lesssim 0.001$ across the entire thermal infrared wavelengths while maintaining their high durability and uniformity. Our novel blackbody sheets would be suitable for a planar standard radiator to calibrate a thermal infrared detector/imager.

ACKNOWLEDGMENTS

This work was supported by JSPS KAKENHI Grant Number JP18K11940. The ion beam irradiation experiment was conducted at Takasaki Ion Accelerators for Advanced Radiation Application (TIARA) of National Institutes for Quantum and Radiological Science and Technology (QST), Takasaki, Japan, which was supported by the Inter-University Program for the Joint Use of JAEA/QST Facilities (proposal no. 19006).

REFERENCES

1. Z.-P. Yang, L. Ci, J. A. Bur, S.-Y. Lin, and P. M. Ajayan, "Experimental Observation of an Extremely Dark Material Made By a Low-Density Nanotube Array," *Nano Lett.* 8(2), 446–451, 2008.
2. J. Lehman, A. Sanders, L. Hanssen, B. Wilthan, J. Zeng, and C. Jensen, "Very Black Infrared Detector from Vertically Aligned Carbon Nanotubes and Electric-Field Poling of Lithium Tantalate," *Nano Lett.* 10(9), 3261–3266, 2010.
3. K. Mizuno, J. Ishii, H. Kishida, Y. Hayamizu, S. Yasuda, D. N. Futaba, M. Yumura, and K. Hata, "A black body absorber from vertically aligned single-walled carbon nanotubes," *Proc. Natl. Acad. Sci.* 106(15), 6044–6047, 2009.
4. K. Amemiya, H. Koshikawa, M. Imbe, T. Yamaki, and H. Shitomi, "Perfect blackbody sheets from nano-precision microtextured elastomers for light and thermal radiation management," *J. Mater. Chem. C* 7(18), 5418–5425, 2019.
5. K. Amemiya, H. Koshikawa, T. Yamaki, Y. Maekawa, H. Shitomi, T. Numata, K. Kinoshita, M. Tanabe, and D. Fukuda, "Fabrication of hard-coated optical absorbers with microstructured surfaces using etched ion tracks: Toward broadband ultra-low reflectance," *Nucl. Instruments Methods Phys. Res. Sect. B Beam Interact. with Mater. Atoms* 356–357, 154–159, 2015.
6. K. Amemiya, D. Fukuda, T. Numata, M. Tanabe, and Y. Ichino, "Comprehensive characterization of broadband ultralow reflectance of a porous nickel–phosphorus black surface by numerical simulation," *Appl. Opt.* 51(29), 6917–6925, 2012.

TSIS Solar Spectral Irradiance Measurements

Odele Coddington¹, Erik Richard¹, Peter Pilewskie^{1,2}, and Dave Harber¹

¹University of Colorado Boulder, Laboratory for Atmospheric and Space Physics, Boulder, USA, ²University of Colorado Boulder, Department of Atmospheric and Oceanic Science, Boulder, USA

Corresponding e-mail address: odele.coddington@lasp.colorado.edu

Solar irradiance is the dominant external source of energy to Earth's atmosphere. Knowledge of solar spectral irradiance (SSI) variability is critical for understanding Earth's atmospheric response to solar forcing. Since early 2018, the Spectral Irradiance Monitor (SIM) instrument on the Total and Spectral Solar Irradiance Sensor (TSIS) mission has observed smaller changes in SSI than previously measured and at unprecedented low uncertainty ($< 0.3\%$) over the majority of the spectrum, traceable to *Système Internationale* (SI) reference standards. TSIS-1 observations provide necessary validation for solar irradiance variability models that prescribe solar forcing at decadal to millennial timescales for climate models.

THE SPACE-BASED SSI RECORD

Space-based measurements of SSI at ultraviolet wavelengths began in 1978 [1] but it was not until the NASA Solar Radiation and Climate Experiment (SORCE) in 2003 that daily, calibrated measurements were made over nearly the entire spectrum, including the visible and near-infrared. The SORCE SSI measurements were crucial in evaluating and improving models on solar rotation (~ 27 days) timescales at most ultraviolet and visible wavelengths, but lacked the stability to quantify the quasi 11-year solar cycle impacts at all wavelengths [2]. Building a long-term SSI climate data record requires continuous instrument calibration in which measurement uncertainties are characterized, and maintained, against SI standards.

THE TSIS SIM INSTRUMENT

The TSIS-1 SIM, covering 200-2400 nm or approximately 96% of the total solar irradiance (TSI), is designed, characterized, calibrated and validated to meet the measurement requirements to quantify and track SSI variability for the climate record [3]. TSIS SIM achieves and maintains this detector-based calibration with an electrical substitution radiometer (ESR). The ESR radiometry is established pre-launch

to better than 0.3% across most of the spectrum (Fig. 1) against an absolute cryogenic radiometer traceable to the NIST Primary Optical Watt Radiometer [4]. The ESR calibration is maintained over time by

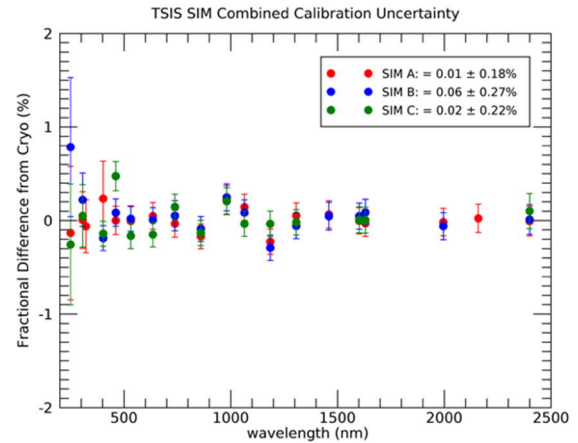


Figure 1. The final pre-launch spectral calibration and $k=1$ uncertainties of all three TSIS SIM channels against the absolute cryogenic radiometer irradiance values.

correcting on-orbit degradation using three independent SIM channels that are operated at different solar exposure rates. In early 2019, the Compact SIM (CSIM) technology demonstration mission [5] under the NASA In-Space Validation of Earth Science Technologies program was launched and demonstrated on-orbit agreement to TSIS-1 SIM to 1% (Fig. 2).

A TSIS SIM REFERENCE SPECTRUM

Solar reference spectra are utilized for varying purposes in atmospheric science and climate model applications. Solar spectra are used to convert measured satellite reflectances to radiances and as top of atmosphere boundary conditions in radiative transfer models for remote sensing applications and renewable energy research. Additionally, some instruments use the Sun for monitoring the stability of their radiometric calibration. Even instruments that assess the stability of their radiometric calibration relative to the Moon rely on a solar reference spectrum.

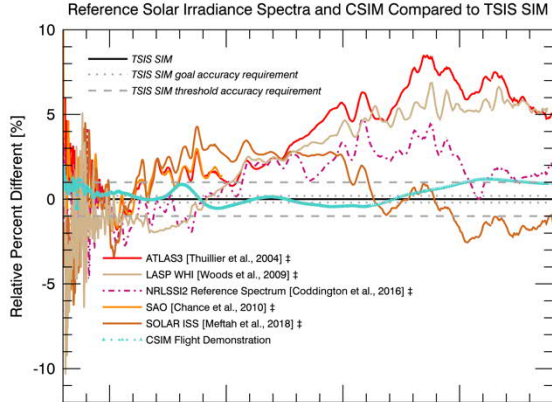


Figure 2. The relative % difference between TSIS SIM and several well-established SSI reference spectra as well as the CSIM flight demonstration mission.

The literature provides a variety of solar reference spectra for these applications [6-10]. A direct comparison of these spectra to TSIS SIM shows differences of as much as 10% in the ultraviolet and up to 8% in the near-infrared (Fig. 2), motivating the need for a new solar reference at the TSIS SIM scale. We are in the progress of developing a new reference spectrum at native TSIS-1 SIM resolution in addition to a higher resolution spectrum using independent, high-resolution solar line data.

DAILY SOLAR VARIABILITY

Even though the Sun is currently in a minimum-activity state, there was a small sunspot occurrence in April and May 2019. The improvements in measurement precision for TSIS-1 SIM relative to concurrent measurements by SORCE SIM are

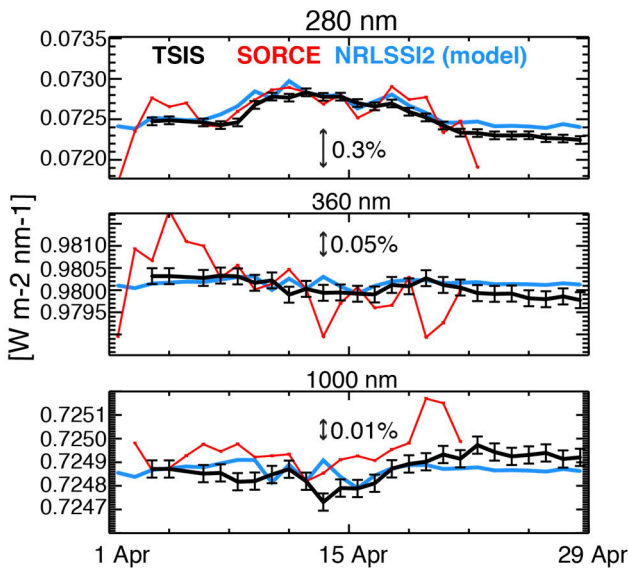


Figure 3. Short-term SSI variability during a sunspot passage in April, 2019 as measured by TSIS SIM (black) and SORCE (red) and estimated by NRLSSI2 (blue).

evident in the passage of this sunspot (Fig. 3). TSIS-1 SIM is resolving 0.01% solar variability at near-infrared wavelengths.

The TSIS-1 SIM precision is helping to improve and validate solar variability models such as version 2 of the Naval Research Laboratory (NRL) SSI model (NRLSSI2) [8]. This model assumes the primary sources of solar irradiance variability are bright faculae and dark sunspots on the Sun's surface and estimates the wavelength-dependent irradiance modulations from multiple linear regression of proxy indices of sunspots and faculae with SORCE SSI observations on short time scales. Development has already begun on a new version of this model to adopt TSIS-1 SIM observations for the absolute scale and in the fidelity at which solar activity is correlated with irradiance, especially between 300-400 nm and longward of 900 nm [11].

REFERENCES

1. B.M. Schlesinger and R. P. Cebula (1992). Solar variation 1979-1987 estimated from an empirical model for changes with time in the sensitivity of the solar backscatter ultraviolet instrument, JGR, 97.
2. Coddington, O., et al. (2019). Solar Irradiance variability: Comparisons of models and measurements. *Earth and Space Science*, 6.
3. NOAA (National Oceanic and Atmospheric Administration), Total and Spectral Solar Irradiance Sensor (TSIS) Requirements Document, Silver Springs, MD, Version 1, 31 Mar. 2010.
4. Richard, E., et al. (2020), Spectral Solar Irradiance, Chapter 7.2, in SI-Traceable Space-based Climate Observing System Workshop Report, CEOS/GSICS Workshop, NPL, London, UK, 9-11 Sept. 2019.
5. Richard, E. et al., 2019, Compact spectral irradiance monitor flight demonstration mission, *Proc. SPIE 11131, CubeSats and SmallSats for Remote Sensing III*, 1113105.
6. Thuillier, G., et al. (2004). Solar irradiance reference spectra for two solar active levels. *Solar Variability and Climate Change*, 34(2), 256-261.
7. Woods, T. N., et al. (2009). Solar Irradiance Reference Spectra (SIRS) for the 2008 Whole Heliosphere Interval (WHI). *Geophysical Research Letters*, 36(1).
8. Coddington, O., et al. (2016). A Solar Irradiance Climate Data Record. *Bulletin of the American Meteorological Society*, 97(7), 1265-1282.
9. Chance, K., & Kurucz, R. L. (2010). An improved high-resolution solar reference spectrum for earth's atmosphere measurements in the ultraviolet, visible, and near infrared. *Journal of Quantitative Spectroscopy & Radiative Transfer*, 111(9), 1289-1295.
10. Meftah, M., et al. (2018). SOLAR-ISS: A new reference spectrum based on SOLAR/SOLSPEC observations. *Astronomy & Astrophysics*, 611.
11. Lean, J. et al. (2020). Solar Irradiance Variability: Modeling the Measurements, *E&SS*, in review.

Planar Absolute Radiometer Operating at Room Temperature for Replacing NIST's Legacy Laser Calorimeter

Anna K. Vaskuri¹, Michelle S. Stephens¹, Nathan A. Tomlin¹, Matthew T. Spidell¹, Christopher S. Yung¹,
Andrew J. Walowitz¹, Cameron Straatsma², David Harber², and John H. Lehman¹

¹*Applied Physics Division, National Institute of Standards and Technology, Boulder, CO, USA*

²*Laboratory for Atmospheric and Space Physics, University of Colorado, Boulder, CO, USA*

Corresponding e-mail address: anna.vaskuri@nist.gov

We have developed a Planar Absolute Radiometer for Room Temperature (PARRoT) that will replace the legacy C-series calorimeter in free-space continuous-wave laser power measurements at the National Institute of Standards and Technology (NIST). PARRoT measures laser powers between 100 μ W and 250 mW from ultraviolet to near-infrared using the electrical power substitution method with active background compensation. Its expanded uncertainty ($k = 2$) reaches 0.13% at laser powers >2 mW. PARRoT's response was compared against a transfer standard silicon trap detector and against the C-series calorimeter. On average these comparisons agreed to better than 0.008% and 0.05%, respectively.

INTRODUCTION

After first lasers became commercially available in the 1960's, West *et al.* [1] at the National Institute of Standards and Technology (NIST) started the development of laser calorimeters to meet the needs of laser-power meter calibrations. The C4-series calorimeters were completed in 1974 [2] and they have been used for calibrating customer detectors at NIST for the past 46 years.

The C-series calorimeter performs free-space laser power measurements with an expanded uncertainty ($k = 2$) of 0.84%, with one measurement cycle taking approximately 15 minutes. Recently, the Laser Interferometer Gravitational-wave Observatory (LIGO) [3, 4] has indicated need for an order of magnitude lower calibration uncertainty at a few 100 mW range.

In this work, we introduce a Planar Absolute Radiometer for Room Temperature (PARRoT) [5], shown in Fig. 1, that will replace the legacy C-series calorimeter. PARRoT is more robust, twice as fast, and it has over a factor of 6 lower measurement uncertainty compared to the C-calorimeter.

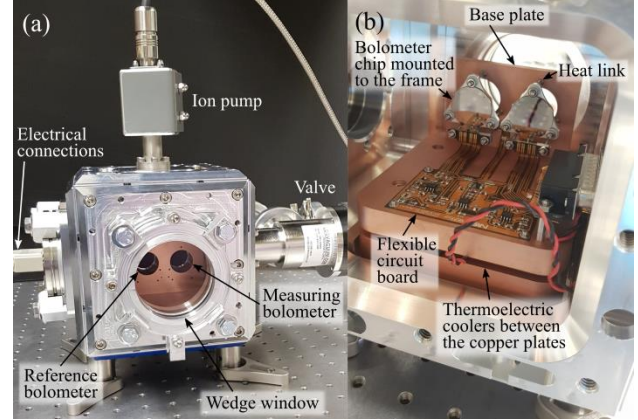


Figure 1. Front side of the radiometer developed (a) and view inside the vacuum chamber (b).

DESIGN OF THE RADIOMETER

PARRoT is based on 20 mm diameter vertically aligned carbon nanotube (VACNT) absorber [6] grown on a microfabricated silicon bolometer chip. PARRoT is operated by closed-loop electrical power substitution method implemented using a field-programmable gate array (FPGA) board with custom electronics. PARRoT's bolometer chip geometry has been optimized by thermal modeling so that its electro-optical inequivalence is less than 0.01% when a laser beam is centered on the absorber [7].

Figure 1 shows photographs of PARRoT. The copper base plate is temperature-stabilized to 295 K with thermoelectric coolers. Two bolometer chips are mounted to aluminum frames that are connected to the base plate via stainless steel cylinders. The bolometers are operated in a vacuum chamber to avoid convective cooling. Laser beam access is provided by an uncoated fused silica window with a wedge angle of 0.5° and diameter of 76.2 mm so that PARRoT can measure across broad spectral range from ultraviolet to near-infrared. Since the laser beam is aligned nearly perpendicular to the VACNT absorber and the vacuum window, PARRoT's response is independent of light polarization.

PARRoT has two identical bolometer chips to compensate radiative coupling to changing ambient environment that reduces drifts in its response. The reference bolometer chip is heated to 325 K by constant electrical power of 290 mW and the measuring bolometer chip's heater is operated in closed loop. When a laser beam hits the measuring bolometer's absorber, the electrical power is reduced to maintain the temperature. Absolute optical power is obtained from the electrical power difference by correcting VACNT absorptance and transmittance of the wedge window that depend on the laser wavelength, correcting the electro-optical inequivalence obtained by thermal modeling, and correcting the parasitic resistance of the wirebonds that electrically connect the heater spirals to the flexible circuit board in Fig. 1.

COMPARISONS AGAINST EXISTING DETECTOR STANDARDS

We compared PARRoT's response against a transfer standard silicon trap detector traceable to NIST's Laser-Optimized Cryogenic Radiometer (LOCR) at a laser wavelength of 633 nm and the C-series calorimeter at laser wavelengths of 405 nm, 532 nm, and 1064 nm. Figure 2 shows that on average PARRoT's laser power measurements agree with the transfer standard trap detector better than 0.008% and with the C-series calorimeter better than 0.05% [5]. These discrepancies are well within PARRoT's expanded measurement uncertainty. At laser powers of a few 100 μ W, PARRoT's expanded uncertainty is limited by the measurement repeatability. At laser powers >2 mW PARRoT's expanded uncertainty ($k = 2$) reaches 0.13% and is limited by an uncertainty of the window transmittance correction ($\pm 0.1\%$ rectangular distribution).

ACKNOWLEDGMENTS

Jenny and Antti Wihuri Foundation, Finland is acknowledged for financially supporting Dr. Vaskuri's postdoctoral research at NIST.

REFERENCES

1. E. D. West, W. E. Case, A. L. Rasmussen, and L. B. Schmidt, "A Reference Calorimeter for Laser Energy Measurements," *J. Res. Natl. Bur. Stand. (U. S.)* **76A**, 13-26 (1972).
2. E. D. West and W. E. Case, "Current Status of NBS Low-Power Laser Energy Measurement," *IEEE Trans. Instrum. Meas.* **23**, 422-425 (1974).

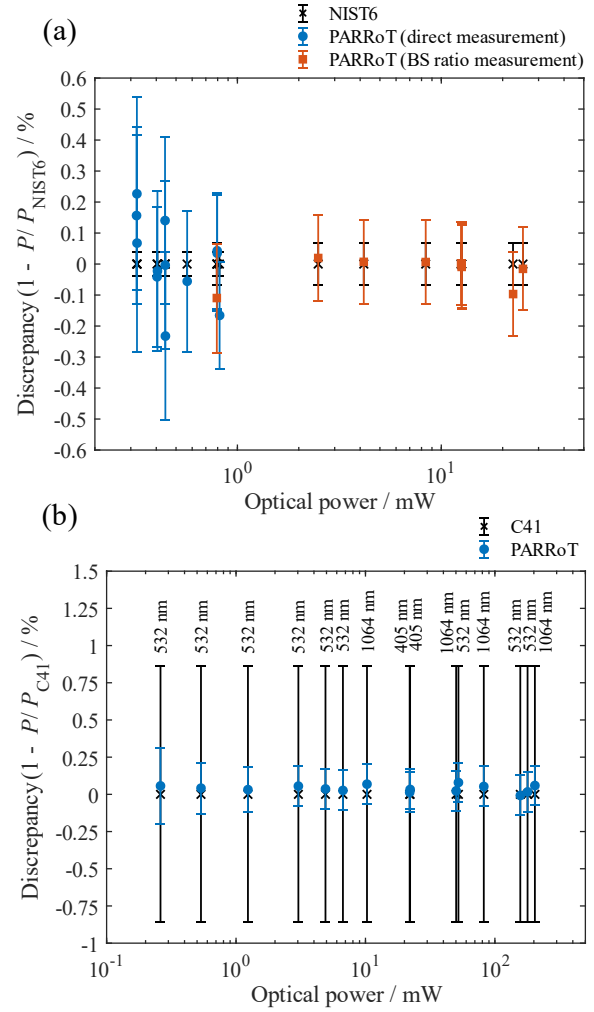


Figure 2. (a) Discrepancies in the optical power measured with PARRoT and the transfer standard silicon trap detector (NIST6). Beamsplitter (BS) ratio measurement was used at laser powers >1 mW. (b) Discrepancies in the optical power measured with PARRoT and the C-series calorimeter (C41). Uncertainty bars depict an expanded uncertainty ($k = 2$).

3. S. Karki, D. Tuyenbayev, S. Kandhasamy *et al.*, "The Advanced LIGO photon calibrators," *Rev. Sci. Instrum.* **87**, 114503 1-12 (2016).
4. D. Bhattacharjee, Y. Lecoecueche, S. Karki *et al.*, "Fiducial displacements with improved accuracy for the global network of gravitational wave detectors," *Classical Quant. Grav.* **38**, 015009 1-22 (2021).
5. A. K. Vaskuri, M. S. Stephens, N. A. Tomlin *et al.*, "High-accuracy room temperature planar absolute radiometer based on vertically aligned carbon nanotubes," (in preparation).
6. J. Lehman, C. Yung, N. Tomlin, D. Conklin, and M. Stephens, "Carbon nanotube-based black coatings," *Appl. Phys. Rev.* **5**, 011103 1-17 (2018).
7. A. Vaskuri, M. S. Stephens, N. A. Tomlin *et al.*, "Microfabricated bolometer based on a vertically aligned carbon nanotube absorber," *Proc. SPIE* **11269**, 112690L 1-12 (2020).

Optical power scale realization using the predictable quantum efficient detector

Kinza Maham¹, Petri Kärhä¹, Farshid Manoocheri¹, and Erkki Ikonen^{1,2}

¹*Metrology Research Institute, Aalto University, Finland,* ²*VTT MIKES, Finland*

Corresponding e-mail address: kinza.maham@aalto.fi

We report realization of an optical power scale based on a predictable quantum efficient detector (PQED) over the spectral range of 400 nm – 800 nm. The PQED is characterized and used to measure the responsivities of a trap detector at four distinct laser lines, with an expanded uncertainty of 0.05%. The measurement results support the concept that the PQED can be used as a primary standard of optical power. We present a comparison of responsivities calibrated against the PQED at Aalto and the cryogenic radiometer at RI.SE, Sweden.

INTRODUCTION

The PQED provides traceability of optical power to SI units [1,2]. Such traceability route is tempting, because the operation of PQEDs is as easy as that of other silicon trap detectors. In most national metrology institutes, the optical power is measured with an absolute cryogenic radiometer (ACR) [3]. These devices can achieve an uncertainty below 0.01%. However, they are expensive to obtain and maintain as they are operated at cryogenic temperatures. Aalto has taken into use a compact PQED [2] as a primary standard of optical power over the spectral range of 400 nm – 800 nm. The PQED consists of high-quality photodiodes with minimal losses for internal quantum deficiency, arranged in a wedged trap configuration to minimize the effects of reflectance correction [4,5]. PQEDs are compact in size and operate at room temperature. They show excellent stability and repeatability of $\sim 0.0016\%$ [2].

In this work, we present an optical power scale realization based on a PQED. A silicon trap detector is calibrated against the new scale and compared to calibration at RI.SE. RI.SE uses an ACR as a primary standard of optical power measurements.

MEASUREMENT PROCEDURE

The new power scale is based on a PQED and a multi-wavelength setup for comparing detectors developed at Aalto [6]. Figure 1 presents a simplified drawing of the setup. Various lasers have been installed in the setup. Lasers available include KrAr⁺, Ar⁺, HeCd,

red and green HeNe, and a couple of diode lasers. The laser beam to be used is selected with a computer-driven mirror on a rail. Unused beams are terminated in beam dumps. The measurement beam is cleaned with a spatial filter based on two off-axis parabolic mirrors (OAP), and a laser power controller (LPC) stabilizes the beam intensity. The PQED and the trap detectors to be calibrated are mounted on a precise XY translation stage, and their photocurrents are recorded with a current-to-voltage converter (CVC) and a digital voltmeter (DVM). A multiplexer (MUX) is used to read various detectors with one set of electronics. The whole setup is computer controlled.

The optical power P is calculated from the

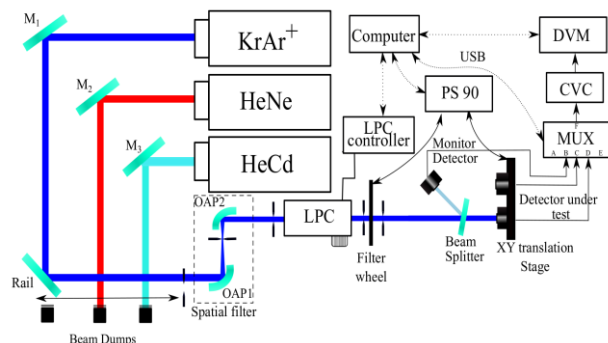


Figure 1. Multi-wavelength setup used for the optical power measurement with the PQED [6]. For abbreviations, see text.

photocurrent I_p of the PQED as

$$P = \frac{l_p \hbar c}{e \lambda [1 - \rho(\lambda)] [1 - \delta(\lambda)]} \quad , \quad (1)$$

where λ is the wavelength of the laser used, $\rho(\lambda)$ is the reflectance of the PQED, $\alpha(\lambda)$ is the internal quantum deficiency of the photodiodes, estimated to be approximately 0.0008% [4], e is the elementary charge, h is Planck's constant and c is the speed of light in the same medium as the wavelength – air or vacuum. The specular reflectances of the PQED are measured at the respective wavelengths using the method described in [2,4].

The PQED is used once a year to calibrate Hamamatsu silicon trap detectors with nitrogen flow serving as transfer standards. The nitrogen flow of

0.5 l/min through the trap detectors reduces the contamination of the photodiodes due to dust.

UNCERTAINTY BUDGET

The uncertainty budget of the new optical power scale is presented in Table 1.

Table 1. Uncertainty budget of spectral responsivity measurement of a trap detector against PQED.

Component	Standard uncertainty, %			
	458 nm	515 nm	543 nm	633 nm
Responsivity of PQED	0.011	0.011	0.011	0.011
Repeatability of results	0.007	0.003	0.003	0.008
Calibration of DVM	0.001			
Calibration of CVC	0.003			
Alignment of detectors	0.001			
Trap's spatial nonuniformity	0.023			
Combined standard uncertainty	0.026	0.026	0.026	0.027
Expanded uncertainty ($k = 2$)	0.053	0.052	0.052	0.054

The responsivity measurements have an expanded uncertainty of 0.052% – 0.054% depending on the wavelength. The highest component of uncertainty is the spatial nonuniformity of the trap detector, 0.023%. Repeatability is the standard deviation of 10 averaged measurements. The error in alignment of detectors was obtained by tilting the detectors by a few degrees and calculating the change in the signal due to a change of 0.5° in the angle.

COMPARISON MEASUREMENT

One silicon trap detector was measured both at RI.SE, Sweden, and at Aalto using the new power scale. Table 2 shows the responsivities measured at the wavelengths of 458 nm, 515 nm, 543 nm, and 633 nm, along with the difference between the two responsivities. The expanded uncertainties presented

in the table are the quadratic sums of the uncertainties of RI.SE and Aalto. The results are only partially in agreement within the uncertainties.

Table 2. Comparison of spectral responsivities of a trap detector measured at Aalto and at RI.SE.

Wave-length / nm	Responsivity A/W		Difference %	Expanded uncertainty ($k = 2$)
	Aalto	RI.SE		
458	0.36446	0.36478	-0.088%	0.080%
515	0.41207	0.41204	0.007 %	0.082%
543	0.43553	0.43555	-0.005 %	0.086%
633	0.50793	0.50798	-0.010 %	0.077%

CONCLUSIONS

Aalto has taken into use a new optical power scale based on the PQED. The PQED is used annually to measure the responsivities of Hamamatsu silicon trap detectors with nitrogen flow working as transfer standards. Comparison with RI.SE using a silicon trap detector showed an agreement between the two scales within the uncertainties of 0.077% – 0.086% for the wavelength range 515 nm – 633 nm. The results indicate the usability of the PQED as a primary standard of optical power.

REFERENCES

1. J. Zwinkels, S. Sperling, T. Goodman, J. Campos Acosta, Y. Ohno, M. L. Rastello, M. Stock, and E. R. Woolliams, Mise en pratique for the definition of the candela and associated derived units for photometric and radiometric quantities in the International System of Units (SI), Metrologia, 53, 1-14, 2016.
2. T. Dönsberg, M. Sildoja, F. Manoocheri, M. Merimaa, L. Petroff, and E. Ikonen, A primary standard of optical power based on induced-junction silicon photodiodes operated at room temperature, Metrologia, 51, 197-202, 2014.
3. J. E. Martin, N. P. Fox, and P. J. Key, A cryogenic radiometer for absolute radiometric measurements, Metrologia, 21, 147-155, 1985.
4. M. Sildoja et al, Predictable quantum efficient detector: I. Photodiodes and predicted responsivity, Metrologia, 50, 385-394, 2013.
5. I. Müller et al, Predictable quantum efficient detector: II. Characterization and confirmed responsivity, Metrologia, 50, 395-401, 2013.
6. A. Vaskuri, Multi-wavelength setup based on lasers for characterizing optical detectors and materials, M.Sc. Thesis, Aalto University, 2014.

Acknowledgement: The authors are grateful to Stefan Källberg of RI.SE, Sweden, for measuring the trap responsivities with ACR.

High efficiency five-element trap detector with low optical losses

Meelis-Mait Sildoja^{1,2*,3*}, Philipp Schneider¹ and Saulius Nevas¹

¹Physikalisch-Technische Bundesanstalt (PTB), Braunschweig and Berlin, Germany, ²Metrosert, Tallinn, Estonia,

³National Institute of Chemical Physics and Biophysics (KBFI), Tallinn, Estonia

Corresponding e-mail address: meelis-mait.sildoja@metrosert.ee

We have constructed a five-element reflectance trap detector consisting of commercial n-on-p type 10 x 10 mm UVG100 photodiodes. The response uniformity of the trap at visible wavelengths is mostly at a level of ± 100 parts per million (ppm) whereas its estimated reflection losses are below 1 ppm throughout most of the visible spectral range. We have measured the linearity of the trap detector as well as its spectral responsivity. The properties of the trap suggest it could be used as a reference detector in photometric and radiometric calibrations.

INTRODUCTION

Most of the photodiode-based reference detectors require calibrations traceable either to a Cryogenic Radiometer (CR) or a Predictable Quantum Efficient Detector (PQED) [1-3]. The need for regular calibrations of conventional silicon detectors based on p-n junction photodiodes (e.g. S1337 by Hamamatsu) comes, among other causes, from their instability caused by short-wavelength radiation and from moisture penetration [4]. UVG-series silicon photodiodes by Opto Diode Corporation are claimed to have no surface recombination and 100 % internal quantum efficiency in the spectral range from 330 nm to 660 nm [5]. We have constructed a trap detector based on these photodiodes to study its properties in terms of possible usage in photometric and radiometric applications. Such a trap could be applied as an absolute detector for calibration of photometers despite the reduced quantum efficiency above 660 nm, i.e. at the tail of the $V(\lambda)$ curve.

DESIGN OF THE DETECTOR

The trap detector is constructed from five selected UVG100-type photodiodes. The first four are aligned under 45° and the last one at 0° angles relative to the incident beam (see figure 1). In such a configuration, the beam encounters 9 reflections before exiting the trap and theoretically has no polarization dependence.

The angular alignment of the last photodiode can be fine adjusted to match the paths of the leaving and incoming beams. The total beam path in the trap is approximately 95 mm. The field of view is estimated to be ± 2 degrees for a 3 mm diameter beam. Also, the holder of the photodiodes can be angularly adjusted relative to the front plane of the trap housing. This allows a good alignment of the trap relative to its housing with an installed radiometric aperture. The photodiodes are connected in parallel and operated without bias voltage.

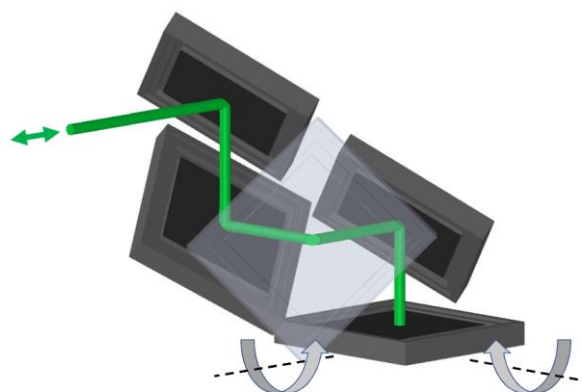


Figure 1. Beam path in the trap detector with five photodiodes. The last photodiode can be fine adjusted to match the incoming and leaving beams.

CHARACTERIZATION

Uniformity

The non-uniformity of the trap was measured at the wavelengths of 490 nm, 680 nm, 750 nm and 800 nm. As the photodiodes are tailored for the UV range, the uniformity is expected to be better at shorter wavelengths. Figure 2 shows the responsivity uniformity at 490 nm. The measured deviations are within ± 75 ppm in the central region with a diameter of 6 mm. At 680 nm, 750 nm and 800 nm the non-uniformity throughout the same central region stays within ± 100 ppm, ± 100 ppm and ± 250 ppm, respectively.

*current institution

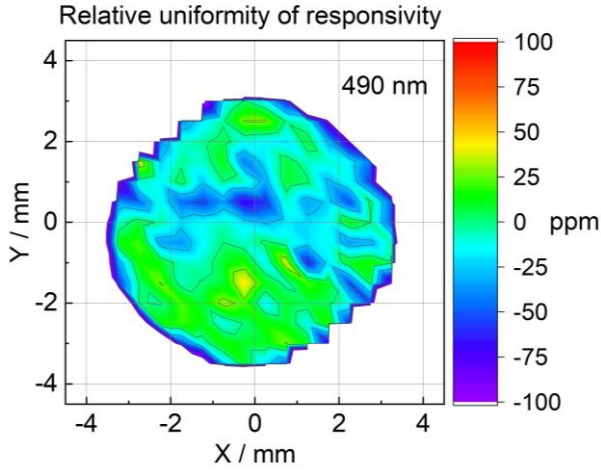


Figure 2. Relative spatial deviation of the responsivity of the trap detector at 490 nm.

Reflectance

Reflectance losses of the trap detector (figure 3) were estimated based on the single-photodiode reflectance curve provided by the manufacturer [5]. The estimated reflectance of the trap has a sharp decline from 360 nm to 500 nm having a change of reflectance from about 3500 ppm down to 0.005 ppm. We confirmed a few percent lower reflectance of a single photodiode at selected wavelengths of 532 nm, 680 nm, 740 nm, 780 and 800 nm. At 490 nm, the measured reflectance was higher than reported by the manufacturer. Despite the small discrepancies, the reflection losses of the trap were confirmed to be below 1 ppm throughout most of the spectral range of interest.

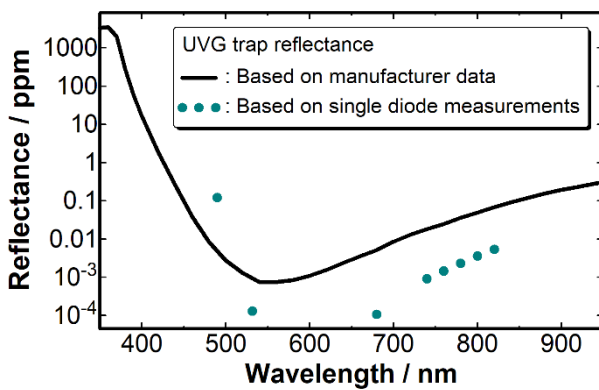


Figure 3. Estimated reflectance of the 5-element trap detector based on the single photodiode reflectance provided by the manufacturer (line). The dots show the values based on our measurements on a single photodiode.

Nonlinearity

The nonlinearity of a single UVG100 photodiode and of the trap detector was measured at 490 nm and at

680 nm, respectively. The beam diameter was about 1 mm FWHM at both wavelengths. The photocurrents were recorded at three different power levels and were compared with the photocurrents of a well-characterised reference trap detector. Up to the level of 100 μ A, limited by the dynamic range of the current-to-voltage converter, both the single photodiode and the trap detector showed no nonlinear behaviour. We tested the photodiodes with -5 V bias as well. No changes were observed between biased and non-biased measurements.

Responsivity

We have carried out preliminary responsivity measurements relative to two calibrated trap detectors at wavelengths of 405 nm, 487 nm, 528 nm and 680 nm. These measurements confirmed a high quantum efficiency of the UVG100-based trap detector within the uncertainties of the measurements. More precise measurements throughout the whole spectral range of interest are planned. The results will be shown at the conference.

CONCLUSIONS

We have constructed a 5-element low-loss trap detector based on commercially available n-on-p photodiodes that are claimed to have a superior long-term stability in responsivity and close to 100% internal quantum efficiency over a broad wavelength range in the visible region. Preliminary tests of spatial response uniformity, linearity and optical losses show an excellent behaviour. The detector is considered as a cheaper and simpler alternative to the custom-made PQED detectors for use in photometric and radiometric applications.

REFERENCES

1. M. Sildoja et al, Predictable quantum efficient detector: I. Photodiodes and predicted responsivity, *Metrologia*, 50, 385–394, 2013.
2. Müller et al, Predictable quantum efficient detector: II. Characterization and confirmed responsivity, *Metrologia*, 50, 395–401, 2013.
3. T. Dönsberg, M. Sildoja, F. Manoocheri, M. Merimaa, L. Petroff and E. Ikonen, A primary standard of optical power based on induced-junction silicon photodiodes operated at room temperature, *Metrologia*, 51, 197–202, 2014.
4. R. Korde and J. Geist, Quantum efficiency stability of silicon photodiodes, *Applied Optics*, 26, 5284–5290, Dec. 1987.
5. <https://optodiode.com/pdf/2. IRD Silicon Photodiodes - UVG Series.pdf>

Calorimetric Measurements for Conversion Efficiency of Optical Devices

Terubumi Saito¹, Takumi Kawana¹, Takumi Naganuma¹

¹*Tohoku Institute of Technology, Sendai, Japan*

Corresponding e-mail address: terubumi.saito@tohotech.ac.jp

Conversion efficiencies of optical devices, both sources and receivers have been measured based on a calorimetric method. Radiant power output of a source can be evaluated by subtracting a heat power from the applied electrical power while radiant power input of a receiver can be evaluated by adding a heat power to the generated electrical power. The technique was validated firstly in the solar cell internal conversion efficiency measurements in a manual operation. To automatize the operation, a negative feedback control circuit to maintain constant temperature by adjusting the electrical power to the heater has been developed and proved to work successfully.

INTRODUCTION

Optoelectronic devices to convert between electrical power and optical power such as photovoltaic cells, laser diodes (LDs), light emitting diodes (LEDs) etc. are widely used in many fields. Among the characteristics of the optoelectronic devices, power conversion efficiency is essentially important.

The external power conversion efficiency is defined as a ratio of output power to the input power. More specifically in the case of solar cell/module, it is the ratio of the electrical power generated to the radiant power incident to the solar cell/module under the defined conditions. While the evaluation of the electrical power can be conducted very easily, the evaluation of the radiant power are usually more complicated and difficult especially when the radiation is spectrally broad as in the case of solar cells. The calorimetric method is advantageous since it enable us to directly determine the internal conversion efficiency of solar cells.

The technique to calorimetrically determine the internal quantum efficiency was developed, for the first time, by T. Inoue et al. for photodiodes receiving a laser beam¹. Inoue et al. applied the similar technique also to measure total radiant power of a laser diode². Our approach is unique in that constant temperature operation, which is required to substitute heat with electrical power, is achieved only by using self-heating of a temperature sensor without an additional heater. In addition, we applied the

calorimetric method to solar cells to determine their internal conversion efficiencies, for the first time³.

In this paper, we focus on the external conversion efficiency measurements of LEDs by using a constant temperature circuit with a platinum resistance thermometer working simultaneously as a heater to replace heat with electrical power.

PRINCIPLE OF OPERATION

The radiant power absorbed (for a receiver) or generated (for a source) can be determined by a calorimetric method in which the heat absorbed or generated in the device is substituted by the electrical power applied to a heater attached to the device.

For receivers such as solar cells, the applied electrical power is adjusted in the dark condition so that the device temperature becomes equal to the one in an illuminated condition. We can assume that the substituted electrical power is equal to the thermal power, or the absorbed radiant power (when an open- or short-circuit condition).

For sources such as LEDs, the electrical power is applied to the heater when the LED is off. When the LED is lit, the electrical power applied to the heater is decreased and adjusted so that the device temperature keeps the same temperature as the one in the dark condition. We can assume that the difference in the electrical power is equal to the thermal power generated when the LED is on and that the emitted radiant power can be given by the input electrical power applied to the LED minus the thermal power difference.

EXPERIMENTAL

Figure 1 shows a test specimen of RGB type LED (OptoSupply OSTCXBCBC1E) attached with a platinum resistance thermometer, Pt100. We have designed and fabricated a negative feedback control circuit to realize automatic temperature control using the Pt100 not only as a temperature sensor but also as an electric heater. The negative feedback control circuit works to automatically adjust the applied electrical power to the Pt100 to maintain a constant temperature, or a constant resistance. The constant

temperature operation has been confirmed to work successfully not only for PTC (positive temperature coefficient) but also for NTC (negative temperature coefficient) sensors.

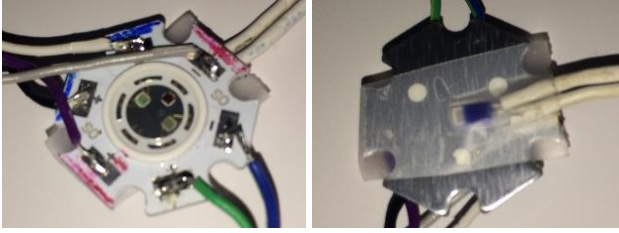


Figure 1. Left: Photograph of front side of RGB type LED. Right: Platinum resistance thermometer, Pt100 attached to the backside of the LED.

RESULTS

As an example of the measurements, Figure 2 shows a result for a red (dominant wavelength of 624 nm) LED. Radiant power of the LED is independently measured by a calibrated silicon photodiode (Hamamatsu S1227-1010BQ) and the square shaped waveform at the bottom clearly shows on and off operation of the LED. The second top curve shows a measured electrical power dissipated at Pt100 and follows with a delay oppositely the curve of emitted radiant power. When the LED is off, about 60 mW is dissipated at Pt100. Once the LED is turned on, the circuit automatically decreases the current flowing Pt100 and therefore the dissipated power to compensate the increased heat caused by LED operation and maintain the same temperature.

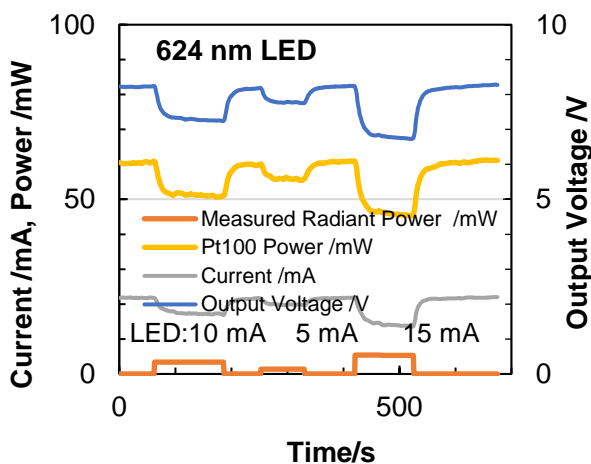


Figure 2. Temporal change in measured radiant power, electrical power dissipated at Pt100, etc..

Figure 3 shows the comparison results between the calorimetric measurements and the optical measurements. Although the calorimetric results correlate linearly with optical results, the former is

about 2 times the latter. The disagreement is highly likely to be caused by the large heat leak through the wires supplying a current to the LEDs. To solve the problem, modifications in thermal design such as replacing the copper wires to high thermal resistance wires and/or adapting thermal anchors are in preparation.

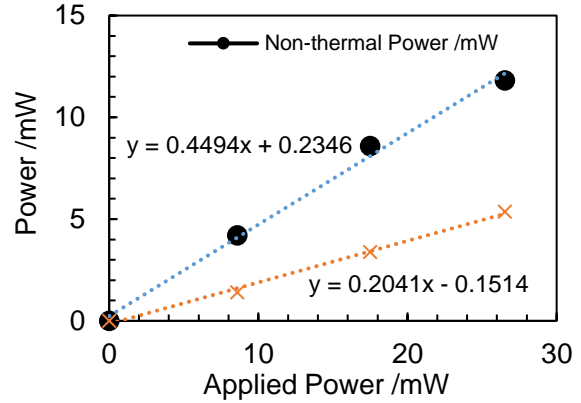


Figure 3. Non-thermal power (input electrical power applied to the LED minus the thermal power difference) and independently measured radiant power.

CONCLUSION

Constant temperature control using a self-heating of a temperature sensor without an additional heater has been proved to work as expected. With this system, it is possible to substitute heat power with electrical power and therefore possible to calorimetrically determine radiant power and conversion efficiency of optical devices, both sources and receivers. Preliminary results for a red LED with the constant temperature controller with Pt100 show two times overestimates for the radiant power. The disagreement is highly likely to be caused by the large heat leak through the wires. Modifications to solve the problem are in preparation.

REFERENCES

1. T. Inoue and K. Yamamura, "Quantum efficiency measurement of a photodiode based on a calorimetric method", J. Appl. Phys., 54, 6782-6784, 1983.
2. T. Inoue and K. Yamamura, "Total Radiant Power Measurement of Laser Diode by a calorimetric method", Electronics Letters, 19, 320-321, 1983.
3. T. Saito, M. Tatsuta, Y. Abe and M. Takesawa, "Calorimetric Measurement for Internal Conversion Efficiency of Photovoltaic Cells/Modules Based on Electrical Substitution Method", J. of Physics: Conf. Series 972, 012019, 1-6, 2018.

Ultraviolet Scale Realization based on a Laser-driven Light Source

Uwe Arp, Edward Hagley, Alex Farrell, Rob Vest

NIST, Gaithersburg, Maryland, United States of America

Corresponding e-mail address: uwe.arp@nist.gov

We report the successful realization of the ultraviolet spectral responsivity scale in the wavelength range between 200 nm and 400 nm at 5 nm intervals with a combined relative standard uncertainty below 0.5 % ($k=1$). This scale realization was based on a laser-driven light source and an absolute-cryogenic radiometer. Since both the scale realization and calibrations are performed using equivalent instruments, any uncertainty caused by differences in bandpass, out-of-band radiation, spectral purity, collimation, or extrapolation will be eliminated, leading to a more robust calibration chain.

INTRODUCTION

A few years ago, we started using a laser-driven light source in ultraviolet detector calibrations at NIST [1,2]. We realized immediately that we had enough optical power to attempt using an absolute-cryogenic radiometer (ACR) with this set up. Several problems made the primary calibration of photodiodes difficult: 1) Feeding a converging beam into the ACR and making sure the beam is not clipped was not trivial; 2) High reflectivity of photodiodes in the ultraviolet spectral region complicated the use of windows spatially close to these diodes; 3) The lack of commercially available damage resistant photodiodes with sufficient spatial uniformity. In the end we successfully calibrated three photodiodes between 200 nm and 400 nm at 5 nm intervals.

EXPERIMENT

After trying out several experimental approaches we concluded that we needed to eliminate the window in front of the photodiodes. Even with an antireflective coating, light reflected from the photodiodes and scattered by the window disturbed the measurement enough to lead to flawed results. Therefore, we settled on the system schematically shown in Fig. 1. This system used a high-quality laser-grade fused silica window in front of the ACR. The photodiodes were operated in air but placed in lens tubes in which apertures the same size and distance as in the ACR were installed, to make sure

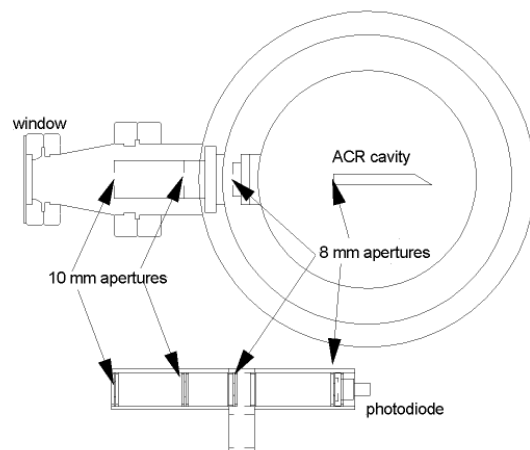


Figure 1. Schematic layout of the experimental set up.

the ACR cavity and the photodiodes were seeing the same light field. The ACR and three identical lens tubes housing three photodiodes were installed on a three-axis motion stage to allow for precise positioning and spatial scanning. The light coming from the laser-driven light source was imaged onto the circular entrance aperture of a double-Czerny-Turner monochromator. An absolute angular encoder was installed on one of the grating mounts. This absolute angular encoder, in combination with a holmium oxide [3] absorption target, was used to establish the wavelength scale. The exit aperture was re-imaged using two off-axis parabolical mirrors into the ACR and the lens tubes. During the first set of measurements we used a 0.5 mm circular exit aperture, which was magnified fourfold to a 2 mm spot. Later we performed a second set of measurements with a 0.3 mm aperture to make sure the ACR cavity was underfilled.

The data acquisition was performed in the following way: The monochromator was tuned to a wavelength λ and active feedback to the absolute angular encoder was enabled to keep the wavelength constant. Then an ACR measurement of the incident optical power was performed, followed by photo current measurements for each of the three photodiodes. At each wavelength on the order of ten measurements were performed in order to identify type A random errors in the spectral responsivity measurements.

The uncertainty in transmission of the window became the largest contributor to the systematic errors in this system. After the ACR measurements were completed, the area illuminated on the window was determined. Then the window was removed, and the transmission was measured at 5 nm intervals in the wavelength range between 200 nm and 400 nm. Using the motion stage, at each wavelength a measurement with and without the window was performed. We performed this measurement six times and used the resulting mean as the window transmission.

UNCERTAINTY ANALYSIS

Careful error analysis is crucial to successful absolute radiometry. In order to quantify type A random errors, we performed about ten measurements at each wavelength and statistically analysed the result. The error analysis is summarized in table 1. The combined relative standard error can be calculated from the relative standard deviation of all systematic contributions and the random contribution divided by the square root of the number of samples.

Table 1. Uncertainty analysis for the measurement with the 500 μm exit aperture.

Type A (random error)		
	Relative Standard Deviation / % (K=1)	
ACR Power (2nW noise)	0.02 to 2	
Photodiode current	0.02 to 0.2	
Type B (systematic error)		
Window transmission	0.27	
Wavelength scale	0.2	
Spectral bandwidth	0.1	
Diode uniformity	0.1	
Stray light	0.1	
Positioning	0.1	
Total systematic	0.39	

RESULTS

To determine the true optical power, the measured optical power had to be divided by the window transmission. For each measurement the diode photo current was divided by the true optical power as measured by the ACR, leading to individual values of the responsivity. The mean of several

responsivity measurements was then determined, and the standard deviation of this mean was used to estimate the type A random error.

The make sure the cavity of the ACR was underfilled, two measurements were performed: The first with a 500 μm -diameter exit aperture in the monochromator and the second with a 300 μm exit aperture. Results from both these measurements agree quite well (See table 2 for details). The differences in table 2 were calculated using equation (1). Using $\sqrt{2}$ instead of 2 in the relative difference scales the result to be equal to the relative standard deviation of the mean, while preserving the direction of the difference.

$$\Delta_R = \sqrt{2} \cdot 100 \cdot (R_2 - R_1) / (R_2 + R_1) \quad (1)$$

Table 2. Differences in the measured spectral responsivity for detector-under-test #1 using 500 μm and 300 μm exit apertures in the monochromator.

Wavelength / nm	Difference / %
250	0.056
290	-0.031
300	0.191
350	0.188
375	-0.242

The total relative standard uncertainty, which combines the systematic and random contributions to the uncertainty is below 0.5 % (k=1) for the whole wavelength range.

CONCLUSION

We successfully performed a primary calibration on a set of three photodiodes using a laser-driven light source and an absolute-cryogenic radiometer. One of the biggest challenges we faced was the unavailability of stable and uniform diodes. The combined relative measurement uncertainty was below 0.5 % for the spectral range from 200 nm to 400 nm.

REFERENCES

1. U. Arp, R. Vest, J. Houston, T. Lucatorto, *Argon mini-arc meets its match: use of a laser-driven plasma source in ultraviolet-detector calibrations*, Applied Optics, **53**(6), 1089, 2014.
2. U. Arp, R. Vest, *Eliminating the Middleman: Streamlined Scale Realization and Reduced Uncertainties in Ultraviolet Detector Calibrations at NIST*, NEWRAD 2014.
3. J. C. Travis et al., *Intrinsic wavelength standard absorption bands in holmium oxide solution for UV/visible molecular absorption spectrophotometry*, J. Phys. Chem. Ref. Data, **34**(1), 41, 2005

A Bilateral Comparison of NIST And PTB Laser Power Standards for Increased Calibration Confidence at LIGO

Matthew Spidell¹, Stefan Kück², Holger Lecher², Marco López², Yannick Lecoecue³, Richard Savage³

¹Sources and Detectors Group, U.S. National Institute of Standards and Technology, Boulder, Colorado USA

²Optics Division, Physikalisch-Technische Bundesanstalt, Braunschweig, Germany

³LIGO Hanford Observatory, Richland, Washington, USA

Corresponding e-mail address: Matthew.Spidell@NIST.GOV

The Laser Interferometric Gravitational Wave Observatory (LIGO) calibrates gravitational strain measurements using photon momentum, with laser power serving as the measurand. Calibration of its laser power meters is currently traceable to the International System of Units through a primary standard maintained by the United States' National Metrology Institute (NMI). Disparity between NMIs indicated in the EUROMET 2010 study impacts confidence in Gravitational Wave (GW) event parameters such as mass, distance and location.

INTRODUCTION

Displacement of mirrored test masses at the extrema of the LIGO interferometer arms is calibrated through photon momentum. Accordingly, uncertainty in the power incident on the mirror is directly proportionate to the uncertainty in the interferometer strain [1].

The EUROMET 2010 study [2] suggests disagreement between various NMIs detector-based representation of the optical watt that exceed stated uncertainties. Inequivalence between NMIs decreases confidence in the absolute accuracy of any given nation's power scale realization.

PREVIOUS INTERNATIONAL COMPARISON

The EUROMET 2010 comparison [2] results for calibrations at 1 W, 1064 nm show discrepancy between calibrations performed by NIST and PTB exceed the 95% measurement confidence interval as described in Table 1. The agreement between NIST and PTB at 514 nm contrasted with the inequivalence at 1064 nm suggests an unaccounted spectral-responsivity. We suggest the discrepancy may be attributable to characteristics of the thermopile transfer standards

Table 1. Comparison of EUROMET 2010 results for PTB and NIST

	1064 nm	
	C.F. Discrepancy	Bilateral Uncertainty
Thermopile		
Ophir	1.03%	1.03%
Molelectron	1.15%	1.10%
	514 nm	
	C.F. Discrepancy	Bilateral Uncertainty
Thermopile		
Ophir	0.12%	0.99%
Molelectron	0.01%	0.99%

THERMOPILE TRANSFER STANDARD INEQUIVALENCE CONTRIBUTIONS

During the EUROMET study NIST applied 1 W for 200 s while PTB applied the same power and wavelength for 600 s. The disparity in injection period, when applied to an uncompensated thermopile such as those used in the EUROMET study, yields an inequivalence of approximately 0.1 % due to increased cold-junction temperature. Figure 1 below depicts decreasing (interpolated) responsivity due to cold-junction heating.

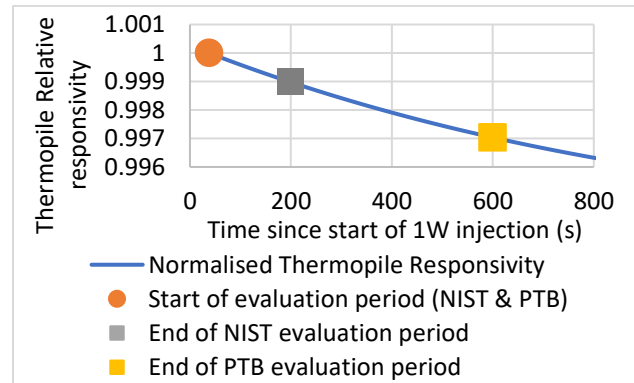


Figure 1. Thermopile relative responsivity versus injection time

Spatial nonuniformity for a thermopile similar to those used during the EUROMET 2010 study, depicted in Figure 2 below, suggests a 2 mm alignment discrepancy can readily yield a responsivity variation exceeding 1 %.

The inequivalence attributable to differing injection periods and spatial nonuniformity suggests the cause of the apparent laboratory inequivalence.

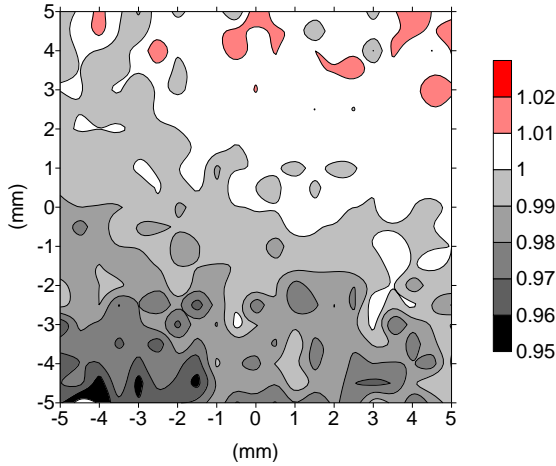


Figure 2. Typical thermopile relative spatial non-uniformity

AN INTEGRATING SPHERE DETECTOR AS AN ALTERNATIVE TRANSFER STANDARD

Integrating sphere detectors, with baffles and apertures configured for laser power measurement, offer an alternative tool for a watt-level comparison between NIST and PTB. For this study, LIGO's calibration group provided a 100 mm fluoropolymer-lined integrating sphere identical to their Photon Calibrator detectors [3]. The spatial non-uniformity of this integrating sphere depicted in Figure 3 is an order-of-magnitude below that of a thermopile. Empirically, the temperature sensitivity coefficient for the system is 0.02 % to 0.1 % per Kelvin [4].

RESULTS AND DISCUSSION

To be presented upon measurement completion at NEWRAD.

CONCLUSION

Observed inequivalence contributions arising from different laser power injection times and typical laser alignment discrepancies combined with spatial non-uniformity

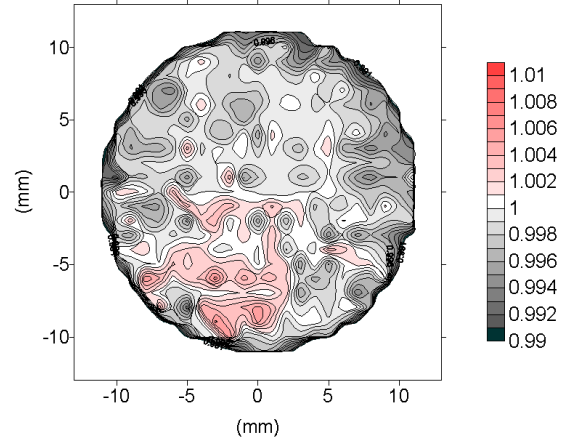


Figure 3. Integrating sphere transfer standard relative spatial non-uniformity

of the transfer standards used in the EUROMET 2010 study suggest the cause of measurement discrepancy between NMIs. Resolution of measurement discrepancy between NIST and PTB validates the competency of both laboratories and the use of integrating spheres as transfer standards. For future comparisons, integrating sphere detectors may be used as transfer standards together with well-matched laboratory environments to reduce these uncertainty contributions by a factor of 10. Successful completion of this bilateral comparison enables a larger comparison validating the power scale of National Metrology Institutes for other GW observatory host countries to serve as an ongoing validation of the LIGO calibration program.

REFERENCES

1. B. P. Abbott, et al., "Calibration of the Advanced LIGO detectors for the discovery of the binary black-hole merger GW150914," *Phys.Rev. D*, 95, 062003, 2017.
2. S. Kück, Final report on EUROMET comparison EUROMET.PR-S2 (Project No. 156): Responsivity of detectors for radiant power of lasers, *Metrologia*, 47, Technical Supplement, 2010.
3. S. Karki, et al., The Advanced LIGO photon calibrators, *Rev. Sci. Inst.*, 87, 114503, 2016.
4. R. Savage, et al. "Displacement fiducials for gravitational-wave detectors with sub-percent accuracy using laser power sensors calibrated at NIST". *Proc. NEWRAD*, 2020.

Implementation of the Spectral Irradiance Standard based on a high-temperature black body

Jan Lalek¹, Andrzej Rybczyński¹, Boris Khlevnoy²

¹GL Optic Polska Sp. z o.o. Sp k, Puszczykowo, Poland,

²All-Russian Research Institute for Optical and Physical Measurements (VNIIOFI), Moscow, Russia

Corresponding e-mail address: andrzej.rybczynski@gloptic.com

The high-temperature black body is widely used as a primary standard source for implementation of spectral irradiance units and can be used for spectral calibration of measuring instruments. Correct determination of a relation between spectral irradiance values of the primary standard and corresponding readings of a measuring instrument, and further obtaining a measurement result from this relation requires a suitably advanced system for making comparative measurements. The presented concept of a measurement system based on modern motion control components helped to achieve a high level of precision and accuracy while achieving better performance of the comparison procedure.

PRIMARY STANDARD

High-temperature black body radiators are widely used in national metrological institutes for implementation and maintenance of radiometric units [1]. The black body BB-PyroG-3000/32 adopted in the GL Optic laboratory was developed and manufactured by All-Russian Research Institute for

current flowing through the stack. The power supply equipped with a feedback system ensures stabilization of the black body temperature ± 0.02 K. During operation, the radiator interior must be filled with argon.

The black body casing is water cooled. In the event of a power failure in the cooling water supply the radiator may be cooled by gravitationally supplied water from a reserve tank. The radiator's properties are shown in Table 1.

MEASUREMENTS AND METHODS

Measurements of the spectral irradiance generated by a high-temperature radiator are carried out using a double monochromator MZDD3504i together with a set of detectors manufactured by SOL Instruments. These detectors are: photomultiplier, silicon diode and InGaS. Each of the Turner-Cherny scheme monochromators is equipped with automated 4-grating turret and automatic slits. The straylight with 20 nm 643.8 nm laser line is below 5×10^{-10} . The instrument can measure spectral irradiance in the range 190-2400 nm.

Table 1. Properties of BB-PyroG-3000/32 high-temperature black body radiator.

Maximum temperature	3200 K
Aperture diameter	25 mm
Cavity diameter	32 mm
Emissivity in UV-VIS-IR	≥ 0.999
Temperature resolution	0.01 K
Temperature stability	± 0.02 K
Support for HTFP	yes

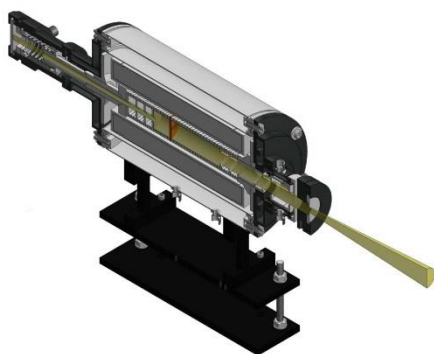


Figure 1. Cross section of the blackbody.

Optical and Physical Measurements (VNIIOFI), Moscow. It belongs to a wide family of radiators developed in this research centre [2].

The radiator is based on a stack of pyrolytic-graphite rings forming a black body cavity. This cavity can be heated up to 3200 K with electric

The Planck's law describes the spectral distribution of the power of optical radiation emitted by a black body in thermal equilibrium based on a set temperature. Correct determination of the temperature is thus crucial for the whole measurement process. To measure the actual temperature, a Chino IR-RST65H pyrometer was used. It is a monochromatic pyrometer using a silicon

photodiode as a detector. The measurement is made at a wavelength of 650 nm. The diameter of the measurement field is 0.6 mm at the distance of 400 mm. It helps to test the homogeneity of the black body emitting area.

To ensure the most accurate temperature measurement, the pyrometer can be calibrated against the rhenium-carbon high temperature fix point (HTFP), when the HTFP cell is installed in the blackbody.

The spectral irradiance measurement procedure consists of alternating measurements of the black body and a tested source for successive wavelengths within the assumed measurement range (Fig. 1).

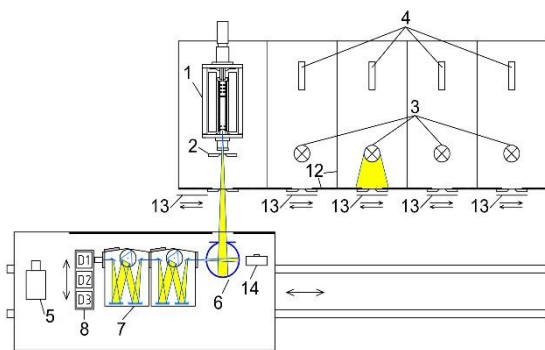


Figure 3. Optical comparator diagram: 1 - blackbody, 2 - diaphragm, 3 - DUTs, 4 – lasers, 5 – pyrometer, 6 – integrating sphere, 7 – double monochromator, 8 – detectors, 13 – shutters, 14 – array spectroradiometer.

Changes in the position of the double monochromator have a significant impact on the total measurement

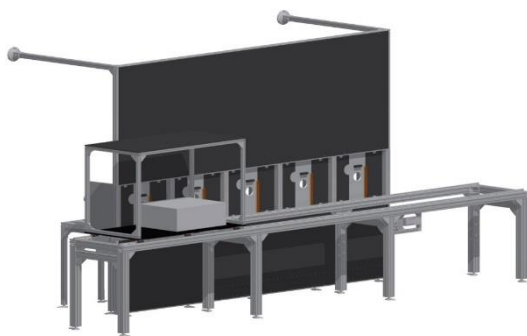


Figure 4. Optical comparator stand design.

time and may introduce additional misalignment errors.

To ensure fast switching between the two measurement positions, the optical comparator uses servomotors with built in 23-bit absolute encoders dedicated to CNC machining tools. The solution used

helped to achieve positioning with standard deviation of 5 μm and with switching time between both positions of about 1.5 s.

The validation procedure revealed a known problem [3] of absorption bands caused by molecular carbon or carbon compounds presented in Figure 3. The additional array spectroradiometer used in combination with a double monochromator helps to identify and correct the deviations from the Planckian spectrum. The results obtained from this instrument are used as input data to the correction algorithm.

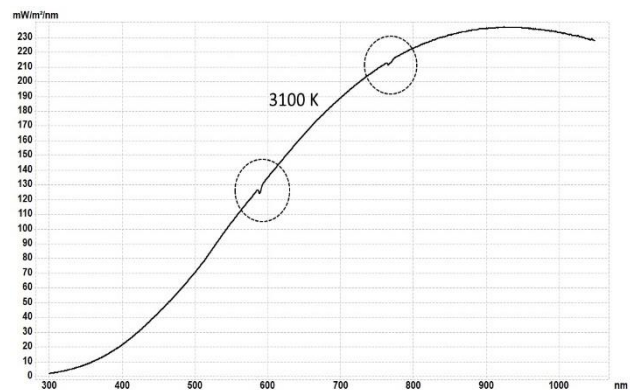


Figure 2. Spectrum with absorption bands.

CONCLUSIONS

The developed Spectral Irradiance Standard facility allows calibration with high efficiency (Figure 4). At the current stage the comparator is a subject of validation and comparative studies with national metrological institutes. The final results of these tests and the obtained calibration procedure times will be presented in the article following this abstract.

REFERENCES

1. Sperfeld, P., Metzdorf, J., Harrison, N. J., Fox, N. P., Khlevnoy, B. B., Khromchenko, V. B., ... & Sapritsky, V. I. (1998). Investigation of high-temperature black body BB3200. *Metrologia*, 35(4), 419.
2. Khlevnoy, B. B., Samoylov, M. L., Grigoryeva, I. A., Ibragimov, N. A., Shapoval, V. I., Puzanov, A. V., & Ogarev, S. A. (2011). Development of high-temperature blackbodies and furnaces for radiation thermometry. *International Journal of Thermophysics*, 32(7-8), 1686-1696.
3. Sperfeld, P., Pape, S., Khlevnoy, B., & Burdakin, A. (2009). Performance limitations of carbon-cavity blackbodies due to absorption bands at the highest temperatures. *Metrologia*, 46(4), S170.

Towards 1 W, High Accuracy, Absolute Radiometer

Florian Stuker¹, Michelle Stephens², Malcolm White^{2,3}, Anna Vaskuri², Nathan Tomlin², Christopher Yung², Ivan Ryger^{2,3}, Peter Blattner¹ and John Lehman²

¹Federal Institute of Metrology METAS, Bern-Wabern, Switzerland, ²National Institute of Standards and Technology NIST, Boulder, CO, USA, ³Department of Physics, University of Colorado, Boulder, CO, USA

Corresponding e-mail address: florian.stuker@metas.ch

Emerging applications require a calibration at 1 W with greater accuracy than is currently available. Conventional free beam absolute electrical substitution radiometers (ESRs) operate at cryogenic conditions have historically provided the highest accuracy but operate at optical power levels < 2 mW. To improve the accuracy of calibrations at 1 W, we compare possible approaches to realize a primary standard for 1 W optical power measurements. We describe and evaluate two diverse concepts based on bolometer detectors: The first design is an adapted cryogenic approach while the second system is operating at room temperature (RT). With the proposed uncertainty budgets, we estimate an expanded uncertainty for the RT layout to be < 0.06 % ($k = 2$) while the cryogenic design approaches 0.02 % ($k = 2$).

INTRODUCTION

Historically absolute ESRs operate at cryogenic temperatures have provided the most accurate laser power calibrations, accepting optical input power levels of up to 1.4 mW [1]. These devices are built for free beam operation where the beam impinges on the absorber area via a Brewster window. Such equipment allows a combined standard uncertainty of < 0.01 %. For higher optical power calibrations, RT primary standards can be used to achieve power levels in the order of several watts but with uncertainty of 0.5 % – 1 % ($k = 2$) in best case. However, there exist applications with the need for lower uncertainties for a 1 W optical power calibration such as the photon calibrator system (P_{cal}) of the LIGO experiment. In that case, the optical calibration of their P_{cal} is directly proportional to the gravitational wave detection performance [2].

A cryogenic primary standard capable of measuring 1 W of optical power has not been demonstrated, and the thermal management challenges are significant. At the same time, there have been advances in room temperature bolometers at moderate optical powers [3,4] that suggest that

high accuracy could be obtained at 1 W with a RT absolute radiometer. If possible, one could realize significant cost savings and possibly better portability over a cryogenic radiometer.

General requirements for a high accuracy 1 W radiometer include a nearly perfect absorber with a diameter > 8 mm to capture Gaussian beams up to 3 mm ($1/e^2$). A free beam operation in vacuum has to be ensured and thus a Brewster entrance window is used to transmit the beam to the absorber.

The aim of this work is to provide a first comparison of the predicted performance of a RT radiometer to a cryogenic version by theoretically estimating the uncertainties associated with new ways of implementing an absolute ESR for measuring 1 W optical power with planar bolometer detectors.

CRYOGENIC DESIGN

One of the major difficulties in a cryogenic high optical power approach is the dissipation of the heat generated by the absorber. We describe the design and modelled the performance of a heat link optimized for high laser powers. According to the heat map of a selected two stage mechanical cryocooler, powers > 2 W at temperatures above 5 K can be handled. We assume a cryocooler-stage plate with 1.4 Hz cyclic thermal fluctuation and an amplitude of ± 200 mK. For precise measurements a first $100\times$ variation damping can be achieved with a thermal low-pass filter consisting of a beryllium copper ring dimensionally matching a readily available holmium copper (HoCu_2) element. With a temperature rise from 7.5 K to 9.5 K the integrated heat flow is 4 W and provides control power to handle 1 W optical power. A similar, size reduced second thermal low-pass filter (lead/ HoCu_2) allows an amplitude modulation suppression to ± 12 μK at a detector stage temperature of 11 K. The screwed-on reference block is made of oxygen free copper (OFC) with high thermal conductivity. A commercial resistance bridge is used to monitor the heat sink thermistor for feedback controlling the integrated cartridge heater. As a heat link (detector/reference block) an

aluminium cylinder with a thermal conductance $G = 1 \text{ W/K}$ is mounted. For a seamless thermal contact, an OFC substrate is explosion bonded to the heat link prior to the spray-on carbon nanotube coating. A heater wire is wound around and is used as the electrical substitution heater for optical power measurements. The detector runs in an open loop where the temperature change is recorded in the centre of the OFC disk with a side mounted thin film resistor.

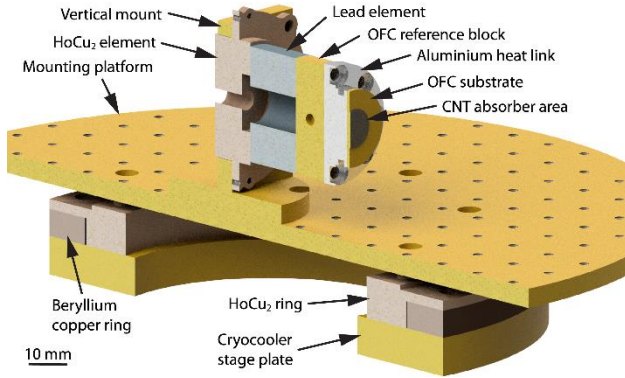


Figure 1. Concept of the cryogenic design

ROOM TEMPERATURE DESIGN

We investigated a design derived from a recently published RT operated compact total irradiance monitor [3] and a RT planar absolute radiometer capable of measuring laser powers up to 300 mW [4]. These differential radiometers are based on vertically aligned carbon nanotubes (VACNTs) grown on silicon substrate [5] and offers an expanded uncertainty of $< 0.06 \%$ ($k = 2$). The operation principle is based on a detector pair: one detector measures the laser power and the other compensates for ambient temperature fluctuations. To adapt the designs presented in Refs. [3,4] to 1 W optical power, we assumed a 1 mm thick and 24 mm diameter silicon substrate. A spiral tungsten heater centred on the back of the detector and four low-noise thermistors near the edges of the detector chip reduces the inequivalence between optical and electrical powers [4]. Temperatures of the two detector chips are matched by connecting thermistors in a custom-made AC driven Wheatstone bridge and varying the electrical power to the measuring detector chip [3,4]. A heat link thermal conductance is designed to keep the detector temperature constantly at 303 K with respect to the temperature controlled base plate at 293 K. The heat link consisting of three stainless steel cylinders transports the heat load to the reference block. The reference block is temperature

controlled with a thermo-electric cooler and a thermistor providing a thermal stability $< 500 \mu\text{K}$.

UNCERTAINTY BUDGET

We estimate uncertainty budgets for both 1 W cryogenic and RT radiometers. The major contributions for the uncertainty budget originate from the bolometer. We have estimated expected electrical heating inequivalence, VACNT properties such as non-uniformity, polarization dependence, the absorber reflectance, and the uncertainty in the transmission of the Brewster window. In the electrical power measurement we summarize the uncertainties in the voltage measurements. The dominant electrical noise component originates for both designs from the commercial resistor bridge for the heat sink thermal loop. The radiative coupling at cryogenic temperatures can be neglected by using highly reflective gold-coated components. However, for the RT layout we estimated the ambient temperature coupling and contributions from the thermal fluctuation in the reference block and heat link. In addition to the uncertainties of the Brewster window transmittance correction, the laser power drift and variations, the laser pointing stability and the changes in background radiation are integrated in the optical contribution.

CONCLUSION

The two presented ESRs having a similar detecting principle but antipodal working conditions result in comparable combined standard uncertainties. A first analysis of a cryogenic design that can manage the thermal load of a 1 W laser beam is described. Such a cryogenic radiometer is estimated to achieve an expanded uncertainty of 0.02% ($k = 2$), a factor of 3 better than the estimated expanded uncertainty of $< 0.06 \%$ ($k = 2$) for a RT design. Both designs show that better accuracy than is currently available is within reach.

REFERENCES

1. J. Martin, et al., A cryogenic radiometer for absolute radiometric measurements, *Metrologia*, 21, 1985
2. S. Karki, et al., The advanced LIGO photon calibrators, *Review of Scientific Instruments*, 87, 2016
3. D. Harber, et al., Compact total irradiance monitor: flight demonstration, *Proc. Vol. 11131*, 11310D, 2019
4. A. Vaskuri et al., Microfabricated bolometer based on a VACNT absorber, *Proc. SPIE Vol. 11269*, 2020, *Subm.*
5. N. Tomlin, et al. Planar electrical-substitution carbon nanotube cryogenic radiometer, *Metrologia*, 52, 2015

Double laser radiometry for study of detector linearity

Mikhail Korpuseenko¹, Farshid Manoocheri¹, and Erkki Ikonen^{1,2}

¹*Metrology Research Institute, Aalto University, Espoo, Finland;* ²*VTT MIKES, Espoo, Finland;*
Corresponding e-mail mikhail.korpuseenko@aalto.fi

An experimental optical system of two laser sources and a silicon photodiode was built to test the double laser radiometry technique. The final goal is to achieve nonlinear region in silicon photodiodes and deactivate surface recombination centres in such a way that photocurrent produced by the photodiode will increase. We observe the present limit of performance of the measurement system at the level of 0.08%

INTRODUCTION

Linearity is a necessary property for high precision optical detector. The absolute responsivity of a photodiode should be stable over a certain period and constant over a certain range of irradiance [1,2]. Nonlinearity is a phenomenon well known in silicon photodiodes. Estimation of photodiode nonlinearity is essential for precise measurements. Activation of recombination centres is one reason of uncertainty in photodiodes. Recombination centres appearing are metallic impurities, most notably silver, which combine with boron in silicon to form latent recombination centres, and which only become active during the passage of several years. Moisture penetration through the package to the device over a long period of time is also a possible cause of observed changes in the quantum efficiency of boron-diffused devices over extended periods of time [2]. Moisture in conjunction with boron is suspected to cause recombination centres near the oxide-silicon interface, and moisture has been reported to neutralize the ionized boron acceptors by hydrogen injection creating a surface region depleted of ionized boron. Deactivation of recombination centres could increase the reliability of measurements. Characterising the supralinear region where recombination centres are deactivated will allow to increase the accuracy of measurements.

In this work, we built a custom developed optical setup to test the idea of double laser radiometry and check the availability of deactivation of surface recombination centers in silicon detectors.

DOUBLE LASER RADIOMETRY SETUP

The idea of the double laser radiometry technique is the usage of two laser sources simultaneously (Fig. 1): near infrared laser as a source of measured signal and blue laser for filling up recombination centres at the

photodiode surface, because of small penetration depth. An optical chopper modulates near infrared light. The light spots from the two lasers coincide on the photodiode active area. The blue beam may deactivate recombination centres, so this technique can increase photodiode responsivity. The set-up consists of two CW diode laser sources with wavelengths of 405 nm and 785 nm. Near infrared light is attenuated with neutral density (ND) filter,

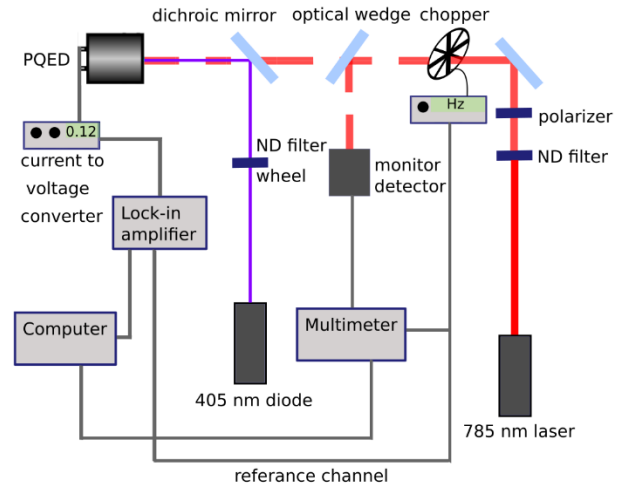


Figure 1. Double laser radiometry optical system.

polarizer and then modulated by optical chopper. Blue light is attenuated with ND filter in a filter wheel. Two beams are brought together with a dichroic mirror so light spots from the lasers overlap on the photodiode active area. We used a monitor detector to check near-infrared laser's stability and a lock-in amplifier to measure the signal from the near-infrared laser. As only 785 nm light is modulated with the optical chopper, the lock-in amplifier measures only the near-infrared signal and the blue light signal is neglected. To detect changes in the weak signal we used a custom-built current-to-voltage converter (CVC) with an amplification of 10^3 and Stanford Research S830 lock-in amplifier. As the detector we chose Hamamatsu S2281 silicon photodiode and a custom-made predictable quantum efficient detector (PQED). The PQED consists of two induced junction photodiodes that are mounted in a wedged trap configuration for the reduction of reflectance losses [3].

The final goal is to study the supralinear region in PQED photodiodes and deactivate surface recombination centres in a such way that the overall

signal will increase when using the double laser technique.

MEASUREMENTS AND DATA PROCESSING

During the measurement process, the automatic filter wheel of blue light changed its position between two states: one with opaque ND filter with high absorbance and another one without any filter. In one position, the set-up records ten measurement points and then the filter wheel switches to another position. The monitor detector allowed correcting the near-infrared laser signal instability. Figure 2 shows the relative difference in lock-in amplifier signal with and without blue light.

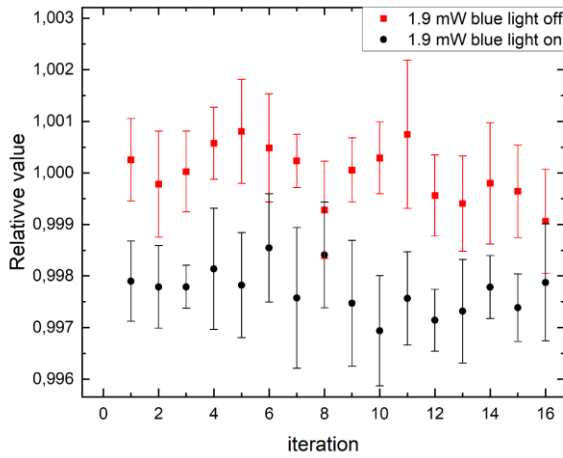


Figure 2. Normalised signal from the lock-in amplifier at $465\ \mu\text{W}$ modulated power of the $785\ \text{nm}$ laser and $1.9\ \text{mW}$ DC power of the $405\ \text{nm}$ laser

We used different power levels of the near-infrared laser to study the tested photodiode (Fig. 3). During data processing all points from one "cycle" were averaged and compared with each other. Such

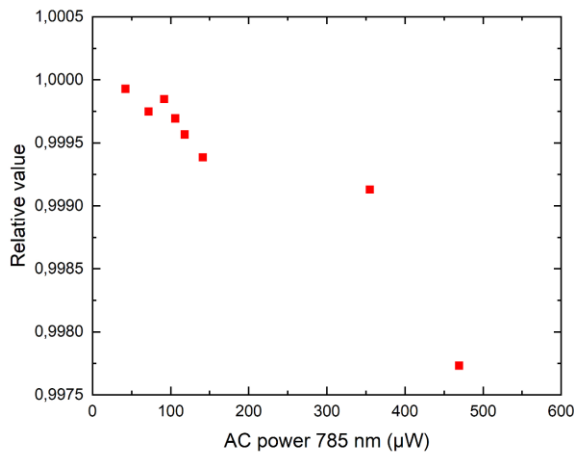


Figure 3. Ratio of near-infrared laser signals from the lock-in amplifier with $1.9\ \text{mW}$ blue light off and blue light on.

measurement allows checking the dependence on laser power, irradiation time, and other conditions. The limit of performance of the measurement is about 0.08% as concluded from data points (Fig. 3). We

seem to start achieving saturation region in the photodiode with the $465\ \mu\text{W}$ signal.

We have also noticed that irradiation of the borders of the photosensitive area with the two lasers leads to reaching supralinear region at various power levels that coincides with results achieved earlier by Tanabe and Kenichi [4]. The next step is to conduct measurements with PQEDs to study possibility of deactivation of surface recombination centres.

ACKNOWLEDGEMENTS

This work was funded by the project chipS·CALe (contract 18SIB10) of the European Metrology Programme for Innovation and Research (EMPIR). The EMPIR is jointly funded by the EMPIR participating countries within EURAMET and the European Union's Horizon 2020 Programme.

REFERENCES

1. A. Schaefer, E. Zalewski, and J. Geist, Silicon detector nonlinearity and related effects, *Applied Optics*, 22(8), p.1232, 1983.
2. R. Korde, J. Geist, Quantum efficiency stability of silicon photodiodes, *Applied Optics*, 26(24), p.5284, 1987.
3. T. Dönsberg, F. Manoocheri, M. Sildoja, M. Juntunen, H. Savin, E. Tuovinen, H. Ronkainen, M. Prunnila, M. Merimaa, C. Tang, J. Gran, I. Müller, L. Werner, B. Rougié, A. Pons, M. Smid, P. Gál, L. Lolli, G. Brida, M. Rastello, and E. Ikonen, Predictable quantum efficient detector based on n-type silicon photodiodes. *Metrologia*, 54(6), p.821, 2017.
4. M. Tanabe and K. Kenichi, Supralinear behavior and its wavelength dependence of silicon photodiodes with over-filled illumination in visible range, *Applied Optics*, 57(13), p.3575, 2018.

Quantum efficiency of Predictable Quantum Efficient Detector in the ultraviolet region

Mikhail Korpuseenko¹, Anna Vaskuri^{1,2}, Farshid Manoocheri¹, and Erkki Ikonen^{1,3}

¹*Metrology Research Institute, Aalto University, Espoo, Finland*

²*National Institute of Standards and Technology (NIST), Boulder, CO, USA*

³*VTT MIKES, Espoo, Finland*

Corresponding e-mail mikhail.korpuseenko@aalto.fi

The internal quantum efficiency of a Predictable Quantum Efficient Detector (PQED) was studied by experiments in the ultraviolet and visible wavelength region. We report and discuss the spectral quantum efficiency behaviour, which is quantitatively different in the PQED photodiodes as compared with Hamamatsu photodiodes.

INTRODUCTION

Accurate optical measurements are of great importance in photometry and radiometry. In these research fields, silicon (Si) photodiodes are widely used and they are the most appropriate photodetector for measuring power levels <1 mW of visible and ultraviolet (UV) light. The spectral responsivity of a quantum detector is given by

$$R(\lambda) = \frac{e\lambda}{hc} (1 - \rho(\lambda))(1 - \delta(\lambda))(1 + g(\lambda)). \quad (1)$$

The factor $e\lambda/hc$ is the responsivity of an ideal quantum detector expressed by fundamental constants and the vacuum wavelength λ of the applied radiation. Parameters $\rho(\lambda)$ and $\delta(\lambda)$ describe the spectral reflectance and internal quantum deficiency (IQD), respectively, and $1 + g(\lambda)$ is the quantum gain. Since Si bandgap is 1.12 eV at room temperature, UV photons have at least twice the energy corresponding to the bandgap energy in Si. For that reason, the generated charge carriers may have so much energy that they produce new electron-hole pairs by impact ionization. Understanding of the behaviour of internal quantum efficiency (IQE) in the UV region of the PQED photodiodes helps to evaluate photon flux more precisely in that spectral range.

COLLECTION EFFICIENCY

Silicon photodiodes can be produced by diffusing thin layers of impurity atoms on the surface of the Si wafer. The resulting collection probability model of charge carriers [1] in Fig. 1 describes the IQE of Hamamatsu photodiodes. In this three-parameter

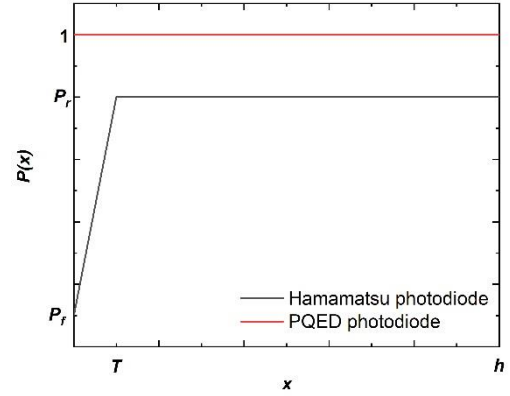


Figure 1. Models for variation of the collection probability $P(x)$ with distance into a photodiode of thickness h . The black line shows the three-parameter model for Hamamatsu photodiodes [1]. The red line shows collection probability for the PQED photodiodes [2, 3].

model the collection probability rises from a value of $P_f \approx 0.98$ at the front of the photodiode to a value $P_r \approx 0.999$ over a distance $T \approx 0.3 \mu\text{m}$ and stays at P_r to the back of the photodiode.

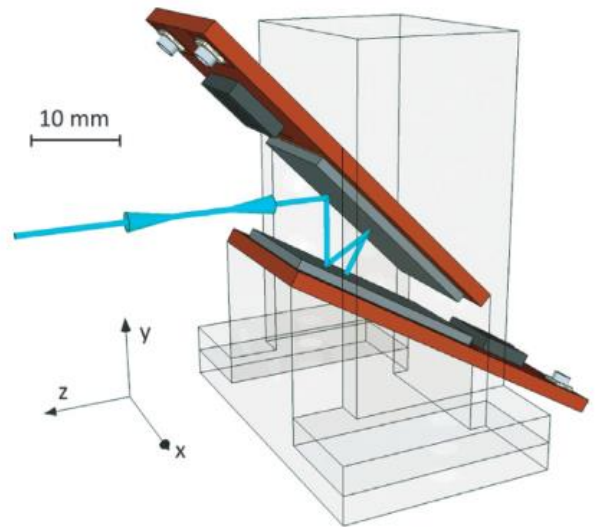


Figure 2. Schematic diagram of the PQED photodiodes' assembly. The blue arrows depict the incident beam. The beam undergoes seven absorptions and reflections at the photodiode surfaces before the remaining fraction of the beam exits through the entrance aperture [2].

For PQED photodiodes, the collection probability model of charge carriers is simple. When the PQED is reverse biased, the value is between 1.0000 and 0.9999 throughout the photodiode thickness [2, 3] as shown in Figure 1. Such charge-carrier collection probability is achieved by the induced-junction structure of the PQED photodiodes, which contains very few recombination centres formed by impurity atoms.

EXPERIMENT AND DATA ANALYSIS

The measurement setup consists of a xenon (Xe) light source, a single monochromator, a detector under test (PQED or a 3-element Si trap detector made of Hamamatsu photodiodes), a broadband wire-grid polarizer for producing light with different polarization states, and a reference pyroelectric radiometer calibrated for measurement of optical power. The PQED consists of two custom-made induced-junction Si photodiodes [2]. The photodiodes in the PQED are aligned so that seven specular reflections take place before the non-absorbed fraction of light leaves the detector (Fig. 2).

Photocurrent signal from the test detectors was divided by the optical power obtained from the pyroelectric radiometer, to determine the measured spectral responsivity $R(\lambda)$ of equation (1). To reduce noise in data, measurements were repeated several times and then averaged. After correcting for the effect of reflectance, factor $1 - \rho(\lambda)$ in equation (1), the IQE values corresponding to $(1 - \delta(\lambda)) \cdot (1 + g(\lambda))$ are obtained.

RESULTS AND DISCUSSION

Figure 3 shows the measured spectral responsivity for the PQED and the trap detector made of Hamamatsu photodiodes. The solid line shows the ideal spectral responsivity $e\lambda/hc$ where each absorbed photon generates one electron-hole pair.

Figure 4 shows the IQE, where it can be clearly seen the differences between the PQED and Hamamatsu photodiodes. As the wavelength decreases below 450 nm, more photons are absorbed near the surface of the Hamamatsu photodiode. According to Figure 1, the collection probability of the trap detector is lower at the surface than in the bulk, and thus the IQE decreases clearly below 1. At the wavelengths below 350 nm, the quantum gain becomes significant and the IQE increases again above 1.

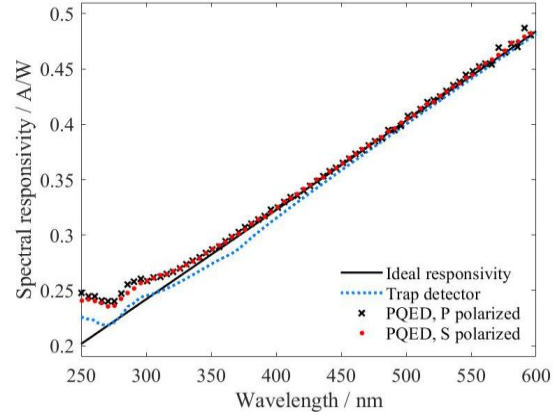


Figure 3. Spectral responsivities of the PQED for S and P polarization, and spectral responsivity of the trap detector. For clarity, only the trend line is shown for the trap detector. The solid line depicts ideal responsivity of a quantum detector.

For the PQED photodiodes, the IQE remains constant for wavelengths down to 400 nm, agreeing with the model of the PQED charge-carrier collection probability of Fig. 1. At the UV wavelengths below 400 nm, the IQE increases due to quantum gain, similar to the behaviour of Hamamatsu photodiodes. Impact ionization is determined by bulk properties of Si, whereas there is a significant difference in the charge-carrier losses due to impurity recombination centres in the two studied types of photodiodes.

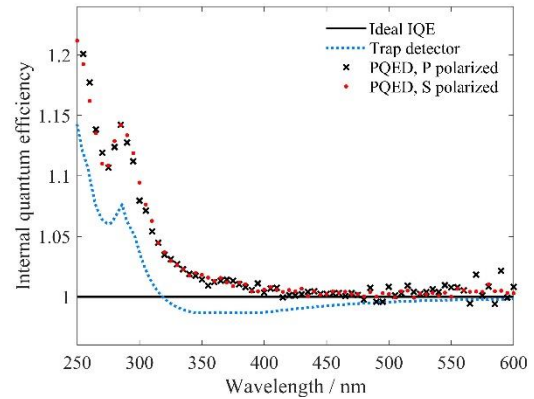


Figure 4. Internal quantum efficiency of the PQED for S and P polarization, IQE of trap detector, and ideal IQE. Measured IQE of PQED is similar for P and S polarizations.

REFERENCES

1. T. Gentile et al., Internal quantum efficiency modeling of silicon photodiodes, *Applied Optics*, 49, 1859-1864, 2010.
2. M. Sildoja et al., Predictable quantum efficient detector: I. Photodiodes and predicted responsivity, *Metrologia*, 50, 385-394, 2013.
3. I. Müller et al., Predictable quantum efficient detector: II. Characterization and confirmed responsivity, *Metrologia*, 50, 395-401, 2013.

Calibration of a modular trap detector system towards a new realization of the luminous intensity unit

Philipp Schneider¹, Saulius Nevas¹, Detlef Lindner¹, Lutz Werner¹, Ulrike Linke¹ and Armin Sperling¹

¹Physikalisch-Technische Bundesanstalt (PTB), Braunschweig and Berlin, Germany

Corresponding e-mail address: philipp.schneider@ptb.de

A modular photometric trap detector system has recently been developed at PTB. All parts of the detector are now completely calibrated. As a result, the new traceability chain for the realisation of the luminous intensity unit can be established for a first time. This contribution shows the results of the individual calibration steps. Improvements in the measurement setup used for carrying out most of the calibration steps in the traceability chain are described and the resulting effect on the measurement uncertainty is shown. The remaining steps along the way towards this new realization of the luminous intensity unit and its implications are discussed.

THE MODULAR DETECTOR APPROACH

The individual steps within the improved calibration strategy for realising the luminous intensity unit at PTB have been shown and described previously [1]. The modular detector system was developed specifically for this purpose. Its suitability for realising the traceability chain were checked beforehand based on thorough characterizations at the TULIP setup [2].

All necessary calibrations of the detector system have now been accomplished, which provides a glance of the final uncertainty achievable while following the new calibration strategy.

CRYOGENIC RADIOMETER-BASED CALIBRATION OF THE TRAP DETECTOR

The trap-detector was calibrated with respect to the spectral power responsivity at the laser-based cryogenic radiometer facility of PTB. It has been designed and is operated in a way to ensure the lowest possible uncertainties. The facility is equipped with a common Brewster window which means that cryogenic radiometer and trap-detector are irradiated through the same window. Thus, the correction for and the uncertainty contribution arising from the measurement of the transmittance of the Brewster window can be avoided. The detector cavity of the cryogenic radiometer and the trap-detector were

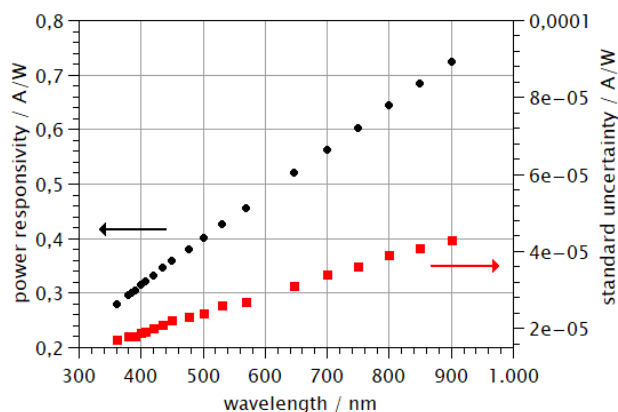


Figure 1. Power responsivity of the trap detector (black symbols) calibrated against the cryogenic radiometer with a preliminary standard uncertainty (red symbols)

irradiated at the same position with respect to the laser beam. Thus, the uncertainty contribution arising from the scattered radiation around the laser beam is drastically reduced. The calibration was carried out at 19 wavelengths covering the spectral range from 360 nm to 900 nm. The results are shown in Figure 1.

The spectral power responsivities at the 19 wavelengths need to be interpolated for further calibrations at the TULIP setup. Since silicon photodiodes are known for their aging and the measurements were done over the course of 5 months, the data points need a correction for this effect. As this detector was measured only once at this uncertainty level, the specific aging correction function is not available yet. Nevertheless, a correction will be estimated with a conservative uncertainty contribution based on known aging rates of similar trap detectors with the same type of photodiodes.

CALIBRATION OF THE PHOTOMETRIC FILTER

The realisation of the luminous intensity unit requires adapting the spectral responsivity of the detector system to the photometric standard observer. For this purpose, the modular trap detector system includes a $V(\lambda)$ filter. The filter transmittance is measured relatively to a precision aperture deposited on a window as described in [1]. The measurements were

carried out using the femtosecond laser system at the TULIP setup. The results are shown in Figure 2.

The major contributions to the uncertainty were yielded by the measurements of the laser wavelength with a spectrometer and the signal to noise ratio of the measured signals, combining the stability of the laser system and the electrical measurement. These uncertainty components of the filter transmittance contribute directly to the measurement uncertainty of the spectral irradiance responsivity of the photometric trap detector system and to the respective uncertainty of the luminous responsivity.

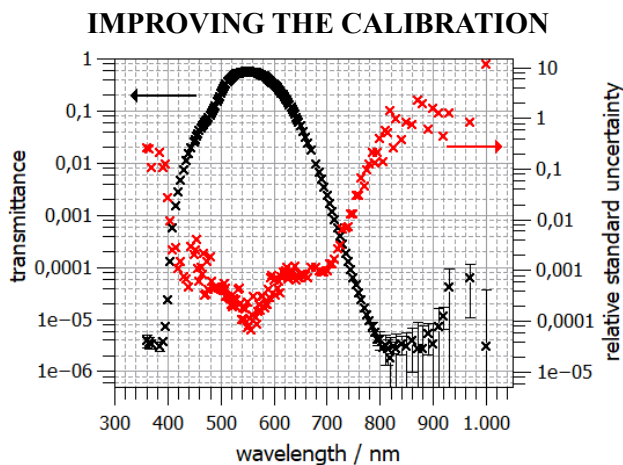


Figure 2. Spectral transmittance of the photometric filter plotted on a logarithmic scale (black symbols) and the corresponding relative standard uncertainty (red symbols).

UNCERTAINTIES

To enable a lower uncertainty of these calibration steps we have done improvements on the TULIP facility. As an additional radiant source, a mode-locked picosecond laser system tuneable from 230 nm to 2300 nm has been installed and is characterized for calibration of the trap detector.

The picosecond laser offers several advantages for the measurements compared to the femtosecond system. The picosecond laser beam has a maximum spectral bandwidth of 0.5 nm within the spectral range of interest. This means that no bandpass additional limiting monochromator is needed. In addition, the wavelength of such a narrow spectral distribution can be measured directly by a laser spectrum analyser with an improved uncertainty compared to the conventional spectrometer that is used for measuring the wavelength of the femtosecond laser.

The measurements of the filter transmission determining the spectral irradiance responsivity of

the trap detector system are repeated following the upgrade of the TULIP setup by the picosecond laser system. The results of the new measurements will be compared to the existing ones.

REALIZATION OF THE LUMINOUS INTENSITY UNIT

Considering the above-mentioned measurements, the detector system can be ascribed with the spectral irradiance responsivity values and the associated uncertainties including correlations. Based on these values, the luminous responsivity can finally be assigned.

A comparison between the current realization of the luminous intensity unit at PTB and the results obtained following the discussed calibration steps will be done. Nevertheless, this is just a first step towards implementing a new strategy for the traceability of the luminous intensity unit at PTB.

Before implementing this new strategy, a thorough investigation of the new realization needs to be done with respect to the stability of this radiometric detector-based approach. This includes establishment of a network of calibrated detectors, determining their individual aging rates, implementing regular calibration of the multiple detectors, apertures, filters and a long-term observation of the values resulting from the new calibration strategy compared to the values of the unit currently maintained by a group of standard incandescent lamps.

REFERENCES

1. P. Schneider et al., Improved calibration strategy for luminous intensity, *J. Phys.: Conf. Ser.*, 972, 012016, 2017
2. M. Schuster et al., Validation of short-pulse-laser-based measurement setup for absolute spectral irradiance responsivity calibration, *Applied Optics*, 53, 13, 2815-2812, 2014

Simultaneous optical and electrical heating in dual-mode photodiode operation at room temperature

Marit Ulset Nordsveen¹ and Jarle Gran¹

¹*Justervesenet, Kjeller, Norway,*

Corresponding e-mail address: mas@justervesenet.no

In this work we investigate an alternative method for thermal detection with the dual-mode optical power detector, which combines both thermal and photocurrent detection of optical power in one device. By applying electrical heat and optical heat simultaneously, rather than in two separate steps, a closed-loop feedback control can be used to maintain the temperature while opening and closing the laser power shutter. Measurements using the new method are compared to the old method, where optical heating was done with an open circuit, with no electrical current flowing. The results demonstrate that simultaneous optical and electrical heating of the photodiode during electrical substitution is possible.

INTRODUCTION

The EMPIR project *chipS·CALe* [1] aims to develop a self-calibrating optical power detector, where thermal detection of incoming radiation is used as a reference to determine the internal losses of the photodiode absorber. The incoming radiation is converted either to a photocurrent, as in a traditional photodiode, or to heat, using electrical substitution to determine the power of the absorbed radiation. The photodiode is used as the absorber in both modes.

The internal quantum deficiency (IQD) of the photodiode is found from:

$$\delta(\lambda) = 1 - \frac{i_{photo}}{\Phi_T} \cdot \frac{hc}{e\lambda}, \quad (1)$$

where Φ_T is the absorbed optical power measured in thermal mode, i_{photo} is the measured photocurrent, λ is the wavelength of the incoming radiation and h, c and e are Planck's constant, the speed of light in vacuum and the elementary charge, respectively.

In thermal mode, all absorbed radiant energy is converted to heat, which is then compared to an equivalent amount of electrical heat with known power. In a conventional electrical substitution radiometer (ESR), the electrical heat is usually applied by an external heater attached to the absorber. However, in the dual-mode detector, the electrical heat is applied by a forward bias voltage across the photodiode. In this way, the electrical heat is

dissipated inside the photodiode, and the amount of power is found from $P = IV$, where I and V are the measured current through and voltage across the photodiode.

In our previous work on the dual-mode detector, optical and electrical heating were applied separately [2]. During optical heating, the electrical circuit was open, so no current could flow. This ensures that all absorbed power is converted to heat.

In this work, we investigate the possibility of applying a forward bias voltage to the photodiode during optical heating. By applying optical and electrical power at the same time, the temperature can be maintained at a constant level, by adjusting the electrical power in a closed feedback loop. In this way, the thermal optical power measurement will be less time-consuming, since there is no need for temperature stabilisation between each time the shutter is opened or closed. The only stabilisation required after toggling the shutter is the settling of the PI control loop, which might take a few seconds.

Furthermore, in designing the thermal link, there is a trade-off between time constant and signal level. Because closed loop operation is faster than the natural time constant of the detector, this method allows the thermal link to be designed to maximise the temperature signal and hence sensitivity. In addition, the detector will be less sensitive to ambient temperature variations, as the measurement can be carried out in less time.

EXPERIMENT

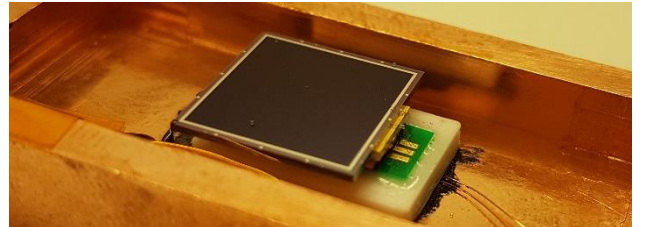


Figure 1. Photograph of the dual-mode detector, showing the 11 mm x 11 mm photodiode, the PLA heat link (white) and the copper carrier heat sink.

The dual-mode detector used in these measurements, shown in Fig. 1, is designed for room-temperature operation. The detector consists of a photodiode of 11

mm x 11 mm, mounted on a PLA heat link and placed in a copper carrier serving as the heat sink. The temperature is monitored with two germanium thermistors, one between the photodiode and the PLA heat link, and the other on the copper carrier heat sink. During measurements, the detector was screwed on to an additional copper heat sink inside a vacuum chamber at room temperature and irradiated with a 488 nm laser source. The heat sink was not temperature stabilised. Reflection losses are the same for both measurement modes and are hence irrelevant for the measurement of photodiode IQD.

In these measurements, made for demonstration purposes only, the electrical substitution was performed by switching between three levels:

- i. Low electrical heating
- ii. Optical + electrical heating
- iii. High electrical heating

The power levels of (i) and (iii) were chosen such that the temperature was slightly below and above the temperature level at (ii), respectively. The total power level of step (ii) was calculated based on the known electrical power levels at steps (i) and (iii). The optical power was then found by subtracting the electrical power from the total power of step (ii). A complete measurement series consisted of an initial photocurrent measurement, followed by five or ten heating cycles, with a second photocurrent measurement at the end. The IQD from four different measurements were compared. In the first two measurements, a forward bias voltage was applied to the photodiode during optical heating, with the addition of 250 μ W and 500 μ W electrical power to the optical power of 500 μ W. The last two measurements were performed with an open circuit during optical heating, the same way as in ref. 2, with an optical power of 500 μ W and 750 μ W.

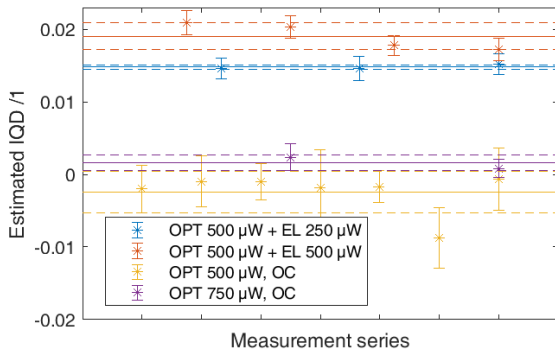


Figure 2. Estimated IQD from dual-mode measurements, with optical power of 500 μ W and additional 250 μ W and 500 μ W electrical power, and optical heating with no additional electrical power at 500 μ W and 750 μ W power.

RESULTS AND FUTURE WORK

The estimated IQD for the four different measurements is plotted in Fig. 2 and summarised in Table 1. The uncertainty given is the standard deviation of the mean.

The results show a deviation between the two methods of optical heating. The IQD when using an open circuit during optical heating is close to zero, and overlapping for different optical power levels, as expected. However, when applying an additional electrical power during optical heating, the estimated IQD increases with increasing electrical power, suggesting somehow an influence on the estimate of Φ_T by unaccounted series resistance. The results vary more than expected, and a more detailed study is needed. However, this work shows that a forward biased operation of the dual-mode detector is possible.

Table 1. Estimated optical power Φ_T and internal losses δ from dual-mode measurements, with and without additional electrical heating during optical heating.

Optical heating step:	Estimated Φ_T (μ W):	Estimated δ :
Opt. 500 μ W + 250 μ W el.	507.5 ± 0.3	0.015 ± 0.0003
Opt. 500 μ W + 500 μ W el.	509.5 ± 1.3	0.019 ± 0.002
Optical 500 μ W, open circuit	499.2 ± 1.4	-0.0024 ± 0.0029
Optical 750 μ W, open circuit	751.5 ± 1.0	0.0016 ± 0.0011

ACKNOWLEDGEMENTS

Thanks to Malcolm G. White for helpful discussions. The version of the dual-mode detector used in these measurements was designed and made at the University of South-Eastern Norway.

This project has received funding from the EMPIR programme co-financed by the Participating States and from the European Union's Horizon 2020 research and innovation programme.

REFERENCES

1. J. Gran. (2019, June 26). Publishable Summary for 18SIB10 *chipS·CALe*. Zenodo. <http://doi.org/10.5281/zenodo.3545677>
2. M. U. Nordsveen, C. K. Tang and J. Gran (2017). Demonstration of a dual-mode Si detector as a self-calibrating device at room temperature, Optics Express 25(8): 8459-8469.

Development of a pyroelectric detector-based method for low uncertainty irradiance and radiance calibrations in the short-wave infrared

Brian G. Alberding, John T. Woodward, Ping-Shine Shaw, Leonard M. Hanssen, Catherine C. Cooksey, and Joseph P. Rice

*National Institute of Standards and Technology, Gaithersburg, MD, USA
brian.alberding@nist.gov*

The uncertainty of detector-based radiance and irradiance responsivity calibrations in the short-wave infrared (SWIR) traditionally has been limited to around 1% or higher by the low spatial uniformity of detectors used to transfer the scale from radiant power. Pyroelectric detectors offer a solution that avoids the spatial uniformity uncertainty, but also introduces additional complications due to alternating current (AC) measurement techniques; there is additional uncertainty when using lock-in amplifiers. Herein, a new method for low uncertainty irradiance responsivity calibrations in the SWIR is presented. An absolute irradiance responsivity scale was placed on a pyro-electric detector with total combined uncertainty ($k=1$) of 0.5% without using a lock-in amplifier.

PYROELECTRIC IRRADIANCE SCALE

At the National Institute of Standards and Technology (NIST), a method for calibrating instruments directly in irradiance or radiance mode using high power, narrow bandwidth lasers has been in use for about 20 years [1,2]. Typically, low uncertainties are achieved by traceability to the NIST Primary Optical Watt Radiometer (POWR) [3] and the NIST Aperture Measurement Facility [4]. In short, a transfer standard detector equipped with a precision aperture is calibrated by POWR with a laser in an underfilled configuration. Irradiance responsivity is therefore determined but the uncertainty is limited by the uniformity of the transfer detector. This method works well in the silicon detector region, where highly uniform trap detectors are available. In the short-wave infrared (SWIR), current indium gallium arsenide (InGaAs) or extended InGaAs (ex-InGaAs) detectors, for example, do not have sufficient uniformity. Pyroelectric detectors offer a potential solution to this problem where an irradiance scale traceable to POWR in the SWIR can be achieved with uncertainties approaching those obtained in the silicon spectral region.

We use a pyroelectric detector with organic black coating as our transfer standard. The coating has low reflectance on the order of a few percent and the transmittance of the coated pyroelectric element is negligible. If the spectral reflectance, $A(\lambda)$, of the detector can be measured independently over a desired wavelength range, then the spectral absorptance, $A(\lambda)$, can be derived using Eq. (1). Because the power or irradiance responsivity of a pyroelectric detector is spectrally flat against absorptance [5], the responsivity of the detector over the entire wavelength range with measured reflectance can be determined by using a single tie point responsivity measured at a single wavelength in the silicon trap spectral range.

$$A(\lambda) = 1 - R(\lambda) \quad (1)$$

ALTERNATING CURRENT SIGNAL PROCESSING

Using a pyroelectric detector also introduces other problems for radiometric calibrations resulting from the requirement that an AC signal is measured. A typical strategy is to modulate the light source by a chopper and process the induced quasi-square waveform detector signal with a lock-in amplifier. The signal output from the lock-in amplifier is derived from the amplitude of the first harmonic of the waveform, which introduces the requirement of calibrating the lock-in amplifier used for a correction factor to determine the DC response of a test detector. Additionally, transient regions in the quasi-square waveform could cause large errors in the resulting output signal (i.e. there is a settling time that must be considered).

In this work, we collected the AC waveform digitally using a modern high-sampling-rate analog-to-digital converter (avoiding the use of a lock-in amplifier) as shown in Fig. 1, and removed unwanted portions of the transient regions to determine the DC offset signal with higher accuracy. For irradiance response measurements, where the pyroelectric detector has a relatively low signal-to-noise, this

method allowed us to maintain the main benefit of a lock-in amplifier, namely picking out modulated signals from high noise, without the added complications. At a chopping frequency of 10 Hz, we could also obtain a relatively large number of samples in a short amount of time (1-minute measurements yield 600 independent measurements) to yield better measurement standard deviation of the mean.

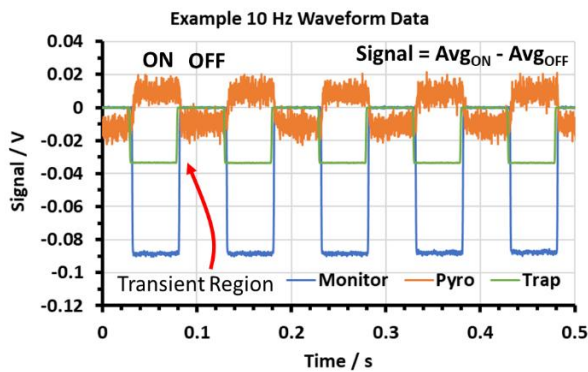


Figure 1: Representative 10 Hz waveform data for the silicon trap (green) pyroelectric (orange) and monitor (blue) detectors.

RESULTS

Using this method, we have performed the scale transfer from a POWR-calibrated Si trap irradiance detector to a pyroelectric irradiance detector as shown in Fig. 2. The reflectance spectrum of the black coating was measured from 834 nm to 3393 nm on a witness pyroelectric detector sample representative of the actual detector absorptance manufactured in such a way to provide complete hemispherical access to the front surface while maintaining optically identical design as a real detector without the electrical connections. The irradiance scale was transferred from the silicon trap irradiance detector at 849 nm yielding the absolute spectral *irradiance* responsivity with a combined standard uncertainty ($k=1$) of 0.5%, where the dominant uncertainty components were the irradiance measurement standard deviation (due to low signal-to-noise of the pyroelectric detector) and the witness sample absorptance.

SUMMARY

Herein, we detail our efforts to provide a low uncertainty absolute irradiance responsivity scale in the SWIR using a pyro-electric detector. We used an AC detection method without a lock-in amplifier that simplifies the overall calibration chain by digitally processing the data. Current state-of-the-art irradiance responsivity calibrations in the SWIR

typically have uncertainties on the order of 1% or more. In this work we achieved 0.5% ($k=1$) uncertainty for absolute *irradiance* responsivity using a pyroelectric detector. It should be noted that there is still room for improvement with these methods as described. First, we have only averaged our measurements over timescales of ~ 1 minute. Further improvements could be made simply for averaging longer time to reduce the measurement standard deviations. Second, there is room for improvement in the design of the pyroelectric detectors. Fabrication with less reflective coatings (for example by adding carbon nanotubes) could yield improvement in the irradiance scale transfer, which is reliant on the absorptance of the detector black coating.

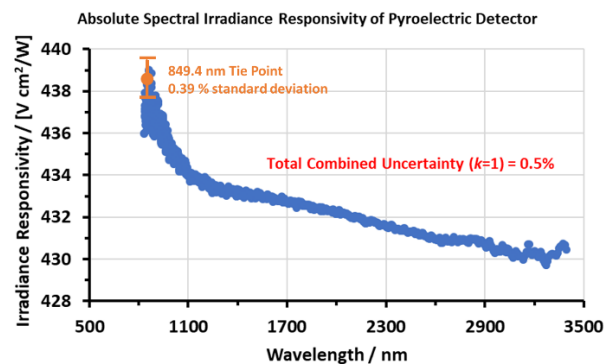


Figure 2: Absolute spectral irradiance responsivity of the pyroelectric detector determined from the witness sample reflectance and a tie point with the silicon trap detector at 849 nm.

REFERENCES

1. Brown, S. W., Eppeldauer, G. P. and Lykke, K. R., Facility for spectral irradiance and radiance responsivity calibrations using uniform sources, Appl. Opt., AO 45, 8218–8237, 2006.
2. Woodward, J. T., Shaw, P.S., Yoon, H.W., Zong, Y., Brown, S.W., and Lykke, K.R., Invited Article: Advances in tunable laser-based radiometric calibration applications at the National Institute of Standards and Technology, USA, Review of Scientific Instruments 89, 091301, 2018.
3. Houston, J. M. & Rice, J. P. NIST reference cryogenic radiometer designed for versatile performance, Metrologia 43, S31, 2006.
4. Fowler, J. and Litorja, M., Geometric area measurements of circular apertures for radiometry at NIST, Metrologia 40, S9–S12, 2003.
5. Eppeldauer, G., Podobedov, V., Hanssen, L., and Cooksey, C., Low-NEP pyroelectric detectors for calibration of UV and IR sources and detectors, Proceedings of SPIE Optical Engineering and Applications, San Diego, California, Proc. Of SPIE Vol. 10378 1037809-1, 2017.

Electrical-Substitution Fourier Transform Spectrometry for Absolute Calibration of Detector Responsivity

J.E. Neira¹, J.E. Proctor¹, S.I. Woods¹, J.P. Rice¹, N.A. Tomlin², M. White², M. Stephens² and J.H. Lehman²

¹National Institute of Standards and Technology (NIST), Gaithersburg, MD 20899, USA

²National Institute of Standards and Technology (NIST), Boulder, CO 80305, USA

Corresponding e-mail address: solomon.woods@nist.gov

We have developed a generalized method for electrical substitution which can operate at time constants compatible with continuous-scan Fourier transform spectrometry, and have applied the method successfully to measure absolute detector spectral responsivity from 1.5 μm to 11 μm . For this project we have also fabricated and characterized a carbon-nanotube planar bolometric radiometer optimized for this application. When combined, the new electrical-substitution electronics and radiometer could provide high-resolution absolute spectral responsivity from 1.5 μm to 50 μm , calibrated directly against a primary standard detector.

INTRODUCTION

Absolute cryogenic radiometers (ACRs) are the basis for most detector-based optical power scale realizations, but these electrical-substitution (ES) primary standards are typically slow ($\tau > 1$ s) and of limited use for spectral calibrations. Cryogenic ES bolometers can be significantly faster [1,2] and the ES method can be generalized beyond shuttered measurements [3], so it is possible to realize a much more versatile and higher-speed ACR. These primary standard detectors can exploit the inherent noise advantage of AC measurements and can be coupled with continuous-scan Fourier transform spectrometers (FTS) for absolute spectral calibrations.

We have developed electronics for electrical-substitution-with-FTS (ES-FTS) and a new planar bolometric radiometer (PBR) with an absorber made from vertically-aligned carbon nanotubes (VACNTs). The electronics and related firmware can actively control the temperature of a bolometer experiencing any periodic optical signal, and the PBR has a time constant of around 10 ms. We have developed the ES-FTS method and verified the function of the electronics with a test ES bolometer (ESB) [1], while fabricating the new PBR in parallel.

The first application for the ES-FTS primary standard radiometer is for a detector comparator

instrument which can measure absolute spectral responsivity of a detector-under-test (DUT) against the ACR. We have built-up and tested such an ES-FTS detector comparator using a commercial FTS and our electronics.

ES-FTS PROCEDURES AND ELECTRONICS

The layout for our ES-FTS detector comparator is shown in Figure 1. Both the high-speed ACR and the DUT measure the same beam from the FTS, which can be focused ($f/8$) onto either detector with a parabolic mirror on a rotation stage. The electrical substitution can “keep up” with the metrology signals from the FTS when operating at a 100 Hz scan rate in continuous-scan mode.

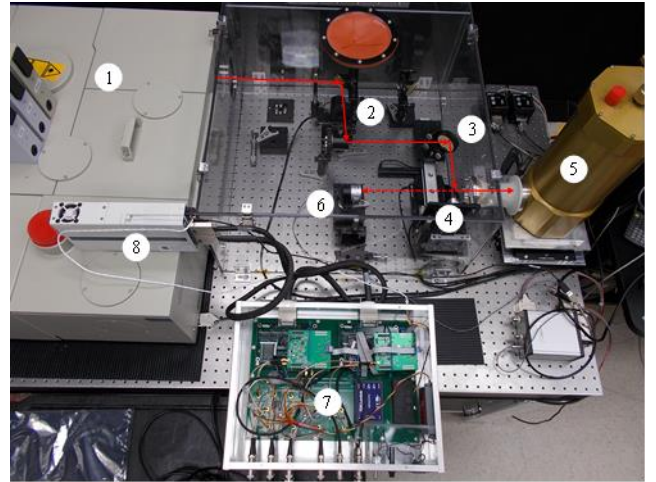


Figure 1. Spectral comparator layout with the following labeled components: 1) FTS, 2) spatial filter, 3) fold mirror, 4) rotating paraboloid, 5) ACR, 6) DUT, 7) ES-FTS electronics, and 8) FPGA.

In typical “DC” electrical substitution an ACR is temperature-controlled while opening and closing a shutter in front of the beam: the extra heat required to maintain the temperature with shutter closed is equivalent to the optical power. Generalized electrical substitution depends on determining the electrical heating waveform which must be applied to the ACR heater in sync with the interferometric optical signal in order to achieve net AC signal near zero from the

ACR thermistor. The governing relation for the ACR thermistor resistance is very similar to standard FTS relations, with the optical spectrum $B(\nu)$ replaced by $B(\nu) \cdot G(\nu)$, where $G(\nu)$ is the complex response (including gain and delays) of the ACR resistance. For a well-made ACR, there is an equivalence between applied optical and electrical power, and the governing relation is identical whether $B(\nu)$ represents the optical or electrical spectrum.

Determination of the required feedback function is made according to the following procedure: first, $G(\nu)$ is estimated by measuring ACR thermistor response to a known electrical heater waveform; second, the estimated $G(\nu)$ is used to calculate the heater waveform required to cancel the measured optical signal; third, this feedback is applied to cancel the optical pulse; then, all these steps are iterated starting from the remainder signal achieved in the third step. Multiple iterations are required to achieve good cancellation because ACR thermistor response as a function of power is not generally linear, but no more than 3 iterations are usually required to achieve cancellation $> 99\%$. Figure 2 is an example of successful cancellation of the ESB signal. After cancellation is achieved, the small leftover portion is averaged over many scans and quantified along with the electrical feedback power required to cancel the optical signal.

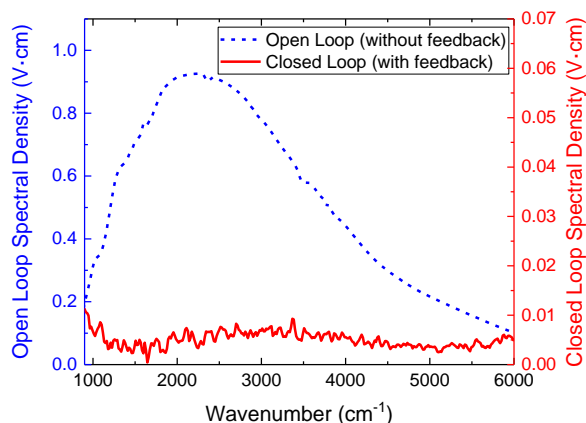


Figure 2. Open and closed loop data for an ES-FTS measurement with the ESB detector, showing $> 99\%$ cancellation by feedback in the closed loop case.

The digital acquisition and feedback are controlled by a commercial field-programmable gate array (FPGA). Timing metrology signals fed from the FTS to the FPGA are used to sync the electrical and optical measurements. Seven channels of analog-to-digital input to the FPGA include: 2 channels for FTS metrology, one for the ACR thermistor, 3 for the ACR

heater, and one for the DUT. One channel of digital-to-analog output sends the feedback signal to the ACR heater.

HIGH-SPEED ES DETECTORS

We have successfully tested our generalized ES method and electronics with a gold-black ESB detector [1], while developing an optimized carbon-nanotube PBR in parallel. The ESB AC response has a 3 dB point (1/2 of max signal) at about 30 Hz, and the gold-black coating provides near-unity absorption out to around $12\ \mu\text{m}$. Used in a cryostat with a BaF_2 window, it can serve as an ACR over the spectral range from $1.5\ \mu\text{m}$ to $11\ \mu\text{m}$. The PBR (which is shown in

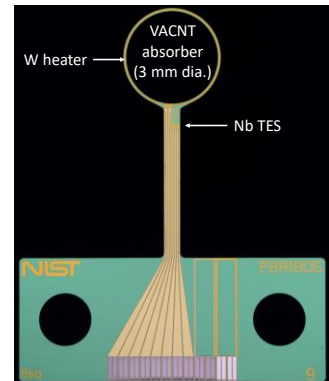


Figure 3. Photo of PBR.

Figure 3) has been fabricated and characterized, and exhibits AC response with a 3 dB point at about 100 Hz. The vertically-aligned carbon nanotubes provide near-unity absorption out to $50\ \mu\text{m}$, and in a cryostat with a CsI window the PBR is expected to serve as a high-speed ACR from $1.5\ \mu\text{m}$ to $50\ \mu\text{m}$.

CONCLUSIONS AND SUMMARY

The ES-FTS method and electronics have been demonstrated, and we have developed a fast carbon nanotube PBR optimized for absolute spectral measurements with an FTS. The ES-FTS method has been applied to a detector spectral responsivity instrument, which can provide absolute spectral responsivity from direct comparison with an optical power primary standard detector. The last step of the project will be to operate the new PBR in ES-FTS mode, and to intercompare its measurements with those of legacy ACRs.

REFERENCES

1. J.P. Rice, An electrically substituted bolometer as a transfer-standard detector, *Metrologia*, 37, 433-436, 2000.
2. N.A. Tomlin, M. White, I. Vayshenker, S.I. Woods, J.H. Lehman, Planar electrical-substitution carbon nanotube cryogenic radiometer, *Metrologia* 52, 376-383, 2015.
3. C.A. Hamilton, G.W. Day, R.J. Phelan, Jr., An electrically calibrated pyroelectric radiometer system, NBS Technical Note 678, National Bureau of Standards, 1976.

NIST's primary optical power responsivity scale realized using a supercontinuum source with automation from 480 nm to 1650 nm

Ping-Shine Shaw and Joseph P. Rice

*Sensor Science Division
National Institute of Standards and Technology
Gaithersburg, MD 20899, USA
Corresponding e-mail address: shaw@nist.gov*

Traditionally, the optical power responsivity scale at NIST was transferred from cryogenic radiometers using various quasi-CW tuneable lasers from the UV to IR. While this technique achieves very low measurement uncertainty, there are several drawbacks that make routine calibration difficult. For example, the complex laser system requires well-trained personnel to operate. Wavelength tuning often requires manual adjustment of laser optics which makes the optical power measurement over many wavelengths very time consuming and labor intensive. Here, we describe a newly-developed system based on the supercontinuum source. This is a truly turn-key system and is fully automated such that many wavelengths over a wide range can be measured without human intervention. Most importantly, the typical detector calibration uncertainty of 0.04 % ($k=1$) obtained in the visible spectral range is very comparable to those achieved with lasers and still better than usually required.

INTRODUCTION

In the last decade, NIST took advantage of the fast-evolving optical technology and used the Primary Optical Watt Radiometer (POWR) cryogenic radiometer [1] in conjunction with tuneable quasi-CW lasers to achieve measurement uncertainty in the 10^{-4} level on optical power responsivity measurements. This forms the primary optical power responsivity scale which has been disseminated to many other metrology measurements at NIST. In the beginning days of the use of lasers as light sources with cryogenic radiometers, the general practice was to measure a few wavelengths in the silicon wavelength range as tie points and rely on the responsivity model [2] to fill in other wavelengths. As measurement uncertainty dropped, the trend today is to use tuneable lasers to directly measure a wide wavelength range at a typical wavelength interval of 5 nm or 10 nm, thus eliminating uncertainties caused

by spectral modelling. While this can be done [3], such fine-wavelength calibration requires months of effort with intensive labor. This is mainly caused by the frequent manual adjustment of the laser from wavelength to wavelength and the switching between several lasers in order to cover the entire wavelength range. An additional problem caused by using a narrow-band laser is the fringing effect which excludes calibration on windowed detectors.

To overcome these problems, we developed a new optical system that employs a broadband Supercontinuum (SC) source for detector optical power responsivity calibration while maintaining uncertainties comparable to those obtained by lasers.

MEASUREMENT SETUP AND RESULTS

Fig. 1 shows the basic schematic for POWR-based detector responsivity calibration using the SC. Our particular SC has a useable wavelength range from 480 nm to just under 2000 nm, and newer versions have broader spectral range. The SC output is fiber-

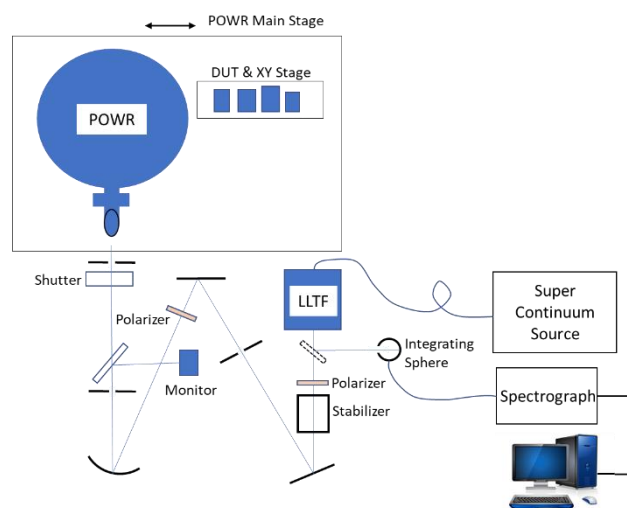


Figure 1. POWR based detector responsivity measurement setup.

coupled to a computer-controlled monochromator (labelled LLTF in Fig. 1). The output is a slightly divergent laser-like beam with about 1 nm bandwidth.

The wavelength of the beam is calibrated by a spectrograph which, in turn, was calibrated by spectral lamps.

Downstream from the LLTF, the beam passes through a polarizer followed by an intensity stabilizer. Then it is spatially filtered, re-polarized, re-collimated, and directed into POWR or the test detectors. The incident light onto POWR and test detectors has a diameter of about 1 mm and a typical power on the order of 100 μ W. Great care was taken to shape the light beam to ensure the beam underfills POWR and the test detectors with minimum stray light. The system is fully automated and controlled by a single computer which commands the wavelength of the LLTF, the stage or the placement of POWR and test detectors, and acquires all signals from POWR, monitor diode, and test detectors.

Fig. 2 shows the calibrated External Quantum Efficiency (EQE) of a 6-element trap detector T04 using the SC/LLTF from 480 nm to 1000 nm at a 5 nm interval.

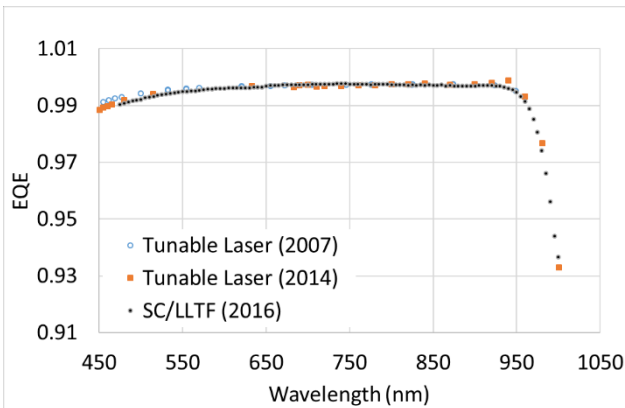


Figure 3. Power responsivity of trap detector T04 measured with tunable lasers and SC.

Also shown in Fig. 2 for comparison are the power responsivities of the same detector measured in previous years using tuneable lasers. Other than the short wavelength end, where the detector is known to degrade over the years, and the long wavelength end, where the detector is subject more to temperature variation, there is good agreement between calibrations using tuneable lasers and SC/LLTF and the variation is well within the measurement uncertainty. Notice the regular and high-density nature of the data for SC/LLTF calibration as compared to the more sparse and irregularly-spaced data points when tuneable lasers were used.

Fig. 3 shows the estimated overall standard uncertainty of the trap detector responsivity using

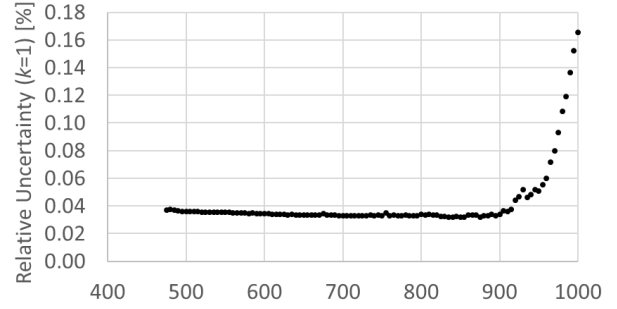


Figure 2. Estimated relative overall uncertainty on the trap responsivity at $k=1$.

SC/LLTF. Other than the long end of the wavelength range, the uncertainty is generally under 0.04 %. This compares favourably with the 0.02 % to 0.03 % uncertainty obtained by calibration using tuneable lasers. The slight increase in overall uncertainty is mainly due to the increased wavelength uncertainty of the much wider bandwidth of ~ 1 nm of the SC/LLTF. In addition to the trap detector calibrations, we have also used this system for calibrating many single element photodiodes, both windowed and non-windowed, such as Si and InGaAs detectors, with satisfactory results.

CONCLUSION AND OUTLOOK

We have shown that SC/LLTF can be used as a light source for ACR-based power responsivity calibration with comparable uncertainty as using tuneable lasers. Without the complex laser system, this much simplified system is fully automated and can calibrate many wavelengths automatically. For calibrations involving a wide wavelength range with many wavelengths, this system can reduce the measurement time from months to days. At NIST, our current strategy for maintaining our power responsivity scale is to use the SC/LLTF system for routine calibration while operating our tuneable lasers only at a few selected wavelengths to serve as a validation of SC/LLTF calibration.

REFERENCES

1. J. M. Houston and J. Rice, "NIST reference cryogenic radiometer designed for versatile performance," *Metrologia*, 43, S31-S35 (2006).
2. T.R. Gentile, S.W. Brown, K.R. Lykke, P.S. Shaw, and J. T. Woodward, "Internal quantum efficiency modeling of silicon photodiodes," *Appl. Opt.* 49, 1859-1864 (1996).
3. J. Woodward, P. S. Shaw, H. Yoon, Y. Zong, S. W. Brown, and K. R. Lykke, "Invited Article: Advances in Tunable Laser-based Radiometric Calibration Applications at the National Institute of Standards and Technology, USA" by *Rev. Sci. Instr.* 89, 091301 (2018).

Novel Integrating Sphere Based Attenuation Method for Single Photon Detector Calibrations

Damian Twerenbold, Florian Stuker and Peter Blattner

Federal Institute of Metrology METAS, Bern-Wabern, Switzerland

Corresponding e-mail address: peter.blattner@metas.ch

The currently used single photon detectors in quantum technology fields are silicon single-photon avalanche diodes (Si-SPADs). The most crucial parameter in those applications is the detection efficiency of those detectors. We have participated in the pilot study of the CCPR WG-SP TG 11 for determining the detection efficiency of Si-SPADs single-photon detectors at a wavelength of 850 nm in free-space beam using the double attenuation filter protocol. Using various lasers, we have extended our measurements from 500 nm to 900 nm. In this paper, we propose a novel method where an integrating sphere is used as the (second) attenuator. Our first experimental results show that the wavelength dependence of the detection efficiency of our Si-SPADs using the sphere attenuation method follow the same curve as the one determined by the absolute detection substitution technique.

INTRODUCTION

For determining the detection efficiency of Si-SPAD detectors two approaches can be used: the two-photon correlation technique [1] or the detection substitution technique, which uses a strongly attenuated laser and a reference detector [2]. In the pilot study of the CCPR WG-SP TG 11, the latter technique is used. We have also participated in this pilot study (measuring detection efficiency at 850 nm) but also extended our measurements to the wavelength range from 500 to 900 nm using various lasers in order to determine the wavelength dependence of the detection efficiency of our Si-SPADs. Because we wanted to use our tuneable-pulsed laser which is tuneable from 200 nm to 2000 nm, we had to develop an alternative method for measuring the detection efficiency. This owing to the fact that the photon flux per laser pulse (100 μ J in a pulse duration of 4 ns) is very high and the standard filter attenuation method fails owing to saturation effects in the reference detector and the impossibility to create single photon flux at the position of the SPAD.

EXPERIMENTAL SETUP

When one uses the detection substitution technique, typically two strong attenuation filters are required in order to link the sensitive range of the Si-reference detector and the single photon-counting mode of the SPAD. In our sphere attenuation setup, we basically replace the second attenuation filter by an integration sphere and decrease the photon flux to the single photon counting level by separating the SPAD by a large distance from one of the exit ports of the sphere. At the same time, we measure the photon flux in the integrating sphere by a Si-reference detector, allowing us to link the single-photon counting rate at the SPAD to the SI-traceable photon flux reference. Figure 1 shows the experimental setup:

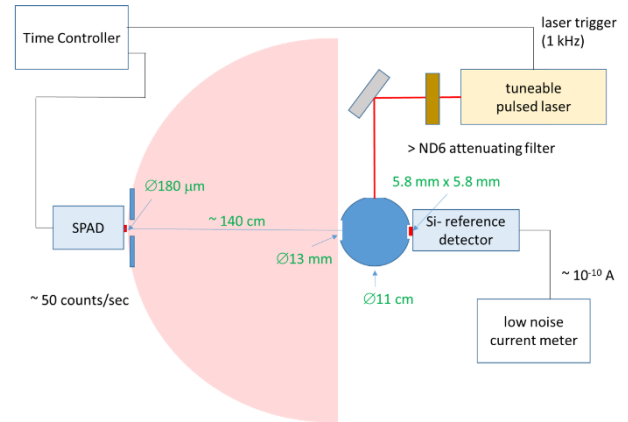


Figure 1. Experimental setup for the integrating sphere attenuation method.

The pulsed laser beam is directed into the entrance port of the integrating sphere. This entry beam is strongly attenuated such that the reference Si-detector can still operate in a linear non-saturating mode. The Si-SPAD is placed at a sufficiently large distance (typically more than 1 m) from a second port of the integrating sphere such that the photon flux is substantially reduced to a single-photon counting level at the position of the Si-SPAD. The Si-reference detector signal is measured by a low-noise current

meter with a good signal-to-noise at 10^{-10} A. The single photon count rate of the SPAD is measured by counting the digital pulses from the SPAD in a time controller which is triggered by the pulsed laser. In order to be sure that one is operating in the single-photon counting mode, typically most laser pulse triggers do not create a SPAD signal. In our setup we measured in the average 30 counts per second at a laser repetition rate of 1 kHz.

RESULTS

Using the detection substitution technique [2] we have measured the absolute detection efficiency of our various Si-SPADs using our tuneable Ti:sapphire laser pumped by a diode-pumped solid-state laser at 532 nm. The following figure 2 shows our experimental results:

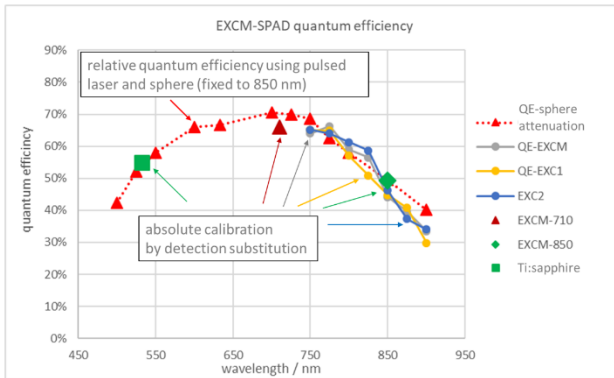


Figure 2. Results comparing our sphere attenuation method (relative measurement) to absolutely calibrated values.

Most of the data points in figure 2 are absolute detection efficiencies for the various Si-SPADs and laser wavelengths using the detection substitution technique. Superimposed are the (relative) detection efficiencies as determined by our pulsed laser and sphere attenuation technique. These results are shown as red triangles, which are connected by a dotted line (for visualization this relative detection efficiencies are fixed to the 850 nm absolute detection efficiency result).

CONCLUSION

Using our sphere attenuation method in combination with a continuously wavelength tuneable pulsed laser, we found a fast way to measure the wavelength dependence of the detection efficiency of a Si-SPAD (relative measurement). We would like to note that this sphere attenuation method could be converted to

an absolute method when all the geometrical factors in figure 1 are known within the required uncertainties. One of the critical issues of our method will be the uncertainties produced by the stray light coming from sources other than the exit window of the integrating sphere directed to the Si-SPAD.

REFERENCES

1. S.V. Polyakov et al., Single-Photon Detector Calibration, Proc. SPIE Vol. 6372, 2006
1. K. Dhoska et al., Improvement of the detection efficiency calibration and homogeneity measurement of Si-SPAD detectors, SpringerPlus, Vol 5, 2016

Recent Progress on Calibration of Spectroradiometers using Tunable Lasers

Yuqin Zong, Ping-Shine Shaw, and C. Cameron Miller

National Institute of Standards and Technology, Gaithersburg, Maryland, USA

Corresponding e-mail address: yuqin.zong@nist.gov

To reduce calibration uncertainties of spectroradiometers, we developed a detector-based method for calibrating spectroradiometers directly (one-step) against transfer-standard trap detectors using a tunable laser. Recently, we conducted more research on spectroradiometer's wavelength calibration and the uncertainty was reduced to approximately 0.25 % ($k = 2$), which is much smaller than that using the conventional calibration method based on transfer-standard lamps. The calibrated spectroradiometer is also a new transfer-standard detector for spectral irradiance or radiance scale.

1. INTRODUCTION

Traditionally, spectroradiometers have been calibrated using transfer-standard broadband light sources such as 1000 W FEL lamps (or deuterium lamps in the ultra-violet region). Using this source-based calibration method, the uncertainty of a spectroradiometer, dominated by the uncertainty of transfer-standard light sources [1], is typically about 1 % in the visible to infrared region and much larger in the ultra-violet region. Compared to transfer-standard detectors the transfer-standard light sources (which are mostly discontinued by the lamp manufacturers) have quite large uncertainties, mainly resulting from the long chain of calibrations to establish their traceability. For example, the spectral irradiance of a 1000 W FEL lamp is derived and transferred in sequence from (1) primary cryogenic radiometer, (2) transfer-standard trap detector, (3) reference field radiometer, (4) gold point blackbody, and (5) high temperature blackbody.

To reduce the calibration uncertainty, we developed a new detector-based method for calibrating spectroradiometers directly (one-step) against transfer-standard trap detectors using a fully automated tuneable laser [2]. This method was improved recently, mainly on spectroradiometer's wavelength calibration and the calibration uncertainty for a spectroradiometer's spectral irradiance responsivity was reduced to approximately 0.25 % ($k = 2$). A spectroradiometer calibrated using

this low-uncertainty method can become a new transfer-standard detector for spectral irradiance or radiance scale which can then be transferred again to other detectors or even sources for further downstream dissemination.

2. THE NEW CALIBRATION METHOD

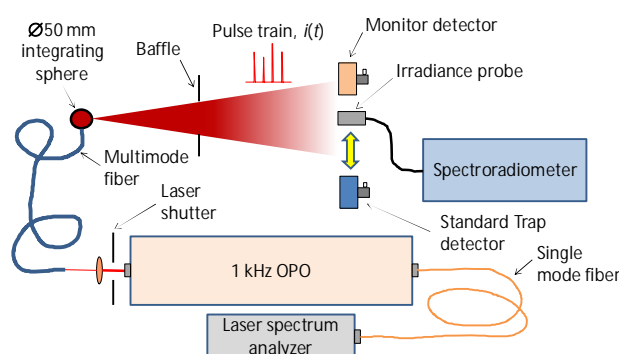


Figure 1. Schematic of the new calibration method

A schematic for calibration of an irradiance spectroradiometer is shown in Figure 1. A 1000 Hz, fully automated tunable (210 nm to 2400 nm) optical parametric oscillator (OPO) laser is used for this calibration. The bandwidth of the OPO laser is approximately 0.2 nm in the visible region. A laser spectrum analyser (LSA) is used for measurement of the wavelength of OPO laser. The wavelength scale of the spectroradiometer is calibrated against the LSA with a standard uncertainty on the order of a picometer [3].

The calibration is based on the measurement of the total energy of a pulsed OPO train. The length of the pulsed OPO train, controlled by a laser shutter, can vary from 1 s to 10 s depending on the laser power. A monitor detector is mounted near the test spectroradiometer or the transfer-standard trap detector to measure the relative total energy of an OPO pulse train. The calibration uses the substitution method where the transfer-standard trap detector and the irradiance probe of the test spectroradiometer are positioned, in turn, to the center of the optical beam. Two charge integrators (not shown in Figure 1) are used for simultaneous measurements of the total electric charge in unit of coulomb: one for the

transfer-standard trap detector and the other for the monitor detector.

Before the calibration, the stray light of the spectroradiometer is characterized such that all ensuing measurements are corrected [4] for out-of-band contribution.

For this calibration, we measured both line spread functions (LSFs) and slit scattering functions (SSFs) of the spectroradiometer under test. An LSF describes the response as a function the pixel for a given wavelength, while an SSF is the response of a pixel as a function of the wavelength for a given pixel. The LSF calibration does not require fine tuning of the laser wavelength to obtain the responsivity at a wavelength. Therefore, fixed wavelength lasers can be used to calibrate or check the responsivities of the spectroradiometer.

3. RESULTS OF CALIBRATION

Several CCD-array spectroradiometers were calibrated to validate the new calibration method. Figure 2 shows a measurement repeatability when

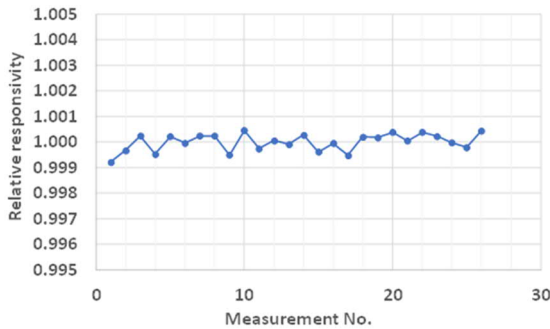


Figure 2. Measurement repeatability

using the LSF method. Also, both LSF method and SSF method were used for calibrating a spectroradiometer. The agreement of the calibration results for this spectroradiometer is shown in Figure 3,

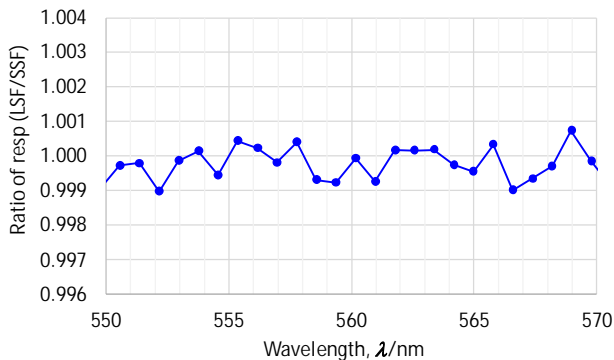


Figure 3. Comparison of LSF method and SSF method which is approximately 0.1 %. The calibration result

using the LSF method is also compared with that obtained using a transfer-standard FEL lamp and the agreement is within the combined expanded uncertainty ($k = 2$) of the two methods (Figure 4).

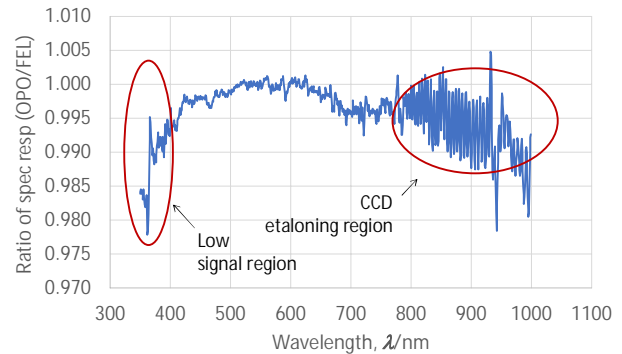


Figure 4. Comparison of spectral irradiance responsivities

4. SUMMARY

A fully automated method was developed for calibrating spectroradiometers directly (one-step) against transfer-standard trap detectors using a tunable laser. This new calibration method not only reduces spectroradiometer's calibration uncertainties but also enables a new approach to realize spectral irradiance or radiance scale. Each calibrated spectroradiometer is, in fact, a new detector-based transfer standard that can further calibrate secondary transfer-standard instruments and even transfer-standard sources for disseminating spectral irradiance and radiance scales with small uncertainties.

ACKNOWLEDGEMENTS

The authors want to thank Steven Brown, Joe Rice, Charles Gibson, John Woodward, Howard Yoon, Benjamin Tsai, Maria Nadal of NIST and Justin Blank of Instrument Systems for their supports on this research.

REFERENCES

1. H. W. Yoon and C. E. Gibson, NIST Special Publication 250-89, NIST Measurement Services - Spectral Irradiance Calibrations, NIST, Gaithersburg, 2011.
2. Y. Zong, P. S. Shaw, J. P. Rice, and C. C. Miller, Calibration of spectroradiometers using tunable lasers, CIE $\times 046:2019$, 569-574, CIE Central Bureau, Vienna, Austria, 2019.
3. Y. Zong, Wavelength Calibration Method for Spectroradiometers with Picometer Uncertainty, CIE $\times 044:2017$, 736-739, CIE Central Bureau, Vienna, Austria, 2017.
4. Y. Zong, S. W. Brown, B. C. Johnson, K. R. Lykke, and Y. Ohno, Simple spectral stray light correction method for array spectroradiometers, Applied Optics, 45, 1111-1119, 2006.

Near Infrared Spectral Responsivity Realization based on Cryogenic Radiometer

Xu Nan, He Yingwei, Liu Wende, Gan Haiyong, Wang Yangyang and Lin Yandong*

National Institute of Metrology, Beijing, China

Corresponding e-mail address: linyd@nim.ac.cn

A new monochromator-based cryogenic radiometer facility has been set up at the China National Institute of Metrology. The realization of the spectral responsivity scale in near infrared spectral range is presented based on the cryogenic radiometer facility which covers spectral range from 900 nm to 1600 nm. The uncertainty of spectral responsivity of the transfer standard detector is analysed.

INTRODUCTION

Lasers are commonly used at discrete wavelengths when calibrating responsivities of photodetectors against a cryogenic radiometer (CR) [1]. However, it is complicated and expensive to set up a laser system covering continuous wide spectrum. A monochromator and broadband source method then becomes a convenient alternative to lasers [2, 3]. A new cryogenic radiometer facility was installed for spectral responsivity realization at NIM, which works with a monochromator and a supercontinuum white light source to increase signal level. InGaAs trap detectors were developed as transfer standards, and their spectral responsivity was calibrated against the new cryogenic radiometer facility.

MONOCHROMATOR-BASED CRYOGENIC RADIOMETER FACILITY

Facility

The configuration of the new facility is shown in Figure 1. The system consists of a light source unit, a double monochromator unit, and a transfer unit. In the light source unit, different types of sources (QTH lamp, laser and supercontinuum light source) are mounted on a linear translation stage for alignment to the monochromator entrance slit. The double monochromator unit includes a predisperser prism and a transmission grating for low stray light and high throughput. The transfer unit includes a Y shape mechanism system connected to the same incident window, two vacuum chambers for

cryogenic radiometer and transfer detector respectively, and a translation stage for switching between the two chambers automatically.

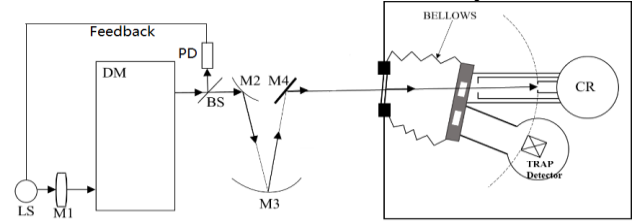


Figure 1. Schematic diagram of the NIM monochromator-based cryogenic radiometer facility for detector calibrations.

Principle

The spectral responsivity measurement process is Detector-CR-Detector type, in which transfer standard detector and cryogenic radiometer are alternatively aligned into the same optical beam. The detector output current is amplified and measured by voltmeter. The spectral responsivity of transfer standard detector at certain wavelength can be calculated as:

$$R = k_{ACR} \frac{[(S_1 - S_{1B}) + (S_2 - S_{2B})] / 2}{P_{EH}} \quad (1)$$

where R is the responsivity of the transfer standard detector to be measured, P_{EH} is the effective heating power measured by cryogenic radiometer, S_1 and S_2 are the detector output current before and after cryogenic radiometer measurement, S_{1B} and S_{2B} are the background current, and k_{ACR} is the correction coefficient for the cavity absorptance, non-equivalent effect and the stray light.

Transfer standard

For near infrared spectral range, a three-element reflection InGaAs trap is used as transfer standard. The photodiodes are with a 10mm diameter circular sensitive area. The non-uniformity, polarization effect and angular dependence of the InGaAs trap detector are measured to ensure its performance as a transfer standard.

Source power stability

For the supercontinuum white light source, the power stability is improved significantly by an external power feedback unit. The power stability measurement, with a standard derivation of roughly 0.01%.

RESULTS

Under the condition of supercontinuum source and monochromator, and an optical power level of $\sim 20\mu\text{W}$ at 1550nm, power responsivity measured by cryogenic radiometer is shown in Figure 2, with a relative standard derivation of less than 0.01%.

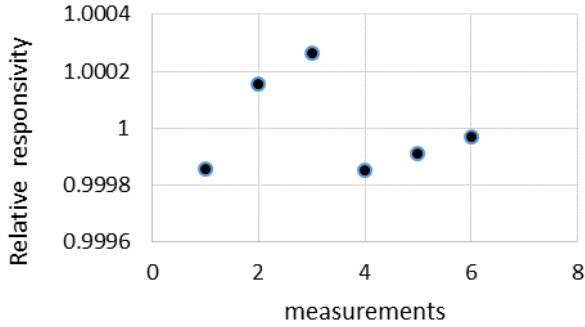


Figure 2. Power responsivity repeatability of transfer standard against cryogenic radiometer at 1550nm.

Spectral responsivity of the InGaAs trap detector calibrated against cryogenic radiometer is shown in Figure 3.

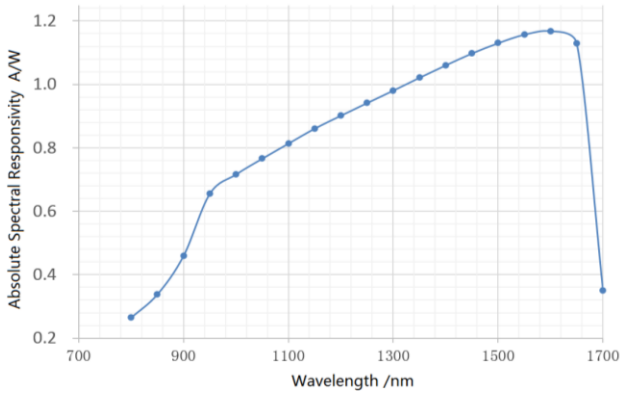


Figure 3. Spectral responsivity measurement result of InGaAs trap detector based on monochromator

Uncertainty induced by stray light, wavelength accuracy, bandwidth effect, geometrical effect, and polarization effect are evaluated. To evaluate uncertainty induced by supercontinuum light source, an InGaAs trap detector is calibrated directly against the cryogenic radiometer using laser and supercontinuum light source both at a certain wavelength. The responsivities of InGaAs trap

detector at 950nm for the two types of sources are measured and analysed.

Measurement uncertainty budget of responsivity of the InGaAs trap detector at 1550nm is shown in Table 1.

Table 1. Uncertainty of responsivity of the InGaAs trap detector at 1550nm

Source	Uncertainty (%)
Cavity absorptance and non-equivalence effects	0.01
Radiometer external electrical calibration	0.01
Beam geometrical effect	0.01
IV amplifier and Voltmeter	0.01
Polarization effect	0.01
Bandwidth effect	0.01
Wavelength accuracy	0.01
Repeatability	0.01
Combined standard uncertainty	0.03

CONCLUSION

A new cryogenic radiometer facility was set up at NIM working with monochromator and a supercontinuum white light source. As a transfer standard, performance of an InGaAs trap detector has been characterized. Spectral responsivity is realized and maintained by transfer standard covering spectral range from 900nm to 1600 nm.

ACKNOWLEDGMENTS

This work is supported by National Key R&D Plan under grant NO. 2018YFB0504601.

REFERENCES

1. Martin J. E., Fox N. P., Key P. J., Cryogenic radiometer for absolute radiometric measurements, *Metrologia*, 21, 147-155, 1985.
2. L. P. Boivin and K. Gibb, Monochromator-based cryogenic radiometry at the NRC, *Metrologia*, 32, 565-570, 1995/96.
3. C. A. Schrama, R. Bosma, K. Gibb, H. Reijn and P. Bloembergen, Comparison of monochromator-based and laser-based cryogenic radiometry, *Metrologia*, 35, 431-435, 1998.

Absolute irradiance responsivity calibration system using diode lasers for tricolour laser applications

Minoru Tanabe¹ and Kenichi Kinoshita¹

¹National Metrology Institute of Japan, Tsukuba, Japan

Corresponding e-mail address: tanabe-m@aist.go.jp

An absolute irradiance responsivity calibration system with diode laser light sources at three wavelengths is presented. This system is based on an optical detector with a silicon photodiode and a uniform light source combined with an integrating sphere. The expanded uncertainty of the absolute irradiance responsivity has been analysed to be 0.55–0.57% ($k = 2$).

INTRODUCTION

Diode lasers emitting red, green, and blue coloured light are favourable for use as light sources in optical products such as laser-based projectors and displays [1,2] and laser-based lighting [3]. In these laser-based products, an immediate advantage of using these tricolour laser lights for displays and lighting is the wide colour gamut that is available in comparison with light-emitting diode and other light emitting devices. The use of diode lasers also helps us to fabricate energy saving and compact optical products, even though gas lasers and solid-state lasers with a wide range of wavelengths are available. The diode lasers used in these products are occasionally quasi-monochromatic spectrum such as multimode oscillation, asymmetric spectrum, and wavelength width more than several nanometres. Accurate measurements are required to manage such light source and to assure the reliability and safety of these laser-based products.

In the fields of using laser-based projectors, displays, and lighting, not only these absolute optical flux evaluations but also photometric evaluations are required because they relate with vision in humans. Colorimetric evaluation is also required to achieve the desired chromaticity coordinate, which is to measure the lasers' spectral distributions and the intensity ratio of the tricolour laser wavelengths. In photometric and colorimetric evaluations, however, large spectral mismatches of the colour matching functions standardized by the CIE would generate within quasi-monochromatic spectrum of the diode laser. These mismatches would cause a white colour imbalance with red, green, and red colour lasers and deviations from the desired photometric values.

Therefore, radiometric evaluation with tricolour laser light sources is an appropriate technique for more accurately evaluating laser-based products with optical detectors. We focus on absolute irradiance responsivity and report on a method to calibrate it using tricolour light source based on diode lasers in order to cover a wide dynamic optical flux range extending over six orders of magnitude. We also discuss the uncertainties of the calibration system.

IRRADIANCE RESPONSIVITY CALIBRATION

A detector-based system with laser diodes was selected for use in calibrating absolute irradiance responsivity values. This calibration system is consisted of a uniform light source combined an integrating sphere with tricolor laser and an optical detector based on a silicon (Si) photodiode (PD) (Hamamatsu S2281) as shown in Figure 1. A knife-edged-aperture was chosen to accurately define the irradiation area of the light source. The standard optical detector was calibrated for the absolute responsivity in units of amperes per watt (A/W) and the linearity of the optical response with respect to the incident flux. The roundness and diameter of the knife-edged-aperture were evaluated.

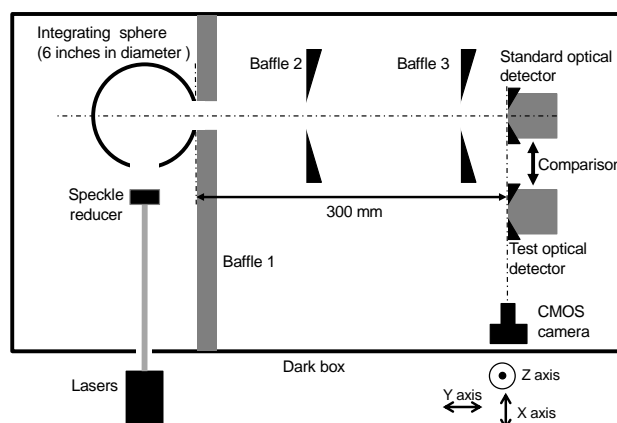


Figure 1. Schematic diagram of irradiance responsivity calibration system with tricolour laser light source.

The light source created with an integrating sphere and tricolor laser is adequate for calibrating the absolute irradiance responsivity of the standard optical detector in terms of its uniformity. The tricolor

laser was produced by two Fabry-Perot laser diodes (FPLDs) and a diode-pumped solid state (DPSS) laser. The incident wavelengths were 452 and 665 nm for the FPLDs and 532 nm for the DPSS laser. A speckle reducer was installed in front of the integrating sphere in order to create a spatially uniform light source.

The light source and the standard optical detector were mounted on the perpendicular and horizontal rotation stages and XYZ axis translation stages. These stages were used so that the detector surface and the light source surface radiated from a port of the integrating sphere were parallel. The center of the detector was adjusted to be at the same height as the center of the light source. Three baffles were installed to shield from the stray light caused by the incident laser light to the integrating sphere and the light emitted from a port of the integrating sphere. To validate the feasibility of our absolute calibration system, a test optical detector was also installed. The test optical detector consisted of a commercial Si PD (Hamamatsu S1227-1010) and an accurate knife-edged-aperture. The detection surfaces of the standard and test optical detectors were adjusted to the same position using a CMOS camera that was vertically installed perpendicular to the two detection surfaces.

The following model formula was applied for evaluating the uncertainty factors for the absolute irradiance responsivity in terms of the standard optical detector and for deriving the combined standard uncertainty.

$$R = \frac{S \cdot \pi \cdot r^2}{(1 - C_\theta \cdot \theta)(1 - C_\varphi \cdot \varphi)} \cdot k_{NL} \cdot k_{uni} \cdot k_{dis} \quad (1)$$

where S is the spectral responsivity of the standard optical detector, r is the radius of the aperture, C_θ and C_φ are the coefficient of the change in irradiance responsivity due to perpendicular and horizontal angular deviations, θ and φ are the perpendicular angular deviation, k_{NL} is the correction of the nonlinearity of the standard optical detector, k_{uni} is the correction due to the non-uniformity of the light source, and k_{dis} is the correction due to the distance difference between the standard and test optical detectors.

Table 1 shows the uncertainty budget for evaluating the irradiance responsivity at 532 nm. A comparison of the irradiance responsivity evaluations conducted on the two optical detectors was performed. The uncertainty of the comparison evaluation was estimated from the standard deviation of the evaluation result. The expanded uncertainty at 532

nm was obtained within 0.55%. In the same manner, the expanded uncertainties at the wavelengths of 452 and 665 nm were obtained within 0.57 and 0.55%, respectively.

Table 1. Uncertainty budget for evaluation of irradiance responsivity at 532 nm.

Uncertainty contribution	Relative uncertainty
Absolute responsivity of the standard optical detector	0.07%
Roundness and diameter of the knife-edged-aperture	0.03%
Linearity of the standard optical detector	0.12%
Uniformity of the light source	0.14%
Horizontal angular deviation of the standard optical detector	0.01%
Perpendicular angular deviation of the standard optical detector	0.02%
Horizontal angular deviation of the light source	0.01%
Perpendicular angular deviation of the light source	0.02%
Distance difference between two detectors	0.19%
Repeated comparison measurement	0.01%
Combined standard uncertainty	0.27%
Expanded uncertainty ($k = 2$)	0.55%

CONSLUTION

A calibration system of the absolute irradiance responsivity using diode laser emitting at three wavelengths has been developed. This system enables us to evaluate the absolute irradiance at the rage of 10^{-4} W/m² to 10^2 W/m². The radiometric performance of the system has been thoroughly investigated by considering all sources of uncertainty and their contributions to the uncertainty budget. The expanded uncertainties from 0.55 to 0.57% ($k = 2$) in irradiance responsivity have been attained. We can conclude that our proposed calibration system of irradiance responsivity based on tricolour laser light was successfully demonstrated. This system is expected to help us to perform radiometric and colorimetric evaluations of the tricolour laser-based products and applications such as displays and lighting.

REFERENCES

- [1] O. Cakmakci *et al*, "Head-worn displays: A review" J. Display Technol. Vol. 2, pp.199–216, (2006).
- [2] K.V. Chellappan *et al*, "Laser-based displays: a review" Appl. Opt. Vol. 49, pp. F79–F98, (2010).
- [3] A. Neumann *et al*, "Four-color laser white illuminant demonstrating high color-rendering quality" Opt. Express Vol. 19, pp.A982–A990, (2011).

Realization and Dissemination of the Spectral Responsivity of Thermal Detectors in the Mid-Infrared Spectral Range at the PTB

Tobias Pohl¹, Peter Meindl¹, Uwe Johannsen¹, Lutz Werner¹, and Jörg Hollandt¹

¹Physikalisch-Technische Bundesanstalt (PTB), Berlin, Germany

Corresponding e-mail address: peter.meindl@ptb.de

The Physikalisch-Technische Bundesanstalt (PTB) has set up a portable collection of mid-infrared (MIR) laser radiation sources for the application at different measurement facilities. Primarily, these lasers can be used at a cryogenic electrical substitution radiometer facility to enable absolute calibrations of the spectral responsivity of MIR detectors traceable to the International System of Units (SI). Besides, it is intended to use the MIR lasers also at a detector comparator facility to disseminate the spectral responsivity from the absolutely calibrated transfer standards to other detectors. As a first step, the expanded cryogenic electrical substitution radiometer facility has been used to calibrate thermopile and pyroelectric detectors for the use as transfer detector standards.

INTRODUCTION

Currently, the calibration of detectors in the spectral range of the near-infrared (NIR) and mid-infrared is of increasing importance, e.g. for remote sensing [1] or radiation thermometry [2]. In general, these applications need traceability to the International System of Units. Therefore, the PTB is expanding its capabilities of realization and dissemination of the spectral responsivity from the NIR into the MIR.

At the PTB, the measurement of radiant power for the calibration of detectors in view of their spectral responsivity is performed with cryogenic electrical substitutions radiometers as national primary detector standards [3]. One of these cryogenic electrical substitution radiometer facilities has been extended with different MIR lasers as radiation sources. Additionally, these MIR lasers can also be used at another MIR detector comparator facility which is set up mainly for the calibration of customer detectors. A number of different thermal detectors have been characterized and calibrated at the extended cryogenic electrical substitution radiometer facility for the use as MIR transfer standards.

CALIBRATION OF MIR TRANSFER STANDARDS WITH CRYOGENIC ELECTRICAL SUBSTITUTION RADIOMETER

Cryogenic electrical substitution radiometers are usually used as national primary standards for the measurement of radiant power. By implementing a CO₂-laser (10.6 μm) and a quantum cascade laser (QCL, 3.96 μm and 9.45 μm) at one of PTB's cryogenic electrical substitution radiometer facilities, absolute detector calibrations of the spectral responsivity in the MIR were enabled (Fig. 1). The calibrations are usually performed at power levels between 1 μW and 1 mW. The laser radiant power can be adjusted by using an attenuator.

The lasers are used to irradiate a diaphragm of 2.4 mm diameter. This diaphragm is then imaged onto the plane of the detector aperture. Additional baffles are used to reduce stray radiation to a minimum which otherwise causes errors if the apertures of the compared detectors are diverging. The MIR beam profile including the amount of stray radiation in the plane of the detector aperture is characterized by scanning the profile using a detector which has a known aperture size. An additional monitor detector can be applied if necessary.

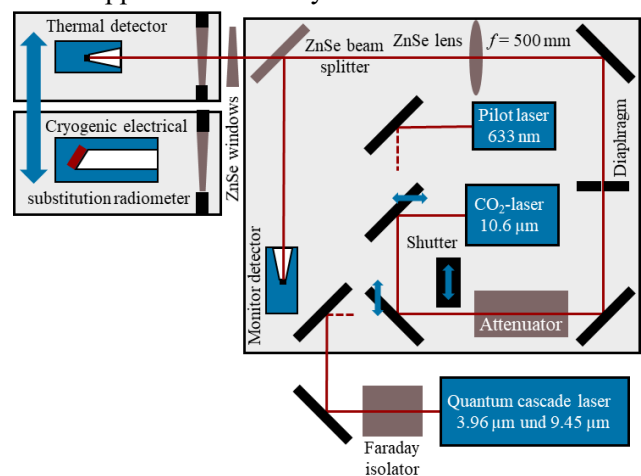


Figure 1. MIR detector calibration facility with cryogenic electrical substitution radiometer and MIR lasers.

The facility was used to calibrate the spectral responsivity of windowless thermopile detectors (TS-76 from the Leibnitz-Institut für Photonische Technologien e.V.) and windowless pyroelectric detectors (InfraTec GmbH). The properties of these types of detectors have been improved by an optimized and thermally stabilized detector housing design [4].

The measurement principle of these thermal detectors is based on the heating effect of an absorber area. Therefore, the detector responsivity should be spectrally more or less constant assuming that the absorptance of the incident radiant power is independent of the wavelength. Fig. 2 shows results of spectral responsivity calibrations of a thermopile detector TS-76. In fact, a slight dependency of the spectral responsivity on the wavelength has been found. A linear approximation seems to be sufficient for an interpolation of the spectral responsivity $s(\lambda)$ between the results at the laser wavelengths. However, this result underlines the importance of measuring the spectral responsivity at different wavelengths.

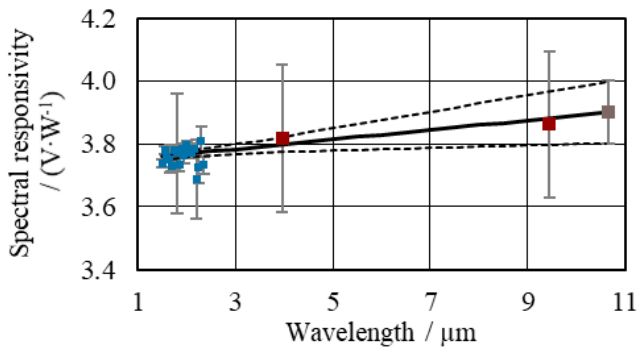


Figure 2. Spectral responsivity $s(\lambda)$ of a thermopile detector TS-76, measured with a supercontinuum laser (blue), a QCL (red) and a CO₂-laser (brown), including the standard measurement uncertainty.

The relative standard measurement uncertainties of the spectral responsivity determined with MIR lasers against the cryogenic electrical substitution radiometer range between 1.3% and 3.6%. The main uncertainty contributions for the calibration of the spectral responsivity is caused by the correction due to stray radiation and the noise of detector, cryogenic radiometer and radiation source. A further uncertainty contribution is caused by the measurement of the ZnSe window transmittances. Based on these calibrations, the TS-76 thermopile detectors and pyroelectric detectors were established as MIR transfer standards for the measurement of radiant power.

OUTLOOK: MIR DETECTOR COMPARATOR FACILITY

The PTB is building a new detector comparator facility for calibrations in the MIR to disseminate the spectral responsivity from the transfer detector standards to other customer detectors (Fig. 3). This facility also uses the portable MIR lasers as radiation sources and furthermore a thermal, broad-band radiation source in combination with a monochromator setup to calibrate detectors at any desired wavelength by using the interpolated spectral responsivity $s(\lambda)$ of the transfer standards.

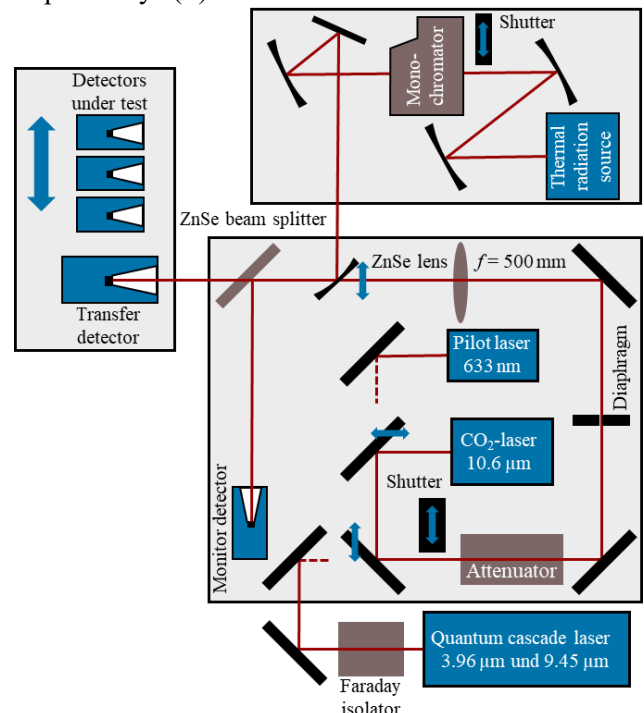


Figure 3. MIR detector comparator facility with MIR lasers and monochromator.

REFERENCES

1. J. A. Sobrino et al., Review of Thermal Infrared Applications and Requirements for Future High-Resolution Sensors, *IEEE Transactions on Geoscience and Remote Sensing* 54(5), 1-10, 2016.
2. N. Noulkow, R. D. Taubert, P. Meindl, and J. Hollandt, Infrared Filter Radiometers for Thermodynamic Temperature Determination below 660 °C, *International Journal of Thermophysics* 30,131-143, 2009.
3. J. Hartmann, J. Hollandt, P. Meindl, D. Taubert and L. Werner, Traceable Radiometric Calibration of Semiconductor Detectors and their Application for Thermodynamic Temperature Measurement, *MAPAN – Journal of Metrology Society of India* 25(1), 3-10, 2010.
4. T. Pohl, P. Meindl, U. Johannsen, D. Taubert, and L. Werner, Measurement of the absolute spectral responsivity in the mid-infrared based on the cryogenic electrical substitution radiometer and an optimized thermopile detector, *Journal of Sensors and Sensor Systems* 8, 195-205, 2019.

Interpolation of Spectral Responsivity of Trap Detectors and Evaluation of Measurement Uncertainties Using Monte Carlo Method

CM Tsui, Brenda HS Lam and Brian HT Lee

The Government of the Hong Kong Special Administrative Region Standards and Calibration Laboratory
cmtsui@itc.gov.hk, hslam@itc.gov.hk, brian.lee@itc.gov.hk,

This paper describes how the Standards and Calibration Laboratory interpolates the responsivity of trap detectors measured by a cryogenic radiometer at 7 wavelengths to the spectral range 400 nm to 800 nm and evaluates the uncertainties using Monte Carlo method.

INTRODUCTION

The Standards and Calibration Laboratory (SCL) has recently set up a cryogenic radiometer for calibration of spectral responsivity of trap detectors built from silicon photodiodes. The spectral responsivity, denoted by S_i , $i = 1$ to 7, are measured at the output wavelengths of a krypton ion laser, namely 406.7 nm, 413.1 nm, 476.2 nm, 530.9 nm, 568.2 nm, 647.1 nm and 799.3 nm. To apply the trap detector for measurement work, these results need to be interpolated to the spectral range of 400 nm to 800 nm and the measurement uncertainties evaluated. The interpolation can be performed by purely mathematical functions such as polynomials or by fitting a physical model for the photodiodes [1]. SCL adopts the latter way to perform the interpolation. This paper also describes how the uncertainties are evaluated using Monte Carlo method (MCM).

RESPONSIVITY MODEL

The spectral responsivity $S(\lambda)$ at wavelength λ is given by,

$$S(\lambda) = \frac{(1-r(\lambda))\eta_i(\lambda)n_{air}\lambda e}{hc} \quad (1)$$

where $r(\lambda)$ and $\eta_i(\lambda)$ are the reflectivity and internal quantum efficiency of the photodiode, n_{air} is the refractive index of air, e is the electron charge and h is the Planck constant. $\eta_i(\lambda)$ can be obtained using the following equation [2][3],

$$\begin{aligned} n_i(\lambda) = & P_f + \frac{1-P_f}{\alpha(\lambda)T} (1 - e^{-\alpha(\lambda)T}) - \\ & \frac{1-P_b}{\alpha(\lambda)(D-T)} (e^{-\alpha(\lambda)T} - e^{-\alpha(\lambda)D}) - P_b e^{-\alpha(\lambda)w} + \\ & R_{back} e^{-\alpha(\lambda)w} P_b \end{aligned} \quad (2)$$

where $\alpha(\lambda)$ and w are the absorption coefficient and thickness of the photodiode, P_f is the collection efficiency at the silicon dioxide/silicon interface and P_b is the value at the bulk, T is the depth of the p-n junction and D is the depth of the bulk region. R_{back} is the reflection coefficient at the back of the photodiode and this term is only required for

interpolation to wavelengths longer than 920 nm [2]. Its value is treated as zero in this paper.

An interpolation function for $\alpha(\lambda)$ is given in [3] as follows where $A_1 = 0.53086 \mu\text{m}^{-1}$, $A_2 = 0.469643 \mu\text{m}$, $A_3 = -0.28801 \mu\text{m}^{-2}$, $A_4 = -0.988739$, $A_5 = 0.282028 \mu\text{m}^{-1}$ and $\lambda_0 = 0.256897 \mu\text{m}$.

$$\alpha(\lambda) = A_1 e^{\frac{A_2}{(\lambda-\lambda_0)}} + A_3 \lambda + A_4 \lambda^{-1} + A_5 \quad (3)$$

The reflectivity $r(\lambda)$ takes the following form with the parameters obtained from prior information or by fitting [3]. In this paper the parameters for $r(\lambda)$ are not fitted since there are insufficient data.

$$r(\lambda) = a e^{\frac{b}{\lambda}} + c \lambda + d \quad (4)$$

INTERPOLATION PROCEDURE AND UNCERTAINTIES EVALUATION

The responsivity $S(\lambda)$ is calculated using (1) to (4). The 4 parameters (P_f , T , P_b , D) of the model are obtained by least squares fitting to the S_i data. The thickness w is assigned a value of 400 μm and not fitted. The Nelder-Mead (NM) algorithm [4] is used for searching the minimum of the residual error.

The interpolation procedure can be viewed as a measurement model in the GUM framework (GUF) [5] having S_i as input quantities and the responsivity $S(\lambda)$ as output quantity. Since the NM algorithm is not a differentiable function, the GUF might not be directly applicable to derive the uncertainties of $S(\lambda)$. According to GUM Supplement 1 [6], MCM may be a suitable choice for this uncertainty evaluation.

A method to derive the uncertainty of $S(\lambda)$ was described in [1]. Responsivity measured at 9 wavelengths were firstly fitted to the model in [2] to obtain the uncertainties and correlations of the 4 parameters P_f , T , P_b and D . These uncertainties were then propagated to $S(\lambda)$ using the physical model.

SCL applies MCM to generate random samples for the input quantities, perform model fitting and calculate $S(\lambda)$ in each trial. The uncertainty is obtained by summing up the results from a large number of trials. In the past, SCL had developed a software tool in Visual C and Visual Basic for Application (VBA) with Microsoft Excel as frontend user interface to evaluate uncertainties using MCM. This software was adapted for this application. The measurement model is encoded in VBA which includes the NM algorithm and equations (1) to (4). The values of S_i are entered in an Excel worksheet with an example shown in Table 1. They are taken to

have Gaussian probability density function (pdf) with relative standard uncertainty of 0.03 % (converted to absolute values in the table). Since these data were measured by the same cryogenic radiometer, they are correlated and the correlations should be considered in the uncertainty evaluation [1]. It is estimated that the correlation coefficient between them is 0.5. A method to generate multivariate Gaussian distribution is described in section 6.4.8 of [6].

λ	pdf *	value	std uncert	Correlation Coefficient						
406.7	G	0.319342	0.000096	1	0.5	0.5	0.5	0.5	0.5	0.5
413.1	G	0.325138	0.000098		1	0.5	0.5	0.5	0.5	0.5
476.2	G	0.380091	0.000114			1	0.5	0.5	0.5	0.5
530.9	G	0.425322	0.000128				1	0.5	0.5	0.5
568.2	G	0.455770	0.000137					1	0.5	0.5
647.1	G	0.519709	0.000156						1	0.5
799.3	G	0.642299	0.000193							1

*G=Gaussian

Table 1. An example of input quantities

Since the responsivity model is non-linear, the user might need to experiment with the starting values of the NM algorithm to achieve good results. It will be a good idea to view the distribution of the fitted parameters to judge if the fitting has worked well. An example of the pdf of the P_f parameter after 100000 MCM trials is shown in Figure 1(a).

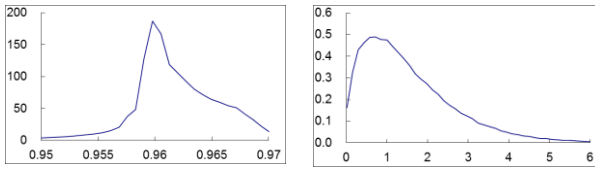


Figure 1. (a) pdf of P_f , (b) Histogram of χ^2

RESULTS AND DISCUSSIONS

Model fitting will not be perfect. There will be residual error in each fitting. The χ^2 parameter defined below can be used to assess the goodness of fit [1]. M is a vector of the fitting errors ($S(\lambda) - S_i$). U_x is the variance covariance matrix of the input quantities. N and P are the number of inputs and fitting parameters. The χ^2 varies vastly for different MCM trials. The histogram of χ^2 for 100000 MCM trials is shown in Figure 1(b)

$$\chi^2 = M^T U_x^{-1} M / (N - P) \quad (6)$$

The residual should be included in the uncertainty of $S(\lambda)$. Different ways to handle this component will have great impact on the reported uncertainty as depicted in the MCM computation results shown in Figure 2. The dots E indicate the uncertainties of the input quantities to facilitate comparison.

Curve A does not include the uncertainty due to fitting. It indicates the uncertainty of $S(\lambda)$ arising from that of S_i alone. Curve C is obtained by adding

to curve A the uncertainty due to individual fitting in each MCM trial. The values are much larger than other curves due to the variation of fitting quality in different MCM trials as shown in Figure 1(b). A possible explanation is that the model might not fit well when random values are added to S_i . Curve C therefore does not represent well the uncertainty of $S(\lambda)$ and should not be used. Curve B is curve A adding a fixed uncertainty component representing the fitting error at S_i . Although the MCM makes a large number of trials, the only set of $S(\lambda)$ that we will use in future work is the set calculated from S_i . Hence curve B is a good representation of the uncertainty of $S(\lambda)$. Curve D is similar to curve A except that the correlations between the input quantities are treated as zero. The result shows the importance of considering the correlations of input quantities.

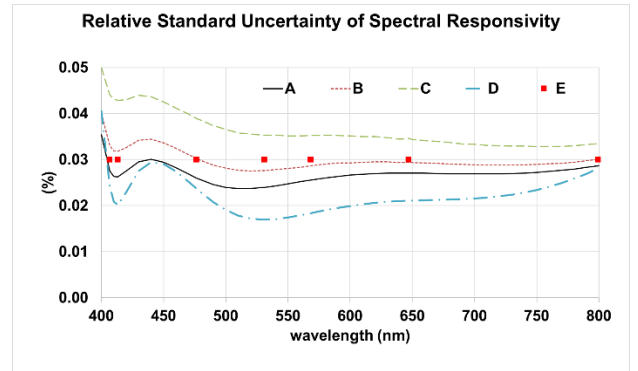


Figure 2. Results of the Monte Carlo computation

CONCLUSION

A procedure for interpolating responsivity and evaluating uncertainty using MCM was described.

ACKNOWLEDGEMENT

The authors would thank Dr Teresa Goodman of NPL, the UK for sharing of trap detectors calibration and interpolation method.

REFERENCES

1. J.L. Gardner, Uncertainty Propagation for NIST Visible Spectral Standards, Journal of Research of the NIST, 109, 305-318, 2004.
2. T.R. Gentile, J.M. Houston and C.L. Cromer, Realization of a scale of absolute spectral response using the National Institute of Standards and Technology high-accuracy cryogenic radiometer, Applied Optics, 35, 4392-4403, 1996.
3. L. Werner, J.Fischer, U. Johannsen and J. Hartmann, Accurate determination of the spectral responsivity of silicon trap detectors between 238 nm and 1015 nm using a laser based cryogenic radiometer, Metrologia, 37, 279-284, 2000.
4. J.A. Nelder and R. Mead, A simplex method for function minimization, The Computer Journal, 7(4), 308-313, 1965.
5. Guide to the expression of uncertainty in measurement, JCGM 100:2008
6. Supplement 1 to the GUM, JCGM 101:2008

Establishment of single-photon detection efficiency calibration system at NRC

Jeongwan Jin¹, Thomas Gerrits², and Angela Gamouras¹

¹National Research Council Canada (NRC), Ottawa, ON K1A 0R6, Canada

²National Institute of Standards and Technology (NIST), Boulder, CO 80305, United States

Corresponding e-mail address: jeongwan.jin@nrc-cnrc.gc.ca

The advent of single-photon detection capabilities has enabled rapid advancements in many areas including quantum measurements and quantum communication [1-2]. Recently, numerous national metrology institutes have established their own detection-efficiency calibration methodologies for single-photon detectors (SPDs) [3-4]. Here, we report the establishment of a free-space SPD efficiency calibration system at NRC utilizing an attenuation-based substitution technique [3]. The measured detection efficiencies of commercial silicon single-photon avalanche photodiodes are traceable to the NRC optical power scale. To validate this new system, SPD detection efficiencies were also measured at NIST, using a calibration set-up described in Ref. [4]. The results of these measurements will be presented.

SI-TRACEABLE QUANTUM RADIOMETRY

The substitution and attenuation technique for measuring detection efficiency enables a single-photon detector (SPD) to be directly compared to a transfer standard detector (TSD), making the calibration traceable to the absolute cryogenic radiometer, the primary standard for the NRC optical power scale (Fig. 1).

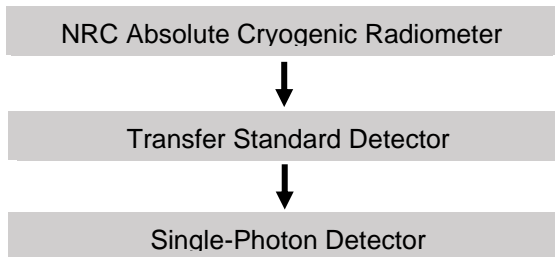


Fig. 1. Traceability chain of a SPD detection-efficiency calibration.

NRC CALIBRATION APPARATUS

Our experimental setup is depicted in Fig. 2. In this calibration method, multiple filters are used to attenuate the incident power of the input laser beam at 850 nm to a level measurable by the SPD, on the order of femtowatt.

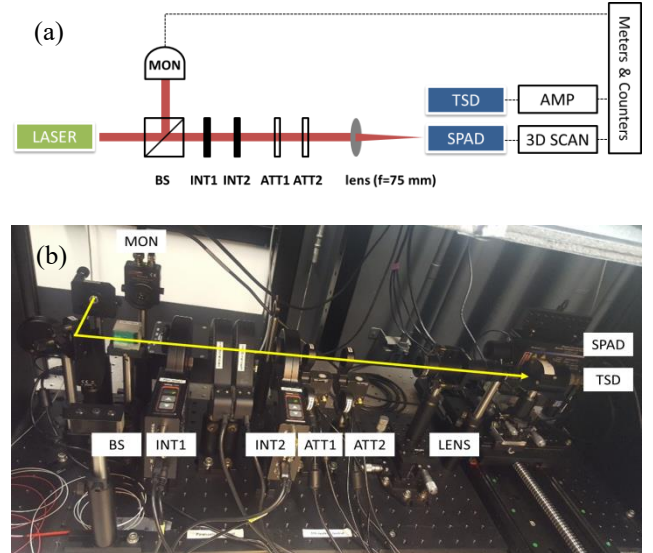


Fig. 2. Measurement setup: (a) a schematic diagram and (b) a photo. AMP: amplifier, BS: beam splitter, MON: laser intensity monitoring detector, INTs: intensity controllers, ATTs: neutral density filters, SPAD: single-photon avalanche diode.

The SPAD under test is mounted on a 3-dimensional computer-controlled stage, allowing the single photons to be optimally positioned on the active area of the SPAD (Fig. 3).

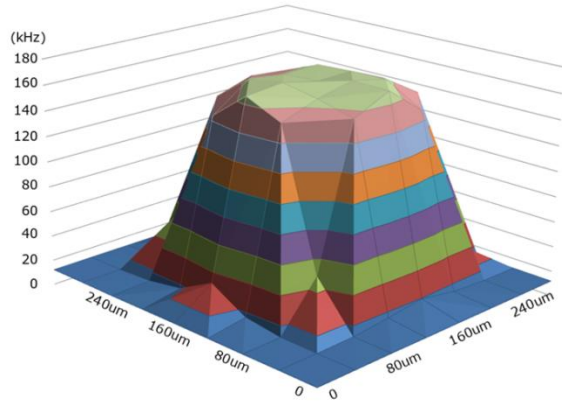


Fig. 3. Detection-response spatial uniformity. A laser beam with a focal size of 17 μm scans the SPAD detection window. An active area diameter (plateau) of 160 μm is measured.

COMPARISON TO NIST CALIBRATION

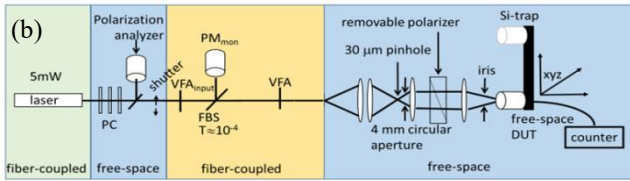
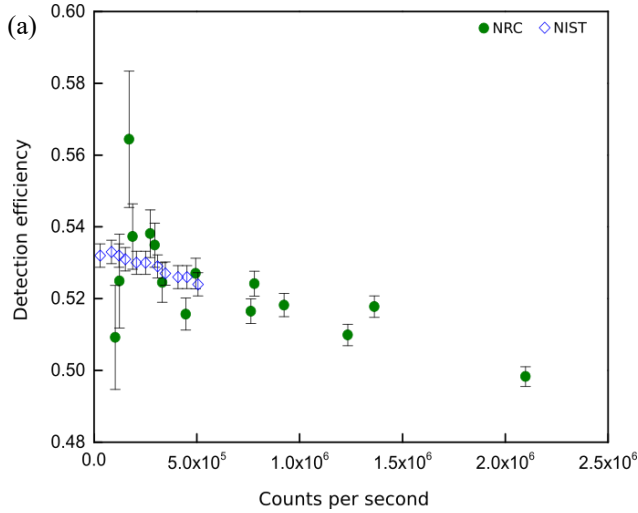


Fig. 4. Measurement results. (a) Detection efficiencies are measured at various input intensity levels, and compared to measurements performed at NIST. (b) The NIST SPAD calibration system [4].

Measurand	Symbol	Unit	Value	Uncertainty	Uncertainty (%)
Wavelength	λ	m	850.63×10^{-9}	6.00×10^{-11}	7.05×10^{-3}
TSD Spectral Responsivity	s	A/W	4.526×10^{-1}	5.93×10^{-4}	1.31×10^{-1}
Amplification	A	V/A	1.00×10^9	5.00×10^6	5.00×10^{-1}
Ratio $V_0/V_{0,\text{mon}}$	Q_0	1	1.14×10^1	1.40×10^{-7}	1.23×10^{-6}
Ratio $V_1/V_{1,\text{mon}}$	Q_1	1	2.25×10^{-1}	2.91×10^{-6}	1.30×10^{-3}
Ratio $V_2/V_{2,\text{mon}}$	Q_2	1	2.64×10^{-2}	1.98×10^{-4}	7.49×10^{-1}
Ratio $N_{\text{SPAD}}/V_{\text{SPAD},\text{mon}}$	Q_{SPAD}	V · s	2.51×10^6	1.38×10^{-6}	5.51×10^{-11}
Efficiency ($n=4$)	η	1	0.522	1.03×10^{-3}	1.98×10^{-1}
Combined uncertainty ($k=1$)					0.93

Table 1. Uncertainty budget. Uncertainties are evaluated at the level of $N_{\text{SPAD}}=102895$ counts per second.

CONCLUSION

We demonstrate a newly constructed apparatus and results for SI-traceable detection-efficiency measurements of free-space single-photon detectors. Our automated system has the capability to measure the uniformity of the active area of the single-photon detector under test which increases measurement accuracy and reproducibility. The measured average detection efficiency agrees with measurements performed at NIST, within measurement uncertainty. Further improvement to reduce measurement uncertainties at the low photon-flux level can be made by utilizing low-noise and high-gain transfer standard detector amplifier and alternate attenuation technique.

REFERENCES

- [1] J. P. Dowling *et al.*, Quantum optical metrology - the lowdown on high-N00N states, *Contemp. Phys.* **49**, 125 (2008).
- [2] J.-G. Ren *et al.*, Ground-to-satellite quantum teleportation, *Nature*. **549**, 70 (2017).
- [3] M. López *et al.*, Detection efficiency calibration of single-photon silicon avalanche photodiodes traceable using double attenuator technique *J. Mod. Opt.* **62**, S21 (2015).
- [4] T. Gerrits *et al.*, Calibration of free-space and fiber-coupled single-photon detectors, *Metrologia* **57**, 015002 (2019).

Recent status of VUV/EUV photodiodes for radiometric scale comparison

Alexander Gottwald, Michael Kolbe, Udo Kroth, Christian Laubis, and Frank Scholze

Physikalisch Technische Bundesanstalt, Berlin, Germany,

Corresponding e-mail address: alexander.gottwald@ptb.de

Semiconductor photodiodes are widely used for the dissemination of radiometric scales. For the extreme and vacuum ultraviolet spectral range (i.e., wavelengths between 10 nm and 200 nm) the performance of these devices does not suffice with respect to homogeneity and stability because of the extreme surface sensitivity. For future scale inter-comparisons, suitable detectors still have to be identified.

INTRODUCTION

In the spectral ranges with wavelengths below 200 nm, synchrotron radiation based realizations of radiometric scales have been established through the last three decades using electric substitution radiometers as primary detector standards [1]. Although different detector types can be used as secondary (transfer) standards, semiconductor photodiodes are widely used, e.g. due to their handiness.

PTB maintains a scale of spectral responsivity using synchrotron radiation from the BESSY II and MLS electron storage rings and electrical substitution radiometers in the spectral ranges from UV (400 nm or 3 eV) to hard X-rays (60 keV or 20 pm). The scale is maintained by the use of different semiconductor photodiodes depending on the respective sub-range, e.g. Si np- and PtSi-nSi Schottky-, and PIN type.

VUV/EUV DETECTOR CALIBRATION UNCERTAINTY BUDGET

The calibration uncertainty and, thus, the possible accuracy of the scale of spectral responsivity, is mainly determined by the contributions listed in Table 1. Main contributions arise from the light source, i.e. the synchrotron radiation from the electron storage ring which is monochromatized by a grating- or crystal monochromator. The monochromatized radiation, however, is not spectrally pure but contains unwanted higher-order and diffuse scatter contributions. The intensity has to be monitored to normalize for the decreasing electron current stored in the storage ring and changes of the

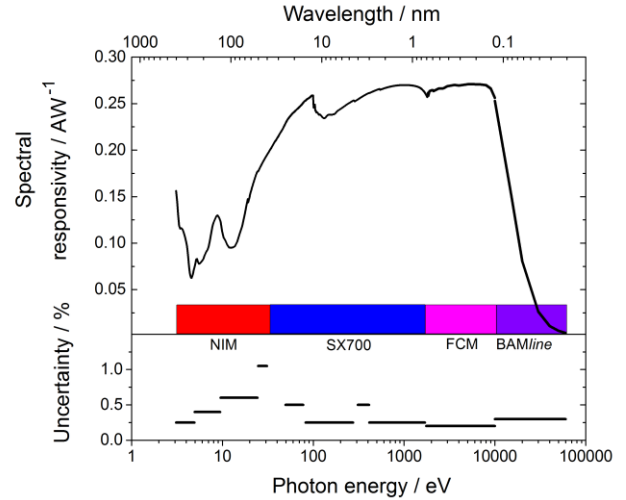


Figure 1. Scale of the spectral responsivity of semiconductor photodiodes by PTB using monochromatized synchrotron radiation at BESSY II (SX700, FCM, BAMline) and MLS (NIM, EUVR/not shown here).

monochromator transmission over wavelength or by aging of optical components.

Table 1. Example uncertainty budget for the measurement of the spectral responsivity of a photodiode at 60 nm using monochromatized synchrotron radiation.

Quantity	Uncertainty contribution ($k=1$)
ESR power	0.04
BL stability (norm.)	0.15
stray light, higher orders	0.15
photocurrent measurement	0.35
detector non-linearity	0.1
detector non-uniformity	0.2
total	0.46

However, the detector itself significantly contributes to the measurement uncertainty if it shows non-uniformity in responsivity over the active surface. Since the beam has a certain (sometimes wavelength-dependent) size, and the position accuracy of the detector with respect to the beam is

limited, this leads to variations of the measured signal. Moreover, in the VUV and EUV spectral ranges, any detector is known to suffer from responsivity degradation (from contamination as well as from radiation-induced damage). It can occur already under illumination in the sub-microwatt radiant power regime during the calibration process. If the non-uniformity exceeds the other uncertainty contributions, the diode quality is not sufficient to act as suitable reference detector.

DETECTOR EXAMPLES

AXUV100G Si-np photodiodes have established as well-proven radiometric standard photodiodes over a wide spectral range since they entered the market decades ago. Their extremely thin top oxide layer makes them suitable also for VUV/EUV radiation, where in certain regions the absorption length is less than 10 nm. However, it got obvious very soon that in particular between 40 nm and 170 nm, already

moderate irradiation causes significant (local) damage [2]. Radiation-hardened photodiodes like the SXUV100 or PtSi-nSi Schottky SUV-100 type have drawbacks e.g. a much lower responsivity. To our knowledge, there is still no commercial semiconductor photodiode which meets all relevant requirements (e.g. high responsivity, size, uniformity, linearity, radiation hardness, availability).

Moreover, in the recent years, we observed significant quality losses (regarding uniformity, Figure 2) of some of commercially available standard detector types. Other, new types of detectors (e.g. B-Si type [3] or metal-SiC-Schottky devices [4]) showed promising results, however, still have not reached a commercial level for VUV use.

PREVIOUS SCALE COMPARISONS

In the decade before 2010, intercomparisons between NMIs took place in the EUV (10 nm to 20 nm) [5] spectral range as well as in the VUV range (135 nm to 250 nm) [6]. Although the results indicated that the scale agreement between the NMIs was well within the combined stated uncertainties, it got obvious already then that the characteristics and use of the transfer devices was the limiting factor. Going beyond these existing results, therefore, first of all requires transfer photodiodes with improved characteristics. Even a reproduction of the previous results will not be possible with the presently available detectors.

REFERENCES

1. B. Beckhoff et al., A quarter-century of metrology using synchrotron radiation by PTB in Berlin, *Phys. Status Solidi B* **246**, 1415, 2009.
2. F. Scholze et al., Irradiation stability of silicon photodiodes for extreme-ultraviolet radiation, *Appl. Opt.* **42**, 5621-5626, 2003.
3. L. Shi et al., High-sensitivity high-stability silicon photodiodes for DUV, VUV and EUV spectral ranges, *Proc. SPIE* **8145**, 81450N, 2011.
4. A. Gottwald et al., Optical properties of a Cr/4H-SiC photodetector in the spectral range from ultraviolet to extreme ultraviolet, *Appl. Opt.* **57**, 8431-8436, 2018.
5. F. Scholze et al., Report on the CCPR Pilot Comparison: Spectral Responsivity 10 nm to 20 nm, *Metrologia* **47**, 02001, 2010.
6. A. Gottwald et al., Bilateral NIST-PTB comparison of spectral responsivity in the VUV, *Metrologia* **48**, 02001, 2011.

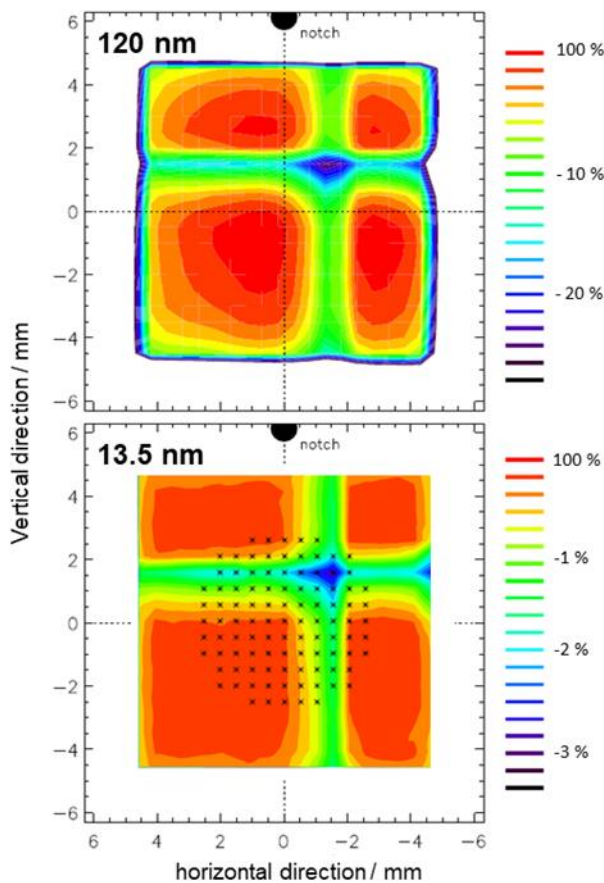


Figure 2. Relative responsivity at wavelengths of 120 nm (VUV) and 13.5 nm (EUV) of a recent example Si photodiode over its active surface area (interpolation with colour scale showing relative changes to the maximum).

Advancements in NRC's Primary Spectral Irradiance Scale Realisation

A. Gamouras, D. J. Woods, É. Côté, and A. A. Gaertner

National Research Council Canada (NRC), Ottawa, Canada

Corresponding e-mail address: angela.gamouras@nrc-cnrc.gc.ca

The primary spectral irradiance scale at the National Research Council (NRC) Canada has transitioned from a detector-based approach in the range of 700 nm to 1600 nm to a detector and source-based realisation from 250 nm to 2500 nm. A high temperature blackbody (HTBB) is now the primary light source for the calibration of FEL spectral irradiance standard lamps. The thermodynamic temperature of the HTBB is measured using an NRC-designed wide-band filter radiometer, with spectral responsivity traceable to the NRC optical power scale. The design of the NRC spectral irradiance facility, measurement procedure, and uncertainty analysis will be discussed.

INTRODUCTION

Over the past decade, the National Research Council (NRC) Canada has been developing a new facility for a source and detector-based primary realisation of the spectral irradiance scale [1]. The previous scale for spectral irradiance measurements from 250 nm to 2500 nm at NRC was a composite of three sources of traceability in different wavelength regions. In the spectral range of 300 nm to 700 nm, the scale was maintained on 500 W quartz-halogen lamps calibrated using the CIE World Mean of 1975 scale. From 250 nm to 300 nm and from 1600 nm to 2500 nm, the scale was traceable to FEL lamps purchased from the National Institute of Standards and Technology in the United States. In the near infrared range from 700 nm to 1600 nm, NRC realised the spectral irradiance scale by using interference filters and absolute radiometers to calibrate tungsten-

halogen lamps [2]. NRC now has a spectral irradiance facility equipped with a high temperature black body (HTBB) which is implemented as a primary light source. The thermodynamic temperature of the HTBB is measured using a wide-band filter radiometer [3], which has a spectral responsivity calibration traceable to the NRC cryogenic radiometer, giving a source and detector-based spectral irradiance scale realisation (Fig. 1).

SPECTRAL IRRADIANCE FACILITY

A simplified diagram of the NRC primary spectral irradiance measurement facility is shown in Figure 2. The HTBB in this facility is model BB3500M, manufactured by VNIIOFI, Russia. Two FEL lamp stations and the HTBB are installed on separate optical tables. The filter radiometer and monochromator system are installed on a third optical table equipped with a rail and lead screw system as well as a linear encoder which facilitates two metres of translation. A custom software program enables the automatic positioning of different sources and detectors: alignment positioning of the HTBB and filter radiometer, the HTBB and monochromator, and of the FEL lamps and monochromator. For spectral data collection, a single grating, one metre focal length, monochromator was used with various combinations of two diffraction gratings (blaze of

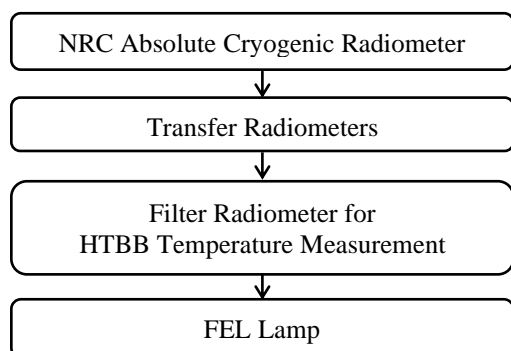


Figure 1. Optical radiation traceability chain for the NRC spectral irradiance scale.

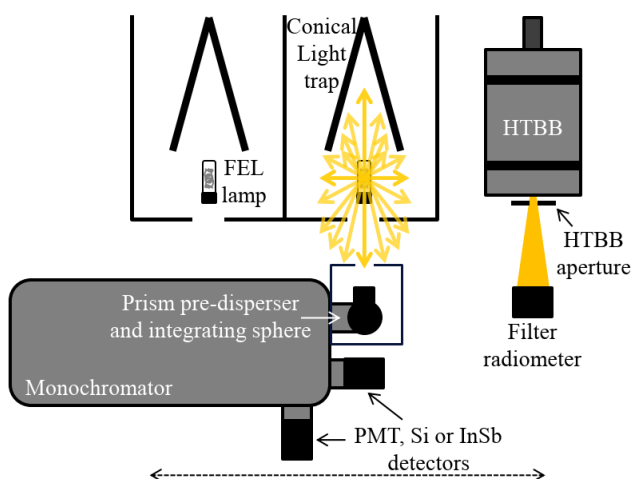


Figure 2. Schematic diagram of the NRC primary spectral irradiance facility.

400 nm or 2700 nm) and three photodetectors (photomultiplier tube (PMT), Si, and InSb detectors) to cover the range of 250 nm to 2500 nm.

MEASUREMENT PROCEDURE

The irradiance of the HTBB depends on its thermodynamic temperature as well as several geometric factors:

$$E_{\lambda,HTBB} = \left(\frac{\pi r_{HTBB}^2}{(d^2 + r_{FR}^2 + r_{HTBB}^2)} \right) \times \left(\frac{2\epsilon h c^2}{\lambda^5 n^2 e^{\frac{hc}{n\lambda kT} - 1}} \right) \quad (1)$$

where T is the thermodynamic temperature of the HTBB, r_{HTBB} and r_{FR} are the radii of the HTBB and filter radiometer precision apertures, d is the distance between these apertures, ϵ is the HTBB emissivity, h is the Planck constant, c is the speed of light, n is the refractive index of air, and k is the Boltzmann constant. For spectral irradiance measurements, the HTBB is operated at a temperature of 2950 K. The first step of the measurement procedure is the determination of T using the wide-band filter radiometer. The monochromator system is then implemented to collect spectral data from the HTBB output. T is then measured a second time to verify temperature stability of the HTBB. Spectral data from an FEL lamp is then collected using the monochromator system. The spectral irradiance of an FEL standard lamp, $E_{\lambda,FEL}$, at a given wavelength λ , is then determined using the equation:

$$E_{\lambda,FEL} = E_{\lambda,HTBB} \frac{S_{\lambda,FEL}}{S_{\lambda,HTBB}} \quad (2)$$

where $S_{\lambda,FEL}$ and $S_{\lambda,HTBB}$ are the measured FEL lamp and HTBB photodetector signals from the monochromator system.

MEASUREMENT UNCERTAINTIES

The total uncertainty for the calibration of FEL standard lamps depends on the uncertainties in the scale realisation as well as in the lamps spectra and electrical current measurements. The majority of the uncertainties in the scale realisation rely on the determination of T , which have been most recently discussed in Ref. 4. A similar approach to uncertainty evaluation is taken in this work, where a sensitivity coefficient is used to convert the relative value of each uncertainty component to an uncertainty in T . Relative values of the filter radiometer calibration, r_{FR} , d , r_{HTBB} , HTBB radiance uniformity, HTBB emissivity, and n [5] are taken into account. For the FEL lamp measurements, the lamp to monochromator

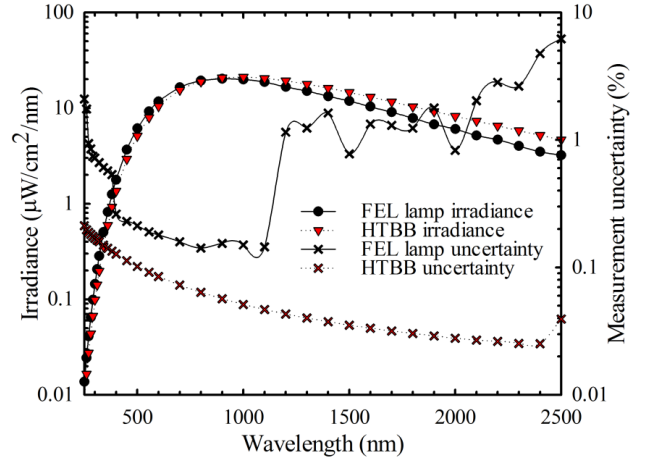


Figure 3. Measured FEL lamp (1000 W) and HTBB (2950 K) irradiance data with associated uncertainties ($k=1$).

distance, current stability as well as repeatability and reproducibility of the spectral measurements are considered. Spectral irradiance data for the HTBB at 2950 K and for a 1000 W FEL lamp, as well as their associated uncertainties, are shown in Figure 3.

SUMMARY

NRC now has a complete primary spectral irradiance scale from 250 nm to 2500 nm. A HTBB is implemented as a standard radiometric source and an NRC-designed filter radiometer, with spectral responsivity traceable to the NRC absolute cryogenic radiometer, is utilized to measure the thermodynamic temperature of the HTBB. This source and detector-based realisation will be the basis for calibrating 1000 W FEL spectral irradiance standard lamps.

REFERENCES

1. A. A. Gaertner, Spectral irradiance calibrations at the National Research Council of Canada (NRC), *Journal of Modern Optics*, 56, 1488-1496, 2009.
2. L. P. Boivin and A. A. Gaertner, Realization of a spectral irradiance scale in the near infrared at the National Research Council of Canada, *Applied Optics*, 31, 6082-6095, 1992.
3. L. P. Boivin, C. Bamber, A. A. Gaertner, R. K. Gerson, D. J. Woods, and E. R. Woolliams, Wideband filter radiometers for blackbody temperature measurements, *Journal of Modern Optics*, 57, 1648-1660, 2010.
4. E. R. Woolliams, *et al.*, Thermodynamic temperature assignment to the point of inflection of the melting curve of high-temperature fixed points, *Philosophical Transactions of the Royal Society A*, 374, 20150044, 2016. (Supplementary Material)
5. A. A. Gaertner, Consultative Committee for Thermometry Working Document CCT/10-11 (2010). https://www.bipm.org/cc/CCT/Allowed/25/D11_CCTdraftAAG.pdf.

Packaging of silicon photodiodes for use as cryogenic electrical substitution radiometer

Eivind Bardalen¹, Marit Ulset Nordsveen², Per Ohlckers¹, and Jarle Gran²

¹ University of South-Eastern Norway, Borre, Norway, ² Justervesenet, Kjeller, Norway,

Corresponding e-mail address: eba@usn.no

A technique for packaging photodiodes for use as a cryogenic electrical substitution radiometer was developed. Thermal simulations were used to design a diffusive thermal link between the photodiode and temperature sensor to ensure equivalence between optical and electrical heating. Tests showed good agreement between the measured and simulated time constant for an assembled module supporting the model accuracy.

INTRODUCTION

The EMPIR research project chipS·CALe aims to develop new experimental techniques for optical power measurements using self-calibrating photodiodes [1]. The dual mode detector (DMD) can be operated both as a predictable quantum efficient detector (PQED) and as an electrical substitution radiometer (ESR). In PQED mode, the optical power is measured directly from the photocurrent, while in ESR mode, a temperature sensor is used to compare optical and electrical heating of the photodiode. The term self-calibrating refers to the fact that the internal losses can be determined by use of the formula:

$$\delta(\lambda) = 1 - \frac{i_{photo}}{\Phi_T} \cdot \frac{hc}{e\lambda}, \quad (1)$$

where Φ_T is the optical power measured in ESR mode and i_{photo} is the measured photocurrent.

A proper design of the photodiode packaging is required to ensure thermal equivalence between optical and electrical heating in ESR mode. Furthermore, the module was designed using COMSOL Multiphysics simulations to give a high signal, while having low time constant.

DESIGN AND MODELLING

A silicon photodiode (PD) with size 11 mm x 11 mm x 0.5 mm functions as both the optical absorber and heater. In optical heating mode, the power is absorbed in the central part of the active layer of the photodiode, while in electrical heating mode, the power is dissipated near the topside cathode ring by applying a forward bias to the photodiode.

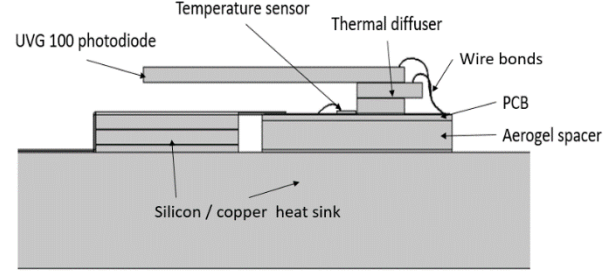


Figure 1: Sketch of DMD-detector

A thin (<200 μm) PCB with 18 μm thick copper tracks is used for electrical connections to the photodiode and temperature sensor via wire bonds and soldered wires. The temperature sensor is bonded with epoxy and wire bonded to the PCB, which is thermally coupled to the photodiode with a thermal diffuser element, consisting of a layered silicon/epoxy structure. The PCB is bonded on a thermally insulating aerogel spacer, which in turn is bonded on a machined copper heat sink. Copper wires are soldered to the edge of the PCB, forming the electrical connections to the external circuitry. These wires also form the main thermal link to the heat sink.

COMSOL's heat transfer module was used to simulate the temperature distribution in the module. The heating of the photodiode was modelled as a constant heat source, P . In the optical mode, the heat source was applied in an elliptical shape in the center of the photodiode, while in electrical heating mode, the heating was applied near the edges of the photodiode. The effect of the different temperature distributions in the photodiode at these different modes (T_{opt} , T_{el}) is evaluated in the photodiode in terms of inequivalence (in ppm), defined as

$$\delta_T = \frac{T_{opt} - T_{el}}{T_{opt}} \cdot 10^6 \quad (2)$$

Simulation results show inequivalence in the temperature sensor below 1 ppm at temperatures 80 K and 35 K, and higher than 100 ppm at 300 K. At 300 K, the grey-body thermal emission from hotspots lead to the higher inequivalence. As shown in Figure 2, the inequivalence is reduced from more than 1000 ppm in the photodiode to less than 1 ppm in the temperature sensor. This is likely due to the low

thermal conductance (k) of the epoxy, which in combination with the high thermally conducting silicon lead to an effectively anisotropic thermal conductance, where $k_z < k_{x,y}$.

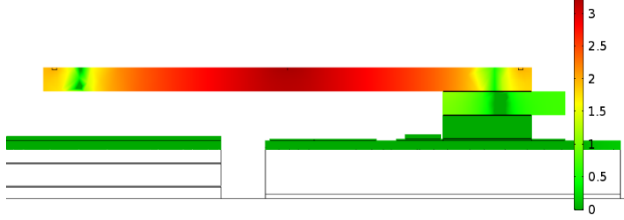


Figure 1: Logarithm of inequivalence at 80 K ($\log(\delta_T)$)

The RC time constant of the system is largely decided by the heat capacity, C_{PD} , of the photodiode and the thermal resistance of the weak link, R . In the ideal case:

$$\tau = R \cdot C_{PD} \quad (3)$$

Since the temperature increase ΔT for an input power P is given by $\Delta T = R \cdot P$, the thermal resistance also takes the meaning of responsivity: $R = \Delta T/P$.

The simulation results, as shown in Figure 4, give a time constant that is around 50% higher than given by eq. (3). This is likely caused by the additional thermal capacitances in the system, such as that of the thermal diffuser, adhesive layers and PCB.

FABRICATION AND TESTS

An assembled module, as shown in Figure 3, was tested in vacuum at 285 K, 80 K and 35 K. Time constant measurements were performed by heating the module both optically and electrically, with cooldown to base temperature between each heating step. The $1/e$ time constant was then found from an exponential fit of the temperature signal. Electrical heating was done by applying a forward bias voltage to the photodiode, while optical heating was done by a 594 nm laser beam hitting the centre active area of the photodiode, while having an open electrical circuit. In both cases, the heating power was 270 μ W.

Table 1 shows the measured and simulated time constant for the device at three temperatures. At 285 K and 80 K, the experimental values agree fairly good, while at 35 K the time constant is significantly higher than the simulated one. The overall good agreement between measured and simulated values supports the accuracy of the model, but more accurate material data is required for low temperatures.

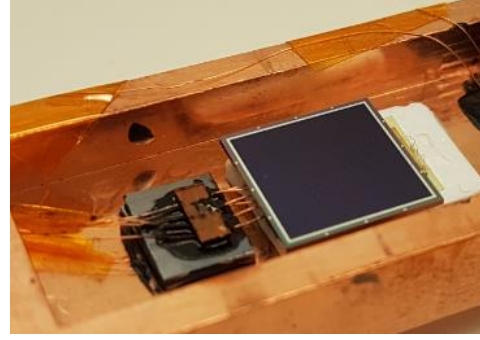


Figure 3: Assembled DMD-module

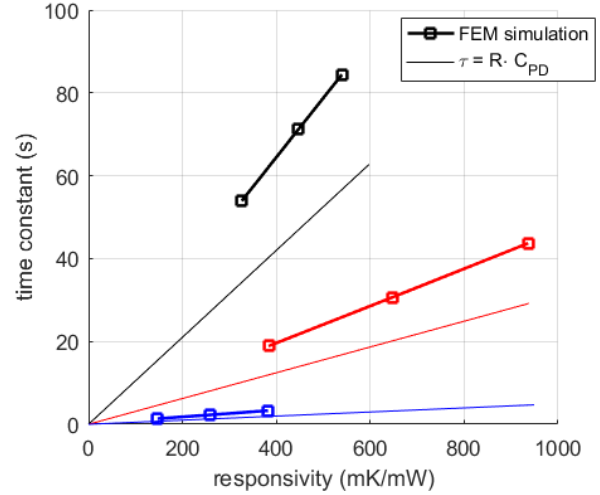


Figure 4: Simulated time constant vs. responsivity at 300 K (black), 80 K (red) and 35 K (blue). Solid lines show theoretical limit given by eq. (2)

Table 1: Experimental and simulated time constant for assembled module.

Temperature	τ (s) (experimental)	τ (s) (simulated)
285 K	83.5	81.2
80 K	41.8	36.8
35 K	10.3	2.8

ACKNOWLEDGEMENT

This project has received funding from the EMPIR programme co-financed by the Participating States and from the European Union's Horizon 2020 research and innovation programme.

REFERENCES

1. Jarle Gran. (2019, June 26). Publishable Summary for 18SIB10 chipS·CALe. Zenodo.
<http://doi.org/10.5281/zenodo.3545677>

Investigation of surface passivation thin film materials for improved predictable quantum efficiency detectors

Ozhan Koybasi¹, Ørnulf Nordseth², Marco Povoli¹, Lars Breivik¹, Anand Summanwar¹, Mauro Rajteri³, Jarle Gran⁴

¹SINTEF MiNaLab, Oslo, Norway; ²Institute for Energy Technology (IFE), Kjeller, Norway; ³INRIM, Turin, Italy;

⁴Justervesent, Kjeller, Norway;

Corresponding e-mail address: Ozhan.koybasi@sintef.no

We report the preliminary results from our study of different surface passivation thin film materials and deposition processes for development of PQEDs with excellent performance and stability at room temperature and cryogenic temperatures. Our work aims at maximizing the fixed charge density in the dielectric and the effective minority charge carrier lifetime as well as reducing the optical absorption of the dielectric in the visible range to a negligible level. We have so far demonstrated a fixed charge density of $> 5 \times 10^{12} \text{cm}^{-2}$ and effective lifetime of $> 4 \text{ ms}$ for p-type FZ wafers passivated with PECVD SiN_x or a stack of thermal SiO_2 and PECVD SiN_x . For n-type FZ wafers passivated with ALD Al_2O_3 , we have obtained an effective lifetime of $\sim 20 \text{ ms}$.

INTRODUCTION

The predictable quantum efficiency detector (PQED) has shown a strong promise to replace the cryogenic radiometer (CR)- which is bulky, expensive and complex - as a primary standard for ultra-high accuracy measurements of optical power¹⁻³. To keep up with the increasing measurement accuracy needs of National Metrology Institutes (NMIs), the internal quantum deficiency (IQD) of PQEDs -which is around 0.01% - needs to be reduced by one order of magnitude, which may require operation at cryogenic temperatures. The aim of our work is therefore to develop PQEDs with superior performance and stability at both room and cryogenic temperatures.

The PQED is made of an induced-junction photodiode in which the p-n junction is formed by the inversion of the silicon surface due to the fixed charges in the passivation dielectric unlike the conventional p-n junction formed by doping. Increasing the fixed charge density $-Q_f$ in the dielectric has been theoretically predicted to improve the quantum efficiency of the diode by decreasing the surface recombination velocity (SRV) at the dielectric-silicon interface, as well as improving the linearity and dynamic range of the detector.

METHODS

We investigate different passivation materials and methods to achieve high fixed charges (Q_f) and low interface traps (D_{it}) that can potentially lead to very low SRVs and consequently to extremely low IQDs. Since it would be too costly to make photodiodes with all possible types of passivation and experimentally difficult to compare their performance at both room temperature and cryogenic temperatures, we follow a different approach. Improved 3D simulation models enable us to limit the study to specific properties of the surface passivation materials. Through this approach, the challenge of improving PQEDs is transformed into high resolution material analysis at various temperatures, which saves cost and makes it possible to predict the response of photodiodes made from the various passivation techniques without having to complete the photodiodes production process. The best passivation material/process for cryogenic temperatures will then be used to manufacture a set of improved PQEDs.

Our research focuses on three different surface passivation dielectrics. For p-type Si wafers, we investigate i) thermally grown SiO_2 , ii) SiN_x deposited by plasma enhanced chemical vapor deposition (PECVD)⁴, and iii) stacks of these two dielectrics, due to their positive fixed charge. Simulations have shown that the IQD of PQEDs made with n-type silicon substrate is a factor of 2-3 times better than that of those made with p-type substrate, if all other parameters are kept the same⁵. For n-type wafers, we study Al_2O_3 deposited by atomic layer deposition (ALD), due to its negative fixed charge, as passivation dielectric for PQEDs.

In our work, we optimize the growth or deposition processes for these dielectrics to minimize the SRV by maximizing Q_f and keeping D_{it} as low as possible. The effective minority charge carrier lifetime (τ_{eff}) is measured by photoluminescence (PL) imaging. Q_f is extracted from C-V measurements on MOS capacitors. The optical characterization of the

dielectric thin films is performed with spectroscopic ellipsometry. The results we have obtained so far were measured at room temperature, but we are currently also working on development of variable temperature setup for lifetime measurements at cryogenic temperatures.

RESULTS AND DISCUSSION

Figure 1 shows the carrier lifetime map of a 6-inch p-type FZ Si wafer with PECVD SiN_x passivation. The PECVD reactor used for deposition is APM from SPTS. The deposition was carried out at temperature of 350 °C and total pressure of 2000 mTorr. The gas flow of both SiH₄ and NH₃ was 60 sccm. The film thickness was measured with ellipsometer to be ~140 nm. As can be seen in Figure 1, a uniform carrier lifetime of 4.1 ms is obtained. The fixed charge density extracted from MOS C-V measurements is about $3 \times 10^{12} \text{ cm}^{-2}$.

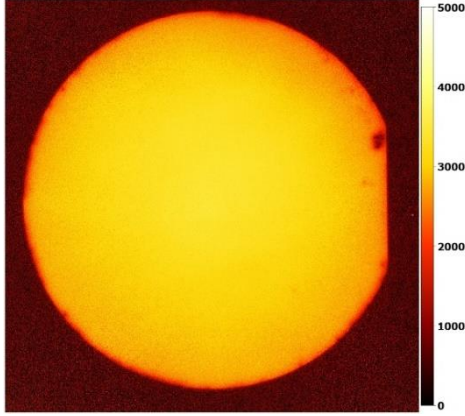


Figure 1. Carrier lifetime map at carrier density of $7.1 \times 10^{14} \text{ cm}^{-3}$ of 6-inch p-type FZ wafer passivated with PECVD SiN_x. The gas flow used for deposition was 60 sccm of SiH₄ and 60 sccm of NH₃. The color bar shows τ_{eff} in μs .

In order to examine the effect of stoichiometric ratio of SiN_x on the lifetime, fixed charge and optical properties of the dielectric, the gas flow ratio of SiH₄ to NH₃ was varied from 1/3 to 3, keeping the NH₃ flow fixed at 60 sccm. Figure 2 shows the C-V characteristics of a MOS capacitor measured at a frequency of 10kHz for each deposition. The C-V shift to more negative values for lower SiH₄ indicate that the Q_f increases with decreasing SiH₄:NH₃ ratio, reaching a value of $6 \times 10^{12} \text{ cm}^{-2}$ for a flow ratio of 1:3. This is ~2 orders of magnitude higher than the Q_f we have obtained in thermally grown SiO₂.

Table I summarizes the key characteristics of SiN_x depositions with different gas flow ratios. The charge and optical characteristics improve significantly with decreasing SiH₄:NH₃ ratio while the carrier lifetime

does not show a strong dependence on the gas flow ratio.

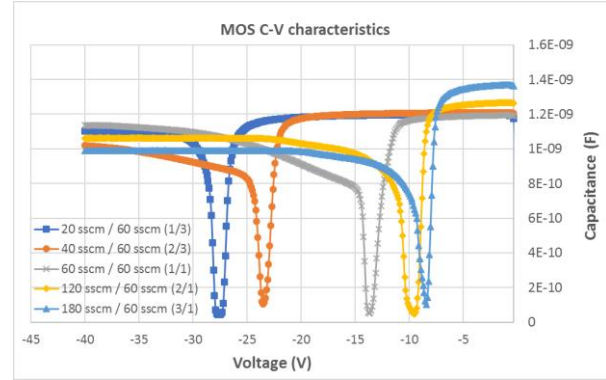


Figure 2. MOS C-V characteristics of PECVD SiN_x films with varied SiH₄/NH₃ gas flow ratio.

Table I: Key characteristics of PECVD SiN_x passivation with different stoichiometric ratios. The NH₃ flow was kept constant at 60 sccm and SiH₄ flow was varied to obtain the given ratios.

SiH ₄ /NH ₃ flow ratio	τ_{eff} (ms @ cm^{-3})	Q_f (cm^{-2})	n @ 632 nm	k @ 632 nm
1/3	4.4 @ 7.1×10^{14}	6.0×10^{12}	1.84	0
2/3	4.2 @ 6.8×10^{14}	5.2×10^{12}	1.98	1.9×10^{-5}
1	4.1 @ 6.5×10^{14}	3.1×10^{12}	2.12	1.9×10^{-3}
2	4.1 @ 6.5×10^{14}	2.2×10^{12}	2.44	1.7×10^{-2}
3	4.1 @ 6.6×10^{14}	2.1×10^{12}	2.67	4.8×10^{-2}

We also investigated the passivation of p-type FZ wafers with a stack of ~5 nm thermal oxide and ~140 nm thick PECVD SiN_x, which leverages the low interface trap density and good stability of thermal SiO₂ as well as high fixed charge density of PECVD SiN_x. This stack has exhibited a few times higher lifetime than bare SiN_x deposited directly on Si.

The preliminary measurement of 60 nm ALD Al₂O₃ films deposited at 300°C shows a τ_{eff} of ~20 ms on n-type FZ Si, n -index of 1.6 and k -index of 3.0×10^{-6} (at wavelength of 632 nm), which is very promising. Further characterization of these films (including Q_f) and optimization of the deposition process is ongoing.

With the results we have obtained so far, there is a good chance of achieving the desired IQD of <1 ppm at room temperature, eliminating the need for cryogenic operation, which is to be verified.

Acknowledgement: This project has received funding from the EMPIR programme co-financed by the Participating States and from the European Union's Horizon 2020 research and innovation programme

REFERENCES

1. M. Sildoja *et al*, Metrologia **50** (2013) 395–401
2. I. Muller *et al*, Metrologia **50** (2013) 395–401
3. K Salffner *et al* 2018 Metrologia **55** 654
4. M. Bazilchuk *et al* 2015 Appl. Phys. Lett. **106**, 143505
5. Timo Dönsberg *et al* 2017 Metrologia **54** 821

Spectral Radiance Scale Traceability Chain by Using Monte Carlo Application

Seval Meric¹, Ozcan Bazkir¹, Mustafa Kilin²

¹National Metrology Institute (TUBITAK-UME), P.O.Box.54, 41470 Kocaeli, Turkey
seval.meric@tubitak.gov.tr, ozcan.bazkir@tubitak.gov.tr

²Engineering Physics Department, Gaziantep University, 27310, Sehitkamil, Gaziantep, Turkey
mkilin@gantep.edu.tr

This work aims to determine the radiance responsivity to be used in the calibration of polychromatic radiation sources with low uncertainty using GUM and GUM Supplement-1. The spectral radiance values of the polychromatic lamps are obtained using the radiance responsivity of the system. The study aims to develop the derivation and better understand traceability of the other radiometric and photometric quantities with low uncertainty from the fundamental radiometric radiance unit. Measurement results obtained in the extended measurement uncertainty scale are determined using both classical and Monte Carlo methods.

INTRODUCTION

In this research, laser-based high-resolution spectra radiometric systems were established. The proposed system calculates the basic radiometric unit radiance with low uncertainty and meets the needs of instrument characterization, which may occur in scientific research activities using other radiometric and photometric quantities. A monochromator that is used for the spectral radiance measurement was first characterized in terms of the wavelength accuracy [1]. Secondly, a reflection-type Si-based trap detector, which is used in the NMIs laboratory as a radiometric transfer standard [2,3] comparatively characterized against an electrical substitution cryogenic radiometry (ESCR) system [4,5]. Thirdly, by using an integrated sphere and laser, the Lambertian distributed radiance beam was determined [6]. In the specific laser wavelength region, radiance values were obtained using a He-Ne tunable (543, 594, 604, 612 and 632.8nm), Argon-Ion (457, 477, 488, and 514 nm), and Nd-Yag (1064 nm) lasers.

MEASUREMENT SETUP

Laser-based measurement system was established, as shown in Fig. 1. First, spectral radiance values were obtained at the laser wavelength using a silicon-based

trap detector [7]. Then, the same system was transferred to the double monochromator system, and the spectral transfer function of the system was obtained. Thus, the spectral radiance values of the unknown polychromatic radiator source were derived using a transfer function obtained with low uncertainty measurements using both the classical and Monte Carlo approaches.

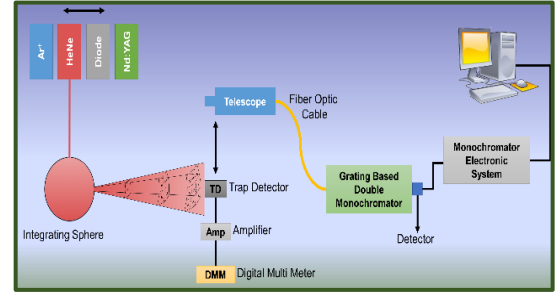


Figure 1: Spectral radiance measurement system.

$$L_{\lambda}(\lambda) = \frac{I^s(\lambda)}{R_s^*(\lambda)} \frac{D^2}{A_s A_d (1 + \delta)} \quad (1)$$

Where $\delta = r_s^2 r_d^2 / D^4$ and $D^2 = r_s^2 + d^2 + r_d^2$ in Eq. 1, and A_s and A_d are the active area of the radiation source and detector, respectively. d represents the distance between the radius of source r_s and detector r_d . In addition, $I^s(\lambda)$ is the measured spectral current, $L_{\lambda}(\lambda)$ is the spectral radiance, and $R_s^*(\lambda)$ is the spectral power responsivity of the detector.

SYSTEM CHARACTERIZATION AND CORRECTION FACTORS

The spectral radiance formula defined in Eq. 1 should include some uncertainty and correction factors caused by the measurement setup in Fig. 1. These are the wavelength accuracy of the monochromator system; trap detector characterization, geometric correction factor owing to the conservation of radiance, the monochromator wavelength shift, and the bandwidth. If the spectral radiance distribution formula of an unknown radiation defined as in Eq. 1 is redefined, it is given as in Eq. 2.

$$L_{\lambda}^U(\lambda) = \frac{I^U(\lambda_M) I^S}{I^M(\lambda_M) R_s^*(\lambda_L) \Delta\lambda \Delta C} \text{CorFac} \quad (2)$$

Where $I^U(\lambda_M)$ and $I^M(\lambda_M)$ monochromator output signal of the unknown and known radiation source respectively. $\Delta\lambda$ is the full width at half maximum (FWHM), which is the spectral band-pass value of the monochromator.

RESULTS

The GUM Supplement-1 (Monte Carlo) [8] method is a relatively new method, and is a useful and practical alternative to the Gum method. Here, the probability density function (PDF) is defined for each measured output quantity, and defines the system and includes pseudo random numbers.

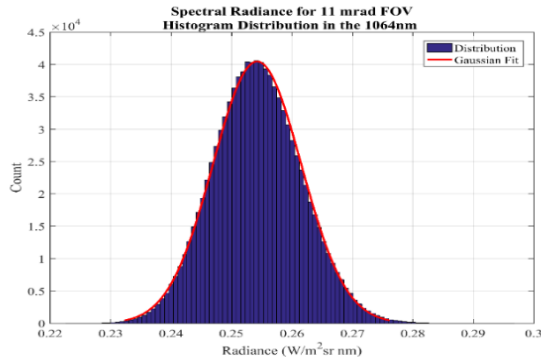


Figure 2: Plot showing 1064-nm spectral radiance histogram distribution and associated Gaussian fit function. The mean value of the function is the spectral radiance value 0.25424 ($\text{Wm}^{-2}\text{sr}^{-1}\text{nm}^{-1}$), and one sigma value of it is 0.007315 ($\text{Wm}^{-2}\text{sr}^{-1}\text{nm}^{-1}$).

Table 1: k=2 Extended standard uncertainty for 11-mrad FOV in terms of both GUM and GUM Supplement-1.

λ (nm)	GUM		Monte Carlo		Ratio
	Radiance ($\text{W/m}^2\text{sr nm}$)	k=2 Extended uncer. ($\text{W/m}^2\text{sr nm}$)	Radiance ($\text{W/m}^2\text{sr nm}$)	k=2 Extended uncer. ($\text{W/m}^2\text{sr nm}$)	
457	0.11952	0.0058	0.11953	0.0057	1.0229
477	0.14892	0.0072	0.14887	0.0071	1.0198
488	0.16825	0.0119	0.16819	0.0108	1.0998
514	0.19524	0.0094	0.19483	0.0093	1.0086
543	0.24632	0.0122	0.24708	0.0121	1.0099
594	0.32095	0.0153	0.32041	0.0153	1.0033
604	0.33359	0.0165	0.33469	0.0162	1.0204
612	0.32635	0.0155	0.32543	0.0155	0.9980
633	0.34347	0.0163	0.34237	0.0163	0.9993
1064	0.25589	0.0150	0.25424	0.0146	1.0253

When the function that defines the measurement system is linear, the Gum method offers an easy

solution, but when the function that defines the system is not linear, the Monte Carlo [32] method is more practical because the partial derivation of the output quantities according to each input quantity makes the calculations difficult.

For different mrad FOV, a Monte Carlo operation was performed, and the uncertainties corresponding to spectral radiance values were calculated.

CONCLUSION

The spectral radiance traceability chain was created, and the radiance value of any radiation source or the surface of an unknown radiance value can be described with ease. In this study, to find a spectral transfer function, uncertainty values were defined by a 95% confidence level by both the classical method and Monte Carlo method.

This study is a guide towards the derivation of radiometric and photometric measurement units. In addition, the Monte Carlo uncertainty, which is often preferred by many national metrology laboratories in recent days, is a guide for calculations.

REFERENCES

1. M. Kilin, H. Tutunculer, S. Meric “Effective measurement of the wavelength accuracy calibration by using Monte Carlo Uncertainty,” AIP conference Proceeding, volume 2178, 2019.
2. N. Mart, “Development of detectors and calibration methods for spectral irradiance and radiometric temperature measurement” Metrology Research Institute Report 25/2005.
3. R. Köhler, R. Goebel, and R. Pello, “Results of an international comparison of spectral responsivity of silicon photodetectors,” Metrologia **32**, 463-468 (1995/96).
4. A.R. Schaefer and K. L. Eckerle, “Spectrophotometric tests using a dye-laser-based radiometric characterization facility,” Appl. Opt. **23**, 250–256 (1984).
5. J. Geist, E. F. Zalewski, and A. R. Schaefer “Spectral response self-calibration and interpolation of silicon photodiodes,” Appl. Opt. **19**, 3795, 3799 (1980).
6. S. Brown, G. Eppeldauer, and K. R. Lykke, “Facility for spectral irradiance and radiance responsivity calibrations using uniform sources,” Appl. Opt. **45**, No. 32, (2006)
7. B. Ozcan, S. Ferhad “Electrical substitution cryogenic radiometer based spectral responsivity scale between 250-2500 nm wavelengths,” Optics and Lasers in Engineering **34** (2004) 427–438.
8. BIPM Joint Committee for Guides in Metrology, “Evaluation of measurement data — Supplement 1 to the “Guide to expression of the uncertainty in measurement” — Propagation of distribution using a Monte Carlo method,” Final draft September (2006).

Improving the spectral radiance and irradiance facility at NPL

Nicole L George¹, William R Servantes¹, and Teresa M Goodman¹

¹The National Physical Laboratory, Teddington, United Kingdom

Corresponding e-mail address: nicole.george@npl.co.uk

The use of blackbodies as a reference standard in spectral irradiance scales is common in many NMIs. This has been the basis of the NPL SRIPS facility for a number of years. This facility has recently been upgraded with new component systems, revised operation processes and analysis software, to improve the uncertainties obtained and robustness of operation. The upgrade has required a re-evaluation of the uncertainty budget. The opportunity was also taken to carry out a detailed health and safety review of the blackbody system and the laboratory environment.

INTRODUCTION

Blackbodies are commonly used as references, by NMIs across the globe, to define spectral radiance and irradiance scales [1, 2, 3]. An ultra-high temperature blackbody source with a pyrolytic graphite core design is implemented at NPL, allows temperatures in the range of 3000 K to 3100 K to be reached, allowing use across the UV to near-IR spectral range while maintaining good stability and uniformity of the source, to 0.0053% and 0.05%, respectfully, with the stability measurement occurring at 800 nm. The blackbody provides an ideal primary source to operate alongside FEL standard lamps and the systems calibrated by them [4, 5].

The ultra-high temperature blackbody is the sourced used within the semi-automated Spectral Radiance and Irradiance Primary Scale (SRIPS) facility. The SRIPS facility is used to calibrate a range of irradiance and radiance standards, from FEL lamps to integrating spheres, in the range of 250 nm to 2500 nm. Within NPL, these standards are used to disseminate calibration references to other spectroradiometer systems, including the NPL Reference Spectroradiometer, as well as to calibrate band & hyperspectral imagers and spectroradiometers for external stakeholders, including those used in ESA, EC Copernicus & national space agency Earth observation (EO) programmes. The dissemination of

the SI through the SRIPS facility creates a crucial link to the pinnacle of the optical radiation traceability chain, the Cryogenic Radiometer, as shown in figure 1. The SRIPS facility also provides the same vital link to a number of industries, including but not limited to, manufacturing, medicine, photobiological safety, and film & television, either directly or indirectly through another NPL facilities.

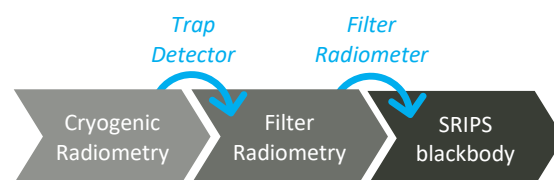


Figure 1. The traceability chain linking various NPL facilities together, from the primary standard for optical measurement, the Cryogenic Radiometer, to the ultra-high temperature blackbody in the SRIPS facility.

NPL SRIPS FACILITY

The blackbody is operated at a nominal 3050 K, a temperature chosen to ensure a balance between producing an adequate output power across the whole spectrum and maintain the longevity of the cavity. Accurate temperature stability and temperature knowledge of the blackbody cavity is needed to meet the radiometric uncertainty requirements. An optical feedback system maintains the stability of the cavity via current control to 0.4 K. To determine the cavity temperature, a calibrated filter radiometer (FR), with a peak response at 800 ± 5 nm, is used, allowing the radiance of the blackbody radiation to be measured over a narrow spectral band [6].

The blackbody emitted radiation is collected by an integrating sphere, and is wavelength selected by a double additive monochromator system, before it exits onto a selection of detectors, the specific detector selected for the wavelength of interest.

The FR measurements are used to calculate the cavity temperature using knowledge of the FR responsivity [7]. The calculated blackbody temperature is then used to determine the spectral radiance output of the blackbody across the spectrum

range. The ratio between the spectral radiance computed using Planck's Law and the spectral data collected after passing through the monochromator system is determined at each individual wavelength and recorded as the system calibration factor (SCF),

$$SCF(\lambda) = \frac{L_{BB}(\lambda)}{S_{BB}(\lambda)} \quad (1)$$

where L is the theoretical radiance, and S is the measured detector signal.

The irradiance source under test is treated in the same way; with the source emission collected by the integrating sphere, passing through the monochromator and sampled by the detector bank. The SCF is applied along with a geometric factor, g , to adjust the units from radiance, L , to irradiance, E , as given by

$$E_{SUT}(\lambda) = \frac{\pi g}{A} \cdot \frac{L_{BB}(\lambda)}{S_{BB}(\lambda)} \cdot S_{SUT}(\lambda) \quad (2)$$

where A is the area of the aperture on the integrating sphere, and S is the signal from the source under test. $E_{SUT}(\lambda)$ gives the final spectral irradiance data [5].

UPGRADING THE SRIPS FACILITY

Since the initial completion of the facility in 2002, SRIPS has undergone a series of upgrade projects. The most recent upgrade has focused on ensuring the long-term reliability of the system.

Within the SRIPS facility, there are key components which are fundamental to operation. Namely, the blackbody pyrolytic graphite core, its power supply & control, the monochromator and integrating sphere, and detector components – all components have been reviewed and either maintained, replaced or their long-term operation de-risked. The blackbody core was replaced, along with sufficient spares to allow SRIPS to operate for the next decade. An additional bespoke power supply has also been procured to safeguard this long-term operation plan. Additionally, the monochromator has been replaced with a new double additive monochromator with larger diffraction gratings, increasing the system throughput at the extremes of the spectral range.

The software used to operate SRIPS has been updated to streamline the data collection and analysis. The uncertainty budgets have also been revised following a complete re-evaluation at the contribution level, with inspiration taken from

collaborations with EO metrology projects, changing the approach to uncertainty analysis to a more visual and coherent style [7].

Finally, all aspects regarding the safe operation of the ultra-high temperature blackbody in a laboratory setting has been reviewed, with the aim of ensuring a best practice approach is undertaken with the spectral irradiance scale systems. All physical safety features required for the operation have been considered, with particular regard for the water-cooling system and argon used to purge air from the blackbody cavity, as well as, the health implications of particulate emission from the cavity.

This paper will describe the upgrade project outcomes and safely best practise conclusions.

This work was supported by the UK government's Department for Business, Energy and Industrial Strategy.

REFERENCES

1. E.R. Woolliams, N.J. Harrison, and N.P. Fox, Preliminary results of the investigation of a 3500 K black body, *Metrologia*, **37**, 501-504, 2000.
2. Zhi-Feng Wu, Caihong Dai, Jia-Lin Yu, Bo Huang, Hui-Quan Ou-Yang, Investigation of Blackbody 3500M, *The International Society for Optical Engineering*, 8192, 2011.
3. V.I. Sapritsky, B.B. Khlevnoy, V.B. Khromchenko, B.E. Lisiansky, S.N. Mekhontsev, U.A. Melenevsky, S.P. Morozova, A.V. Prokhorov, L.N. Samoilov, V.I. Shapoval, K.A. Sudarev, and M.F. Zelener, Precision blackbody sources for radiometric standards, *Applied Optics*, **36**(22), 5403-5408, 1997.
4. B.B. Khlevnoy, M.L. Samoylov, I.A. Grigoryeva, N.A. Ibragimov, V.I. Shapoval, A.V. Puzanov, S.A. Ogarev, Development of High-Temperature Blackbodies and Furnaces for Radiation Thermometry, *International Journal of Thermophysics*, **32**, 1686–1696, 2011.
5. E.R. Woolliams, Development and evaluation of a high temperature blackbody source for the realisation of NPL's primary spectral irradiance scale, PhD, University of Manchester, 2003.
6. E.R. Woolliams, Uncertainty Analysis for Filter Radiometry Based on the Uncertainty Associated with Integrated Quantities, *International Journal of Thermophysics*, **35**, 1353-1365, 2014.
7. J. Mittaz, C.J. Merchant, and E.R. Woolliams, Applying principles of metrology to historical Earth observations from satellites, *Metrologia*, **56**(3), 032002, 2003.

Upgrade of cryogenic radiometer control electronics and software

Stefan Källberg and Mikael Lindgren

RISE Research Institutes of Sweden, Borås, SWEDEN

Corresponding e-mail address: Stefan.Kallberg@ri.se

The successful upgrade of control electronics and software for a cryogenic radiometer is described. A commercially available temperature controller using ac resistance thermometry was used with an existing radiometer. The upgrade did not involve any change to the radiometer hardware except the controller electronics. The upgrade was therefore relatively easy to implement. New software in LabView was also developed. Initial results show an improvement in performance and calibration results in line with expectations.

INTRODUCTION

Absolute Cryogenic Radiometers (ACRs) are commonly used at National Metrology Institutes (NMIs) for the realization of absolute radiant flux. These devices, based on electrical-substitution radiometry carried out at cryogenic temperatures in vacuum, provide the lowest achievable uncertainties for a wide range of power levels and wavelengths [1]. However, given their operating principles, there are generally large costs associated with building or purchasing such systems. Hence, it is worthwhile to prolong the lifetime of already existing older systems. Many NMIs are still using ACR systems that were manufactured in the 1990s, although the electronics and software may not be compatible with modern technology.

The photometry and radiometry group at RISE Research Institutes of Sweden has since 1995 been using the commercial LaseRad ACR from Cambridge Research & Instrumentation Inc. (CRi). It is used for realization of absolute radiant flux in the visible and NIR wavelength range. Due to increasing communication problems and excess noise in the electronics, in 2016 a decision was made to rebuild the LaseRad ACR using a commercially available cryogenic temperature controller. This paper describes the steps taken for this upgrade to be successful, including initial performance evaluation of the upgraded system.

METHOD

The cryogenic radiometer operates by absorbing radiation in a Receiver, see Figure 1. The Receiver has blackened surfaces which act to absorb incident radiation, thereby leading to a certain Receiver temperature. Typical sensitivity is 0.6 K/mW. The Receiver temperature is accurately monitored by the use of a carbon film resistor thermometer.

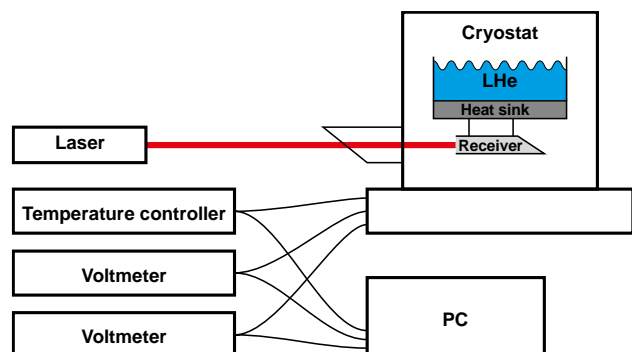


Figure 1. Schematic setup of the ACR with new control electronics.

The Receiver is thermally connected to a Heat sink which is used to provide a long-term stable temperature. The Heat sink temperature is monitored by a Germanium thermistor and can be controlled by means of a heater.

In operation, the radiation is blocked, and electrical power is fed to the Receiver via a small resistive heater, placed near the location where the radiation is absorbed. By measuring this electrical power by external means, a measure for the radiation power is obtained.

The basis for the operation is that two control loops are used to stabilize the temperatures of both the Receiver and Heat sink. The control loops were realized in the supplied Control electronics, together with AC bridge measurement of the two thermometer resistances.

RISE ACR experienced difficulties in obtaining a stable control of the two temperatures. The reason was attributed to self-oscillation in the control electronics and could not easily be remedied. For this reason, a new temperature controller (TC) was

acquired from Lakeshore Cryotronics [2] and interfaced to the existing ACR. A similar controller has been used in another ACR and proved suitable [3]. The internal hardware (thermometers and heaters) of the ACR was left unchanged, but some electronic PCBs which were originally placed in the base of the cryostat were removed.

The TC is a Model 372 AC Resistance Bridge and Temperature Controller. It has provisions for two independent closed-loop PID controls, each using a range of thermistor resistances. The measuring principle is *ac* measurement of resistance in tandem with an internal lock-in amplifier in order to extract small measurement signals. This enables very low excitation currents to be used and excellent rejection of noise.

The TC is directly connected to the internal hardware of the ACR, by the use of standard shielded twisted-pair wires. The only component placed thermally isolated in the cryostat housing was a 1000- Ω precision resistor, used for measuring the Receiver heater current. The voltages across the resistor and across the heater are each measured with an 8 $\frac{1}{2}$ -digit voltmeter and the product constitutes the measurand (electrical power = optical power).

The software originally provided with the ACR ran in a DOS-like environment and was directly interfaced to the original electronics. Consequently, it was most desirable to also exchange it when the new TC was implemented. New software for control was developed in LabView and subsequently used for evaluation of system performance and performing calibrations.

RESULTS

In addition to the up-to-date software and communications of the upgraded ACR, enabling easy and stable operations, the electrical performance of the ACR was improved compared to before the upgrade. Even though the system has not yet been fully optimized regarding shielding of cables and TC settings, the RMS noise of the Receiver heater power at 400 μ W is around 0.01 %, see Figure 2.

In May 2019, the first calibration of silicon trap detectors was done using the upgraded ACR. When comparing the obtained detector responsivities to historical data, see Figure 3, the results are in line with what was expected, clearly indicating that the ACR is functioning properly.

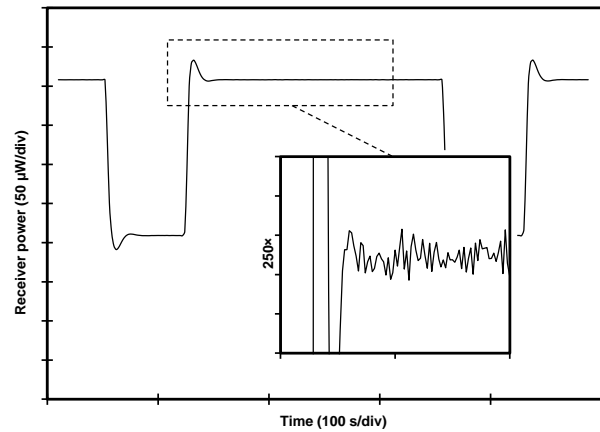


Figure 2. Results from system performance study with incident radiation of 200 μ W being switched on and off, resulting in a rapid change in the measured temperature of the Receiver.

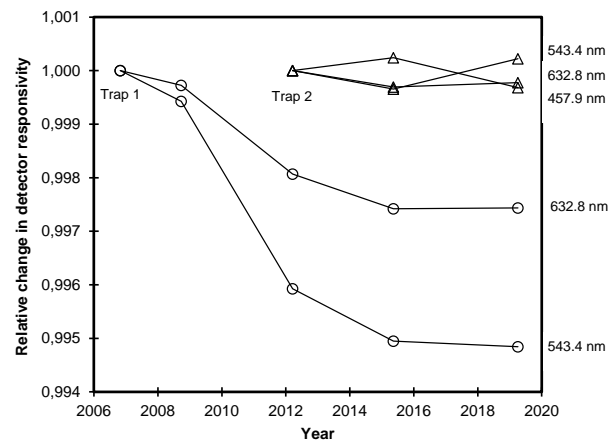


Figure 3. Results from trap calibration. The results from 2019 are using the upgraded control electronics. Measurement uncertainties ($k=2$) are typically 0.05–0.06 %.

REFERENCES

1. A. Parr *et al.*, Optical Radiometry Vol. 41, Academic Press, 2005.
2. Lake Shore Cryotronics, Inc. www.lakeshore.com
3. S. M. Carr *et al.*, Experimental measurements and noise analysis of a cryogenic radiometer, Rev. Sci. Instr. 85, 075105, 2014.

Measurements of monolithic GaInP₂/InGaAs/Ge triple-junction solar cells

Haifeng Meng, Junchao Zhang, Limin Xiong, Yingwei He, Bifeng Zhang, Chuan Cai, Shuai Man and Meng Wang

National Institute of Metrology, Beijing, P. R. China

Corresponding e-mail address: menghf@nim.ac.cn

For the sake of the three composed sub-cells, that is GaInP₂, InGaAs and Ge sub-cell, the monolithic GaInP₂/InGaAs/Ge triple-junction solar cells can make use of solar irradiance in the wavelength range of 300 nm to 1800 nm, so that achieve high efficiency. They have become the main energy source for space on-orbit applications, and should be assembled into space solar array for use. Their photo-electric parameters were critical for space energy system setting. In this paper, we will present methods for their spectral responsivity and I-V characteristic measurement.

INTRODUCTION

Because of the high efficiency and high power weight ratio, triple-junction GaInP₂/InGaAs/Ge solar cells were always assembled into arrays and wings for space energy use. Three composed sub-cells, GaInP₂, InGaAs and Ge are epitaxial grown on one substrate and sub-cells are interconnected in series by tunnel diodes leading to a standard two-terminal contact, as the scheme shown in Figure 1. Efficiency more than 30% and V_{OC} higher than 2.5 V were previously reported [1,2]. Before assembled to an array, their current-voltage characteristics under AM0 STC should be measured to obtain key parameters, such as short circuit current, open circuit voltage and maximum output power, etc. Solar cells with similar current would be picked out for an array to achieve rated performance parameters, also to avoid power shortage or other safety problems causing by current mismatch. And match the link voltage of the spacecraft system by making use of reasonable series and parallel design.

In this paper, by appropriately adjusting the wavelength range and irradiance intensity of the bias light, the direction and value of the bias voltage, we would present the measurement of spectral responsivity for monolithic GaInP₂/InGaAs/Ge triple-junction solar cells. Then combine with spectral mismatch analysis technique, we employ a high spectral matched double-light solar simulator to measure the I-V characteristic for monolithic triple-junction GaInP₂/InGaAs/Ge solar cells. Small mismatch error makes our results more reliable. Hope it will help to obtain reliable results for multi-junction solar cells' photo-electric parameters under AM0 STC.

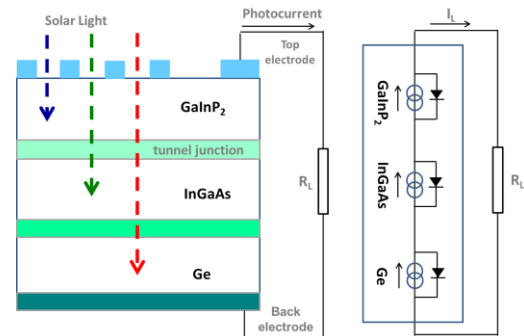


Figure 1. Scheme of structure of monolithic triple-junction GaInP₂/InGaAs/Ge solar cells.

CALIBRATION

As shown in Figure 2, a facility of spectral responsivity measurement for monolithic GaInP₂/InGaAs/Ge triple-junction solar cells based on monochromatic light system was built [3]. It is aimed to measure the spectral responsivity for monolithic multi-junction solar cells, but it also suitable for single-junction solar cells. Various bias light and optional bias voltage were critical for multi-junction solar cell's measurement, which made the untested junctions saturated and the junction under test to be the current-limiting junction.

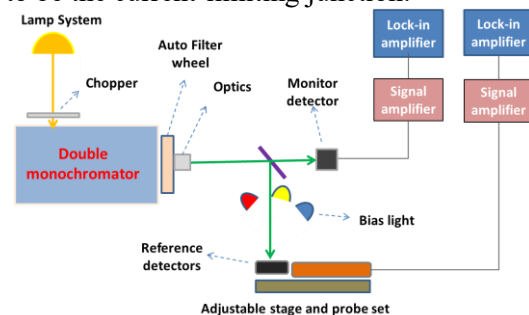


Figure 2. Scheme of the spectral responsivity measurement facility for monolithic triple-junction solar cells.

By using calibrated Si detector and Ge detector as standard, the measurement wavelength range can cover 300 nm to 1800 nm, and directly traceable to the national standard equipment for detector's spectral responsivity in NIM (National Institute of Metrology, China). Figure 3 was shown the measurement results for two types (S1 and S2) of GaInP₂/InGaAs/Ge triple-junction solar cells with different band-gap design. Because the Ge bottom

junction's current is far greater than other two junctions, it cannot be the current-limiting junction. So we only discuss about the top and middle junction herein. According to Figure 3, red-shift was obviously observed when compare S2 to S1.

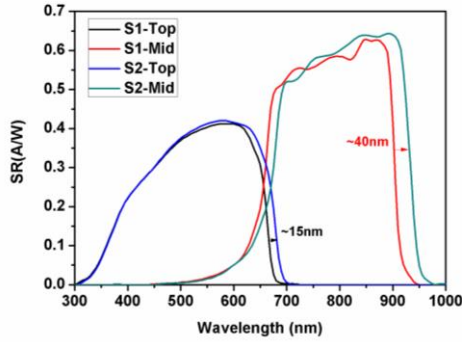


Figure 3. Curves of the spectral responsivity for two types monolithic GaInP₂/InGaAs/Ge triple-junction solar cells.

Based on the spectral responsivity results, a high spectral matched double-light AM0 solar simulator was employed for I-V measurement. Firstly, according to IEC 60904-7 [4], we theoretically calculate the mismatch error caused by solar simulator's spectrum. Table 1 shown that the errors for S1 were both smaller than 1%, an acceptable value, while for S2, it is different.

Table 1. Mismatch error calculation results of two types of triple-junction solar cells, by using a high spectral matched solar simulator.

	S1-Top	S1-Mid	S2-Top	S2-Mid
I_{STC}	71.15	72.02	75.13	75.67
I_{SS}	71.21	71.40	75.31	74.41
Error	0.09%	-0.85%	0.24%	-1.66%

Then we change the route, isotypes were used. Figure 4 was shown the spectral responsivity curves for all-structure monolithic GaInP₂/InGaAs/Ge triple-junction solar cells and their isotypes.

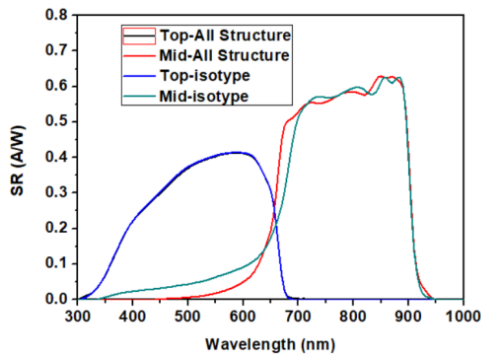


Figure 4. Curves of the spectral responsivity for all-structure monolithic GaInP₂/InGaAs/Ge triple-junction solar cells and their isotypes.

Further analysis was conducted for spectral mismatch according to equation (1).

$$MMF = \frac{\int_{\lambda_1}^{\lambda_2} E_{ref}(\lambda) s_{ref}(\lambda) d\lambda \int_{\lambda_1}^{\lambda_2} E_{source}(\lambda) s_{test}(\lambda) d\lambda}{\int_{\lambda_1}^{\lambda_2} E_{ref}(\lambda) s_{test}(\lambda) d\lambda \int_{\lambda_1}^{\lambda_2} E_{source}(\lambda) s_{ref}(\lambda) d\lambda} \quad (1)$$

It turns out the error for top junction and middle junction was 0 and 0.06%, both were negligible. So, we use the isotypes to calibrate the double light AM0 solar simulator, and keep the state unchanged to measure the I-V curve for monolithic triple-junction solar cells. Temperature also should be controlled and monitored. Figure 5 demonstrated the measured I-V curves of four monolithic GaInP₂/InGaAs/Ge triple-junction solar cells.

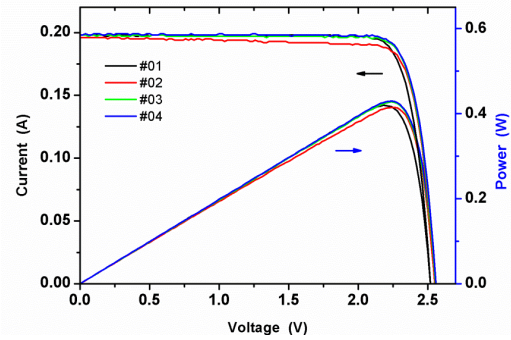


Figure 5. I-V curves for four monolithic GaInP₂/InGaAs/Ge triple-junction solar cells measured under AM0 STC.

CONCLUSIONS

This work stated the measurement for monolithic triple-junction GaInP₂/InGaAs/Ge solar cells, including spectral responsivity and I-V characteristic. It will provide strong support for their space application.

REFERENCES

1. S. Bailey, R. Raffaele, [Handbook of Photovoltaic Science and Engineering]. Edited by A. Luque and S. Hegedus, John Wiley & Sons, Ltd, Space Solar Cells and Arrays, 413-448, 2003.
2. M. A. Green, K. Emery, Y. Hishikawa, W. Warta, E. D. Dunlop, D. H. Levi, A. W. Y. Ho-Baillie, Solar cell efficiency tables (version 49). Progress in Photovoltaics: Research and Applications, 25 (1) 3-13, 2016.
3. H. Meng, L. Xiong, J. Zhang, Y. He, B. Zhang, C. Cai, Spectral responsivity measurements of monolithic GaInP₂/InGaAs/Ge triple-junction solar cells, Proc. SPIE, 2019.
4. IEC 60904-7 (Ed. 3.0) Photovoltaic devices - Part 7: Computation of the spectral mismatch correction for measurements of photovoltaic devices, 2008.

UV spectral irradiance responsivity calibrations using a scanning method in a monochromator-based facility

Jeanne M. Houston, Maritoni Litorja, Howard W. Yoon

*Sensor Science Division
National Institute of Standards and Technology
Gaithersburg, USA*

Corresponding e-mail address: hyoon@nist.gov

The use of the NIST monochromator-based facility for irradiance responsivity calibration of filter radiometers from 300 nm to 1800 nm is described. Spectral irradiance responsivities are determined using a combination of the measured spectral power responsivity and the effective aperture areas. The effective aperture area is measured using a focussed output beam which is raster-scanned over a grid which overfills the aperture diameter of the filter radiometer. We show that if a uniform irradiance field is projected at the plane of the filter radiometer, then the exact aperture area of the filter radiometer need not be determined. We also show that irradiance responsivities can be measured using a variable-sized, rectangular output beam which is larger than the aperture diameter. Total uncertainties of 0.4 % ($k=2$) have been achieved in spectral irradiance responsivity measurements of < 1 mm diameter UV filter radiometers.

INTRODUCTION

Although National Measurement Institutes (NMI) routinely issue spectral power responsivity calibrations, there are often requests for spectral irradiance responsivity calibrations of detectors and filter radiometers [1]. The knowledge of the incident irradiance or the optical power incident on a surface area is a much more relevant quantity in the areas of ultra-violet (UV) disinfection or materials curing. In the past, irradiance responsivities were determined using a two-step, source-based approach, where the relative or absolute power responsivities were calibrated and then referenced to a calibrated detector using a uniform UV source.

We describe the process and uncertainties of UV spectral irradiance responsivity calibrations using the NIST Visible Spectral Calibration Facility (VisSCF) [2]. The VisSCF is a monochromator-based facility

with precision, calibrated x- and y-scanning stages which has been configured to measure spatial uniformities and effective aperture areas along with providing spectral power responsivity calibrations. The advantages of using a well characterized spectral power responsivity calibration setup for spectral irradiance responsivity calibration are many. Most of the instrument characterizations and uncertainty analysis will have been already performed in setting up a power responsivity calibration facility. Also, the spatial-scanning method has been extensively used by NMIs for measurements of aperture area primarily using scanned laser beams [3]. Here we show that this method can be used to measure UV spectral irradiance responsivities of small < 1 mm diameter filter radiometer with low additional uncertainties even when the size of the output beam is larger than the area of the filter radiometer.

EXPERIMENTAL SETUP

A calibrated spectral irradiance responsivity of a 365 nm UV filter radiometer is shown in Fig. 1. The UV filter radiometer is aligned into detector positions and first measured for initially for effective spectral power responsivity by comparisons to NIST working standard Si diodes.

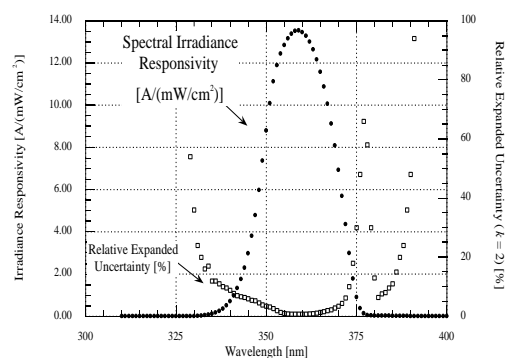


Figure 1. The irradiance responsivity of a ~ 1 mm diameter UV filter radiometer which is centered at 365 nm.

Since the optical beam can be larger than the opening of the filter radiometer, this measurement mode does not determine the correct spectral power responsivities. The rectangular optical output beam from the monochromator is shaped in the horizontal direction using variable-width slits on the monochromator and the height is adjusted using independently adjustable vertical slits. This separation of the two axes are to preserve the wavelength calibration as the optical beam size is changed. For the measurements shown in Fig. 1 a 1.0 mm by 1.0 mm square optical beam was used.

After the effective spectral power responsivities are measured, the UV filter photometers are also scanned to determine the effective aperture area at the peak of the spectral responsivity. A plot of the spatial power responsivity scan is shown in Fig. 2. The plot is

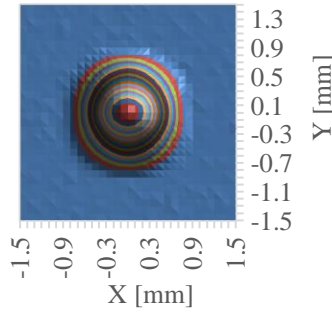


Figure 2. Spatial mapping of the 365 nm filter radiometer with a 1 mm diameter opening using a 0.85 mm square optical beam. The spatial contours show the convolved shape.

normalized to the center and the effective area is determined using,

$$A_{eff} = \Delta x \Delta y \sum_{j=n_x}^{n_x} \sum_{k=n_y}^{n_y} \frac{\phi_{j,k}}{\phi_L}, \quad (1)$$

where Δx and Δy are the horizontal and vertical step sizes of the measurements and the double summation denotes a total sum of the normalized intensities [3]. The determined effective areas for the same filter radiometer can vary greatly depending on the optical beam size as shown in Fig. 3.

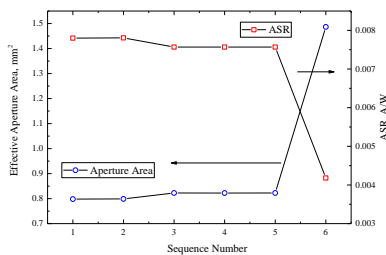


Figure 3. Effective aperture areas and ASR measured using different optical output beam sizes.

The irradiance responsivities in Fig. 4 are determined using the product of the effective area and the effective ASR,

$$S_E = A_{eff} * ASR_{eff}, \quad (2)$$

where S_E is the spectral irradiance responsivity.

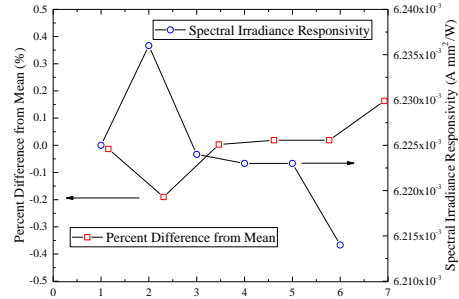


Figure 4. Spectral irradiance responsivities of the 435 nm filter radiometer measured using different optical beam sizes. The large variations in Fig. 3 collapses to variations of only 0.2 % in irradiance responsivities.

The total uncertainties of the measurements shown in Fig. 4 are about 0.45 % ($k=2$) at 435 nm.

CONCLUSIONS

We demonstrate that monochromator-based facilities designed for spectral power responsivity calibrations can be adopted for irradiance responsivity calibrations of UV filter radiometers with resulting uncertainties of 0.45 % ($k=2$). This has been achieved by scanning optical beams which can vary in sizes and which can be larger than the detector aperture areas. These different irradiance responsivities are within the combined uncertainties of the measurements. This scanning approach can be easier and faster in practice than the traditional two-step method currently utilized at NMIs while achieving lower uncertainties than the presently utilized methods.

REFERENCES

1. D R Taubert, R Friedrich, J Hartmann and J Hollandt, "Improved calibration of the spectral responsivity of interference filter radiometers in the visible and near infrared spectral range at PTB," *Metrologia*, **40**, 2003.
2. T. C. Larason and J. M. Houston, "Spectroradiometric Detector Measurements: Ultraviolet, Visible, and Near-Infrared Detectors for Spectral Power," NIST Special Publication 250-41 (2008).
3. E. Ikonen, P. Toivanen, A. Lassila, "A new optical method of high-accuracy determination of aperture area," *Metrologia*, **35**, 1998.

Nonlinearity corrections of spectrographs using combinatorial methods

Howard W. Yoon, Thomas C. Larason, John T. Woodward

*Sensor Science Division
National Institute of Standards and Technology
Gaithersburg, USA*

Corresponding e-mail address: hyoon@nist.gov

Signal or gray-level linearities of spectrographs have been determined using a dual-path combinatorial method. Spectrographs were characterized for nonlinearities at fixed integration times using the NIST beamconjoiner apparatus. The 120 dependent signals were then analysed using nonlinear least squares fit with 40 independent signals and a 6th order polynomial as variables. The uncertainties of the nonlinearity corrections determined from the residuals of the fits were found to be 0.2 % ($k=2$) over the range of signals from 30 to 30,000. The resulting nonlinearity corrections were also compared with those measured using a constant optical source and varying integration times.

INTRODUCTION

The uses of spectrographs in radiometry and photometry are increasing due to the need for spectral information which can be used to better interpret measurement results. Since calibrations of these spectrographs can be performed only over a limited set of experimental conditions while the instruments can be used to measure widely varying optical levels, lack of knowledge about the linearities of these instruments can lead to large uncertainties in the final data products.

In the past, some laboratories have based their linearity characterizations of spectrographs on separately calibrated reference photodiodes which are used to simultaneously monitor the incident radiation on the spectrographs [1]. Others have used a dual-path method and measured mean-signal ratios which are then multiplied together to determine nonlinearity correction factors [2]. Both techniques have deficiencies, such as sparsity of points in the first method or the need to form a product of all the signal ratios to determine nonlinearity factors.

In this work, we describe the use of the NIST beamconjoiner setup [3] to determine nonlinearity correction factors of spectrographs.

EXPERIMENTAL SETUP

Briefly, the beamconjoiner is a dual-path setup using a single 100 W quartz-tungsten halogen (QTH) lamp with an MR16 reflector. The single beam is split into two paths as shown in Fig. 1 and then recombined onto the detector or the device-under-test. A total of 120 signals can be measured during a single run. Each of the 40 independent fluxes along with polynomial correction terms are solved using nonlinear least-square fit of the over-determined system of equations.

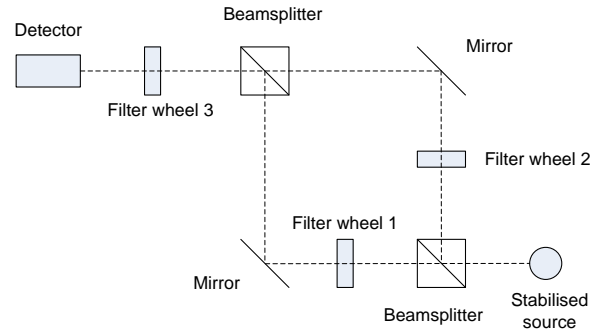


Figure 1 The NIST beamconjoiner apparatus for linearity testing of optical sensors. A 100 W QTH lamp was used as the source for these measurements.

Each signal can be written as a response to the incident flux or conversely, each flux results in signal as a function of the flux,

$$\Phi(i, j, k) = \Phi(i, j) + \phi(j, k) = r_0 + s(i, j, k) + r_2 \cdot s^2(i, j, k) + \dots + r_n \cdot s^n(i, j, k) \quad (1)$$

where $\phi(i, j, k)$ denote the flux, $s(i, j, k)$ is the measured signal at the detector, and r_0, r_2, \dots, r_n are the coefficients which relate the signal to the flux.

A typical measurement run with 120 spectra is shown in Fig. 2. Before each run, the filter wheels are positioned to the maximum transmittance, and then integration time of the spectrograph is adjusted such that signals are not saturated. A spectrum is taken for

each filter wheel combination and plotted as digital number (DN) over the integration time. For the analysis, only the averaged signals from the plateau region near the center of the spectra are analysed. This is to have constant nonlinearity corrections for pixel-averaged signals.

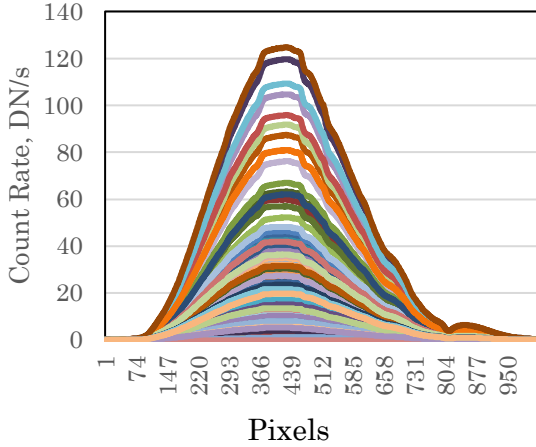


Figure 2. 120 spectra taken using a spectrograph during a single measurement run using the beamconjoiner. Integration time of 240 ms was used. The spectral range is from about 300 nm to 1100 nm. The averaged signals at the middle plateau were used for linearity fits.

ANALYSIS

The measured net signals ratioed to calculated fluxes are plotted in Fig. 3a as a function of the net signal along with the 6th order polynomial to correct the

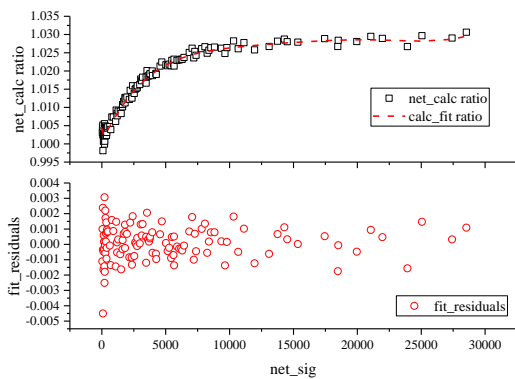


Figure 3. (a) The ratios of net measured signals to the fitted signals without the polynomial corrections. Nonlinearities of up to 3 % can be perceived. The polynomial correction function is also plotted. (b) The residuals of the fit showing 0.2 % ($k=2$) residuals.

nonlinearity. Without any corrections, the deviation of ratios from unity clearly indicates the presence of nonlinear behavior of up to 3 %. Introducing a 6th order polynomial correction reduces the deviations to about 0.2 % ($k=2$) as observed in Fig. 3b.

These nonlinearity corrections were further checked by measuring a constant radiation source with changing integration times to examine whether the count rates were linear. The 3 % nonlinearity could be clearly measured in the deviations of the count rate although with higher noise and at fewer signal levels as can be measured using the beamconjoiner setup.

DISCUSSION AND CONCLUSIONS

We demonstrate that the combinatorial method can be used to characterize the nonlinearity corrections of spectrographs. These focal-plane arrays exhibit substantially greater nonlinearities than single element detectors.

In this work, only the gray-level or the signal-dependent nonlinearity was characterized. Spectrographs could have integration-time-dependent nonlinearities, and methods to examine such dependences using the beamconjoiner method are being explored.

REFERENCES

1. T. Pulli, S. Nevas, O. El Gawhary, S. van den Berg, J. Askola, P. Kärhä, F. Manoocheri, and E. Ikonen, "Nonlinearity characterization of array spectroradiometers for the solar UV measurements," *Appl. Opt.* 56, 3077-3086, 2017.
2. M. Tanabe and K. Godo, "Effect of spectroradiometer characteristics on chromaticity for tricolor laser light sources," *J. Opt. Soc. Am. A* 36, 1379-1384, 2019.
3. D.R. White, M.T. Clarkson, P. Saunders, and H.W. Yoon, "A General Technique for Calibrating Indicating Instruments," *Metrologia* 45, 199-210 2008.
4. J. Pacheco-Labrador, A. Ferrero, and M. Pilar Martín, "Characterizing integration time and gray-level-related nonlinearities in a NMOS sensor," *Appl. Opt.* 53, 7778-7786, 2014.

Cantilever-based photoacoustic detection of electromagnetic radiation

Sucheta Sharma¹, Toni Laurila¹, Jussi Rossi², Markku Vainio^{2,3} and Erkki Ikonen^{1,4}

¹*Metrology Research Institute, Aalto University, Espoo, Finland,*

²*Photonics Laboratory, Physics Unit, Tampere University, Tampere, Finland,*

³*Department of Chemistry, University of Helsinki, Helsinki, Finland,*

⁴*VTT MIKES, Espoo, Finland*

Corresponding e-mail address: sucheta.sharma@aalto.fi

We report here on a highly sensitive silicon cantilever-based photoacoustic electromagnetic radiation detector of broad spectral bandwidth. The developed detector can be used for measuring the power of radiation in the 100 nW to 10 mW range. Experiments have been carried out using 633 nm and 1523 nm lasers. The results show very good linearity and dynamic range.

INTRODUCTION

For monitoring environmental pollution or detecting toxic, inflammable and explosive gases [1-2], which pose major risk on health, safety and security, photoacoustic (PA) spectroscopy is one of the applied detection methods because of its high sensitivity and selectivity [3-4]. In the gas sensing applications, the non-radiative relaxation processes of electromagnetic-radiation-induced excited molecules generate heat and consequently produce pressure waves, which give rise to the PA signal. One of the common methods for detecting the PA signal employs a capacitive microphone. However, a capacitive microphone has several limitations including the nonlinear response of the membrane in sensing the external pressure. Apart from that, for improving the sensitivity, the gap between the membrane and the backplane of the capacitive condenser cannot be reduced below a certain limit, as the gas cannot anymore flow freely through such narrow region due to viscous effect [5]. An alternative approach has been developed for PA signal detection where optical beam deflection and micro-mechanical silicon (Si)-cantilevers are used. The cantilever-based approach does not have such drawbacks and it has been successfully used in many applications requiring very sensitive PA signal detection [6]. The cantilever-based PA signal detection method employs a compact interferometer for measuring the deflection of the cantilever tip [7]. In this study, we report on a Si-cantilever-based PA detection system for electromagnetic power measurements. Benefits of the new power measurement method include good

linearity and broad spectral bandwidth. In contrast, most available power detectors are highly dependent on the operating wavelengths. Si-photodiode detectors, for example, work mainly in 200 nm-1100 nm range whereas, for infrared wavelengths, InGaAs detectors are used. However, the PA principle employs absorption of radiation into a black absorber material and this can be made rather independent of the operating wavelength over a large spectral range.

EXPERIMENT

Figure 1 shows the schematic diagram of the experimental setup. The system comprises three main modules: (1) an electromagnetic radiation source, the power of which falls on the absorbing material (for this experiment, candle soot was used) to generate heat, (2) the acoustic section consisting of a gas cell (in this case, it was filled with air) which contains the sample and a cantilever, (3) the optical readout system, to measure the cantilever deflection using a compact Michelson interferometer. The incident radiation first passes through a chopper and gets absorbed by the black absorber material to produce heat. The generated periodic heating causes volume expansion of the gaseous medium within the closed PA cell and produces pressure waves, which are finally detected by monitoring the position of the cantilever tip by using the optical interferometer.

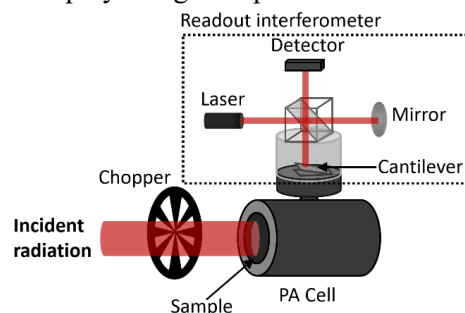


Figure 1. Schematic diagram of the experimental setup.

RESULTS

Experiments were performed using two incident wavelengths: 633 nm and 1523 nm. In both cases, the

frequency of the chopper was at 43 Hz and the generated PA signals were measured by varying the input power of the incident radiation. Figure 2 shows the linearity of the PA signal amplitude with the input power. The data shows good linearity with R^2 values of 0.99985 and 0.99982 for 633 nm and 1523 nm wavelengths respectively.

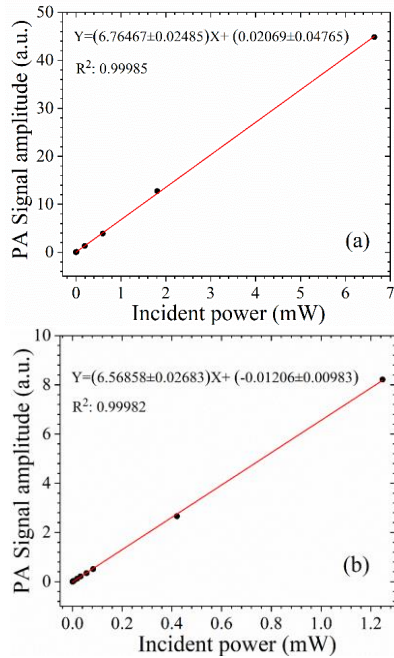


Figure 2. Linear response of PA signal with incident power of input radiation (a) 633 nm and (b) 1523 nm.

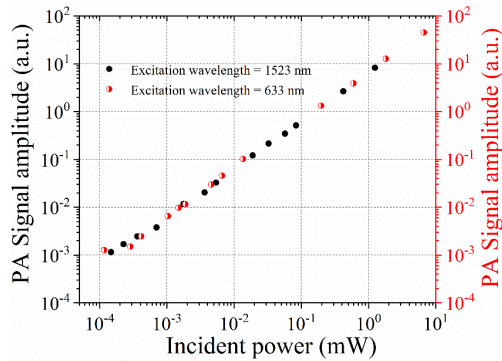


Figure 3. Peak amplitude of PA signal depicts no dependency on the incident wavelength.

The incident power was varied from 116 nW to 6.64 mW for 633 nm and from 147 nW to 1.25 mW for 1523 nm wavelength input radiation. As shown in Figure 2, the dynamic range is nearly five orders of magnitude. According to theoretical estimation the highest power, which can be measured using the system, is close to 1W. Hence, the dynamic range can still be further extended. As Figure 3 demonstrates, the PA response is practically independent of the incident wavelengths. Thus, this process has potential to get extended to cover spectral ranges from Ultraviolet (UV) to Terahertz (THz) with suitable window materials of the PA cell.

CONCLUSION

We have presented a cantilever-based PA power detection technique, which is capable of measuring incident power from approximately 100 nW to 10 mW. This detection mechanism has the potential to measure up to 1 W making the dynamic range significantly large. In future, the detection scheme will be applied for power measurements of UV, infrared and THz (30 μm – 300 μm) radiation sources. Currently, no single power detector can operate under all the required wavelengths. The new PA power detection technology will be useful not only for scientific research but it can be applied also to medical and chemical industries where power measurement is one of the key necessities.

ACKNOWLEDGEMENT

This work is a part of Universal electromagnetic radiation detector (UNIDET) research project, which is funded by the Academy of Finland (Project numbers 314363 and 314364).

REFERENCES

1. K. Chen, B. Zhang, S. Liu, Q. Yu, Parts-per-billion-level detection of hydrogen sulfide based on near-infrared all-optical photoacoustic spectroscopy, *Sensors and Actuators B: Chemical*, 283, 1–5, 2019.
2. J. Rossi, J. Uotila, T. Laurila, E. Ikonen and M. Vainio, Broadband Electromagnetic Radiation Detector Based on Photoacoustic Effect, *Proceedings of OIE 2019*, Edited by: Petri Kärh , Erkki Ikonen, Yoshio Hayasaki, and Kai Peiponen, 89-90, Espoo and Tallinn, 2019.
3. T. Tomberg, T. Hieta, M. Vainio and L. Halonen, Cavity-enhanced cantilever-enhanced photo-acoustic spectroscopy, *Analyst*, 144, 2291–2296, 2019.
4. R. A. Coutu Jr., I. R. Medvedev and D.T. Petkie, Improved Sensitivity MEMS Cantilever Sensor for Terahertz Photoacoustic Spectroscopy, *Sensors*, 16, 251(1-11), 2016.
5. I. Kauppinen, A. Branders, J. Uotila, J. Kauppinen and T. Kuusela, Sensitive and fast gas sensor for wide variety of applications based on novel differential infrared photoacoustic principle, *Proceedings IRS², SENSOR+TEST Conferences*, 71 – 75, N rnberg, 2011.
6. V. Koskinen, J. Fonsen, K. Roth and J. Kauppinen, Cantilever enhanced photoacoustic detection of carbon dioxide using a tunable diode laser source, *Applied Physics B*, 86, 451–454, 2007.
7. T. Laurila, H. Cattaneo, T. P yh nen, V. Koskinen, J. Kauppinen and R. Hernberg, Cantilever-based photoacoustic detection of carbon dioxide using a fiber-amplified diode laser, *Applied Physics B*, 83, 285–288, 2006.

Differential spectral responsivity measurements of large bifacial solar cells

Petri Kärhä¹, Janne Askola¹, Kinza Maham¹, Timo Dönsberg², and Erkki Ikonen^{1,3}

¹Aalto University, Espoo, Finland, ²Hehkulab Ltd, Espoo, Finland, ³VTT MIKES, Espoo, Finland

Corresponding e-mail address: petri.karha@aalto.fi

We report on measurements of large bifacial solar cells using a new LED-based measurement setup for wavelength range 290 – 1300 nm. The measurement uncertainty in visible is 1.7% ($k=2$). Main challenges in the measurements are the spatial uniformity and the measurement of short circuit current. These topics are discussed in detail.

INTRODUCTION

Differential spectral responsivity is needed for solar cell development and analysis. It can also be used in testing to correct for the spectral mismatch between the light source used in the measurement and the standardized reference spectrum. Spectral responsivity has to be measured for a cell under biased conditions due to possible nonlinearity [1], which poses challenges.

In this paper, we present our setup for differential spectral responsivity. We also discuss its use for and challenges in measuring large bifacial solar cells.

Quasi-monochromatic radiation for measuring the spectral responsivity is provided with 30 temperature-stabilized LEDs assembled on a rotatable carousel, covering the wavelength range of 290 – 1300 nm. LEDs are driven with pulsed current at a frequency of 177 Hz. The signal produced is measured from the cell current using a lock-in amplifier and a shunt resistor.

The relative spectra of the LEDs have been measured. In cell measurements, the absolute levels of the spectra are measured with a silicon trap detector and an aperture with a diameter of 3 mm. The relatively large bandwidths of the LEDs are taken into account in the data analysis using a recursive iteration process, similar to the method used earlier for analysing spectral irradiance of halogen lamps from filter radiometer measurements [3]. The method gives accurate values for spectral responsivity at the effective wavelengths of the LEDs, and an interpolation function.

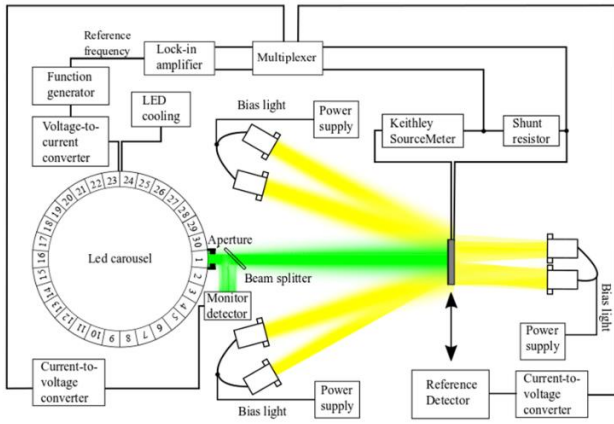


Figure 1. Setup for measuring differential spectral responsivities of bifacial solar cells. [2]

MEASUREMENT SETUP

Our setup for measuring differential spectral responsivity of solar cells [2] is presented in Fig. 1. Bias lighting is provided by towers of halogen lamps, 7 x 50 W in each tower. Four towers in the front provide up to 1000 W/m² irradiance on the cell. Two additional towers are used to light the back side of bifacial cells e.g. with 1/3 of the intensity on the front side.

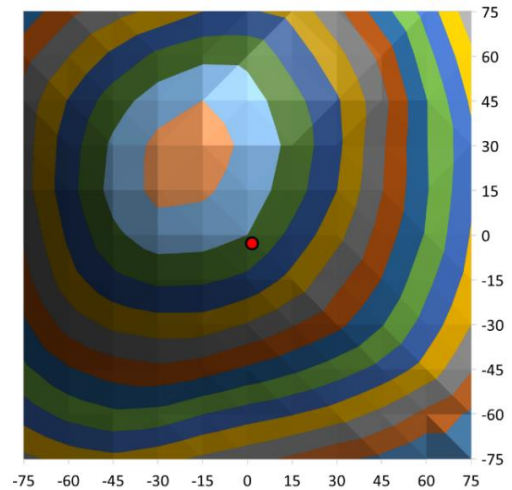


Figure 2. Spatial uniformity of the 727 nm LED irradiance. The axis values are given in mm. The difference between the contour lines is 2.5%. The red circle in the center shows the size and location of the 3 mm aperture of the trap detector used in measuring the spectral irradiance.

RESULTS AND DISCUSSION

The setup has been used to measure the spectral responsivities of bifacial solar cells with a large area of 15 x 15 cm². The large size poses challenges due

to non-uniformities of the measurement beams and the large dynamic range of the measurement signal.

Radiation field in the sample location was scanned for spatial uniformity for all the 30 LEDs used. Figure 2 shows the spatial uniformity of the 727 nm LED which had the largest non-uniformity. The radiation field of this LED is narrow and slightly misaligned. The uniformity is taken into account in data analysis by dividing the irradiance measured in the center of the field with the average of the irradiance measured across the large cell area.

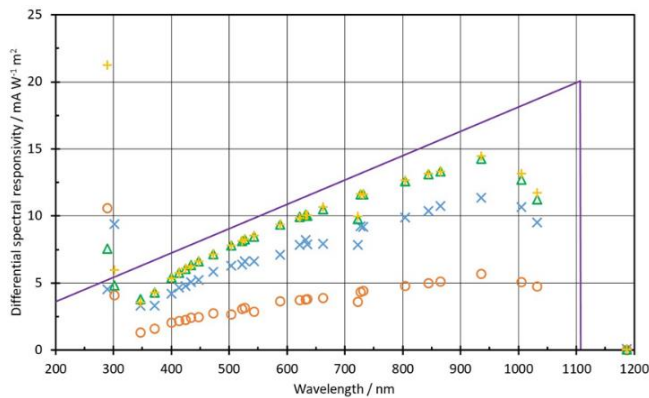


Figure 3. Differential spectral responsivity for a 15 x 15 cm² bifacial solar cell at different bias light conditions. Green triangles indicate results with no bias, yellow pluses with 500 W/m² on the front surface, blue crosses with 1000 W/m² on the front surface, and red circles with 1000 W/m² on the front and 300 W/m² on the back. The solid purple line represents the ideal responsivity assuming 100% quantum efficiency. [2]

Despite the large area and bifaciality, the open circuit voltage of the bifacial solar cell is only 0.565 V. Yet the current produced exceeds 7 A with the front surface exposed to 1000 W/m² and even higher with the back-side exposed. According to [1], the voltage over the cell should remain below 3% of the open circuit voltage, thus, the maximum impedance for the measurement electronics is 2.4 mΩ.

For currents smaller than 3 A, we have a Keithley source meter forcing the voltage across the cell to zero as seen in Fig. 1. For currents above 3 A, we have tested a zero-flux sensor DS200ID-CD1000 from Danisense, and a newly acquired source meter from Hehkulab providing zero voltage up to 10 A.

Figure 3 shows measurement results obtained with the zero-flux current sensor. With zero-flux, the solar cell is short circuited with a cable going through the sensor, and the sensor gives out a current without loading the cell.

The measurements without bias lights and with 500 W/m² applied on the front surface are in good

agreement indicating linearity. The current level at the latter condition is 3.5 A. With the higher irradiance levels producing currents of 7.1 A and 8.4 A, the responsivity drops due to nonlinearity. One cause of this nonlinearity is the resistance of the wire used to short circuit the cell, 15 mΩ. The results indicate that active control of the cell voltage is needed to reach these high irradiance levels. Another possible reason is heating of the cell due to bias light.

The uncertainty of the measurements is shown in Fig. 4. The expanded uncertainty of the obtained differential spectral responsivities over the visible region 400 – 730 nm is on the average 1.7% ($k = 2$). In the UV and IR regions the uncertainties are significantly higher. The main components are the standard uncertainties of the alignment and distance (0.25 – 0.5%), gain of the lock-in amplifier (0.5 %), short term stability of the LED sources (0.02 – 0.9%), absolute spectral irradiance (0.11 – 15%), relative spectral irradiance (0.5 – 8%), data analysis (0.1%), resolution of the current measurement (0.02 – 30%), and the spatial uniformity measurement (0.03 – 0.9%).

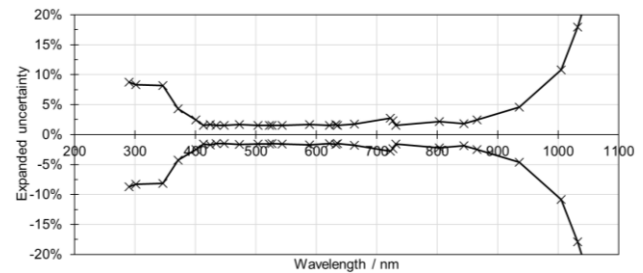


Figure 4. Expanded uncertainties ($k = 2$) of the obtained differential spectral responsivity values.

REFERENCES

1. IEC 60904-8:2014, Photovoltaic devices - Part 8: Measurement of spectral response of a photovoltaic (PV) device (The International Electrotechnical Commission IEC, Geneva, 2014).
2. P. Kärhä, H. Baumgartner, J. Askola, K. Kylmänen, B. Oksanen, K. Maham, V. Huynh, and E. Ikonen, Measurement setup for differential spectral responsivity of solar cells, "Measurement setup for differential spectral responsivity of solar cells," Opt. Rev. 27, 195–204, 2020.
3. P. Kärhä, P. Toivanen, F. Manoochchri, A. Haapalinna, and E. Ikonen, Development of a detector-based absolute spectral irradiance scale in the 380-900-nm spectral range, Appl. Opt. 36, 8909 – 8918, 1997.

Acknowledgement: The project 19ENG01 (Metro-PV) leading to this publication has received funding from the EMPIR programme co-financed by the Participating States and from the European Union's Horizon 2020 research and innovation programme.

Application of a Tuneable Pulsed Laser for Spectral Responsivity Measurements of UV Radiometers Based on Wide-Bandgap Photodiodes

Saulius Nevas¹, Philipp Schneider¹, Peter Sperfeld¹, and Niklas Papathanasiou²

¹ *Physikalisch-Technische Bundesanstalt (PTB), Braunschweig and Berlin, Germany,*

² *sglux GmbH, Berlin, Germany*

Corresponding e-mail address: saulius.nevas@ptb.de

Compact nanosecond-pulsed and slow repetition-rate lasers can be used for direct spectral calibrations of radiometers for high irradiance level applications. UV radiometers are often built around wide-bandgap photodiodes. In this contribution we demonstrate that the radiometers may show deviations from linearity throughout the dynamic range of such measurements. This complicates the application of the pulsed lasers. The metrological problem, possible solutions and application examples are discussed in this contribution.

INTRODUCTION

Ultraviolet (UV) radiometers are widely used in various industrial applications to monitor UV radiation-induced processes like UV curing of polymers in the production of plastic parts and coatings, water disinfection, etc. There are several advantages to build the radiometers for the high UV-irradiance measurements around wide-bandgap photodiodes.

Determination of spectral responsivity functions of the UV radiometers conditioned for a high-level UV radiation is often a challenging task. Classical double-monochromator-based setups may not be capable of providing spectrally narrow and high enough irradiance levels to yield measurable signals. One metrological possibility to cope with the task is application of continuous-wave (cw) or mode-locked spectrally tuneable lasers. However, such laser systems are not widely affordable for the radiometric application due to their high costs and complexity.

Compact optical parametric oscillators (OPO) generating nanosecond pulses at repetition rates of tens to hundreds of Hz are available on the market. In contrast to cw or mode-locked systems, they are affordable to a wider range of users such as calibration and testing laboratories. It has been demonstrated that the ns-OPO systems can be successfully applied for spectral measurements of radiometric detectors using synchronised measurement techniques based on an oscilloscope [1,

2, 3] or electrometers [4]. One of the highest obstacles in the measurement application of such tuneable sources is posed by the huge energies of the laser pulses, which limits the dynamic range of the measurements due to pulse peak saturation.

Additionally, nonlinearities can be caused also by other semiconductor-related effects. For instance, solid-state detectors may exhibit supra-linearities both at low and at high irradiance levels due to semiconductor defects like charge carrier traps [5].

In this contribution we will discuss nonlinearities observed for UV radiometers irradiated by a ns-pulsed OPO source. We will also demonstrate that despite their strongly nonlinear behaviour under the pulsed irradiation the spectral calibration of the radiometers is still possible under certain conditions.

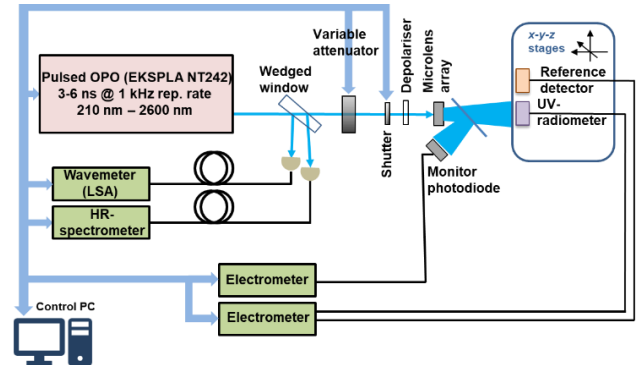


Figure 1. PTB setup based on a ns-OPO source used for the radiometric characterisations and calibrations.

PTB SETUP BASED ON A NANOSECOND-PULSED OPO

The setup based on a pulsed OPO (5 ns at 1 kHz) used at PTB for radiometric characterisations and calibrations is shown schematically in Figure 1. It has recently been taken into use as an upgrade for the PLACOS setup built around a ns-OPO at 20 Hz repetition rate [6]. While exposed to a homogenised field of the OPO radiation, the signal of the UV radiometer under test is compared to that of a calibrated reference detector based on a Hamamatsu S1227-type photodiode. An identical photodiode is also used as a linear monitor detector. For a

synchronised readout of the radiometer and monitor-photodiode signals either a two-channel oscilloscope or two electrometers are used.

MEASUREMENT PROBLEM

Considering the short-pulse and low-duty cycle of the irradiating field, the first step in the measurement procedure for spectral calibration of a radiometer under test is to proof the linearity of the detector under test throughout the dynamic range of the measurements. In the setup of Figure 1, the linearity is checked by varying the irradiance level at a fixed OPO wavelength and recording signals from the detector under test and the monitor photodiode. In case of UV-radiometers based on widely used silicon photodiodes, only normal peak saturation-type nonlinearities have been observed so far, similarly to the results reported in [4].

However, for UV-radiometers including certain models of wide-bandgap photodiodes severe nonlinearities have been measured throughout the whole dynamic range. Figure 2 shows exemplary nonlinearities of two SiC photodiodes of different models. Model 2 is affected just by the peak pulse saturation while model 1 exhibits also a severe supra-linearity at lower signals. Hence, such nonlinearities may substantially limit the dynamic range of the measurements and, thus, affect the calibration significantly.

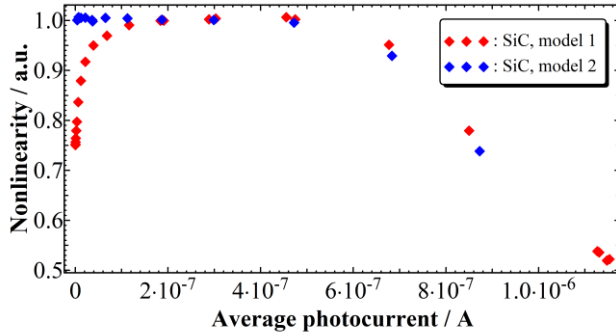


Figure 2. Deviation from linearity for two models of SiC photodiodes irradiated by the ns-pulsed OPO source at 310 nm in irradiance mode. It is shown as a function of average photodiode current.

SOLUTION AND VALIDATION

Despite the non-linearities, the UV radiometers can still be spectrally calibrated provided that the deviations from linearity under the pulsed irradiation are measured and approximated by respective correction functions. As an example, Figure 3 shows

calibration results of a UV radiometer with such a nonlinearity correction applied and without it.

In the conference contribution we present results for several UV radiometers obtained using the pulsed ns-OPO setup at PTB. The results of the characterisations and responsivity calibrations are compared to those of other measurements carried out at the quasi-cw-laser setup of PTB. Moreover, the obtained spectral irradiance responsivities are also validated radiometrically by measuring several high-power UV sources.

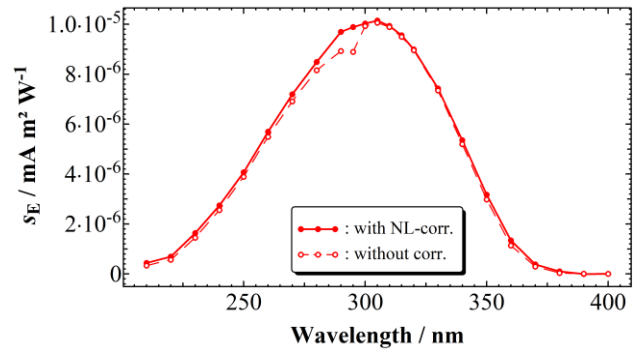


Figure 3. Spectral irradiance responsivity of a UV radiometer based on a SiC photodiode of model 1. Due to the nonlinearity, an abrupt decrease of the laser power below 300 nm causes the observed responsivity drop-off.

REFERENCES

1. M. Ojanen, P. Kärh , S. Nevas, A. Sperling, H. M ntynen and E. Ikonen, Double-coiled tungsten filament lamps as absolute spectral irradiance reference sources, *Metrologia*, 49, S53–S58, 2012.
2. S. Nevas, U. K hler, F. Sch nenborn, and G. McConville, Characterisation of Dobson spectrophotometers using a tuneable pulsed laser, in *Proceedings of NEWRAD 2017*, edited by Local Organizing Committee (LOC) of NEWRAD 2017, 173–175, 2017.
3. K.-S. Hong, S. Park, J. Hwang, E. Atkinson, P. Manson and D.-H. Lee, Spectral responsivity measurement of photovoltaic detectors by comparison with a pyroelectric detector on individual nano-second laser pulses, *Metrologia*, 54, 355–364, 2017.
4. Y. Zong, S. W. Brown, G. P. Eppeldauer, K. R. Lykke and Y. Ohno, A new method for spectral irradiance and radiance responsivity calibrations using kilohertz pulsed tunable optical parametric oscillators, *Metrologia*, 49, S124–S129, 2012.
5. J. Metzdorf, W. M ller, T. Wittchen and D. H nerhof, Principle and application of differential spectroradiometry, *Metrologia*, 28, 247–250, 1991.
6. S. Nevas, M. Lindemann, A. Sperling, A. Teuber and R. Maass, Colorimetry of LEDs with array spectroradiometers, *MAPAN—J. Metrol. Soc. India*, 24, 153–162, 2009.

Broadband absolute radiometers for far infrared sensing

Christopher Yung¹, Nathan Tomlin¹, Cameron Straatsma², David Harber², John Lehman¹ and Michelle Stephens¹

¹National Institute of Standards and Technology (NIST), Boulder, CO, USA, ²Laboratory for Atmospheric and Space Physics (LASP), University of Colorado, Boulder, CO, USA,

Corresponding e-mail address: christopher.yung@nist.gov

Currently the Earth's outgoing longwave radiation (OLR, 3 μm – 100 μm) is being imaged with scanning, single-element radiometers on the NASA CERES satellite instrument. Despite the need for increased spatial resolution, scanning radiometers are slated for future missions due to lack of a better alternative. For example, microbolometer staring arrays, which are technologically mature, do not possess the accuracy or broadband absorption required by climate scientists for OLR imaging. I will discuss our efforts to develop a new type of uncooled microbolometer consisting of electrical substitution radiometers (ESRs) capable of sensing out to 100 μm for smallsat remote sensing.

INTRODUCTION

Absolute radiometry using an electrical substitution radiometer (ESR) has not fundamentally changed since its conception by Kurlbaum (1892) and Ångström (1893) [1]. To this day, incident optical power is determined by measuring the ohmic heating required to achieve an equivalent signal in a transducer (e.g. thermistor or thermopile) when non-illuminated. Thus, the measurement does not depend upon a calibrated transducer or material properties of the thermal absorber (i.e. knowledge of specific heat or thermal conductance is not required). A significant improvement to the concept of the ESR has been the development of the active cavity radiometer (ACR) [2], which has improved accuracy, broadband absorption and total absorption. However, ACRs typically possess time constants on the order of tens of seconds and are cm-scale; thus, making them incompatible for imaging.

In the 1970s, Honeywell developed the microbolometer for low size, weight, and power (SWaP) imaging of thermal radiation from 7 μm – 15 μm . While microbolometers are fast (video frame rates) and uncooled making them ideal for CubeSats, OLR imaging is problematic since their absorption is narrowband and calibration of each pixel's thermistor is required for radiometric grade imaging. Recently,

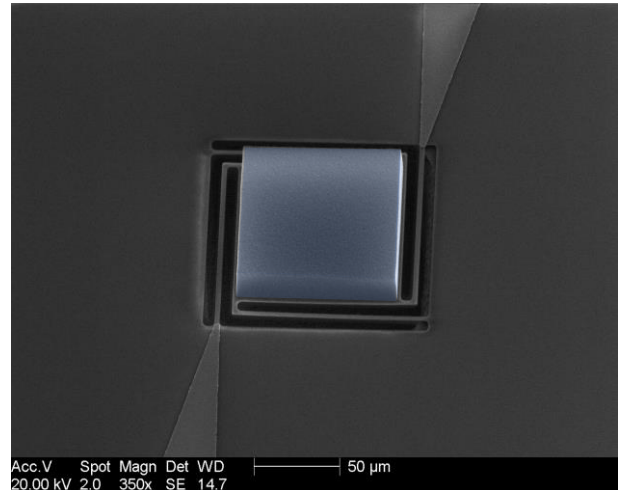


Figure 1. Scanning electron microscope image of a prototype single-element ESR. The element is thermally decoupled from the substrate by four silicon nitride legs. The broadband VACNT absorber (false colored blue) is approximately 22 μm tall and sits above a thin film VO_x thermistor.

several research groups have adapted microbolometer arrays in a number of ways for satellite based OLR sensing. Deposition of gold black on the pixels to increase absorption out to 100 μm [3,4], as well as ESR operation of a silicon micromachined pixel have both been demonstrated [5].

In collaboration with LASP, we have demonstrated cm-scale ESRs using vertically aligned carbon nanotubes (VACNTs) as broadband absorbers for CubeSat applications. The Compact Solar Irradiance Measurement (CSIM) [6], currently in space, uses a NIST/LASP developed ESR to track degradation of the photodiodes. The ESR is a silicon micromachined, cm-scale device with hand placed thermistors. We aim to further advance this technology to develop an active microradiometer (AMR) - an imaging array combining the benefits of both microbolometers and ACRs.

DISCUSSION

Figure 1 is an SEM image of a silicon micromachined prototype pixel/element to demonstrate the feasibility of integrating VACNTs with microbolometers. VACNTs were chosen specifically for their

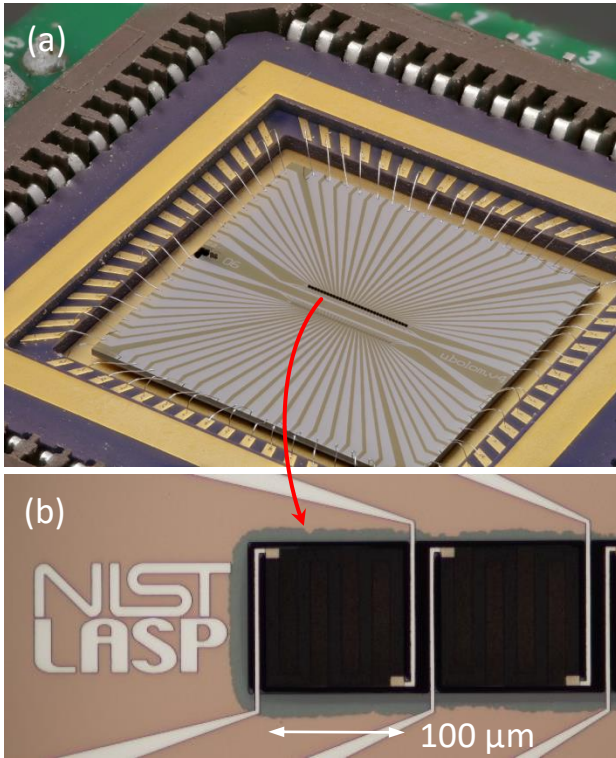


Figure 2. (a) Linear array of 32 ESR elements wire bonded and packaged in a leadless chip carrier. (b) Microscope image of the first two pixels of the linear array. Elements are similar to the prototype in Fig. 1., but with two silicon nitride support legs.

broadband absorptance ($> 99\%$) out to $100\ \mu\text{m}$. Pixels were fabricated on $2\ \mu\text{m}$ thick silicon nitride membranes with further thermal isolation provided by etching four legs ($5\ \mu\text{m} \times 126\ \mu\text{m}$) into the membrane. Thin film vanadium oxide (VO_x) thermistors were lithographically defined and sputtered on the pixel. Fe/AlO_x catalyst was co-located over the VO_x thermistor and VACNTs were grown at $800\ ^\circ\text{C}$ in a mixture of $\text{Ar}/\text{H}_2/\text{C}_2\text{H}_4$ for 20 min. VO_x thermistors display a temperature coefficient of resistance (TCR) of approximately $-1\ \%/K$ after VACNT growth [6]. In addition, we have demonstrated ACR-like operation of the pixel by using the thermistor as a heater as well. Actively controlling the ohmic heat dissipated in the pixel, we can reduce the natural time constant from 50 ms to 10 ms.

Figure 2 is an optical image of a full 32-element linear imaging array. The top line of pixels (look black due to the VACNTs) are the active sensing elements, while the bottom row of 32 pixels (without VACNTs) are compensating elements used for common mode rejection of substrate temperature fluctuations if placed in a bridge with the sensing pixels.

Future work entails increasing the TCR of the thermistor while minimizing the $1/f$ noise, developing the electronics to support active control/readout of a 32-element array, and radiometric bench testing to evaluate ultimate performance.

SUMMARY

Active microradiometers are a nascent technology potentially meeting the requirements of imaging Earth's OLR. Simple modifications of operating the individual pixels in similar fashion to active cavity radiometers and integrating VACNTs as broadband absorbers will allow for absolute radiometric imaging into the far infrared.

REFERENCES

1. F. Hengstberger, 1.3 - The Absolute Measurement of Radiant Power, in *Absol. Radiom.*, edited by F. Hengstberger, 30-33, Academic Press, 1989.
2. R. C. Willson, Active Cavity Radiometer, *Appl. Opt.*, 12, 810-817, 1973.
3. G. Mariani, M. Kenyon, B. Eom, et al., Far-infrared room-temperature focal plane modules for polar radiant energy in the far infrared experiment, *Int. Conf. Infrared, Millimeter, Terahertz Waves, IRMMW-THz.*, 1-2, 2016.
4. F. Génèreux, B. Tremblay, D. Gay, et al., Small uncooled bolometers with a broad spectral response, *Proc. SPIE*, 106241D, 2018.
5. G. Allègre, B. Guillet, D. Robbes, et al., A room temperature $\text{Si}_3\text{N}_4/\text{SiO}_2$ membrane-type electrical substitution radiometer using thin film platinum thermometers, *Meas. Sci. Technol.*, 18, 183-189, 2007.
6. E. Richard, D. Harber, G. Drake, et al., Compact spectral irradiance monitor flight demonstration mission, *Proc. SPIE*, 1113105, 2019.
7. C. Yung, N. Tomlin, C. Straatsma, et al., BABAR: black array of broadband absolute radiometers for far infrared sensing, *Proc. SPIE*, 109800F, 2019.

The Nature of Fibre Beam-Splitters for Absolute Radiometric Measurements

M G WHITE^{1,2}, E BAUMANN^{1,2}, I VAYSHENKER³, Z E RUIZ⁴, M S STEPHENS³, J H LEHMAN³

¹Associate of National Institute of Standards and Technology, Boulder, Colorado 80305 USA

²Department of Physics, University of Colorado, Boulder, Colorado 80309, USA

³National Institute of Standards and Technology, Boulder, Colorado, 80305 USA

⁴Centro Nacional de Metrología, Querétaro, México

Corresponding e-mail address: m.white@boulder.nist.gov

We have investigated the performance of several fibre beam-splitters in order to fully understand their contribution to the uncertainty of radiometric measurements. The temperature dependence of the polarisation dependent loss was evaluated for fused biconical and planar beam-splitters at 1310 nm and 1550 nm over the range 10 °C to 40 °C and is reported for SMF-28 Ultra and polarisation maintaining fibre beam-splitters, analysed using the Mueller matrix method. The variation in signal ratio between the output ports of multi-port PM splitters was also investigated to determine the baseline uncertainty in such a ratio measurement.

INTRODUCTION

Often with radiant power measurements there is some optical element in the setup between the device under test (DUT) and standard that requires characterisation. This could be a Brewster window or even a plane wedged window, a turning mirror or a beam-splitter. Each adds uncertainty to the measurement. We are interested in evaluating the performance limit of fibre beam-splitters, especially polarisation maintaining (PM) splitters, as the variability of the splitter ratio dominates the DUT responsivity measurement uncertainty of our calibration facility [1]. This work improves and helps assure the performance of our optical fibre-coupled cryogenic radiometer facility.

Fibre beam-splitters are very useful in the field of radiometry. The work discussed here is not only relevant to our fibre-coupled radiometer but is also relevant to the area of few-photon radiometry, where fibre-coupled detectors are calibrated for detection efficiency [2] or compared directly to many other few-photon detectors, including superconducting nanowire single-photon detectors [3].

Passive optical components such as fibre beam-splitters and couplers, exhibit polarisation dependent loss (PDL), whereby the output signal of the device varies as a function of the input polarisation state S . Many references can be found in the literature to

application notes and standards discussing PDL measurement techniques for fibre components [4]. We use the Mueller matrix method to assess the temperature dependent PDL of the beam-splitters tested.

Further, we assess the impact the optical power level and spectral modal stability of Fabry-Pérot laser diode sources have on the stability of the beam-splitter ratio between any two output ports of multiport PM fibre beam-splitters. The beam-splitter ratio between DUT and radiometer channels is required to relate the power incident on the DUT to the power incident on the standard detector. Splitters are convenient as they enable simultaneous measurement of the DUT and radiometer output signals. For high-accuracy measurements it is important to understand the behaviour of the beam-splitter and the consequence of selecting specific output channels. The variability of the fibre beam-splitter ratio dominates the DUT responsivity measurement uncertainty, hence this investigation.

METHOD

The measurement of the response of a beam-splitter to four separately applied input polarisation states, whose power is known, is enough for the first-row coefficients of the 4 x 4 Mueller matrix to be determined. The minimum and maximum throughput of the DUT can be calculated from these four matrix coefficient values. A 1 x 3 SMF-28 wavelength independent splitter and two planar 1 x 4 PM splitters were in turn placed in an environmental chamber and cycled from 10 °C to 40 °C, being soaked for an hour at each temperature. Measurements were recorded for each of four input polarisation states; 0°, 45°, 90°, and RHC generated by a polarisation synthesiser. A schematic of the experimental setup is shown in Fig. 1. The polarisation dependent loss is calculated from Eq. 1;

$$\text{PDL (dB)} = 10 \log_{10} \frac{T_{\max}}{T_{\min}} \quad (1)$$

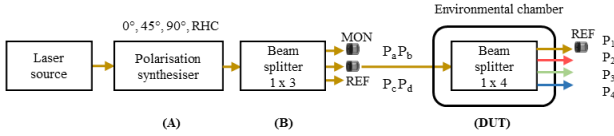


Fig. 1. Setup for the temperature dependent PDL measurement. The input power to the DUT (P_a , P_b , P_c , P_d) and the output power of the DUT (P_1 , P_2 , P_3 , P_4) for each of four input polarisation states; 0° , 45° , 90° , RHC, is measured relative to the power of the monitor photodiode (MON). (A) General Photonics PSY-101 polarisation synthesiser for selecting input polarisation states. (B) 1×3 beam-splitter with monitoring channel. The four coloured fibre outputs from the DUT illustrated (1×4 PM beam-splitter; 25 % each channel) relate to the colours on charts 2a and 2b below.

A two-detector technique was used to determine the ratio between any two output ports of the beam-splitter, given by Eq. 2;

$$BSR = \sqrt{\frac{M_1(DUT)}{M_2(RAD)}} \times \frac{M_2(DUT)}{M_1(RAD)} \quad (2)$$

where BSR is the beam-splitter ratio and M_1 , M_2 the detector signals of the fibre-coupled outputs DUT and radiometer (RAD). The Fabry-Pérot laser diode source was fibre coupled to the beam-splitter via a variable optical attenuator (not illustrated) which is used to set the optical power level.

RESULTS

Figures 2a and 2b highlight the decrease in PDL when changing from SMF-28 type splitters to PM type splitters. The PDL of the PM beam-splitters is of the order 1 % at 20°C , exhibiting a temperature coefficient $\Delta PDL / ^\circ\text{C}$ of approximately -0.03 . This represents the maximum excursion in fibre output signal given all states of input polarisation. We include a rectangular bounded uncertainty of 0.05 % in our uncertainty budget to account for the PDL of the PM splitters we use.

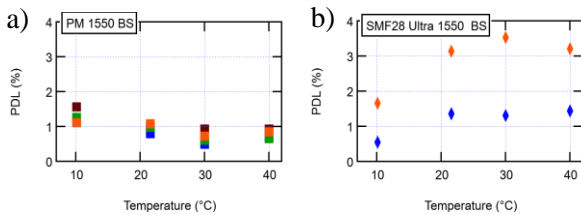


Fig. 2(a). Plot of the temperature dependence of the PDL (%) of 1550 nm 4 channel PM fibre beam-splitter. The four colours; blue, green, red, brown represent the four output channels of the splitter. Fig. 2(b). Plot of the temp. dependence of the PDL (%) of 1550 nm SMF-28 3 port

fibre beam-splitter – only 2 channels shown.

The standard deviation of the ratio of the power output from any two fibre ports of the 3 and 4 port beam-splitters tested is 0.03 % maximum over a measurement period of 5 hours. Single element InGaAs photodiodes were used for this purpose at wavelengths 1310 nm and 1550 nm. This represents a quantitative measure of the effect of the temperature dependent PDL of the fibre beam-splitters. It results from temperature fluctuations of $\pm 0.3^\circ\text{C} / \text{day}$ in the laboratory environment and small changes in the polarisation state of the propagating light, caused by coupling between the slow and fast axes of the optical fibre components, and variability in the modal stability of the laser diode source. The polarisation extinction ratio (PER) is a measure of the strength of this coupling. For the PM splitters tested the PER was 20 dB. An additional uncertainty of 0.02 % was attributed to each fibre as a result of swapping fibres between detectors during a beam-splitter ratio measurement. Summing these contributions in quadrature with the 0.03 % mentioned above, yields an expanded uncertainty of 0.08 %.

CONCLUSION

We have evaluated several fibre beam-splitters in order to understand their characteristics. Results confirm that current beam-splitter technology limits our fibre-coupled cryogenic power responsivity calibration uncertainty to 0.1 % ($k=2$). However, this work has resulted in a 4x improvement in the NIST optical fibre coupled power responsivity calibration uncertainty.

REFERENCES

1. M.G. White, Z.E. Ruiz, C.S. Yung, I. Vayshenker, N.A. Tomlin, M.S. Stephens, and J.H. Lehman, “Cryogenic primary standard for optical fibre power measurement”, *Metrologia* **55**(5), 706-715 2018.
2. T. Gerrits, A. Migdal, J. Bienfang, J. Lehman, S.W. Nam, J. Splett, I. Vayshenker, and J. Wang, “Calibration of free-space and fiber-coupled single photon detectors”, *Metrologia* **57**(1) 2020.
3. I. Mueller, R.D. Horansky, J.H. Lehman, S.W. Nam, I. Vayshenker, L. Werner, G. Wuebbeler, and M.G. White, “Verification of calibration methods for determining photon-counting detection efficiency using superconducting nano-wire single photon detectors”, *Opt. Express* **25**(18) 21483-21495 2017.
4. IEC 61300-3-2 Fibre Optic Interconnecting Devices and Passive Components – Basic Test and Measurement Procedures – Part 3-2: Examination and Measurements – Polarization Dependent Loss in a Single-Mode Fibre Optic Device IEC:2009 3rd edn (Geneva: IEC).

Development of UVC Measurement Tools at NIST to Combat Healthcare-Associated Infections (HAIs)

C. Cameron Miller¹, Thomas Larason¹, Dianne Poster¹, and Richard A. Martinello²

¹National Institute of Standards & Technology, Gaithersburg, Maryland, United States of America, ²Yale School of Medicine, New Haven, Connecticut, United States of America

Corresponding e-mail address: c.miller@nist.gov

In the United States (U.S.), healthcare-associated infections (HAIs) infect one in every 25 hospital patients, account for more than 99,000 deaths and increase medical costs by more than \$35 billion, each year. Ultraviolet-C (UV-C) antimicrobial devices are shown to reduce the incidence of many of these HAIs by 35% or more. The adoption of UV-C technology by the healthcare industry has been sporadic largely due to the lack of measures for efficacy. NIST has leveraged our new UV scale realizations to provide multiple calibration facilities for a variety of source technologies through the implementation of straylight corrected spectroradiometers calibrated against UV standard detectors.

HEALTHCARE PROBLEM

HAIs are one of the leading causes of death in the U.S. HAI statistics are difficult to obtained. HAI are not as newsworthy as other causes of death, until a facility is closed for sanitation reasons. Nationwide, HAIs infect about one in every 25 hospital patients.[1] Each year this translates to approximately 1.7 million HAIs occurring in U.S. hospitals, resulting in approximately 100,000 or more unnecessary deaths and an estimated \$20 billion in U.S. dollars in healthcare costs. [2] The overall costs due to operational or occupational losses of productivity are estimated at more than \$100+ billion.

Comparing these economic data to information obtained from the U.S. Centers for Disease Control and Prevention shown in Figure 1, the deaths from HAIs place HAI deaths nearly at the level of those attributed to Alzheimer's disease and above the seventh leading cause of death in the U.S., that is, above diabetes. [3] In 2015, diabetes claimed 79,535 deaths, which is only about three-quarters of the deaths attributed to HAIs. The U.S. currently recognizes an "Opioid Crisis" where in 2016, about 63,000 drug overdose deaths in the US were reported, while terrible is lower than those attributed to HAIs.

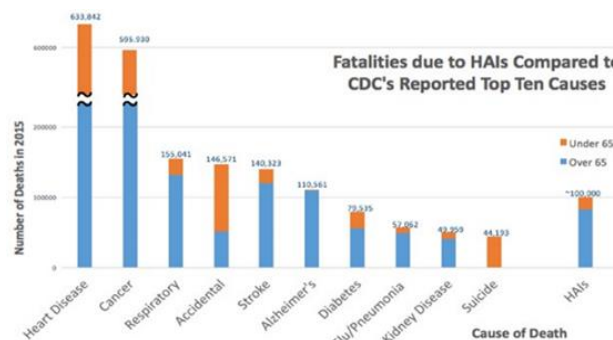


Figure 1 - CDC reported top ten causes of death in 2015 (CDC 2018) compared to the reported number of HAI fatalities (SRT&SOCS 2014)

NIST'S ROLE

Multiple UV-C light source technologies and disinfection mechanisms at multiple wavelengths (Hg lamps, Xe lamps, LED, excimer) contribute to the confusion and difficulty in comparing devices. Levelling of the playing field with scientifically certifiable data of the efficacy of antimicrobial devices will help facilitate science-based decision making.

NIST has developed three new facilities and working with the International Ultraviolet Association (IUVA) and Illuminating Engineering Society (IES) on several standard methods to support the UV-C measurement community. The first facility is a 25 cm integrating sphere system for the measurement of UV-C LEDs. The second facility is a small frame goniometer coupled to the new NIST photometric bench used for measuring radiant intensity distributions of UV-C LEDs. The third facility is 1.5 m sphere that has been recoated with a PTFE film which is highly reflective down to 200 nm.

UV-C LED SPHERE SYSTEM

The UV-C LED Sphere System is composed of a 25 cm sphere that is coupled to CCD based array spectroradiometer and a halogen/deuterium source via two fibers. The port entrance is 25 mm in diameter with a mounted precision aperture mounted. The system is calibrated for spectral irradiance using

a pulsed laser-based system that is directly compared to silicon single element and trap detectors calibrated on the NIST cryogenic radiometer. [4] Calibration by this method creates a stray-light correction matrix for the system. [5] The UV-C LED Sphere System has a fiber coupled halogen/deuterium lamp system that holds the calibration scale. On days when the system is used the fiber coupled lamp validates the calibration.

As completion of the calibration loop, deuterium lamps calibrated at the NIST Synchrotron Ultraviolet Radiation Facility (SURF) described in another abstract submitted to NEWRAD2020 are compared using the detector-based UV-C LED Sphere System. The results of the source-based scale to the detector-based scale will be presented.

UV-C LED GONIOMETER SYSTEM

The UV-C LED Goniometer System is a compact goniometer that acts as a source on the new NIST Photometric Bench, shown in Fig. 2. The goniometer is a Type-D goniometer according to LM-75 capable of positioning thermal electrical temperature-controlled LEDs. [6]

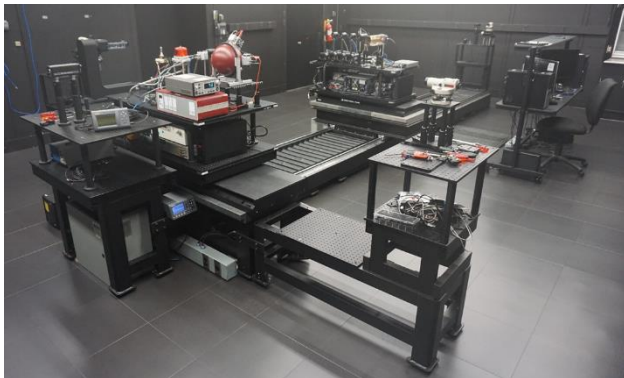


Figure 2 – New NIST Photometric Bench. UV-C LED Goniometer is to the left on the source table.

Using the NIST Photometric Bench and the alignment techniques developed at NIST using microscopes, the angular dependent radiant intensity of the LEDs can be measured and verified at various distances. The total radiant flux using the UV-C LED Goniometer System will be presented compared to the UV-C LED Sphere System.

IES DOCUMENT DEVELOPMENT

NIST along with the Illuminating Engineering Society (IES) and the International Ultraviolet Association (IUVA) are supporting the UV-C disinfection community by leveraging the standards

developed to support the infrastructure of the general lighting community. Four topics have been identified as areas of need for documentary test measurement standards: Total radiant flux and radiant intensity distribution measurement of discharge sources; Total radiant flux and radiant intensity distribution measurement of LED chips and arrays; Total radiant flux and radiant intensity distribution of complete UV devices; and the Application distance radiometry of UVC devices.

SUMMARY

NIST is taking an active role by improving UV measurement scales and UV measurement facilities to support the application of the documentary standards for the UV-C disinfection community.

REFERENCES

1. Centers for Disease Control and Prevention, (CDC) (2018) National Center for Emerging and Zoonotic Infectious Diseases, “Healthcare-associated infections (HAI), HAI data and statistics,” <https://www.cdc.gov/hai/surveillance/index.html>.
2. Joint Hearing Before the Subcommittee on Research and Technology & Subcommittee on Oversight Committee on Science, Space, and Technology, (SRT&SOCS) (2014) House of Representatives, “Technology for patient safety at veterans’ hospitals,” 113th Congress, 2nd Session, Serial No. 113–83; p. 12; Washington, D.C., <https://www.gpo.gov/fdsys/pkg/CHRG-113hhrg89412/pdf/CHRG-113hhrg89412.pdf>.
3. Centers for Disease Control and Prevention, (CDC) (2017) National Center for Health Statistics, “Health, United States, 2016: with chartbook on long-term trends in health,” Library of Congress Catalog Number 76–641496, [https://www.cdc.gov/nchs/data/16.pdf#019](https://www.cdc.gov/nchs/data/hus/16.pdf#019).
4. Yuqin Zong, et al, “Calibration of spectroradiometers using tunable lasers,” Proc. of the CIE, CIE x046:2019, 569-574.
5. Yuqin Zong, et al. 2006 Simple Spectral Stray Light Correction Method for Array Spectroradiometers. Applied Optics, 45, 1111-1119.
6. Illuminating Engineering Society, IES LM-75-20 “IES Guide to Goniometer Measurements and Types, and Photometric Coordinate Systems,” 2020.

Absolute Calibration Setup for Spectral Responsivity of a NIR radiation thermometer

Thada Keawprasert and Kanokwan Nontapot

National Institute of Metrology Thailand, Pathumthani, Thailand

Corresponding e-mail address: thada@nimt.or.th

A new calibration facility was setup for the absolute spectral responsivity measurement of a NIR radiation thermometer at the NIMT. The concept of the setup is to measure the absolute spectral responsivity in the wavelength range of 1550 nm to 1650 nm matching to the spectral bandpass of a NIMT radiation thermometer. The new setup uses a tuneable laser as infrared source and an integrating sphere as Lambertian source. The laser output is guided with a fibre optic into the integrating sphere equipped with an precision aperture with known effective area. The spectral radiance of the source is determined via the spectral irradiance measured by an InGaAs detector with known absolute spectral power responsivity traceable to the primary detector of the PTB. First results of the spectral responsivity calibration of the NIR radiation thermometer are presented, and estimations of uncertainty for the absolute spectral responsivity are given.

INTRODUCTION

Recently the redefinition of the new kelvin allows spectral-band primary radiometry to realise the thermodynamic temperature [1]. So far many NMIs have developed capabilities for directly measuring thermodynamic temperatures at high temperatures [2,3,4]. However some NMIs have developed capabilities for directly measuring thermodynamic temperature in the middle temperature range using a NIR radiation thermometer [5,6].

Presently a cryogenic radiometer was setup at the NIMT and established as a primary standard of the absolute radiant power in the visible region. Using a fiber optic tuneable laser, the capability can be extended to the wavelength range from 1550 nm to 1650 nm, which match with the spectral bandpass of a 1600 nm radiation thermometer already used to disseminate the ITS-90. Therefore, the realisation of the new kelvin using the NIR radiation thermometer

can be done at the NIMT by developing the absolute calibration setup for spectral radiance responsivity in the wavelength range. The aim of this calibration is to assign the thermodynamic temperature to fixed-point blackbodies used at the middle temperature range as shown in **Figure 1**.

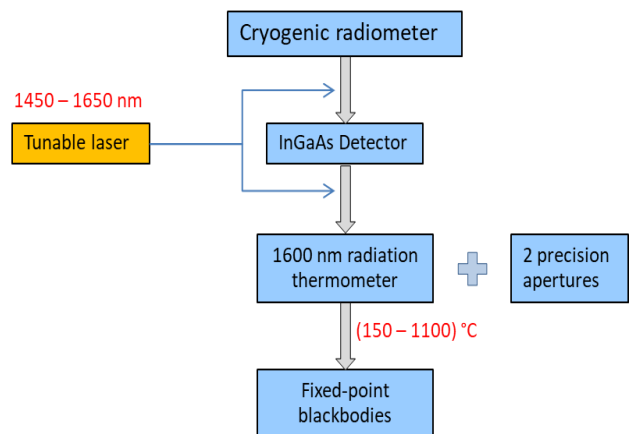


Figure 1. Traceability chain of thermodynamic temperature in the middle temperature range

CALIBRATION SETUP

A schematic diagram of the new calibration setup at the NIMT is shown in **Figure 2**. A tuneable laser is used as radiation source. By operating in constant current (CC) mode, the laser output is controlled to be stable within 0.2 %. To enable calibrating radiation thermometer, the laser radiation is introduced to an 9.75 inch integrating sphere through a 1 m fiber optics. The opening port of the sphere is equipped with a precision aperture of 10 mm in diameter due to large target spot of the radiation thermometer (3 mm). A direct substitution comparison was performed by using translation stages to move the InGsAs detector and the radiation thermometer to the measurement position. Due to the low output, the spectral radiance measured by the InGaAs detector is performed at the one half of the measuring distance of the radiation thermometer.

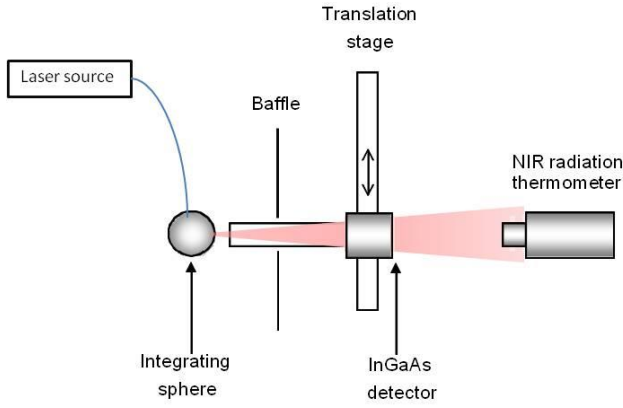


Figure 2. Calibration setup for absolute calibration for a NIR radiation thermometer

The spectral absolute radiance responsivity of the NIR radiation thermometer at each wavelength ($S_{RT}(\lambda)$) is calculated from the spectral responsivity of the InGaAs ($S_{InGaAs}(\lambda)$) by

$$S_{RT}^L = G \cdot \frac{I_{ph,RT} - I_{d,RT}}{I_{ph,InGaAs} - I_{d,InGaAs}} \cdot S_{InGaAs}^E \quad (1)$$

where G is the geometric factor of the measurement set up, $I_{ph,InGaAs}$ and $I_{d,InGaAs}$ is the photocurrent and the dark current of the InGaAs detector, $I_{ph,RT}$ and, $I_{d,RT}$ is the photocurrent and the dark current of the radiation thermometer.

In combination with the relative spectral responsivity measured at the spectral responsivity measurement facility [7], the absolute spectral responsivity can be determined for the whole range from 1000 nm to 2200 nm.

RESULTS AND DISCUSSION

Preliminary result for absolute spectral responsivity of the NIR radiation thermometer is graphically shown in **Figure 3**.

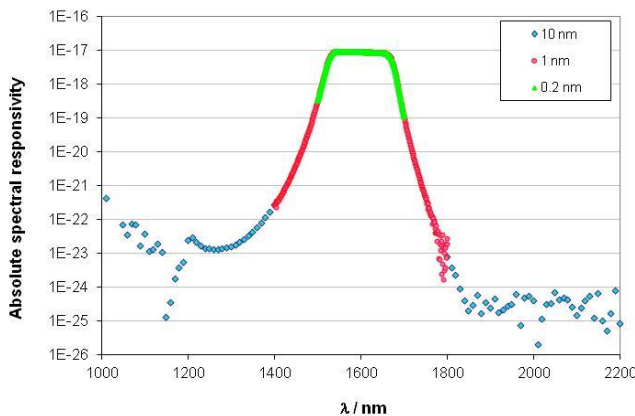


Figure 3. Preliminary measurement results for absolute spectral responsivity of the test NIR radiation thermometer

In the **figure 3**, only the calibration result at 1600 nm comes from the absolute calibration setup while the related responsivity for the whole range comes from the relative spectral responsivity facility.

The main contributions of the uncertainty for the absolute spectral responsivity of the NIR radiation thermometer are shown in **Table 1**.

Table 1. Contributions to uncertainty at 1600 nm.

Contributions of uncertainty, %	Preliminary	Provision
Homogeneity across the sphere	0.2	0.1
Stability of output signals	0.1	0.05
Calibration uncertainty	0.4	0.05
Calibration of Aperture	0.05	0.023
Distance measurement	0.1	0.05
Noise of radiation thermometer	0.005	0.005
Combine uncertainty, % ($k=1$)	0.47	0.13
Expand uncertainty, % ($k=2$)	0.94	0.26

In the present setup, the calibration uncertainty of the InGaAs detector contributes most to the overall uncertainty, which is limited to 0.94% ($k=2$). By improving the calibration uncertainty of the InGaAs detector to a value of 0.1%, which is straightforward, the overall uncertainty will reduce to 0.23% ($k=2$) corresponding to 53 mK at 150 °C, 143 mK at 420 C and 563 mK at 1100 °C.

REFERENCES

1. Mise en pratique for the definition of the Kelvin in the SI, Appendix 2 of 9th edition SI Brochure, 2019.
2. K. Anhalt, G. Machin, Thermodynamic temperature by primary radiometry, Phil. Trans. R. Soc. A 374: 20150041, 2016.
3. Y. Yamaguchi, Y. Yamada, J. Ishii, Supercontinuum-Source-Based Facility for Absolute Calibration of Radiation Thermometers, Int J Thermophys. 36, 1825–1833, 2015.
4. M.J. et.al., Performance of different light sources for the absolute calibration of radiation thermometers, In J Thermophys, 38:138, 2017.
5. L. Bungler, R.D. Taubert, B. Gutschwager, K Anhalt, S. Briaudeau and M. Sadli, Absolute radiation thermometry in the NIR, In J Thermophys , 38, 2017
6. H.W. Yoon, T.J. Woodward H. McEvoy, G. Machin, Thermodynamic measurements of Zn and Al freezing temperature using an InGaAs-based, near-infrared radiation thermometer 3 (NIR3), IOP Conf. Series: Journal of Physics: Conf. Series 1065 122023, 2018.
7. T. Keawprasert, P. Wongnut, U. Norranim, Detector-based absolute calibration of a 1.6 um radiation thermometer for validation of source-based ITS-90 temperature scale, In Proceeding of NEWRAD 2014.

Increased response of trap detectors with apertures due to nitrogen flow

Janne Askola¹, Kinza Maham¹, Mikhail Korpusenko¹, Petri Kärhä¹, and Erkki Ikonen^{1,2}

¹*Metrology Research Institute, Aalto University, Espoo, Finland,* ²*VTT MIKES, VTT Technical Research Centre of Finland Ltd, Espoo, Finland,*

Corresponding e-mail address: janne.askola@aalto.fi

According to our experimental results and simulations, a nitrogen flow used to prevent dust and moisture entering the detector may influence measurements performed with trap detectors in overfilled conditions. Based on simulations, the nitrogen flow through the detector forms a nitrogen beam that might act as a gradient-index lens increasing the effective aperture area of the detector and thus the photocurrent. The turbulence of the flow increases standard deviation of the measurements. The shape of the nitrogen beam depends on the size of the limiting aperture of the detector. Thus, the maximum usable nitrogen flow should be determined separately for each configuration.

INTRODUCTION

Measurements using trap detectors are carried out daily in optical metrology. Typically, the photodiodes in the detector are exposed to ambient conditions of the laboratory. Dust and moisture accumulating on the diodes increases the uncertainty of the measurements and reduces the calibration interval.

A nitrogen flow system can be used to prevent the moisture and dust collection on the diodes [1]. A constant flow of dry nitrogen is introduced through the detector, where it exits the detector aperture preventing unwanted particles and moisture entering the detector. The optical properties of nitrogen are rather similar to those of air. Based on this, the flow should tentatively not introduce any errors into the measurements. However, our results indicate that the nitrogen flow can increase signals in overfilled measurement conditions.

RESPONSIVITY MEASUREMENTS

In our measurements of a 5-cm diameter LED source at the distance of 4.5 m using methods presented in [2], we have noticed that the nitrogen flow influences the results. Measurements were carried out with a wedged trap detector of two photodiodes and a precision aperture with a diameter of 4 mm. Figure 1 presents the normalized photocurrents from the trap

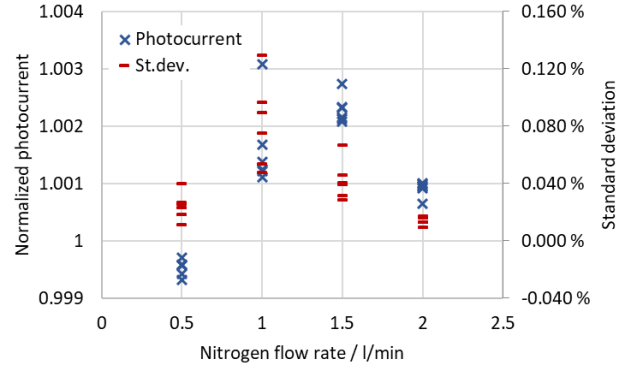


Figure 1. Relative photocurrents and their standard deviations of 6 measurements using stable white LED source with a trap detector and a 4-mm diameter limiting aperture in overfilled condition ($>100 \times d_{\text{aperture}}$).

detector at nitrogen flow rates of 0.5 – 2.0 l/min. The standard deviations of the results are also indicated. It can be noticed that with flow rates of 1.0 and 1.5 l/min, both the photocurrent and the standard deviation are clearly elevated when compared to the results at the flow rate of 0.5 l/min.

Measurements were also carried out for the responsivity in underfilled mode utilizing different flow rates. The normalized results are shown in Figure 2, where it can be seen that the changes in responsivity are approximately two orders of magnitude smaller than the changes in the measurements made in the overfilled mode. These results link the responsivity changes of Figure 1 to light passing close to the aperture edge in overfilled conditions.

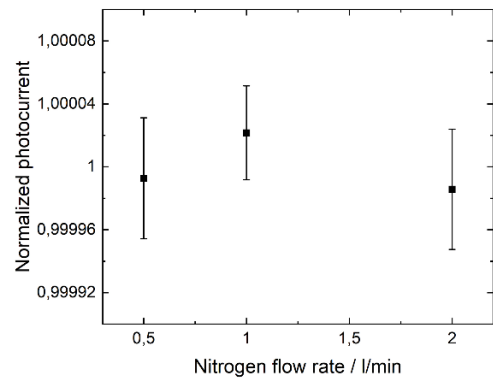


Figure 2. Normalized responsivity of the trap detector with 10-mm diameter aperture measured with 488-nm laser beam of 1.6-mm diameter at different nitrogen flow rates.

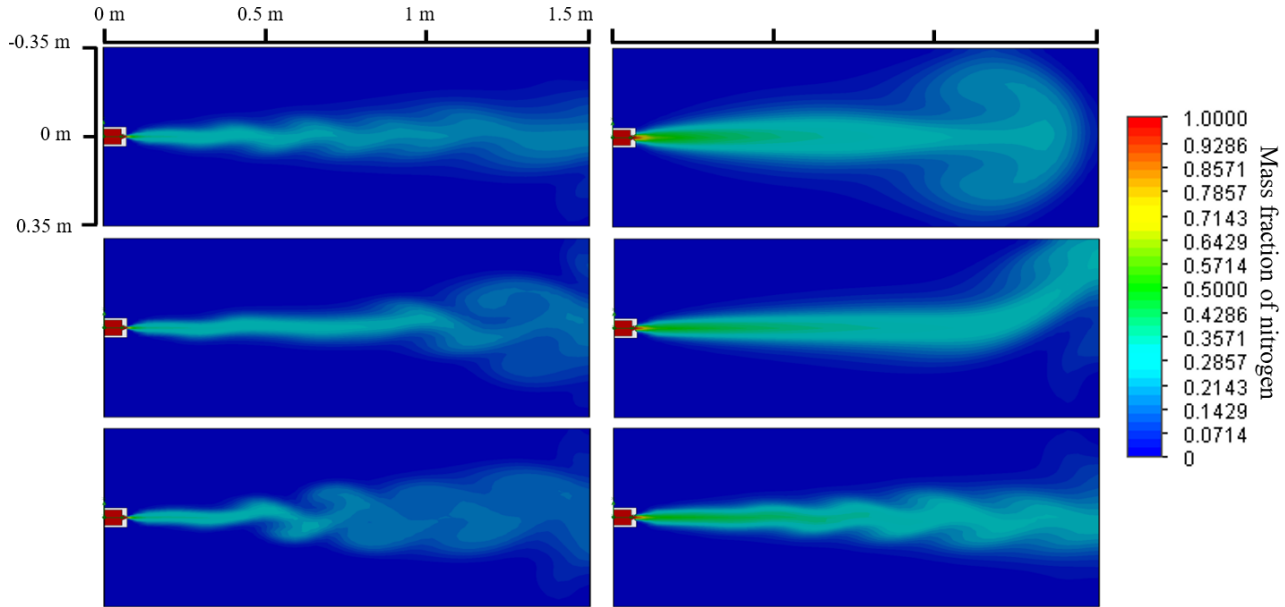


Figure 3. Simulated nitrogen flow distributions of a detector with 4 mm (left) and 10 mm (right) aperture openings with flow rates of 0.5 (top), 1.0 (middle), and 1.5 l/min (bottom). The length and the width of the simulated area are 1.5m and 0.7 m, respectively. The simulated result is shown at the steady state of the system.

SIMULATION OF NITROGEN FLOW

To further analyse the reason for the response increase, the distributions of the nitrogen fraction, pressure, and the relative humidity were simulated with Solidworks. Detector housings with aperture diameters of 4 mm and 10 mm were modelled. A turbulent flow was assumed as the inlet flow.

Figure 3 shows the simulation results at the steady state for flow rates of 0.5, 1.0 and 1.5 l/min with both aperture diameters. The pressure difference between the inside of the detector and the ambient is 0.2 Pa when using the 4-mm diameter aperture and 1.5 l/min flow rate. The turbulence makes the flow distribution change over time with higher flow rates, and the nitrogen profile in front of the detector is unstable. This is also seen in the LED measurements in Figure 1 as increased standard deviation of the photocurrent.

The nitrogen flow appears to produce a tube-like structure in front of the aperture. The refractive index of nitrogen is about 5 ppm larger than that of air [3] and thus nitrogen appears to form a gradient-index type gas lens in front of the detector. Paraxial light paths passing close to the aperture edge are expected to slightly bend towards the optical axis. As a result, the area of the detector aperture may effectively increase for a large-area LED source because of the lensing effect. For a laser source in underfilled mode,

the lensing effect is expected to be much smaller, in agreement with Figure 2.

DISCUSSION

Based on our measurements, the nitrogen flow affects the response of trap detectors in overfill conditions. The gradual radial change of the nitrogen fraction, and thus the refractive index, may act as a gradient-index lens and effectively increase the aperture area of the detector.

Simulations were made for two different aperture diameters and different nitrogen flow rates to evaluate the nitrogen profile in front of the detector and its turbulence. The standard deviations of the overfill measurements support the hypothesis of the flow affecting the results. Having a small enough flow rate minimizes the effect on the measurements. At the same time, the flow rate should be kept large enough to prevent moisture and dust entering the detector.

REFERENCES

1. T. Dönsberg et. al., A primary standard of optical power based on induced-junction silicon photodiodes operated at room temperature, *Metrologia*, 51(3), 197, 2014.
2. T. Pulli et. al., Advantages of white LED lamps and new detector technology in photometry, *Light: Science & Applications*, 4(9), e332, 2015.
3. J.A. Smith, *Engineering Metrology Toolbox: Refractive Index of Air*, <http://emtoolbox.nist.gov/Main/Main.asp>

Radiometric calibration method for dim sources

Maritoni Litorja, Yuqin Zong and Cameron Miller

National Institute of Standards and Technology

Gaithersburg, MD, USA

Corresponding e-mail address: litorja@nist.gov

Light sources with total emittance at or lower than femtowatt power can be used to calibrate sensitive cameras used for biomedical imaging. We employ a system to calibrate these dim sources by using a light source split by a high ratio (99:1) bifurcated optical fiber. The measured transmittance ratio along with the calibration of the high emittance branch using current measurement capabilities with low uncertainties facilitates calibration of dim sources.

INTRODUCTION

Fluorescence and bioluminescence-guided imaging devices are used to help clinicians visualize the extent and distribution of cancerous tissue, especially during surgical excisions. Driven by the goal of minimizing toxicity from both the fluorescent contrast agent and the excitation source intensity, the luminescence emitted at the tissue surface is very dim. This necessitates the use of dim light sources, which may be electrically - driven (light bulbs) or optically driven (fluorescent polymeric tissue phantoms) as monitoring artifacts to track the performance of an imaging device during its development or in preclinical studies (Fig. 1). [1]

The camera systems in luminescence-guided imaging vary in form factors (e.g endoscope, robotic-

assisted surgical systems), the types of sensors and associated electronics, and operate in different wavebands depending on the contrast agent emission band which can vary from the blue to near infrared spectral region. Thus, it is convenient to have these portable dim light sources presented to the imager at the site of use. These sources have been generally used as monitoring artifacts; with radiometric calibration, they can transfer SI-traceable scale to the imager.

METHOD

We have set up a system to calibrate dim sources using commercially available components, as shown in Fig. 2. This consists of a light emitting diode (A) at the desired waveband matching the unit under test

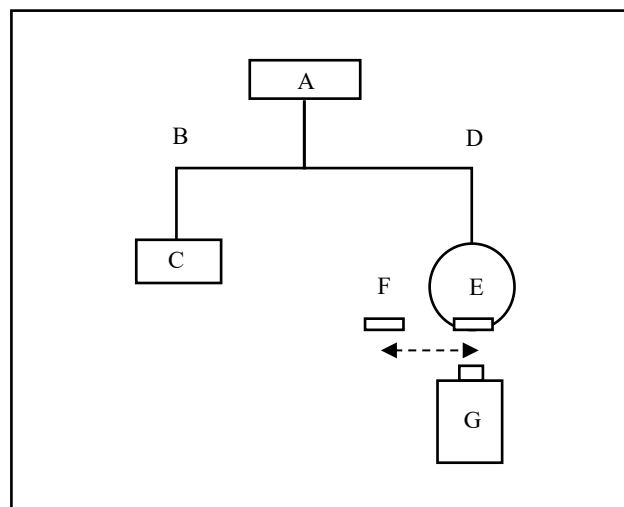


Figure 2. Illustration of the bifurcated optical fiber system for calibrating dim light sources.

(F), input into a high-ratio bifurcated optical fiber (B,D) (99:1 ratio). The higher emittance branch (B) is coupled to a photodiode (C) calibrated by the NIST SCF. [2] The low-emittance branch of the fiber (D) is input into a 50.8 mm (two-inch) diameter integrating sphere with a 12.7 mm (half inch) exit port (E), attenuating it further. The optical fiber and integrating sphere are calibrated for their transmittance and throughput respectively. The integrating sphere exit port is presented to a low-noise camera (G), used here as a transfer imager, alternated with the dim light

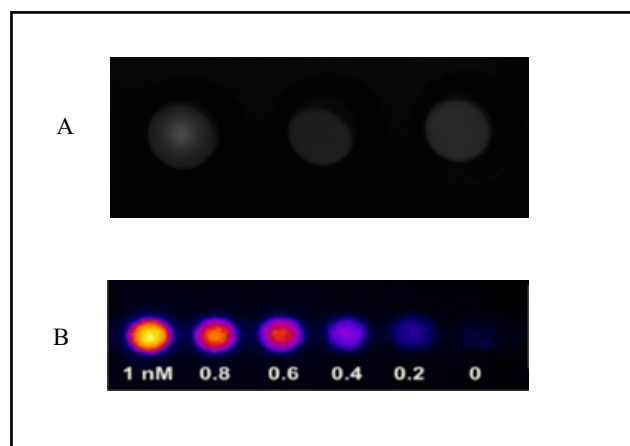


Figure 1. Example of a light-emitting diode artifact (A) and a fluorescent tissue phantom (B).

source being tested (F); the light emitting diode source drive current is adjusted such that the radiance of the sphere source matches the dim source under test as imaged on the transfer camera. The radiance of the sphere source is calculated from the responsivity of the calibrated photodiode and the fiber transmittance and sphere throughput. The dim source derives its radiance value through the comparison with the sphere output.

The calibration is done at higher flux, where measurement uncertainties are lower and utilizes commercially available components.

REFERENCES

1. B.W. Pogue et al, "Fluorescence-guided surgery and intervention—an AAPM emerging technology blue paper", *Medical Physics* 45, 2681-2688, 2018.
2. T.C Larason and J.M. Houston, "NIST Measurement Services: Spectroradiometric Detector Measurements: Ultraviolet, Visible and Near-Infrared Detectors for Spectral Power," NIST Special Publications 250-41, 2008.

A fast AC mode measurement system for detector response and spatial uniformity characterization

Ping-Shine Shaw and Yuqin Zong

*Sensor Science Division
National Institute of Standards and Technology
Gaithersburg, MD 20899, USA
Corresponding e-mail address: shaw@nist.gov*

When high-accuracy radiometric measurements for photodetectors such as Si photodiodes are required, the prevailing practice is to perform DC measurements on the detector's response. For example, the signal from the detector is typically acquired and integrated over seconds if not longer for each input light configuration. The idea is that long integrating time helps in reducing noise related uncertainty. Here, we demonstrate an alternative to this paradigm with a radiometric measurement system that performs a versatile AC mode of operations. This system achieves not just fast but accurate measurements mainly by three components: a fast steering mirror that can position the probe beam rapidly, a fast data acquisition module that acquires responses from all detectors, and a computer algorithm for digital signal processing. This system enables fast data collection using a variety of measurement configurations. We illustrate the benefits of the system using two examples; measuring detector response using a chopped beam, and measuring detector spatial uniformity map with high density of pixels.

INTRODUCTION

In modern radiometry from UV to IR, the use of several types of solid-state photodetectors like Si and InGaAs photodiodes has been ubiquitous. Pyroelectric detectors are also gaining popularity. For photodiodes, while the frequency range of response typically extends from DC to several hundreds of kHz, it is a general tradition to perform radiometric measurements only at DC mode with a time constant of seconds. For example, a photodiode's response is integrated up to seconds with a fixed light configuration followed by the same measurement but with light blocked for background response. The difference of the two measurements is then the true response of the detector. Little was done to explore photodiode response using AC mode of measurement.

As for the pyroelectric detectors, they can only be operated in AC mode at a frequency of tens of Hz. Consequently, the traditional measurement system for pyroelectric detectors often incorporates a chopper and a lock-in amplifier. Here, we introduce a measurement setup capable of AC measurements for both types of detectors without using conventional choppers and lock-in amplifiers. The versatile nature of the setup offers a variety of measurement modes that is very time-consuming to do using conventional systems.

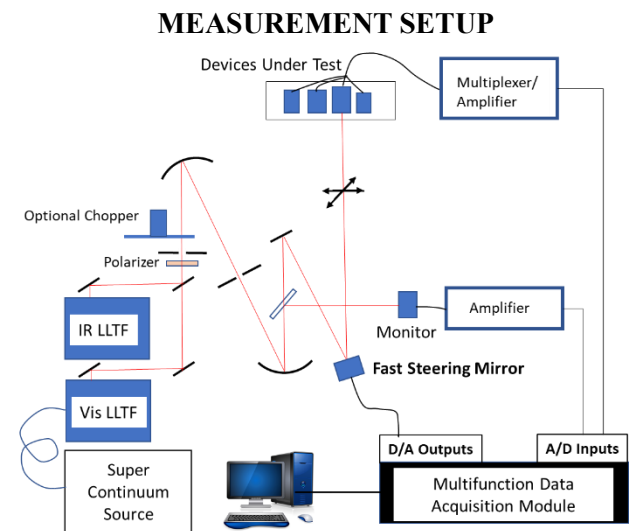


Figure 1. Setup for detector response measurement using AC/DC mode.

The setup is depicted in Fig. 1. The vis/IR light used by this setup is generated by a Super-Continuum (SC) source and filtered by a monochromator (labelled as LLTF in Fig.1). The light is directed to test detectors and steered by a Fast Steering Mirror (FSM). The FSM is capable of tilting along two perpendicular axis and the angles of the tilt are controlled by voltages from two D/A outputs of a Multifunction Data Acquisition (MDA) module. The response of the test detector is sent back to the A/D input of the MDA. The MDA is commanded by a computer and can

perform synchronous A/D and D/A operation up to a sampling rate of 500 kHz.

DETECTOR RESPONSE MEASUREMENT USING CHOPPED BEAM

In the first example, we programmed the MDA such that the FSM steered the light beam and alternated between two positions, one inside the detector's active area and the other outside the detector's active area. At the same time, the detector's response was digitized synchronously with the steering operation. Fig. 2 shows the raw response data from a Si detector and a pyroelectric detector with a chopping frequency of 10 Hz and a sampling rate of 10k/s. The DC responses of the detectors were derived from the raw data using a Digital Signal Processing (DSP) algorithm which (1) eliminates data from the transient regions, (2) averages the flat response regions of the light-on and light-off periods, and (3) calculates the DC response from their difference. Using this method, we found excellent repeatability at the 10^{-4} level for the photodiode with 1 sec acquisition time. It is somewhat higher for the pyroelectric detector because of the intrinsic detector noise as evident from Fig. 2.

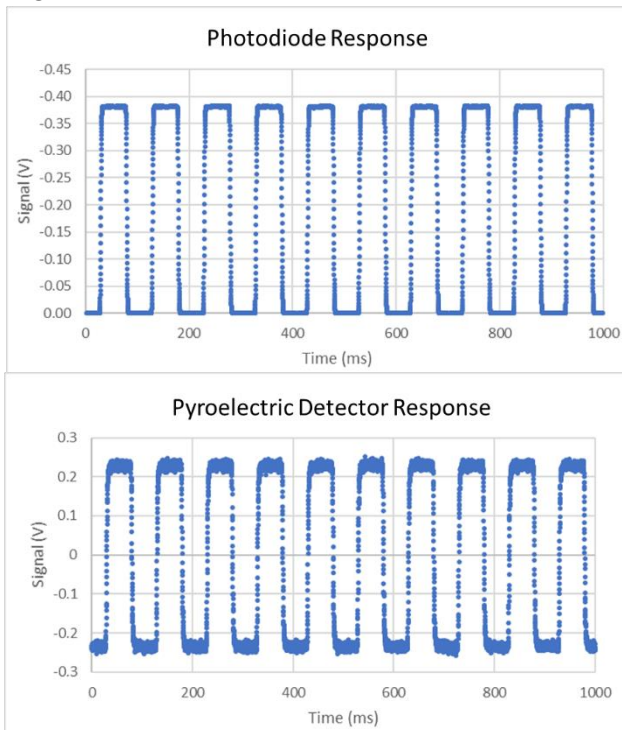


Figure 3. Data acquired by MDA from of a Si photodiode and a pyroelectric detector by chopped light using FSM.

DETECTOR SPATIAL UNIFORMITY SCAN

As a second example, the FSM was used to raster scan the light beam across a detector for uniformity

mapping. The scanning sequence is controlled by the MDA which also collects data from the detector synchronously with the position of the light beam. Fig. 3 shows the contour plot at 0.1% contour level of a scan on a trap detector with a 4 mm aperture. The area of the scan is 8 mm x 8 mm with a 128 x 128 mesh with corresponds to more than 16,000 data points from the scan and the whole scan took about 3 minutes to complete. Notice the details exhibited in the plot especially the depressed hole near the bottom of the plot. It is believed to be caused by a speck of dust stuck on the detector surface.

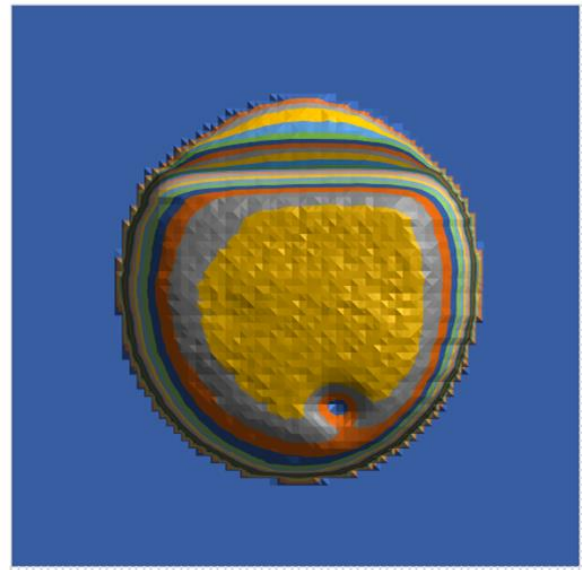


Figure 2. Uniformity contour plot of a trap detector. For clarity, only the contour lines of the top 2% are plotted and the adjacent contour lines represent 0.1% change in responsivity. This plot is generated using 128 x 128 data points.

SUMMARY

We have shown that a simple system with FSM, MDA, and DSP processing of data can extract DC response using AC measurement for detectors like photodiodes and pyroelectric detector. This technique is a variation of the conventional phase-sensitive lock-in measurement and is good at out-of-band noise reduction. This contrasts with the traditional DC measurements which is subject to possible slow drift from the system. In addition, we showed that this system can perform fast and high-density detector uniformity scan. Such scan can take many hours using a conventional DC system. This scanning technique can be a good diagnostic tool for evaluating a detector's general conditions.

Power and wavelength-meter in one for lasers and other narrow-band light sources based on the dual-photodiode radiometer concept

Dong-Joo Shin, Seongchong Park, Yong Shim Yoo, Jae-Keun Yoo, and Dong-Hoon Lee

Korea Research Institute of Standards and Science (KRISS), Daejeon, Korea

Corresponding e-mail address: djshin@kriss.re.kr

We are developing a radiometer, which can simultaneously measure radiant power and centroid wavelength of narrow-band light sources in a wavelength range from 400 nm to 900 nm. The device consists of an integrating sphere and two photodiodes attached on that. One of the photodiodes is accompanied with a dielectric filter to make its spectral responsivity different from the other. The accuracy of the power and wavelength measurements using this device is being tested both numerically and experimentally.

MOTIVATION

Wavelength-tunable narrowband light sources with a spectral bandwidth of less than 10 nm, including lasers, are widely used in the field of radiometry, especially for spectral characterization and calibration of optical sensors and detector systems. The radiant power and centroid wavelength of such a source are the important quantities, which need be monitored by using two separate instruments, a power-meter (i.e., a radiometer calibrated against radiant flux) and a wavelength-meter (or a spectro-radiometer).

Our motivation is to develop a two-in-one instrument, which can simultaneously measure radiant power and centroid wavelength in a single reading. The concept of the dual-photodiode radiometer is applied, which is described and

demonstrated in Ref. [1]. The main challenge of our experimental realisation of this concept is to cover a wide wavelength range from 400 nm to 900 nm. As the development is still in progress, we present in this paper the preliminary results achieved so far.

CONSTRUCTION

Figure 1 shows the schematic design of the dual-photodiode radiometer developed. The flux to be measured is entered into a small-sized integrating sphere with an inner diameter of 50 mm, which is attached with two Si photodiodes. One of them is accompanied with a dielectrically coated filter, which makes the spectral responsivity of one detector different from the other.

As described in Ref. [1], the dual-photodiode radiometer concept works only when the following conditions are fulfilled: First, spectral responsivity of each detector should be a linear function against wavelength within the bandwidth of the incident light. Second, the responsivity ratio of the both photodiodes should be a monotonic function against wavelength. The measured spectral responsivities of each photodiode are shown in Figure 2 together with their ratio as a function of wavelength. The condition of the linear function seems to be fulfilled from 400 nm to 900 nm. However, the ratio is not a monotonic function below 500 nm. Therefore, the device constructed for the first test can be used only in a

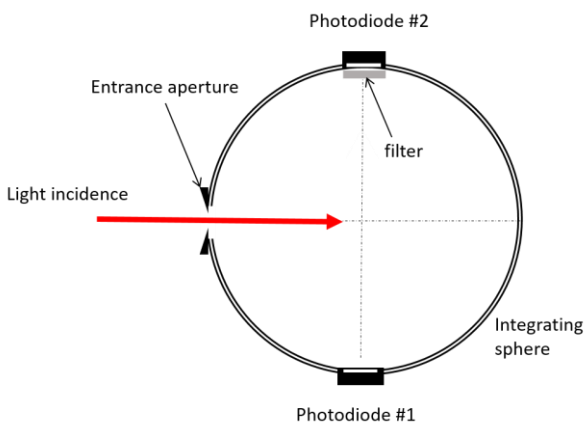


Figure 1. Schematic design of the dual-photodiode radiometer for simultaneous measurement of radiant flux and centroid wavelength.

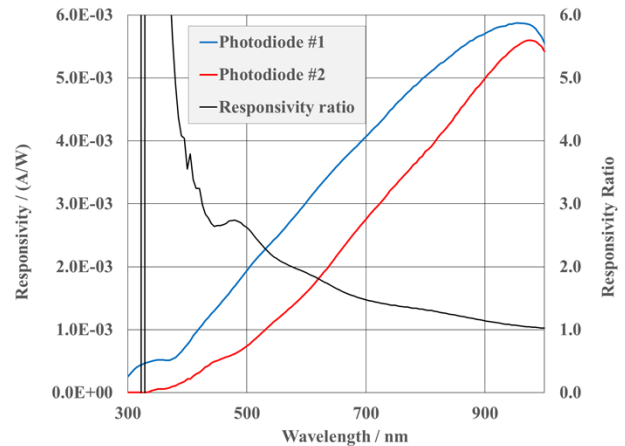


Figure 2. Measured spectral responsivity of the photodiodes #1 and #2, and their ratio of the dual-photodiode radiometer shown in Fig. 1.

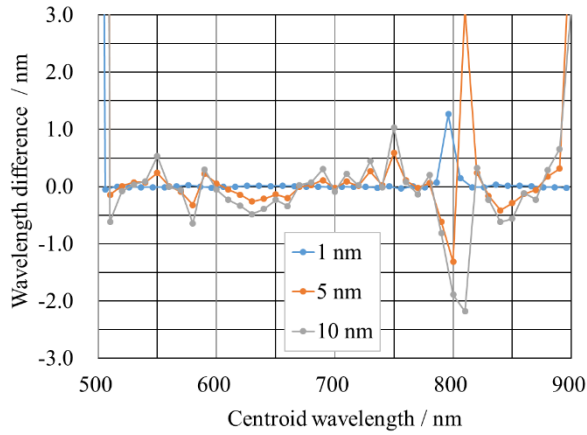


Figure 3. Measurement errors for centroid wavelength expected from the numerical simulation based on the measured spectral responsivities of Fig. 2 and a Gaussian function input with a spectral bandwidth of 1 nm (blue), 5 nm (red), and 10 nm (grey).

wavelength range from 500 nm to 900 nm. A revision of the filter coating is required to extend the working range.

NUMERICAL TEST RESULTS

The expected accuracy of the dual-photodiode radiometer is first tested based on a numerical simulation. Similar to Ref. [1], we took a Gaussian function with a spectral bandwidth (FWHM) of 1 nm, 5 nm, and 10 nm at various centroid wavelength as the input light. For each input light, we calculated the centroid wavelength and radiant power by using the measurement equations of the dual-photodiode radiometer based on the measured data of Fig. 2.

Figure 3 and Fig. 4 show the simulation results for centroid wavelength and radiant power, respectively: the difference of the “measured” values and the “true” values are plotted as a function of wavelength from 500 nm to 900 nm for different values of source spectral bandwidth.

We see in the results of Fig. 3 and Fig. 4 that a high measurement error is expected in the near of 500 nm, 900 nm, and 800 nm, where the spectral responsivity of the photodiode #1 severely deviates from a linear function. Except these regions, the maximum errors are kept small. For a spectral bandwidth of less than 1 nm, the expected errors for centroid wavelength and radiant power are less 0.1 nm and 0.1 %, respectively. The errors generally increase as the spectral bandwidth of the source increases, but well below 0.5 nm and 0.3 % for centroid wavelength and radiant power, respectively, except several problematic regions where the spectral

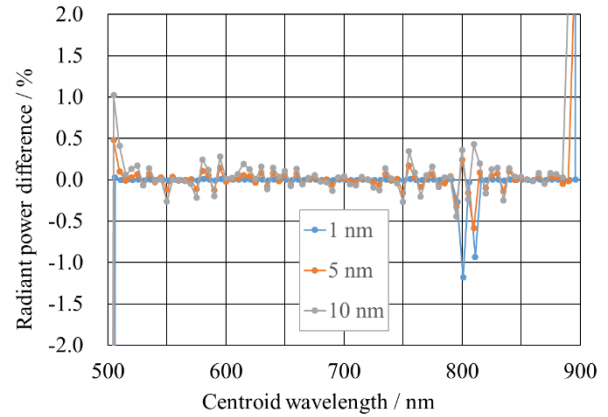


Figure 4. Measurement errors for radiant power expected from the numerical simulation based on the measured spectral responsivities of Fig. 2 and a Gaussian function input with a spectral bandwidth of 1 nm (blue), 5 nm (red), and 10 nm (grey).

responsivity is strongly non-linear against wavelength.

Based on the numerical test results with the measured spectral responsivities, we obtained valuable information on how to modify the spectral transmittance of the filter to achieve the high accuracy in the whole target range from 400 nm to 900 nm.

FURTHER TESTS IN PLAN

To be a practical measurement device, the proposed dual-photodiode radiometer needs to be also tested for various response characteristics such as angular and spatial uniformity, stability, and non-linearity against incident power. For application with lasers, polarization dependence will be also tested. As the target application of this two-in-one device, we will monitor the radiant power and centroid wavelength of a tunable laser and of a monochromator-based tunable light source.

REFERENCES

1. Dong-Joo Shin *et al.*, Dual-photodiode radiometer design for simultaneous measurement of irradiance and centroid wavelength of light sources with finite spectral bandwidth, *Applied Optics*, 58, 8262-8271, 2019

Stable spectrally tunable source based on supercontinuum laser and monochromator for detectors radiometric calibration

A. Yu. Dunaev, S. P. Morozova, N.L. Dovgilov, A.S. Baturin, V.S. Bormashov, V.R. Gavrilov and V.I. Sapritsky

All-Russian Research Institute for Optical and Physical measurements, Moscow, Russia

Corresponding e-mail address: dunaev@vniiofi.ru

A stable spectrally tunable source for calibration of radiometric detectors in radiance or power mode has been developed and characterized. It consists of a supercontinuum laser with expander and focusing optics, subtractive monochromator, power stabilization feedback control scheme, and output coupling optics.

The commercial supercontinuum laser Fianium SC400-4 was used. It has wavelength range from 0.4 to 2.5 μm with full spectrum power of 4 W.

A power stabilization feedback control scheme has been incorporated that stabilizes the source to better than 0.02% for averaging times longer than 1200 s.

INTRODUCTION

When developing facilities for spectroradiometric instrument calibrations, including detectors, spectroradiometers, video spectrometers, etc., one of the main components of uncertainty budget of radiance or radiant power measurements is the instability of the radiation source used.

While radiant sources based on lamps and blackbodies provide sufficient measurement accuracy in the visible range of the spectrum, for example, for the detectors spectral responsivity, the radiant power level of these sources does not provide the required accuracy in the infrared. A partial solution to the problems of measurements in the infrared spectral range is to using lasers at fixed wavelengths.

Nowadays, lasers with a wide spectral range are available [1,2]. These lasers are called supercontinuum and covered the spectral range from 0.4 to 2.5 μm with full power up to 14 watts. Using of these lasers significantly expands the capabilities of the metrological assurance of spectroradiometric instruments calibrations, while the stability is certain.

This work is devoted to stabilization of supercontinuum laser power, while it used as a radiant source of detector spectral responsivity calibration facility based on a cryogenic radiometer.

STABLE SPECTRALLY TUNABLE MONOCHROMATIC SOURCE

Figure 1 shows the VNIIOFI stable spectrally

tunable monochromatic source for the spectral range from 0.4 to 2.5 μm .

The main parts of the facility are: (i) radiation source unit with the optical system, which focuses the radiation on the input slit of the monochromator; (ii) subtractive double monochromator, (iii) laser feedback system, (iv) output coupling optics and (v) detector under test.

The facility includes powerful supercontinuum laser Fianium WhiteLase SC 400-4 for the spectral range from 0.4 μm to 2.5 μm . Special laser beam mirror expander with focusing unit are used to irradiate entrance slit of double monochromator and fill its $f/4,8$ aperture angle. This expander consists of 2 spherical mirrors with expansion ratio of 6^\times . The focusing unit includes flat and off-axis parabolic mirrors. The spectral mercury lamp is used for monochromator wavelength calibration.

Radiation of source is directed to monochromator input slit, in front of which the order-sorting filter wheel is located. Subtractive double monochromator McPherson 2035D uses gratings of 600 grooves/mm for the spectral range from 0.4 to 2.5 μm . Monochromator technical characteristics allow selecting radiation with the spectral bandwidth of 6 nm in this spectral range.

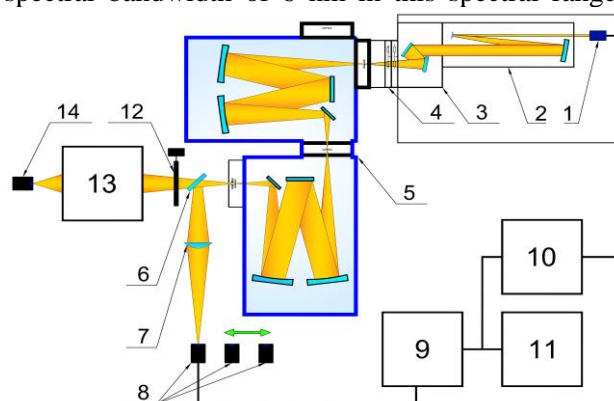


Figure 1. VNIIOFI stable spectrally tunable monochromatic source

1 – supercontinuum laser emitter, 2 – laser beam mirror expander, 3 – focusing unit, 4 – order-sorting filter wheel, 5 – subtractive double monochromator, 6 – quartz beamsplitter, 7 – quartz lens, 8 – feedback monitor detector, 9 – transimpedance amplifier, 10 – supercontinuum laser unit, 11 – digital voltmeter, 12 – shutter; 13 – output coupling optics; 14 – detectors under test (DUT).

For stabilization of monochromatic radiant power the feedback control is used. It consists of thin quartz plate beamsplitter (6), quartz lens (7), feedback monitor (8), transimpedance amplifier (9), supercontinuum laser unit (10) and digital voltmeter (11). Thin quartz plate beamsplitter is installed after output slit of monochromator. The reflected beam is directed to feedback monitor detector with focusing quartz lens. Silicon trap-detector is used as feedback monitor in the spectral range from 0.4 to 1.0 μm . InGaAs and Extended-InGaAs photodiodes are used as feedback monitor in the spectral range from 0.9 to 1.6 μm and from 1.6 to 2.5 μm respectively. Spectral responsivities of this feedback monitor detectors are presented in Figure 2.

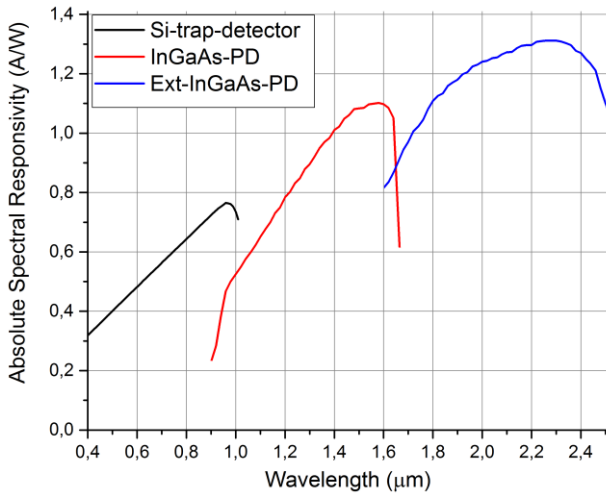


Figure 2. Spectral responsivities of feedback monitor detectors

Feedback monitor detectors are connected to transimpedance amplifier that outputs feedback DC voltage in the range from 0 to +5V. Adjusting DC Voltage of feedback is provided by changing the gain of transimpedance amplifier. Output of amplifier is connected to supercontinuum laser unit that has own internal feedback interface. A PID (Proportional-Integral-Differential) control loop is used to adjust the drive levels to the laser.

Optionally optical program-controlled shutter is placed after feedback beamsplitter in transmitted beam.

Developed monochromatic laser-based source has been established at VNIIOFI Primary Standard for Optical Radiant Power based on Absolute Cryogenic Radiometer (ACR) [3]. Output coupling optics (13) is provided by using two off-axis parabolic mirrors to the entrance window of the vacuum chamber, which forms a common vacuum volume for the ACR and detectors under test.

Spectral responsivity scale realization consists in measuring the radiant power absorbed by the receiving cavity of the radiometer, irradiating the

photodetector with this flux, measuring its signal and calculating its spectral responsivity by the formulas:

$$S_I(\lambda) = \frac{I(\lambda)}{P_o(\lambda)}; \quad S_U(\lambda) = \frac{U(\lambda)}{P_o(\lambda)},$$

Where $S_I(\lambda)$, $S_U(\lambda)$ - current and voltage spectral responsivities of calibrating detector, $I(\lambda)$, $U(\lambda)$ - current and voltage of calibrating detector, $P_o(\lambda)$ - spectral radiant power.

The measured spectral radiant power of developed monochromatic laser-based source in the spectral band of 6 nm is presented in Figure 3.

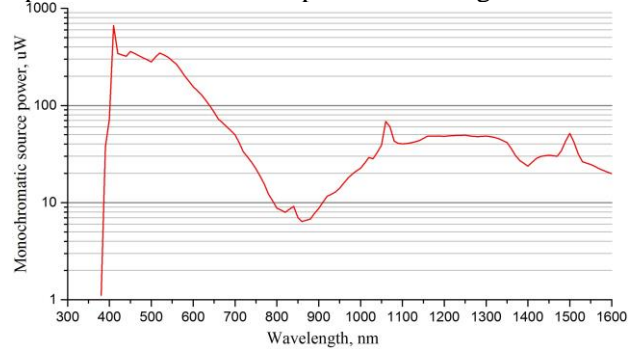


Figure 3. Spectral radiant power of developed monochromatic laser-based source in the spectral band of 6 nm

A power stabilization feedback control scheme has been incorporated and it stabilizes the monochromatic radiant power better than 0.02% for time interval longer about 1200 s. Spectral radiant power stability is presented in Figure 4.

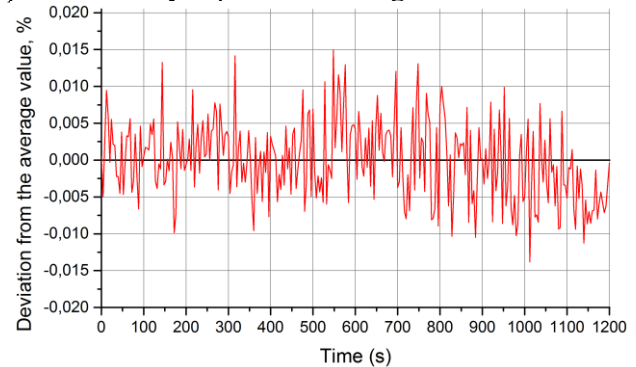


Figure 4. Temporary stability of spectral radiant power

REFERENCES

1. J T Woodward et al., Supercontinuum sources for metrology, *Metrologia* 46 (2009) S277–S282.
2. Andrew P. Levick et al., Spectral radiance source based on supercontinuum laser and wavelength tunable bandpass filter: the spectrally tunable absolute irradiance and radiance source, *APPLIED OPTICS* / Vol. 53, No. 16 / 1 June 2014.
3. Gavrilov V.R. et al., National Primary Standard for the Units of Absolute and Relative Spectral Sensitivity at Wavelengths from 0.25 to 14.00 μm Get 213–2014, *Measurement Techniques*, February 2016, Volume 58, Issue 11, pp 1200–120.

Thermal Characterization of Fiber-Coupled Spectrographs

B. Carol Johnson, Steven W. Brown, Thomas Larason, and John Woodward

Sensor Science Division

National Institute of Standards and Technology

Corresponding e-mail address: cjohnson@nist.gov

Accurate spectral radiometry utilizing spectrographs requires thorough instrument characterization. The performance of spectrographs with silicon photo-diode or CCD arrays demands increased scrutiny as applications continue to push for lower uncertainties and incandescent lamp sources are being replaced by non-Planckian radiators. In this work we characterized the sensitivity of the wavelength registration and the system radiometric responsivity of five commercial spectrographs to ambient temperature using a lamp illuminated integrating sphere source, emission line lamps, and an environmental chamber. The temperature was varied between 6°C and 45°C. We developed correction functions for the two effects and validated them with test data.

INTRODUCTION

Several projects in the Sensor Science Division at the National Institute of Standards and Technology (NIST) require accurate radiometric measurements during field work, where the ambient temperatures differ from the laboratories at NIST. In the future, solid-state sources such as LEDs may supplement or replace incandescent lamps in radiometric sources. As the latter are proxies for primary standards via Planck's Law, while the former are not, performance requirements on spectroradiometers will become more stringent, and sensitivity to temperature will be a critical aspect of instrument characterization.

Three different field projects were involved in this study, one where a source and spectroradiometer system are required to be stable over intervals of 6 months to 1 year, during which time the system is transported by a cargo ship inside a shipping container [1], a second where a spectroradiometer is calibrated in an unairconditioned aircraft hangar and then flown on a National Aeronautics and Space Administration (NASA) ER-2 aircraft [2], and a third where the spectroradiometer is calibrated and operated at high altitude (Mt. Hopkins or Mauna Loa) under conditions of varying ambient temperature [3].

For all three projects, insensitivity to temperature changes is mandatory.

In this work we report the sensitivity to ambient temperature for five fiber-coupled CCD spectrographs, see Table 1.

Table 1. Description of the spectroradiometers (BF = bare fiber, CC = cosine collector).

Name	Spectral Coverage, nm	Foreoptic
MOBY	298 to 1103	BF
UV	200 to 876	BF
LUSI	299 to 1104	CC
STARS	380 to 1050	BF
XSTARS	379 to 1040	CC

EXPERIMENTAL SETUP

The spectrographs (devices) under test (DUTs) were operated inside an environmental chamber with the relative humidity allowed to vary while the temperature was controlled at various set points. Two ports, one for electrical cables and one for the optical fibers, allowed for remote control of the DUTs, incorporation of additional temperature sensors, and simultaneous illumination of the DUTs using a lamp-illuminated integrating sphere source (ISS). The ISS and a fiber-coupled monitor spectrograph (MS) were outside the environmental chamber, where the temperature was 24.3°C±0.3°C. The stability of the ISS was recorded by the MS with occasional manual readings of the ISS' internal photopic monitor photodiode. When the chamber temperature was stable at the set point, the ISS measurements were interrupted for a sequence of wavelength stability tests using HgNe or Ne emission pen lamps.

Multiple, independent records of chamber and laboratory ambient temperature and relative humidity were recorded utilizing the chamber sensors, a two-channel digital thermometer-hygrometer, and a 10 kΩ thermistor. The thermistor was mounted on one of the DUTs. Temperature profiles were operated daily, always beginning and ending near ambient, with durations of 90 min or 120 min. The MOBY, UV, LUSI, and STARS were operated over 11 days in the fall of 2018; XSTARS was operated on a single day

in April 2019. The set temperature varied between 5°C and 40°C, which was deliberately outside the stated operating range for the two of the DUT in order to replicate collects on prior field experiments.

ANALYSIS

The experiment generated 24,618 data files, as much of the data logging was on a 10 s, 30 s, or 60 s cadence (wavelength calibrations were the exception), so the processing was designed to be automated.

For both the wavelength and system response dependence on ambient temperature, the thermistor serves as the reference. The observed emission lines were fit to a Gaussian. The results were independent of which lamp (HgNe or Ne) as well as wavelength. The temperature-induced wavelength shifts were modelled by a quadratic and the sensitivity factors determined from the derivative, see Fig. 1.

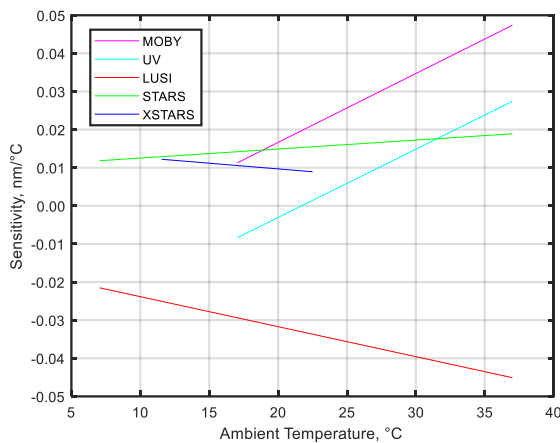


Figure 1. Sensitivity of wavelength shift to ambient temperature for the five DUTs.

After correcting for the wavelength dependence on temperature, the observations of the ISS were corrected for known effects (e.g. stray light, changes in alignment of the optical heads viewing the ISS, and drift in the ISS output over the 92 h burn time). DUT files acquired for 10 min to 20 min when the thermistor reading had stabilized were averaged, see Fig. 2 for MOBY. These results are for all 43 temperature plateaus, normalized to 24°C. Interpolation in these data results in a responsivity correction factor as a function of ambient temperature and wavelength. At 600 nm, these preliminary results correspond to a responsivity temperature sensitivity for MOBY of about 0.1%/°C.

Results to date have modelled the sphere drift in terms of a Planckian distribution fit for CCT using the

MS data. Correlation studies between the MS and the DUTs support the hypothesis that the responsivity of the MS was invariant, and it was the ISS that drifted.

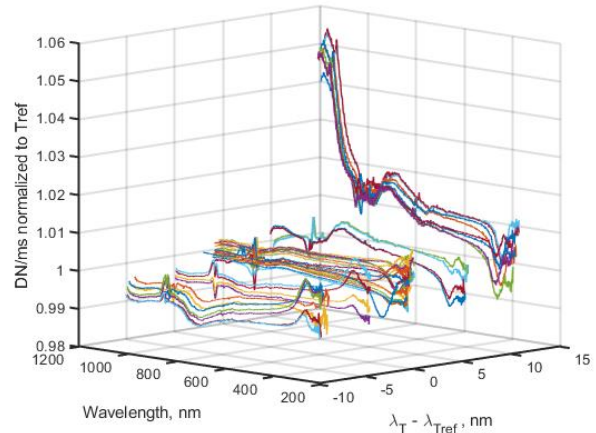


Figure 2. Normalized MOBY output as a function of wavelength and difference from the reference temperature.

DISCUSSION AND CONCLUSIONS

The five DUTs were all from the same manufacturer and the same general model number, manufactured between 2005 and 2015. The wavelength sensitivity with ambient temperature differed for each, indicating individual characterization is required. The system response demonstrated increased sensitivity to temperature for wavelengths greater than about 900 nm and ambient temperatures above 32°C. For all DUTs, the responsivity sensitivity depends on wavelength.

The lead author acknowledges Stephanie Flora of Moss Landing Marine Laboratories for software support. NASA support was provided through agreements NNN15AZ021 and the Airborne Instrument Technology Transition (AITT) program.

REFERENCES

1. K. Voss et al., Developing a MOBY-Net instrument, Suitable for a Federation Network for Vicarious Calibration of Ocean Colour Satellites, NASA, 2014.
2. <https://www.nasa.gov/feature/goddard/2019/new-moon-seeking-sensor-aims-to-improve-earth-observations>
3. Cramer, et al., SI-traceable calibrations of celestial objects, in Calibration and Standardization of Missions and Large Surveys in Astronomy and Astrophysics, Astron. Soc. Pacific Conf. Ser., 503, 135-143, 2016.

Experimental Correction of Temperature Dependence for LED Filament Lamps

Zhao Weiqiang¹, Liu Hui, Yan Jinyun, Su Ying

National Institute of Metrology, Beijing, China

¹Corresponding e-mail address: zhaowq@nim.ac.cn

Experimental correction model of temperature dependence for LED filament lamps is reported. The quantities approximate relations of the ambient temperature, the voltage and the flux are analysed. The flux deviation is nearly linearly to voltage deviation while the ambient temperature changes in a small range. While flux correction method applied according to voltage deviation, the experimental results show that the flux fluctuation of the LED filament lamp is less than 0.03% without any thermal control.

1. MOTIVATION

Since the incandescent lamps are phasing out and alternative LEDs become popular in the lighting market, the research of LED standard lamp now are an active topic in field of photometry and radiometry [1]. The National Institute of Metrology (NIM) is developing LED filament standard lamps. They are two types of standard lamps, one is for total luminous flux, other is for luminous intensity. In our design, the lamps are made of LED filaments, mimicking the classical tungsten filament type. As the temperature control module is cumbersome in our case, we measure the ambient temperature-dependence and propose a flux correction method according to the voltage. The temperature effect of LED filament is compressed.

2. CORRECTION MODEL

As well-known, the temperature-dependence of flux can be describe as following:

$$\Phi(T) = \Phi(T_0)e^{k(T-T_0)} \quad (1)$$

Here $\Phi(T)$ is the flux at temperature T , $\Phi(T_0)$ is flux at temperature T_0 , k is temperature coefficient. Since the $\Phi(T)/\Phi(T_0) \approx 1$, it deduces:

$$\frac{\Phi(T)-\Phi(T_0)}{\Phi(T_0)} = k(T - T_0) \quad (2)$$

Also, the voltage deviation is linearly to PN junction temperature deviation. Due to thermal equilibrium, the ambient temperature deviation is the same as the junction temperature deviation. So,

$$\frac{\Phi(T)-\Phi(T_0)}{\Phi(T_0)} = k(T - T_0) = k_2(V(T) - V(T_0)) \quad (3)$$

Here $V(T)$ is the voltage at temperature T , $V(T_0)$ is the voltage at temperature T_0 , k_2 is voltage coefficient. Approximately, at a certain current, we get a fitting equation used as the correction model:

$$\Phi(V) = k_3 \cdot V + b_3 \quad (4)$$

and other two fitting equations:

$$\Phi(T) = k_4 \cdot T + b_4 \quad (5)$$

$$V(T) = k_5 \cdot T + b_5 \quad (5)$$

Here k_3 , b_3 , k_4 , b_4 , k_5 , and b_5 are the fitting parameters.

3. FITTING PARAMETERS MEASUREMENT

A spherical photometer is used to measure the fitting parameters. 4-wire connection is applied for voltage remote sensing. Ambient temperature sensor is installed inside the sphere and close to the baffle, placed in the shadow side. Auxiliary halogen lamp is used to be reference lamp to reduce the temperature influence of photometer. We test one LED filament lamp, GQ#67, which are made of 12 filaments, and proposed to be luminous intensity standard lamp. The experimental results are shown in Figure 1, 2 and 3.

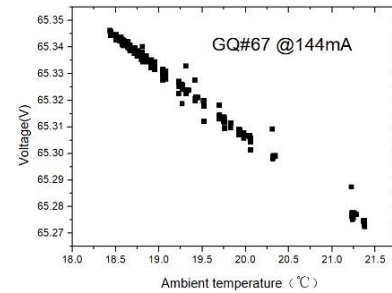


Figure1. Voltage vs temperature

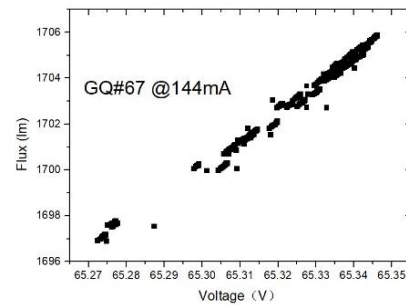


Figure 2 Flux vs voltage

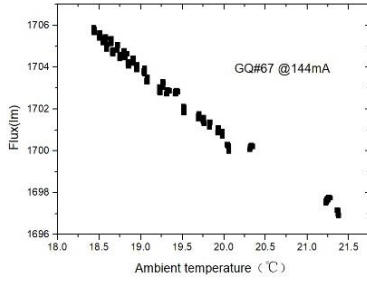


Figure 3. Flux vs temperature

Using least square fit, the fitting equations are described as:

$$\Phi(V) = 119.397 \cdot V(T) - 6096.52 \quad (6)$$

$$\Phi(T) = -2.94165 \cdot T + 1759.82 \quad (7)$$

$$V(T) = -0.0245994 \cdot T + 65.7995 \quad (8)$$

The calculated temperature coefficient is $-0.17\%/^{\circ}\text{C}$

4. EXPERIMENTAL RESULTS

The test of stability of GQ#67 is ongoing following the produce. After 500 hours aging, the lamp operates for 1 hour every day and then the flux, the voltage and the ambient temperature are monitored and recorded in 3 minutes.

We compared these two correction ways, one is based on equation (6) according to voltage, the other is based on equation (7) according to the ambient temperature as a contrast. $T=25^{\circ}\text{C}$ is the temperature reference point. $V(25^{\circ}\text{C})=65.1845\text{ V}$ according to the equation (8) is the voltage reference point.

With correction applied, 19 days results are shown in figure 4.

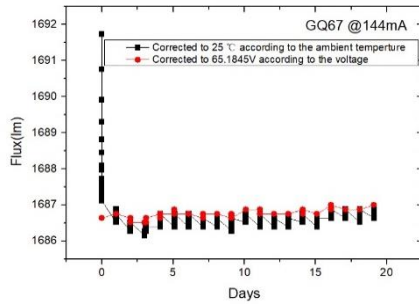


Figure 4. Flux stability in 19 days

In day 1, when using temperature correction, the flux drops from 1692 lm to 1687 lm due to the thermal non-balance in 3 minutes. However, using voltage correction, the flux multiple readings in 3 minutes are consistent. The voltage of lamp indicated the PN-junction temperature, related to the output flux. Voltage is a direct way to response to the flux. Use voltage correction is a better choice than temperature correction.

We show the corrected fluxes vs ambient temperature results in figure 5 and 6.

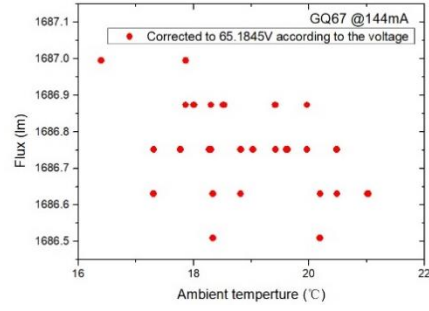


Figure 5. Voltage corrected flux vs temperature

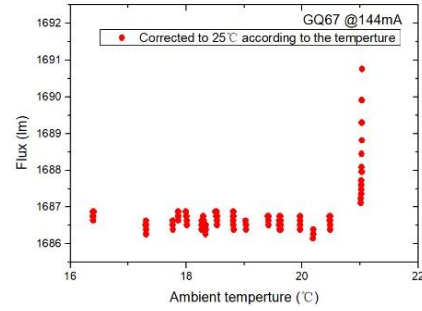


Figure 6. temperature corrected flux vs temperature

The figure 5 shows the voltage corrected flux is in the range of $(1686.5 \sim 1687.0)$ lm in these 19 days, that means less than 0.03% fluctuation when the ambient temperature varies. The related ambient temperature is in the range of $(16 \sim 21)$ $^{\circ}\text{C}$. No obvious decay is observed according to the figure 4.

Figure 6 shows a larger fluctuation of temperature corrected flux in same temperature variation range

5. CONCLUSION

NIM is developing LED filament standard lamps. An experimental correction method of temperature dependence for LED filament lamps is discussed in this report. The correction method is based on voltage deviation. After correction, flux fluctuation is less than 0.03% when the ambient temperature varies in range of $(16 \sim 21)$ $^{\circ}\text{C}$.

ACKNOWLEDGMENT

The authors are thankful to NIM colleague Mr. Lin Yandong for helpful discussion.

REFERENCES

1. CCPR Strategy Document for Rolling Development Programme, 2017.
2. Yan J.Y. etc, LED filament standard lamps for total luminous flux and luminous intensity, Proceedings of 29th CIE Session 2019

A Lens-free InGaAs-Radiation Thermometer with improved Detectivity at 1.6 μm to cover the Temperature Range from 80 $^{\circ}\text{C}$ to 962 $^{\circ}\text{C}$

Ingmar Mueller¹, Jonas Bories¹, Berndt Gutschwager¹, and Christian Monte¹

¹Physikalisch-Technische Bundesanstalt, Braunschweig and Berlin, Germany

Corresponding e-mail address: ingmar.mueller@ptb.de

In the last decade the specific detectivity of InGaAs-photodiodes has improved significantly. Hence, the lower detection limit of InGaAs-photodiode based radiation thermometers at 1.6 μm can be extended. Here, an existing radiation thermometer was equipped with a state-of-the-art InGaAs-photodiode. The radiation thermometer was characterized and calibrated and a reference function has been compiled. The lower temperature limit could be extended from 150 $^{\circ}\text{C}$ down to 80 $^{\circ}\text{C}$.

INTRODUCTION

The working group “Infrared Radiation Thermometry” of the Physikalisch-Technische Bundesanstalt (PTB) provides non-contact temperature measurements in the range from -170 $^{\circ}\text{C}$ to 962 $^{\circ}\text{C}$ at the highest metrological level. High-quality infrared radiation thermometers are used as transfer instruments as well as for comparison measurements. InGaAs-photodiode instruments are superior to instruments based on thermal detectors in terms of temporal stability and achievable uncertainties in the short wavelength range. However, wavelengths around 1.6 μm limit the minimal detectable temperature of InGaAs-radiation thermometers to typically 150 $^{\circ}\text{C}$ to 200 $^{\circ}\text{C}$. In the last decade, the performance of InGaAs-photodiodes increased by several orders in magnitude in terms of specific detectivity. By using a commercial two-stage cooled InGaAs-photodiode, the minimal detectable temperature of a 15 years old lens-free radiation thermometer (LF-IRRT2) was improved from 150 $^{\circ}\text{C}$ to 80 $^{\circ}\text{C}$.

Table 1. Specifications of the LF-IRRT3. See also Figure 1.

Component	Nominal specification
Aperture stop \varnothing	6.00 mm
Field stop \varnothing	3.706 mm
Distance aperture stop to field stop	243.8 mm
Detectivity (data sheet)	$6.7 \times 10^{13} \text{ cmHz}^{1/2}/\text{W}$
Bandpass of filter	1.55 μm - 1.65 μm
Maximum transmission of filter	81% at 1.6 μm

DESIGN OF THE RADIATION THERMOMETER LF-IRRT3

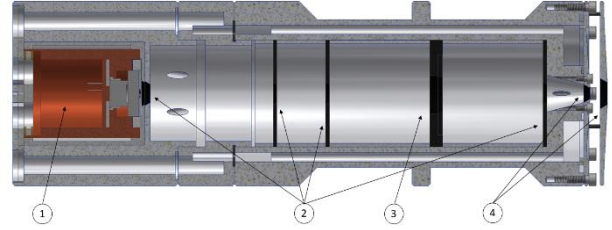


Figure 1 Cut presentation of the InGaAs-radiation thermometer LF-IRRT3. The main parts are listed in the text.

Figure 1 shows a cut presentation of the LF-IRRT3. The main parts are:

1. Water cooled detector housing including an interference filter and the field stop (see Table 1).
2. Set of stray light baffles in a water-cooled housing.
3. Motorized optical shutter.
4. Water-cooled front aperture (aperture stop) with additional heat-shield.

The photodiode is a two-stage cooled InGaAs-photodiode with an active area of 5 mm in diameter. The photodiode is operated at a temperature of approximately $-20 \text{ }^{\circ}\text{C} \pm 0.005 \text{ }^{\circ}\text{C}$ to reduce the wear and tear of the TE-cooler. The temperature is controlled by a custom-built temperature controller. The controller housing also includes a custom-built transimpedance amplifier, tailored for the photodiode. Gains can be set from 10^5 to 10^{10} . An additional voltage gain factor of 10 can be set at every gain to increase the signal level.

By means of a so-called reference function [2] the output signal is converted into a temperature reading.

The reference function is given by:

$$i = \frac{A_1 \cdot A_2}{D^2} \int_{\lambda_1}^{\lambda_2} L_{\lambda}(\lambda, t_{90}) \cdot s(\lambda) \cdot \tau(\lambda) \cdot d\lambda \quad (1)$$

with the photocurrent i , $A_{1,2}$ the active areas of the aperture stop and field stop, $\lambda_{1,2}$ the limiting wavelengths, $L_{\lambda}(\lambda, t_{90})$ the spectral radiance of the blackbody at the temperature t_{90} , $s(\lambda)$ the spectral responsivity of the photodiode, $\tau(\lambda)$ the transmission of the interference filter. Assuming a linear responsivity, the input values of Eq. (1) can be

determined by measuring the photocurrent i at several known temperatures $t_{s,90}$ and applying a least square fit. In order to obtain a radiation temperature $t_{s,90}$ from the photocurrent i , the temperature is inversely calculated by comparing the measured photocurrent with the photocurrent according to Eq. (1).

CALIBRATION OF THE LF-IRRT3

The LF-IRRT3 has been calibrated at the Thermal Imager Calibration Facility (ThermICF) [1] (see Figure 2) of PTB. The ThermICF completely covers the temperature range from -60 °C to 962 °C by means of heatpipe blackbodies. Additional surface radiators are available in the temperature range from -15 °C to 500 °C for the full field of view characterization of thermal imagers.

The photocurrent of the LF-IRRT3 was measured at

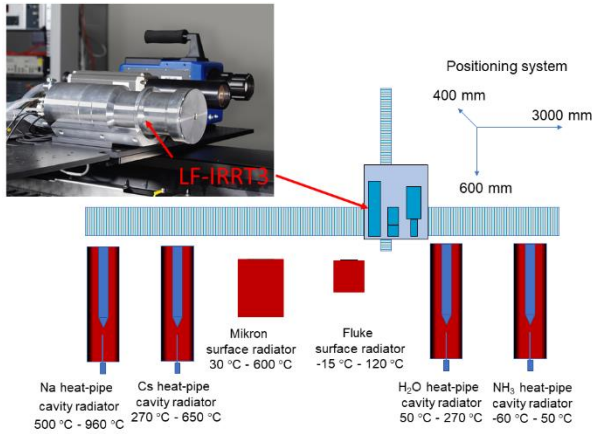


Figure 3 Schematic of the Thermal Imager Calibration Facility (ThermICF) of PTB. The facility uses four heatpipe blackbodies to provide radiation temperatures traceable to the ITS-90. The LF-IRRT3 is shown mounted on a long-range x-y-z-translation system in front of the heatpipe blackbodies and a surface radiator. The inserted photograph shows the LF-IRRT3 together with a pyrometer and a thermal imager.

several temperatures in the range from 80 °C to 960 °C and the input parameters for Eq. (1) were determined. The LF-IRRT3 together with the read-out electronics (DMM and transimpedance amplifier) was treated as a “blackbox”, i.e. only the spectral radiance $L_\lambda(\lambda, t_{90})$ and the output signal were used for the calibration. However, in the observed temperature range, the photocurrent increases from $\approx 10^{-14}$ A to $\approx 10^{-6}$ A. Hence, the full range of gains of the transimpedance amplifier has to be used. The gain ratios were determined at four different temperatures to allow an overlap of different gain settings. To

simplify the evaluation of the radiation temperature, an approximation of Eq. (1):

$$i = c \cdot \int_{\lambda_1}^{\lambda_2} L_\lambda(\lambda, t_{90}) d\lambda \quad (2)$$

with $c = A_1 A_2 \tau_{0S0} / D^2$ is used. The resulting input parameters are given in Table 2.

Table 2 Input parameters for Eq. (2) obtained by calibration of LF-IRRT3 against high-quality heatpipe blackbodies of PTB.

Parameter (see text)	Value
Instrument const. c	$4.040989 \cdot 10^{-9} \text{ Am}^2 \text{srW}^{-1}$
wavelength limit λ_1	$1.542945 \cdot 10^{-6} \text{ m}$
wavelength limit λ_2	$1.645718 \cdot 10^{-6} \text{ m}$

The resulting difference of the radiation temperature obtained according to Eq. (2) $t_{\text{Instrument}}$ and the radiation temperature $t_{s,90}$ is given in Figure 3.

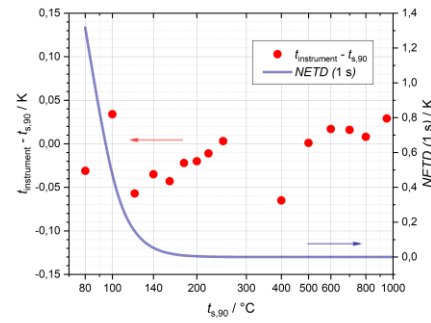


Figure 2 Difference of measured radiation temperature $t_{\text{Instrument}}$ and radiation temperature $t_{s,90}$ (red dots) and noise equivalent temperature difference / (NETD) (blue curve) for 1 s integration time plotted over the radiation temperature $t_{s,90}$.

CONCLUSION

The LF-IRRT3 was developed and calibrated against high-quality heatpipe blackbodies of PTB. The difference $t_{\text{Instrument}} - t_{s,90}$ is below 65 mK and within the expanded uncertainties of the blackbodies for all observed temperatures. However, the integration time increases for temperatures below 120 °C to approximately 5 minutes at 80 °C.

REFERENCES

1. I. Müller, et al., “Non-contact Temperature Measurement at the Physikalisch-Technische Bundesanstalt (PTB)” submitted to QIRT Journal
2. B. Gutschwager and J. Fischer, “An InGaAs radiation thermometer with an accurate reference function as transfer standard from 150 °C to 960 °C”, in “Proceedings TEMPMEKO ’99”, edited by J. F. Dubbeldam and M. J. de Groot, 567-572, IMEKO/NMI Delft, 1999.

Absolute Calibration of the Spectral Responsivity of Thermal Detectors at a High-Temperature Blackbody at the PTB

Tobias Pohl¹, Peter Meindl¹, Lutz Werner¹, Uwe Johannsen¹, Christian Monte¹, Richard Dieter Taubert¹, and Jörg Hollandt¹

¹Physikalisch-Technische Bundesanstalt (PTB), Berlin, Germany

Corresponding e-mail address: lutz.werner@ptb.de

The Physikalisch-Technische Bundesanstalt (PTB) is setting up an additional measurement approach for the absolute calibration of the spectral responsivity in the near- and mid-infrared by using a high-temperature blackbody operating at about 1200 K with a precision aperture. The blackbody radiation is described by Planck's law and is spectrally selected by accurately characterized optical bandpass filters. Thus, the detector under calibration is irradiated by a calculable spectral irradiance within the bandpass of the applied transmission filters. First results for the spectral responsivity of thermopile detectors agree within the uncertainty with previous calibrations at PTB's national primary detector standards.

INTRODUCTION

Currently, the calibration of detectors in view of their spectral responsivity in the spectral range of the near-infrared (NIR) and mid-infrared (MIR) is of increasing interest and market importance, e.g. for remote sensing [1] or radiation thermometry [2].

These applications need traceability to the International System of Units (SI). Therefore, the Physikalisch-Technische Bundesanstalt (PTB) operates cryogenic electrical substitution radiometers as primary detector standards to measure radiant power and to calibrate detectors in view of their spectral responsivity [3]. Furthermore, different types of transfer detectors which have been calibrated absolutely against the primary detector standards are used for the dissemination of the spectral responsivity.

In the NIR and MIR, these transfer detectors are partially thermal detectors, whose measurement principle is based on the heating effect of an absorber. Therefore, the detector responsivity is spectrally more or less constant as long as the absorptance of the incident radiant power is independent of the wavelength [4]. This enables a sufficiently accurate interpolation of the spectral responsivity between widely separated calibration wavelengths.

Currently, the PTB realizes an additional approach for detector calibrations in view of the spectral responsivity traceable to the SI by using a high-temperature blackbody operating at about 1200 K with a precision aperture as a standard of spectral irradiance.

DETECTOR CALIBRATION AT A HIGH-TEMPERATURE BLACKBODY

The calibration facility is a cavity radiator named Large-Area Blackbody (LABB) assembled of two concentrically stacked heat pipes and a temperature stabilized precision aperture with a radius of 10 mm. The LABB is temperature controlled with calibrated standard platinum resistance thermometers. With an emissivity of 0.9999 it is an almost ideal realization of a blackbody radiator [5] whose spectral radiance is described by Planck's law.

The blackbody radiation is spectrally selected by optical bandpass filters with characterized transmissions. By this means, the detector is irradiated by a calculable spectral irradiance within the bandpass of the applied transmission filters. The radiant power reaching the detector absorber can be calculated, considering the input aperture of the detector.

Fig. 1 shows the LABB measurement setup for the calibration of thermopile transfer detectors called TS-76 (Leibnitz-Institut für Photonische Technologien e.V.). This type of detector is a well characterized and calibrated MIR transfer standard at

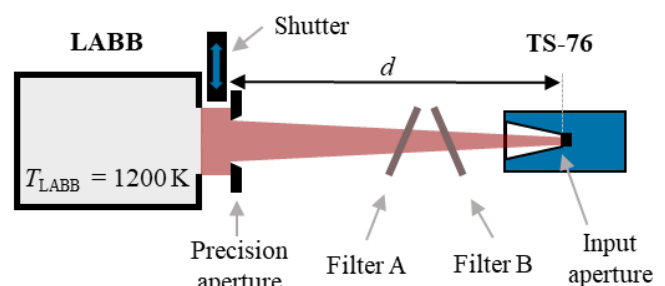


Figure 1. Calibration setup for the thermopile detector TS-76 at the high-temperature blackbody LABB with two transmission filters.

the PTB with an aperture radius of 2.9 mm. The distance d between the apertures of the LABB and the detector was varied between 350 mm and 650 mm.

FILTER TRANSMISSION MEASUREMENT

To calibrate detectors in terms of their spectral responsivity with blackbody radiation, well characterized optical transmission filters are needed: A bandpass filter (“Filter A”, see Fig. 1) is combined with an additional wider bandpass filter or an edge filter (“Filter B”). In fact, the combination of two filters reduces the maximum bandpass transmission slightly but realizes significantly better blocking of the out-of-bandpass radiation.

As a first step, three pairs of filters were chosen and characterized in view of their bandpass and blocking transmission at a Fourier Transform Spectrometer (FTS). Fig. 2 shows the calculated transmittance of a filter pair for calibrations at 1.55 μm . Similar pairs were characterized for calibrations at 2.7 μm and 3.9 μm .

Typically, power levels of about 30 μW at the detector were realized considering the filter transmission and measurement geometry. The two filters are slightly tilted to avoid interreflections between them.

FIRST MEASUREMENT RESULTS

First results for the spectral responsivity of the thermopile transfer detectors TS-76 at the LABB agree with their calibrations at the cryogenic electrical substitution radiometer within the uncertainty considering corrections due to absorption in air. Main uncertainty contributions are given by the filter transmission measurement resulting in a combined measurement uncertainty in the range of several percent. A detailed uncertainty budget will be given.

This measurement approach is SI traceable and independent from the calibration with the cryogenic electrical substitution radiometer.

Furthermore, the calibration at the LABB offers calibrations at wavelengths, where no laser radiation sources at the cryogenic electrical substitution radiometer exist. This is especially of interest for the spectral range above 10.6 μm .

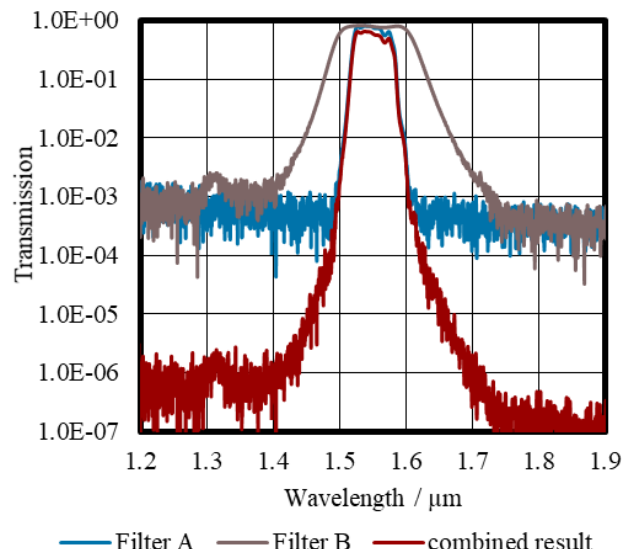


Figure 2. With FTS measured filter transmittances of two filters with bandpass at 1.55 μm (blue and brown) and the calculated resulting transmission of both filters combined (red) with better blocking.

OUTLOOK

Currently, more optical filters are characterized to conduct calibrations at the LABB at further wavelengths. Furthermore, this measurement approach will be used for calibrations of other detectors, such as pyroelectric detectors serving as MIR transfer detectors at the PTB.

REFERENCES

1. J. A. Sobrino et al., Review of Thermal Infrared Applications and Requirements for Future High-Resolution Sensors, *IEEE Transactions on Geoscience and Remote Sensing*, 54(5), 1-10, 2016.
2. N. Noulkow, R. D. Taubert, P. Meindl, and J. Hollandt, Infrared Filter Radiometers for Thermodynamic Temperature Determination below 660 °C, *International Journal of Thermophysics* 30, 131-143, 2009.
3. J. Hartmann, J. Hollandt, P. Meindl, D. Taubert and L. Werner, Traceable Radiometric Calibration of Semiconductor Detectors and their Application for Thermodynamic Temperature Measurement, *MAPAN – Journal of Metrology Society of India* 25(1), 3-10, 2010.
4. T. Pohl, P. Meindl, U. Johannsen, D. Taubert, and L. Werner, Measurement of the absolute spectral responsivity in the mid-infrared based on the cryogenic electrical substitution radiometer and an optimized thermopile detector, *Journal of Sensors and Sensor Systems* 8, 195-205, 2019.
5. D. R. Taubert, Radiometrische Messung thermodynamischer Temperaturen und Vergleich mit der Internationalen Temperaturskala (ITS-90) im Bereich von 419 °C bis 660 °C, Dissertation, Berlin, 2003.

A Blackbody for Calibration of Hemispherical Infrared Detectors

Moritz Feierabend¹, Max Reiniger¹, Jonas Bories¹, Julian Gröbner², and Christian Monte¹

¹ Physikalisch-Technische Bundesanstalt (PTB), Berlin, Germany, ² Physikalisch-Meteorologisches Observatorium Davos (PMOD) / World Radiation Center (WRC), Davos, Switzerland.

Corresponding e-mail address: moritz.feierabend@ptb.de

A new blackbody has been developed at the Physikalisch-Technische Bundesanstalt (PTB) to allow accurate calibration of infrared detectors with a hemispherical acceptance angle. The aim is to significantly reduce the uncertainty of long-wave downward irradiance measurements that are fundamental for investigation of the energy budget of the Earth – a key topic in climate research. The new Hemispherical Blackbody was designed to specifically meet the requirements for tracing such measurements to the SI.

PROJECT OBJECTIVE

Ground-based, low-uncertainty measurements of the hemispherical long-wave downward atmospheric radiation, which is strongly connected to the greenhouse effect of the earth, are performed globally with pyrgeometers and are for example organised within the Baseline Surface Radiation Network (BSRN). To achieve low measurement uncertainties highly accurate detector calibration is necessary. Such calibration measurements are performed as comparisons to the World Infrared Standard Group (WISG), operated at the World Radiation Center (WRC) in Davos. For an improved traceability of the WISG to the SI, a new blackbody as a dedicated calibration source for pyrgeometers is proposed in the framework of the EU co-funded research project MetEOC3 – “Further metrology for Earth Observation and Climate” [1]. One of the aims in this project is to reduce the uncertainty of hemispherical long-wave downward irradiance measurements from currently 5 W/m² to less than 2 W/m². As a substantial uncertainty component contributing to the overall uncertainty of this irradiance measurement, the new blackbody calibration source needs to feature an irradiance uncertainty of less than 0.5 W/m². In combination with the “Infrared Integrating Sphere” (IRIS) instruments [2] calibrated against the blackbody, irradiance responsivity traceable to the SI can be transferred to the WISG with the required uncertainty.

DESIGN OF THE BLACKBODY

Based on numerical simulations with the Monte-Carlo ray tracing software “STEEP3” [3], the design for the new blackbody was optimised. Particular attention was given to the specific requirements for calibrating detectors with a hemispherical acceptance angle. Several design aspects such as geometry and coating were considered in the simulations in order to identify an ideal design with high effective emissivity and low angular variation. A selection of the most promising candidates is pictured in Figure 1. A low dependence of the effective emissivity on the opening angle is advantageous for transferring measured radiation temperatures at normal incidence to the hemispherical opening angle and therefore to the irradiance of the blackbody onto the aperture area.

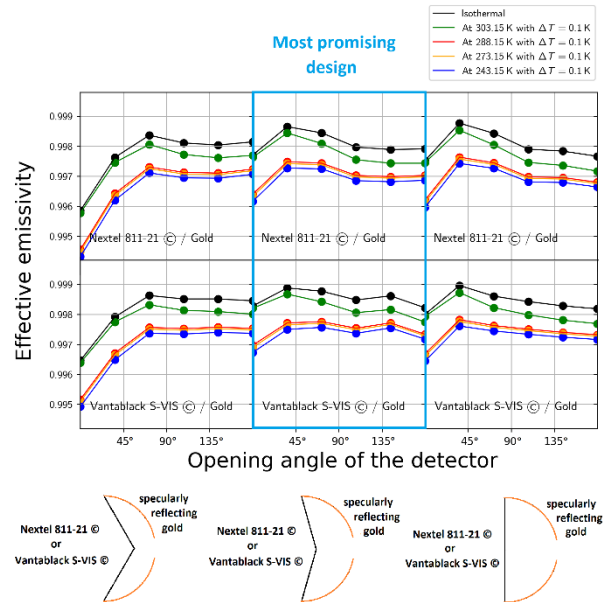


Figure 1. Monte-Carlo ray tracing simulations were carried out to obtain the effective emissivity for several design candidates of the new blackbody. Attention was given to the geometry and coating to identify a design with high effective emissivity in combination with low angular variation.

In addition, a highly reflecting golden hemisphere surrounding the highly emitting black cone is considered beneficial regarding the temperature non-uniformity of the blackbody cavity [4].

The Hemispherical Blackbody, presented in Figure 2, was designed, developed and brought into operation at the Physikalisch-Technische Bundesanstalt (PTB). To characterise the blackbody, simulations and comparison measurements were carried out. The latter took place against one of several heatpipe blackbodies that serve as national standards for the radiation temperature scale at the PTB [5].

REFERENCES

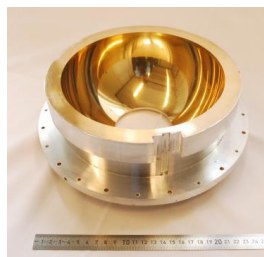
1. *Metrology for Earth Observation and Climate*. www.meteoc.org. Visited 18th December 2019. National Physical Laboratory.
2. J. Gröbner, A Transfer Standard Radiometer for Atmospheric Longwave Irradiance Measurements, *Metrologia*, 49.2, S105-S111, 2012.
3. A. Prokhorov, Monte Carlo Method in Optical Radiometry, *Metrologia* 35.4, 465-471, 1998.
4. T. Quinn et al., A Black-Body Cavity for Total Radiation Thermometry, *Metrologia* 23.2, 111-114, 1986.
5. J. Hollandt et al., High-Accuracy Radiation Thermometry at the National Metrology Institute of Germany, the PTB, *High Temperatures – High Pressures*, 35/36.4, 379-415, 2003-2004.



(a)



(b)



(c)

Figure 2. The Hemispherical Blackbody dedicated for the calibration of hemispherical infrared detectors. The design (a) includes a highly emitting black cone (b) and a highly specularly reflecting golden hemisphere (c).

SCOPE OF THE PRESENTATION

The development, the thorough characterisation process and first applications of the Hemispherical Blackbody will be presented as well as the main technical features and objectives.

Low Light Level Realization at Near Correlated Color Temperature

Wu Zhifeng, Dai Caihong, Li Ling, Wang Yanfei, Xie Yihang, and Cheng Qiutong

National Institute of Metrology, Beijing, China

Corresponding e-mail address: wuzf@nim.ac.cn

Integrating sphere lamp is usually used as the normal spectral radiance calibration source. The spectral radiance can be adjusted by using a variable aperture between the integrating sphere and the lamp. However, the relative spectral in the red region increases rapidly when the luminance is decreased from 30000 cd/m² to 0.01 cd/m². The variation of correlated color temperature is as high as 255 K. By using another integrating sphere, low light level radiation source at nearly constant spectral distribution is obtained. The variation of correlated color temperature is 60 K with the luminance decreased to 0.0033 cd/m².

INTRODUCTION

Integrating sphere and tungsten lamp are the most popular spectral radiance light sources, covering from 250 nm to 2500 nm. However, the spectral radiance is hard to cover a large range using the tungsten lamp and diffuse plate. If the distance between the tungsten lamp and diffuse plate is varied from 50 cm to 500 cm, the spectral radiance changes 100 times. If the current of the tungsten lamp is changed, the correlated color temperature (CCT) will be different. With the new needs in remote sensing such as weather forecast, the early-morning orbit satellite is required to fill the gaps on the global scale every 6 hours. The spectral radiance changes more than six orders of magnitude from day to night. The spectral radiance can be as low as 10⁻⁵ W/(m²·sr·nm). In order to calibrate spectral radiance responsivity at low light level, integrating sphere lamp must be used to establish a low light level facility.

EXPERIMENT AND RESULT

Variable aperture is usually mounted between the lamp and integrating sphere to change the luminance at the exit port. In our experiment, OL 455 integrating sphere lamp is used. By continuous adjusting the aperture, the sphere luminance can be decreased at least 10⁶ times. Figure 1 shows the relative spectral distribution at different luminance.

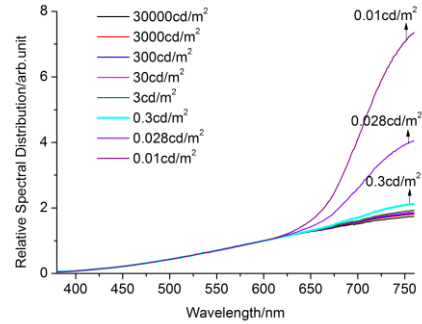


Figure 1. The spectral distribution of OL455

The spectra are all normalized by the spectral radiance at 600 nm. When the luminance is decreased from 30000 cd/m² to 3 cd/m², the difference is less than 10% at 760 nm. The corresponding CCT decreased from 2808 K to 2770 K. However, the difference increases to 20% when the luminance is decreased to 0.3 cd/m². Further, the spectral difference exceeds 300% when the luminance is decreased to 0.01 cd/m². And the corresponding spectral irradiance at 380 nm is still higher than 10⁻⁴ W/(m²·sr·nm). The corresponding CCT is only 2553 K, 255K lower than that of 30000 cd/m².

For the obvious increase in the infrared region, it may be due to the fact that the variation of the aperture influences the structure of the integrating sphere. The integrating sphere is made of PTFE or BaSO₄, while the aperture is not. The reflectivity of the aperture in the red region may be higher. Also, radiation from different part of the lamp enters the

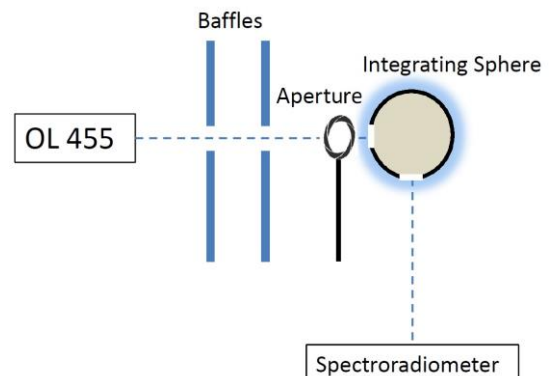


Figure 2. Low light integrating sphere facility

integrating sphere when the aperture is changed.

Figure 2 shows the facility consists of OL 455, baffles and an integrating sphere with an inner diameter of 50 mm. The integrating sphere has two ports which situate at perpendicular directions. The entrance port has a diameter of 25.4 mm, and the exit port has a diameter of 12.7 mm. The baffles are used to screen the stray light. The integrating sphere is mounted on the other side of the baffles. An variable aperture is placed in front of the integrating sphere limiting the spectral flux entering the integrating sphere. The distance between the aperture and the entrance of the integrating sphere is about 6 cm.

First, the luminance of OL 455 is fixed at 30000 cd/m^2 . The aperture is at its maximum with a diameter of 10 mm. The luminance at the exit port of the integrating sphere is 12.2 cd/m^2 and CCT is about 2760 K. By decreasing the diameter of the aperture, spectral radiance at three different levels is recorded, as shown in figure 3. The relative spectral distribution differs by more than 70% at 760 nm when the luminance is decreased to 0.07 cd/m^2 .

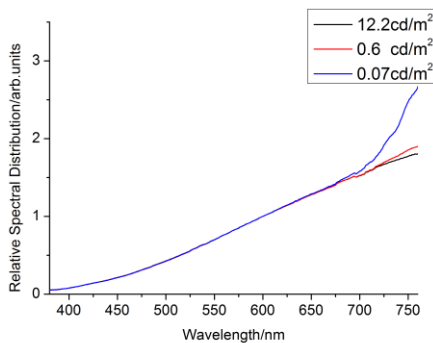


Figure 3. The variation of the relative spectra

Meanwhile the difference is less than 1.5% between 400 nm and 600nm. According to the ratio 12.2 to 0.6, the diameter of the aperture is about 2.2 mm for 0.6 cd/m^2 . The difference is less than 6% at 760 nm for 0.6 cd/m^2 . It seems that there is a turning point in the role of the diameter. The red region will increase rapidly below the turning point. The aperture has a decisive influence for 0.07 cd/m^2 .

Second, the variable aperture in figure 2 is removed. By adjusting the luminance of OL 455, the spectral radiance is recorded at four different levels. When the luminance of OL 455 is about 3 cd/m^2 , the luminance at the exit port of the integrating sphere is 0.0033 cd/m^2 and the corresponding CCT is about

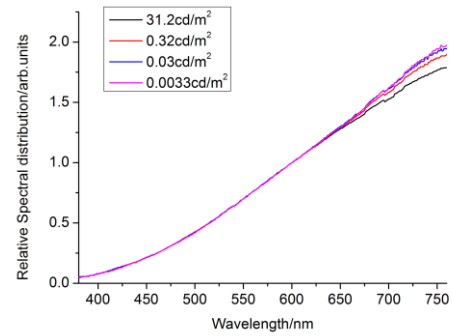


Figure 4. The variation of the relative spectra

2748 K. Comparing to the result in figure 1, CCT is nearly 200 K higher than that of the luminance 0.01 cd/m^2 in figure 1. Therefore, the variation of CCT is reduced significantly using the facility in figure 2.

The spectral radiance from 380 nm to 430 nm is in the range $(3-9) \times 10^{-5} \text{ W}/(\text{m}^2 \cdot \text{sr} \cdot \text{nm})$ when the luminance is 0.0033 cd/m^2 . If the spectral radiance less than $10^{-4} \text{ W}/(\text{m}^2 \cdot \text{sr} \cdot \text{nm})$ is needed at 760 nm, the luminance should be smaller than 0.00028 cd/m^2 . By increasing the diameter of the integrating sphere and distance between the integrating sphere and OL 455, the spectral radiance can be realized with CCT near 2748 K.

CONCLUSION

If the relative spectrum is nearly constant throughout a high dynamic range, low light level spectral radiance can be obtained with the help of a photodetector. By measuring the ratio from normal spectral radiance to low light level using a silicon detector, the spectral radiance at low light level can be calculated.

ACKNOWLEDGEMENT

This work was supported by the National Key R&d Program of China, 2018YFB0504800 (2018YFB-0504804) and National Institute of Metrology Fundamental Research Funds under grant No.23-AKY1513.

REFERENCES

1. C-Y Cao, Preliminary study for improving the VIIRS DNB low light calibration accuracy with ground based active light source, in Proceedings of SPIE, 9607, 96070D, 2015.
2. Joe Laveigne, Calibration of a high dynamic range, low light level visible source, Proc. of SPIE, 8014, 801415-10, 2011.

New spectral irradiance traceability scale at LNE-CNAM

Mai Huong VALIN¹, Bernard ROUGIE¹, Alain VISSIERE¹, Gaël OBEIN¹, Thierry VALIN²

¹LNE-CNAM, Conservatoire national des arts et métiers, ²LNE-CNAM, Laboratoire national de métrologie et d'essais

Paris, France

Corresponding e-mail address: mai-huong-christine.valin@lecnam.net

The LNE-CNAM developed a new spectral irradiance measurement facility covering the spectral range from 250 nm to 2500 nm. This bench allows calibration of irradiance spectral density of a source using a high temperature black body (HTBB) and a filter radiometer. The filter radiometer used is traceable to the cryogenic radiometer which is our radiometric reference. It extends our measurement capacity up to 250 nm and reduces by at least a factor two our measurement uncertainties over the entire range. This paper shows our new traceability scheme for spectral irradiance, the method used, and its validation.

NEW TRACEABILITY SCHEME

Up to now, the irradiance spectral density measurement is based on the thermodynamic temperature reference at LNE-CNAM [1] and our Calibration and Measurement Capabilities (CMC) is between 300 nm and 2500 nm.

We have recently simplified our traceability scheme in order to reduce our measurement uncertainties and to extend our measurement capacity up to 250 nm. For this, we have set up a new measurement facility. It allows calibration of absolute spectral irradiance of a lamp based on the comparison with a black body (HTBB) whose temperature is assessed by measuring the irradiance with a calibrated filter radiometer and calculating the spectral radiance at one wavelength. The calibration method is similar to those previously developed in other National Measurement Institutes [2]. The HTBB temperature measurement follows the method detailed in [6].

Spectral responsivity of the radiometer is obtained in three steps: the calibration of spectral responsivity of the Silicon trap detector with our cryogenic radiometer [3], the calibration of the spectral regular transmittance of its bandpass filter with our primary spectrophotometer [4] and the calibration of its aperture with our devoted setup [5].

The traceability of spectral irradiance with national realisation of watt and meter is shown on Figure 1.

To minimize uncertainties, corrections on temperature homogeneity and emissivity of HTBB are applied [6].

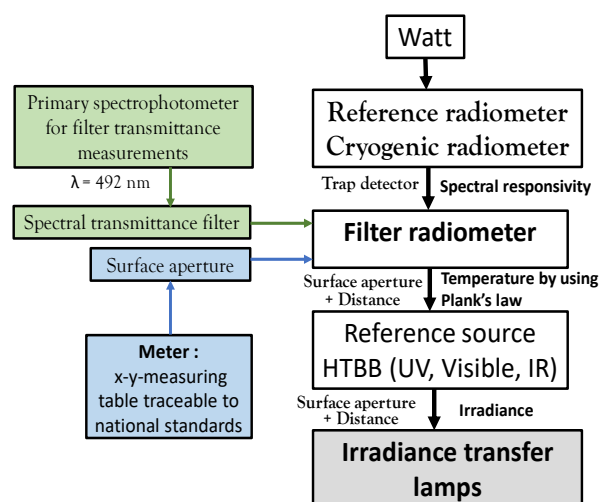


Figure 1. Traceability chain for the spectral irradiance calibration at LNE-CNAM.

DESCRIPTION OF THE BENCH

The spectroradiometer of the LNE-CNAM is described in Figure 2.

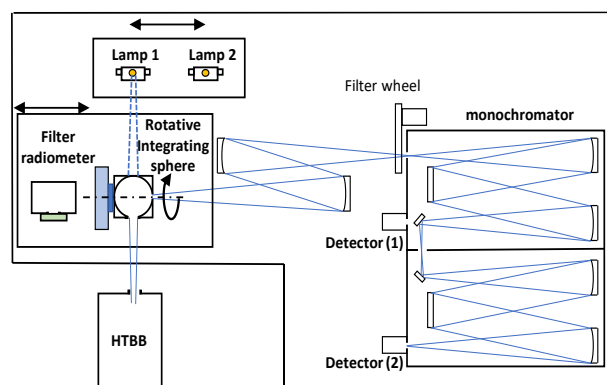


Figure 2. Diagram of LNE-CNAM calibration facility.

The HTBB is used as an irradiance reference for the calibration of transfer sources. A cavity heated up to 3100 K provides radiation which can be used in the 250 nm to 2500 nm range. A spectroradiometric system compares the spectral irradiance of HTBB and

transfer lamps (Lamp1 and Lamp2). It is composed of:

- an integrating sphere that receives the flux from the sources with an entrance port equipped with a circular diaphragm. The sphere has an output port located at 90° with a rectangular slit shape of 2 mm x 15 mm.
- two Ø 150 mm spherical mirrors that focus the image of the sphere exit slit on to the entrance slit of a dual monochromator.
- a filter radiometer with a transmittance centred on 492 nm.
- a Jobin Yvon HRD640 double monochromator on which the manual wavelength selection mechanism has been replaced by a high precision motorized translation stage and equipped with three pairs of gratings to cover the wavelength range.

The filter radiometer and the integrating sphere are placed on the same translation stage. That allows to perform in one cycle the blackbody temperature measurement with the calibrated filter radiometer and the irradiance spectral comparison of the HTBB and the lamps. The integrating sphere is rotated by 180° around the axis centred on the exit slit. This allows to collect either the HTBB or the transfer lamps flux.

The entire facility is placed in a box with two compartments, one for the source part and one for the monochromator, in order to avoid stray light.

The bench is fully automated and controlled by a custom LabVIEW software.

VALIDATION

For the validation of this new measurement setup, our set of four reference transfer lamps have been measured and compared with their historical values on the range 300 nm to 2500 nm. The historical and new measurement uncertainties ($k=2$) of a lamp are showed in the Table 1.

Table 1. Historical and new measurement uncertainties of a lamp.

Wavelength (nm)	Relative expanded uncertainty ($k = 2$) / (%)	
	2016	2019
250		7.2
260 - 290		3.0 - 1.4
300 - 310	3.9	1.2
320 - 390	2.6	< 1.2
400 - 1400	2.2	0.5 - 1.6
1500 - 2300	2.6	0.4 - 1.2
2400 - 2500	5.0	2.3 - 7.6

At the spectrum extremities at 250 nm and 2500 nm, the large uncertainties are due to the lack of flux.

The comparison results are showed in Table 2.

Table 2. Results of our lamps with the new bench.

Wavelength (nm)	Mean deviation 2019/2016 (%)	Comparison uncertainties 2019/2016 ($k=2$) / (%)
300	4.5	4.1
320-380	< 1.3	2.8
400-1050	< 0.6	2.3 - 2.6
1100 - 2200	0.1 - 2.6	2.3 - 2.8
2300 -2500	4.6 - 8.5	3.0 - 9.0

Most of the mean deviations 2019/2016 observed are smaller than the expanded uncertainty of the comparison. At 300 nm, the significant deviation observed seems to correct the deviation that we had during the last CCPR K1-a in 2005. It could be explained by lack of flux and the stray light of former simple monochromator.

CONCLUSION

From now on, LNE-CNAM spectral irradiance reference is based on the radiometric reference.

Thanks to the new setup, it is possible to measure the absolute irradiance of transfer lamps with a direct traceability to our cryogenic radiometer. This bench extends our measurement capacity up to 250 nm and reduces at least by a factor two our measurement uncertainties (excepted at 2500 nm).

In the future, optimisation of measurement facility will allow:

- a further reduction of uncertainties between 2400 nm and 2500 nm.
- an extension of our measurements up to 200 nm.
- an extension of our measurements up to 3000 nm.
- a radiance calibration in this spectral range.

REFERENCES

1. Rougie B, Bastie J, Realization of irradiance reference at the Institut National de Métrologie, Rev. Française métrologie n° 5, Volume 2006-1, 31-40, 2006.
2. P. Sperfeld, S. Pape and S. Nevas, The Spectral Irradiance Traceability Chain at PTB, Radiation Processes in the Atmosphere and Ocean (IRS2012), AIP Conf. Proc. 1531, 801-804, 2013.
3. Coutin J and Rougie B, Characterization and validation of a new cryogenic radiometer at the LNE-LCM Rev. Française métrologie 2016-1 11-20, 2016.
4. Obein G and Bastie J, Report on the key comparison EUROMET-PR-K6: Spectral regular transmittance Metrologia 48, 2011.
5. A. Razet, J. Bastie, "Uncertainty evaluation in non-contact aperture area measurements", Metrologia, 43, 2006, 361-366.
6. Rougie B, Valin M H, Thermodynamic measurement and validation of a high temperature blackbody for spectral radiance and irradiance reference, NEWRAD 2017 Proceedings, Tokyo, Japan, 2017.

Development, implementation and validation of a high-power LED-based radiation source for goniometric spectral radiance factor measurements

Irina Santourian¹, Sven Teichert¹, Kai-Olaf Hauer¹, Tatjana Quast¹, and Alfred Schirmacher¹

¹*Physikalisch-Technische Bundesanstalt (PTB), Braunschweig und Berlin, Germany*

Corresponding e-mail address: Irina.Santourian@ptb.de

To improve the accuracy in spectral radiance factor measurements with the robot-based gonireflectometer at PTB the suitability of LEDs as additional radiation sources in the short-wavelength visible spectral range was investigated. An LED sphere radiation source (LED-SR) was constructed. Its performance with respect to the spectral range and coverage, the temporal stability, and the homogeneity of the radiation field is presented. Comparative measurements of the spectral radiance factor between the currently used radiation source and the LED-SR were performed and the results indicate that the LED-SR is an appropriate radiation source for goniometric spectral radiance factor measurements at the border between the visible and the UVA spectral range.

INTRODUCTION

LEDs have the potential to be used in a variety of applications due to their long lifetime, efficiency and the available high radiation power. Also, recent advances in LED technology are leading to an increase in accessible spectral ranges and open even more application areas.

For the currently used sphere radiation source, equipped with an internal 400 W quartz-tungsten halogen lamp, the achievable measurement uncertainty of the setup at wavelengths around 400 nm is dominated by statistic effects according to the decreasing available output power. By using LEDs a considerably higher sample irradiance in the short wavelength range is achievable which was the main reason to investigate the use of LEDs as an additional radiation source for the gonireflectometer.

GONIOREFLECTOMETER AT PTB

The gonireflectometer at PTB is the national standard for the determination of the absolute spectral radiance factor $\beta(\lambda)$ of diffusely reflecting materials in a variety of bidirectional measurement geometries [1]. It consists of a large rotation stage

carrying the mentioned sphere radiation source. This source can thus be rotated around the sample, which is placed on a five-axes robot in the centre of the apparatus. This setup enables, in combination with a fixed detection path, highly precise measurements of the spectral radiance factor with almost arbitrary bidirectional geometries. It is well described in several publications [1-3].

LED SPHERE RADIATION SOURCE

The currently used sphere radiator creates a highly homogeneous and Lambertian beam profile on the sample which is required by the measuring principle. Based on this principle an LED sphere radiation source was constructed to improve the available radiant power in the short wavelength spectral range (preliminary studies described in [4]). As sphere wall coating sintered PTFE was used for the LED-SR instead of a standard barium sulphate coating because of its higher diffuse reflection in this spectral range. As primary source a board with 21 surface-mounted device LEDs covering the spectral range from 365 nm to 410 nm was designed by using LEDs with three different peak wavelengths. To obtain a temperature independent temporal stability an active temperature regulation with thermoelectric cooling was added. This new LED-SR maintains the advantages of the existing system and provides a higher radiation power level in the design spectral range.

RESULTS

Prior to implementation in the gonireflectometer setup the LED-SR was characterized for the spectral coverage, the temporal stability, and the homogeneity of the emitted radiation field. As expected by design, the LED-SR has a fairly smooth spectrum consisting of a composition of the three peaks of the LEDs used (peaks at 365 nm, 385 nm, 405 nm) for the designed LED board. Below 430 nm the LED-SR delivers a significantly higher signal compared to the currently used source. Moreover, the LED-SR also meets all other requirements, e.g.

the homogeneity of the radiation beam is about $\pm 1\%$ and thus comparable to the halogen-lamp based radiator [2]. Based on the high-precision actively regulated temperature control a photocurrent change of only 1 % in 286 h operation time of the LED-SR is achieved and allows measurements with high precision.

For validation the LED-SR was implemented in the gonireflectometer to perform comparative measurements with the currently used radiator. A silicon diode (Hamamatsu S1337-66 BR) was used for detection in the entire spectral range. The absolute spectral radiance factor $\beta(\lambda)$ of a white and red ceramic, representing a high and a low reflectance, were measured for geometry $45^\circ:0^\circ$ with both sources. For each sample the resulting relative uncertainty ($k=1$) of the mean spectral radiance factor for seven (white) respectively ten repetitions (red ceramic) measured with both radiators are given in Fig. 1.

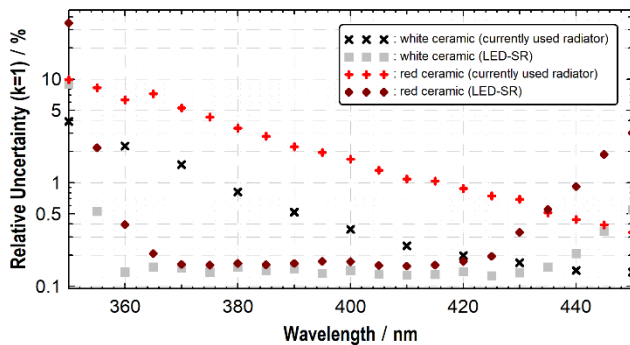


Figure 1. Relative uncertainty ($k=1$) of the average absolute spectral radiance factor for a white and red matte ceramic sample measured with the currently used sphere radiator and the LED-SR in $45^\circ:0^\circ$ geometry.

The measurement uncertainty was determined by considering various systematic and statistical effects. In case of the white ceramic measured with the standard source statistical uncertainties begin to dominate the total uncertainty below 430 nm and result in a rise towards shorter wavelengths. In ordinary calibrations this would have to be compensated by a higher number of repetitions or by switching to a more sensitive detector type. The uncertainty resulting from the LED-SR however stays constant and only rises below 360 nm when the available power decreases. Therefore, one can conclude that the statistical contributions are very small for this source in its design wavelength range. This is underlined by the results for the low-reflective red sample, which are only slightly higher

than for the white standard. The break-even point is at 435 nm for the measurements on the red sample.

It is therefore shown that the application of the LED-SR results in a considerable improvement with respect to the achievable measurement uncertainty.

CONCLUSION

A newly developed LED sphere radiation source equipped with a high-power LED board and an active temperature regulation was developed. The basic properties such as spectral range, temporal stability and homogeneity of the radiation field were characterized and fulfill the necessary requirements for applying this radiation source at the gonireflectometer to determine the spectral radiance factor. Validation measurements show that achievable measurement uncertainties in the spectral range between 360 nm and 430 nm can be reduced significantly. The results demonstrate that the LED-SR is an appropriate radiation source for measurements at the border between visible and UVA wavelengths and that the main objectives such as the reduction of the measuring time and reducing measurement uncertainties were achieved.

ACKNOWLEDGMENTS

The authors thank the members of the mechanical workshop Jörn Hauffe, Morten John, Marcel Janik and Henry Ganz for the construction of several parts of the LED sphere radiation source. Also, we thank Rouven Krake and Stefan Pendsa for the electrical layout of the LED board and the TEC unit. We gratefully acknowledge the support of the Braunschweig International Graduate School of Metrology B-IGSM.

REFERENCES

1. D. Hünerhoff, U. Grusemann, and A. Höpe, New robot-based gonireflectometer for measuring spectral diffuse reflection, *Metrologia*, BIPM and IOP Publishing Ltd, Vol. 43, No. 2, pp. 1-10, March 2006.
2. K. Hauer and A. Höpe, High-grade uniform light source for radiometric and photometric applications, *MAPAN*, Springer Science+Business Media S.A., Vol. 24, No. 3, pp. 175-182, September 2009.
3. C. Strothkämper et al., Multilateral spectral radiance factor scale comparison, *Applied Optics*, OSA Publishing, Vol. 56, No.7, pp. 1996-2006, March 2017.
4. I. Santourian, S. Teichert, K.-O. Hauer, A. Schirmacher, Investigation of the suitability of high-power LEDs for the use as radiation source for PTB's gonireflectometer, *TU Ilmenau, Lux junior 2019*, pp. 43-50, 2019.

New Facility for Deuterium Lamp Calibrations at SURF III

Robert E. Vest¹, Mitchell L. Furst¹, Edward W. Hagley¹, and Thomas B. Lucatorto¹

¹Sensor Science Division, NIST, Gaithersburg, MD, USA

Corresponding e-mail address: rvest@nist.gov

A new facility for the irradiance calibration of deuterium lamps has been constructed and commissioned at the Synchrotron Ultraviolet Radiation Facility (SURF III) at NIST's Gaithersburg, MD campus. This facility enables the calibration of the irradiance from a lamp under test against the primary standard of irradiance from the NIST synchrotron in the spectral range from 200 nm to 400 nm and longer wavelengths. The uncertainty achieved is on the order of 1% throughout this spectral range.

CALIBRATION FACILITY

The primary standard of irradiance is the synchrotron radiation from the SURF III electron storage ring. The irradiance as a function of wavelength is calculated from a few accelerator parameters: the magnetic field strength, the bending radius of the electron orbit, and the stored electron beam current. BL-2 has been rebuilt with improved baffling and stray light control for the new calibration facility.

The beamline is fitted with two fused silica windows that transmit the synchrotron radiation while maintaining the vacuum integrity of the storage ring and beamline. The transmission of these windows is measured and accounted for as part of the calibration process.

The spectrally resolving detector system is a diffuser, monochromator, photodiode, and amplifier system. The diffuser is a fused silica optical flat that incorporates a high density of scattering centers. The

transmitted light is well diffused and is completely unpolarized, even for the linearly polarized incident radiation from the synchrotron. The monochromator is a commercial Czerny-Turner monochromator which has been modified by removing internal heat sources and mounting on a thermally conducting base plate. These modifications significantly improved the thermal stability of the system. The detector is a commercial Si photodiode, and the photocurrent is converted to voltage by a specially constructed low-noise transimpedance amplifier in the same housing as the photodiode. The amplifier has a fixed gain of 3×10^{10} V / A. The output is measured by a digital voltmeter.

The detector system is mounted on a yaw rotation stage. After measurement of the synchrotron radiation, the stage is rotated so the irradiance from the deuterium lamp is incident on the diffuser at the entrance aperture.

The irradiance from the lamp is determined by comparison of the detector signal when looking at the lamp under test to that when looking at the known SURF irradiance. An overview of the system is shown in Fig. 1 and a detail of the detector system in Fig. 2.

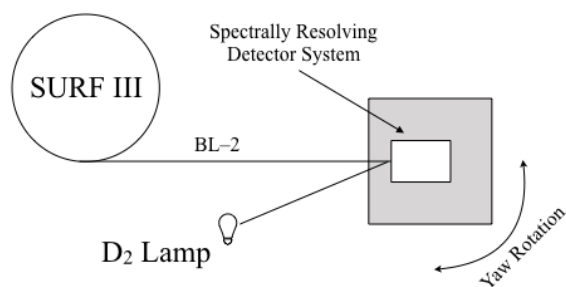


Figure 1. Overview of the calibration system for comparing the irradiance from a deuterium lamp to

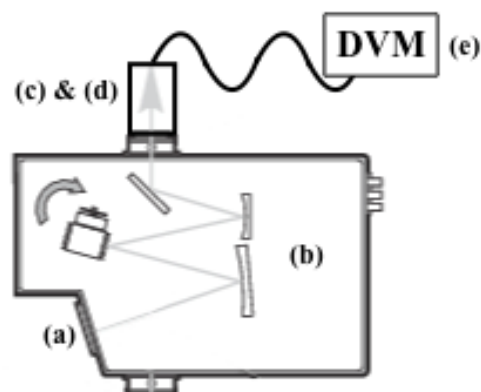


Figure 2. Layout of the spectrally resolving detector system showing the (a) diffuser, (b) monochromator, (c) detector, (d) amplifier, and (e) digital voltmeter.

CALIBRATION PROCEDURE

The calibration procedure begins with a determination of the detector system's responsivity by measuring the voltage signal produced by the known incident irradiance from the synchrotron. In the absence of the intervening fused silica windows, this would be a simple measurement. However, this determination must be made from a set of three measurements to properly account for the window transmission. The first window is mounted in the gate of a high-vacuum gate valve and is inserted by closing the valve. The second window is mounted on a vacuum-seal flange at the end of the beamline and is inserted by installing the flange. Removal of the second window vents the beamline from the end up to the first window.

The responsivity η_0 of the monochromator is given by:

$$\eta_0 = \frac{\eta_1 \eta_2}{\eta_{1,2}^{air}}, \quad (1)$$

where η_1 is the responsivity measured with only the first window inserted in the beam, η_2 is the responsivity measured with only the second window inserted in the beam, and $\eta_{1,2}^{air}$ is the responsivity measured with both windows inserted in the beam. The beamline section between the windows is vented for the measurement with both windows.

In practice, a fourth measurement is made of $\eta_{1,2}^{vac}$ with both windows inserted but the intervening section under vacuum. This allows a determination of the transmission of the first window T_1 without any effect from air absorption at short wavelengths.

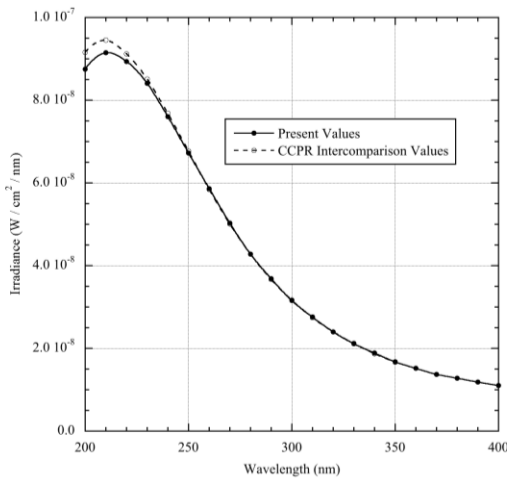


Figure 3. The calibrated irradiance from a deuterium lamp measured on the new facility (solid circles) and prior values from a CCPR intercomparison (open circles).

Once the detector system's responsivity η_0 is known, the irradiance from the lamp E_{lamp} is determined from η_0 and the lamp signal V_{lamp} :

$$E_{lamp} = \frac{V_{lamp}}{\eta_0}. \quad (2)$$

Figure 3 shows the results of the calibration of a deuterium lamp and historic data from a prior CCPR intercomparison.

UNCERTAINTY BUDGET

The full assessment of the uncertainty in the final lamp irradiance calibration is ongoing. Table 1 shows the preliminary uncertainty budget.

The uncertainty is dominated by the statistical (Type A) uncertainty in the repeatability of the detector system calibration. The total uncertainty ($k = 1$) in the irradiance from the deuterium lamp is about 0.7%.

Table 1. Preliminary uncertainty u_c in the irradiance calibration of a deuterium lamp.

Uncertainty Component	u_c in Irradiance
Detector System Calibration	
Statistics	0.60%
Electron energy	0.10%
Electron current	0.20%
Distance to tangent point	0.01%
<i>Uncertainty in Detector</i>	<i>0.64%</i>
Lamp Calibration	
Statistics	0.10%
Distance to lamp	0.01%
Monochromator stability	0.20%
<i>Uncertainty in Lamp</i>	<i>0.22%</i>
Comparison (common mode)	
Scattered light	0.20%
Entrance aperture area	0.01%
<i>Uncertainty in Comparison</i>	<i>0.20%</i>
Total Uncertainty	0.71%

Spectral Mismatch Correction for the Calibration of UVA Radiometers

Peter Sperfeld¹, Saulius Nevas¹

¹Physikalisch-Technische Bundesanstalt (PTB), Braunschweig & Berlin, Germany

Corresponding e-mail address: Peter.Sperfeld@ptb.de

Using examples of the calibration of UVA radiometers, the influence of spectral mismatch will be discussed. As the spectral responsivity of so-called UVA radiometers is never spectrally flat, it will be shown that this can lead to significant differences between measurement results even of narrow-band UVA sources typically used for calibrations. This should be taken into account both for routine calibrations of UVA radiometers and for carrying out intercomparisons.

INTRODUCTION

The ideal UVA radiometer does not exist because no device can simulate the "UVA" interval. In practice, the term "UVA radiometer" usually refers to measuring devices that provide values for irradiance in a defined spectral (sub-)range between 315 nm and 400 nm.

A frequent application is the non-destructive testing of materials using UVA radiation according to DIN EN ISO 3059 [1]. Here, a defined irradiance in the UVA spectral range is required (1 W/m² - 50 W/m²). The irradiation source should have a spectral distribution with maximum value at 365 nm ± 5 nm and a full-width at half-maximum (FWHM) of 30 nm. For this application, the UVA radiometers should be calibrated using a narrowband radiation at 365 nm.

The required calibration is, thus, a comparatively simple measurement task in which the radiometer to be calibrated is compared under narrowband radiation at 365 nm against a calibrated reference detector. A respective correction factor is calculated for the display readout of the UVA radiometer and a simple measurement uncertainty estimate is obtained:

$$k_{dut,UVA} = \frac{E_{UVA}}{Y_{dut}} = \frac{1}{s_{0,r}} \cdot \frac{Y_r(365 \text{ nm})}{Y_{dut}},$$

$$u^2(k_{dut,UVA}) = u^2(s_r) + u^2(Y_r) + u^2(Y_{dut}). \quad (1)$$

Here $s_{0,r}$ is the spectral irradiance responsivity of the calibrated reference detector at 365 nm, $Y_r(365 \text{ nm})$ is its photosignal and Y_{dut} is the readout value of the UVA radiometer. A standard measurement uncertainty typically in the range of 1 % can be estimated for the correction factor.

However, this simple estimation of the calibration uncertainty does not consider substantial contributions. This becomes apparent in particular if the application on site runs under different conditions or calibration results of different origins are compared, which has also been observed during different intercomparisons. Obviously, some other elements can contribute significantly to the measurement uncertainty making it considerably higher.

The EURAMET comparison EURAMET.PR-S4 [2] included a comparison of the calibrations of two UVA radiometers at 365 nm between ten participants. After spectral characterizations of the radiometers it became clear that the relative spectral responsivity of the UVA radiometers will have a huge impact on the results and must be taken into account even though narrow-band irradiation sources were used during the calibrations.

SPECTRAL MISMATCH

The (relative) spectral responsivity of a UVA radiometer is not, as demanded, spectrally flat. Therefore, even if a narrow-band source is selected for the calibration, a strong local change in the spectral responsivity may cause a displacement of the measurement result. In general, the weighted spectral deviation of a radiometer depends on the relative spectral irradiance distribution of the calibration source "C", $E_{\lambda,C,rel}(\lambda)$, and the relative spectral responsivity of the radiometer, $s_{rel}(\lambda)$,

$$m_{UVA,C} = \frac{\int E_{\lambda,C,rel}(\lambda) d\lambda}{\int E_{\lambda,C,rel}(\lambda) s_{rel}(\lambda) d\lambda}. \quad (2)$$

In addition to the correction of the weighted spectral deviation, further corrections must be considered for the calibration. This is achieved by extending the calibration equation by means of adjustment factors a_j and the calibration equation (1) extends to

$$k_{dut,UVA,C} = \frac{1}{s_{0,r}} \cdot m_{r,UVA,C} \cdot \frac{Y_{r,C}}{Y_{dut,C}} \cdot \prod_{j=1}^n a_j, \quad (3)$$

with $m_{UVA,r,C}$ being the weighted spectral deviation of the reference detector responsivity. At this point, for the calibration source "C", the weighted deviation

of the device under test needs not to be considered. Only the reference detector responsivity around 365 nm needs to be considered. Knowledge of the weighted spectral deviation of the device under test is required if a source with a different spectral distribution is used for the application or for other calibration being compared with. Then the weighted spectral deviations with respect to the calibration source “C” and the reference source “R” must be considered and the so-called spectral mismatch is obtained [3],

$$a_{dut,UVA,R,C}^* = \frac{k_{dut,UVA,R}}{k_{dut,UVA,C}} = \frac{m_{dut,UVA,R}}{m_{dut,UVA,C}}. \quad (4)$$

The reciprocal value of this spectral mismatch $F_{r,UVA,R,C}^* = 1/a_{r,UVA,R,C}^*$ is called the spectral mismatch correction factor and so the correction factor for the reference source “R” can be calculated:

$$\begin{aligned} k_{dut,UVA,R} &= k_{dut,UVA,C} \cdot F_{dut,UVA,R,C}^* \\ &= k_{dut,UVA,C} \cdot \frac{m_{dut,UVA,C}}{m_{dut,UVA,R}} \end{aligned} \quad (5)$$

PRACTICLE EXAMPLES

For the Euramet.PR-S4 intercomparison, two different UVA radiometers were measured. In contrast to the manufacturers' specifications, the radiometers showed a significant change in relative spectral responsivity around 365 nm. Figure 1 shows that one detector (DUT1) has a local slope of 3 %/nm, and the other one (DUT2) shows -13%/nm. The reference standard detector (REF) based on a Si

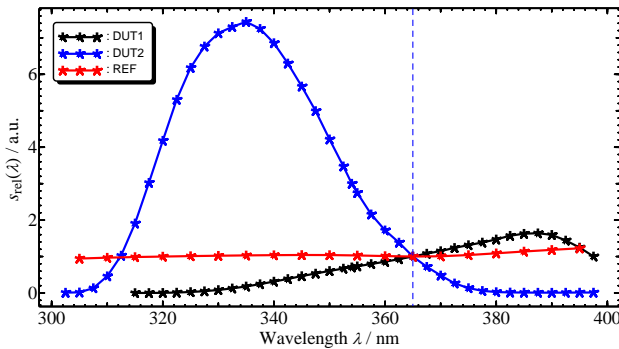


Figure 1. Relative spectral responsivity of two UVA radiometers (DUT1, DUT2) and a Si reference photodiode (REF).

photodiode features a minor local minimum symmetric around 365 nm.

The calibration source “C” used at PTB is a filtered HgXe high-pressure lamp. The relative spectral irradiance distribution has a centroid wavelength of 365.3 nm and a bandwidth (FWHM) of 2.2 nm (Figure 2). For the intercomparison, a reference spectrum “R” with a centroid wavelength

of 365.7 nm and FWHM of 5 nm was provided by the pilot and is shown in Figure 2 as well. The resulting weighted deviations related to the reference spectrum are up to $m_{DUT2,UVA,R} = 7\%$ for DUT2 and its resulting spectral correction factor is in the range of $F_{DUT2,UVA,R,C}^* = 4\%$ (Table 1). For the evaluation of the intercomparison results, appropriate spectral corrections are therefore indispensable.

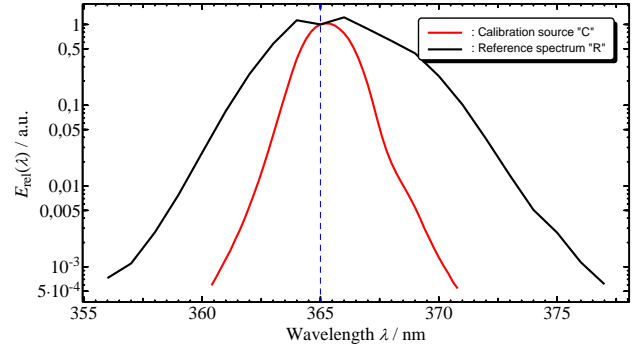


Figure 2. Relative spectral irradiance distribution of the calibration source “C” used for calibration and the reference spectrum “R” for the intercomparison.

Table 1. Weighted spectral deviation and mismatch correction factor for three different radiometers.

Radiometer	$m_{x,UVA,C}$	$m_{x,UVA,R}$	$F_{x,UVA,R,C}^*$
DUT1	0.989	0.974	1.016
DUT 2	1.025	1.066	0.962
REF	0.999	0.996	1.003

CONCLUSION

Even if sources with narrow-band spectral distributions are used for calibrations, it is necessary to perform a spectral mismatch correction of radiometers. This is the only way to achieve comparability between measurement results by different radiometers and institutes. The corrections require knowledge of the relative spectral responsivity of radiometers and the spectral distribution of the relevant emitters. However, such measurements are often not included in routine calibrations. Nevertheless, even if no spectral characterization can be made, a conservative estimate of the contribution to measurement uncertainty should be made.

REFERENCES

1. [DIN EN ISO 3059:2013-03](#) Non-destructive testing - Penetrant testing and magnetic particle testing - Viewing conditions.
2. EURAMET.PR-S4 Calibration of UVA power meters at relatively high irradiance levels, <https://www.bipm.org/kcdb/comparison?id=1084>
3. [CIE 220:2016](#), “characterization and calibration methods of UV radiometers.

Novel LED standard source for absolute radiometry in the visible wavelength range

Gerloff, T.¹, Kallenbach, L.¹, Schrader, C.¹, Sperling, A.¹, Šmid, M.², Kliment, P.², Poikonen, T.³

¹ PTB, Braunschweig, GERMANY, ² ČMI, Prague, CZECH REPUBLIC, ³ VTT, Espoo, FINLAND

Corresponding e-mail address: Thorsten.gerloff@ptb.de

Source-based radiometric calibrations are mainly based on the use of scientific grade incandescent lamps that are traceable to a black body radiators. In this publication we discuss the advantages and disadvantages of a radiometric standard based on LEDs.

Major advantages of thermal radiation sources are the continuous and calculable spectral distribution in a large wavelength range. However, the very large infrared component of thermal sources can lead to problems.

The LED standard source presented here has a very high reproducibility and is particularly suitable for the calibration of radiometric detectors in the visible spectral range.

LED REFERENCE SPECTRA

The European research project “Future photometry based on solid-state lighting products” (EMPIR 15SIB07 PhotoLED) has investigated the fundamental requirements for photometry based on white light-emitting diode (LED) sources. Many hundreds of LED spectra were analyzed and suitable LED reference spectra for photometric calibrations were derived [1,2]. In the CIE publication “Colorimetry” were 5 spectral distributions of typical phosphor-converted blue LEDs at colour temperatures, which are commonly used, published.[3]

LED STANDARD SOURCE LIS-A

The construction of the LED source (LIS-A) consists of an aluminium cylinder with a diameter of 100 mm and a length of 70 mm.

The heat exchange takes place via an internal heat sink to achieve a high degree of insensitivity to ambient temperature and air currents. The heat sink is actively cooled by a fan on the back. The temperature of the LED chip is controlled by an underlying Peltier element via an integrated active temperature controller.

24 SMD LEDs are arranged on the printed circuit board. Their typical correlated colour temperature in the standard configuration is between 4000 K and 4100 K.

Originally, the LED source LIS-A was developed as a luminous intensity standard.

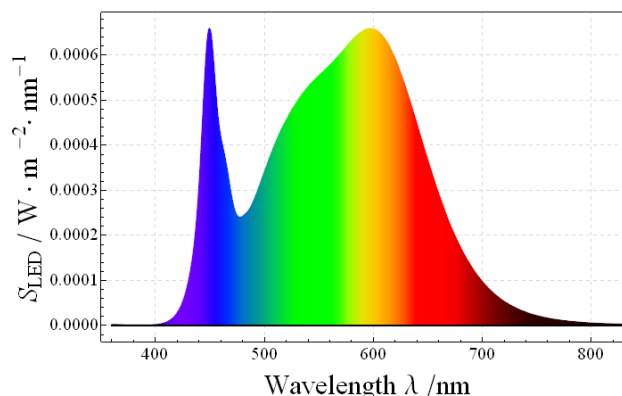
During the subsequent characterization, however, it was shown that photometric as well as integral and spectrally resolving radiometric detectors can be calibrated with the LED standard source with low uncertainty.

The investigations include photometers, radiometers, trap detectors, PQEDs and spectroradiometers and show the general usability of the LED standard source.

SPECTRAL IRRADIANCE MEASUREMENT

The spectral irradiance of the LIS-A sources was calibrated with scanning double monochromators and array spectroradiometers and also shows good agreement between different NMIs.

The measured spectrum is shown in the figure below.

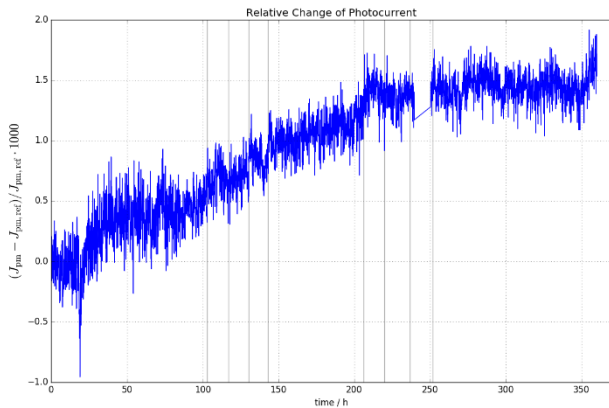


SEASONING

The LIS-A standard lamps are operated with an external direct current of about 65 mA at a supply voltage of about 75 V.

The built-in temperature control unit keeps the surface of the LED board at a temperature of about 45°C. All LEDs have been seasoned for at least 1000

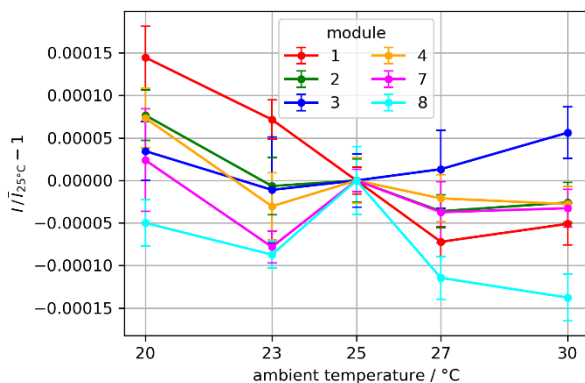
hours to reduce aging effects and ensure stability during operation. The relative changes of the photocurrent of a monitor detector during the last 360 hours of ageing are shown in the figure below.



The average photocurrent change is significantly less than 0.1% for the last 100 hours of seasoning.

EFFECTS OF AMBIENT TEMPERATURE

The figure below shows the relative changes of the detector photocurrent with temperature in relation to the value at the nominal temperature 25°C for 6 different LED modules. The influence of ambient temperature and humidity was determined in a climate chamber with an external photometer. The ambient temperature was varied between 20°C and 30°C and each measurement was performed after 20 minutes of stabilisation time. All measurements were performed at 50% relative humidity.



The deviations are below $1.5 \cdot 10^{-4}$, which can be considered negligible, especially considering the standard deviations at each measurement point.

SUMMARY

The presented LED standard source can be used for a variety of applications. Due to its very good stability and reproducibility, with very low noise, the standard

can be used for both photometric and radiometric applications.

In the presentation the special possibilities are highlighted and quantified by analysis of the measurement uncertainties.

REFERENCES

1. Jost, S. et al, „Determination of illuminants representing typical white light emitting diodes sources”, CIE x044:2017
2. Development of white LED illuminants for colorimetry and recommendation of white LED reference spectrum for photometry. Metrologia. 55. 526-534
3. CIE 015:2018. Colorimetry, 4th Edition. Vienna: CIE.

Spectral Irradiance Measurement Based on Large-area WC-C Fixed Point Blackbody

Yanfei Wang¹, Caihong Dai¹, Boris Khlevnoy², Irina Grigoryeva², Ling Li¹, Zhifeng Wu¹, Yihang Xie¹, and Shufang He¹

¹ National Institute of Metrology (NIM), Beijing, China, ² All-Russian Research Institute for Optical and Physical Measurements (VNIIOFI), Moscow, Russia

Corresponding e-mail address: daicaihong@nim.ac.cn

We realized spectral irradiance measurement of standard lamp based on large-area WC-C fixed-point blackbody for the first time. The wavelength range is from 390 nm to 1000 nm. We measured spectral irradiance of standard lamp based on traditional variable temperature blackbody and large-area WC-C fixed-point blackbody respectively. The average measurement difference of the two methods is 0.29% within this wavelength range. Compared with the traditional measurement method, the fixed-point method could reduce the average measurement uncertainty from 0.53% ($k=2$) to 0.39% ($k=2$).

INTRODUCTION

Spectral irradiance from 250 nm to 2500 nm is CCPR K1-a Key Comparison [1]. The tungsten halogen lamps are used for the transfer lamps. The lamps are also the most widely used for spectral irradiance measurement. In many national metrology labs, the lamps are measured against the variable high temperature blackbody. The temperature is measured by pyrometer. This is the most common traceability chain for source based method. For this method, the major uncertainty is the temperature measurement uncertainty of the blackbody.

The melting temperature of WC-C fixed point is 3021 K around, which is close to the colour temperature of the tungsten halogen lamps (about 3000 K) [2]. Therefore, this kind of fixed point is very useful for spectral irradiance measurement. For the purpose of spectral irradiance measurement, the large-area WC-C fixed point has been developed [3]. In the following, we will introduce the fixed-point method for spectral irradiance measurement. This is the first time that fixed-point method is used for the spectral irradiance measurement directly.

MEASUREMENT METHOD AND RESULTS

The experimental schematics is shown in Fig. 1. Blackbody A is a variable high temperature

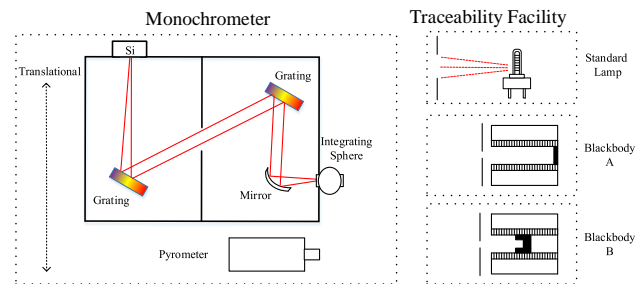


Figure 1. Experimental schematics.

blackbody. Blackbody B is large-area WC-C fixed point blackbody. The opening diameter of the fixed point is 14 mm, which is large enough for spectral irradiance measurement.

Firstly, we set the temperature of blackbody A at the temperature of 2972.09 K. The temperature is measured by the pyrometer. The system including the monochromator and Si detector is calibrated by blackbody A. And then, we measure the spectral irradiance of the standard lamp. The wavelength range is from 390 nm to 1000 nm, which is limited by the detector and the gratings. This is method A.

For the fixed point method, we use the melting plateau as the primary standard. We could know the temperature exactly without the pyrometer. The plateau shape is shown in Fig. 2. Using the first and the second derivative of the melting curve, which is shown in Fig. 3, we can obtain the duration of the melting plateau [4-5], about 14.7 min. We also use the same pyrometer to measure a small WC-C fixed point. Then, we obtain the temperature of the large cell,

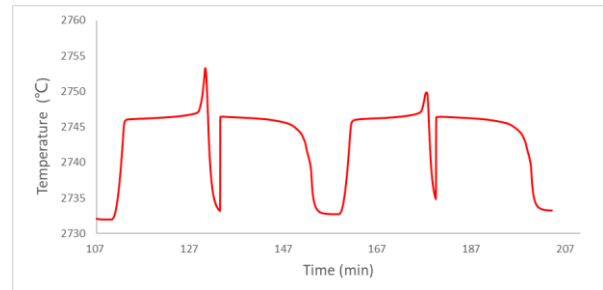


Figure 2. Plateau shape of large-area WC-C fixed point.

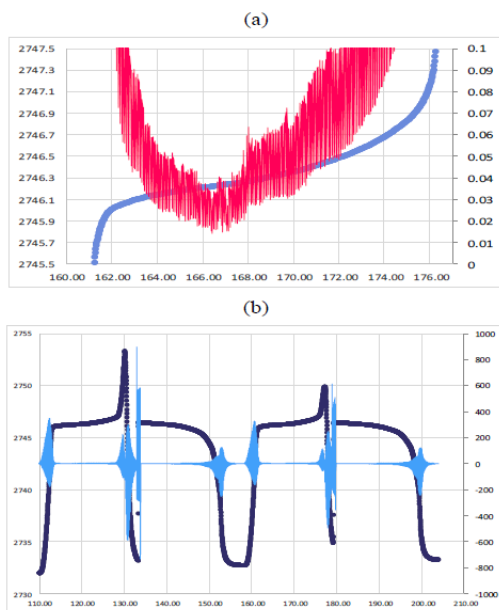


Figure 3. (a) First derivative of the melting curve. (b) Second derivative of the melting curve.

3020.02 K. By the second, third, and fourth melting plateau, which is shown in Fig. 4, we calibrate the system. The blank of the melting plateau means the calibration is going on. We repeat the measurement for three times. The curve shape is not good enough because we put a small diaphragm in front of the blackbody. However, it will not affect the results. This is Method B.

The measurement results are shown in Table. 1. The average measurement difference of the two methods is 0.29%. Compared with Method A, Method B could reduce the average measurement uncertainty from 0.53% ($k=2$) to 0.39% ($k=2$).

CONCLUSION

We realized a fixed point method for spectral irradiance measurement of tungsten halogen lamps. The measurement results agreed very well with the

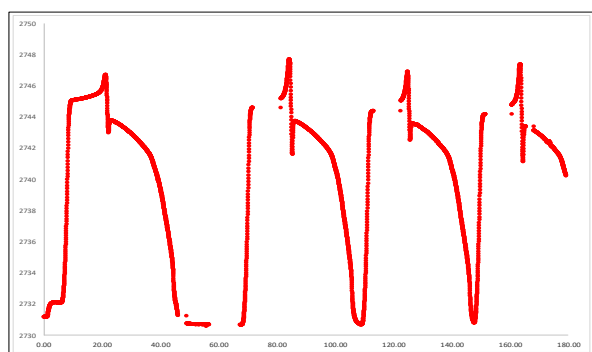


Figure 4. Melting curve for the spectral irradiance measurement.

Table 1. Measurement results.

Wavelength (nm)	Method A ($\mu\text{Wcm}^{-2}\text{nm}^{-1}$)	Uncertainty A (% $k=2$)	Method B ($\mu\text{Wcm}^{-2}\text{nm}^{-1}$)	Uncertainty B (% $k=2$)	Difference (% B-A)
390	1.44E+00	0.71	1.43E+00	0.44	-0.66
450	3.54E+00	0.64	3.55E+00	0.43	0.47
500	5.94E+00	0.60	5.96E+00	0.42	0.24
550	8.67E+00	0.52	8.69E+00	0.35	0.20
600	1.14E+01	0.50	1.14E+01	0.35	0.10
650	1.39E+01	0.47	1.40E+01	0.34	0.28
800	1.88E+01	0.46	1.89E+01	0.37	0.32
900	1.99E+01	0.46	1.98E+01	0.40	-0.12
1000	1.95E+01	0.45	1.95E+01	0.40	-0.20

traditional variable blackbody method. The fixed point method could shorten the traceability chain and reduce the measurement uncertainty of the primary spectral irradiance scale significantly. The method could be extended to the whole wavelength range from 250 nm to 2500 nm in the near future.

ACKNOWLEDGEMENTS

The authors thank Yandong Lin and Xiaofeng Lu for helpful discussion. This work was supported by National Key Research and Development Program of China (Grant No. 2016YFF0200304) and Quality Technology Capacity Improvement Program (Grant No. ANL1909).

REFERENCES

1. E. R. Woolliams, N. P. Fox, M. G. Cox et al., Final report on CCPR K1-a: Spectral irradiance from 250 nm to 2500 nm, Metrologia, 43, 02003, 2006.
2. B. B. Khlevnoy, I. A. Grigoryeva, D. A. Otryaskin, Development and investigation of WC-C fixed-point cells, Metrologia, 55, S59-S67, 2012.
3. B. B. Khlevnoy, I. A. Grigoryeva, K. Anhalt et al., Development of large-area high-temperature fixed-point blackbodies for photometry and radiometry, Metrologia, 55, S43-S51, 2018.
4. E. R. Woolliams, K. Anhalt, M. Ballico et al., Thermodynamic temperature assignment to the point of inflection of the melting curve of high-temperature fixed points, Philosophical Transactions of the Royal Society A: Mathematical, Physical and Engineering Sciences, 374, 20150044, 2016.
5. Y. Yamada, K. Anhalt, M. Battuello et al., Evaluation and Selection of High-Temperature Fixed-Point Cells for Thermodynamic Temperature Assignment, International Journal of Thermophysics 36, 1834-1847, 2015.

High-temperature behavior of diffraction effects in blackbody calibrations: higher-order effects

Eric L. Shirley

Sensor Science Division, NIST

Since the early work by Blevin [1], it has been well known that diffraction effects in the calibration of blackbodies generate an error in measured power led by a term varying as $1/T$. Higher-order corrections are also of increasing importance in cases of (1.) low (source) temperature, and (2.) multi-staged optical systems. This talk will include presentation of results related to these two aspects. For low temperatures and in the case of a single intervening aperture consisting of the blackbody, cryogenic radiometer and aperture, diffraction corrections on total power involve a series expansion in terms of $1/T$ and the logarithm of T [2]. For cases with more than one aperture between the source and detector, other effects arise that mostly vary as $1/T^2$, but often with contributions scaling as $1/T^3$, $1/T^4$ or $1/T^5$. By use of a higher-order boundary diffraction wave formulation [3], these terms can be identified, and the larger terms can be computed efficiently in a method that automatically integrates over the Planck spectrum, eliminating the need to carry out calculations at multiple wavelengths before such integration. This talk will emphasize the new, unpublished developments that have taken place most recently and apply the results of this work to a recent calibration at NIST.

[1] W. R. Blevin, *Metrologia* **6**, 39 (1970).

[2] E.L. Shirley, *J. Opt. Soc. Am. A* **33**, 1509 (2016).

[3] E.L. Shirley, *J. Mod. Opt.* **54**, 515 (2007).

Characterisation of high irradiance level 254 nm UV sources for UVmeter calibration

J. Dubard¹, F. Buteau¹, O. Enouf¹

¹LCM/LNE-CNAM, Trappes, FRANCE

Corresponding e-mail address: jimmy.dubrad@lne.fr

UVC light around 254 nm is used in many applications that requires high irradiance levels up to 150 W/m². We have investigated several types of sources to determine their ability to produce such level of irradiance for the purpose of the calibration of UVC radiometer. Low-pressure mercury lamps with amalgam as well as newly developed UVC LED show good performances. We present the results of the characterisation in irradiance level and spatial uniformity for both sources.

INTRODUCTION

UVC light is use in many applications and particularly for the disinfection of water, air and surfaces, but also for sterilisation in the medical field. For all these application high irradiance levels are used on the order of 150 W/m² and there is a need for calibration of UV meters on this level range.

However today calibration laboratories have limited irradiance range less than 20 W/m² at 254 nm due to the type of sources used.

We have investigated several UVC sources in order to determine their suitability to produce the required irradiance levels. In this paper we present the results of the characterisation performed on two parameter: irradiance level and spatial uniformity.

SOURCE PARAMETERS

The sources investigated will be used for UVC meter calibration. Therefore they have to comply with some characteristics that are :

- Irradiance level that should be about 150 W/m²
- The spatial uniformity should be limited to 5% on a circular area of 3 cm²
- A temporal stability less than 1% over one hour

The focus was made on the first two parameters but a rough estimation of the temporal stability was evaluated. In complement to these physical

parameters, the cost of the source was also taken into account.

We have investigated four types of sources:

- Laser and laser diodes
- Laser driven light source (LDLS)
- Mercury lamps with amalgam
- UV LED

SOURCE CHARACTERISATION RESULTS

UVC laser can reach the required irradiance levels. However such source is not cost effective. UVC laser diode s are not available yet on the market.

LDLS needs a UV filter and a lot of light is wasted limiting the UVC output level.

Low pressure mercury lamps with amalgam [1] exhibit high UVC throughput with about 85% of 254 nm light.

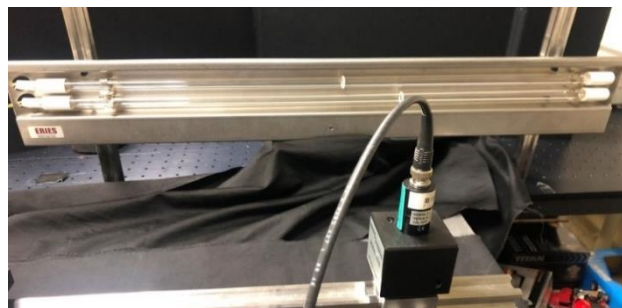


Figure 1. Amalgam UVC source.

Using the set-up shown on figure 1 with two 1m long lamps an irradiance level > 200 W/m² was reached at a distance of 10 cm from the lamp. The spatial uniformity was better than $\pm 2\%$ over a disc of one inch in diameter.

A new device like the one shown on figure 1 is under development and will integrate shorter lamps: 4x57 W with 36 cm in length. The beam profile based on simulation is shown on figure 2.

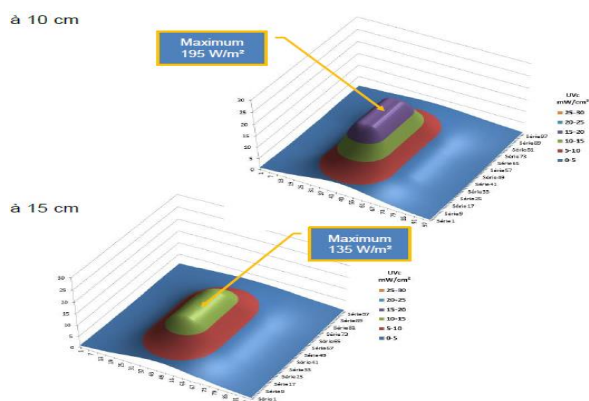


Figure 2. Beam profile of the new Amalgam UVC source.

UV LED are developing rapidly and recently 5W are made available for UVC applications. These LED have a 10 nm spectral bandwidth and can have a angular distribution of 7°, 35°, 120°. Figure 3 shows the angular distribution of the 35° wide LED.

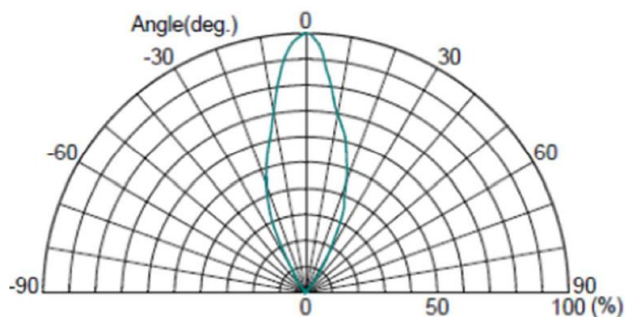


Figure 3. Angular distribution of the UVC LED.

In order to obtain the required irradiance level the LED should be set in an array and an optic should be added. Optical simulation based on the following parameters has been made:

- Data from figure 3
- Radiometric specifications from the manufacturer
- A 5x5 array with 32 mm x and y dimensions
- A focusing lens in the 2f optical configuration

The results of the simulation is show on figure 4. At a distance of 90 mm from the source, the

irradiance level is about 290 W/m² and the spatial uniformity is $\pm 2.2\%$ over a disc of 1 inch in diameter.

The UVC LED were delivered by mid of January 2020. By the time of the conference experimental results will be available

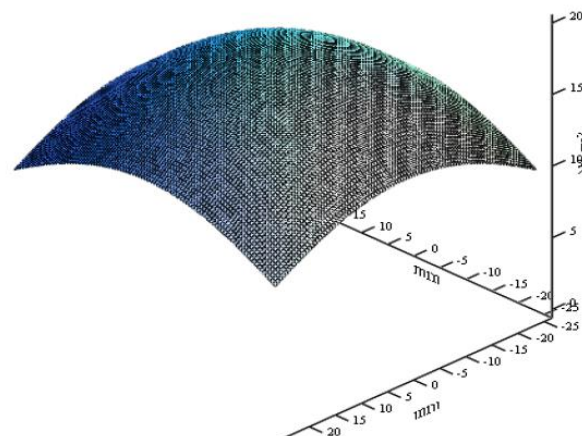


Figure 4. Simulation of the beam profile of the 35° wide UVC LED source.

CONCLUSION

Low pressure mercury lamps with amalgam and newly developed UVC LED show good performance to allow high irradiance level and can be used in calibration set-ups for UV radiometer.

REFERENCES

1. Ultraviolet Light in Food Technology: Principles and Applications, Larry J. Forney, Carmen I. Moraru à ISBN10 1281993689 à ISBN13 9781281993687.

Intercomparison of indoor and outdoor spectral irradiance measurements between INTI and INMETRO

Thiago Ferreira da Silva¹, Juan Pablo Babaro^{2,*}, Alberto Zinzallari², and Valeria Jesiotr²

¹National Institute of Metrology, Quality and Technology – INMETRO, Duque de Caxias – RJ, Brazil

²Instituto Nacional de Metrología Industrial – INTI, Buenos Aires, Argentina

*Corresponding e-mail address: jbabaro@inti.gob.ar

National institutes of metrology of Argentina and Brazil perform an intercomparison of spectral irradiance. Each institute developed its own secondary calibration facilities and provided a calibrated lamp. These lamps and a third one are alternately measured using their characterized spectroradiometers in the range from 250 nm to 1100 nm. The spectroradiometers are then taken outdoor to simultaneous solar measurements in UV range. Agreement between the results assess the institute's calibration capability.

INTRODUCTION

Spectral irradiance scale is usually materialized in standard lamps ultimately traced to a high-temperature blackbody [1] and to an electric-substitution cryogenic radiometer [2] as primary standards. Direct comparison using a spectroradiometer allows the transference of calibration between different artefacts. The *Instituto Nacional de Metrología Industrial* (INTI / Argentina) and the *National Institute of Metrology, Quality and Technology* (INMETRO / Brazil) have developed their own facilities for secondary calibration of lamps based on direct comparison to FEL 1000 W reference standards (traced to the *Physikalisch-Technische Bundesanstalt*, PTB/Germany) using fully-characterized spectroradiometers.

Here we report the results of the intercomparison of indoor and outdoor spectral irradiance measurements performed at INTI's installations in Buenos Aires (Argentina) between May 27th and June 5th, 2019 [3]. Spectral irradiance lamps are measured by the participants against their own secondary standards using their spectroradiometers. The instruments are then taken outdoor for comparative measurements of UV solar spectral irradiance.

EQUIPMENT

INTI uses a double monochromator scanning spectroradiometer with a photomultiplier detector equipped with an integrating sphere and an optical

diffuser for solar and indoor measurements, respectively. INMETRO [4] uses a 2048 pixels, Si CCD-based array spectroradiometer with a cosine-response PTFE diffuser. Both devices use optical fibers and are beforehand characterized for intensity and time linearity, spectral straylight, wavelength scale, spectral bandwidth, cosine response and optical plane of incidence. Each participant provides a certified secondary FEL 1000W lamp which has been calibrated in its own facility against their reference standards, according to Table 1, and also a third lamp.

Table 1. Standard lamps used in the intercomparison.

Lamp	A	B	C
Certificate	INTI	INMETRO	Neither

MEASUREMENT PROTOCOL

Each lamp is aligned in the optical bench and measured at a distance of 700 mm with both spectroradiometers. The results for each test lamp are obtained as $L_T(\lambda) = L_S(\lambda) M_T(\lambda)/M_S(\lambda)$, where $L_S(\lambda)$ is the certified spectral irradiance of each participant's own standard lamp (A or B) and $M_{T,S}(\lambda)$ are the *in-locus* spectral measurements.

For outdoor measurements, participants calibrate their spectroradiometers against the same reference (lamp A). The instruments are positioned in the rooftop of INTI's installations (34.57° S, 58.52° W) and their input are aligned towards zenith. Total acquisition period is matched between systems and measurements rounds start synchronously. Global measurements include both direct Sun and hemispherical scattering of the sky dome. Diffuse irradiance is obtained by shading the entrance optics. Direct irradiance is computed as their difference.

RESULTS

Figure 1 shows an example (lamp B) of spectral irradiance measurement performed by the participants in the range from 250 nm to 1100 nm. The achieved calibration uncertainty values (k=2) are compared. Relative difference between results

obtained by the institutes for lamps A, B and C are shown in Fig. 2.

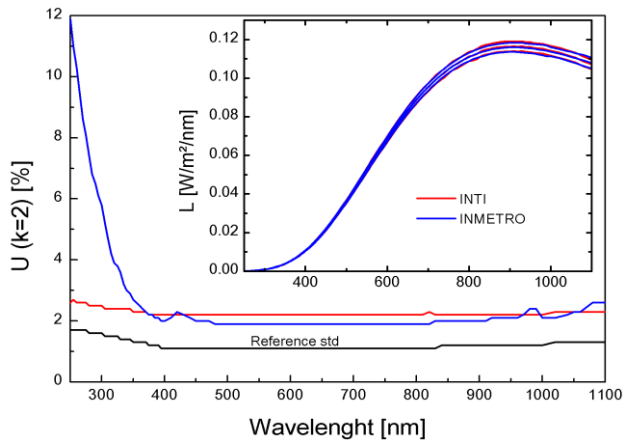


Figure 1. Calibration uncertainty of secondary standards of both institutes (primary lamp uncertainty shown in black). Inset shows spectral irradiance of lamp B.

Region between outer lines in Fig. 2(a-c) indicate combined uncertainty. This range touched the zero line, indicating agreement between data. Normalized error (En) between measurements (the absolute difference over their combined uncertainty) in Fig. 2d are within acceptance criterion of $En \leq 1$, except for few data points. INMETRO's higher uncertainty in UV is due to reduced sensitivity of its array spectroradiometer in this spectral region

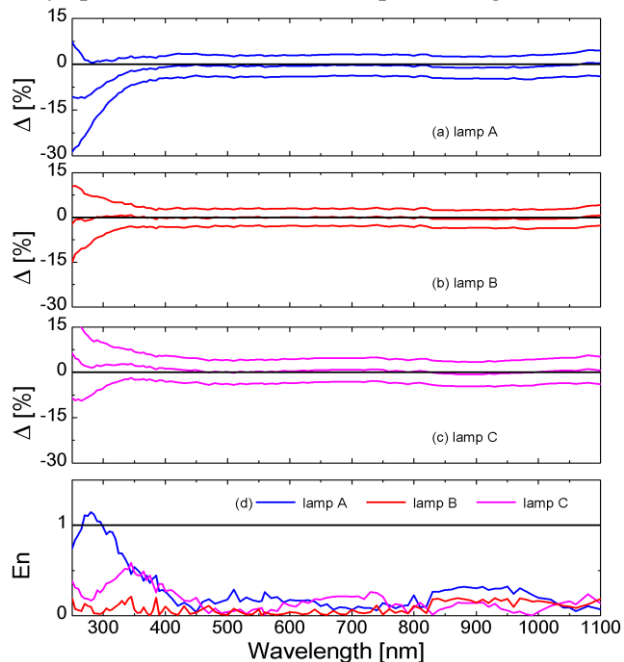


Figure 2. (a, b, c) Relative differences and (d) En computed over measurements of lamps A, B and C.

Five complete rounds of outdoor measurements were performed in June 3rd, between 12:49 and 13:32. Simultaneous results of both institutes obtained with their spectroradiometers in UV range are shown in

Fig. 3, and also the normalized error. The observed spectral pattern is due to difference in spectral bandwidth of the instruments. Histograms of En (inset in Fig. 3d) reveals the value is mostly below unit, indicating good agreement between data, except for the lowest wavelengths, where INMETRO's instrument is less sensitive.

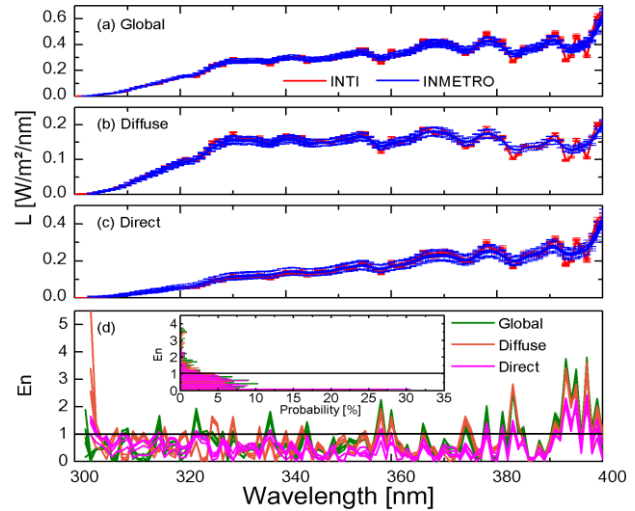


Figure 3. Measurements of (a) global, (b) diffuse and (c) direct UV solar spectral irradiance measured by INTI and INMETRO and (d) normalized error (inset: histogram).

CONCLUSION

Normalized error below unit for three lamps indicate agreement between INTI and INMETRO, assessing their independent secondary spectral irradiance calibration systems. Although solar measurements are performed in a rather experimental purpose, results exhibit good agreement, indicating the spectroradiometers are well characterized.

ACKNOWLEDGEMENTS

Authors thank Dr. Peter Sperfeld and Dr. Saulius Nevas for technical support and enlightening discussions, and the PTB/Germany for financial support under the Regional Fund Quality Infrastructure for Biodiversity and Climate Protection.

REFERENCES

1. P. Sperfeld *et al.*, "The spectral irradiance traceability chain at PTB," AIP Conf. Proc. 1531, 801-804, 2013.
2. H. W. Yoon *et al.*, "The realization of the NIST detector-based spectral irradiance scale," Metrologia 40, S172-S176, 2003.
3. J. P. Babaro *et al.*, "Intercomparison in secondary standard lamps of spectral irradiance and solar spectrum measurement," Final report, October 2019.
4. T. Ferreira da Silva, "Secondary calibration of lamps in spectral irradiance," in proc. of Brazilian Congress of Optical Metrology (CBMO), November 2019.

Development of illuminance meter calibration system with LED spectrally tunable light source

Kenji Godo¹, Yutaka Tamura², and Osamu Watari²

¹NMIJ, AIST, 1-1-1 Umezono, Tsukuba, Ibaraki, JAPAN

²Cell System Co., Ltd, 1-2-8 Azamino-minami, Aoba-ku, Yokohama, Kanagawa

Corresponding e-mail address: kenji-goudo@aist.go.jp

Calibration of an illuminance meter is usually done using a photometric bench and a luminous intensity standard lamp. To replace standard lamp method, we constructed an illuminance meter calibration system based on an LED based spectrally tunable light source (LSTL). CIE Illuminant A approximate spectra realized by the LSTL was controlled at various illuminance values. A test illuminance meter was calibrated by comparison against a reference photometer with the realized Illuminant A approximate spectra.

INTRODUCTION

Illuminance meters are normally used to measure the degree to which incident light from indoor lighting and sunlight illuminates a surface. Calibration of an illuminance meter is usually done using a photometric bench and a luminous intensity standard lamp¹. The luminous intensity standard lamp is an incandescent lamp that realizes a spectrum of the CIE standard illuminant A (Illuminant A), i.e., its relative spectral distribution is that of Planck radiation at a temperature of about 2856 K².

In recent years, by increasing replacement of incandescent lamps with white LED lamps, it has become difficult to obtain the standard lamps. Although LED lighting is used widely, it is important to measure illuminance from sunlight. Therefore, the calibration of illuminance meter based on an Illuminant A approximate spectrum is continued to need for industrial and testing laboratory too.

As a candidate calibration source to take the place of traditional lamp sources, including incandescent lamps, an LED-based spectrally tunable light source (LSTL) has been investigated in several fields³⁻⁵. The main benefit of LSTLs is that it allows realization of different spectral and various optical intensities with only one lighting system without exchange of several light sources.

In this study, we constructed an illuminance meter calibration system based on LSTL as a pilot study. In the system, test illuminance meters are calibrated by

comparison against a reference photometer using an Illuminant A approximate spectrum realized by the LSTL.

CALIBRATION SYSTEM DEVELOPMENT

The calibration system was constructed by modifying an LSTL developed for a solar simulator in the photovoltaic field. An overview of our constructed calibration system is depicted in Figure 1. Overall dimensions of the calibration system are about 1.5 m (H) × 0.8 m (W) × 0.8 m (D). The calibration system consists of the LSTL, two CCD cameras for ascertaining the measurement position, a reference photometer, and a spectroradiometer. In addition, the measurement instruments including a test photometer are installed on a two-axis automatic movement stage (travel length of both axes: 300 mm), which enables accurate comparison measurement at the same position. The measurement distance from the LSTL to the measurement plane is 400 – 450 mm. The measurement distance is limited by the based solar simulator system.

The LSTL was constructed from 21 types of monochromatic HP-LEDs and two quasi-green yellow LEDs based on white HP-LED at wavelengths

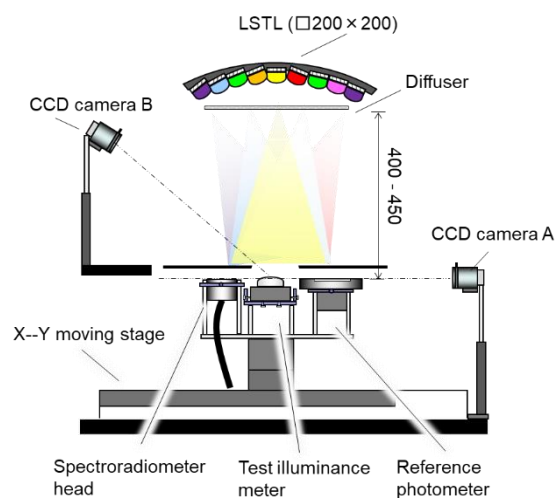


Figure 1. Schematic drawing of the illuminance meter calibration system based on LSTL.

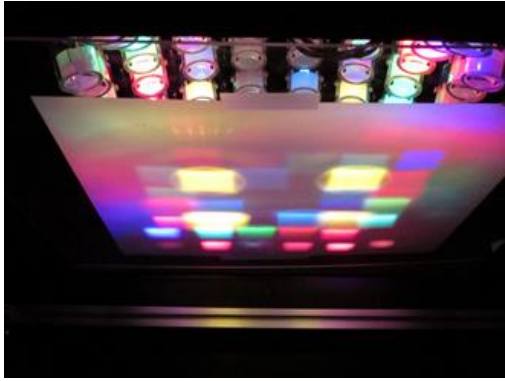


Figure 2. Photograph of LSTL (21 types of monochromatic HP-LEDs and two quasi-green yellow LEDs based on white HP-LED).

of 340 – 800 nm for covering the UV–visible range. Two or four of the same type HP-LEDs were used in one wavelength band. A total of 54 LEDs was used in LSTL. Figure 2 shows a photograph of the LSTL. Their maximum operated current depends on the LED type (500 – 3,000 mA maximum rated current). The optical power can be changed by individual constant current control of each LED from 10 mA to 3000 mA. The overall LSTL shape is a dome-shaped frame. HP-LEDs of the same type were placed diagonally on the LSTL dome frame, with total emission area of the 54 mounted LEDs as 200 mm square.

To improve illuminance power and illuminance uniformity on the measurement plane, individual HP-LEDs have compact magnifier optics. The magnifier optics was constructed with a light pipe (10 mm square, 135 mm length) and a condensing lens ($f=25$ mm). It was designed to form a uniform illuminance plane of 200 mm square at the measurement plane with individual HP-LEDs.

Test illuminance meters were calibrated by comparison against the reference photometer using an Illuminant A approximate spectrum realized by the LSTL: the illuminance value of Illuminant A approximate spectrum is determined using the reference photometer. The test illuminance meter is calibrated from that value. This method is generally called as the detector-based method¹. Using this method, the illuminance scale is provided using a reference photometer, not by a standard lamp.

Figure 3 shows a spectral distribution of an Illuminant A approximate spectrum realized by the LSTL. The chromaticity coordinate of the approximate spectrum is $(u',v')=(0.239, 0.538)$. The illuminance is about 10,000 lx. Above condition,

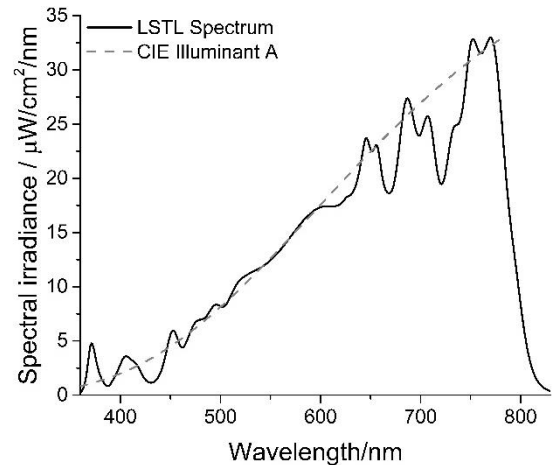


Figure 3. Spectral distribution of an Illuminant A approximate spectrum realized by the LSTL.

diffuser was not inserted for the maximum illuminance. The Illuminant A approximate spectrum in Figure 3 achieves very high illuminance that are difficult to achieve using traditional standard lamps. The Illuminant A approximate spectrum can achieve various illuminance values (800 lx to 10,000 lx) and diffuse characteristics by controlling the current value and inserting a diffuser.

CONCLUSION

In this study, the illuminance meter calibration system based on the LSTL was constructed to replace standard lamp methods. To construct the LSTL to cover wavelengths of 340–800 nm, 23 types were used. The Illuminant A approximate spectrum realized by the LSTL was controlled at various illuminance values from 800 lx to 10,000 lx

REFERENCES

1. Y. Zong, NIST SP 250-95 NIST Measurement Services Photometric Calibrations, 2018.
2. ISO 11664-2:2007(E)/CIE S 014-2/E:2006 Colorimetry – Part 2: CIE Standard Illuminants, 2006.
3. I. Fryc I, S W. Brown, G P. Eppeldauer, and Y. Ohno, LED-based spectrally tunable source for radiometric photometric and colorimetric applications, *Opt Eng*, 44(11), 111309, 2005.
4. S. Kohaku and K. Kurokawa, New methods for solar cells measurement by LED solar simulator, *Proc of Third World Conference on Photovoltaic Energy Conversion*, 1977–1980, 2003.
5. K. Godo, Y. Tamura, and O. Watari, Study of spectrally tunable light source based on LED for development of practical lighting booth, *Proc of NEWRAD 2017*, 116–117, 2017.

Comparison of Two Methods for Total Luminous Flux Measurement of White LEDs

Yuri Nakazawa¹, Kenji Godo¹, Yoshiki Yamaji² and Shinya Matsuoka²

¹NMIJ, AIST, Tsukuba, Ibaraki, Japan

²Nichia Corporation, Anan, Tokushima, Japan

Corresponding e-mail address: y-nakazawa@aist.go.jp

Total luminous flux of commercial white LEDs measured with sphere-spectroradiometer method in 2π geometry and goniophotometer method were compared. The measured values in sphere-spectroradiometer method were smaller than that of goniophotometer method by 1% to 5%. Near field absorption and spatial response distribution function of an integrating sphere were estimated as main uncertainty factors of this difference.

INTRODUCTION

For total luminous flux evaluation of LED products, total spectral radiant flux (TSRF) measurement is necessary. A sphere-spectroradiometer constructed with an integrating sphere and a spectroradiometer is commonly used for total luminous flux evaluation of LED products. The sphere-spectroradiometer is calibrated against TSRF standard. In the sphere-spectroradiometer method, test sources that emit light only forward direction are recommended mounted on a port of the integrating sphere wall (2π geometry) [1]. A reference standard source should be mounted at same geometry of the test sources, however, there was no suitable reference standard source for TSRF measurement in 2π geometry until recently. Thus, very few studies had done about total luminous flux measurement of LED products in 2π geometry.

Recently, we developed a new LED-based standard source (2π standard LED) that is suitable for spectral measurement in 2π geometry [2] and TSRF scale for 2π geometry was realized in NMIJ (National Metrology Institute of Japan). Thereby, it has become possible to evaluate total luminous flux of commercial LED products with sphere-spectroradiometer method in 2π geometry. In this study, TSRF and total luminous flux values of commercial white LEDs were measured with two method, sphere-spectroradiometer method using the 2π standard LED as a reference standard source and goniophotometer method. By comparison of the measurement, the uncertainty factors of commercial white LEDs measurement were examined.

EXPERIMENT

In the measurement, 10 types of commercial white LEDs were used as a test white LED. Figure 1 shows spectra of the test white LEDs. Total luminous flux values of the white LEDs were 100 lm to 320 lm and corrected color temperature (CCT) of the white LEDs were from 3000 K to 8000 K. Each white LED was operated at a constant current and mounted on the socket with a built-in thermo-module. The stabilities of total luminous flux of each white LED were $\pm 0.2\%$ by the temperature control.

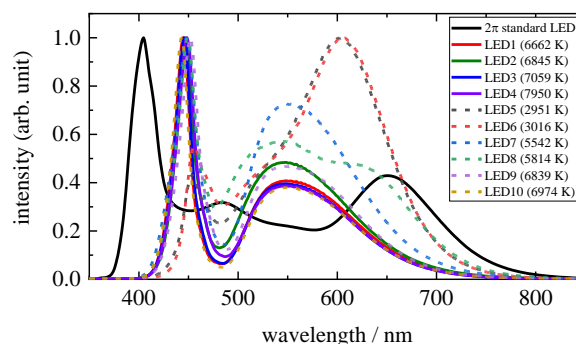


Figure 1. Spectra of 10 types of the test white LEDs and 2π standard LED.

Figure 2 shows angular intensity distributions of 4 types of the white LEDs. The white LEDs emitting light only in the forward direction was selected for a test source, however, LED5–LED10 have radiant intensity even over $\theta = 90^\circ$ direction when measured (e.g., LED6 and LED9 as shown in Fig. 2). In addition, the spatial uniformity of some white LEDs such as LED2 and LED6 were greatly different from that of the 2π standard LED. The angular intensity distribution of the 2π standard LED is almost equal to the Lambertian beam pattern.

In sphere-spectroradiometer method, TSRF of the white LEDs were measured in 2π geometry that calibrated against the 2π standard LED as a reference standard source. Total luminous flux of the white LED was calculated from TSRF. The diameter of the integrating sphere in the sphere-spectroradiometer

was 1.65 m. In the measurement, self-absorption correction was performed using a halogen lamp.

In goniophotometer method, total luminous flux of the white LEDs were measured using a $V(\lambda)$ -matched detector. An array spectroradiometer was used for measuring a spatially averaged spectrum of the white LED for calculation of spectral mismatch correction factor and TSRF. The illuminance responsivity of the $V(\lambda)$ -matched detector was calibrated against luminous intensity standard and the relative spectral responsivity of the array spectroradiometer was calibrated against spectral irradiance standard. The measurement distance was 1.15 m.

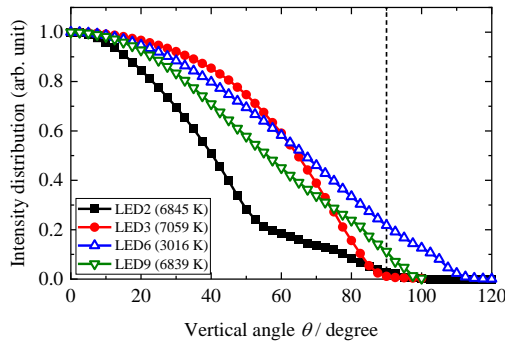


Figure 2. Angular intensity distributions of the white LEDs.

RESULT AND DISCUSSION

Figure 3 shows the differences between total luminous flux measured with two method. As shown in Fig. 3, almost all the results with sphere-spectroradiometer method were smaller than that measured with goniophotometer method by 1% to 5%. For the differences between TSRF measured with two method, similar tendency was also obtained. There was no clear relation between the differences of total luminous flux value and characteristics of the white LEDs, such as spectrum shape and CCT.

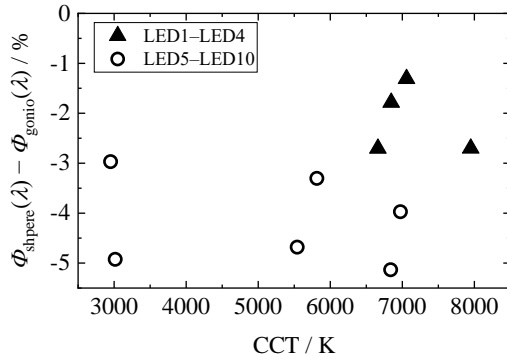


Figure 3. Difference of measured total luminous flux between sphere-spectroradiometer method $\Phi_{\text{sphere}}(\lambda)$ and goniophotometer $\Phi_{\text{gonio}}(\lambda)$.

The uncertainty of the total luminous flux measurement with each two method was about 1% respectively, then these differences between two method were considered to come from other factors mainly. As shown in Fig. 2, some of the white LEDs have backward radiation over $\theta = 90^\circ$ direction. In Fig. 3, these white LEDs has the difference of about 3%–5% (open circles in Fig. 3). In contrast, the white LEDs that emit light only forward direction has the difference of about 1%–3% (closed triangles in Fig. 3).

From this result, two uncertainty factors were considered as the reason of the difference. One important uncertainty factor related to an angular intensity distribution is near field absorption that cannot be corrected by self-absorption correction. This factor was expected to become larger in 2π geometry when the white LED emits light over $\theta = 90^\circ$ direction. In 2π geometry, printed circuit boards and mount jigs cut off the light emitted in the backward direction over $\theta = 90^\circ$. Other uncertainty factor is nonuniformity of spatial response distribution function (SRDF) of the integrating sphere that causes error when a test source has different spatial radiant intensity distribution from that of a standard source.

A quantitative analysis for relation between intensity distributions of white LEDs and measured total luminous flux value is needed as future work.

CONCLUSION

Total luminous flux of commercial white LEDs were compared with two method. As a result, total luminous flux values measured with sphere-spectroradiometer method in 2π geometry using the 2π standard LED as a reference standard source were smaller than that measured with gonio-measurement by 1% to 5%. This difference come from uncertainties related to characteristics of the commercial white LEDs, such as near field absorption effect and SRDF of the integrating sphere.

ACKNOWLEDGEMENT

A part of this work was supported by a grant from Japan LED Association.

REFERENCES

1. CIE S 025/E: 2015, Test Method for LED Lamps, LED Luminaires and LED Modules, CIE.
2. Y. Nakazawa, K. Godo, K. Niwa, T. Zama, Y. Yamaji and S. Matsuoka, Lighting Res. Technol., 51, 870-882, 2019.

Enhancement of the state primary standard of the unit of total radiance

Iu. A. Sild, E.V. Vizulaynen, M.A. Ivanova

D.I. Mendeleyev Institute for Metrology (VNIIM), Saint-Petersburg, Russian Federation

Corresponding e-mail address: y.a.sild@vniim.ru

The State primary standard of the total radiance unit, which was approved in the end of 2018, is described. The range of the total radiance reproduced by the standard is from 54,36 to $61 \cdot 10^3$ W/(sr·m²) with the expanded uncertainty not more than $1,5 \cdot 10^{-3}$ relative units.

INTRODUCTION

The first work on creating standards in the field of the total radiation in Russia was started at VNIIM in 1964. In 1974, the first radiometric state primary standard of total radiation unit (SPS) was approved. Work directed at expanding the range and improving accuracy continued, which was reflected in the SPS approved in 2001.

Due to the increased measurement tasks to provide measuring instruments with higher metrological characteristics, the improvement of the SPS was required. In addition, there was a need to increase the reliability of unit transfer from SPS to secondary and working standards.

Thus, in 2015, the enhancement of the state primary standard of the unit of total radiance was started, which was successfully completed at the end of 2018.

DESCRIPTION OF THE STANDART

The main parts of the standard created in 2001 were blackbodies sources based on the phase transitions of pure substances [1].

Preserving the ideology of construction the standard, the main efforts in its improvement were aimed at creating a new blackbody source based on the triple point of mercury (BB-Hg).

As a result of work in the framework of enhancement of the SPS, a black body was developed [2]. The new blackbody based on the triple point of mercury reproduces value of total radiance 54.36 W/(sr·m²) at a phase transition temperature of 234.32 K in accordance with ITS-90.

In addition, modernization of the blackbody sources of reference points of pure elements: tin (BB-O), indium (BB-I), aluminum (BB-A) [3] and copper (BB-C).

A fundamental element of any blackbody

sources is the cell filled corresponding pure substance. Construction the cell must enforce mandatory requirements for the external dimensions of the cell, thickness the wall and emissivity parameters of cavity.

With the enhancement of the SPS, the development of new designs of the cell of blackbody sources based on phase transitions of pure metals was done. New cells were made and filled with high-purity metals. The new three-zone furnaces were development for blackbody sources placement and subsequent implementation.

The reproducible values of units total radiation for BB-O, BB-I, BB-A, BB-C compose 1173.4, 4151.0, 13691 and 61282 W/(sr·m²) respectively.

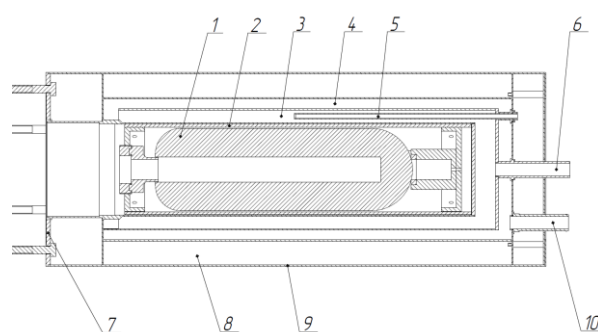
The use of new cells designs has significantly increased the life of the blackbody sources.

Also, a novel blackbody sources based on a triple point of water (BB-TPW) was developed.

BB-TPW include the following main units:

- Cell of the triple point of water fixed point;
- Passive thermostat for placing the cell of triple point of water;
- Cryostat, designed to provide the necessary thermal regime for the realization of a triple point of water;
- Connecting elements.

Passive thermostat and cryostat form a thermostatic device.



1 - the cell of triple point; 2 - container; 3 - the internal cavity of a heat exchanger; 4 - the outer cavity of a heat exchanger; 5 - thermometer channel; 6 - inlet branch pipe; 7 - connecting flange; 8 - thermal insulation; 9 - envelope; 10 - outlet branch pipe;

Figure 1. Design of a passive thermostat

Design of a passive thermostat is based on heat exchanger in the form of the “pipe in the pipe” that working in the opposite connection. The coolant, enters to the inlet branch pipe (6) and flows through the internal cavity of the heat exchanger (3). After passing through the internal cavity of the heat exchanger, the coolant is poured through the specialized technological slots into the outer cavity of the heat exchanger (4) and through an outlet branch pipe (10) it returns to the cryostat.

The temperature of the cavity is controlled by the resistance thermometer located in the channel (5). The attachment to the vacuum chamber of the primary standard is carried out by means of the connecting flange (7).

The results of the measurements are showed, that the metrological characteristics of the thermostatic device satisfy the requirements necessary for the realization and maintenance of the fixed point of water. Reproducible value of total radiance of BB-TPW is $100.39 \text{ W}/(\text{sr}\cdot\text{m}^2)$.

As part of the enhancement of the standard, a new thermostat was developed for the blackbody source of gallium. Its use allowed to reduce the non-uniformity of the temperature field during the implementation of the melting plateau of high-purity gallium.

CONCLUSIONS

The SPS was enhancement, within the framework new blackbodies source were developed. Also blackbodies sources from the previous state primary standard were modernized. Research done have shown that the expanded value of the uncertainty does not exceed $1,5\cdot 10^{-3}$ relative units at $k = 2$.

REFERENCES

1. I. I. Dolgikh, A. I. Pokhodun, O. V. Rybolovleva, V. V. Smirnova, State Primary Standard of the Unit of Infrared Radiance, Measurement Techniques, Volume 44, Issue 10, 965-971, October 2001.
2. Iu. A. Sild, M.S. Matveyev, E.V. Vizulaynen, M.A. Ivanova, Development novel blackbody source based on the mercury triple point., in Proceedings of NEWRAD 2017, Conference in Tokyo, Japan, 2017.
3. Iu. A. Sild, E.V. Vizulaynen, Improving cell for black body sources of aluminum fixed point, in Proceedings of NEWRAD 2014, edited by Seongchong Park, Petri Kärhä, Erkki Ikonen, 151-152, Conference in Espoo, Finland, 2014.

Simulation of Thermal Processes in High-Temperature Blackbodies and Fixed-Point Cells for Improving their Characteristics

Vladislav Zemlyanoy^{1,2}, Boris Khlevnoy^{1,2} and Andrey Baturin^{1,2}

¹*All-Russian Research Institute for Optical and Physical Measurements (VNIIOFI), Moscow, Russia*

²*Moscow Institute of Physics and Technology (MIPT), Dolgoprudny, Russia*

Corresponding e-mail address: khlevnoy-m4@vniiofi.ru

The finite element method (FEM) has been applied to develop a model of a high-temperature blackbody (HTBB) for simulation of thermal processes and the temperature distribution in HTBB and high-temperature fixed points (HTFPs) installed in HTBB as a furnace. This simulation instrument is being applied for further improvement of HTBB and for clarifying the parameters of HTFPs used in HTBB.

INTRODUCTION

25 year ago, the first high-temperature blackbody (HTBB) was developed at VNIIOFI and applied as a standard radiometric source [1]. Later, HTBBs were supplied to 15 National Metrology Institutes and used at national standard facilities for spectral irradiance and spectral radiance realization, as well as for photometry and radiation thermometry applications.

Unique HTBB parameters, such as wide operating temperature range (up to 3500 K), large radiating cavity, high stability, uniformity, and emissivity make it the best planckian metrological source and a convenient furnace for high-temperature fixed points (HTFPs) [2]. However, further improvement of HTBB is desirable in order to increase the emissivity and/or decrease its uncertainty, which is currently estimated as about 0.9995 ± 0.0005 . The HTBB emissivity significantly depends on temperature uniformity of the radiating cavity. Therefore, the HTBB design should be modified in such a way as to improve the uniformity. Experimental investigation of influence of possible modification to the uniformity and, therefore, the temperature distribution in the HTBB elements is quite difficult (or in some cases impossible) due to high operating temperatures.

This paper presents a computer simulation of thermal processes in HTBB, which takes into account the furnace geometry and the physical properties of the materials used. The model allows computing the temperature distribution in the HTBB (along the radiating cavity walls, heat shield, and

other parts) for two cases: the stationary case (when the HTBB temperature is stable – the usual blackbody regime) and the dynamic case (when the temperature is increasing or decreasing). The latter is applied to simulate the melting and freezing processes of HTFPs.

SIMULATION OF HTBB

HTBB has a cylindrical heater formed by a stack of graphite rings, which is heated by electrical current passing through the rings. The heater and a surrounding heat shield, made of graphite and carbon felt, are assembled horizontally in a stainless-steel water-cooled cylindrical housing. The space between the furnace construction elements is filled with argon gas.

The model of HTBB is purely axis-symmetrical. Although it ignores gravity effects, it still captures the most important features of the process.

The finite element method (FEM) [3] is used to solve numerically the stationary equations for electric heating and heat transfer, thus computing the temperature field in the HTBB model. The model takes into account electrical resistivity, thermal conductivity and specific heat capacity of the materials used depending on temperature. Heat radiation is taken into account as a boundary condition for all furnace surfaces. The emissivity of graphite is taken equal to 0.85, wavelength independently.

Fig.1 shows the cross-section of the HTBB model with computed temperature distribution (presented in colours) in the stationary case at the cavity temperature of 3000 K.

The simulation is being applied to improve HTBB, namely to find a way of such modification of HTBB design and the parameters of the heater and heat shield materials, which allows improving the temperature uniformity of the blackbody radiating cavity and, thus, increasing the emissivity and/or more accurate determining of the emissivity uncertainty.

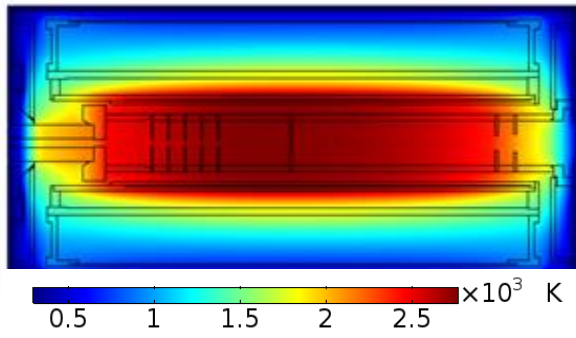


Figure 1. Computed temperature distribution in HTBB.

SIMULATION OF HTFP

When simulating the HTFP transition experiment the model includes only the heater and the HTFP cell itself excluding other parts of the furnace. The temperature distribution along the heater outer surface (see above) is treated as a boundary condition. To simulate a melting plateau the heater temperature is slowly increased by certain step, linearly in time.

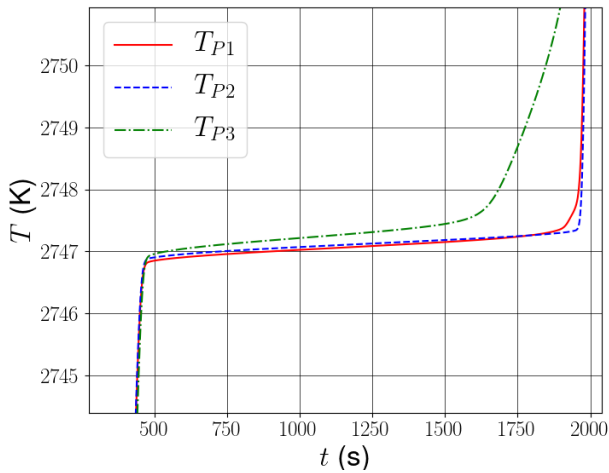


Figure 2. Melting plateaus of Re-C cell in point P1, P2 and P3 shown in Fig.3.

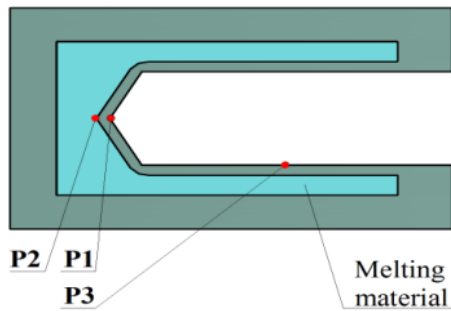


Figure 3. Diagram of HTFP cell

Phase transition is simulated as an additional specific heat of the melting material in a narrow temperature range around the melting point. The value of the range is varied around 1 K in different simulations. Difference in specific volume of solid and liquid phases is neglected, assuming equal densities at the melting point.

Fig. 2 presents melting plateaus computed for a Re-C cell in the points P1, P2 and P3 shown in Fig.3. The difference between the points P2 and P1 is the “temperature drop”, and the difference between P3 and P1 indicates the temperature gradient along the cavity wall. The shape of computed the curves and the temperature differences depends on uniformity of the temperature field around HTFP. Therefore, varying the temperature profile or the position of the cell in the furnace, one can investigate their influence on the cell characteristics.

The simulation is being used as an instrument to investigate the temperature drop effect in HTFP cells and the temperature gradient along the cell cavity, and for optimising the thermal conditions for the cells.

CONCLUSION

A model of a high-temperature blackbody (HTBB) based on finite element method (FEM) has been developed for simulating thermal processes and temperature distribution in HTBB and HTFPs. This simulation instrument is being applied for further improvement of HTBB uniformity and, therefore, more accurate determination of the emissivity. Another application is investigation of HTFP cells conditions and characteristics, in particular better evaluation of the temperature drop correction and its uncertainty.

REFERENCES

1. V. Sapritsky et al., Precision blackbody sources for radiometric standards, *Appl. Opt.*, 36, 5403-5408, 1997.
2. B. Khlevnoy, et al., Investigation of Furnace Uniformity and its Effect on High-Temperature Fixed-Point Performance, *Int. J. Thermophys* 29, 271–284, 2008.
3. O. Zienkiewicz et al., *The Finite Element Method: Its Basis and Fundamentals*, 7th Edition, Butterworth-Heinemann, 2013.
4. J.M. Bergheau and R. Fortunier, *Finite element simulation of heat transfer*, Wiley-ISTE, 2008.

High-Temperature Fixed-Point Blackbody with Temperature of about 2856 K Based on Melting Phase Transition of $\delta(\text{MoC})\text{-C}$

Boris Khlevnoy^{1,2}, Irina Grigoryeva¹, Denis Otryaskin¹, Maxim Solodilov¹ and Evgeniy Ivashin¹

¹All-Russian Research Institute for Optical and Physical Measurements (VNIIOFI), Moscow, Russia

²Moscow Institute of Physics and Technology (MIPT), Dolgoprudny, Russia

Corresponding e-mail address: khlevnoy-m4@vniiofi.ru

Large-area HTFP blackbody of $\delta(\text{MoC})\text{-C}$ type with temperature of about 2856 K has been developed. The $\delta(\text{MoC})\text{-C}$ HTFP has been investigated using several $\delta(\text{MoC})\text{-C}$ cells of different sizes. Thermodynamic temperature of the $\delta(\text{MoC})\text{-C}$ fixed point (POI) has been determined equals to 2856.93 K with standard uncertainty of 0.35 K, while the temperature of the large-area blackbody has been measured to be 2856. 25 K.

INTRODUCTION

Creation of high-temperature fixed-points (HTFPs) and inclusion them in the *Mise en pratique* for the definition of the kelvin (*MeP-K*) have significantly contributed to the development of the source-based (namely, blackbody-based) radiometry/photometry by means of increasing accuracy and reliability of temperature measurements of high-temperature blackbodies (HTBB).

The radiometry/photometry can further benefit from the development of large-area HTFP cells and, thus, creation of high-temperature fixed-point blackbodies with relatively large apertures capable of operating in irradiance mode and realizing such quantities as spectral radiance or luminous intensity.

VNIIOFI traditionally has been dealing with development of large HTFP cells. The last research presented the development and investigation of Re-C and WC-C large cells [1] and announced the development of $\delta(\text{MoC})\text{-C}$. The point $\delta(\text{MoC})\text{-C}$, first suggested by Sasajima [2], with melting temperature of about 2856 K is particular interesting for photometry as a base of the photometric Type-A standard blackbody.

Recently at VNIIOFI the $\delta(\text{MoC})\text{-C}$ blackbody based on a large cell was created. The several $\delta(\text{MoC})\text{-C}$ cells, large and small (“normal”) size, were built and investigated. Thermodynamic temperature of the $\delta(\text{MoC})\text{-C}$ fixed point was determined. This paper presents design of the developed cells and the blackbody as well as the results of the investigations.

DESIGN

Design of new $\delta(\text{MoC})\text{-C}$ blackbody is similar to that described in [1] for Re-C and WC-C. Its cross-sections is shown in Fig.1. The blackbody is based on the largest VNIIOFI-developed high-temperature furnace BB3500MP [3] with the cavity diameter of 59 mm, which contains a large $\delta(\text{MoC})\text{-C}$ fixed-point cell. The cell has a blackbody cavity with the diameter and length of 14 mm and 45 mm, respectively.

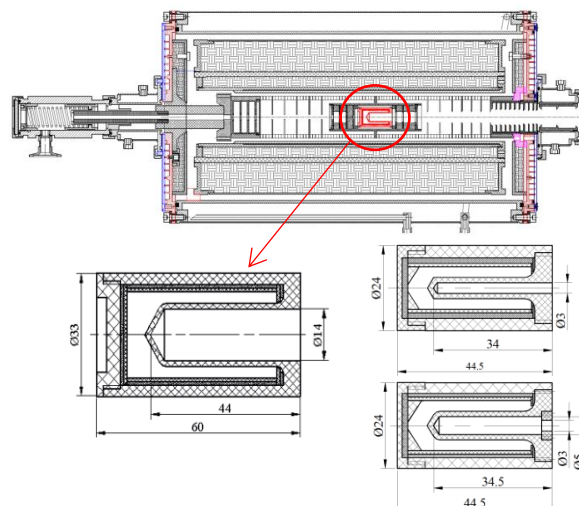


Figure 1. Cross-section of the $\delta(\text{MoC})\text{-C}$ blackbody.

Although the cell cavity is not deep, together with the furnace it has an emissivity of 0.9996. The dimensions of the cell and furnace allow using an outer aperture in front of the blackbody of about 5 mm, when calibrating a sensor of 5 mm at the distance of 500 mm. In this configuration the blackbody reproduces luminous intensity and illuminance of about 400 cd and 1600 lx.

To study the fixed point itself, three small cells, shown in the bottom right of Fig.2, have been built and investigated: one with cavity diameter of 3 mm and two with cavity of 5 mm and opening of 3 mm.

The same materials with nominal purity of 99.999 % were used for all the cells, small and large: molybdenum powder from American elements and graphite R4550 from “SGL Group” (Germany).

MELTING PLATEAUS

The melting plateaus shape of $\delta(\text{MoC})\text{-C}$ and repeatability were investigated using the temperature stabilized radiation thermometer of LP5 type. The plateau of the large-cell $\delta(\text{MoC})\text{-C}$ blackbody was also observed by a photometer head in “irradiance” mode. Fig.3 shows the typical melting/freezing plateaus of a small cell measured by LP5 and a melting plateau the large-cell blackbody recorded by the photometer. The cells showed high-quality melting plateau with melting range, varied for the small cells from 120 mK to 250 mK, which is less than that of the well-studied Re-C fixed point. The “best” cell, MoC-C7, demonstrated typical melting range of (120-150) mK that comparable with WC-C. The melting range of the large $\delta(\text{MoC})\text{-C}$ cell was a bit larger, 200 to 350 mK, which is explainable for the bigger ingot. The good shape of the melting plateau allows determining of the point of inflection (POI) with accuracy within ± 20 mK. Repeatability of melting temperature, determined as the standard deviation of POI, was 10 to 20 mK, which is typical for HTFPs.

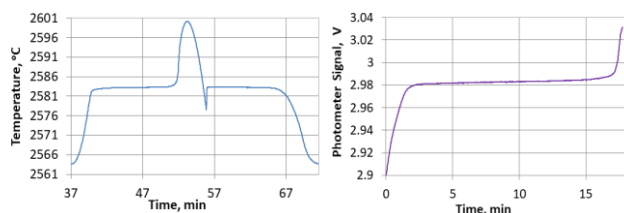


Figure 3. Left: melting/freezing plateaus of small cell. Right: melting plateau of large cell measured by photometer in irradiance mode.

$\delta(\text{MoC})\text{-C}$ TEMPERATURE MEASUREMENT

Thermodynamic temperature of all tested $\delta(\text{MoC})\text{-C}$ cells has been measured as POI temperature by means of comparison with Re-C fixed point, whose thermodynamic temperature was determined as 2747.84 K with standard uncertainty of 0.18 K at the international complain [4]. The same Re-C cell was compared with all the $\delta(\text{MoC})\text{-C}$ cells. When comparing, a $\delta(\text{MoC})\text{-C}$ cell was placed in BB3500MP, while the Re-C cell – in another HTBB furnace. Both furnaces stood next to each other in front of the radiation thermometer LP5 and mounted on the translation stage. Relative spectral responsivity of LP5 was measured against a trap-detector using a 1-m double monochromator. To avoid possible drift, the cells were compared at the same day, wherein the Re-C cell was measured twice, before and after the $\delta(\text{MoC})\text{-C}$ cell.

The standard uncertainty of the $\delta(\text{MoC})\text{-C}$ thermodynamic temperature has been estimated to be 0.35 K. The major components have been related to the realisation of the Re-C fixed point.

The measured values are presented in Table 1. For the small cells the temperature varied from 2856.81 K to 2856.93 K with the average value of 2856.85 K. The cell with the smallest melting range showed the highest temperature. The large cell was measured as it was and with an additional aperture of 3 mm. Temperature shown with the aperture equalled to that average for small cells. Without any aperture the 14mm cell $\delta(\text{MoC})\text{-C}$ blackbody showed the temperature slammed by 0.6 K, similar to Re-C and WC-C large-area blackbodies [1].

Table 1. Measured thermodynamic temperatures of $\delta(\text{MoC})\text{-C}$ blackbodies.

Cell ID	Cavity /opening diameter, mm	T, K
MoC-C7	3/3	2856.93
MoC-C8	5/3	2856.84
MoC-C9	5/3	2856.81
MoC-C10D14	14/3	2856.85
	14/14	2856.25

ROBUSTNESS

The cavity walls of all built cells cracked during the filling or in the early stage of use. Fortunately, no one cell has leaked. All the measurements described above were done with the cracks. Probably the thermal expansion of the graphite used does not match well to the Mo-C alloy. Therefore, proper type of graphite has to be tested searched and selected for the $\delta(\text{MoC})\text{-C}$ fixed point.

REFERENCES

1. B. Khlevnoy et al., Development of large-area high-temperature fixed-point blackbodies for photometry and radiometry, *Metrologia*, 55, S43-S41, 2018.
2. N. Sasajima, Y. Yamada, and F. Sakuma, Investigation of fixed points exceeding 2500 °C using metal carbide-carbon eutectics, *Temperature: Its Measurement and Control in Science and Industry*, V.7, edited by D.C. Ripple, 79-284, AIP, 2, 2003.
3. S. Ogarev et al., High-temperature blackbody models for use in photometry, radiometry and radiation thermometry, *Measurement Techniques*, 58, 1255–1260, 2016.
4. E. Woolliams et al., Thermodynamic temperature assignment to the point of inflection of the melting curve of high-temperature fixed points, *Philosophical Transactions of the Royal Society A*, p. 374: 20150044, 2015.

Reference UVC LED Source

S.V. Nikanenko, A.V. Danilchik, E.V. Lutsenko

*B. I. Stepanov Institute of Physics National Academy of Sciences of Belarus, Minsk, Belarus
s.nikonenko@dragon.bas-net.by*

A compact reference UVC source based on state-of-the-art commercially available LED has been developed at B.I. Stepanov Institute of Physics NAS of Belarus. The paper presents the design and results of the study of the optical characteristics of the radiation of the reference UVC LED source.

INTRODUCTION

UV radiation is widely used to solve various engineering and scientific problems. Efficiency, quality and safety of work performed using UV radiation, is largely determined by the quality of the preliminary metrological support of these works.

There are a number of problems in metrological insurance in the UV spectral region. First of all, it is a significant reduction in the accuracy of the transfer of measured units size from national standards of the corresponding optical quantities to working units in the CIE UV ranges. Second, when measuring in the UV CIE ranges, it is necessary to use a power meter with constant spectral sensitivity inside these ranges and zero outside it, which is very problematic due to the lack of high-quality UV filters. Third, the accuracy of the results of measuring optical characteristics of UV radiation is reduced significantly due to the difference in spectral distributions of the radiation intensity of the test and reference radiation sources.

One of the promising ways to improve the accuracy of measurements in the UV spectral region is the use of reference radiation sources created on the basis of LEDs, due to their stability and long lifetime. Earlier, the Institute of Physics of the NAS of Belarus has developed a number of reference radiation sources for the CIE UV ranges based on LEDs [1 - 3]. In the article the design of the created new reference CIE UVC LED source describes.

DESIGN UVC LED SOURCE

A reference UVC LED source (RUVCS) based on state-of-the-art commercially available one LED emitting at wavelength of 265 nm.

The source operates as follows: the injection

current is supplied to the LED chip 1, the temperature of which is regulated by the Peltier element 4 based on the resistance value of the thermistor 5. The heat generated by the Peltier element is removed through the base 6 and is additionally cooled by a radiator of water or air cooling 11. A temperature controller Arroyo TECSOURCE 5305 were used to stabilize temperature of the RUVCS.

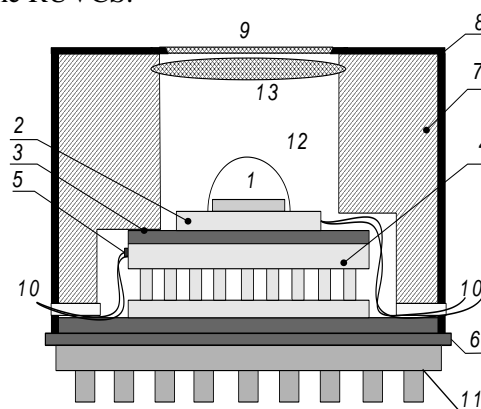


Figure 1. Picture of reference UVC LED source

OPTICAL CHARACTERISTICS OF THE SOURCE

The measurement of optical characteristics of LEDs and RUVCS was carried out using setup for the measurement of optical characteristics of UV-NIR SSL sources emission [4]. The measurements of the were performed at 25°C stabilized temperature.

The inset in figure 2 shows the angular distribution of the radiation intensity of the LED chip. As can be seen from the far field, the radiation intensity is approximately the same within the cone 20°. The observed jumps in the radiation intensity are due to the fact that the LED lens projects an image of the chip to infinity. The radiation intensity jump corresponds to the electrode of the LED chip. To reduce the intensity heterogeneity in this angle, we used a 5° holographic diffuser (inset on Fig. 2).

However, the obtained radiation intensity levels of the RUVCS are insufficient for calibrating UV radiometers. Therefore, a correcting lens 13 and a holographic diffuser 9 are included in the design of the reference source (Fig. 1).

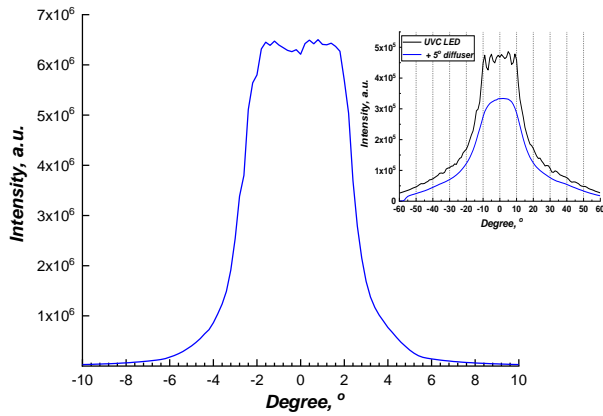


Figure 2 Radiation intensity of reference UVC LED source as a function of angle. Inset shows radiation intensity of UVC LED and UVC LED at 5° diffuser

As can be seen from Fig. 2, only the use of the correcting lens made it possible to increase the power density of the RUVCS by an order of magnitude and significantly reducing the inhomogeneity of radiation intensity in the far field. Fig. 3 shows the dependence of the power density on the injection current at measurement distance 0.5 m from RUVCS and the LED chip.

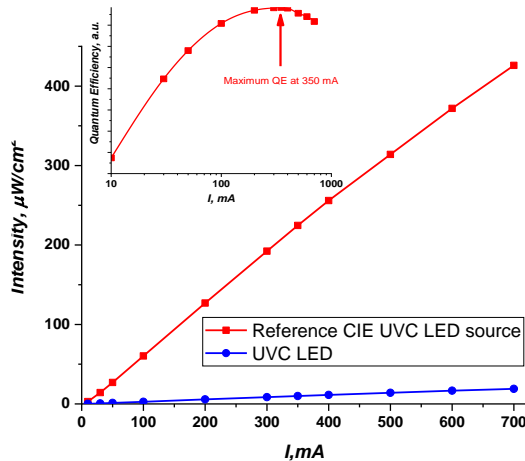


Figure 3 Intensity of reference UVC LED source as a function of injection current. Inset shows radiation intensity of UVC LED and UVC LED at $\pm 5^\circ$ diffuser

As can be seen in the inset in Fig. 3, the maximum quantum efficiency is achieved at an injection current of 350 mA. This corresponds to a power density of $>200 \mu\text{W}/\text{cm}^2$, which provides a fine level for calibrating UV radiometers. Therefore, we recommend this injection current level for source operation. At this level, the radiation spectrum is independent of the viewing angle within the essential radiation intensity levels ($\pm 5^\circ$).

As can be seen from Fig. 4, the radiation intensity of RUVCS are about 5% at the boundary between UVC and UVB ranges.

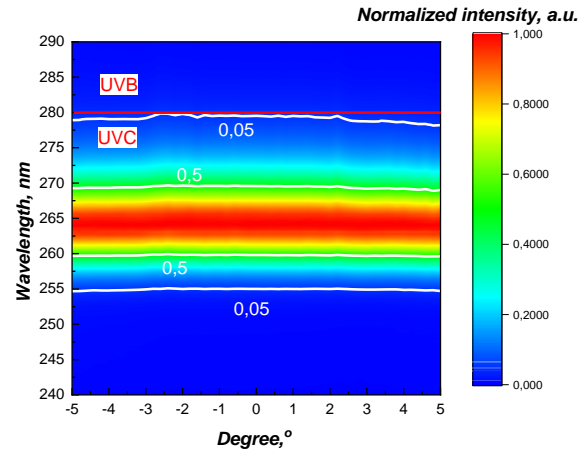


Figure 4 2D color mapping of reference UVC LED source normalized spectra as a function of angle

Fig. 5 show the distribution ($\pm 2\%$) of the radiation intensity of RUVCS without holographic diffuser in the working area at distance 0.5m. The additional use of 1° holographic diffuser in the source leads to an improvement in the uniformity of the distribution of the radiation intensity density up to $\pm 1\%$.

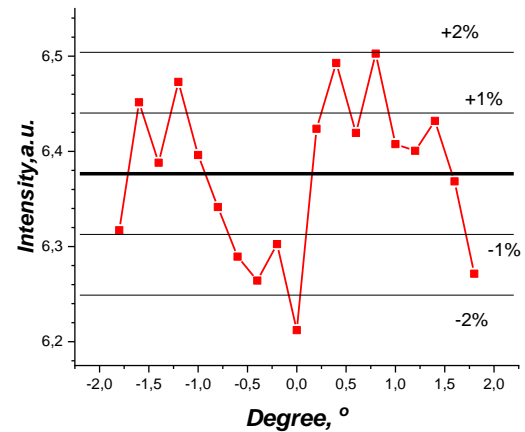


Figure 5 Intensity of reference UVC LED source in the working area

REFERENCES

1. S.V. Nikanenko, *et al.*, A practical method for determination of averaged spectral radiance of UV LED, in Proceedings of 28th CIE session, CIE 216:2015, Vol. 1, Part 2, 1396–1400, 2015.
2. S.V. Nikanenko, *et al.*, Reference UV LED Sources, in Smart Lighting for Better Life: Proc. of the Conf. at the CIE Midterm Meeting 2017, 984–989, 2017.
3. S.V. Nikanenko, A.V. Danilchuk, E.V. Lutsenko, Compact reference UV-LEDs sources with conical diffuse reflectors, in Proceedings of 29th CIE session, CIE x046:2019, Vol. 1, Part 2, 1193–1194/4, 2019.
4. S.V. Nikanenko, *et al.*, Setup for measurement of the optical characteristics of UV-NIR solid-state light sources emission, Proceedings of NEWRAD 2014, ed. S.Park *et al.*, 350-351, 2014.

NATIONAL STANDARD OF BELARUS OF THE UNITS OF RADIANT INTENSITY, SPECTRAL RADIANCE AND IRRADIANCE IN THE SPECTRAL RANGE FROM 0.2 μm TO 3.0 μm

S.V. Nikanenka¹, V.A. Dlugunovich¹, A.V. Kreidzich¹, M.V. Rzhetski¹, D.V. Scums² and E.V. Lutsenko¹

¹*B. I. Stepanov Institute of Physics of the National Academy of Sciences of Belarus, Minsk, Belarus,*

²*Belarusian state institute of metrology - BelGIM, Minsk, Belarus*

s.nikonenko@dragon.bas-net.by

In 2019, a National standard of Belarus of the units of radiant intensity, spectral radiance and irradiance in the wavelengths range from 0.2 μm to 3.0 μm was created. This report describes the details of a based spectral irradiance and radiance facilities.

INTRODUCTION

Spectral irradiance and radiance is one of the most important fundamental radiometric units. It is a key quantity with wide spread applications in industry, medical research, remote sensing and in our day to day life. In 2019, the National standard of Belarus of the units of radiant intensity, spectral radiance and irradiance in wavelengths range from 0.2 μm to 3.0 μm (NSSRI) was developed and constructed in the Institute of Physics of the NAS of Belarus together with the National Metrology Institute of Belarus (BelGIM). The purpose of establishing national standard is to provide metrological services to various R&D laboratories and industries.

NATIONAL STANDARD OF BELARUS OF THE UNITS OF RADIANT INTENSITY, SPECTRAL RADIANCE AND IRRADIANCE IN THE SPECTRAL RANGE FROM 0.2 TO 3.0 μm

The main components of NSSRI are: high-temperature blackbody radiator BB3500M, Linearpyrometer LP5, set-up of the multifunctional spectral facility (MSF), integrating sphere source (ISS), monochrome radiation source (MRS), standard lamps.

The high-temperature blackbody radiator BB3500M is used as the national primary standard for spectral radiance and irradiance in the spectral range from 0.2 μm to 3.0 μm . It was constructed by the All-Russian Institute for Optical and Physical Measurements (VNIIOFI), Moscow. The radiometric temperature of the blackbody is determined with Linearpyrometer LP5 at the

distance of 0.7 m. A precision aperture, which circulating cooling water, is placed in front of the blackbody to define the area of uniform radiance.

Spectral radiance of the blackbody is calculated by the Planck's law. Spectral irradiance on a measurement plane is calculated by using the spectral radiance of the blackbody, precision aperture area and distance between the aperture and input aperture of integrating sphere. A water cooling system has been developed for the BB3500M black body that maintains the temperature of the water in the system with an accuracy of 0.2 °C.

The set-up of the multifunctional spectroradiometrical facility consists two spectral systems, translation table (2.8 m) and portable radiometric benches. Spectral systems consist of UV-VIS and VIS-NIR double monochromators on base monochromators MS266 (SolarLS, Belarus) for ranges 0.20-1.20 μm and 0.35-3.00 μm respectively. The double monochromators there is one entrance and three output ports. To input radiation into the monochromators, an entrance optics block based on a toroidal mirror is installed on the input port. At the output ports, detectors are installed.

The spectral irradiance of the lamp is obtained by using the measured ratio of the multifunctional spectroradiometrical facility output signal for the lamp to that of the spectral irradiance of blackbody at the entrance aperture of the entrance optics.

The working standards used for the spectral irradiance in the spectral range from 250 nm up to 2500 nm are 1000 W FEL-type quartz-halogen lamps (Gigahertz-Optik, Germany) and in the spectral range from 200 nm up to 400 nm are deuterium lamps. The working standards used for the spectral radiance in the spectral range from 350 nm up to 2500 nm are temperature lamps 1000 W TRU 1100-2350 and 200 W SIRSh 8.5-200-1 (Lisma LLC, Russia). The whole NSSRI is optimized for such lamp standards.

The working standards used for the radiant intensity in the spectral range from 250 nm up to

1100 nm are filter radiometers based on 3-element trap detectors (Hohenheide OÜ, Estonia).

SPECTRAL IRRADIANCE CALIBRATION FACILITY

Fig. 1 shows the schematic diagram of spectral irradiance calibration facility.

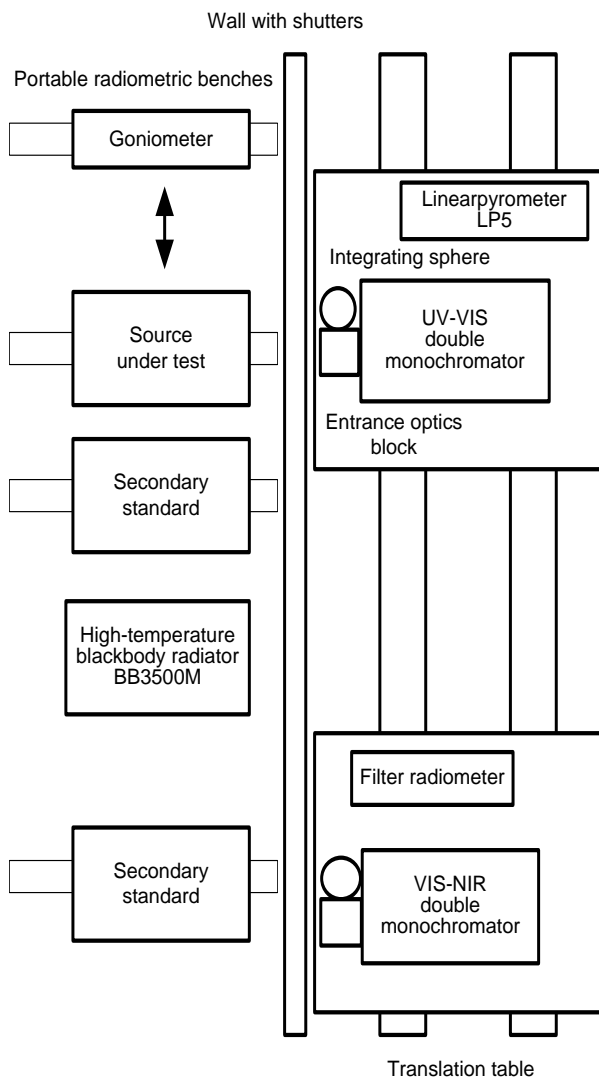


Figure 1. Schematic diagram of the spectral irradiance calibration facility

For measurement of the spectral irradiance an integrating sphere is installed on the input optics block. The inner surface of the integrating sphere used as a diffuser is made of PTFE with inside diameter of 50.8 mm. Its entrance aperture is aligned to radiation sources.

The four gratings with different blazed wavelengths are used by changing one by one corresponding to wavelengths. A PMT, Si-photodiode and InAs infrared detector are used to

measure the output signal from the spectral systems from 200 nm to 800 nm, from 650 nm to 1200 nm and from 1200 nm to 3000 nm respectively. Among detectors, the IR enhanced InAs detector is operated in combination with chopper and lock-in amplifier to measure the small signal at long wavelengths.

The sources can be placed at distances from 4 mm up to 2 m to the opening of the entrance optics.

The design of the spectral irradiance calibration facility allows to measure the spectral irradiance of any radiation sources at distances from 4 mm to 2 m.

In addition, to measure the optical characteristics of LEDs, as well as small-sized sources, the spectral irradiance calibration facility includes an automated goniometer and a number of power supplies and TEC.

SPECTRAL RADIANCE CALIBRATION FACILITY

To measure the spectral radiance two mirrors are placed in front of the input optics block. Its entrance aperture is aligned to radiation sources. As well as when measuring spectral irradiance the four gratings with different blazed wavelengths are used.

A PMT, Si-photodiode, CCD matrix, InAs infrared detector and InGaAs linear imaging sensor are used to measure the output signal from the spectral systems from 350 nm to 800 nm, from 650 nm to 1200 nm, from 350 nm to 1200 nm, from 1200 nm to 3000 nm respectively.

For calibration of spectroradiometers by spectral radiance sources MRS and ISS are used. The MRS is used for measurements of relative spectral responsivity of the devices, and the ISS is used for determining of absolute responsivity. The MRS is based on the monochromator M266-IV (SolarLS) and a temperature lamp SIRSh 8.5-200-1.

The diameter of the ISS is 0.6 m. It has an aperture with diameter of 0.24 m. The ISS is equipped with a set of 6 tungsten halogen lamps of 150 W and 6 tungsten halogen lamps of 250 W each located inside the sphere along the aperture perimeter. The ISS realizes 28 levels of spectral radiance. Radiance homogeneity of the ISS at 650 nm is within about 2 % over the aperture area, whereas the central-point radiance differs from the weighted average radiance by about 0.5 %. Calibration of ISS is carried out by comparison with a blackbody.

Calibration of silicon single-photon avalanche diode detectors using a narrow-bandwidth quantum emitter

Hristina Georgieva¹, Marco López¹, Helmuth Hofer¹, Beatrice Rodiek¹, Justus Christinck¹, Peter Schnauber², Arseny Kaganskiy², Tobias Heindel², Sven Rodt², Stephan Reitzenstein², and Stefan Kück¹

¹Physikalisch-Technische Bundesanstalt, Braunschweig, Germany,

²Institut für Festkörperphysik, Technische Universität Berlin, Berlin, Germany

Corresponding e-mail address: hristina.georgieva@ptb.de

A narrow-bandwidth, traceable single-photon source is used to improve the calibration of single-photon avalanche diode (SPAD) detectors. The near-infrared emission of a single InGaAs quantum dot under non-resonant pulsed excitation is detected simultaneously by two SPAD detectors of the same type, and the ratio of their detection efficiencies has been determined to be 1.059 with a relative standard uncertainty of 0.7 %. This result is validated by a comparison with a standard calibration using an attenuated laser.

INTRODUCTION

Standard calibration methods for SPAD detectors use attenuated laser light, which follows the Poisson statistics. Therefore, even at very low photon fluxes, there is still a nonzero probability for a multiphoton event, which cannot be resolved by an avalanche photodiode operating in the Geiger mode. To circumvent this problem imposed by the photon statistics, it is favourable to use a non-classical light source, a single quantum emitter with a high single-photon purity. Additionally, this new source should simultaneously fulfil the requirement of a directed monochromatic emission, needed for calibration purposes. The narrow emission bandwidth of semiconductor quantum dots makes them perfect candidates for this task.

SINGLE-PHOTON SOURCE

We aim for a high photon flux reaching the detection area of a SPAD detector by means of an efficient quantum emitter combined with a low-loss optical setup. A single InGaAs quantum dot (QD) is embedded into a monolithic microlens, which directs the emitted light into a small solid angle, thus increasing the extraction efficiency into the first lens of the setup (Figure 1.a). The sample is cooled down to 10 K and is non-resonantly excited at 850 nm at a repetition frequency of 80 MHz (see Figure 1.b). Figure 2.a shows a micro-photoluminescence scan of

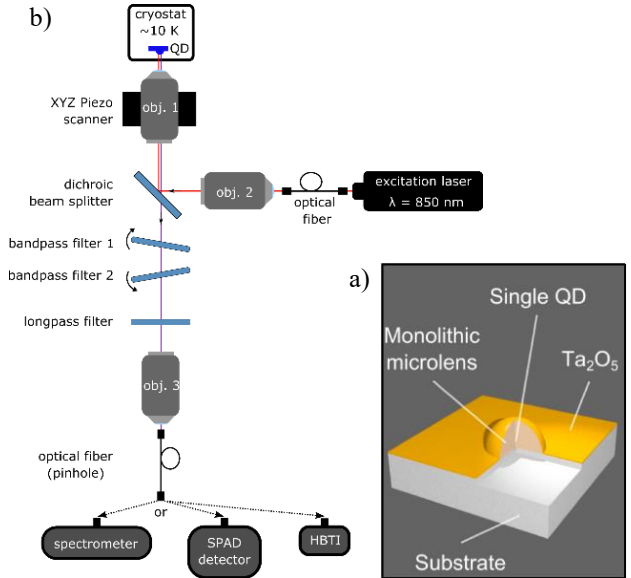


Figure 1. a) Scheme of a deterministic quantum dot microlens [1]. b) Confocal setup.

the QD layer, obtained by confocal imaging. One of the quantum dots, marked by a white circle, is placed in focus for spectral analysis.

To minimize the optical losses, we are using two ultra-narrow bandpass filters for the spectral filtering instead of a monochromator. Each filter transmits about 90% of the incoming near-infrared emission. The exciton recombination line with highest intensity is selected by shifting the transmission window through filter rotation. Figure 2.b shows the presence of a single spectral peak having a full width of half maximum of only 0.04 nm. The emission wavelength is determined to be (922.37 ± 0.02) nm. Finally, the single-photon purity of the emission has been verified with a Hanbury-Brown and Twiss interferometer (Figure 2.c). The histogram of normalized coincidences yields a $g^{(2)}(\tau = 0)$ value of 0.25.

CALIBRATION METHOD

Simultaneous measurement of the photon flux with two SPAD detectors of the same type (SPCM-AQRH-13-FC, Perkin Elmer) employing the fiber exchange

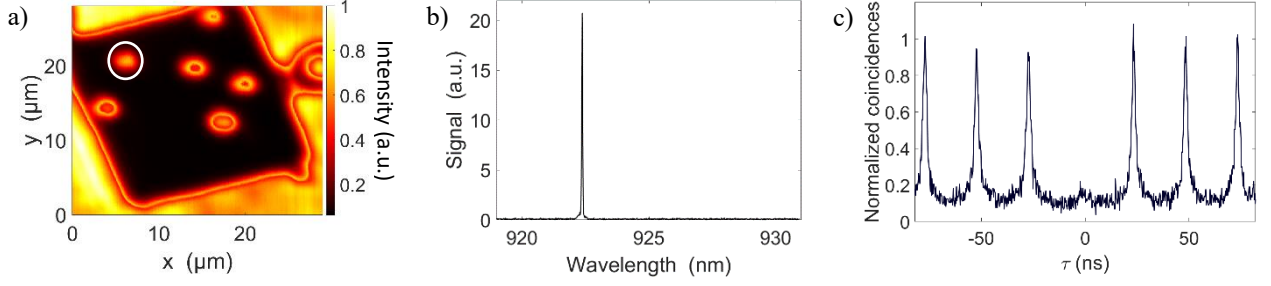


Figure 2. a) Micro-photoluminescence scan of the quantum dot layer at 10 K. b) Spectrum of the spectrally filtered quantum dot emission under non-resonant excitation. c) Corresponding second-order correlation measurement for pulsed excitation.

calibration technique [2] enables us to determine the ratio of detection efficiencies r according to:

$$r = \frac{\eta_{\text{SPAD1}}}{\eta_{\text{SPAD2}}} = \sqrt{\frac{\dot{N}_{\text{A}}^{\text{I}}}{\dot{N}_{\text{B}}^{\text{I}}} \cdot \frac{\dot{N}_{\text{B}}^{\text{II}}}{\dot{N}_{\text{A}}^{\text{II}}}} \cdot f_{\text{cr}}, \quad (2)$$

where $\dot{N}_{\text{A,B}}^{\text{I,II}}$ denotes the measured detector counts per second. The intrinsic dark counts have been subtracted from the measured values. The single-photon emission of the quantum dot is split into two optical fibres A and B, which are connected to detectors 1 and 2 correspondingly. For the second (II) measurement, the positions of the detectors are switched, so that equation 2 becomes independent of the coupling ratio of the beam splitter.

An additional correction factor f_{cr} takes into account the temporal stability of the light source, as well as the reproducibility deduced from repeating the measurement ten times. An Allan deviation analysis was conducted to determine the optimal averaging time. The influence of after-pulse probability and dead time can be neglected due to the very low mean photon number (below 0.002) used for the calibration.

RESULTS

The SPAD calibration is conducted with a photon flux of approx. 120 kHz, originating from a single spectral line of the quantum dot emission spectrum. This photon flux corresponds to an optical power of 26 fW and falls into the linear regime of the silicon SPAD detectors, so that no attenuation is needed and a lower overall uncertainty can be reached. The detection efficiency ratio was determined to be $r_{\text{QD}} = 1.059 \pm 0.008$. As expected, the value for r_{QD} is very close to unity since we are comparing two detectors of the same type with very similar properties. Additionally, both detectors were calibrated against a reference analogue detector by means of the double attenuator technique [3]: $\eta_{\text{SPAD1}} = 0.324$, $\eta_{\text{SPAD2}} = 0.305$ with a

relative standard uncertainty of 1%. This yields a ratio of $\eta_{\text{laser}} = 1.063 \pm 0.015$. The results from both independent methods are in a very good agreement.

In conclusion, the presented light source fulfils the criteria of an efficient, directed, monochromatic single-photon emission. Moreover, we have demonstrated its usefulness for detector calibrations in the near infrared in the field of quantum radiometry. Next steps will be to increase the photon flux of the single-photon source by using more sophisticated structures allowing for a higher collection efficiency.

ACKNOWLEDGEMENT

This work was funded by the project EMPIR-17FUN06 SIQUEST. This project received funding from the EMPIR programme co-financed by the Participating States and from the European Union's Horizon 2020 research and innovation programme. We gratefully acknowledge the support of the Braunschweig International Graduate School of Metrology B-IGSM and the DFG Research Training Group 1952 Metrology for Complex Nanosystems.

REFERENCES

1. P. Schnauber et al., Bright single-photon sources based on anti-reflection coated deterministic quantum-dot microlenses, *Technologies* 4, 1, 2016.
2. W. Schmunk et al., Radiometric calibration of single photon detectors by a single photon source based on NV-centers in diamond, *Journal of Modern Optics*, 58:14, 1252-1259, 2011.
3. M. López et al., Detection efficiency calibration of single-photon silicon avalanche photodiodes traceable using double attenuator technique, *Journal of Modern Optics*, 62:20, 1732, 2015.

Calibration of free-space and fiber-coupled single-photon detectors

Thomas Gerrits¹, Alan Migdall², Joshua C. Bienfang², John Lehman¹, Sae Woo Nam¹, Jolene Splett¹, Igor Vayshenker¹, Jack Wang¹

¹National Institute of Standards and Technology, Boulder, CO, 80305 (USA)

²Joint Quantum Institute, University of Maryland, National Institute of Standards and Technology, Gaithersburg, MD, 20899 (USA)

Corresponding e-mail address: gerrits@nist.gov

We present our measurements of the detection efficiency of free-space and fiber-coupled single-photon detectors at wavelengths near 851 nm and 1533.6 nm. We investigate the spatial uniformity of one free-space-coupled silicon single-photon avalanche diode (SPAD) and present a comparison between fusion-spliced and connectorized fiber-coupled single-photon detectors. We find that our expanded relative uncertainty for a single measurement of the detection efficiency is as low as 0.7 % for fiber-coupled measurements at 1533.6 nm and as high as 1.8 % for our free-space characterization at 851.8 nm [1].

Future Optical Quantum Networks will need components based on single-photon quantum technologies and those components will require characterization. We start with single-photon detectors, which in turn can be used to characterize other quantum network components such as single-photon sources, fiber losses, network switches, etc.

We measure detection efficiency using a calibrated attenuation stage and a calibrated optical power meter as shown in Figure 1. Laser power is first roughly set using a variable fiber attenuator (VFA_{input}) and then sent to a splitter/attenuator unit, which has a highly attenuated output and high-light-level monitor. The ratio of the output to the monitor ($R_{out/mon}$) is $\approx 10^{-5}$ and is measured using an optical power meter (PM) and monitor optical power meter (PM_{mon}). Both, PM and PM_{mon}, require a nonlinearity (relative) calibration, whereas only PM requires an absolute responsivity calibration. Key to the measurements are the transmittance of the splitter/attenuator unit and the output-to-monitor ratio of the splitter/attenuator unit. Both are determined from the fiber beam splitter (FBS) splitting ratio and the attenuation of VFA, using the power meter and the monitor power meter. In addition, this method relies on the stability of the splitter/attenuator unit's output-to-monitor ratio, the polarization and wavelength of the light versus time, and the independence of the output-to-monitor ratio

with input optical power. We verify each of these either during the measurement or by prior characterization.

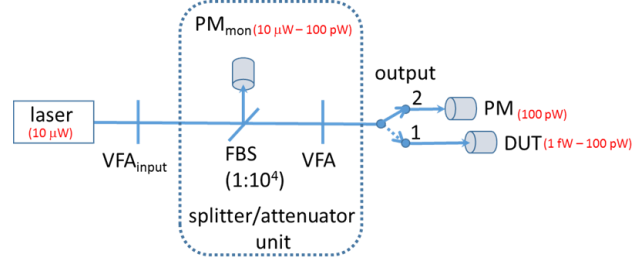


Figure 1. Schematic of the measurement setup.

Detection efficiency results are shown (fig. 2) for a free-space-coupled silicon single-photon avalanche detector (SPAD) measured in two modes. One using a continuous wave (CW) and another using a mode-locked Ti:sapphire laser. Detection efficiency (DE) is measured at a range of detector count rates so that the DE can be determined at 1 cnt/s and 10^5 cnt/s. Setup stability and repeatability is achieved for the extracted detection efficiencies at the two rates of 1 cnt/s and 10^5 cnt/s (fig. 2).

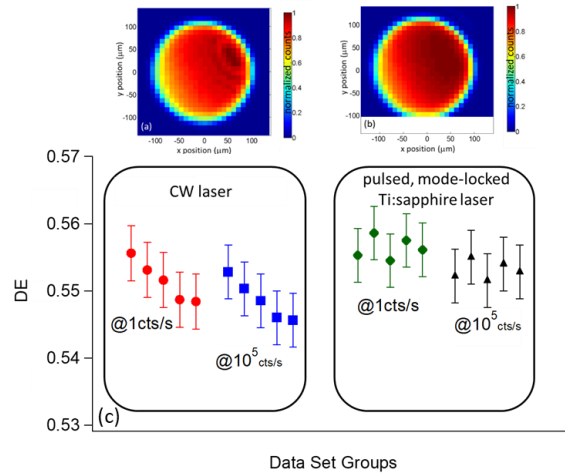


Figure 2. Measured DE for the NIST8103 detector at 1 cnt/s and 10^5 cnt/s made with CW laser and a pulsed Ti:sapphire laser, as labelled. Error bars represent the extracted standard uncertainties ($k=1$) for each measurement.

The CW laser results show a larger variation in the extracted DE at both count rates. The spatial response of the SPAD using the CW and Ti:sapphire laser, measurements are also shown. The CW laser results show fringes in the spatial response. Thus, it will have higher sensitivity to slight spatial misalignments than for the measurements made with the Ti:sapphire laser.

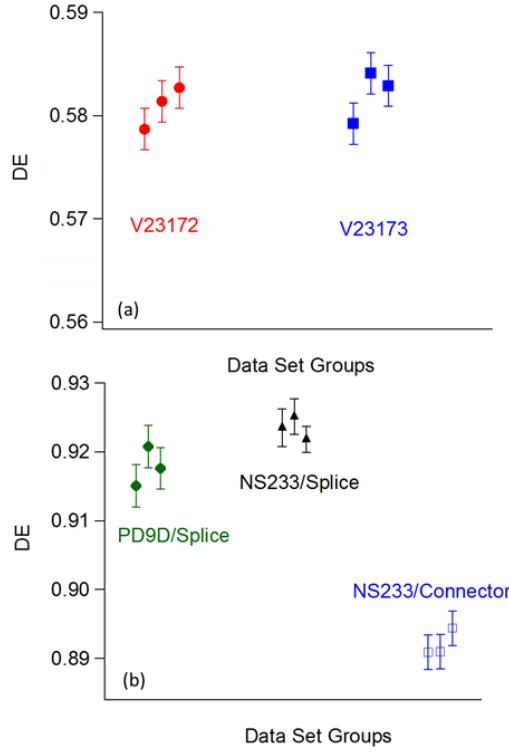


Figure 3. Summary of measurements for fiber-coupled detectors (a) V23172, V23173, and PD9D at 851.8 nm and (b) NS233 at 1533.6 nm. For detector NS233, fusion splicing and FC/PC connectors were used to connect the DUT fiber to the output of the FBS as indicated. Error bars are the extracted standard uncertainties ($k=1$) of each measurement

Figure 3 shows the extracted detection efficiencies at 10^5 cnt/s of three fiber-coupled detectors, two SPADs: V23172 and V23173 and one superconducting nanowire single photon detector (SNSPD): PD9D at a wavelength of 851.8 nm. The DEs for both SPADs were determined with an FC/PC fiber connector at the output fiber of the FPC, whereas the SNSPD's DE was determined by fusion splicing the detector fiber. Good setup reproducibility is observed for all three detectors. Figure 3 also shows the calibration results of an SNSPD optimized for 1550 nm (NS233) at a measurement wavelength of 1533.6 nm. The DE of NS233 was determined with an FC/PC fiber-to-fiber connector union and by fusion splicing the detector fiber to the output fiber of the FPC. The measured extracted DE at 10^5 cnt/s through a fusion splice is

higher than that measured through an FC/PC connector, as expected. The repeatability between individual runs for both cases is comparable to the repeatability achieved for the 851.8 nm fiber-coupled measurement.

Table 1 summarizes the results of this work for all detectors at a count rate of 10^5 cnt/s. The DE and 95 % coverage intervals were calculated with the NIST consensus builder [2] and linear opinion pooling for the individual measurement outcomes for each detector. Relative expanded uncertainties as low as 0.70 % are achieved in the case of a fiber-coupled SNSPD at 1533.6 nm. Whereas for the free-space measurements at 851.8 nm, the relative expanded uncertainty is 1.8 % with a CW laser. The main source of uncertainty for the free-space measurements is the uncertainty in the detector response due to laser-beam-detector alignment. For all-fiber-coupled detectors this uncertainty is not relevant but is replaced with a connector and fiber-end reflection-loss uncertainty. In this study, we were not able to compare several FC/PC connectors to establish an uncertainty associated with different commercially available fiber connectors. However, we believe that for many different FC/PC connectors the loss uncertainty will be larger than our overall uncertainty budget. For the NS233 detector, we observe a ≈ 3.5 % lower system DE than when splicing the fibers. In the extreme case, an FC/PC connection may have very low losses (close to 0 %). Therefore, we speculate that this measurement already reveals a variation of at least 3.5 % in the extracted DE for the FC/PC connector method.

detector		DE at 10^5 cnt/s	95 % cov. int.	rel. exp. unc.(%)
NIST8103	fs, Ti:Sa	0.5532	[0.5449, 0.5615]	1.5
NIST8103	fs, CW	0.5490	[0.5397, 0.5587]	1.8
V23172	fc, FC/PC	0.5811	[0.5708, 0.5911]	1.8
V23173	fc, FC/PC	0.5821	[0.5735, 0.5911]	1.6
PD9D	fc, splice	0.9178	[0.9066, 0.9292]	1.1
NS233	fc, FC/PC	0.8921	[0.8859, 0.8996]	0.73
NS233	fc, splice	0.9234	[0.9171, 0.9298]	0.70

Table 1. Summary of results for all measured single photon detectors. Quoted are the photon delivery method (fc: fiber-coupled, fs: free-space, Ti:Sa: Ti:sapphire laser, CW: CW laser, splice: fusion spliced, FC/PC: FC/PC fiber connector), mean DEs at 10^5 cnt/s, the 95 % coverage intervals and the relative expanded uncertainties ($k=2$).

REFERENCES

- [1] T. Gerrits et al., *Metrologia* **57**, 015002 (2020)
- [2] <https://consensus.nist.gov/>

Molecule-based single photon source for quantum radiometry

Stefan Kück¹, Marco López¹, Pietro Lombardi², Constanza Toninelli², Marco Trapuzzano³, Maja Colautti⁴, Giancarlo Margheri⁵, Ivo P. Degiovanni⁶

¹Physikalisch-Technische Bundesanstalt (PTB), Braunschweig, Germany, ²Istituto Nazionale di Ottica (CNR-INO), Florence, Italy, ³Università degli Studi di Firenze, Florence, Italy, ⁴LENS, Università degli Studi di Firenze, Florence, Italy, ⁵Istituto dei Sistemi Complessi (CNR-ISC), Florence, Italy, ⁶Istituto Nazionale di Ricerca Metrologica (INRiM), Torino, Italy

Corresponding e-mail address: stefan.kueck@ptb.de

In this paper we report on the calibration of the detection efficiency of a Silicon photon avalanche detector via comparison against an analogue, calibrated Silicon photodiode using a single-photon source based on the emission of an organic dye molecule. The single-photon source used had a total photon flux of 1.32×10^6 photon per second (corresponding to ≈ 334 fW), an emission linewidth of < 0.2 nm and a single-photon purity given by a $g^{(2)}(t=0)$ value < 0.1 . The obtained standard measurement uncertainty is between 2 % and 6 %, main contribution is the Silicon photodiode detector noise.

INTRODUCTION

Single-photon sources are considered being one of the major building blocks in many quantum optical applications, so e.g. in quantum key distribution, quantum computing and quantum enhanced optical measurements [1]. Besides these applications, also they are considered being ideal sources for radiometry, especially considering the field of quantum radiometry, i.e. where low photon fluxes need to be measured with low uncertainty [2]. Furthermore, single-photon sources in principle offer the possibility to become new standard photon sources [3, 4], complementing the blackbody radiator and the synchrotron radiation source. This is simply due to the fact, that the optical flux is given by $\Phi = fhc/\lambda$, where f is the repetition rate of the excitation laser, h is the Planck constant, c is the speed of light and λ is the wavelength of the emitted radiation. However, current single-photon sources are far from being that ideal, due to non-unity collection and quantum efficiency. In this paper, a single-photon source based on the dibenzoterrylene (DBT) molecule is used as single-photon source for the calibration of a single-photon detector (Si-SPAD) directly against a classical Silicon photodiode, which is traced to the primary standard for optical radiant flux, i.e. the cryogenic radiometer.

THE SINGLE-PHOTON SOURCE

The single-photon source used in the experiments is constituted by an isolated dibenzoterrylene (DBT) molecule embedded into an anthracene (AC) host matrix. Details of the source can be found in [5]. The monochromatic single-photon source has an operating wavelength of (785.6 ± 0.1) nm and generated an adjustable photon flux at the location of the detectors between 144000 photon per second and 1320000 photons per second, corresponding to an optical radiant flux between 36.5 fW and 334 fW. The source showed a high single-photon purity indicated by a second-order autocorrelation function at zero time delay below 0.1 throughout the whole flux range. The single-photon source is operated in continuous wave at a temperature of 3 K.

CALIBRATION OF STANDARD DETECTOR

The standard detector used for the photon flux measurement of the single-photon source was an analogue ultra-low noise Si detector (Femto, FWPR-20-s). It is a fibre coupled Si-photodiode with an active area of $1.1 \text{ mm} \times 1.1 \text{ mm}$ and a transimpedance amplifier with a gain of $1 \times 10^{12} \text{ V/A}$. The minimum noise equivalent power (NEP) of the detector is $0.7 \text{ fW/Hz}^{1/2}$. Its spectral responsivity $s_{\text{Si}}(\lambda)$ was determined by calibrating it against a working standard traceable to PTB's primary standard for optical power, the cryogenic radiometer [6]. The spectral responsivity of the low noise Si detector obtained at 786 nm is:

$$s_{\text{Si}}(\lambda=786 \text{ nm}) = (0.5752 \pm 58 \times 10^{-4}) \text{ A/W} \quad (1)$$

This value was used for the calibration of the Si-SPAD detector in the experiments with the single-photon source.

CALIBRATION OF SI-SPAD

The detection efficiency of a Si-SPAD detector (Perkin Elmer, SPCM-AQRH-13-FC) is determined

by comparing the photon flux measurements of the single-photon source carried out with the SPAD detector with those of an analogue reference Si-detector. Both detectors are fibre-coupled, equipped with a FC/PC fibre connector, optimized for a multi-mode fibre. The detection efficiency of the Si-SPAD detector, η_{SPAD} , is determined by

$$\eta_{\text{SPAD}} = \langle N_{\text{SPAD}} \rangle / \langle N_{\text{ref}} \rangle = \langle N_{\text{SPAD}} \rangle / (\langle \Phi_s \rangle E) \\ = \langle N_{\text{SPAD}} \rangle / (\langle I_f \rangle s_{\text{ref}} E) \quad (2)$$

where N_{SPAD} is the count rate measured with the Si-SPAD detector, N_{ref} is the photon flux rate derived from the measurement of the optical flux Φ_s and the photon energy E (with $E = 2.53 \times 10^{-19}$ J for photons at a wavelength of 785.6 nm). Φ_s is obtained as the ratio between the measured average photocurrent $\langle I_f \rangle$ and the reference detector responsivity s_{ref} . In the experiments, photon fluxes between 0.144×10^6 photons per second and 1.32×10^6 photons per second, which corresponds to an optical power range between 36.5 fW and 334 fW, were applied.

In Figure 1 the detection efficiency of the Si-SPAD detector is shown as a function of the photon rate at the detector. As can be seen, the detection efficiency starts to decrease slightly towards higher photon fluxes, caused by the detector deadtime. This is because the emission rate of the molecule already reaches regimes, where the deadtime of the detector already influences the measured detection efficiency η_{SPAD} , because due to the short emission decay time of the DBT molecule of about 4 ns, there are already multiple emission events within the detector deadtime.

The standard uncertainty of the detection efficiency was also determined. The model equation for the calculation is given by:

$$\eta_{\text{SPAD}} = hc/\lambda s_{\text{si}} F_{\text{Amp}} N_{\text{SPAD}} / (V_f (1 - F_{\text{Lin}})) \quad (3)$$

where h is the Planck constant, c is the speed of the light, λ is the wavelength, F_{Amp} is the amplification factor of the internal amplifier of the reference detector, V_f is the photo-voltage measurement of the Si-detector measurement, F_{Lin} is the linearity factor correction of the Si reference detector and N_{SPAD} are the Si-SPAD counts including dark counts correction. The different contributions for a photon rate of $\approx 7.64 \times 10^5$ photons per second, which corresponds to an optical power of ≈ 193 fW, are as follows: $u(h) = 0\%$, $u(\lambda) = 0.01\%$, $u(c) = 0\%$, $u(s_{\text{si}}) = 0.40\%$, $u(V_f) = 1.87\%$, $u(F_{\text{Amp}}) = 0.10\%$, $u(F_{\text{Lin}}) = 0.03\%$, $u(N_{\text{SPAD}}) = 0.02\%$, giving a combined standard uncertainty u_c

$= 1.92\%$. In general, the standard uncertainties are in the range between 2 % and 6 %, depending on the photon rate. The lower the photon rate, the higher the uncertainty, because of the increasing reference detector noise. The final value obtained for the Si-SPAD detection efficiency is $\eta_{\text{SPAD}} = (0.603 \pm 0.012)$.

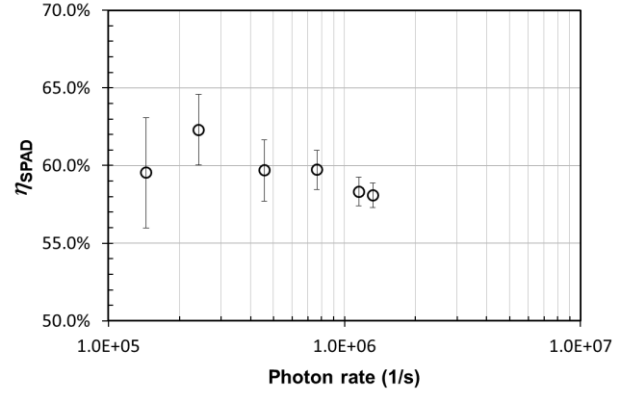


Figure 1. Detection efficiency as a function of the photon rate at the detector. The standard uncertainties are also shown as error bars. (Adapted from [5]).

SUMMARY

The direct calibration of the detection efficiency of a Si-SPAD detector with a calibrated analogue Si-photodiode, traceable to the cryogenic radiometer, using a true, nearly monochromatic single-photon source was presented. The obtained uncertainties were between 2 % and 6 %, mainly caused by the standard detector noise. Next steps will be the implementation of pulsed excitation in order to avoid detector dead time effects on the calibration result.

ACKNOWLEDGEMENT

This work was funded by the project EMPIR-17FUN06 SIQUST. This project received funding from the EMPIR programme co-financed by the Participating States and from the European Union's Horizon 2020 research and innovation programme.

REFERENCES

1. N. Sangouard et al., Journal of Modern Optics 59, 1458 (2012).
2. C. J. Chunnillall et al., Optical Engineering 53, 081910 (2014).
3. J. Y. Cheung et al., Journal of Modern Optics 54, 373 (2007).
4. B. Rodiek et al., Optica 4, 71 (2017).
5. P. Lombardi et al., Adv. Quantum Technology (2019), doi:10.1002/qute.201900083.
6. L. Werner et al., Metrologia, 37, 279 (2000).

Pilot study on the detection efficiency measurement of InGaAs/InP single-photon detectors

Marco López¹, Alice Meda², Geiland Porrovecchio³, Robert Kirkwood⁴, Marco Genovese², Giorgio Brida², Marek Šmid³, Christopher Chunnillall⁴, Ivo Pietro Degiovanni² and Stefan Kück¹

¹ *Physikalisch-Technische Bundesanstalt (PTB), Braunschweig, Germany,*

² *Istituto Nazionale di Ricerca Metrologica (INRIM), Torino, Italy,*

³ *Cesky Metrologický Institut (CMI), Brno, Czech,*

⁴ *Republic, National Physical Laboratory (NPL), Hampton Road, Teddington, TW11 0LW, United Kingdom*

Corresponding e-mail address: marco.lopez@ptb.de

We present the results of a pilot study on the detection efficiency calibration of a free-running fibre-coupled InGaAs/InP single-photon avalanche detector carried out by four European national metrology institutes (NMIs). The calibration is performed using different experimental setups and reference standards with independent traceability chains at the wavelength of 1550 nm. The detection efficiency of the single-photon detector under test was determined for a mean photon number from 0.07 to 1.8, which correspond to approx. from 16250 photons/s to 203 000 photons/s, respectively.

INTRODUCTION

InGaAs/InP single-photon avalanche detectors (SPADs) are today the most frequently used detectors in ultra-high sensitivity applications such as quantum communication and quantum information processing, specifically fibre-based Quantum Key Distribution (QKD) [1-2] usually operated at the wavelength of 1550 nm. The traceable calibration of such detector is of great importance to fully guarantee the reliability of a quantum detection systems. Therefore, several national metrological institutes (NMIs) are currently putting great efforts into developing novel measurement methods and calibration facilities, enabling the performance of traceable calibration of such detectors by using reference standards.

In this paper we present the results of the pilot study on the detection efficiency measurements carried out by four European metrology institutes: CMI, INRIM, NPL and PTB, whose main purpose is to provide a snapshot of their measurement capabilities in the field of photon counting detection at telecom wavelengths.

DEVICE UNDER TEST

The device under test (DUT) used in this study was a fibre-coupled free-running InGaAs/InP single-photon avalanche detector from ID Quantique, model: ID-220, see Figure 1(a). Previous to the calibration, the detection probability level and the dead time of the DUT were configured to 10 % and 10 μ s, respectively. Furthermore, to achieve high reproducibility of the measurements, the DUT was operated with a single-mode FC/PC fibre patch cable connected to its input optical port, where the measurement setups of all participating laboratories were connected by means of an FC/PC mating sleeve. Thus, the detection efficiency measured by all participating laboratories is referenced to this optical connection.

MEASUREMENT PRINCIPLE

The measurement principle used by all participating laboratories for determining the detection efficiency of the DUT η_{DUT} is based on the substitution method

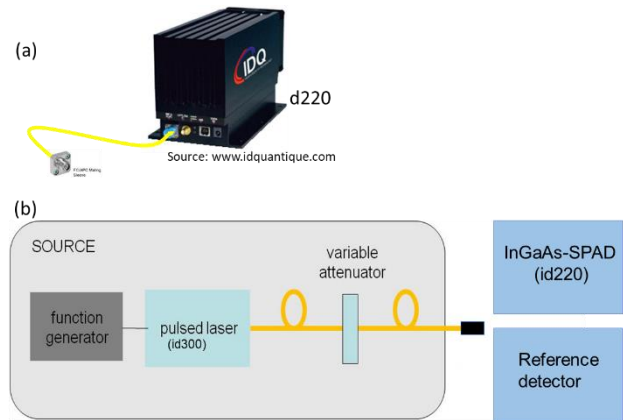


Figure 1. (a) InGaAs/InP free-running single-photon avalanche detector (ID Quantique ID-220). (b) Simplified scheme of the measurement principle (substitution method) used for determining the detection efficiency of the SPAD detector.

(see the simplified setup in Figure 1(b)). This method consists in comparing the optical power, corresponding to the effective number of photons per second, registered by the SPAD detector with the incident mean optical power per laser pulse determined by using a reference analogue detector. That is, $\eta_{\text{DUT}} = P_c / \alpha \cdot P_0$, where P_0 is the optical power measured with the variable attenuator set to 0 dB, α is the attenuation factor of the variable attenuator and P_c is the average optical power corresponding to the effective photon rate measured by the DUT. P_c is calculated from the photon rate ρ absorbed by the DUT, corrected for dead time and dark counts, and the energy of the photon $h \cdot c / \lambda$, that is, $P_c = \rho \cdot h \cdot c / \lambda$.

The light source used for the detector calibration was a short-pulse laser source (ID Quantique, id300) externally triggered to produce sub-nanosecond pulses of approximately 300 ps duration at a repetition rate $f_{\text{laser}} = 110$ kHz. Thus, the value of the photon rate absorbed by the DUT is calculated by $\rho = -f_{\text{laser}} \cdot (1 - q)$, where q is the probability of having a “click” per laser pulse during the detection process. However, since the dead time D of the DUT is larger than $\tau = 1/f_{\text{laser}}$, i.e. $\tau < D < 2\tau$, a correction to obtain the real value of q is required. The model developed in this work for q corrects the influence of the dark counts and the dead time D of the detector during the detection process. That is,

$$q = \frac{\rho_{\text{click}}}{f_{\text{laser}} - \rho_{\text{click}}} + \frac{f_{\text{laser}} \cdot (\rho_{\text{click}} - \rho_{\text{click}}^2 \cdot D + f_{\text{laser}} \cdot (\rho_{\text{click}} \cdot D + \rho_{\text{click}}^2 \cdot D^2 - 1))}{D \cdot (f_{\text{laser}} - \rho_{\text{click}})^2 (f_{\text{laser}} - \rho_{\text{click}} + \rho_{\text{click}} \cdot f_{\text{laser}} \cdot D)} \quad (1)$$

where ρ_{click} is the photon rate counted by the DUT and ρ_{dark} is the dark counts. In addition, since the detector dead time D also affects the detector dark counts, we corrected it by $\rho_{\text{dark}} = \rho'_{\text{click,dark}} / (1 - \rho'_{\text{click,dark}} \cdot D)$, where $\rho'_{\text{click,dark}}$ is the dark counts measured in absence of light.

RESULTS

Figure 2 shows the detection efficiency of the DUT determined by all participants for a mean photon number per pulse between 0.07 and 1.8, which corresponds to a photon rate of approx. 16250 photons/s and 203 000 photons/s, respectively. The detection efficiency without dead time corrections, obtained from the measurements performed by CMI, is also included, which clearly shows the typical detection efficiency saturation of the detector. Moreover, the average value and the expanded

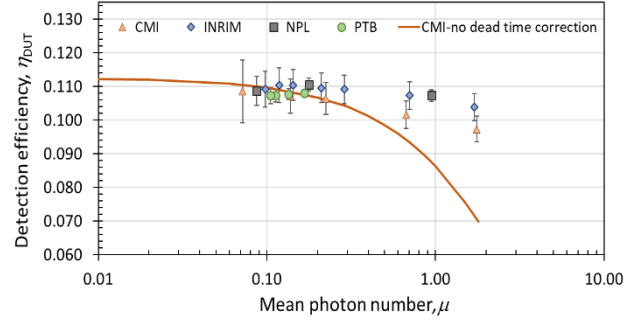


Figure 2. Detection efficiency of the InGaAs/InP SPAD detector measured by all participants between the mean photon number per pulse from 0.07 and 1.8, which correspond to a photon rate of approx. 16250 photons/s and 203 000 photons/s, respectively. Error bars: expanded uncertainty ($k=2$). Solid line: detection efficiency without detector dead time correction.

uncertainty reported by the participants are shown in Table 1.

Table 1. Average and expanded uncertainty of the detection efficiency reported by each participant laboratory.

Laboratory	Participant detection efficiency, η_p	Expanded uncertainty
CMI	0.1042	0.0054 (5.2%)
INRIM	0.1086	0.0050 (4.7%)
NPL	0.1089	0.0026 (2.4%)
PTB	0.1076	0.0024 (2.2%)

CONCLUSIONS

A pilot study on the measurement of the detection efficiency of fibre-coupled free-running InGaAs/InP-SPAD detectors was presented. The evaluation of the detection efficiency included the correction of the dead time of the device under test. The measured values reported by all participants are within the expanded uncertainty of the mean.

Acknowledgment: The work reported on this paper was funded by project EMPIR 14IND05 “MIQC2” and 17FUN06 SIQUST. This project received funding from the EMPIR program co-financed by the Participating States and from the European Union Horizon 2020 research and innovation program.

REFERENCES

1. R. H. Hadfield, Nature Photonics 3, 696–705 (2009).
2. D. Stucki, et al., Journal of Modern Optics, 48, Issue 13, 1967-1981 (2001).

Optical frequency metrology based on photon counting

Thiago Ferreira da Silva¹

¹National Institute of Metrology, Quality and Technology - INMETRO, Duque de Caxias – RJ, Brazil

Corresponding e-mail address: tfsilva@inmetro.gov.br

Low power can be a concern for traditional calibration of frequency-stabilized laser sources against a reference using the heterodyne beating technique. Here, the relative difference between standard and test sources is obtained at few-photon level from correlated photon counts in a Hong-Ou-Mandel interferometer. Uncertainty is computed and results are validated against traditional heterodyne measurement system.

INTRODUCTION

Practical realization of the meter is based on standard frequencies recommended by the International Committee for Weights and Measures – CIPM [1], including stabilized laser sources (for example, a He-Ne laser referenced to a hyperfine transition $^{127}\text{I}_2$ molecule). A secondary laser is calibrated against this reference standard by heterodyne beating of optical frequencies. This well-known technique translates optical frequencies into their difference, f_{beat} , as $I(t) \propto \sqrt{I_1 I_2} \cos(2\pi f_{\text{beat}} t)$, where $I_{1,2}$ are optical intensities. The resulting signal is measurable in the RF range, provided the frequency difference, $f_{\text{beat}} = |\nu_1 - \nu_2|$, is within the bandwidth of the detection instrumentation. However, low intensity limitation is a practical concern that can jeopardize the measurement capability.

Two-photon interference in a Hong-Ou-Mandel (HOM) interferometer is also a well-known phenomenon [2]: two photons entering a symmetric beam splitter (BS) through different ports tend to bunch together at a random output whenever they are fundamentally indistinguishable. Thus, scanning the relative output temporal modes while monitoring the coincidences between single-photon detectors (SPDs) results in the HOM dip. Furthermore, frequency displacement between photons may result in an oscillatory pattern within the dip [3], even for weak coherent states, as in the case of faint laser sources. This feature is explored in the few-photon heterodyne spectroscopy (FPHS) technique [4,5].

Here, the FPHS technique is used as a tool for calibration of the frequency difference between a test laser and a reference laser traced to CIPM standard radiation. Two frequency-stabilized He-Ne lasers are

attenuated and their frequency difference is measured from the interferogram obtained with photon counting. Uncertainty is computed and the method is validated against traditional heterodyne system.

EXPERIMENTAL SETUP

Experimental setup for the measurement system is depicted in Fig. 1. Two independent laser sources (633 nm) couple into optical fibers and feed the HOM interferometer. Single-mode optical fibers ensure spatial modes overlap. The Si avalanche photodiode-based SPDs operate in free-running Geiger mode and are connected to the *start* and *stop* ports of the high-resolution TIC. Time intervals are arranged in a histogram of coincidences per time interval, later converted into an interferogram over relative temporal mode. A delay line at *stop* channel displaces the matched times 3.4 ns from zero. States of polarization (SOP) are made parallel using the auxiliary setting setup and additional quarter- (QWP) and half-wave plates (HWP). Intensities are tuned down to few-photon level and matched by tilting the lenses (L) used to couple laser into fiber.

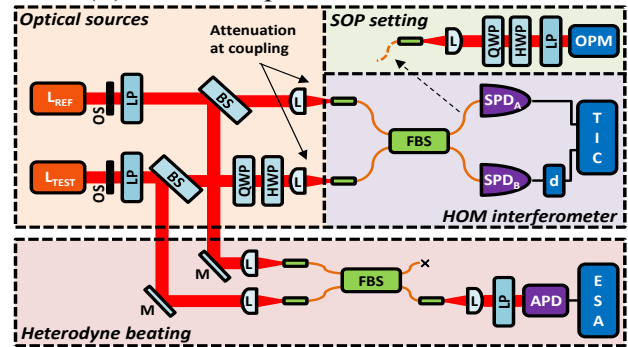


Figure 1. Experimental setup.

Samples of each beam (before attenuation) are also superposed in a photodiode and the heterodyne beating signal is observed in an ESA for validation.

RESULTS

After warm-up of the lasers, time intervals between the SPDs are collected during an one-hour period (~250k samples) into a histogram (Fig. 2a.1). Exponential decay of data (due to Poisson statistics of the photon flux [6]) is corrected and the interferogram is obtained, as depicted in Fig. 2a. The envelope of the interferogram is associated to the mutual

coherence of the laser sources, whilst the oscillatory pattern (zoom in shown in Fig. 2a.2) depends on the beat frequency.

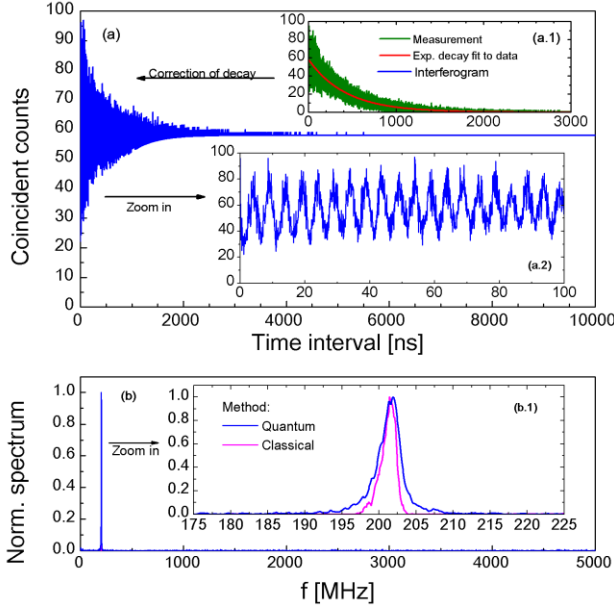


Figure 2. Experimental results: (a) interferogram obtained from histogram (see inset a.1), with first 100 ns in the detail of inset a.2; (b) Power spectrum of the FFT of the interferogram and comparison to results with higher power levels (inset b.1).

Fourier transform of the interferogram results in the convolution of the spectral lines [5]. Figure 2b show the power spectrum obtained with an FFT over the interferogram. The oscillatory pattern at ~ 200 MHz results in the evident peak at this frequency. Result is compared in Fig. 2b.1 to the heterodyne beating observed in the ESA through classical method. Central frequencies are obtained by computing the first moment of the distribution, $f_{beat} = \sum f(i)P(i)/\sum P(i)$. Evaluation range is taken as full-width at 0.1 of maximum. Uncertainty of centroid, u_{f0} , is computed using $u_f(i)$ and $u_p(i)$ through uncertainty propagation techniques over the first moment and combined to the RMS variance of distribution (second moment).

Histogram is computed up to $10 \mu s$ with bin width of 0.1 ns, resulting in sample period $t_s = 0.1$ ns and $N = 10^5$ points. Single-sample resolution of TIC is computed as $u_{TIC} = 45.1$ ps, including timing jitter of the SPDs (characterized using [7]). Combining $\Delta f/(2\sqrt{3})$ and u_{TIC}/\sqrt{C} , where C is average number of coincident counts, results in $u_{ts} = 0.041$ ns. Frequency step of the FFT is $\Delta f = (t_s N)^{-1} = 0.100$ MHz, thus $u_f(i) = 0.041$ MHz. $u_p(i)$ is taken as square root of the number of events in the (amplitude) spectrum.

ESA was previously verified using a frequency synthesizer driven by a calibrated quartz clock traced to national standards as input, and frequency offset is within instrument resolution bandwidth (10 kHz). Spectral span is sampled at 0.100 MHz, thus $u_f(i) = 0.041$ MHz. $u_p(i)$ is computed from the standard deviation over ~ 2000 traces.

Results are shown in Table 1. The difference of 0.02 MHz, much smaller than uncertainty values, indicates agreement between methods. Note that the ambiguity in absolute frequency, which also appears in the classical case ($\nu_{Test} = \nu_{Ref} \pm f_{beat}$), could be resolved by a second measurement using a frequency shifter or a second reference laser.

Table 1. Results for frequency difference using quantum and classical methods. All values in [MHz].

	f_{beat}	u_{f0}	σ_f	u_c^*
FFT	201.27	0.00067	1.48	1.48
ESA	201.25	0.00076	0.88	0.88

CONCLUSIONS

Relative frequency of a faint stabilized laser sources is determined based on photon counting and validated through conventional heterodyne beating. The method constitutes a practical solution for low power frequency metrology.

ACKNOWLEDGEMENTS

Author thanks Dr. Ivan L. M. Silva for helpful discussions. This work is partially funded by *Conselho Nacional de Desenvolvimento Científico e Tecnológico* – CNPq (408661/2016-0).

REFERENCES

1. www.bipm.org/en/publications/mises-en-pratique/stand-ard-frequencies.html
2. C. K. Hong, Z. Y. Ou, and L. Mandel, “Measurement of subpicosecond time intervals between two photons by interference,” *Phys. Rev. Lett.* 59, 2044–2046 (1987).
3. T. Legero *et al.*, “Time-resolved two-photon quantum interference,” *Appl. Phys. B* 77, 797–802 (2003).
4. T. Ferreira da Silva *et al.*, “Spectral characterization of weak coherent state sources based on two-photon interference,” *J. Opt. Soc. Am. B* 32, 545–549, 2015.
5. G. C. Amaral, T. Ferreira da Silva *et al.*, “Few-photon heterodyne spectroscopy,” *Opt. Lett.* 41, 1502–1505, 2016.
6. T. Ferreira da Silva, “Self-triggered method for characterization of single-photon detectors,” *App. Opt.* 55, 1565–1570 (2016).
7. T. Ferreira da Silva *et al.*, “Real-time characterization of gated-mode single-photon detectors,” *IEEE J. Quantum Electron.* 47, 1251–1256 (2011).

Nanowire-based Sources of Non-classical Light

R.L. Williams¹, P. Laferrière^{1,2}, K. Mnaymneh¹, S. Haffouz¹, D.B. Northeast¹, P. J. Poole¹ and D. Dalacu¹

¹National Research council of Canada, Ottawa, Canada, ²University of Ottawa, Ottawa, Canada

Corresponding e-mail address: robin.williams@nrc-cnrc.gc.ca

Sources of non-classical light based upon semiconductor quantum dots embedded within a photonic nanowire are reviewed. Details of the epitaxial growth and photonic nanowire design are examined in relation to optimising source performance metrics such as brightness, emission linewidth and single photon purity. Multiplexed sources using multiple quantum dots coupled to a single photonic nanowire as well as efforts to extend the emission wavelength to those suitable for telecoms applications are discussed, along with possible routes to integration with the silicon photonics platform.

INTRODUCTION

Sources of non-classical light, single photons or entangled photon pairs, are a necessary resource for many quantum information, communications and imaging applications. On-demand sources with high emission rate, high generation and collection efficiency and high purity are desirable; traits that have been convincingly demonstrated by solid state emitters such as semiconductor quantum dots [1,2].

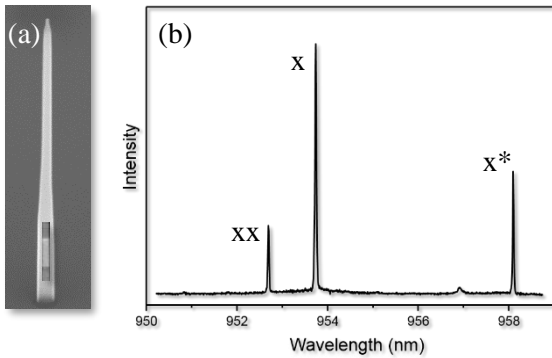


Figure 1. (a) Scanning electron microscope image of a nanowire with the quantum dot shown schematically in the wire core. (b) Photoluminescence spectrum of quantum dot emission.

In the work presented here we discuss the design and realisation of InAs-InP semiconductor quantum dot sources in which the emitter is placed along the axis of a Wurtzite InP nanowire grown by Chemical Beam Epitaxy. A scanning electron microscopy image of a typical nanowire along with a

representative emission spectrum is shown in Fig. 1. The nanowire core is grown using a vapour-liquid-solid epitaxy technique, with the nanowire core and quantum dot diameter ($\sim 20\text{nm}$) controlled to within a few nm by the size of a gold catalyst located within a dielectric-defined opening on the substrate surface. After growth of the nanowire core and quantum dot emitter, growth conditions are altered to promote radial growth in contrast to axial growth, producing a tapered InP photonic nanowire with a base diameter

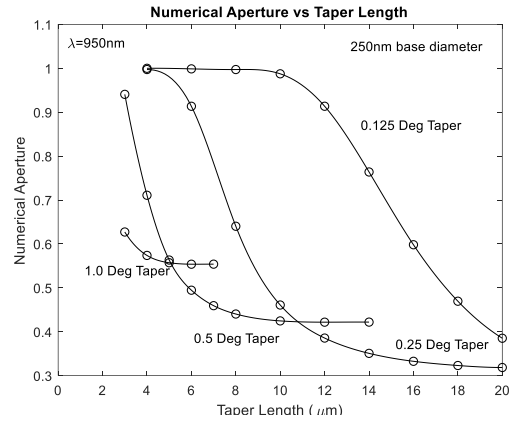


Figure 2. Effect of taper length and angle on the numerical aperture of the source.

of $\sim 250\text{nm}$, suitable for efficient coupling of photons from the quantum dot into the Gaussian-like HE11 mode of the nanowire waveguide. The effects of taper length and angle on the numerical aperture of the nanowire source are shown in Fig. 2. With appropriate taper design, efficiencies in excess of 90% can be achieved for coupling of the HE11 mode to single mode optical fibre [3].

OPTICAL PROPERTIES

InAs-InP quantum dot nanowires emitting around $\lambda=950\text{nm}$ have demonstrated $>85\%$ coupling efficiency into the nanowire HE11 mode, with a multi-photon emission probability $g^{(2)}(0)=0.002$ and near transform limited line widths of $4\mu\text{eV}$. By modifying the growth conditions, the emission wavelength can be tuned in the range from approximately $\lambda=880\text{nm}$ to beyond $\lambda=1500\text{nm}$, suitable for fibre-based transmission, as shown in Fig.

3. However, as can be seen in the inset of Fig. 3, the shift of emission to longer wavelengths is accompanied by a considerable drop in emission rate.

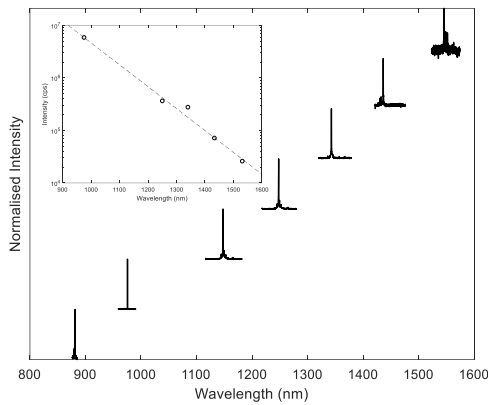


Figure 3. Normalised Photoluminescence spectra showing emission tuning with variation in growth parameters. Inset shows the drop in measured count rates.

ROUTES TO PHOTONIC INTEGRATION

The tapered nature of the InP nanowire described above produces an expanding, less confined optical mode as photons propagate towards the nanowire tip. If the nanowire is brought into the vicinity of a SiN waveguide, photons can be transferred from the nanowire, into the waveguide and can be made available for further processing as part of a photonic integrated circuit. Such a coupled nanowire-waveguide is shown below in Fig. 4.

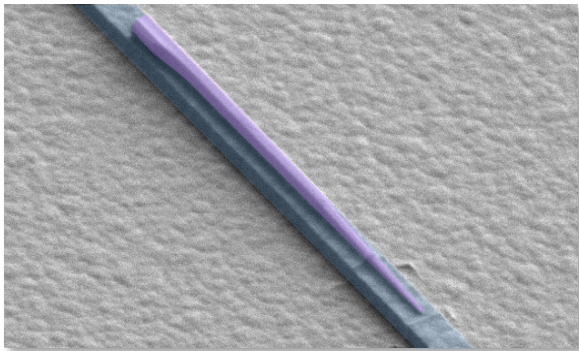


Figure 4. Scanning electron microscope image of an InAs-InP quantum dot nanowire placed on top of a SiN waveguide for evanescent coupling.

A coupling efficiency of 74% for photons propagating towards the nanowire tip has been demonstrated for structures of this type along with a single photon purity ($1 - g^{(2)}(0)$) of 89% [4].

This work was supported by the Natural Sciences and Engineering Research Council and the Canadian Space Agency.

REFERENCES

1. D. Dalacu, K. Mnaymneh, J. Lapointe, X. Wu, P. J. Poole, G. Bulgarini, V. Zwiller, M. Reimer, "Ultraclean Emission from InAsP Quantum Dots in Defect-Free Wurtzite InP Nanowires", *Nano Letters* 2012 12 (11), 5919-5923 DOI: 10.1021/nl303327h.
2. M. Versteegh, M.E. Reimer, K.D. Jons, D. Dalacu, P.J. Poole, A. Gulinatti, A. Giudice, V. Zwiller, "Observation of strongly entangled photon pairs from a nanowire quantum dot", *Nat Commun* 5, 5298 (2014). <https://doi.org/10.1038/ncomms6298>.
3. G. Bulgarini, M.E. Reimer, M.B. Bavinck, K.D. Jöns, D. Dalacu, P.J. Poole, E. Bakkers, V. Zwiller, "Nanowire Waveguides Launching Single Photons in a Gaussian Mode for Ideal Fiber Coupling", *Nano Letters* 2014 14 (7), 4102-4106. DOI: 10.1021/nl501648f.
4. K. Mnaymneh, D. Dalacu, J. McKee, J. Lapointe, S. Haffouz, J. F. Weber, D. B. Northeast, P. J. Poole, G. C. Aers, R. L. Williams, "On-Chip Integration of Single Photon Sources via Evanescent Coupling of Tapered Nanowires to SiN Waveguides", *Adv. Quantum Technol.* 2019, 2, 1900021.

Core-shell CdSe/CdS quantum dot based single-photon emitter for SPAD calibration at room temperature

Beatrice Rodiek^{1,2}, Justus Christinck^{1,2}, Hristina Georgieva¹, Helmuth Hofer^{1,2}, Marco López¹, Xiao-Liu Chu^{3,4}, Stephan Götzinger^{3,4} and Stefan Kück^{1,2}

¹Physikalisch-Technische Bundesanstalt, Braunschweig, Germany

²Laboratory for Emerging Nanometrology (LENA), Braunschweig, Germany

³Friedrich-Alexander-Universität Erlangen-Nürnberg, Erlangen, Germany

⁴Max Planck Institute for the Science of Light, Erlangen, Germany

Corresponding e-mail address: beatrice.rodiek@ptb.de

The characterization of a core-shell CdSe/CdS quantum dot emitter at room temperature will be presented. For the characterization, the photon flux, the spectral distribution and the single-photon purity are determined. The central wavelength of the quantum dot is 642 nm, the bandwidth (FWHM) is about 18 nm. Furthermore, the relative detector calibration of two single-photon detectors (SPADs) will be shown using this quantum emitter.

INTRODUCTION

Single-photon emitters receive more attention in several quantum technology fields e.g. in quantum key distribution, quantum computing and quantum-enhanced optical measurements [1]. They are also interesting for the radiometry and metrology, because of, ideally, the absence of background and multi-photon emission. Such source has the potential to become a standard source in radiometry [2]. Moreover, a single-photon source is ideal for calibrating single-photon detectors, because of the omitted influence of the photon statistics on the calibration results [3].

For that reason, PTB is focussing on the development of different kinds of single-photon emitters at different wavelengths. In this contribution, the results of the characterization of a core-shell CdSe/CdS quantum dot emitter as well as a detector calibration using this emitter are presented. Here, core-shell quantum dots were used because of their brightness and narrow spectral bandwidth (compared to the already absolute characterized nitrogen-vacancy centers in nanodiamond) at room temperature [4].

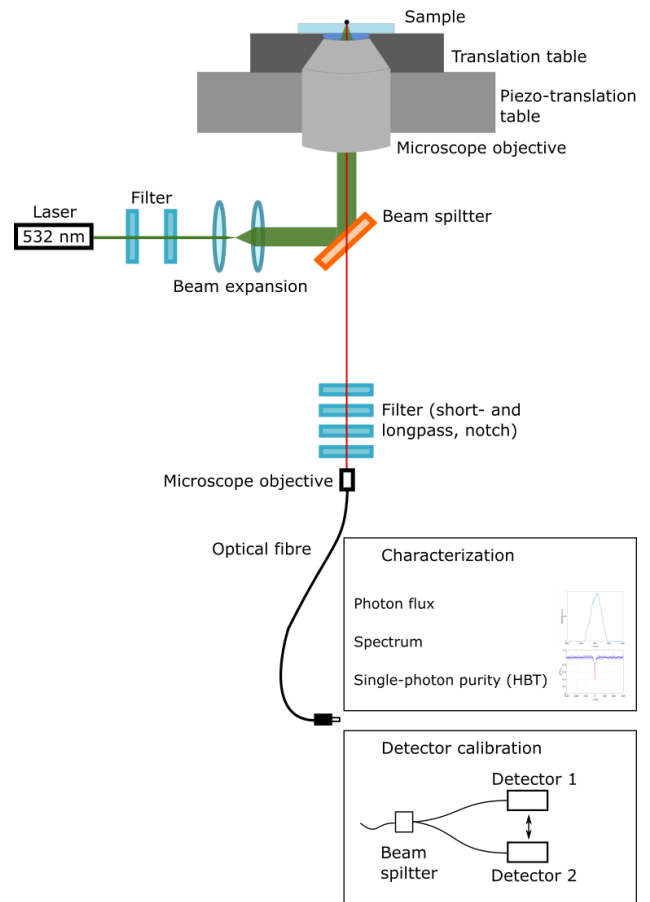


Figure 1. Measurement setup used for the characterization and the relative detector calibration.

EMITTER AND SETUP

As an emitter, core-shell quantum dots consisting of a CdSe core and a CdS shell placed on a standard cover glass were used, which were prepared by the Friedrich Alexander University (FAU) [4].

The sample is placed in a confocal microscope setup (see Figure 1) and is excited by a continuous wave laser operating at a wavelength of 532 nm. An oil immersion objective (NA 1.4) is used for a high collection of the emission. In the first case, the

characterization, the confocal setup is consecutively connected to a detector, spectrometer as well as a Hanbury-Brown and Twiss interferometer (HBTI). In the second case, the detector calibration, two detectors are linked to the confocal microscope via a 50/50 beam splitter.

All measurements were carried out at room temperature.

CHARACTERIZATION

By scanning the sample, one quantum dot was selected for further investigations. The photon flux of the core-shell quantum dot was determined to be approx. 390 kcounts per second. The second order correlation function $g^{(2)}(\tau)$, as an indicator for the single-photon purity, was measured with a Hanbury-Brown and Twiss interferometer (HBTI), at $\tau = 0$ its value is approx. 0.4, indicating the non-classical character of the source, see Fig. 2a.

The spectral distribution of the quantum dot emitter is shown in Figure 2b, the central wavelength

is at 642 nm, the FWHM is approximately 18 nm (Figure 2b). The lifetime of the quantum dot was determined to approx. 7ns.

DETECTOR CALIBRATION

For the relative calibration the single-photon emission is divided by a 50/50 beam splitter. Two single-photon detectors (SPADs) are connected to the beam splitter. The detectors are of the same type (COUNT-T100-FC). After measuring the photon flux rate at both detectors at the same time, the detectors are switched and the photon flux rate is measured again. By analysing the measured photon fluxes, the ratio of the detection efficiency can be determined [5]. Preliminary evaluation gives a detection efficiency ratio of:

$$r = 1.023 \pm 0.086 . \quad (1)$$

Further details and results will be shown at the conference.

ACKNOWLEDGEMENT

This work was funded by the project EMPIR-17FUN06 SIQUEST. This project received funding from the EMPIR programme co-financed by the Participating States and from the European Union's Horizon 2020 research and innovation programme.

This work was also funded by the Deutsche Forschungsgemeinschaft (DFG, German Research Foundation) under Germany's Excellence Strategy – EXC 2123 QuantumFrontiers, Project-ID 390837967.

REFERENCES

1. M. D. Eisaman, J. Fan, A. Migdall, and S. V. Polyakov, "Single-photon sources and detectors," *Rev. Sci. Instrum.* 82, 071101, 2011.
2. W. Schmunk et al., Photon number statistics of NV centre emission, *Metrologia* 49, 156-160, 2012.
3. B. Rodiek et al., Experimental realization of an absolute single-photon source based on a single nitrogen vacancy center in a nanodiamond, *Optica* 4 (1), 71-76, 2017.
4. X.-L. Chu et al., Experimental realization of an optical antenna designed for collecting 99% of photons from a quantum emitter, *Optica* 1(4), 203-208, 2014.
5. W. Schmunk et al., Radiometric calibration of single photon detectors by a single photon source based on NV-centers in diamond, *Journal of Modern Optics*, 58:14, 1252-1259, 2011.

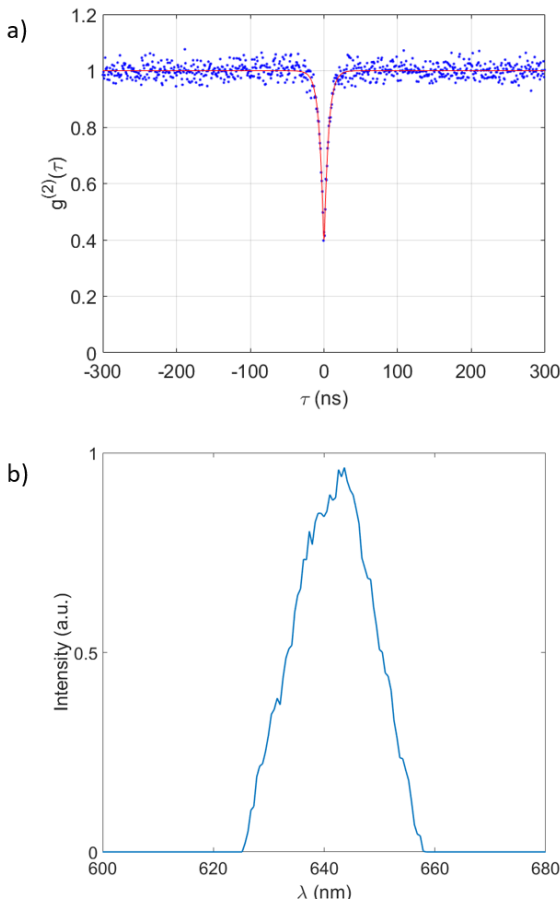


Figure 2. a) Single-photon purity of the CdSe/CdS quantum dot and b) its spectral distribution.

Calibration of InGaAs/InP single-photon avalanche detectors

Robin Eßling, Helmuth Hofer, S. M. F. Raupach, Hristina Georgieva, Beatrice Rodiek, Justus Christinck, Stefan Kück and Marco López

Physikalisch-Technische Bundesanstalt (PTB), Braunschweig, Germany

Corresponding e-mail address: marco.lopez@ptb.de

We present our latest results on the calibration of the detection efficiency of free-running and external-gated InGaAs/InP single-photon avalanche detectors at the wavelength of 1550 nm. This includes the characterisation of the gate window temporal response and the after-pulse probability, which, depending on the detector operation mode, significantly affect the detection efficiency.

INTRODUCTION

InGaAs/InP- single-photon avalanche detectors (SPADs) operated in external-gating and free-running mode are frequently used in many quantum technologies, such as quantum communication, quantum key distribution, etc. The precise characterization of relevant parameters such as, among others, detection efficiency, dead time, after-pulse probability, temporal photon detection probability profile and dark count probability, is mandatory for their use in quantum-sensitive detection systems. Therefore, several National Metrology Institutes (NMIs), such as PTB, and standardisation organisations such as the European Telecommunications Standards Institute (ETSI) are currently undertaking large efforts in developing and standardizing measurement methods and procedures, which will allow the traceable characterisation of all relevant parameters. From radiometric point of view, the detection efficiency is the parameter that can be determined with traceability to the primary standard for optical power, the cryogenic radiometer.

MEASUREMENT METHOD AND SETUP

The detection efficiency η of an InGaAs/InP SPAD detector is obtained by determining the probability P_i to detect a photon at each illuminated gate as a function of the mean number of photons per laser pulse, $\langle\mu\rangle$. That is,

$$\eta = \frac{P_i - P_d}{\langle\mu\rangle} \cdot \frac{1}{1 + P_{\text{after}}} \quad (1)$$

where P_d is the dark count probability and P_{after} is the after-pulse probability. The mean number of photons per laser pulse $\langle\mu\rangle$ is given by,

$$\langle\mu\rangle = \frac{P}{f \cdot (h \cdot c / \lambda)} \cdot A \quad (2)$$

where P is the optical power of the laser, f is the repetition rate of the laser pulses, hc/λ is the photon energy and A is the attenuation factor required to attenuate the laser source down to single-photon levels (fW).

The setup used for the calibration of the detection efficiency of the free-running and gated fiber-coupled InGaAs/InP SPAD detectors is shown in Figure 1. In this setup, a strongly attenuated short-pulsed laser with a pulse duration of approx. 300 ps operating at a wavelength of 1550 nm, triggered with a frequency of $f_{\text{Trigger}} = 90$ kHz, is used as a radiation source. The optical power of the laser is attenuated down to single-photon levels (fW) by two attenuators, which attenuation factors A_1 and A_2 are previously calibrated at a higher optical power by using the double attenuator technique [1]. Thus, the attenuation factor A is calculated by $A_1 \cdot A_2$. A low noise InGaAs photodiode (Hamamatsu G8605-23) cooled to -20°C and traceable to the PTB's primary standard for optical power (cryogenic radiometer) is used as reference standard for the measurement of the optical power. The photocurrent generated by the InGaAs photodiode is directly measured with a Femto/Pico-ammeter (Keysight B2981A, see Figure 1(b)). When a SPAD operated in external gating mode is calibrated, a delay generator is used to precisely synchronise the photon detection time within the gate.

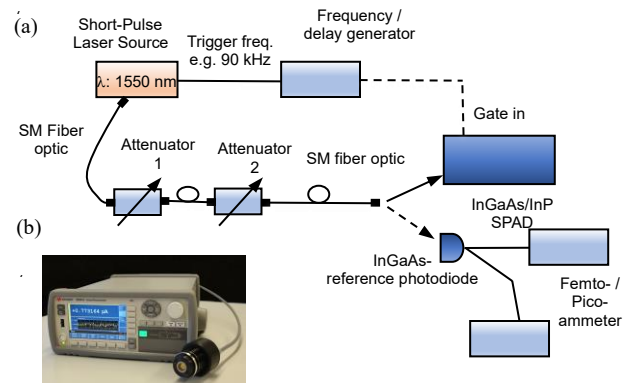


Figure 1. (a) Setup for determining the detection efficiency of fibre optic coupled InGaAs/InP SPAD detector. (b) InGaAs reference photodiode (Hamamatsu G8605-23) and Femto-/Pico-ammeter (Keysight B2981A) used as photocurrent meter.

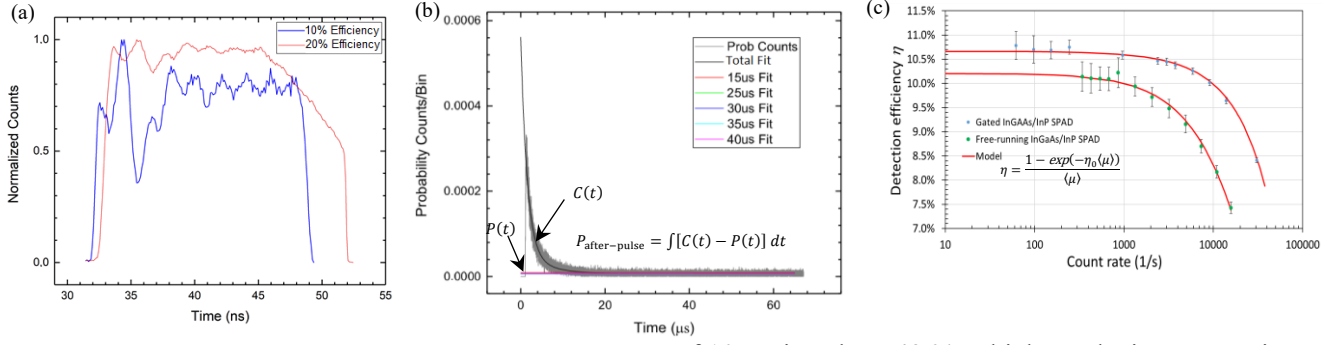


Figure 2. (a) Normalized gate window temporal response of the gated InGaAs/InP SPAD (ID201) for different detection efficiency configurations. (b) Histogram of the probability counts obtained for determining the after-pulse probability of the free-running InGaAs/InP SPAD (ID220). (c) Detection efficiency of the gated and the free-running InGaAs/InP SPAD detector (ID201 and ID220, respectively) as a function of the count rate. Solid points: measurement results, error bars: standard uncertainty, solid line (red): fitted model.

The after-pulse probability of the SPADs is determined as described in [2]. This method consists in determining the time-correlation between two consecutive output pulses generated by the SPAD detector in absence of light. The after-pulse probability is quantified by fitting a model function $C(t)$ and $P(t)$ to the registered time-correlation events for a timing period range with and without after-pulses events, respectively. Both fitting model functions $C(t)$ and $P(t)$ have the form $x_0 \cdot e^{-R \cdot t}$, where x_0 and R are the photon detection probability per unit time slot and the average photon counting rate, respectively. Finally, the after-pulse probability is calculated by $P_{\text{after-pulse}} = \int [C(t) - P(t)] dt$.

RESULTS

The measurement of the gate window temporal response of the external-gating SPAD detector (ID201), set to a nominal detection efficiency of 10 % and 20 %, respectively, is shown in Figure 2(a). As can be observed, the detector count rate strongly depends on the photon detection within the gate window. The count rate changes, relative to the maximum value measured, up to approx. 60 % and 10 %, for a detector efficiency setting of 10 % and 20 %, respectively.

Figure 2(b) shows the histogram of the probability counts and the corresponding fitted functions for the free-running SPAD detector (ID220). The after-pulse probability obtained, for a setting detector dead time

of 10 μs, is to be 7.43 %, which results in a correction factor $\frac{1}{1+P_{\text{after}}} = 0.931$ in equation (1).

The detection efficiency measurements of the gated and free-running InGaAs/InP SPAD detector (ID201 and ID220, respectively) as a function of the count rate is shown in Figure 2(c). The detection efficiency of the gated SPAD detector was determined by gating it at approx. 43 ns within the gate window shown in Figure 2(a). The dead time and efficiency of both detectors were configured to 10 μs and 10 %, respectively. As can be observed, the detection efficiency decreases once the saturation of the detectors is reached, as described in [2]. The relative standard uncertainty achieved is less than 1.2 %. The maximal deviation of the detection efficiency of the gated SPAD obtained within its gate window, and relative to an efficiency of 10 %, is to be 7.97 %.

In summary, the calibration of the detection efficiency of an external gating and a free-running InGaAs/InP SPAD detector was presented. The after-pulsing probability correction obtained for the free-running SPAD was approx. 7.0 % @10 μs dead time. For the external gating SPAD, a variation of the detection efficiency of up to approx. 8.0 % was obtained within its gate window.

Acknowledgment: The work reported on this paper was funded by project EMPIR 17FUN06 SIQUST. This project received funding from the EMPIR program co-financed by the Participating States and from the European Union Horizon 2020 research and innovation program.

REFERENCES

1. Marco López, et. al. "Detection efficiency calibration of InGaAs/InP single-photon detectors", NewRad 2017 Proceedings, Tokyo 13 - 16 June, 2017.
2. Hee Jung Lee et. al. "Wavelength-scanning calibration of detection efficiency of single photon detectors by direct comparison with a photodiode", Metrologia 53, 908-917, 2016.

The SIQUEST-project – towards single-photon sources as new quantum standards

S. Kück¹, H. Georgieva¹, M. López¹, B. Rodiek¹, F. Manoocheri², G. Porrovecchio³, M. Smid³, G. Brida⁴, P. Traina⁴, T. Kubarseppe⁵, C. Giusca⁶, P. Dolan⁶, L. Hao⁶, C. J. Chunnillall⁶, T. Dönsberg⁷, P. Lombardi⁸, C. Toninelli⁸, B. Alén⁹, S. Götzinger¹⁰, J. Forneris¹¹, S. Rodt¹², S. Reitzenstein¹², P. Fuchs¹³, C. Becher¹³, P. Olivero¹⁴, S. Ditalia Tchernij¹⁴, M. Jetter¹⁵, P. Michler¹⁵, S. L. Portalupi¹⁵

¹Physikalisch-Technische Bundesanstalt (PTB), Braunschweig, Germany, ²Aalto-korkeakoulusäätiö sr (Aalto), Espoo, Finland, ³Ceský Metrologický Institut (CMI), Brno, Czech Republic, ⁴Istituto Nazionale di Ricerca Metrologica (INRIM), Torino, Italy, ⁵AS Metroserf (Metroserf), Tallinn, Estonia, ⁶National Physical Laboratory (NPL), Teddington, U.K., ⁷Teknologian tutkimuskeskus VTT Oy (VTT), Espoo, Finland, ⁸Istituto Nazionale di Ottica (CNR-INO), Florence, Italy, ⁹Instituto de Micro y Nanotecnología, IMN-CNM, CSIC (CEI UAM+CSIC), Madrid, Spain, ¹⁰Friedrich-Alexander-Universität Erlangen – Nürnberg (FAU), Erlangen, Germany, ¹¹Istituto Nazionale di Fisica Nucleare (INFN), Torino, Italy, ¹²Technische Universität Berlin (TUB), Berlin, Germany, ¹³Universität des Saarlandes (UdS), Saarbrücken, Germany, ¹⁴Physics Department, University of Torino (UNITO), Torino, Italy, ¹⁵Institut für Halbleiteroptik und Funktionelle Grenzflächen, Center for Integrated Quantum Science and Technology (IQST) and SCoPE, University of Stuttgart (USTUTT), Stuttgart, Germany
Corresponding e-mail address: stefan.kueck@ptb.de

In this presentation, the EURAMET joint research project “Single-photon sources as new quantum standards” (SIQUEST) [1], funded within the European Union Horizon 2020 research and innovation programme, will be presented.

INTRODUCTION

The aim of this project is to develop new absolute standard radiation sources, which exploit the discrete and quantum nature of photons, and the necessary metrological infrastructure. These sources will be based on single-photon emitters with a calculable photon emission rate and high purity, i.e. with a very low multiple photon emission probability. Such sources hold promise as new quantum standards which will have a large number of applications, e.g. for use in the calibration of single-photon detectors, for the realisation of the SI base unit candela, for quantum random number generation, for quantum key distribution, for subshot noise metrology, for quantum enhanced metrology, and for photon-based quantum computation.

OBJECTIVES AND RESULTS

This project focuses on the development of single-photon sources as new quantum standards. Results obtained within the first half of the project are:

Type-IIa diamond bulk crystals have been implanted with several different ions. Samples implanted with Sn and Pb demonstrated single-photon emission at room temperature under 520 nm

and 532 nm laser excitation. The SnV centre exhibited $g^{(2)}(0)$ values down to 0.29 ± 0.02 with a saturation photon rate of approx. 1.4×10^6 photons/s. Samples treated differently after the ion-implantation process exhibit enhanced single-photon purities, with $g^{(2)}(0)$ value down to 0.05. Single-photon sources based on InGaAs QDs in micro-structured GaAs were fabricated and for the first time used for a relative calibration of two Silicon single-photon avalanche diode detectors. The photon rate measured for a specific QD was around 3×10^5 photons/s with a $g^{(2)}(0)$ -value of 0.23 at a wavelength of (922.37 ± 0.02) nm. The measurement uncertainty for this relative calibration is about 0.7 %. Several single-photon emitters based on a single molecule (dibenzoterrylene in anthracene, DBT:Ac) were designed and fabricated. In order to efficiently collect the emission, a planar antenna design which is simple and cheap to fabricate, and which provides hundreds of source candidates per fabrication run, was developed. A bright single-photon emitters based on a single molecule (dibenzoterrylene in anthracene, DBT:Ac) was metrologically characterized, the parameters are, simultaneously: photon flux up to 1.4×10^6 photons/s at the wavelength of (785.6 ± 0.1) nm with a $g^{(2)}(0)$ -value < 0.1 and a spectral bandwidth (FWHM) < 2 nm. The photon flux was measured with a traceable low-noise analogue reference Si detector. This source was used to directly calibrate a Silicon single photon avalanche diode detector against a Silicon photodiode, which is in turn traceable to the cryogenic radiometer.

The impact of different excitation schemes on the quantum optical properties of single-photon sources is investigated for InGaAs QDs (emitting around 930 nm) in GaAs matrix. A strong linewidth decrease is observed from above-band ($\Delta\nu \approx 11$ GHz) via phonon-assisted ($\Delta\nu \approx 7.1$ GHz) to direct resonant excitation ($\Delta\nu \approx 3.1$ GHz). Furthermore, two-photon excitation was applied and high purity ($g^{(2)}(0) = 0.072 \pm 0.104$) and highly indistinguishable ($V = 0.894 \pm 0.109$) single photons were observed.

Indistinguishability of photons emitted by a single molecule has been demonstrated. Setup upgrades to enhance emission purity and spectral filtering, as well to refine indistinguishability measurement are in progress.

The setup for ODMR measurements was upgraded resulting in an increase of magnetic field sensitivity of ODMR-based magnetometry protocols ultimately for applications of sensing in biological systems. Specifically, an optimized diamond sample with a very narrow layer of NV centres is used and the possibility to drive simultaneously all three hyperfine peaks corresponding to one spin orientation was implemented. A new state-of-the-art experimental setup for the implementation of single-photon confocal photoluminescence and ODMR measurements down to 4 K temperature was established.

The new paradigm dubbed the genetic quantum measurement, specifically the possibility to exploit this new approach with quantum dots and colour centres in diamond, has been investigated with respect to understand if there is some peculiar observable of these quantum systems that can take advantage of this novel technique.

A cooled Predictable Quantum Efficient Detector (PQED) in a liquid nitrogen operated cryostat for use in performing SI traceable measurements of low power sources was constructed and characterised. The device uses electronics developed within the project and is capable to detect 1 000 000 photons/s with an uncertainty of $< 1\%$ in the wavelength range between 650 nm and 750 nm.

A portable single-photon source was designed and constructed and currently undergoes compaction to reduce the size to approx. only 40 cm x 27.5 cm x 20 cm. This source delivered with a molecule emitter (terrylene in p-terphenyl) approx. 2×10^6 photons/s at room temperature. The $g^{(2)}(0)$ value was approx. 0.2 and the emission covered the spectral region between

550 nm and 700 nm with emission peaks at approx. 580 nm, 630 nm and 680 nm.

First results were achieved using techniques for measuring the $g^{(2)}(0)$ value. A pilot study on the characterisation with respect to the $g^{(2)}(t=0)$ value of a pulsed-pumped single-photon source, based on a NV centre in nanodiamond, was performed by INRIM, NPL and PTB. The main result of this study was the development of a standardised measurement technique as well as an uncertainty estimation procedure. The validity of the technique (system-independent and unaffected by the non-ideality of the apparatus) was demonstrated by the results which yielded estimated values of $g^{(2)}(0)$ that were compatible within the uncertainty ($k=2$) for all of the participants. This study will greatly benefit the single-photon metrology community, as well as rapidly growing quantum-technology-related industries. At the conference, an overview about the project itself as well as on the results obtained until then will be given.

ACKNOWLEDGEMENT

This work was funded by the project EMPIR-17FUN06 SIQUEST. This project received funding from the EMPIR programme co-financed by the Participating States and from the European Union's Horizon 2020 research and innovation programme.

REFERENCES

1. <https://www.siqust.eu>

Performance evaluation of a thermoelectrically-cooled SiC single photon avalanche photodiode

In-Ho Bae^{1,2}, Young-Jin, Koh³, Seongchong Park¹, Kee Suk Hong², and Dong-Hoon Lee^{1,2}

¹ Division of Physical Metrology, Korea Research Institute of Standards and Science, Daejeon 34113, Republic of Korea

² Quantum Technology Institute, Korea Research Institute of Standards and Science, Daejeon, 34113, Republic of Korea

³ Chem-Bio Division, Agency for Defense Development, Daejeon, 34186, Republic of Korea

Corresponding e-mail address: inhobae@kriss.re.kr

In this paper, we report on the characteristics of a lab-assembled UV single photon avalanche photodiode (SPAD) based on a thermoelectrically cooled silicon carbide (4H-SiC) avalanche photodiode (APD). A SiC avalanche photodiode (APD) fabricated with bevelled mesa structure was integrated into a lab-assembled SiC SPAD working in a passive Geiger-mode. A 4-stage thermoelectric cooler (TEC) was used for adjusting the APD temperature. Changing bias voltage and comparator level, we evaluated after-pulse characteristics and dark count rates at different APD temperatures.

MOTIVATION

The development of sensitive detectors for UV light has attracted great attention in solar-blind applications such as flame detection, aerosol measurement and missile tracking [1]. In particular, avalanche photodiodes (APDs) based on a silicon carbide (SiC) are known as suitable candidates for sensitive UV detectors because they have excellent spectral responsibility only in the UV region [2]. Further work is underway to develop SiC-based single photon avalanche photodiodes (SPADs) that are sensitive enough to measure UV photons in an extremely low light level [3]. Therefore, in order to guarantee the successful studies on the development of such SPADs, the characteristics of single photon detectors such as dark count rate, afterpulsing probability and detection efficiency must be evaluated in the UV region [4].

In this paper, we report on the performance evaluation of lab-assembled SiC-SPAD working in passive Geiger-mode. 4H SiC-APDs are demonstrated through eUPBAS (enhanced Ultraviolet Photodiode for Biological Aerosol Sensors) program lead by ADD, CCDC-CBC and CCDC-ARL. The APD fabricated with bevelled mesa structure was integrated into the SPAD and the passive quenching circuit enables the Geiger-mode

operation of the APD. We measured photon counting rates as a function of incident UV LED power. Dark count rate (DCR) and afterpulsing probability are also measured at different APD temperatures.

EXPERIMENTAL SETUP

Figure 1 shows an experimental setup to evaluate DCR and afterpulsing probability of our SPAD module. We used two source meters to apply stable voltage to the APD and comparator level, respectively. The SiC-APD was attached on a TEC element to control its temperature. The metal housing and cooling fan were used as a heat sink which consumes heat from the TEC element. To test the response of the SPAD on input photons, we used a deep UV LED of 285 nm. This system to measure dark count rates and afterpulsing probability consists of a level translator (Phillips Scientific, 726), a time-to-

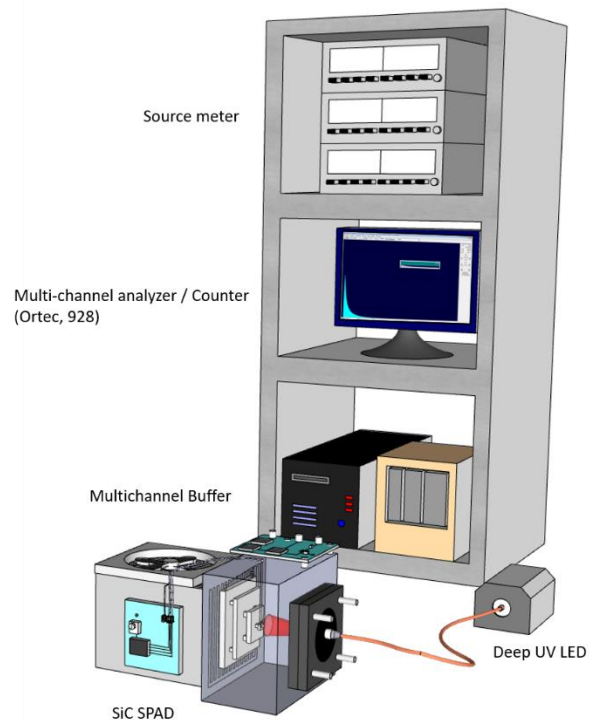


Figure 1. Experimental schematics for the performance evaluation of the SiC-based SPAD.

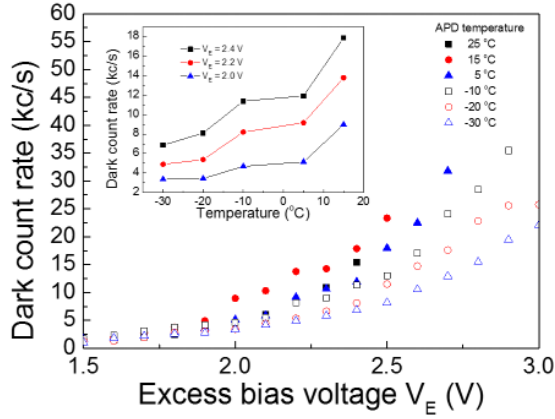


Figure 2. Dark count rates at various temperatures as a function of bias voltage.

amplitude converter (Ortec, 567) and a multi-channel analyser (Ortec, 928).

EXPERIMENTAL RESULTS

As shown in Fig. 2, measurement of DCRs at six different APD temperatures were performed in steps of excess bias voltage applied to the SPAD; the filled squares, circles, and triangles represent the DCRs measured at 25 °C, 15 °C and 5 °C, respectively, while the hollowed squares, circles, and triangles represent DCRs at -10 °C, -20 °C and -30 °C, respectively. Inset figure shows the DCRs at different excess bias voltages of 2.0 V, 2.2V and 2.4 V. From the results we observed that DCRs are reduced with decreasing the APD temperature. The reason for this reduction is resulted from decrease of the thermally generated carriers in the APD junction.

Finally, we measured afterpulse characteristics at APD temperatures as shown in Fig. 3. When the APD temperature reached 0 °C we observed appearance of afterpulse events. At the APD temperature of -30 °C, we clearly confirmed the afterpulse characteristics. With a simple equation in Ref. [4], we can assume that the afterpulsing probability was less than 0.01% at the APD temperature of -30 °C.

CONCLUSION

In this paper, we introduce lab-assembled SPAD based on temperature-controlled SiC-APD. The dark count rates were measured as a function of APD temperature. By using the time-correlated photon counting method, we evaluated afterpulsing probability of our lab-assembled SiC-SPAD.

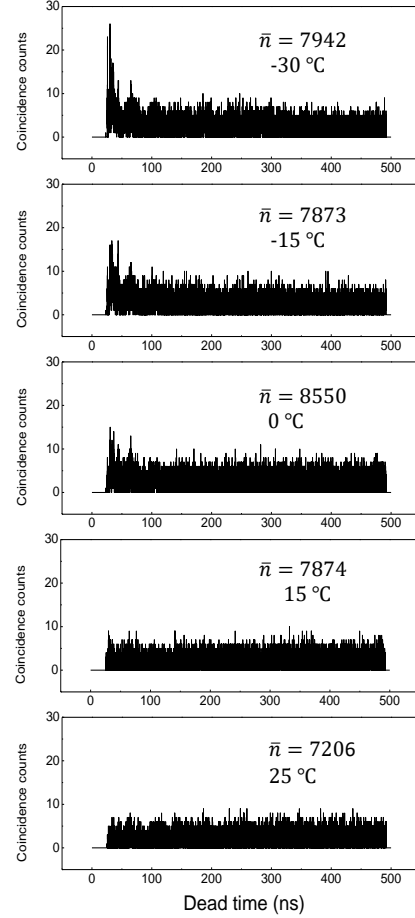


Figure 3. Afterpulse characteristics of the SiC-SPAD as a function of APD temperature. Coincidence count and photon count rates were recorded by a start-stop correlator and photon counting module, respectively.

REFERENCES

1. A. Vert, S. Soloviev, J. Fronheiser, and P. Sandvik, Solar-blind 4H-SiC single-photon avalanche diode operating in Geiger mode, *IEEE Photon. Technol. Lett.* 20, 1587–1589, 2008.
2. E. Chong, Y. J. Koh, D.-H. Lee, I.-H. Bae, J.-S. Kim, Y.-S. Jeong, J. Y. Ryu, J.-Y. Lee, M.-J. Kang, J.-H. Park, K.-K. Choi, Effect of beveled mesa angle on the leakage performance of 4H-SiC avalanche photodiodes, *Solid-State Electron.* 156, 1, 2019.
3. I.-H. Bae, S. Park, K. S. Hong, B. Park, E. Chong, and D.-H. Lee, Development of SPAD based on thermoelectrically controlled silicon carbide avalanche photodiode, in 2019 Conference on Lasers and Electro-Optics Europe and European Quantum Electronics Conference, OSA Technical Digest (Optical Society of America), paper ch_p_3, 2019.
4. I.-H. Bae, S. Park, K. S. Hong, H. S. Park, H. J. Lee, H. S. Moon, J. S. Borbely, and D.-H. Lee, Detection efficiency measurement of single photon avalanche photodiodes by using a focused monochromatic beam tunable from 250 nm to 1000 nm, *Metrologia*, 56, 035003, 2019.

Comparison of back focal plane imaging of nitrogen vacancy centers in nanodiamond and core-shell CdSe/CdS quantum dots

Justus Christinck^{1,2}, Beatrice Rodiek^{1,2}, Marco Lopéz¹, Hristina Georgieva¹, Helmuth Hofer^{1,2}, Xiao-Liu Chu^{3,4}, Stephan Götzinger^{3,4} and Stefan Kück^{1,2}

¹Physikalisch-Technische Bundesanstalt (PTB), Braunschweig, Germany

²Laboratory for Emerging Nanometrology (LENA), Braunschweig, Germany

³Max Planck Institute for the Science of Light, Erlangen, Germany

⁴Friedrich Alexander University Erlangen-Nürnberg (FAU), Erlangen, Germany

Corresponding e-mail address: justus.christinck@ptb.de

We report on the characterization of the angular-dependent emission of two different single-photon emitters based on nitrogen-vacancy centers in nanodiamond and core-shell CdSe/CdS quantum dot nanoparticles.

The emitters were characterized in a confocal microscope setup by spectroscopy and Hanbury-Brown and Twiss interferometry. The angular-dependent emission is measured using back focal plane imaging technique. A theoretical model of the angular emission patterns of the 2D dipoles of the emitters is developed to determine their orientation. Experiment and model agree well with each other.

EXPERIMENTAL SETUP

Both emitters were characterized in a similar confocal microscope setup using a laser operating at a wavelength of 532nm for excitation and an oil-immersion objective with a numerical aperture (NA) of 1.4 for the quantum dots (QD) and 1.45 for the nitrogen-vacancy (NV-) centers. Spectral filters were used to cut off wavelengths below 550 nm and above 750 nm and a fiber with core diameter of 9 μm was used as a pinhole. Two single avalanche photodiodes were used in the Hanbury-Brown and Twiss interferometer and for the sample scanning. Back focal plane imaging was carried out using a sCMOS camera.

The nitrogen-vacancy center nanodiamonds have a size of about 75 nm and the core-shell CdSe/CdS quantum dot nanoparticles are of about 15 nm in diameter.

MODEL OF THE ANGULAR EMISSION

Lukosz [1] developed a model for the angular-dependent emission patterns of a dipole at a dielectric interface. Nitrogen-vacancy centers consist of two perpendicular dipoles in plane perpendicular to the

symmetry axis of the NV-center [2]. The quantum dot emission is also originated from 2D dipoles [3]. The orientation of the emitters refers to the orientation angles θ and φ of the normal vector of the dipole emission plane, because the orientation of the two dipoles is unambiguously described. The angular-dependent emission patterns were calculated as the sum of the patterns of the two dipoles.

EXPERIMENTAL RESULTS

After sample scanning, one emitter on each sample has been chosen for further characterization. While the nitrogen-vacancy center emits a broad spectrum between about 600 nm and 750 nm, the QD emission is relatively narrow at about 640 nm (FWHM=18 nm) as shown in Figure 1. The Hanbury-Brown and Twiss measurement prove non-classical emission for both emitters with $g^{(2)}(0)$ values of 0.09 for the NV-center and 0.31 for the QD, respectively,

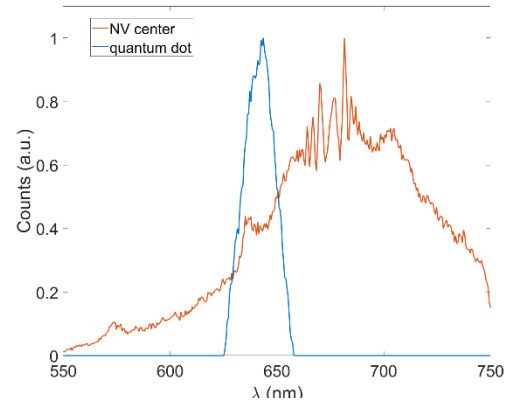


Figure 1. Spectra of the quantum dot and nitrogen-vacancy center emission.

as can be seen in Figure 2.

Background corrected back focal plane images were taken by first collecting the emission for about 60 seconds and then imaging the background light near the emitter for the same time. In the insets of Figure 3 and 4 back focal plane images of the emitters are shown.

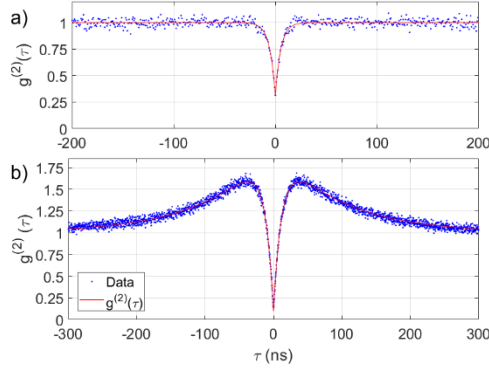


Figure 2. Intensity correlation function $g^{(2)}(\tau)$ for a) quantum dot and b) nitrogen-vacancy center.

For better comparison angular-dependent emission patterns were calculated from the back focal plane images along a line that is shown in their respective back focal plane image. In Figure 3 and 4 the angular-dependent emission patterns are shown together with calculated data from the model. The angle α is the angle against the optical axis. The NV-

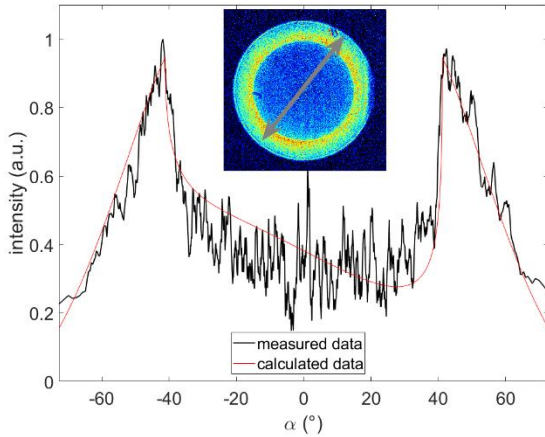


Figure 3. Comparison of model and experimental data of the angular-dependent emission of the quantum dot. In

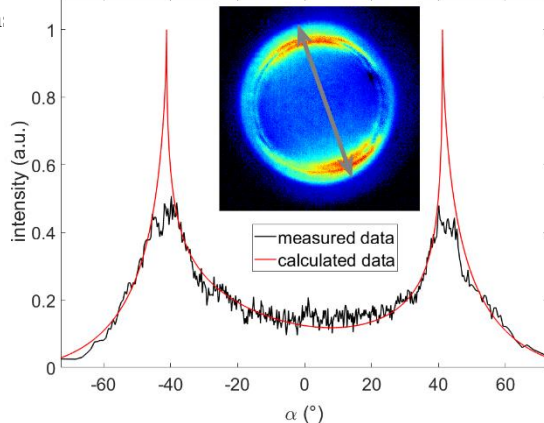


Figure 4. Comparison of model and experimental data of the angular-dependent emission of the nitrogen-vacancy center. Inset: back focal plane image of the nitrogen-vacancy center.

center emission is in good agreement with the model. The difference at the peaks may be caused by

blurriness in the picture. The QD emission is accurately reproduced by the model of the 2D dipoles. The orientation angles of the nitrogen-vacancy center are $\theta = 60^\circ$ and $\phi = 334^\circ$, while for the quantum dot they are $\theta = 30^\circ$ and $\phi = 35^\circ$.

CONCLUSION

Back focal plane imaging has been successfully shown on nitrogen-vacancy centers in nanodiamond and core-shell CdSe/CdS quantum dots. Model and experiment agree well for both emitters. The orientation of the 2D emission dipoles of the quantum dot and the orientation of the symmetry axis of the nitrogen-vacancy center were calculated. Further details will be presented at the conference.

ACKNOWLEDGEMENT

This work was funded by the project EMPIR-17FUN06 SIQUEST. This project received funding from the EMPIR programme co-financed by the Participating States and from the European Union's Horizon 2020 research and innovation programme.

This work was also funded by the Deutsche Forschungsgemeinschaft (DFG, German Research Foundation) under Germany's Excellence Strategy – EXC 2123 QuantumFrontiers, Project-ID 390837967.

REFERENCES

1. W. Lukosz et al., Light emission by magnetic and electric dipoles close to a plane dielectric interface II. Radiation patterns of perpendicular oriented dipoles, J. Opt. Soc. Am. 67:12, 1615-1619, 1977
2. R. J. Epstein et al., Anisotropic interactions of a single spin and dark-spin spectroscopy in diamond, Nature Physics 1, 94-98, 2005
3. I. Chung et al., Room temperature measurements of the 3D orientation CdSe quantum dots using polarization microscopy, Proc. Natl. Acad. Sci. USA 100, 405-408, 2003

Simulated internal quantum deficiency of induced junction photodiodes

Trinh Tran¹ and Jarle Gran¹

¹Justervesenet, Kjeller, Norway,

Corresponding e-mail address: ttr@justervesenet.no

The paper presents a study of the internal quantum deficiency of the predictable quantum photodetector (PQED) using 3D device simulation. It is shown that surface recombination velocity and fixed oxide charge density are the key parameters that have to be optimised in an effort to develop improved PQED photodiodes.

INTRODUCTION

The PQED is accepted as a new primary standard for radiant power measurement due to its low loss and predictable response [1]. This detector is constructed from two self-induced p-n junction photodiodes. The p-n junction is formed by the fixed charge between a dielectric surface layer and a silicon substrate. By optimising materials and fabrication processes to minimize surface recombination and to maximize fixed charge density, it is suggested that PQED photodiode with internal quantum deficiency (IQD) below ppm can be constructed [2]. Work is ongoing to develop improved induced junction photodiodes in the common European 18SIB10 *chipS·CALe* project [3], where expected response from simulations are an essential input to achieve the goal.

RESULTS AND DISCUSSION

The photodiode response is studied by using 3D simulation model developed in Genius Device Simulator from Cogenda [4]. The simulation structure is shown in Fig. 1. In order to save time and memory, only 1/8 of the real device is simulated and the symmetry boundary conditions are applied to obtain the response to the whole photodiode structure. The simulation structure consists of a low doped p-type silicon substrate with an oxide passivation layer on the surface which induces a fixed surface charge density Q_f at the silicon-oxide interface. The silicon substrate thickness is 500 μm . The electrodes are defined as p^+ doping and n^+ doping areas that have the width of 100 μm and separation distance of 300 μm . The rear side is also implemented with a p^+ doping that has the same doping concentration as the

front side contact doping. The fixed simulation parameters used here are shown in the Table 1.

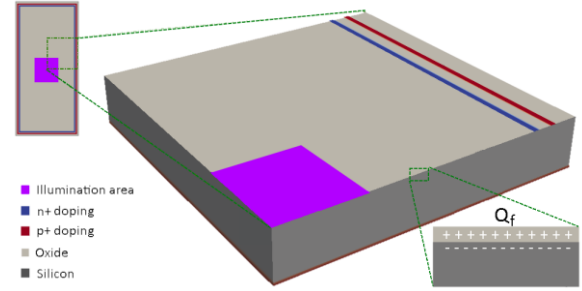


Figure 1. Simulation structure of a PQED photodiode.

Table 1. Simulation parameters.

Parameters	Value
Simulation structure	6mm×6 mm
Illumination area	1.5mm×1.5mm
Substrate doping concentration	$1.5 \times 10^{12} \text{cm}^{-3}$
Shockley-Read-Hall bulk lifetime	$2.9 \times 10^{-3} \text{s}$
Temperature	300K

IQD caused by charge carrier recombination is calculated by the following equation:

$$IQD = Rec/G_{opt} \quad (1)$$

where G_{opt} is the total rate of optically generation and Rec the total recombination rate of e-h pairs. Both G_{opt} and Rec can be extracted from simulation. We choose to decompose the total recombination in surface recombination and bulk recombination.

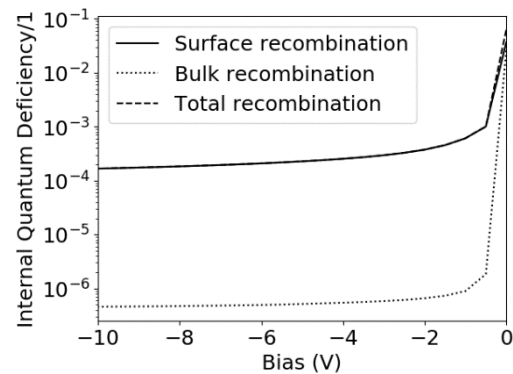


Figure 2. IQD response of photodiode with reversed bias.

A plot of typical IQD response of PQED photodiode with illumination at 450 nm with reversed bias is shown in Fig. 2. The simulation is done using Q_f of $6 \times 10^{11} \text{ cm}^{-2}$, surface recombination velocity (SRV) of $1.2 \times 10^4 \text{ cm/s}$ and absorbed optical power of $1 \times 10^{-4} \text{ W}$. By applying reversed bias up to -10V, the total IQD is reduced from 6.2×10^{-2} to 1.7×10^{-4} with the largest reduction from 0 V to -0.5 V bias.

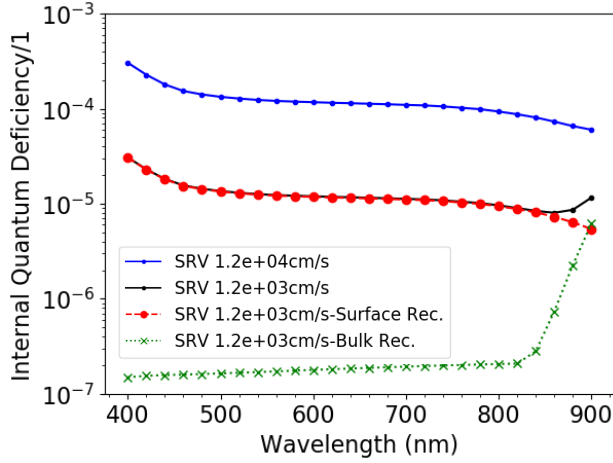


Figure 3. IQD as a function of wavelength of photodiode at two values of SRV.

Fig. 3 shows the spectrally dependent IQD with two different values of SRV with -10V reversed bias at room temperature. The simulations are performed with Q_f equals $6.5 \times 10^{11} \text{ cm}^{-2}$ and SRV is varied from $1.2 \times 10^3 \text{ cm/s}$ to $1.2 \times 10^4 \text{ cm/s}$. It is seen that IQD changes one order of magnitude when the SRV is varied with one order of magnitude. Additionally, the decomposed IQD caused by SRV and bulk recombination at SRV $1.2 \times 10^3 \text{ cm/s}$ are shown in the plot. With the parameter values of the SRV and bulk lifetime used here it is evident that the SRV limits the IQD over the whole visible spectral range.

The dependence of total IQD loss with 0 V reverse bias as a function of absorbed optical power with different Q_f is shown in Fig. 4. Fixed SRV value of $1.2 \times 10^4 \text{ cm/s}$ and illumination wavelength of 450 nm are used as input parameters for the simulations. The same trend is observed on all curves. IQD does not change much at low power level. At higher absorbed optical power, IQD shows a sharp increase and becomes saturated. At low absorbed optical power, there is not much loss that comes from bulk recombination. As absorbed optical power increases, bulk recombination begins to contribute more to the total IQD until it reaches its saturated value at very high optical power. Q_f also has a field effect passivation influence of the surface, but this effect saturates with charge density $2 \times 10^{12} \text{ cm}^{-2}$.

Above this value we see little influence of increasing the fixed charge from a passivation point of view, but a slight increase in linearity is still observed (not shown).

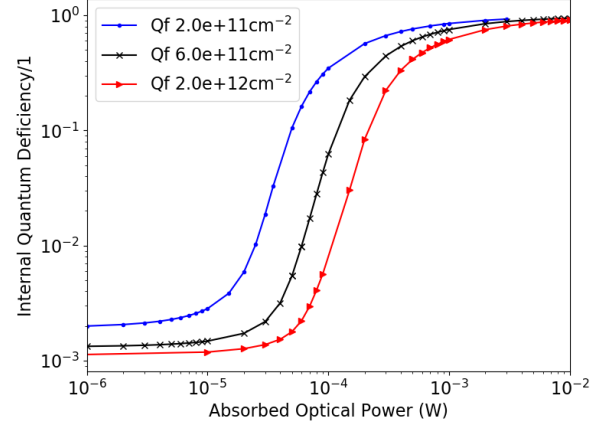


Figure 4. IQD as a function of absorbed optical power with different Q_f .

CONCLUSIONS

The PQED spectrally dependent IQD is limited by the SRV whereas the fixed oxide charge Q_f limits the linearity of the photodiode. High Q_f improves the performance of the photodiodes with lower IQD and better linearity. The photodiodes should be operated with sufficient bias for low IQD. However, IQD below 0.1% losses can be achieved with unbiased diodes at low power levels.

ACKNOWLEDGMENT

This work has received funding from the EMPIR programme co-financed by the Participating States and from the European Union's Horizon 2020 research and innovation programme.

REFERENCES

1. I. Müller *et al.*, "Predictable quantum efficient detector: II. Characterization and confirmed responsivity," *Metrologia*, vol. 50, no. 4, pp. 395–401, Jul. 2013, doi: 10.1088/0026-1394/50/4/395.
2. T. S. Stokkan, H. Haug, C. K. Tang, E. S. Marstein, and J. Gran, "Enhanced surface passivation of predictable quantum efficient detectors by silicon nitride and silicon oxynitride/silicon nitride stack," *J. Appl. Phys.*, vol. 124, no. 21, p. 214502, Dec. 2018, doi: 10.1063/1.5054696.
3. J. Gran, Publishable Summary for 18SIB10 chipS.CALe. Zenodo, Jun. 2019. <http://doi.org/10.5281/zenodo.354567>.
4. <https://www.cogenda.com/>.

HALO – High Amplification Laser-pressure Optic

Alexandra Artusio-Glimpse, Kyle Rogers, Paul Williams, and John Lehman

National Institute of Standards and Technology, Boulder CO, USA

Corresponding e-mail address: alexandra.artusio-glimpse@nist.gov

Efforts are underway at the National Institute of Standards and Technology to drastically reduce the uncertainty of laser power measurements using radiation pressure. The High Amplification Laser-pressure Optic (HALO) system is a cornerstone of this effort as it enables amplification of the laser pressure on a high-quality mirror attached to a precision force sensor. We discuss the HALO architecture here.

MOTIVATION

Laser power measurements based on radiation pressure (RP) use the force of light as it reflects from a mirror to characterize the optical power. Here, we work to reduce measurement uncertainty by amplifying the force of the laser light. If the same light reflects multiple times from the sensing mirror of an RP detector, a passive gain can be realized [1,2]. For decades, the cryogenic radiometer standard has yielded relative measurement uncertainties of 10^{-4} at the milliwatt level. Meanwhile, power measurements above 100 W have relative uncertainties near 10^{-2} for both calorimetric-based and RP-based measurements. By amplifying the force of RP with a multi-reflection optical system, we expect laser power measurement uncertainties to approach 10^{-4} for kilowatt level incident powers.

For a RP measurement where the light reflects N times off the sensing mirror having reflectance R given a round-trip scattering and absorption loss L the signal to noise ratio (SNR) goes as

$$SNR \propto \sum_{j=1}^N ((1-L)R)^{j-1}, \quad (1)$$

which approaches N as $(1-L)R \rightarrow 1$. Absorption in the sensing mirror can heat the force sensor and produce a measurement error $N\eta_T\Delta T_1$ where η_T is the temperature-dependent error coefficient and ΔT_1 is the change in temperature of the force sensor for a single reflection. Thus, for low-loss, high-reflectivity optics, we approximate the fractional measurement error as

$$\varepsilon \approx (\eta_1/N + \eta_T\Delta T_1)/F_1, \quad (2)$$

where η_1 represents the averaged noise and F_1 the measured force, both for a single reflection. We see

that amplifying the force of a single reflection with N reflections, we effectively reduce the fractional contribution of the fixed noise by N , but have no effect on the thermal contribution.

Here we describe a system designed for $N \leq 15$ bounces and accommodating the 40 mm diameter beam from a 10 kW infrared laser. Current efforts emphasize the design and system tolerances, while forthcoming efforts will develop an alignment procedure and mirror reflectance and scatter measurements to meet preliminary tolerances. These are steps toward our goal of achieving relative measurement uncertainties approaching those currently found only in cryogenic radiometers. Moreover, our multi-reflection system can be used to amplify lower power lasers, enabling us to reduce the measurement uncertainty of any RP measurements.

HALO DESIGN

The NIST High Amplification Laser-pressure Optic (HALO) system is depicted in Fig. 1 with a green HeNe laser (5 mW) illuminating the beam path, reflecting off the sensing mirror 14 times, and leaving the system to the upper right.

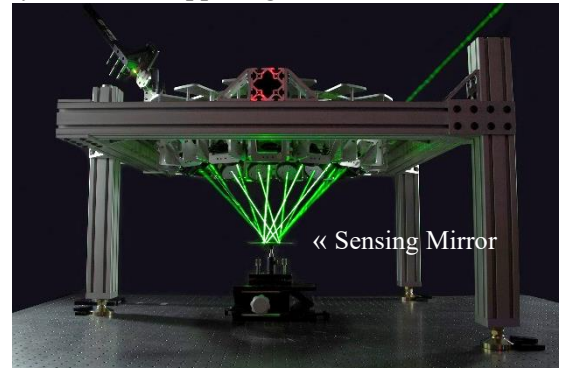


Figure 1. HALO system photograph. A green HeNe illuminates the laser path through 14-bounces and out the system to a beam dump (not shown) at the upper right.

HALO is a pentadecagonal structure with an entrance port and up to 14 upper mirror modules (“ring mirrors”, see Fig. 2) that direct the input laser beam to a lower sensing mirror. Importantly, the laser incidence angle on the sensing mirror is always 45° . This both protects the mirror from thermal flexing as the reflectance need only be optimized for a single

angle and simplifies propagation of uncertainties. The total structure fills a volume of about 1 m^3 . Like toroidal multipass cells used for laser spectroscopy [3], the laser beam traces out a star polygon (Fig. 2). However, here the ring mirrors are pitched downward to the sensing mirror placed at the center of the star pattern. When all 14 ring mirrors are in place, the total beam path in the system is 10.124 m.

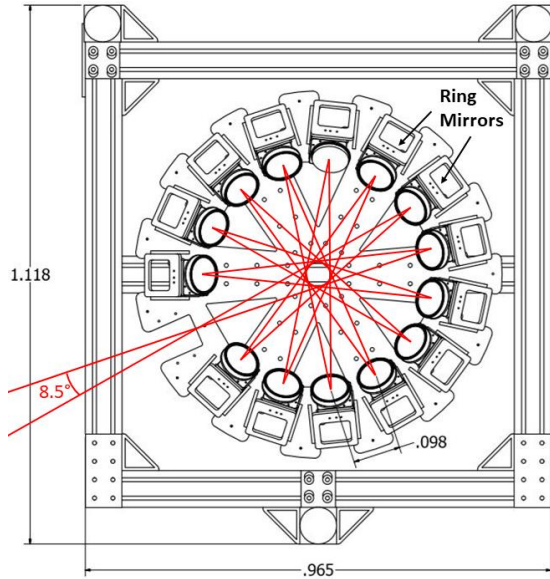


Figure 2. Upper ring mirror modules and star polygon laser path when all 14 mirrors (76.2 mm diameter) are in place. Laser enters through the empty port and exits through the same port, rotated by 8.5° . Alternatively, the laser may exit through any other port when the respective mirror module is removed. (labels in meters)

The spot pattern of the laser on the 150 mm diameter sensing mirror forms two open crescent shapes as the laser beam rotates and expands through the system (Fig. 3). Given the short ($90 \mu\text{m}$) coherence length of our laser and the large incidence angles and long path length differences between adjacent spots in this system, interference is not a concern.

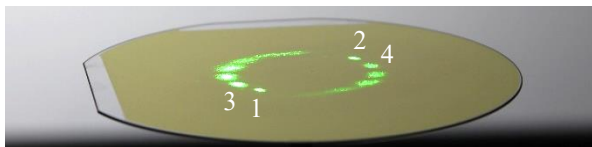


Figure 3. Green HeNe laser spot pattern is visible on the surface of a gold coated fused silica 150 mm diameter wafer. First four bounces of 14 total are labeled.

TIGHT TOLERANCES AND OUTLOOK

In order to reach 10^{-4} uncertainty, near perfect laser alignment and highly-accurate optical characterization of each mirror (reflectance, scatter,

absorptance) will be required. As such, our first goal is to reach a relative measurement uncertainty of 10^{-3} at 10 kW.

We simulated laser propagation through the HALO system and modulated geometric and optical parameters to obtain system tolerances. The results of the ray-tracer and Monte Carlo algorithm are listed in Table 1 (totals exclude the force sensor [4]).

Table 1. Alignment and optical measurement tolerances needed to reach two relative uncertainty goals.

Rel. Unc. Goal	10^{-3}	10^{-4}
Sensing Mirror Angle	$60 \mu\text{rad}$	$30 \mu\text{rad}$
Ring Mirror Angle	$300 \mu\text{rad}$	$30 \mu\text{rad}$
All Mirrors 3D Position	2 mm	2 mm
Reflectance/Scatter	20×10^{-6}	1×10^{-6}
Total Optical Rel. Unc	0.7×10^{-3}	0.75×10^{-4}

In addition to tight system tolerances, if the sensing mirror is bowed, the laser will accumulate astigmatism, as is the case in Fig. 3 where the spots grow in ellipticity as the number of bounces increases. The HALO structure must also be rigid and isolated from vibrations to maintain these tolerances. To reach the 10^{-4} uncertainty goal, simply knowing total scattered power is not enough. The full bidirectional scatter distribution function must be accounted for in the momentum calculations else the calculated laser power from the measured force will be in error by an order of 10^{-4} .

The NIST HALO system has been built and its alignment demonstrated with a low-power, small diameter laser. We now set our attention to alignment with high reflectivity IR mirrors and measurement of a 500 W laser. This incremental advancement is necessary as we progress toward a RP laser power measurement system that will yield measurement uncertainties of 10^{-4} at 10 kW.

This publication is a contribution of the U.S. government and is not subject to copyright.

REFERENCES

1. S. Vasilyan, et al., Total momentum transfer produced by the photons of a multi-pass laser beam as an evident avenue for optical and mass metrology, *Opt. Express*, 25, 20798-20816, 2017.
2. G. Shaw, et al., Comparison of electrostatic and photon pressure force references at the nanonewton level, *Metrologia*, 56, 2019.
3. B. Tuzson, et al., Compact multipass optical cell for laser spectroscopy, *Opt. Letters*, 38, 257-259, 2013.
4. G. Shaw, et al., SI traceable electrostatic balance to measure laser power, *NewRad 2020 extended abstract*.

SI traceable electrostatic balance to measure laser power

G. Shaw¹, F. Seifert¹, J.R. Pratt¹, D.B. Newell¹ and S. Schlamminger¹

¹National Institute of Standards and Technology, Gaithersburg, U.S.A.

Corresponding e-mail address: stephan.schlamminger@nist.gov

We have built an electrostatic balance that can insitu measure laser power traceable to the SI in the range of 10 W to 100 kW. The photon pressure force on a mirror attached to the balance is compensated by an electrostatic force transducer. The balance is capable of measuring the force equivalent to photon pressure from a 100 kW laser with a relative uncertainty of approximately 10^{-4} .

INTRODUCTION

In normal incident reflection, a laser beam with optical power P will exert a force of $2P/c$ on the mirror with c denoting the speed of light. Measurement of this force has become a tool for measurement of laser power [1,2]. A laser beam with 100 kW optical power produces a force of 667 μN , so to achieve a relative uncertainty of 10^{-4} , the force needs to be measured with an absolute uncertainty of 67 nN. In this abstract we focus on the mechanics and electrostatics of the system. The optical layout is designed by our colleagues at the NIST Boulder laboratories [3].

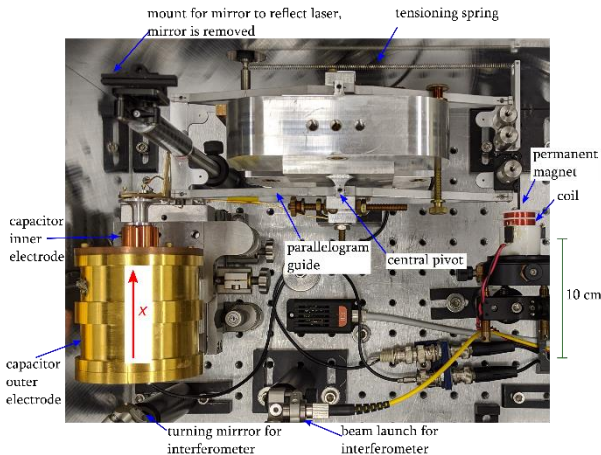


Figure 1. Photo of the electrostatic balance from the top.

A photograph taken from the top of the balancing mechanism is shown in Fig. 1. A four-bar linkage provides nearly parallel movement of the mounting platforms on the left and the right side of the balance along the x-axis (indicated by the red arrow in the photograph). The light reflects off a mirror mounted on the short arm on the left of the balance mechanism. On the same arm, the inner electrode of a concentric

cylinder capacitor is affixed. The balance and outer electrode are mounted to an optical table and a commercial fiber interferometer is used to measure the position of the inner electrode. During force measurements, the balance position is held at a nominal zero position by a digital feedback controller that changes the output of a high voltage amplifier connected to the inner cylinder. The force generated by the electrostatic attraction is given by

$$F = \frac{1}{2} \frac{dC}{dx} V^2, \quad (1)$$

where V is the difference in potential between the cylinders forming the capacitor. The capacitance gradient (dC/dx) is calculated from measurements of the capacitance as a function of position $C(x)$. A second order polynomial $f(x)$, shown in Fig.2, is fitted to the data. The derivative of the polynomial with respect to x gives the capacitance gradient with an average value of -1.12 nF/m.

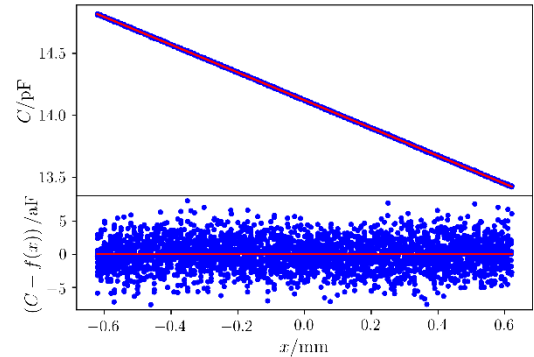


Figure 2. The measured capacitance as a function of position of the inner electrode. The lower graph shows the absolute differences of the measured values from a second order polynomial.

For the capacitance measurements, the balance position must be controlled to a specified target without using the electrostatic force transducer. Therefore, a second actuator consisting of a weak permanent magnet attached to the right mounting platform inside a stationary coil was built. The balance is controlled by supplying current to the coil using the same digital feedback control mentioned above. The dynamic range of the position control is

1.2 mm. The capacitance C was measured using a commercial LCR meter.

SENSITIVITY

The magnetic actuator gives us the opportunity to check the sensitivity of the electrostatic feedback without relying on optical power. An electrical current in a square waveform was supplied to the coil producing a force of about ± 80 nN. The feedback system maintained the balance null position by changing the voltage on the electrostatic actuator. The voltage on the capacitor cylinders is measured with a commercial voltmeter, and from it's reading and the previously measured capacitance gradient the electrostatic force was calculated. Figure 3 shows the electrostatic force for a 3.5-minute-long data taking window.

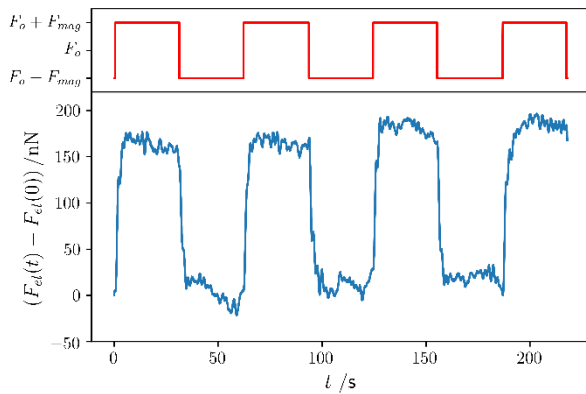


Figure 3. Compensation of the magnetic force (top) with an electrostatic force (bottom).

Figure 4 shows the amplitude of the differential electrostatic force as a function of time for a day. The mean value of the signal is 168 nN with a standard deviation of 18 nN. The data is consistent with a slight

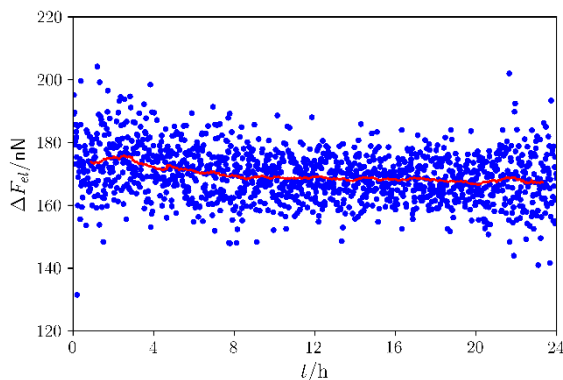


Figure 4. The measurement of the signal amplitude as a function of time (blue dots). The red line represents a moving average over 100 points.

linear drift of about -0.56 nN/h which we believe is caused by the temperature dependence of the magnetization of the permanent magnet that is used to provide the signal. The standard deviation of the signal is smaller at night, around $t=12$ h in Figure 4. At night time standard deviations of 7 nN are achieved. At day time, standard deviations are 50 % higher, an increase that is probably caused by vibrations in the building due to human activity.

SUMMARY AND OUTLOOK

In summary, an electromagnetic signal that represented approximately 2×10^{-4} of a 100 kW optical force was resolved at the 1 W level. Hence, the mechanical, electrical, and control systems are sufficient for the task. However, before the balance can be used to measure light, two important considerations need to be addressed. First, the alignment of the force axis of the balance must be made parallel to the light beam within 0.8° for a relative measurement uncertainty of 10^{-4} . Second, the thermal gradients must be managed. Any absorbed light will cause heating, which will couple into the mechanical system in two ways: (a) the elastic properties of the balance system will change causing a shift in the force required to maintain the balance at 0 and (b) thermal currents in the air surrounding the mirror can produce spurious forces on the mirror. These effects are currently under investigation.

REFERENCES

1. G.A. Shaw, J. Stirling, J. Kramar, P. Williams, M. Spidell, R. Mirin, Comparison of electrostatic and photon pressure force references at the nanonewton level, *Metrologia*, 56, 025002, 2019.
2. P. Williams, M.T. Spidell, J.A. Hadler, T. Gerrits, A. Koepke, D. Livigni, M.S. Stephens, N.A. Tomlin, G.A. Shaw, J.D. Splett, I. Vayshenker, M.G. White, C.S. Yung, J.H. Lehman, Meta-study of laser power calibrations ranging 20 orders of magnitude with traceability to the kilogram, *Metrologia*, 57, 015001, 2019.
3. A. Artusio-Glimpse, K. Rogers, P. Williams, and J. Lehman, HALO – High Amplification Laser-pressure Optic, Newrad 2020 extended abstract.

USE OF PHOTON PRESSURE IN SMALL MASS AND FORCE CALIBRATION

Gordon A. Shaw¹, Julian Stirling², Ryan Wagner³, Paul Williams⁴, Matthew Spidell⁴

¹ Gordon A. Shaw, Mass and Force Group, U.S. National Institute of Standards and Technology (NIST), USA

² Department of Physics, University of Bath, UK

³ Asylum Research, Oxford Instruments, Santa Barbara, CA

⁴ Sources and Detectors Group, U.S. National Institute of Standards and Technology (NIST), USA

Corresponding e-mail address: gshaw@nist.gov

The recent redefinition of the International System of Units (SI) provides opportunities to improve scaling in mass and force metrology. The use of photon pressure force to improve metrology in the nanonewton to piconewton range has the potential to overcome difficulties encountered in developing traceability for this range of forces. Several experiments conducted to compare photon pressure force calibration to other existing methods demonstrate the feasibility of this approach to small mass and force calibration.

INTRODUCTION

Mass and force calibration are typically carried out using calibrated weights. This approach becomes problematic moving to mass below about 100 micrograms (force less than 1 micronewton.) The difficulty in handling the small calibration weights and the uncertainty in their mass values increases the smaller the weights become. The use of a photon pressure force is one way to circumvent these problems, as it provides a reference force in a direction defined by the reflecting surface that is traceable to the SI via laser power calibration methods. Several experiments have been carried out to examine the validity of this approach

EXPERIMENTS

The NIST Electrostatic Force Balance (EFB) has been used to measure photon pressure force at the nanonewton level. The EFB is an electromechanical balance system that uses traceable measurements of capacitance, displacement and voltage to provide a primary reference for mass and force [1]. By attaching high-reflectivity distributed Bragg reflector (DBR) mirrors to the top and bottom of the EFB, and alternately reflecting a laser from these mirrors, a differential force is generated while minimizing thermal drift [2]. A second measurement used a

parallel-mirror etalon to increase the photon pressure force, and data is shown in Fig. 1. The single- and multiple-reflection force measurements were consistent with each other, but both differed from the photon pressure force predicted from an in-situ measurement of laser power by approximately 5 %. The operating conditions of the reference laser power detector used for the in-situ measurement may have contributed to the difference, since the detector was calibrated in air but used in vacuum during the EFB comparison. By using the optical switch in pulsed mode, the force could be continuously varied with high linearity by varying pulse duty cycle.

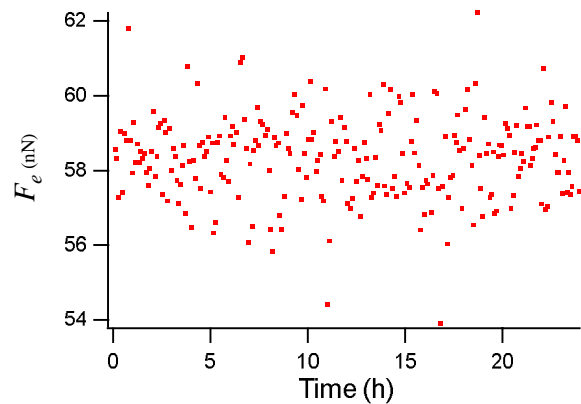


Figure 1. EFB force measurement in multiple reflection configuration.

Force below 1 nanonewton has been measured using chip-scale optomechanical systems. The mechanical sensors are millimeter-scale fused silica parallelogram flexures. Integrated optical fibers provide both a means to apply the photon pressure force, and an interferometer to read out the resulting displacement. When low-finesse fiber optical cavities are used, femtonewton resolution can be obtained with a maximum force of approximately 100 pN [3]. A cross-check of the mechanical flexure stiffness using a calibrated mass shows sub-percent agreement

with the photon pressure force predicted by measuring the power of the laser used to drive the optomechanical system. The use of higher-finesse optical cavities allows for a larger maximum force of several nanonewtons, due to the buildup of circulating optical power within the cavity. The displacement response at the sensor's mechanical resonance frequency is shown in Fig. 2. In this case, the maximum photon pressure force is several nanonewtons. The accuracy of the reference force provided by measuring the optical power delivered to the sensor is heavily dependent on the modelling of the optical properties of the cavity, however [4]. The properties of the sensor itself are very stable, with the laser power force calibration varying less than 2 % over approximately two years of testing. This indicates these types of devices are useful as transfer artifacts.

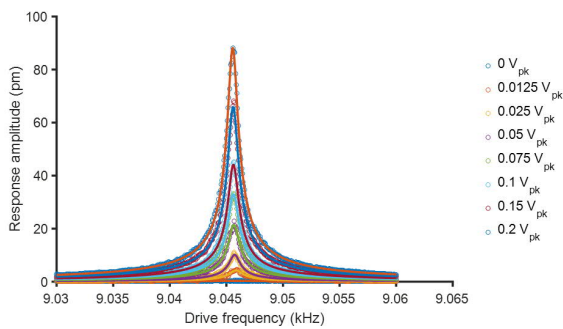


Figure 2. Displacement response to modulated photon pressure force on a flexure sensor from a high-finesse fiber optic cavity. Legend shows uncalibrated modulation amplitude for laser.

Table 1. Calibration strategies for different force ranges.

Force Range	Sensor Type	Reference
300 μ N – 1 nN	EFB	[2]
10 nN – 10 pN	Flexure, resonant optical cavity	[4]
50 pN – 10 fN	Flexure, low finesse cavity	[3]

CONCLUSION

A suite of techniques is available that allows the use of photon pressure to provide force references that are traceable to the SI. Different techniques are appropriate for different force ranges and accuracy requirements. The use of photon pressure forces is potentially useful for a wide variety of small force

calibrations, such as those used in atomic force microscopy (AFM,) gravitational wave detectors, instrumented indentation, and particulate mass measurement.

REFERENCES

1. G.A. Shaw, J. Stirling, J.A. Kramar, A. Moses, P. Abbott, R. Steiner, A. Koffman, J.R. Pratt, Z.J. Kubarych, Milligram mass metrology using an electrostatic force balance, *Metrologia*, 53, A86, 2016.
2. G.A. Shaw, J. Stirling, J. Kramar, P. Williams, M. Spidell, R. Mirin, Comparison of electrostatic and photon pressure force references at the nanonewton level, *Metrologia*, 56, 025002, 2019.3.
3. J. Melcher, J. Stirling, F. Guzmán Cervantes, J.R. Pratt, G.A. Shaw, A self-calibrating optomechanical force sensor with femtonewton resolution, *Appl. Phys. Lett.*, 105, 233109, 2014.
4. R. Wagner, F. Guzmán, A. Chijioke, G.K. Gulati, M. Keller, G.A. Shaw, Direct measurement of radiation pressure and circulating power inside a passive optical cavity, *Optics Express*, 26, 23492, 2019.

Optical power measurements via photon momentum and its comparison with SI-traceable reference methods

Suren Vasilyan^{1,2}, Marco López², Holger Lecher², Marcel Pastuschek², Stefan Kück², Norbert Rogge¹, Eberhard Manske¹ and Thomas Fröhlich¹

¹ Institute of Process Measurement and Sensor Technology, Ilmenau, Germany,

² Physikalisch-Technische Bundesanstalt (PTB), Braunschweig, Germany

Corresponding e-mail address: suren.vasilyan@tu-ilmenau.de

We present the comparison results of the optical power measurements performed by using a calibrated reference standard detector (Thermopile and Si-diode) against those performed by a differential electromagnetic force compensation balance via the photon-momentum generated force measurements in the optical power range between 1 W and 10 W levels. A multi-reflection principle is used to amplify the generated effective forces with an optical cavity created by two quasi-parallel ultra-high reflective mirrors. At different configurations, the measurements of the forces and the optical powers were simultaneously monitored and the relative standard deviations were obtained. Dependent from the computation principle and the absolute value of the applied laser power level the improvements of the measurement uncertainties are discussed.

INTRODUCTION

In recent years, the use of photon momentum to determine the optical power of lasers or to generate precision/calibration small forces [1, 2, 3] has made important progress, especially for the measurements of optical laser power at kilowatt levels [4]. The measuring principle is based on the measurement of the force which is exerted due to the transfer of the photon momentum upon reflection of the radiant power from high-reflective mirror. A measurement device developed by Williams *et. al.* uses this measurement technique with which a relative expanded measurement uncertainty of 1.6 % has been achieved for optical power levels between 1 kW and 50 kW [4]. In the core of the device is a force sensor, consisting of a commercial off-the-shelf electromagnetic force compensation (EMFC) weighing balance and a mirror with high reflectivity ($R=0.9998$) attached to it. Vasilyan *et. al.* [1, 2] carried out measurements with a device having similar components, however, here two force sensors adapted for differential measurements were used, by which the noise level have been reduced. Here, for the stability considerations a low power laser system (around 1 W) was used in multi-reflection

configuration to generate a calibration forces at the currently existing lowest end of the small force standard from 10 nN up to 10 μ N. Despite the statistical error observed as an oversight between the measurements and simplified theoretical calculations, under the multi-reflection configuration the total measured force was amplified at least with an order of magnitude in comparison to single reflection configuration. Furthermore, with the usage of single- and multi-reflection configuration, a possible standard for the force calibration routine, or reversed, standard for the optical (laser) power calibration routine with direct and more simplified traceable chain to the recently renewed SI base units [2, 5, 6] was already established.

EXPERIMENTAL RESULTS

In this paper we present a new, an improved set of measurements of the photon-momentum generated forces at the multi-reflection configuration with the use of differential EMFC setup ([1, 2]) at the laser power levels from 1 W to 10 W and their comparison with the optical power measurements made with the

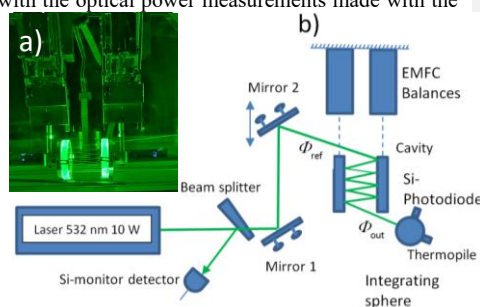


Figure 1. Setup for measuring optical power via photon momentum and vice versa; i.e. calibration of the EMFC using reference optical power.

calibrated reference standard detector.

The measurements were carried out at PTB with an optical system established in accordance to schematics presented in fig. 1(b) and with an integrated portable differential force measurement setup developed at TU Ilmenau. The input optical power Φ_{ref} is measured after mirror 2 with a calibrated

Formatted: Font color: Text 1

reference detector (consisting of a Si-photodiode and a Thermopile attached to an integrating sphere) and simultaneously with the monitor detector. Then the monitor detector is able to determine the laser power at the input of the cavity during the measurements assuming the conversion factor including the reflectivity of the mirrors 1 and 2. The output optical power Φ_{out} , measured with the same calibrated reference detector together with the input optical power, measured with the monitor detector, allows to determine the power loss due to the cavity see fig. 1(b) and fig. 2 (bottom).

With the pre-set laser power of up to 10 W and the multi-reflection (at 21, 33, and 41 cases) configuration we have substantially enlarged the limit of the upper margin of the existing experimental data in continuous force (sub-10 μ N level) and laser power measurements. Additionally, to reduce the optical losses in the cavity, we replaced the conventional high reflective mirrors $R=99.5\%$ with ultra-high reflective mirrors with $R=99.997\%$ reflectivity (for a wavelength of 532 nm) that were used to create our optical cavity like configuration. Results showed a major improvement on reliability of the comparison

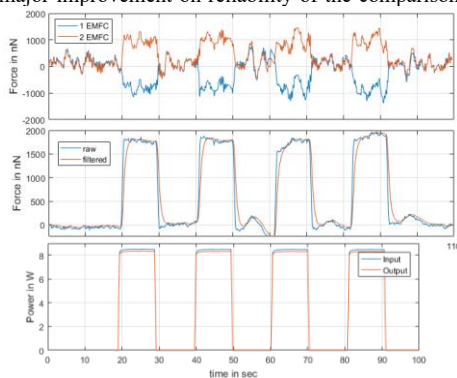


Figure 2. Example of the static force measurements with a periodically applied laser power (10 s) in the case of 33 reflections. (Top) Measured force signal from each balance, (Middle) the difference signal. A feed backward averaging filter was chosen for the last 15 bins to filter raw data. (Bottom) Input and Output power.

of actual photon-momentum generated forces obtained from the real measurement data against the simplified theoretical computations presented in [1, 2, 3]. Thus, the force measurements are performed in combination with the optical schematics as is presented in the fig. 1. The optical power values were used to calculate theoretically the expected photon-momentum generated forces for comparison with the data from the measurements. In this configuration we

are able to directly compare the reference for the force measurements and the reference for the optical power measurements, towards the SI based traceable comparison (actually to the Planck constant) of the force/mass and laser power references.

In fig. 2 we show one of the typical set of force and the corresponding laser power measurements. At the first glance, from the raw data of the force measurements at 33 reflection configuration (mirror reflectivity: 99.997 %, input power: 8.5 W, output power: 8.3 W), the mean value of 1873 nN is obtained with the relative combined standard deviation of 1.71 % (32 nN), if the calculations are made assuming the sample standard deviation then the value is 0.23 %. However, the relative standard error was 3.7 % due to unforeseen environmental noise (temperature and mechanical vibrations) which was detected during the measurement process. As a comparison, the standard uncertainty of the optical power measurements using the calibrated reference standard detector was 0.3 %. Furthermore, in this particular case, the mean value of the measured forces in comparison to the value calculated theoretically differs by 0.2 %, from all measurements this difference is within 3 %.

REFERENCES

1. S. Vasilyan, T. Fröhlich, E. Manske "Total momentum transfer produced by the photons of a multi-pass laser beam as an evident avenue for optical and mass metrology," *Optics Express*, 25, 20798-20816, 2017. DOI: 10.1364/OE.25.020798.
2. E. Manske, T. Fröhlich, S. Vasilyan, „Photon momentum induced precision small forces: a static and dynamic check,“ *Meas. Sci. Technol.* 30 105004, 2019. DOI: 10.1088/1361-6501/ab257e.
3. G. A. Shaw, J. Stirling, J. Kramar, P. Williams, M. Spidell, R. Mirin, "Comparison of electrostatic and photon pressure force references at the nanonewton level", *Metrologia*, 56, 025002, 2019. DOI: 10.1088/1681-7575/aaf9e2.
4. P. Williams, et. al "Portable, high-accuracy, non-absorbing laser power measurement at kilowatt levels by means of radiation pressure" *Opt. Express* 25 4382–92 2017. DOI: 10.1364/OE.25.004382.
5. P. A. Williams, et. al, "Meta-study of laser power calibrations ranging 20 orders of magnitude with traceability to the kilogram" *Metrologia*, 57, 015001, 2020. DOI: 10.1088/1681-7575/ab4641.
6. C. Rothleitner, J. Schleichert, L. Günther, S. Vasilyan, N. Rogge, D. Knopf, T. Fröhlich, F. Härtig, "The Planck-Balance – Using a fixed value of the Planck constant to calibrate E1/E2-weights," *Meas. Sci. Technol.*, 29, 074003, 2018. DOI: 10.1088/1361-6501/aabc9e.

Validation of a compact radiation pressure power meter at hundreds of watts

Alexandra Artusio-Glimpse¹, Ivan Ryger², Natalia Azarova¹, Paul Williams¹, Josh Hadler¹, John Lehman¹

¹National Institute of Standards and Technology, Boulder CO, USA, ²Formerly at NIST, Boulder CO, USA

Corresponding e-mail address: alexandra.artusio-glimpse@nist.gov

We report on the operation of a small-package radiation pressure laser power meter and detail its measurement uncertainties. Given the small package of this device and its non-destructive interaction with the laser, this power meter is attractive for real-time, high-accuracy power measurements in industrial applications. We measure laser power from 25 W to 400 W with a 260 mW/ $\sqrt{\text{Hz}}$ noise floor and 3.1-4.6 % expanded uncertainty. We validate our device against a calibrated thermopile by simultaneous measurements of an unpolarized 1070 nm laser and report good agreement between the two.

INTRODUCTION

In recent years, radiation pressure-based laser power metrology has developed significant interest from the metrology community. In contrast to traditional thermal and quantum techniques for measuring optical power, radiation pressure-based techniques allow for real-time, full beam, in situ monitoring. This offers a unique opportunity to embed SI traceable detectors into laser sources producing what effectively becomes a traceable source system.

Radiation pressure laser power meters have been demonstrated by multiple groups measuring power levels below 1 W [1-5] and above 500 W [6-8]; however, there exists a gap in demonstrated measurements at the few hundred watts level. This middle range in power is applicable to laser-based manufacturing processes like metal additive manufacturing. For this reason, we report on laser power measurements from 25 W to 400 W using our recently developed compact, room temperature, ambient radiation pressure force transducer.

DETECTOR DESIGN

Our compact radiation pressure power meter is diagrammed in Fig. 1. The device consists of two identical spiral flexures made from micromachined crystalline silicon (like the flexures introduced by Ryger [9]) and three fiber-coupled interferometer heads for position detection. The full package

(excluding the interferometer laser, receivers, and electronics) fits within a 4 cm x 4 cm x 2 cm box.

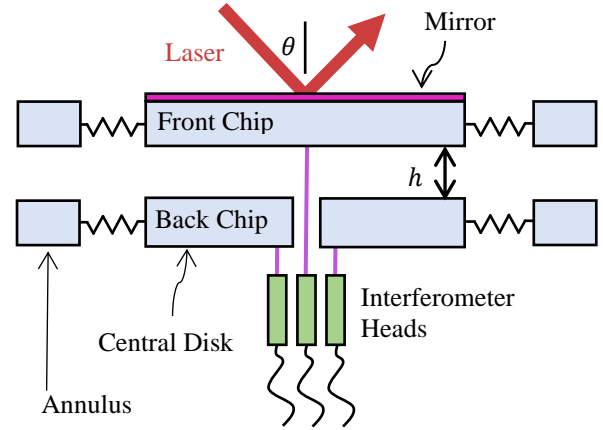


Figure 1. Cross-section view of dual-spring compact power meter (front and back chips have circular symmetry in the plane perpendicular to the page).

Upon laser illumination of the mirror coating (reflectivity greater than 0.9999), the front chip deflects relative to the back chip by Δh , where h is the inter-plate spacing determined from the position measurements of the front chip and back chips made by one interferometer tracing the front and two tracking the back (to account for off-center tilting errors). The power of the laser is directly related to the force of radiation pressure on the front chip and is calculated by balancing this optical force with the restoring spring force of the front chip:

$$P = \Delta h k c / [2R + \alpha(1 - R)] \cos \theta, \quad (1)$$

where $k = 74.5 \pm 0.2$ N/m is the calibrated stiffness of the front chip, c is the speed of light, R is the mirror reflectivity, α is the fraction of non-reflected light that is absorbed, and $\theta = 45^\circ$ is the laser incidence angle with the mirror surface normal.

MEASUREMENTS AND UNCERTAINTY

To overcome small baseline drifting of the measurement signal from air current disturbances and differential heating of the flexure, we modulate the incident laser at 0.5 Hz with 50 % duty cycle and perform a baseline correction. Squeezed air damping between the two chips over-damps ringing of the

spring and results in an exponential time constant of 30 ms on the rising edge of the measurement. Figure 2 shows the baseline corrected power measurement from our compact device. Twenty-nine modulation cycles are overlaid (blue curve) and averaged (black curve). In comparing against the calibrated thermopile, we defined the measured power as the averaged signal in a window from 0.4 s to 0.9 s. In this region, the average noise equivalent power is 260 mW/ $\sqrt{\text{Hz}}$.

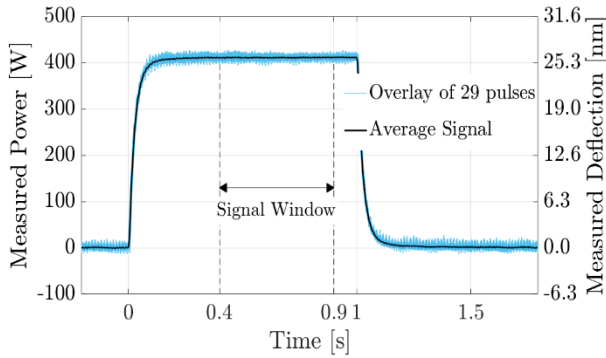


Figure 2. Measurement trace of 400 W laser modulated at 0.5 Hz with 29 cycles overlaid (blue) and averaged (black). The final power measurement is the averaged signal in the window from 0.4 s to 0.9 s.

Over a range of power levels, measured power from our device is compared to the thermopile in Fig. 3, where percent discrepancy is defined $100 \times (P^* - P_0)/P_0$, P^* is the power measured by our compact radiation pressure meter and P_0 is the power measured by the calibrated thermopile (1.2 % expanded uncertainty). Taking an uncertainty weighted average of the measured discrepancies, we find our device reads 1.6 % lower than the thermopile.

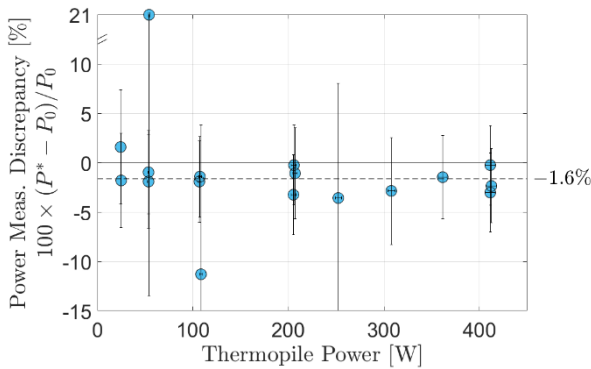


Figure 3. Percent discrepancy in simultaneous power measurements between our device and a calibrated thermopile showing agreement within expanded uncertainties (error bars represent combined uncertainty of both devices, $k=2$).

Fractional uncertainties of our compact radiation pressure measurements are reported in Table 1. Calibration uncertainty components (reflectance and spring constant) and set-up uncertainty components are independent of the laser power, whereas the fractional uncertainty in the measured deflection (Δh) decreases with power.

Table 1. Fractional measurement uncertainty components ($k=2$). Power dependent uncertainties given at two power levels as example.

Component	Dist, Type	Unc. (%)
Reflectance	rect, B	0.010
Spring constant		0.302
Fit	norm, A	0.054
Repeatability	norm, A	0.292
Alignment with gravity	rect, B	0.030
Mass decentering	rect, B	0.044
Laser incidence angle	rect, B	3.126
Laser decentering	rect, B	0.044
Interferometer alignment	rect, B	0.062
Thermal drift correction	rect, B	0.008
Meas. deflection at 25 W	norm, A	3.352
Meas. deflection at 400 W	norm, A	0.186
Combined Uncertainty at 25 W		4.626
Combined Uncertainty at 400 W		3.148

REFERENCES

1. K. Agatsuma, et al., Precise measurement of laser power using an optomechanical system, *Opt. Express*, 22, 2013-2030, 2014.
2. S. Vasilyan, et al., Total momentum transfer produced by the photons of a multi-pass laser beam as an evident avenue for optical and mass metrology, *Opt. Express*, 25, 20798-20816, 2017.
3. R. Wagner, et al., Direct measurement of radiation pressure and circulating power inside a passive optical cavity, *Opt. Express*, 26, 23492-23506, 2018.
4. G. Shaw, et al., Comparison of electrostatic and photon pressure force references at the nanonewton level, *Metrologia*, 56, 2019.
5. P. Pinot, et al., Optical power meter using radiation pressure measurement, *Measurement*, 131, 109-119, 2019.
6. P. Williams, et al., Portable, high-accuracy, non-absorbing laser power measurement at kilowatt levels by means of radiation pressure, *Opt. Express*, 25, 4382-4392, 2017.
7. J. Lehman, et al., Inline laser power measurement by photon momentum, *Appl. Opt.*, 58, 1239-1241, 2019.
8. P. Williams, et al., Radiation-pressure-enabled traceable laser sources at CW powers up to 50 kW, *IEEE Trans. on Inst. Meas.*, 68, 1833-1839, 2019.
9. I. Ryger, Micromachined force scale for optical power measurement by radiation pressure sensing, *IEEE Sensors J.*, 18, 7941-7948, 2018.

Design and calibration of a radiation-pressure based laser power meter and force sensor

Jonathan Cripe¹, Matthew Spidell², and Gordon Shaw¹

¹National Institute of Standards and Technology, Gaithersburg, USA

² National Institute of Standards and Technology, Boulder, USA

Corresponding e-mail address: jonathan.cripe@nist.gov

Photons impart a back-action force when they reflect from a surface. When combined with simple interferometry the radiation pressure force can be used to calibrate an optomechanical sensor. We describe the design and calibration of a radiation-pressure based laser power meter and force sensor. We propose calibrating the optomechanical sensor in two ways, with photon momentum and with the force of gravity using calibrated masses and comparing the results. Once calibrated the sensor will provide a metrological link between mass & force and laser power at the 1 W and 10 nN scales with a goal of 1 % uncertainty and provide traceability to the kilogram.

INTRODUCTION

Traditional means of measuring laser power require the light to be absorbed. For example, thermal power meters absorb photons and measure the increase in temperature. The drawback of absorptive power measurements is that one cannot directly measure the power without introducing a beamsplitter to sample the light, which in turns adds uncertainty to the measurement.

An alternative to absorptive power measurements is using radiation pressure or photon momentum. When light reflects off a mirror, the change in momentum provides a radiation pressure force given by

$$F_{RP} = \frac{2P}{c} r \cos \theta \quad (1)$$

where P is the power, c is the speed of light, r is the reflectivity of the surface, and θ is the angle of incidence with respect to the normal. By attaching the mirror to a spring-like transducer, the radiation pressure force creates a displacement, as seen in Figure 1, that can be measured using interferometry shown in Figure 2. NIST has previously developed this approach for measuring kilowatt [1] and milliwatt [2] level laser powers. Here we describe the design and calibration for measuring power on the order of 1 W and force on the order of 10 nN.

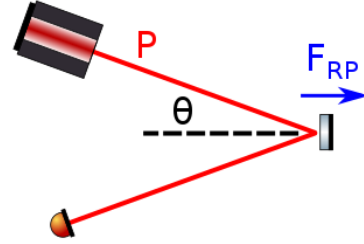


Figure 1. Schematic of radiation pressure force on a movable mirror.

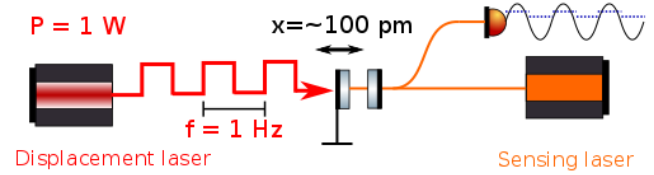


Figure 2. Schematic of radiation pressure force and displacement readout. The displacement laser causes a length change, x , in the Fabry Perot cavity which is read out using as separate sensing laser as a change in voltage on a photodiode in reflection of the cavity.

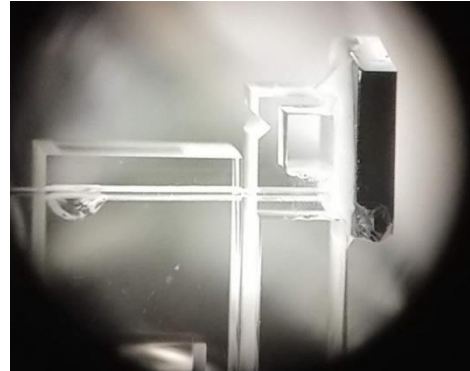


Figure 3. Image of the optomechanical sensor. The sensor consists of a reference (left) and flexible cantilever (right). A highly reflective mirror is attached to the flexible cantilever. A cleaved fiber is attached to each side to create a low finesse Fabry Perot cavity for measuring displacement.

CALIBRATION USING RADIATION PRESSURE

To calibrate the sensor using radiation pressure, we use a 1 W laser to provide a radiation pressure force which causes a 100 pm displacement of the sensor. The laser light will pass through a switch to modulate

the radiation pressure force exerted on the mirror with a frequency of approximately 1 Hz. We collect the light reflected by the sensor with a calibrated integrating sphere to serve as a record of the amount of force applied to the sensor.

We measure the displacement of the sensor using a second sensing laser and a low finesse Fabry Perot cavity made up of two optical fibers. The intensity and frequency of the sensing laser is stabilized with feedback control loops to reduce the influence of intensity and frequency noise in the displacement measurement. The radiation pressure force from the displacement laser cause the cavity length to change, which in turn affects the optical interference within the cavity. We calibrate the cavity voltage signal detected in reflection by sweeping the wavelength of the widely tuneable sensing laser. Relating the calibrated force from the integrating sphere measurement to the displacement measurement allows us to calibrate the mechanical response or stiffness of the sensor and is traceable to a NIST standard laser absorption calorimeter.

CALIBRATION USING THE FORCE OF GRAVITY

A second approach to calibrating the sensor's low frequency response is to use the force of gravity from a calibrated mass to create a displacement. This method of calibration is traceable to the kilogram. By using a mass robot to load and unload the mass, we can generate a large number of repeatable trials to reduce the uncertainty of the measurements. The displacement readout is the same as described in the previous section.

Using a similar but stiffer sensor as that shown in Figure 1, we conducted 10 separate trial sets consisting of between 200 and 700 individual measurements each. Figure 4 shows a histogram of an example set of trials consisting of 300 measurements using a 200 mg mass. Using the mass robot and conducting the measurements in a stable, temperature-controlled environment allow us to achieve a population standard deviation of approximately 1 % for each set of measurements.

Having developed this method of calibration and provided a proof of principle, we will repeat the process with a smaller mass for the more flexible radiation pressure-based sensor shown in Figure 3. Calibrating the sensor using both the radiation pressure method and the mass method will allow us

to compare results and create a metrological link between optical power and mass and provide a calibrated and portable sensor for measuring optical powers on the order of 1 W and forces on the order of 10 nN.

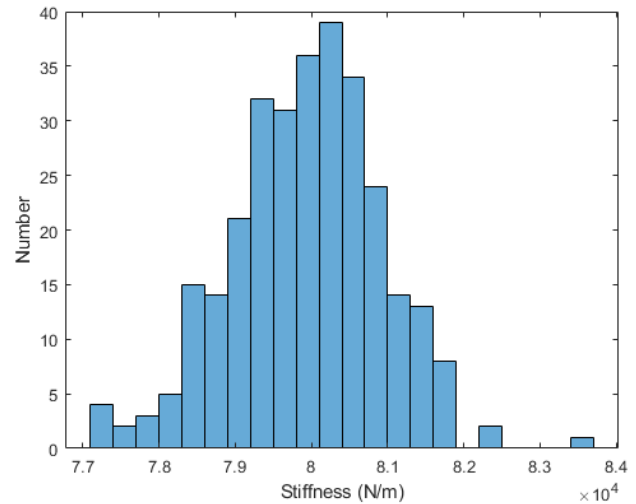


Figure 4. Histogram of results of the static stiffness using the force of gravity calibration method. The mean of the data is 79,900 N/m with a population standard deviation of 1000 N/m.

REFERENCES

1. P. Williams, et al. Portable, high-accuracy, non-absorbing laser power measurement at kilowatt levels by means of radiation pressure, *Optics Express*, **25**, 4382-4392, 2017.
2. J. Melcher, et al. A self-calibrating optomechanical force sensor with femtonewton resolution, *Appl. Phys. Lett.*, **105**, 233109, 2014.

A Simple Method of UV Stray Light Correction for Field Spectrometers in Ground Validation Sites

Ling Li^{1*}, Zhifeng Wu¹, Caihong Dai¹, Yanfei Wang¹ and Emma Woolliams²

¹Division of Optics, National Institute of Metrology, China, Beijing, China

²National Physical Laboratory, Queens Road, Teddington, Middx, TW11 0LW, UK

Corresponding e-mail address: liling@nim.ac.cn

Field spectrometers are widely applied in ground validation sites for remote sensing and earth observation. However, the stray light is one of the most important factors on accurate measurements, since the spectral distribution of target source differs significantly from the incandescent calibration source. Here, a simple UV stray light correction method for continuously distributed wide-spectrum light sources was established by using bandpass filters. The UV stray lights of field spectrometers in situ measurement was reduced obviously.

INTRODUCTION

With the goal of climate change prediction and disaster weather prevention, high accurate spectral radiometric calibration is essential for remote sensing and earth observation¹. Ground vicarious calibration is one of the most feasible ways to realize SI-traceable radiometric calibration for on-orbit satellites. However, the spectral distribution of solar radiance is different from calibration light source (incandescent lamp). The stray light is a main uncertainty source of laboratory calibrated spectrometers which are transferred to the ground-based validation sites, since CCD spectrometers have problems such as internal structural defects and unsatisfactory optical components, which seriously affect the accurate radiance measurements. Several approaches have been proposed to correct the stray light in CCD spectrometers²⁻⁵. Zong et al.³ proposed an efficient and accurate correction method that obtained the spectral line spread functions for every pixel by using a set of monochromatic laser sources. But the tunable lasers are relatively expensive and hard to maintain for most laboratories.

In this paper, the stray light properties of various typical field spectrometers were characterized. A simple, economic correction method was established for continuously distributed wide-spectrum light sources by using bandpass filters. The mathematical correction model was also proposed.

EXPERIMENTS

The stray light properties of four various typical field spectrometers were characterized by using a cut-off filter, which blocks the wavelengths shorter than 450 nm. These spectrometers, FieldSpec4 (ASD), HR-1024i (SVC), PSR+3500 (Spectral Evolution), and CR280 (Colorimetry Research), were calibrated by reflectance plaque and standard lamp. Then the 450 nm cut-off filter was placed in front of each spectrometer, with the same measurement settings, including position, integration time, and the average number of time.

The stray light ratios (σ) in UV wavelengths were calculated by dividing the radiance results with cut-off filter by calibration ones, the formula is $\sigma = L_x/L_c \times 100$. As is shown in Fig.1, The stray light ratios are more than 5% in the wavelength around 350 nm, and σ value of the more compact spectrometer is much higher, such as CR 280.

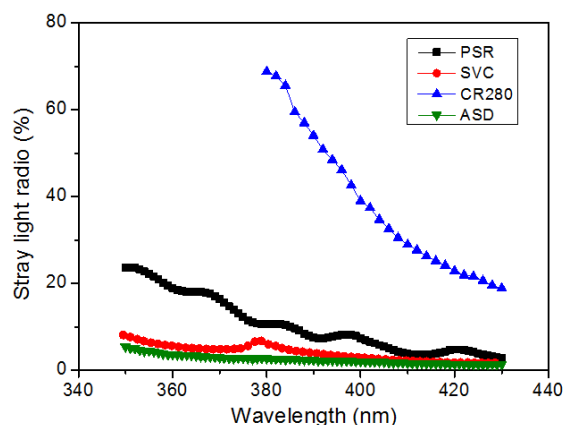


Figure 1. The stray light ratios of four field spectrometers.

As is shown in Fig.2, the UV stray light ratios owing to different wavelength ranges of CR 280 spectrometer were measured by a set of bandpass filters. The stray light at 380 nm originating from 550nm to infrared wavelengths could be defined as $Y_{\text{stray a},380}$. The stray light at 380 nm originating from 650nm to infrared range could be defined as $Y_{\text{stray b},380}$. Then stray light portion at 380 nm owing to the wavelength range from 550nm to 650nm could be

obtained by subtracting $Y_{\text{stray } b,380}$ from $Y_{\text{stray } a,380}$. Thus, the stray light ratio of UV wavelength could be calculated by dividing $(Y_{\text{stray } a,380} - Y_{\text{stray } b,380})$ by integral radiance between 550 nm and 650 nm.

$$R_{\text{stray } 380,550\text{nm}-650\text{nm}} = \frac{Y_{\text{stray } a,380} - Y_{\text{stray } b,380}}{Y_{\text{meas}, 550\text{nm}-650\text{nm}}}$$

Similarly, the UV stray light ratios owing to 650 nm to 800 nm, and 800 nm to near infrared ranges could be obtained, respectively.

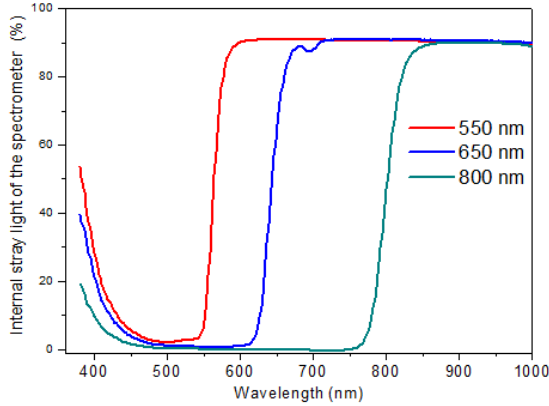


Figure 2. Stray light ratios of CR280 by different bandpass filters.

CORRECTION METHOD

The total signal from spectral stray light at a given wavelength (λ_i) is the sum of all spectral stray light contributions from the broadband source spectra falling on the elements. For continuously distributed wide-spectrum light sources, the stray light effect of longer wavelengths on UV adjacent wavelengths is similar. Therefore, the true signal $Y_{\text{true}, 380}$ of spectrometer can be calculated by the equation below:

$$\begin{aligned} Y_{\text{true}, 380} &= Y_{\text{meas}, 380} - Y_{\text{stray}, 380} \\ &= Y_{\text{meas}, 380} - [Y_{\text{stray } 380,550\text{nm}-650\text{nm}} \\ &\quad + Y_{\text{stray } 380,650\text{nm}-800\text{nm}} + Y_{\text{stray } 380,800\text{nm}-1080\text{nm}}] \\ &= Y_{\text{meas}, 380} - [R_{\text{stray } 380,550\text{nm}-650\text{nm}} \cdot Y_{550\text{nm}-650\text{nm}} \\ &\quad + R_{\text{stray } 380,650\text{nm}-800\text{nm}} \cdot Y_{650\text{nm}-800\text{nm}} \\ &\quad + R_{\text{stray } 380,800\text{nm}-1080\text{nm}} \cdot Y_{800\text{nm}-1080\text{nm}}] \end{aligned}$$

This mathematical model can be easily used to calculate the correction results of stray light at UV wavelengths. As shown in Fig. 3, the spectral radiance results of the solar radiance on the ground-based verification site was corrected, the stray light effect of visible and infrared range on UV 380nm~400nm was significantly reduced.

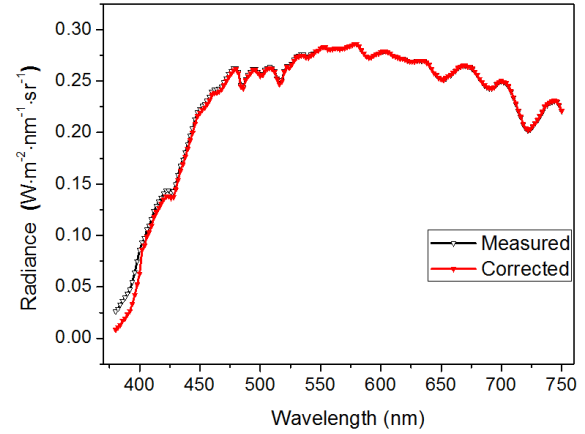


Figure 3. The measured result and corrected result of CR280 used in ground-based sites.

CONCLUSION

Here, a set of the bandpass filters with specific transmittances were used to measure UV stray light signals, and the mathematical correction model was established to realize the efficient evaluation and simple correction. The method with bandpass filter can be widely used due to simple experimental conditions and efficient work process for the continuously distributed wide-spectrum light sources.

ACKNOWLEDGMENTS

This work was supported by the National Key R&D Program of China, No. 2018YFB0504800 (2018YFB0504804).

REFERENCES

1. M. Jehle, A. Hueni, K. Lenhard, A. Baumgartner, M. E. Schaepman Detection and Correction of Radiance Variations During Spectral Calibration in APEX IEEE, Geoscience & Remote Sensing Letters, 12(5), 1023-1027, 2015.
2. S. W. Brown, B. C. Johnson, M. E. Feinholz, M. A. Yarbrough, S. J. Flora, K. R. Lykke, D. K. Clark, Stray-light correction algorithm for spectrographs, Metrologia, 40(1), 81-84, 2003.
3. Y. Zong, S. W. Brown, B. C. Johnson, K. R. Lykke, Y. Ohno, Simple spectral stray light correction method for array Spectroradiometers, Applied Optics, 45(6), 1111-1119, 2006.
4. S. G. R. Salim, N. P. Fox, W. S. Hartree, E. R. Woolliams, T. Sun, K. T. V. Grattan, Stray light correction for diode-array-based spectrometers using a monochromator, Applied Optics, 50(26), 5130-5138, 2011.
5. S. Nevas, J. Gröbner, L. Egli, M. Blumthale, Stray light correction of array spectroradiometers for solar UV measurements, Applied Optics, 53(19), 4313-4319, 2014.

Traceable Radiometry Underpinning Terrestrial- and Helio- Studies (TRUTHS): Enabling a Space-based Climate and Calibration Observatory - An ESA Earth Watch mission.

Nigel Fox¹, Paul Green¹ Javier Gorron¹

National Physical Laboratory (NPL), Teddington, United Kingdom

Corresponding e-mail address: nigel.fox@npl.co.uk

TRUTHS, will create a ‘metrology laboratory in space’. Designed explicitly to meet the requirements of climate the mission establishes SI traceability on-board the space-craft through mimicking the ground-based radiometric calibration chain fully-linked to a space cryogenic radiometer. TRUTHS measures incoming and reflected radiation from the sun spectrally and spatially resolved with accuracy, typically an order of magnitude better than current satellites. This data will provide a benchmark of the radiation state of the planet from which change can be detected in <half time of existing sensors constraining climate forecasts. The data also allows an upgrade in performance of other sensors, ensuring their SI traceability through reference calibration from space.

INTRODUCTION

In November 2019 the TRUTHS mission [1, 2] was funded and adopted into the ESA Earth watch program. The mission is based on a concept conceived and prototyped by a UK team led by the National Physical Laboratory (NPL) the UK national metrology institute and selected by the UK space agency (UKSA) from a national competition. The first phase of implementation will be carried out by an industrial consortium drawn from subscribing member states: UK, Greece, Switzerland, Czech Republic and Romania with a view to a target launch date in 2026.

TRUTHS is a mission designed explicitly to meet the exacting needs of climate. Its primary goal is to establish a benchmark dataset of the radiation state of the planet, spectrally and spatially resolved with sufficient accuracy that trends can be detected limited only by natural variability, immune from biases and ambiguities of sensor performance and degradation. It measures incoming and reflected solar radiation from ~320 nm to 2450 nm with an uncertainty of 0.3% (k=2) (a factor ten improvement over existing sensors), globally sampled at 50 m spatial resolution and spectrally continuous with a bandwidth of 5-10 nm. This allows it not only to

quantify change in radiation balance but also to attribute effects to key climate feedbacks such as Cloud and Albedo as well as account for potential variations in energy inputs total and spectral solar irradiance - facilitating testing of climate forecast models in the shortest time possible.

TRUTHS will be the scientific forerunner of a paradigm shift in how the Earth is observed, delivering data not constrained to a single discipline but deliberately specified to allow it to be configured to support applications in and at the boundaries of Land, Ocean and Atmosphere and meet the exacting needs of many Essential Climate Variables (ECVs) e.g. Land and Ocean Carbon cycle,

Additionally, it will be a ‘metrology laboratory in space’, providing and enabling SI-traceable measurements of improved and unequivocal accuracy from other sensors through in-flight calibration. TRUTHS will be an enabling element of the internationally requested ‘space-based climate observatory’, ideally in conjunction with other benchmark sensors such as NASA CLARREO [3].

MISSION CONCEPT

The TRUTHS payload comprises a hyperspectral imaging Spectrometer (HIS), which whilst of state-of-the-art performance is not significantly different than that flying or designed for other missions. The disruptive differentiator of TRUTHS is the on-board calibration system. This mimics the primary terrestrial traceability chain of a typical NMI – cryogenic radiometer – intensity stabilised lasers – Transfer Radiometers – Flat plate diffusers all implemented within in a small ~1 m³ satellite.

This on-board calibration system facilitates a spectral radiance calibration of the HIS on a daily basis, removing not only effects of launch but also corrections for normal in-flight degradation of both the HIS and the calibration system. The space-based cryogenic radiometer of TRUTHS called CSAR (Cryogenic Solar Absolute Radiometer) not only serves as a primary SI standard but also measures incoming total solar irradiance with an uncertainty of

0.02% $k=2$. The CSAR for TRUTHS is based on an evolution of the first prototype currently serving as a terrestrial reference for solar irradiance at the World Radiation Centre in Davos for the last decade [4]. A CSAR v2, 1/3rd of the mass, was built and tested coupled to a space cooler as part of pre-development studies in 2016.

In addition to making high accuracy observations of the Earth for climate and other applications TRUTHS will improve the accuracy of other missions through reference calibration. The choice of a true non-sun-synchronous polar orbit allows TRUTHS to simultaneously view the same scene as other satellites on a regular basis. The high spatial and spectral resolution of TRUTHS facilitating a match to the footprint of other sensors and when viewing relatively uniform targets like deserts and snowfields calibrations can be transferred in a traceable manner.

RESULTS

The paper will not only present the concept but also results of testing of the prototype calibration system under vacuum and simulations of cross-calibrations and performance improvements of other sensors such as Sentinel 2 where a factor 5 improvement in radiometric uncertainty has been demonstrated.

ACKNOWLEDGEMENTS

The authors wish to acknowledge the work of the international science team, particularly those from NASA CLARREO team that helped develop the science case for TRUTHS and UK space agency through its Centre for Earth Observation Instrumentation for funding of the prototype together with the UK national measurement system. The work was also supported by the project (16ENV03), which has received funding from the EMPIR programme co-financed by the Participating States and from the European Union's Horizon 2020 research and innovation programme.

REFERENCES

1. TRUTHS - NPL [Internet]. [cited 2020 Jan 21]. Available from: <https://www.npl.co.uk/earth-observation/truths>
2. N. Fox, A. Kaiser-Weiss, W. Schmutz et al, Phil. Trans. R. Soc A, 369, 4028-4063, 2011.
3. Wielicki et al BAMS ([https://doi.org/10.1175/BAMS-D-](https://doi.org/10.1175/BAMS-D-12-00149.1)

- 12-00149.1) 2013,
4. Winkler R. Cryogenic Solar Absolute Radiometer A potential SI standard for Solar Irradiance. University College London; 2012.

CubeSat spectroradiometer calibration with a laser-based tunable radiance source

Steven van den Berg¹, Paul Dekker¹, Gerard Otter², Marcela Pelica Páscoa² and Niels Dijkhuizen²

¹VSL, Delft, The Netherlands, ²TNO, Delft, The Netherlands

Corresponding e-mail address: svdberg@vsl.nl

We have developed an SI-traceable laser-based tunable radiance source for the calibration of spectroradiometers. As a demonstration of the calibration method, a CubeSat spectrometer has been calibrated for radiance in the UV-VIS wavelength range. For comparison, the spectrometer has also been calibrated with a traditional setup based on a calibrated diffuser and a FEL lamp. Both routes show good agreement within the combined measurement uncertainty. The laser-based approach could be an interesting alternative to the traditional method, not only because of reduced measurement uncertainty, but also because it directly allows for characterization of the instrumental spectral response function and stray light effects, reducing calibration time and cost.

INTRODUCTION

SI-traceable calibration of satellite instruments, such as spectroradiometers, gets increasingly important in space-based observation for various reasons. First, requirements on measurements in terms of accuracy, dynamic range and wavelength range get more and more demanding. Second, long-term observations require SI-traceability for comparability of data records that are acquired over a long time-interval (decades) and with different instruments. Traditionally, radiance response calibration is performed with a FEL lamp, combined with a calibrated diffuser as a radiance source. The disadvantages of such a source are the limited lifetime of the FEL lamp and its large spectral width. Additional measurements are therefore required to determine stray light characteristics and the instrumental spectral response function (slit function) of the spectroradiometer.

In this contribution we present the application of a laser-based tunable radiance source for the calibration of spectroradiometers. Such sources have been shown to be an interesting alternative to lamp-based sources, as e.g. demonstrated for the calibration of spectral (ir-)radiance responsivity of detectors [1]. As demonstration of the calibration method, a

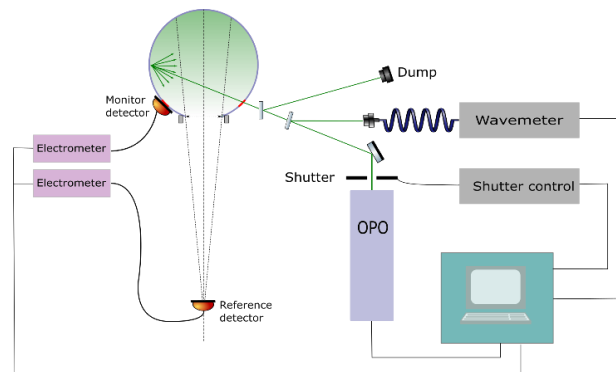


Figure 1. Schematic of laser-based radiance source.

CubeSat spectroradiometer (TROPOLITE BB, TNO [2]) has been calibrated in the UV-VIS wavelength range with this source. For comparison the spectroradiometer has also been calibrated with a radiance source based on a FEL lamp and a diffuser.

SPECTROMETER CALIBRATION WITH A LASER BASED RADIANCE SOURCE

The radiance source consists of a 30 cm-diameter integrating sphere, that is fed with the light from a tunable nanosecond optical parametric oscillator (OPO) offering a wide tuning range (210 nm – 2400 nm). The integrating sphere is equipped with a monitor detector to measure the irradiance at the sphere wall, accounting for any potential source instability. A schematic of the setup is shown in **Figure 1**. More details on the design requirements can be found in [3]. The radiance source is calibrated with a reference detector that is positioned at a well-defined distance from the sphere aperture (**Figure 2**). Both the reference detector and the integrating sphere are equipped with calibrated apertures. The radiance emitted from the integrating sphere's exit aperture is determined from the measured flux and the geometry of the system. This calibration is performed as a function of wavelength by tuning the laser. The signals from reference detector and monitor detector are measured simultaneously with a charge meter, thus linking the emitted radiance from the sphere aperture to the monitor detector signal. Charge meters are used here because of the pulsed nature of the source [1].

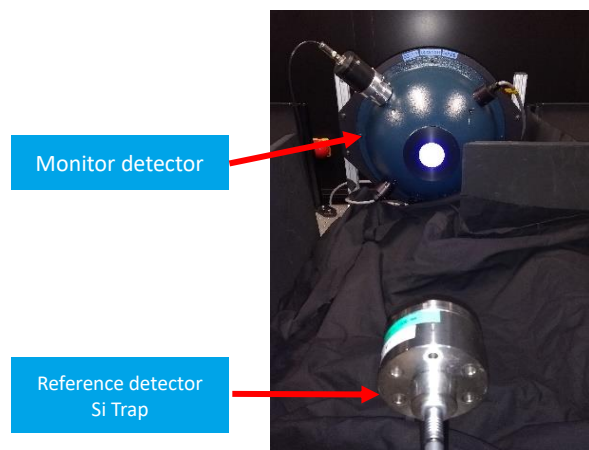


Figure 3. Setup for the calibration of radiance from the integrating sphere with a reference trap detector.

As an additional check of the method and to estimate residual stray light effects, the calibration of the source has been performed at 2 positions of the reference detector (50 cm and 75 cm from the source). The measured radiance at both positions agrees within 0.2% for wavelengths ranging from 250 nm to 950 nm. Here the reference detector is a Si trap detector traceable to the absolute cryogenic radiometer of VSL. The total measurement uncertainty of the source radiance calibration is preliminary estimated to be about 1%.

The TROPOLITE spectroradiometer has been calibrated with the laser-based radiance by positioning it in front of the radiance source (replacing the reference detector in **Figure 2**). The calibration is performed by tuning the OPO from 370 nm to 480 nm in steps of 10 nm. The measurement range is determined by the operating range of the TROPOLITE instrument. For each wavelength setting a set of images is acquired by the spectroradiometer, while the current from the monitor detector is measured simultaneously.

VALIDATION OF THE METHOD

To validate the laser-based method, a traditional calibration of the TROPOLITE instrument has been performed with a FEL lamp with a setup schematically shown in **Figure 3**. The FEL lamp has been calibrated by VSL for spectral irradiance with an uncertainty of (2% - 3%, $k=2$, wavelength dependent). To convert the lamp irradiance into radiance a diffuser is used. The diffuser has been applied for several satellite instrument calibrations and has been thoroughly characterized. The calibration has been performed for various distances between FEL lamp and diffuser. A preliminary

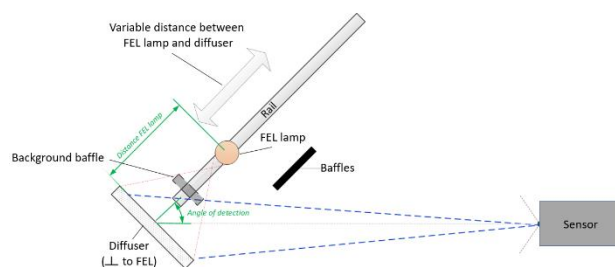


Figure 2. Schematic of a setup for calibration of a spectroradiometer (the sensor on the right-hand side) with an FEL lamp and a diffuser.

analysis of the TROPOLITE calibration data shows that the traditional method and the laser-based method agree within 1-2% over the full wavelength range.

CONCLUSIONS

We have developed a tunable laser-based radiance source, which was successfully applied for the calibration of a CubeSat spectroradiometer. The results were validated by comparison with a traditional FEL lamp-based calibration. The laser-based approach not only delivers radiance calibration, it also offers the opportunity to simultaneously measure other instrument characteristics such as stray-light effects and the instrument spectral response function.

This work was funded by the European Metrology Programme for Innovation and Research (EMPIR), Project 16ENV03, MetEOC-3, 'Further metrology for Earth Observation and Climate'. EMPIR is co-funded by the European Union's Horizon 2020 research and innovation programme and the EMPIR Participating States.

REFERENCES

1. B.T. G De Goeij *et al.*, "First aircraft test results of a compact, low cost hyperspectral imager for earth observation from space", in Proceedings of International Conference on Space Optics — ICSO 2016, Proc. SPIE, 10562N, 2017.
2. Zong, Y., Brown, S. W., Eppeldauer, G. P., Lykke, K. R. and Ohno, Y., "A new method for spectral irradiance and radiance responsivity calibrations using kilohertz pulsed tunable optical parametric oscillators", Metrologia 49, S124-S129, 2012.
3. S.A. van den Berg *et al.*, Traceable radiance source for spectroradiometer calibration, in Proceedings of International Conference on Space Optics — ICSO 2018, Proc. SPIE, 1118068
<https://doi.org/10.1117/12.2536143>, 2019

THE REDUCED BACKGROUND CALIBRATION FACILITY 2 FOR INFRARED DETECTORS, CAMERAS AND SOURCES

C. Monte, M. Reiniger, A. Adibekyan, C. Baltruschat, J. Bories, J. Gieseler,
B. Gutschwager, R. Häfner, I. Müller, and J. Hollandt

Physikalisch-Technische Bundesanstalt (PTB), Braunschweig and Berlin, Germany

Corresponding e-mail address: Christian.Monte@ptb.de

The Reduced Background Calibration Facility 2 (RBCF2) as the successor of the Reduced Background Calibration Facility (RBCF) was recently brought into operation at PTB. It provides traceable calibrations of space based infrared remote sensing experiments in terms of radiation temperature and spectral radiance under cryogenic and / or vacuum conditions.

INTRODUCTION

The Physikalisch-Technische Bundesanstalt (PTB) designed a new calibration facility, the Reduced Background Calibration Facility 2 (RBCF2) as the successor of the Reduced Background Calibration Facility (RBCF) [1], and brought it recently into operation. It provides traceable calibrations of air born and space based infrared remote sensing experiments in terms of radiance temperature and spectral radiance. Traceable remote measurements require the use of calibrated stable detector systems and/or source-based calibration standards on board of the instrumentation. In any case they should be calibrated under operational conditions to ensure traceability with the smallest possible uncertainty. The RBCF2 enables therefore the calibration of radiators and detectors and cameras under cryogenic and/or vacuum conditions. The integration of the instrument under test into the RBCF2 can be done under ISO 5 clean room conditions.

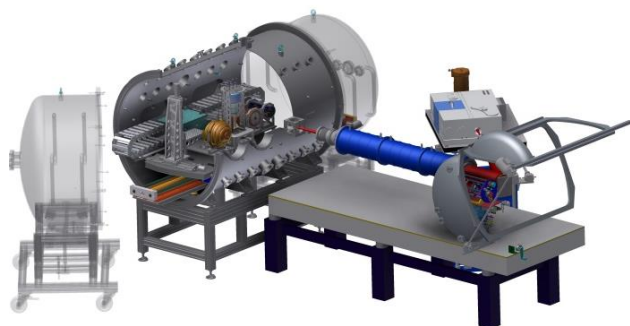


Figure 1 The Reduced Background Calibration Facility 2 (RBCF2) of PTB with source- (left) and detector (right) chamber.

CONCEPT OF THE RBCF2

The general concept of the RBCF2, shown in Figure 1, is to connect different sources in the source chamber and detectors in the detector chamber via a liquid nitrogen cooled beam line. Source- and detector chamber also incorporate cooling facilities. Translation units in both chambers enable the RBCF2 to automatically compare and calibrate different sources and detectors with stable comparison instruments at cryogenic ambient temperatures and under a common vacuum.

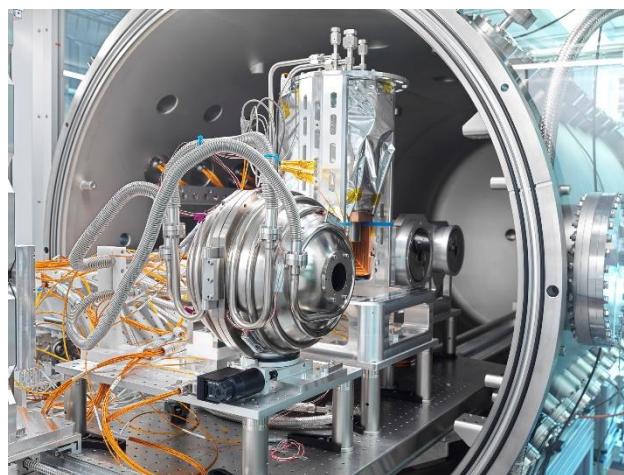


Figure 2 View into the source chamber of the RBCF2: emissivity sample holder, LN2-blackbody, VLTBB and VMTBB from left to right.

Reference sources for comparisons are dedicated vacuum variable temperature blackbodies (compare Figure 2), for example the vacuum medium temperature blackbody (VMTBB, 150 °C to 430 °C) [2], the vacuum low temperature blackbody (VLTBB, -173 °C to 177 °C) [3], the large area heatpipe blackbody (LAHBB, -60 °C to 50 °C) featuring a radiating diameter of 250 mm, the liquid nitrogen blackbody (LNBB, -196 °C) and calibrated vacuum integrating sphere radiators for UV-VIS and SWIR applications (Figure 3). The radiation temperatures of the reference blackbodies and the spectral radiance of the integrating sphere radiators are traceable to the ITS-90 via the primary standards

of PTB. Using the calibrated vacuum infrared standard radiation thermometer (VIRST) [4] direct calibrations of sources in terms of radiance temperature in the wavelength range from 8 μm to 14 μm can be performed.

For spectrally resolved measurements the radiation of the reference sources and the sources under test is imaged on a vacuum Fourier-Transform Spectrometer (FTS). The FTS covers the wavelength range from 0.4 μm to 1000 μm by employing detectors ranging from photomultipliers to liquid helium cooled bolometers. The different reference blackbodies enable measurements with respect to at least two reference temperatures, simultaneously. Hereby disturbances in the infrared by background radiation resulting from inside the FTS can be effectively compensated. Sources can be also spatially mapped and characterized for the lateral distribution of their spectral radiance. The flexible design of the facility also allows large aperture camera characterizations and modifications for customer needs and the measurement of directional spectral emissivities over a wide temperature and wavelength range.

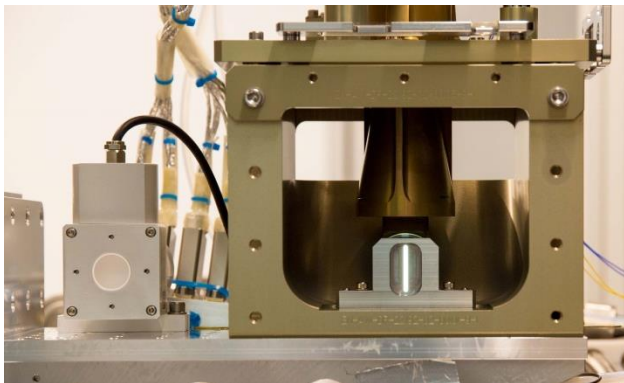


Figure 3 PTB's vacuum integrated sphere radiance transfer standard (RTS) (left) and EnMAP's onboard calibration assembly (OBICA) with illuminated exit aperture (right) inside the source chamber of the RBCF2.

EXEMPLARY APPLICATIONS

As a critical consistency check to the former RBCF vacuum emissivity measurements were performed at the RBCF2. For example, the results of the directional spectral emissivity of SiC depicted in Figure 4 show no deviation between past and current measurements within the standard uncertainty. Additionally, comparison measurements performed with the emissivity measurement facility in air (EMAF) show no significant deviation.

Recent calibrations of the large aperture on-board blackbodies of the airborne GLORIA limb-sounder [5] in the MIR spectral range and of the on-board calibrations assembly (OBICA) of the EnMAP satellite [6] in the VIS-NIR spectral range will be shown during the presentation to illustrate the capabilities of the RBCF2.

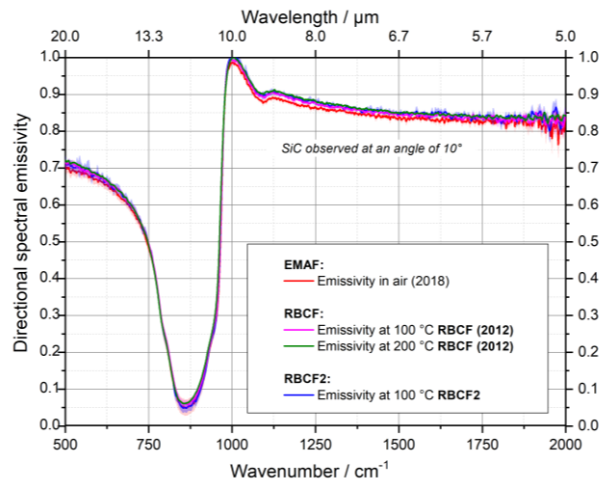


Figure 4 Directional spectral emissivity of SiC recorded 2012 at the RBCF in vacuum, 2018 at the EMAF and 2019 at the RBCF2 show no significant deviation.

REFERENCES

1. C. Monte et al., The Reduced Background Calibration Facility for Detectors and Radiators at the Physikalisch-Technische Bundesanstalt, in: Sensors, Systems, and Next-Generation Satellites XIII, edited by: Meynart, R., Neeck, S. P., and Shimoda, H., Vol. 7474, Proceedings of SPIE/747414, Berlin, 2009a..
2. S. P. Morozova et al., Vacuum Variable Medium Temperature Blackbody (VMTBB), Int. J. Thermophys, 31, 1809-1820, 20103.
3. S. P. Morozova et al., Vacuum Variable Temperature Blackbody VLTBB100, Int. J. Thermophys., 29, 341-351, 2008.
4. B. Gutschwager et al., An Infrared Precision Radiation Thermometer for the Calibration of Remote Sensing Instrumentations under Vacuum, in: Image and Signal Processing for Remote Sensing XV, edited by: Bruzzone, L., Notar-nicola, C., and Posa, F., Vol. 7477, Proceedings of SPIE, 747719, Berlin, 2009.
5. C. Monte et al., Radiometric calibration of the in-flight blackbody calibration system of the GLORIA interferometer, Atmos. Meas. Tech., 7, 13-27, 2014.
6. L. Guanter et al., The EnMAP Spaceborne Imaging Spectroscopy Mission for Earth Observation. Remote Sens., 7, 8830-8857, 2015.

VNIIOFI's developments in measurement assurance of Earth remote sensing

Valeriy Gavrilov¹, Svetlana Morozova¹, Boris Khlevnoy¹, Alexander Dunaev¹, Andrey Burdakin¹, Ekaterina Us¹, and Vitaly Bormashov¹

¹All-Russian Research Institute for Optical and Physical Measurements (VNIIOFI), Moscow, Russia,

Corresponding e-mail address: gavrilov@vniiofi.ru

The results of VNIIOFI's developments during last decade and current activities in measurement assurance of Earth remote sensing are presented. Two standard radiometric facilities developed at VNIIOFI for preflight calibration of the remote sensing instruments are briefly characterized. The first facility is intended for calibrations in the visible and near IR spectral range, and the second facility based on a vacuum cryogenic chamber is for the thermal IR spectral range. A brief overview of performed calibrations of the instruments launched on board satellites for scientific and the Earth resources investigations is also presented. Completed and upcoming space-flight experiments aimed at creating space-born fixed-point blackbodies for onboard calibrations of IR remote sensing instruments are also described.

STANDARD RADIOMETRIC FACILITIES FOR PREFLIGHT CALIBRATION OF REMOTE SENSING INSTRUMENTS

For preflight radiometric calibration of remote sensing instruments with apertures up to 500 mm in the solar reflective range (from 0.3 to 3.0 μm) VNIIOFI has developed and created at 2010 the standard radiometric facility consisting of two large-area radiant sources [1]. The first is a monochromatic collimated radiation source (MCRS) measured for relative distribution of spectral radiant power with traceability to VNIIFI's cryogenic radiometer. The MCRS is intended for measuring the relative spectral responsivity of the remote sensing instruments with broadband spectral channels. The second is an integrating sphere diffuse source (ISDS) measured for spectral radiance against VNIIOFI's high-temperature fixed-point blackbodies (see [2] and refs therein). Calibration against the ISDS results in measuring the absolute radiance responsivity of hyperspectral remote sensing instruments.

Standard radiometric facility for preflight radiometric calibration of remote sensing instruments in the thermal IR spectral range (from 3 to 14 μm) was designed by VNIIOFI on the basis

of vacuum cryogenic chamber modelling space environment conditions for the instruments under calibration inside it [3]. Monochromatic source of IR radiation for measuring the relative spectral responsivity consists of placed outside the chamber a set of detectors with traceability to VNIIFI's cryogenic radiometer, a monochromator, a high temperature blackbody and located inside an optomechanical system for spectral comparing. A set of low temperature blackbodies developed and manufactured at VNIIOFI and a Fourier-spectrometer are used for measuring the absolute spectral responsivity [4]. The gallium fixed-point black body is used as reference radiation source, and large-area blackbody in the form of a V-shaped 500 mm diameter aluminium-alloy plate covered by the black Aeroglaze Z306 dull paint stands for illuminating the instrument under calibration.

PERFORMED PREFLIGHT RADIOMETRIC CALIBRATIONS

Regular radiometric calibrations for spectral radiance responsivity of hyperspectral remote sensing instruments GSA-RP are performed against the ISDS [5]. GSA-RP was designed and manufactured by JSC «Krasnogorsky Zavod» under the contract with Progress Space Rocket Centre for hyperspectral imaging on board the Earth observation spacecraft of Resurs-P series [6]. Launches of the first three spacecrafts Resurs-P No.1, Resurs-P No.2 and Resurs-P No.3 with GSA-RP on board were performed on June 25, 2013, December 26, 2014 and March 13, 2016.

Multispectral Imaging System KMSS-2, consisting of two identical 3-channel multispectral imaging units MSU-100TM, was launched aboard satellite Meteor-M No.2-2 in a sun-synchronous orbit on July 5, 2019. KMSS-2 was developed by the Space Research Institute of the Russian Academy of Sciences (IKI RAN) for satellite monitoring of weather and climate. Measurements of the relative spectral responsivity against the MCRS and the subsequent measurements of the absolute radiance responsivity against the ISDS for

each channel of the both units MSU-100TM were performed during the preflight radiometric calibration [7].

Four surveillance cameras are installed on the surface platform of the ExoMars 2020 mission for obtaining overview colour, radiometrically corrected static images of the surface and atmosphere of Mars in the visible spectral range, formation of circular closed panorama of the landing site and measuring the spectral radiance of surrounding objects at three wavelengths - 0.45, 0.55 and 0.65 μm [8]. IKI RAN has developed the cameras and the radiometric calibration of the cameras was performed against the ISDS at VNIIOFI.

TOWARDS TO IN-FLIGHT CALIBRATIONS

Since 2008, VNIIOFI has continued activities aimed at creating a highly stable space-born fixed-point blackbodies for onboard radiometric calibrations of IR remote sensing instruments.

One series of space-flight experiments is testing the performance of low temperature blackbody prototypes with radiating cavity surrounded by a phase-changing working substance. The first experiment of this series was performed in 2014 on board the "Foton-M" No.4 reentrant vehicle. As a result of the experiment, stable melting plateaus of Ga (29.8 °C) were obtained with the temperature drift no more than 30 mK [9]. The next analogous experiment is planned for In-Bi eutectic system fixed point (72.5 °C) on board the "Bion-M" No.2 reentrant vehicle in 2024.

The second series of experiments is planned on board the International Space Station and consists in experimental studies of the microgravity influence on phase transitions of working substances with those melting/freezing temperature fixed points in the range interesting from the remote sensing viewpoint. The first experiment of this series for the fixed points Ga-In (17.7 °C), Ga-Sn (20.5 °C), (Ga-Zn (25.2 °C), Ga (29.8 °C) is planned in 2020, and the second experiment is for the fixed points H₂O (0 °C) and In-Bi (72.5 °C).

CURRENT ACTIVITIES

At present, VNIIOFI develops a comprehensive system of measurement assurance for remote sensing instruments of the visible, near IR and thermal IR spectral ranges during their development, preflight testing and orbital operation.

Implementation of the system involves the following activities.

1. Development, manufacturing and certification of a complex of facilities for preflight radiometric, spectral and photogrammetric calibrations, including the harmonized with the international document "Quality Assurance Framework for Earth Observation" regulatory and methodological base that ensures traceability of the instrument characteristics to VNIIOFI's measurement standards.

2. Development and creation of a center for pursuance remote calibration, remotely sensed data verification and associated products validation on the basis of

- onboard facilities for radiometric calibration including diffused plates, LED based integrating spheres, large-area blackbodies and blackbodies with radiating cavity on the fixed points;
- ground sites equipped with a mobile instrumentation providing spectral surface reflectance and atmospheric conditions.

REFERENCES

1. V.I. Sapritsky et al, Current activity of Russia in measurement assurance of Earth optical observation, *Metrologia*, 49, pp. S9–S16, 2012.
2. Boris Khlevnoy et al, Development of large-area high-temperature fixed-point blackbodies for photometry and radiometry, *Metrologia*, 55, pp. S43–S51, 2018.
3. V.I. Sapritsky et al, "Standard radiometric facility for preflight calibration of space borne Earth observation instruments in IR spectral range", *Proceedings of NEWRAD 2014*, pp. 27-28, Jun. 2014.
4. S.P. Morozova et al, "Preflight Spectral Radiance Infrared Calibration Facility", *Int J Thermophys*, 35, pp. 1330–1340, 2014.
5. Nikolay Butiyaykin et al, "Hyperspectral Earth Observation Instrument and its Preflight Calibration", *Proceedings of NEWRAD 2014*, pp. 35-36, Jun. 2014.
6. https://en.samspace.ru/products/earth_remote_sensing_satellites/ka_resurs_p/
7. Valeriy Gavrilov et al, "Radiometric Calibration of Satellite Multispectral Imaging System KMSS-2", *Proceedings of NEWRAD 2017*, pp. 38-39, Jun. 2014.
8. <https://exploration.esa.int/web/mars/-/56933-exomars-2020-surface-platform>
9. A. Burdakin et al, "Space-Flight Experiment on Board the "Foton-M" No.4 Reentrant Vehicle – First Step Towards Space-Borne High-Stability Fixed-Point Reference Blackbody", *Proceedings of NEWRAD 2017*, pp. 28-29, Jun. 2017.

Design and Development of a Tuneable Portable Radiation Source for In Situ Characterisation of Dobson Spectrometers

M. Smid¹, G. Porrovecchio¹, T. Burnitt², P. Linduska¹, M. Stanek³ and L. Egli⁴

¹ Czech Metrology Institute, Brno, Czech Republic, ²Principal Optics, Reading, UK, ³ Czech Hydrometeorological Institute, Hradec Kralove, Czech Republic, ⁴Physikalisch-Meteorologisches Observatorium Davos / World Radiation Center, Davos, Switzerland

Corresponding e-mail address: msmid@cmi.cz

A tuneable and portable radiation source (TuPS) has been developed for the in-field characterization of the wavelength scale (290 nm to 350 nm) and slit function of Dobson spectrometers. TuPS emits radiation with a bandwidth of 0.1 nm and an uncertainty less than 0.02 nm in the wavelength scale, while the radiant power of emitted beam exceeds 20 nW over the spectral range of interest. The past two years of operation have included two in-field calibration campaigns that have required shipping and in-field installations, and during which more than 14 Dobson spectrometers were calibrated. Over this period the long-term stability of both slit function and wavelength scale were determined to be as high as 0.02 nm.

TuPS was designed so that only minor modifications are necessary to extend/shift its spectral range towards visible and near-infrared spectral regions, thereby extending its application to the spectral characterisation of other spectrometers.

MOTIVATION AND OBJECTIVE

Dobson and Brewer spectrometers are key instruments used to monitor the ozone layer. Although networks using a specific instrument are self-consistent to better than ± 0.5 % level, total column ozone retrieved from the two instrument types differ by up to 3 %. This large discrepancy currently prevents a merging of both datasets and an eventual replacement of one instrument with another type. Therefore, improved characterization and calibration of Dobson instruments would be of great benefit.

The bandwidth and wavelength scale accuracy of Dobson spectrometers are not known for each instrument, but are assumed to be equal to the world reference Dobson. Currently, tuneable monochromatic sources which could be used for characterisation of Dobsons are complex and systems

that are only found in a few laboratories world-wide and cannot be used for in-field calibrations as needed by the global spectrometer network.

Laboratory based characterisations have been performed at CMI and PTB [1] having requested typically two days time for each spectrometer plus additional time necessary for shipping of often heavy and large DUTs from their permanent in-field installation down to the metrology laboratory.

Here we describe the design and development of a tuneable and portable radiation source (TuPS) for the in-field characterization of Dobson spectrometers. TuPS operates over wavelength range 290 nm to 350 nm. This light engine emits the radiation with the bandwidth of 0.1 nm with uncertainty lower than 0.02 nm in wavelength scale, while the radiant power of emitted beam exceeds the level of 20 nW over all spectral range of interest.

THE OPTICAL DESIGN

The TuPS is a combination of a broadband source and an optical tuneable dispersion system; the latter rejecting all but a narrow wavelength band. Optimal level of total radiant flux emitted from TuPS was found experimentally during the laboratory-based characterization of Dobson 074 [1] as a value that ranges from 10 nW to 100 nW. The optical layout was designed using Zemax, an important consideration in

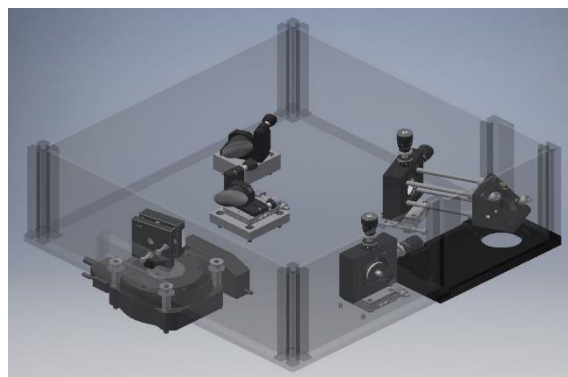


Figure 1. TuPSs' optical configuration of.

the design being that TuPS would be easily transportable thus enabling its use as an in-field source for Dobson spectrometers.

TuPS is contained within a 400 mm x 400 mm optical board, with the grating and the second parabolic mirror positions fixed; and the input pinhole, the first parabolic mirror and the output slit mounted on high precision micro-metric linear stages to provide the fine adjustment needed to compensate for the focal length tolerance of the parabolic mirrors. Both parabolic mirrors and the grating are mounted on adjustable stages to optimize the mirrors' optical alignment. A motorized rotation stage, which sets the grating angle, uses a high resolution encoder that has an accuracy of better than 0.001° . The optical configuration of the TuPS is shown in Figure 1.

TUPS OPTICAL CHARACTERISATION

The optical characterisation of TuPS light engine was performed using the fibre coupled CMI tuneable optical parametric oscillator laser facility (OPO). The OPO laser radiation wavelength and its stability is monitored by calibrated wavemeter with accuracy better than 0.01 nm [2]. Schematic diagram of the measurement setup is shown in Figure 2

For each wavelength the angular position of the peak A_{λ_i} relative to the laser line λ is calculated using the centroid formula, using this the relationship between the TuPS grating angle and the TuPS wavelength at the output slit can be determined. Using the same data set, and the linear relationship between the grating angle and wavelength it is also possible to assess the bandwidth performance of the TuPS. With the same measurement setup used for the TuPS wavelength and bandwidth calibration the optical power output of TuPS over all spectral region of interest was measured using a calibrated Si photodiode located at the TuPS output port.

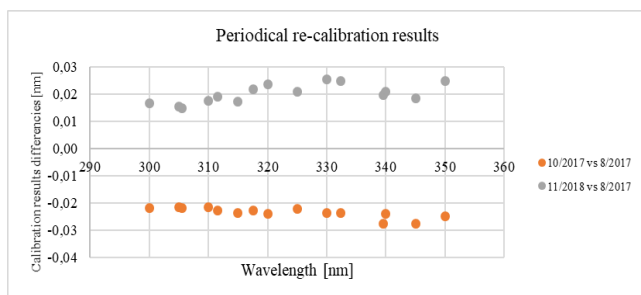


Figure 3. TuPS results of periodical recalibration of the wavelength scale after each in-field measurement.

The temporal stability of TuPS was investigated over a period of 2 years. During 2017 TuPS participated in five measurement campaigns, where it characterized 14 Dobson spectrometers. Before and after each measurement campaign the TuPS wavelength scale

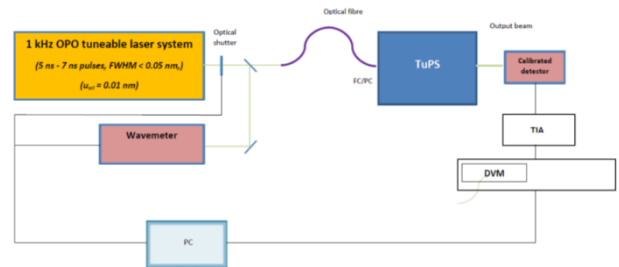


Figure 2. The schematic diagram of the TuPS characterisation measurement setup.

was recalibrated at CMI, using the OPO laser facility. The results for the calibrations before and after each campaign are shown in Figure 3. The largest difference in the wavelength scale of about 0.025 nm was recorded between the measurements in AEMET Izana (Spain) and the Deutscher Wetterdienst (Germany), a time interval of 45 days.

CONCLUSION

TuPS is an instrument for determining the slit function and centre wavelength of Dobsons. TuPS has been characterised for bandwidth and the central wavelength accuracy over the spectral range of interest. This characterisation was done using the fibre coupled CMI tuneable laser facility, this is a 1 kHz ns pulsed OPO in combination with the CMI reference wavemeter being demonstrated better than 0.1 nm and 0.02 nm respectively. The stability of TuPS over two years has been shown to be 0.02 nm for both key parameters.

REFERENCES

1. Köhler, U. et al., 2018. Optical characterisation of three reference dobsons in ATMOZ project - verification of G.M.B. Dobson's original specification. *Atmospheric Measurements Technology*, November, Volume 11, pp. 1989-1999.
2. Balling, P., Masika, P., Kren, P. & Dolezal, M., 2012. Length and refractive index measurement by Fourier transform interferometry. *Measurement Science and Technology*, Volume 23

Acknowledgement: This work has been supported by the European Metrology Research Programme (EMRP) within the joint research project EMRP ENV59 ATMOZ “Traceability for atmospheric total column ozone”. The EMRP is jointly funded by the EMRP participating countries within EURAMET and the European Union

Gonioreflectometric properties of the sand from RadCalNet Gobabeb test site

Dmitri Lanevski¹, Agnieszka Bialek¹, Emma Woolliams², Farshid Manoocheri¹,
Nigel Fox² and Erkki Ikonen^{1,3}

¹*Metrology Research Institute, Aalto University, Espoo, Finland;* ²*NPL, Teddington, UK;* ³*VTT MIKES, Espoo, Finland*

Corresponding e-mail address: Dmitri.lanevski@aalto.fi

Gobabeb test site is one of the instrumented semi-invariant locations on Earth that is used for vicarious post-launch calibration of satellite optical sensors. Recent studies suggest that a more site specific model of ground BRDF might decrease the uncertainty of such calibrations. For this reason a sample of sand from Gobabeb test site was collected and measured in a laboratory using a 3D goniometer. Data are compared to on-site measurements and suggested as an empirical base for a new site-specific BRDF model.

INTRODUCTION

In order to provide accurate data regarding our planet, optical sensors of Earth observation satellites require precise calibration. While large satellites often have on-board calibration devices, such devices age in orbit and vicarious calibration methods provide a valuable check of stability and inter-sensor biases. The move towards smaller and cheaper satellites also demand vicarious solutions. For this reason ground based reference test sites were developed. They are represented by optically semi-invariant locations on Earth that can be simultaneously observed by the satellites and by the automated ground stations [1]. Data from these sites coupled with site-specific Top-Of-Atmosphere (TOA) models provide satellite operators with SI-traceable spectrally-resolved reflectances to aid in the post-launch radiometric calibration and validation of optical imaging sensors.

The Gobabeb test site is a part of the Radiometric Calibration Network (RadCalNet) and is located on the edge of the Namib desert [2]. Its TOA model is based on radiative transfer code MODTRAN [3] that requires information about the atmospheric conditions and surface reflectance as an input. The latter is derived from in situ measurements and application of Roujean BRDF model that was developed firstly for la Crau site [4]. Studies showed that this approach provides quite consistent calibration results with an uncertainty of 1%-4%. Further developments of the test-site, however, suggest that application of more

site-specific BRDF model will reduce the uncertainty associated with non-nadir observations.

Development of a new BRDF model for a site requires a set of SI-traceable empirical data. This is challenging on-site due to the changing solar illumination and relatively long data acquisition times, field conditions vary significantly during in situ measurements and increase uncertainty levels up to 2%. For this reason, laboratory measurements of test site ground samples are required. This article describes the Gobabeb test site sample, equipment, and procedures required for such measurements as well as results compared to the in situ measurements.

GOBABEB TEST SITE GROUND SAMPLE



Figure 1. Photograph of the ground from Gobabeb test site. 5cm long screw (marked with red ellipse) is placed on the ground for scale.

Figure 1 shows that the Gobabeb ground consists mostly of sand and relatively small-sized gravel. Only a small fraction of dried out vegetation and animal remnants are present. A sample of this ground was collected into 3-litre container and transported to the laboratories at NPL and Aalto for further characterization and gonioreflectometric BRDF measurements. The sample consisted mostly of fine sand with the grain size less than 200 μm and gravel with diameter ranging from 1.5 mm to 15 mm with the average diameter of 6.2 mm. Fractions of intermediate size were rare.

MEASUREMENT EQUIPMENT AND PROCEDURES

Since the main fraction of the sample of interest is sand that is highly loose and volatile material, the only way to reliably measure its gonireflectometric properties is to place the sample horizontally and minimize its movement during measurements. For this reason, a specific 3D goniometer developed at Aalto was used (figure 2).

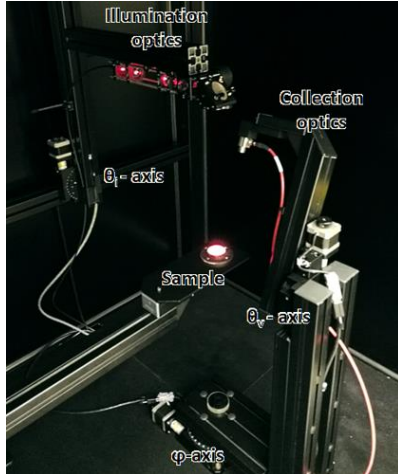


Figure 2. Photograph of the gonireflectometer used to perform BRDF measurements.

The gonireflectometer consists of a horizontal sample holder and multiple arms that move illumination and detector around the sample. The device allowed in-and out-of-plane 3D BRDF measurements with a 4° blind spot around the illumination. An NKT photonics supercontinuum laser coupled with laser line tuneable filters (LLTF) was used as the illumination source that allowed the illumination wavelength to vary from 400 nm to 2200 nm with spectral bandwidth of 2.5 nm to 5 nm. The optics allowed to change the beam size from 5 mm to 20 mm. The light reflected by the sample was collected by a parabolic mirror into optical fibre that guided collected light to the detection system, which allowed 3 different detectors to be chosen: silicon photodiode for visible wavelength range, InGaAs detector for NIR spectral region (900 nm to 1700 nm) and extended InGaAs allowing to expand sensing span up to 2070 nm. The repeatability of the instrument was better than 0.5%.

SI-traceability of the 3D goniometer was achieved by measuring a spectralon PTFE sample, the BRDF of which had been characterised by an absolute reference goniometer with an uncertainty of 0.2%. Correction factors were derived from the ratio between absolute and relative spectralon BRDF measurements, giving an estimate of the BRDF of Gobabeb test site ground samples with an uncertainty of less than 1 %.

PRELIMINARY RESULTS

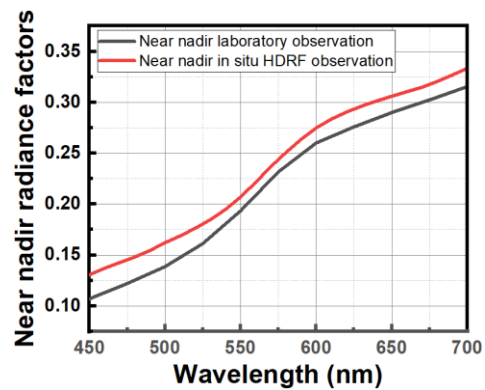


Figure 3. Radiance factors of near nadir observations of Gobabeb sand in visible spectral range in laboratory and in situ (RadCalNet data measured on 01.11.2019 at 09:00).

Several measurements of the BRDF of Gobabeb sand were performed in the visible range with the illumination angle of 0°. Results depicted in figure 3 show that near-nadir BRDF values measured in laboratory are similar in shape, yet lower in value compared to in situ values. This is likely due to the significantly smaller illumination area which doesn't include bigger gravel pebbles in the measurement sample and because of the 4° blind spot around illumination that didn't collect the full reflectance data at nadir. This problem, however, should have less effect on off-nadir BRDF measurements, which are currently in progress.

ACKNOWLEDGEMENTS

This work was funded by the project MetEOC-3 (16ENV03) of the European Metrology Programme for Innovation and Research (EMPIR). The EMPIR is jointly funded by the EMPIR participating countries within EURAMET and the European Union's Horizon 2020 program.

REFERENCES

1. Bouvet, M. et al, RadCalNet: A radiometric calibration network for Earth observing imagers operating in the visible to shortwave infrared spectral range. *Remote Sens.*, 11(20), 2401. 2019
2. A Bialek, Greenwell et al., New radiometric calibration site located at Gobabeb Namib desert, *Proc. IGARSS*, 6094-6097, 2016.
3. Meygret, A.; Santer, R.; Berthelot, B. ROSAS: A robotic station for atmosphere and surface characterization dedicated to on-orbit calibration. In *Proceedings of the Earth Observing Systems XVI*, San Diego, CA, USA, 13 September 2011.
4. J. Roujean, M. Leroy et al., A bidirectional reflectance model of the Earth surface for the correction of remote sensing data, *J. Geophys. Res.*, 97(D18), 20455– 20468, 1992.

Experience with the radiometric traceability concept for the Network for Detection of Mesospheric Change (NDMC)

Max Reiniger¹, Christian Monte¹, Berndt Gutschwager¹, Jörg Hollandt¹, Paul Dekker², Steven van den Berg², Carsten Schmidt³, Sabine Wüst³, Michael Bittner³

¹Physikalisch-Technische Bundesanstalt (PTB), Berlin - Germany,

²VSL – Dutch Metrology Institute, Delft – The Netherlands,

³Deutsches Zentrum für Luft- und Raumfahrt (DLR), Oberpfaffenhofen - Germany

Corresponding e-mail address: Max.Reiniger@ptb.de

We have implemented a radiometric traceability concept to provide calibrations to the NDMC. With transportable instruments we are able to calibrate the typically used GRIPS instruments in the spectral range from 1500 nm to 1600 nm with a thermal radiance source at radiance temperatures of around 110 °C. Here we present our experience with this concept exemplarily by the results of the calibration at two different NDMC sites.

INTRODUCTION

The NDMC [1] is an international network of currently 55 ground-based experiments with emphasis on observing the airglow emissions from excited OH- and O radicals as well as excited O₂ molecules in the mesopause region. About one third of these instruments are of the so-called GRIPS type (Ground-based Infrared P-branch Spectrometer) determining the rotational temperature of the OH(3-1) vibrational transition.

We focus on providing radiometric traceability to measurements of these GRIPS instruments to determine the mesopause temperature with sufficiently low uncertainty to identify temperature changes at the level of 1 K per decade. By Monte-Carlo simulations we determined the required uncertainty in terms of the relative radiance responsivity calibration of the GRIPS instrument to achieve this goal. It needs to be better than 0.5 % ($k=1$) in the wavelength range between 1500 nm and 1600 nm. Furthermore, an absolute radiance responsivity calibration of the GRIPS instruments within the NDMC would allow the determination of the OH* radical concentration which is directly correlated to the concentration of atomic oxygen in the mesopause.

CALIBRATION CONCEPT

The emission measurements of the OH* radicals are performed between 1500 nm and 1600 nm at very low radiance levels (around 350 Wm⁻¹sr⁻¹m⁻² - equivalent to a blackbody radiance temperature of around 110 °C at 1550 nm) caused by their low density in the mesopause. At these radiance levels and wavelengths, the required radiance uncertainty was just achievable for laboratory-based calibration procedures at National Metrology Institutes. To obtain this low level of uncertainty for the NDMC in the field we developed a traceability concept (**Figure 1**) based on a radiometrically well-characterized Traveling Radiance Source (TRSO) and a likewise characterized Traveling Reference Spectrometer (TRSP).

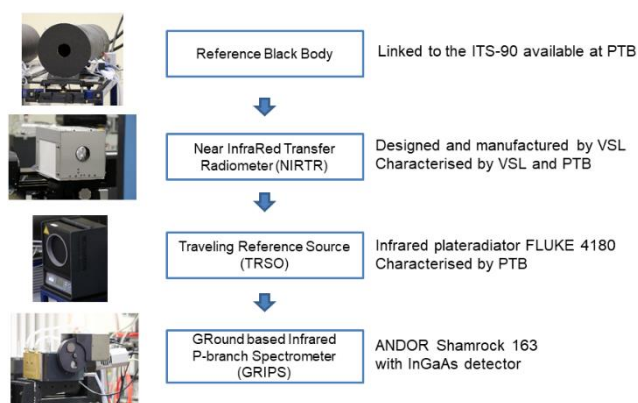


Figure 1. Calibration concept of the GRIPS instrument

We identified, characterized, optimized and calibrated two suitable instruments for this concept: a commercially available infrared plate radiator (Fluke 4180) as the TRSO and a GRIPS instrument (Andor Shamrock 163) typically used by DLR as the TRSP.

For the transfer of the spectral radiance scale from the primary radiance standards of the PTB [3] to the TRSO with lowest possible uncertainty a dedicated Near InfraRed Transfer Radiometer (NIRTR) has been developed by the VSL [2] which is able to detect the low radiance levels with a sufficiently good signal-to-noise ratio and matches closely the optical imaging properties of the GRIPS instruments.

Several optimisations of the GRIPS were necessary to reach these low uncertainties. The most important improvements are a temperature stabilised enclosure and a temperature stabilised aperture system to minimize the size-of-source effect (SSE) of the GRIPS. Furthermore, we have investigated the long-term stability of different types of the TRSO with the NIRTR.

RESULTS

With this calibration concept and the improved and metrologically well characterized instruments we were able to calibrate the GRIPS instruments with uncertainties ($k=2$) from 0.8% to 1.2% (**Figure 2**)

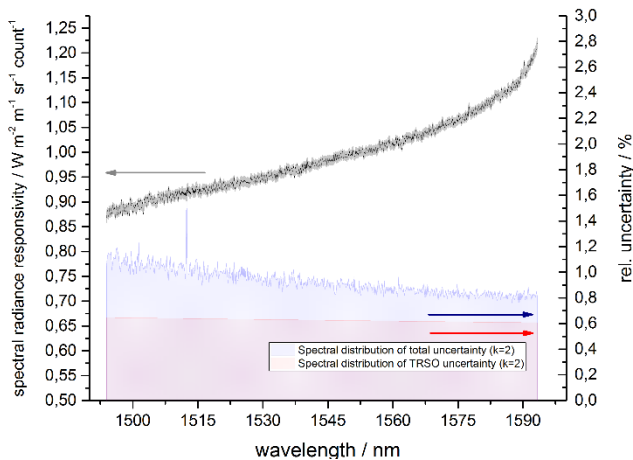


Figure 2. Result of the spectral radiance responsivity calibration of the GRIPS instrument and its uncertainty.

We have validated the long-term stability of the GRIPS calibration with multiple calibrations of the same instruments at different sites within different measurement campaigns. The deviation between the calibration which took place at Oberpfaffenhofen (OPN) and at the Environmental Research Station Schneefernerhaus (UFS) at Zugspitze are shown in Figure 3. The deviation between these two calibrations is well within the combined uncertainty. This clearly shows that there is practically no significant impact of the transport of the calibration

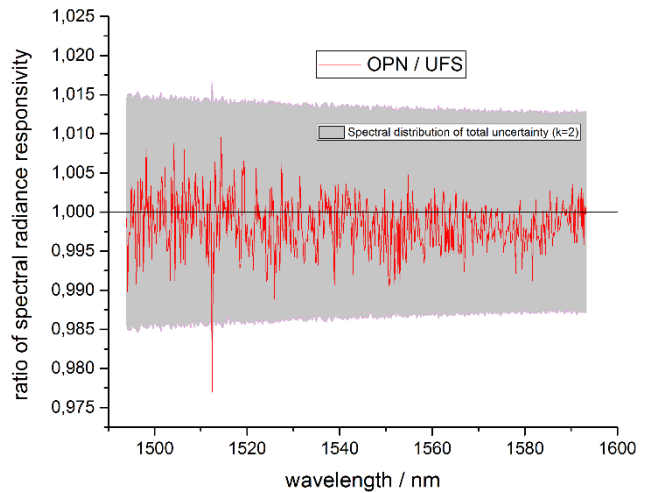


Figure 3. Ratio of spectral radiance between to measurement campaigns which took place at OPN and UFS.

instrumentation and that the calibration concept is able to provide sufficiently good traceability to the NDMC. Part of the radiometric characterization of the TRSP was, additionally, the wavelength calibration which was done with a high precision narrowband tuneable laser source in combination with an integrating sphere. These measurements provide precisely the wavelength scale but, furthermore, give information about spectral straylight and the spectral response function of the instruments. This enables a spectral deconvolution of the measured spectra and thus an improved determination of the required line intensities.

CONCLUSION

We will show the results of the first on-site calibrations with the combination of TRSP and TRSO with respect to their transportability, radiometric stability and the achievable uncertainties

REFERENCES

1. <https://ndmc.dlr.de>
2. S. van den Berg et al., Traceability of the Network for Detection of the Mesospheric Change (NDMC) to radiometric standards via a Near Infrared Filter Radiometer, 2018, J. Phys.: Conf. Ser. **972** 012006.
3. I. Müller et al., Calibration capabilities at PTB for radiation thermometry, quantitative thermography and emissivity, 14th Quantitative InfraRed Thermography Conference, 2018, 10.21611/qirt.2018.015.

Measurements of absolute, SI traceable lunar irradiance with the airborne Lunar Spectral Irradiance (air-LUSI) Mission

Steven W. Brown¹, John T. Woodward¹, S. Andrew Gadsden², Thomas C. Stone⁴, Kevin R. Turpie³, Steven E. Grantham¹, Thomas C. Larason¹, Stephen E. Maxwell¹, and Andrew Newton²

¹National Institute of Standards and Technology (NIST), Gaithersburg MD (USA), ²University of Guelph, Guelph, ON, CAN, ³University of Maryland Baltimore Campus, Baltimore County MD, USA, ⁴US Geological Survey, Flagstaff AZ, USA

Corresponding e-mail address: K. R. Turpie <kturpie@umbc.edu>

The air-LUSI instrument is developed around a spectrograph fiber-coupled to a telescope. The system is designed to make highly accurate SI-traceable measurements of the lunar spectral irradiance in the VNIR region from an aircraft at elevations from 60,000 feet to 70,000 feet. Five air-LUSI Demonstration Flights were conducted in November 2019 corresponding to lunar phase angles ranging from 10° to 60°. This presentation discusses the lunar irradiance measurements, the resultant uncertainty budgets, and the path forward to achieve uncertainties of 0.5 % or less in lunar irradiance.

INTRODUCTION

The Moon is an attractive exo-atmospheric calibration target for space-based sensors that observe the Earth because the lunar surface is photometrically stable, flux levels approximate those from the Earth, and no atmospheric corrections need to be applied for the calibration. While many sources of uncertainty that arise when vicariously calibrating sensors using land targets are eliminated, lunar measurements are complicated – though predictable – because the lunar irradiance is a function of the relative positions of the Sun, Moon, and Observer (spacecraft) among other variables. The United States Geological Survey (USGS) has developed the Robotic Lunar Observatory (ROLO) Model of Top-Of-the-Atmosphere (TOA) lunar reflectance/irradiance, which accounts for changes in lunar irradiance as a function of these variables. The USGS ROLO model - and the Global Space-based Inter-Calibration System (GSICS) Implementation of the ROLO model (the GIRO model) - represent the most precise knowledge of lunar spectral irradiance and are used frequently as a relative calibration standard by spaceborne Earth-observing sensors. However, the current uncertainties in the ROLO Model are estimated to be between 5 % and 10 % in the Visible

to Near InfraRed (VNIR) spectral region and are not traceable to the International System of Units (SI); consequently, the Moon is not used as an absolute standard.

The objective of the air-LUSI project is to make highly accurate (sub-0.5 % uncertainty), SI-traceable measurements of the lunar spectral irradiance in the VNIR region from an aircraft at altitudes from 60,000 feet to 70,000 feet. Air-LUSI measurements, corrected for residual atmospheric attenuation, are designed to provide a data set of low uncertainty TOA lunar irradiances at known lunar phase and libration angles to be compared and integrated with other lunar irradiance data sets.

AIR-LUSI INSTRUMENT

A schematic diagram of air-LUSI is shown in Figure 1 as it is mounted in the aircraft. The instrument is mounted on one of two ER-2 wing pods. Each pod has three sections: an aft-body, a mid-body and a fore-body. The aft-body is open to the environment and during lunar measurements is at an atmospheric pressure $\approx 0.06 \text{ atm}$ and a temperature $\approx -60^\circ\text{C}$. The mid-body is kept at a pressure of $1/3 \text{ atm}$ and a temperature of 0°C . The instrument enclosure is mounted in the mid-body and fiber-coupled through the bulkhead to the telescope mounted in the aft-body.

Heaters control the temperatures of the instrument enclosure, the fiber-optic bundles, the integrating

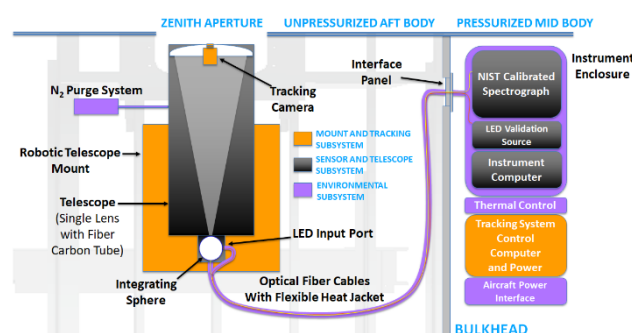


Figure 1. Schematic design of air-LUSI.

sphere detector on the telescope and the actuators that control pointing of the system.

MEASUREMENTS OF LUNAR IRRADIANCE

The instrument was successfully integrated into a wing pod of an ER-2 research aircraft at NASA's Armstrong Flight Research Center and five Demonstration Flights were conducted in November 2019 covering lunar phase angles from $\approx 10^\circ$ (Flight 1) to $\approx 60^\circ$ (Flight 5).

The lunar irradiance averaged over the full lunar data sets from each night of measurements is shown in Figure 1. Estimated uncertainties in the measurements of lunar irradiance are shown in Figure 2. Only one uncertainty budget is shown because there is only a small difference in the uncertainty budget as the phase changes from 10° to 60° . The uncertainty is less than 1 % from 400 nm to 1000 nm.

DISCUSSION

While the target uncertainties are less than 0.5 %, SI-traceable TOA lunar irradiances with higher uncertainties are very useful. An SI-traceable, TOA lunar irradiance data set with uncertainties less than 1% could meet many sensor calibration uncertainty requirements and include the ability to bring inter-

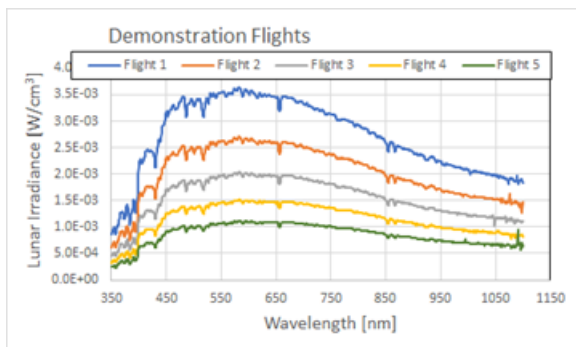


Figure 1. Mean lunar irradiances measured by air-LUSI during Demonstration Flights in November 2019.

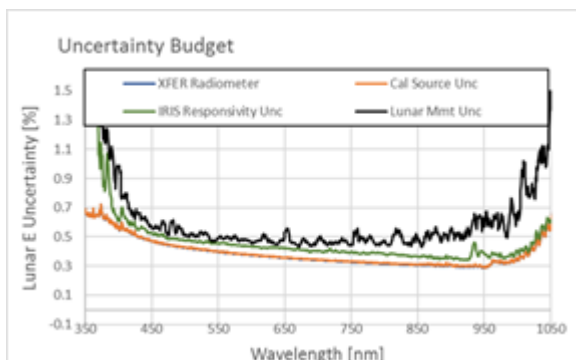


Figure 2. Lunar irradiance uncertainty budget.

consistently between contemporary missions and across series of missions by using a common, stable reference.

The air-LUSI measurements may also resolve questions about the origin of differences between sensor measurements of the lunar irradiances and model predictions. Figure 3 shows the ratio of measurements by seven different instruments to the ROLO Model, 6 US instruments and 1 non-US instrument, shown in red in Figure 3. Instrument 6 is the only ground-based instrument in the comparison; it measured the lunar irradiance at two different phases, 6.9° and 16.9° .

This presentation discusses the results of the air-LUSI Demonstration Flights, focusing on the development of the uncertainty budget.

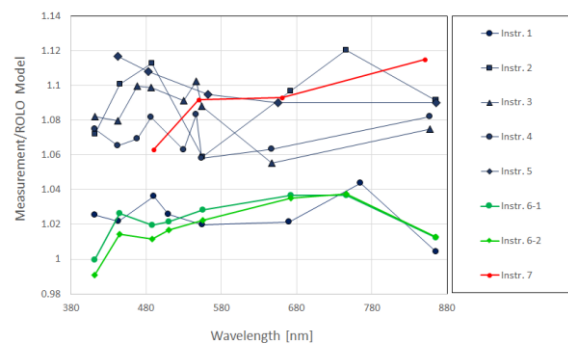


Figure 3. Ratio of measurements by different instruments to the ROLO Model.

ACKNOWLEDGEMENT

The air-LUSI team would like to thank Gene Eplee, NASA's Goddard Space Flight Center, and Aimé Meygret, CNES - DSO/SI/MO, for contributing data sets to Figure 3.

The STAR-CC-OGSE system for pre-flight sensor calibration

Paul D Green¹, Sean Devlin¹, William Kingett¹ and Nigel P Fox¹

¹The National Physical Laboratory, Teddington, United Kingdom

Corresponding e-mail address: paul.green@npl.co.uk

A robust SI-traceable pre-flight characterisation and radiometric calibration of satellite Earth Observation sensors is critical to maximising the value obtained from the data provided by our on-orbit environmental monitoring infrastructure. The NPL STAR-CC-OGSE pre-flight satellite sensor calibration and characterisation system has been designed as a generic OGSE facility capable of meeting the needs of the next generation of sensors. The STAR-CC-OGSE incorporates a fully automated tuneable CW laser system and is available on a lease basis to provide a cost-effective OGSE solution to the EO community.

INTRODUCTION

Reliable characterisation and radiometric calibration of satellite sensors are critical to their optimal performance on-orbit. Only through a robust understanding of the instrument behaviour, performance and degradation mechanisms will the significant effort and expense invested into the flight hardware be fully exploited.

The evolution of the uses of satellite sensor data, with their increased use in long-term environmental monitoring and climate studies mean that the performance and data quality provided by a single sensor can no longer be considered in isolation but needs to be considered as a part of the international Earth Observation (EO) infrastructure. Sensor data is increasingly used synergistically; across individual platforms & constellations, across space agency providers and across spectral domains and measurement techniques.

The drive for improved performance, increased sensitivity to geophysical phenomena, together with the desire for inter-operability between sensors creates increased demands on the pre-flight characterisation and radiometric calibration of sensors and the facilities needed to undertake these activities. This paper describes the developments made at NPL to create the facilities needed to service the next generation of optical band and hyperspectral satellite sensors.

OPTICAL GROUND SUPPORT EQUIPMENT REQUIREMENTS

Sensor pre-flight characterisation and calibration facilities are better known as optical ground support equipment (OGSE). The purpose of an OGSE is to determine the sensor performance over a few broad categories including:

- Geometric performance / Image quality
- Channel/Band co-registration
- Spectral calibration / Out-of-band rejection
- Radiometric calibration
- Polarisation sensitivity
- Non-linearity, non-uniformity response etc.

The methods employed have advanced over time but routinely use broadband white light and emission lamp sources projected through an optical test card providing a known illumination against which to test the sensor performance. The specific requirements of the sensor, determined by its footprint, FoV, spectral extent & resolution, nominal radiance and required sensitivity typically results in a bespoke OGSE needed to meet the specific sensor requirements. For large-scale multi-sensor series programmes, a bespoke solution may remain the preferred solution. However, for single/few unit explorer missions, commercial constellations and more agile sensor development programmes, the expense & post-use redundancy of a bespoke OGSE system may be prohibitive.

THE STAR-CC-OGSE SYSTEM

NPL has developed a generic OGSE system, the Spectroscopically Tuneable Absolute Radiometric calibration & characterisation OGSE (STAR-CC-OGSE), a versatile facility for the radiometric calibration and calibration of satellite sensors, available through a cost-effective lease arrangement.

The system is provided fully characterised, calibrated and performance verified, with an easy to

use software interface that allows fully automated remote operation from the customer interface. The system can be installed at a customer cleanroom facility or operated at NPL with a customer-supplied sensor. The main components of the STAR-CC-OGSE system are:

- A large aperture integrating sphere source for radiometric calibration
- A collimated beam source, equipped with an interchangeable, position fine-tuneable feature field mask for optical performance characterisation
- A CW laser allowing monochromatic continuous tuneability from 270 nm to 2700 nm, with a broadband (white light) source extending over the same spectral extent.
- A vacuum-compatible SI-traceable radiance detector module containing both broadband photodiodes & a spectrometer.

The laser illumination interface to either the small mask illumination sphere, large radiance sphere or direct to the field mask allows fully tuneable monochromatic illumination for all characterisation and calibration modes. Figure 1 shows a CAD model of the on-table assemblies.

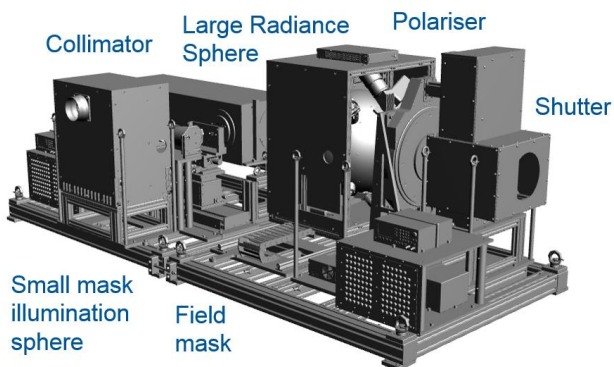


Figure 1. A CAD rendering of the STAR-CC-OGSE system. The collimator setup is to the left, the large sphere radiance source to the right, together with the polariser and shutter assemblies. The laser system and electronics rack (not shown) are connected to the on-table assembly via fibre & cable links.

SI-traceability via a vacuum-compatible detector-based module, that can be installed at the sensor-under-test entrance aperture, ensures the radiance at the sensor-under-test is directly measured with an uncertainty far superior to a source-derived

calibration reliant on additional transmission measurements and modelling. Some of the system performance parameters are given in Figure 2 & Figure 3

Radiometric	
Monochromatic spectral range	260 nm to 2700 nm.
Broadband spectral range	250 nm to 2500 nm (eqv. to 3000K blackbody). Can be extended into UV
Monochromatic typical radiance	Max. 0.5 W.m ⁻² .sr ⁻¹ (@800nm)
Broadband typical radiance	Max. 2000 W.m ⁻² .sr ⁻¹ .nm ⁻¹ (@1200nm)
Radiance spatial uniformity	Typically <0.15% PV (application dependant)
Radiance temporal uniformity	Mono (0.2% PV), BB (0.02% rms)
Monochromatic source line width	<0.1 pm
Monochromatic source tuning step size	~few pm
Monochromatic source wavelength calibration	<0.2 pm (PV)
Calibrated TVAC-compatible radiance monitor	<0.5% (k=1) [TBC]
Collimator focal length & F/#	1000 mm & F/5
Polarisation	
Contrast ratio	>1:10 ⁴
Rotation extent, resolution & accuracy	>360° , <0.1° , <0.2°

Figure 2. The STAR-CC-OGSE system radiometric and polarisation performance parameters.

Physical	
Physical size	2.6m (L) x 1.2m (W) x 1.0m (H)
Mass	<500Kg
Transport	Crane-able & transported in sections
Beam diameter	200 mm
Field mask features	Slit, squares, MTF, high intensity point source.
Field mask rotation stage	± 5°
Cleanliness	ISO6 (external surfaces compliant to ISO5)
Shutter response time	< 5 seconds
Operations	Completely remote controlled, interfaced to customer control systems.
Data management	Customer-tailored data interfacing system.
Environmental (operations)	Temp: 18° C ± 2° C, Pressure: 900 hPa - 1084 hPa, humidity: 40 %rh – 70 %rh
Environmental (transport/storage)	Temp: 0° C - 40° C, Pressure: 900 hPa - 1084 hPa, humidity: 40 %rh – 70 %rh
Compliance	CE & ROHS

Figure 3 The STAR-CC-OGSE physical performance parameters.

SYSTEM STATUS

At the time of writing the STAR-CC-OGSE is undergoing final performance testing, with delivery to the initial lease customer in Spring 2020. This paper will describe the STAR-CC-OGSE system, the outcome of the verification testing and system performance.

The HyperSpectral Imager for Climate Science (HySICS) on the CLARREO Pathfinder Mission

Greg Kopp¹, Gary Fleming², Peter Pilewskie¹, Paul Smith¹, Greg Ucker¹, Bruce Wielicki²

¹Laboratory for Atmospheric and Space Physics, Univ. of Colorado, Boulder, CO, U.S.A., ²NASA Langley Research Center, Hampton, VA, U.S.A.

Greg.Kopp@LASP.Colorado.edu

The HyperSpectral Imager for Climate Science (HySICS), to be flown as the CLARREO Pathfinder payload in 2023, is a spatial/spectral pushbroom imager achieving 6 nm of spectral resolution with 0.5-km spatial resolution for Earth scenes viewed from its platform on the International Space Station. Covering 350 to 2300 nm and having a 70-km swath, the HySICS will acquire images of the Earth's ground and atmosphere with unprecedented radiometric accuracies of $<0.3\%$ ($k=1$) achieved via on-orbit calibrations using the spectral solar irradiance. These high radiometric accuracies enable benchmarking of Earth radiances for climate studies and provide reference calibrations for other on-orbit Earth-viewing sensors.

CLARREO RADIOMETRY

The 2007 U.S. Academy of Sciences Decadal Survey for Earth Science recommended the Tier 1 mission CLARREO (Climate Absolute Radiance and Refractivity Observatory) [2] to acquire high-accuracy, climate-benchmarking spatial/spectral radiances of the Earth's surface and to provide reference calibrations for other on-orbit sensors. The more recent 2018 Decadal Survey similarly prioritized reference radiance inter-calibrations as one of its "Most Important Targeted Observables," providing on-orbit SI traceability for other programs such as the Global Space Based Inter-Calibration System. To achieve these climate-benchmarking and inter-calibration capabilities, the space-borne imaging spectrometer for the CLARREO requires radiometric-accuracy improvements that are 4 to 8x better than any currently-flying spectrometer provides, necessitating innovative new on-orbit measurement techniques.

The HyperSpectral Imager for Climate Science (HySICS) is currently in development for the NASA CLARREO Pathfinder (CPF), a low-cost, Class-D mission planned for launch to the International Space Station (ISS) in 2023 for a 1-year mission to demonstrate both the CLARREO-needed on-orbit

radiometric accuracies and reference calibrations of other space-based assets. The two primary goals of this mission are to demonstrate 1) on-orbit, high-accuracy, SI-traceable calibrations for measurements of Earth-reflected radiances in the solar-spectral region, and 2) the ability to transfer calibrations to other on-orbit sensors, in particular the VIIRS and CERES as proof-of-concept. The instrument will also acquire lunar radiances at various phase and libration angles to improve the knowledge of the Moon as an on-orbit calibration source. A two-axis HySICS pointing system enables target selection (Earth-nadir, Sun, Moon, and off-nadir for reference-calibration coincidence pointing with other instruments).

The CLARREO Pathfinder is currently in Phase C with intended installation in the ISS ExPRESS Logistics Carrier #1 Site #3.

HYRICS CALIBRATION APPROACH

The radiometric uncertainty goal for the Pathfinder HySICS is 0.3% ($k=1$), which is much better than any current spaceflight reference detector or calibration light source is capable of providing. Instead of either of these traditional detector- or source-based calibration approaches, the HySICS relies on on-orbit calibrations provided by direct views of the spectral solar irradiance (SSI), which is known on an absolute SI-traceable scale to $\sim 0.2\%$ from other space-based instruments such as the TSIS-1 Spectral Irradiance Monitor [2].

Two signal-attenuation approaches enable the HySICS's direct views of the Sun for these SSI cross-calibrations: 1) knife-edged apertures of different sizes prior to the telescope entrance limit the amount of entering light by precisely-known amounts, giving $\sim 10^{-3}$ attenuation due to geometric area between a 2-cm diameter Earth-viewing aperture and a 500- μm diameter Sun-viewing aperture; and 2) changes in focal-plane-array (FPA) integration times coupled with well-characterized detector linearity provide similar levels of attenuation. In conjunction, these two attenuation methods enable viewing both the Earth and the Sun with the same optical system

despite the 10^6 difference in radiances. A prototype HySICS demonstrated these attenuation approaches and the desired radiometric accuracy improvements during two high-altitude balloon flights under a NASA Earth Science Technology Office program [1].

Estimated CPF HySICS uncertainties across the spectral range are shown in **Figure 1**.

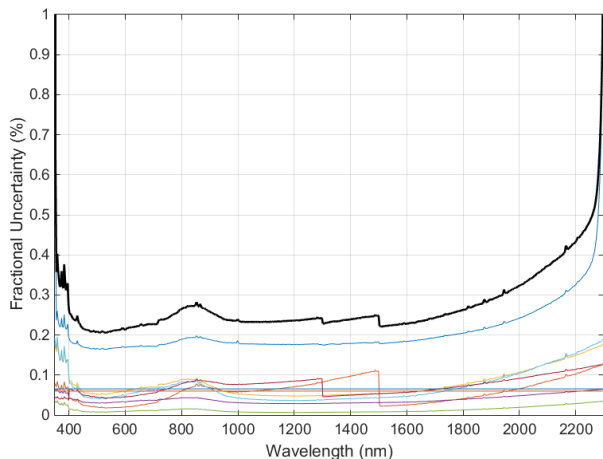


Figure 1. Estimated HySICS uncertainties with dominant contributors (colored curves) are summed in quadrature (black curve) to give a mean radiometric uncertainty of 0.27% across the spectrum.

HYSICS OPTICAL DESIGN

The HySICS is an Offner-based imaging spectrometer that contiguously covers 350 to 2300 nm with 6-nm spectral resolution (3.1-nm sampling). The nadir-looking instantaneous field-of-view is 130 m (instrument-intrinsic 67 arcsec) sampling a cross-track swath width of 71 km with a 10.1° field of view from the ISS's orbit altitude. An orthogonal arrangement of the optical planes of the four-mirror anastigmat telescope (4MA), providing imaging for the spectrometer, and the Offner reduces instrument-induced polarization to $<0.1\%$ from 350 to 1800 nm and $<0.2\%$ above 1800 nm. These low polarization sensitivities are needed for maintaining radiometric accuracy from scenes of unknown polarization. An aperture wheel prior to the imager's 4MA allows selection of Earth- and solar-viewing apertures.

Cross-track observations of Earth scenes acquire spatial/spectral information of the ground and atmosphere. Cross-slit scans of the Sun give composite measurements of the SSI, to which the HySICS is radiometrically referenced to SI. Along-slit solar scans enable flat fielding in the instrument's solar-viewing configuration, while a transmissive diffuser in the aperture wheel enables Earth-viewing-geometry flat fielding. A Hg/Ar pen-ray lamp

provides on-orbit wavelength calibrations across the spectral range.

This full spectral range is spanned by a single HgCdTe FPA with 100% fill-factor pixels in a 640x480 format to acquire spatial/spectral images. The high-speed CMOS design includes an electronic global shutter allowing precise control of integration timing needed for known attenuation control. With nominal 15-Hz sampling, ground images have an along-track smear-limited 500-m spatial resolution; cross-track pixels are binned to the same resolution in Level-1 data products. Read-out noise is $<100\text{ e}^-$. Dark current and thermal backgrounds are reduced with the FPA's 150 K operating temperature, reducing uncertainties.

SUMMARY

The Sun is the most accurately-known and most stable radiometric light source in space. Using direct views of the spectral solar irradiance to provide on-orbit radiometric calibrations, the HySICS transfers this SI-traceable source to Earth reflectances with 0.3% uncertainties. This methodology is intended to provide needed radiometric accuracies for long-term climate studies and to improve, via inter-calibrations, measurements from other on-orbit sensors. The CLARREO Pathfinder is implementing the HySICS and this SI-traceable on-orbit calibration approach from the ISS starting in 2023. This mission is intended to demonstrate: current state-of-the-art in establishing traceability in orbit; new observations and climate-sensitivity detection capabilities and concepts; needed measurements, timescales, and accuracies for long-term climate studies; and reference calibrations to other on-orbit assets using identical viewing-geometries of targets.

REFERENCES

1. G. Kopp, P. Smith, C. Belting, Z. Castleman, G. Drake, J. Espejo, K. Heuerman, J. Lanzi, and D. Stuchlik, "Radiometric flight results from the HyperSpectral Imager for Climate Science (HySICS)," *Geoscientific Instrumentation Method. Data Syst.*, 6, pp. 169-191, 2017, doi:10.5194/gi-6-169-2017
2. <http://lasp.colorado.edu/home/tsis/instruments/sim-spectral-irradiance-monitor/>
3. B. Wielicki et al., "Achieving Climate Change Absolute Accuracy in Orbit," *BAMS*, Oct. 2013, doi:10.1175/BAMS-D-12-00149.1

New fixed point on the basis of In-Bi eutectic system for perspective space-borne standard low-temperature fixed-point blackbodies

Andrei Burdakin, Valeriy Gavrilov, Ekaterina Us, and Vitaly Bormashov

All-Russian Research Institute for Optical and Physical Measurements (VNIIOFI), Moscow, Russia

Corresponding e-mail address: burdakin-m4@vniiofi.ru

Reliable climate change monitoring requires high-quality long-term time series of atmospheric and surface remote temperature measured with space-borne radiometric IR instruments. This task can be solved through the development of incorporating the phase transition phenomenon space-borne blackbodies with an increased stability intended for IR instruments in-flight calibration. For the said purpose a number of phase-change materials (PCMs) with melt-freeze temperatures/fixed points located in the dynamic temperature range of Earth observation systems ($\sim 230\div 350$ K) are potentially applicable [1, 2]. Space-flight experiments on the melt-freeze transition in zero gravity of potentially applicable PCMs – individual substances and eutectic alloys – are absolutely necessary in the sequence of works on developing the novel space-borne standard fixed-point blackbodies.

SPACE-FLIGHT EXPERIMENT "KALIBR" – AN ESSENTIAL STEP ON THE WAY

The need for space-flight experiments follows from the fact that phase transition thermometric characteristics of a blackbody's working substance/PCM may alter in zero gravity. And for this reason characteristics of a fixed-point blackbody itself may alter in zero gravity as well.

In the line with this, the space-flight experiment "Kalibr" had been performed in 2014 on board the "Foton-M" #4 reentrant vehicle by using the space-borne standard blackbody test model (KALIBR) based on the melt transition of Ga (~ 303 K). The melting plateaus of Ga in zero gravity had been obtained, and performance of the space-borne low-temperature fixed-point blackbody test model/prototype KALIBR was investigated [3, 4].

NEW In-Bi EUTECTIC FIXED POINT

Along with Ga, the eutectic alloys Ga-In, Ga-Sn, and Ga-Zn as potentially suitable PCMs will be examined in zero gravity in the upcoming experiment on board the ISS ("Reper-Kalibr", stage 1). On ground

preliminary experiments showed that these substances are really promising regarding the task of developing space-borne fixed-point blackbodies [5]. At the same time, having the melt temperatures quite close to each other they form a rather narrow "on-orbit calibration scale" ($\sim 289\div 303$ K).

This makes highly desirable to involve some other PCMs in addition to the aforesaid substances. With the use for this purpose the In-Bi eutectic system (~ 345 K) and water "the on-orbit calibration scale" will be significantly expanded ($\sim 273\div 345$ K).

For this reason, the In-Bi eutectic system was chosen as a PCM for the space-borne fixed-point blackbody test model KALIBR-2 being developed for the same name space-flight experiment on board the "Bion-M" #2 reentrant vehicle.

Laboratory study of the new In-Bi fixed point. In compliance with the specificity of space application the new fixed point on the basis of the In-Bi eutectic system was preliminary studied in small cells (in the same way as in previous work [5]). More precisely, the "In-Bi fixed point" (~ 345 K / $\sim 72,5$ °C) is the melt temperature of the In-In₂Bi eutectic alloy – a domain in the In-Bi phase diagram [6]. Three samples of the In-In₂Bi alloy of different compositions were studied; typical melting plateaus are showed in the figure 1.

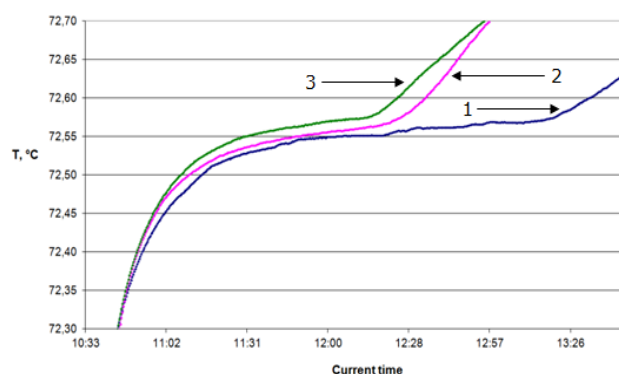


Figure 1. Melting plateaus of three samples of In-In₂Bi:

- 1 - 33,3 mass % Bi (approximate eutectic composition)
- 2 - 37,1 mass % Bi (hypereutectic composition)
- 3 - 24,0 mass % Bi (hypoeutectic composition)

In agreement with the theory melting plateaus of the sample close to eutectic composition and two other samples are found in practically the same temperature range. Though the melting plateaus of the hyper- and hypoeutectic alloys are shorter than one of the alloy close to eutectic composition (also in agreement with the theory) their quality is nevertheless quite appropriate: they last long enough, and irrespective of the plateau duration temperature drift at all plateaus does not exceed 30 mK (Fig. 1).

What is even more important regarding the final goal to ensure in-flight stability of space-borne IR instruments characteristics at the required level [2] – through the development of the novel high-stable space-borne blackbodies – that is a very good repeatability ~ 3 mK (1σ) of the In-Bi melting fixed point discovered in these experiments. (For simplicity, hereinafter we shall use the term "the In-Bi fixed point": by constituent elements.)

So, the ground-based study showed that the In-Bi eutectic system is a promising PCM for a space-borne fixed-point blackbody what explains the orientation of the space-flight experiment "Kalibr-2".

FUTURE SPACE-FLIGHT EXPERIMENTS INVOLVING THE In-Bi FIXED POINT INVESTIGATION IN ZERO GRAVITY

Space-flight experiment "Kalibr-2". Just like the experiment "Kalibr", the "Kalibr-2" pursues two interrelated goals. Firstly, investigation in zero gravity of the In-Bi eutectic system as a PCM for the perspective space-borne fixed-point blackbody with operational temperature ~ 345 K. The availability of such a blackbody should noticeably improve the quality of in-flight calibrations. And plus, testing of the space-borne standard blackbody prototype per se (in this case – utilizing the In-Bi fixed point).

Space-flight experiment "Reper-Kalibr". The space-flight experiment "Reper-Kalibr" as a whole (stages 1, 2) implies more thorough investigation of zero gravity influence on characteristics of a row of eutectic fixed points in connection with their use in the perspective space-borne calibration blackbodies. As for the In-Bi eutectic fixed point, it will be examined at the stage 2 of the "Reper-Kalibr".

As compared with the eutectic alloys on the basis of Ga (Ga-In, Ga-Sn, and Ga-Zn) which are the objects of investigation at the stage 1, the In-Bi eutectic system is even more interesting from a scientific perspective. (Another object of the stage 2

of the "Reper-Kalibr" – water – is also highly interesting from a scientific viewpoint.) The thing is, atomic weights of In and Bi differs among themselves more than atomic weight of Ga, on the one hand, differs from ones of In, Sn, and Zn, on the other hand. This fact makes the In-Bi eutectic system more "sensitive" to gravity.

Space-borne fixed-point blackbody prototype KALIBR-2 based on the In-Bi eutectic system.

Coming back to the "Kalibr-2" space-flight experiment, it should be pointed out that its primary goal is nevertheless rather practical than scientific: testing the space-borne standard fixed-point blackbody prototype. This experiment will be helpful for developing a reasonable number of the space-borne calibration blackbodies with an increased stability which operational/fixed-point temperatures are within the dynamic temperature range of Earth observation systems ($\sim 230\div 350$ K).

The use of the new In-Bi eutectic fixed point for the said purpose enables to create a space-borne blackbody with operational temperature almost at the upper limit of the dynamic temperature range. Such a noticeable expansion of "the on-orbit calibration scale" ensures more qualified in-flight calibration of space-borne radiometric IR instruments operating in the dynamic temperature range, whose measurements are critical for reliable climate change monitoring.

REFERENCES

1. V.N. Krutikov, V.I. Sapritsky, B.B. Khlevnoy et al, "The Global Earth Observation System of Systems (GEOSS) and Metrological Support for Measuring Radiometric Properties of Objects of Observations", *Metrologia*, vol. 43, no. 2, pp. 94-97, Apr. 2006.
2. V.I. Sapritsky, A.A. Burdakin, A.S. Panfilov et al, "On metrological support for climatic time series of satellite radiometric data", *JARS.*, vol. 3, no. 1, Jan. 2009.
3. V.I. Sapritsky, A.A. Burdakin, V.S. Ivanov et al, "Experiment "Kalibr" on Board the "Foton-M" № 4 Spacecraft – a First Step Towards the Establishment of the High-Stable Spaceborne Standard Radiation Sources", *Issledovanie Zemli iz Kosmosa*, no 4, pp. 85-55, Oct. 2016 (in Russian).
4. A. Burdakin, B. Khlevnoy, V. Krutikov et al, "Space-Flight Experiment on Board the "Foton-M" # 4 Reentrant Vehicle – First Step Towards Space-Borne High-Stability Fixed-Point Reference Blackbody.", *Proceedings of NEWRAD 2017*, pp. 28-29, Jun. 2017.
5. A. Burdakin et al., Melting points of gallium and of binary eutectics with gallium realized in small cells, *Metrologia*, 45, 75-82, 2008
6. N.P. Lyakishev, Diagrammy sostoyaniya dvoynykh metallicheskih sistem, Tom 1, "Mashinostroenie", Moskva, 1996 (in Russian)

Development of a laser-based satellite sensor illumination system to advance the capabilities of Earth observing systems

Steven W. Brown* and Brian Alberding

National Institute of Standards and Technology (NIST), Gaithersburg MD (USA)

Timothy A. Berkoff and Constantine Lukashin

National Aeronautics and Space Administration's (NASA's) Langley Research Center, Hampton VA (USA)

Abstract

An Earth observing satellite sensor's capability to robustly demonstrate SI traceability on-orbit at the uncertainty levels required by science data products is challenging. Dedicated on-orbit instrumentation and measurements of solar, lunar, and world reference calibration/validation sites established by the international Committee on Earth observation satellites (CEOS) are used to evaluate system performance and constrain measurement uncertainties. To meet future mission objectives such as climate quality observations by SI-traceable space-based reference observatories, for example the US Climate Absolute Radiance and Refractivity Observatory (CLARREO) [1] and EU Traceable Radiometry Underpinning Terrestrial and Heliostudies (TRUTHS) [2] instruments, the current state-of-the-art satellite sensor measurement uncertainties need to be reduced by an order of magnitude. Clearly, advancement of current technologies for establishing SI traceability as well as development of new characterization and calibration capabilities will be necessary to achieve future mission uncertainty requirements.

The objective of the program is to develop a dynamic Ground-to-Space Laser Characterization (GSLC) system that advances the capabilities of Earth observing satellite sensors. SI-Traceable Space-based Climate Observing Systems (COS) have the lowest uncertainty requirements and illumination of sensors on these systems by the GSLC system would provide a robust evaluation of the concept. Possible COS sensors to illuminate would include the Reflected Solar spectrometer of the CLARREO Pathfinder Mission on the International Space Station starting in 2023 [1], and the hyperspectral imager for measurements of Earth reflected solar radiation of the TRUTHS mission. Both will be in Lower Earth Orbits (LEO orbits) and can point, a requirement for experiments using the GSLC system. The TRUTHS mission includes a Cryogenic Solar Absolute Radiometer (CSAR) that holds the scale for the TRUTHS mission and up to 10 lasers to transfer the scale to the hyperspectral instrument.

In this presentation, development of a Ground-to-Space Laser Characterization (GSLC) system that provides extensive on-orbit diagnostic capabilities for Earth remote sensing systems is discussed [3, 4]. In its simplest configuration, broadly tunable narrow-band lasers are introduced into the GSLC system, for example using NASA's GLAMR system [5] or NIST's SIRCUS system [6]. In this configuration, the GSLC can illuminate an instrument similar to TRUTHS and use its on-board SI-traceable reference instrument, for example the CSAR on TRUTHS, to transfer the scale and thus, absolute SI-traceable measurements by the satellite sensor is feasible. Demonstrating

additional capabilities, the GSLC system can project dynamic, user-defined calibration source distributions, in principle.

Previous demonstration studies include successful illumination of the Global Lightning Mapper on GOES-16 and 17 [7]. The GSLC system has leveraged advances in free-space optical communications technologies, including demonstrations such as the Lunar Laser Communications Demonstration [8], and laser beam transmittance through the atmosphere. The performance of illumination systems designed to reduce scintillation will be evaluated using sensors mounted on aircraft. Satellite sensor measurements of the GSLC illumination system, if successful, lay the foundation for an entirely new approach to *in situ* characterizations of satellite sensors.

*point-of-contact. (address) NIST, 100 Bureau Drive, Mail Stop 8444, Gaithersburg, MD 20899; (email) swbrown@nist.gov; (phone) 301.975.5167.

References

- [1] Wielicki, Bruce A., et al., Pathfinder Mission for Climate Absolute Radiance and Refractivity Observatory, CLARREO Pathfinder Mission Team Report, 2016, (https://clarreo.larc.nasa.gov/pdf/CLARREO_Pathfinder_Report.pdf).
- [2] Fox, Nigel P., et al., Traceable Radiometry Underpinning Terrestrial– and Helio–Studies (TRUTHS): Establishing a Climate and Calibration Observatory in Space, Proc. SPIE 10563, 1056325 (2014).
- [3] C. Lukashin and B. Wielicki, patent US 8767210 B1, "Method for Ground-to-Space Laser Calibration System," July 1, 2014.
- [4] C. Lukashin and B. Wielicki, patent US 9052236 B2, "Method for Ground-to-Space Laser Calibration System," June 9, 2015.
- [5] Goddard Laser for Absolute Measurement of Radiance (GLAMR), (<https://glamr.gsfc.nasa.gov/>).
- [6] Woodward, John T., et al., Advances in tunable laser-based radiometric calibration applications at the National Institute of Standards and Technology, USA, Rev. Sci. Instr. 89 (9): 091301 (2018).
- [7] Buechler, Dennis, *et al.*, On-orbit validation of the geolocation accuracy of GOES-16 Geostationary Lightning Mapper (GLM) flashes using ground-based laser beacons, Proc. SPIE 10764, 107640J (2018).
- [8] Boroson, Don M., *et al.*, Overview and results of the Lunar Laser Communication Demonstration, Proc. SPIE 8971, 89710S (2014).

Recent developments in the VUV transfer source calibration based on calculable synchrotron radiation

Annett Barboutis, Roman Klein, Simone Kroth, Wolfgang Paustian, Reiner Thornagel

Physikalisch-Technische Bundesanstalt, Berlin, Germany

Corresponding e-mail address: roman.klein@ptb.de

The spectral radiant intensity of synchrotron radiation can be accurately calculated by the Schwinger formula, thus making electron storage rings primary sources. This fact has been used by PTB at several electron storage rings, which have been optimized to be operated as primary source standards, for the calibration of transfer sources in the spectral range of the UV and VUV for almost 30 years. Currently, we operate the electron storage rings BESSY II and MLS as primary source standards. The transfer sources are compared to the respective primary source standard by means of a suitable, wavelength-dispersive transfer station at each of the storage rings. The spectral region from 7 nm to 400 nm is covered, which is unique in the world. For the dissemination of this radiometric scale in the short wavelength spectral region, PTB operates transfer sources that are based on a hollow cathode discharge. We report on the status of these VUV transfer sources.

INTRODUCTION

Electron storage rings optimized for radiometry can be used as primary radiation source standards, the spectral intensity of which can be accurately calculated within classical electrodynamics by the so-called Schwinger formula [1]. So, using synchrotron radiation for radiometry gives access to the UV, VUV and X-ray spectral region [2, 3] and thus considerably expands the spectral region as compared to that covered, e.g., by blackbody radiators.

Since the late seventies, PTB has been taking advantage of this (besides a multitude of other applications [4]) for the traceable calibration of radiation sources.

CALIBRATION OF TRANSFER SOURCES

Transfer sources are compared to the primary source by means of wavelength-dispersive transfer stations. The transfer station either accepts radiation from the primary source or from the transfer source under test.

The source point of either source is imaged into an entrance aperture of a wavelength-dispersive monochromator, which represents the core of the transfer station. In the first orientation, the spectral sensitivity of the transfer device is determined and in the second orientation it is used then for a traceable calibration of the transfer source. PTB operates a transfer station [5] at the electron storage ring BESSY II primary source standard [6] which covers the spectral range from 40 nm to 400 nm and a station at the MLS primary source standard [7], which covers the spectral range from 7 nm to 40 nm [8, 9]. The transfer source can be either characterized in terms of spectral radiance or spectral radiant intensity. In the first case, only a part of the radiating source area is accepted by the entrance aperture of the transfer device. Details of the calibration principle and the uncertainty budget can be found in [8, 9].

At PTB, source-based calibrations in the short wavelength range below 120 nm are mainly performed within scientific co-operations, focusing on the calibration of space instruments [10, 11] and related transfer sources. In this paper we focus at these transfer sources. In the spectral region with wavelengths longer than 116 nm, i.e. the spectral region where the radiometric scale can be straightforwardly disseminated by means of deuterium (D₂) lamps as transfer standards, calibrations are handled within the normal PTB calibration service [12].

VUV TRANSFER SOURCES

Currently PTB operates two VUV transfer sources, both of which are based on a hollow cathode of the same kind. These sources have been developed by PTB in the 1980s for the calibration of the CDS spectrometer and SUMER spectrometer of the SOHO mission, respectively. The CDS source uses a Wolter telescope for the collimation of the radiation to a beam with 5 mm in diameter and works in the spectral range from 7 nm upwards. The SUMER source uses an Au coated mirror under NI reflection

for collimation. It delivers a beam of 10 mm in diameter, but due to the NI reflection its use has been limited to wavelengths longer than about 50 nm. To benefit from this larger beam diameter also in the shorter spectral range, the Au coated mirror was recently replaced by a multilayer mirror with reflectivity as shown in Fig.1. The comparison of the SUMER source signal before and after the modification is shown in Fig. 2. The short wavelength Ne spectral lines are now also emitted by the source with only moderate less output at the longer wavelength spectral region.

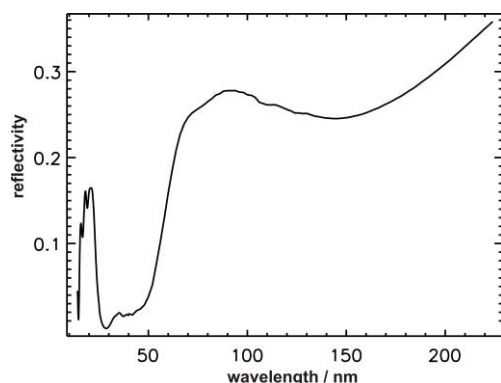


Figure 1. Measured reflectivity of the new SUMER transfer source collimation mirror.

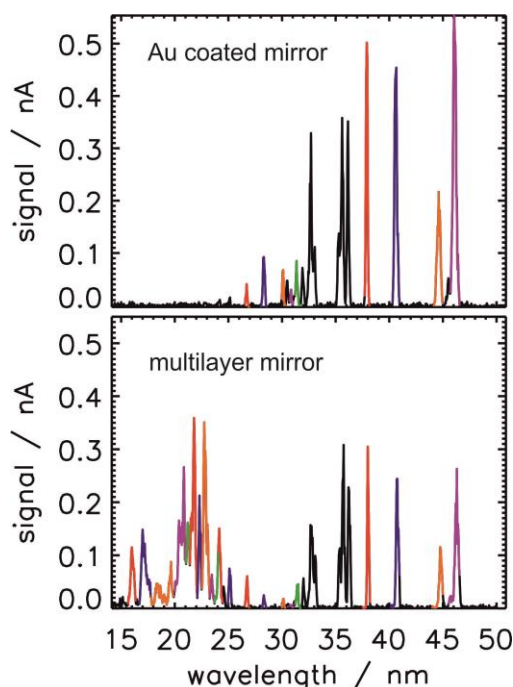


Figure 2. Example for the short wavelength range covered with the SUMER transfer source operated with Ne discharge before (top trace) and after (bottom trace) replacement of the collimation mirror.

After this replacement, the spectral range, which previously could only be covered by the CDS source, now also is served with the SUMER source. This enables the calibration over a wide spectral range with only one source and thus considerably facilitates the calibration procedure.

REFERENCES

1. J. Schwinger On the classical radiation of accelerated electrons *Phys. Rev.* **75** (1949) 1912.
2. J. Hollandt, J. Seidel, R. Klein, G. Ulm, M. Ware, A. Migdall in: 'Optical Radiometry', ed. by A. Parr, R. Datla, J. Garner, Vol. **41** of Experimental Methods in the Physical Sciences, Elsevier (2005) p. 213.
3. G. Ulm Radiometry with synchrotron radiation *Metrologia* **40** (2003) S101.
4. B. Beckhoff, A. Gottwald, R. Klein, M. Krumrey, R. Müller, M. Richter, F. Scholze, R. Thornagel, G. Ulm A quarter-century of metrology using synchrotron radiation by PTB in Berlin *Phys. Status Solidi B* **246** (2009) 1415.
5. M. Richter, J. Hollandt, U. Kroth, W. Paustian, H. Rabus, R. Thornagel, G. Ulm Source and detector calibration in the UV and VUV at BESSY II *Metrologia* **40** (2003) S107.
6. R. Thornagel, R. Klein, G. Ulm The electron storage ring BESSY II as a primary source standard from the visible to the X-ray range *Metrologia* **38**, (2001) 385.
7. R. Klein, G. Brandt, R. Fliegauf, A. Hoehl, R. Müller, R. Thornagel, G. Ulm, M. Abo-Bakr, J. Feikes, M. v. Hartrott, K. Höldack, G. Wüstefeld Operation of the Metrology Light Source as a primary radiation source standard *Phys. Rev. Special Topics - Accelerators and Beams (PRST-AB)* **11** (2008) 110701.
8. R. Thornagel, R. Klein, S. Kroth, W. Paustian, M. Richter Validation of a new facility at the Metrology Light Source for the calibration of radiation sources in the wavelength range from 116 nm to 400 nm *Metrologia* **51** (2014) 528-538.
9. R. Thornagel, R. Fliegauf, R. Klein, S. Kroth, W. Paustian, M. Richter A new facility for the synchrotron radiation-based calibration of transfer radiation sources in the ultraviolet and vacuum ultraviolet spectral range *Rev. Sci. Instrum.* **86** (2015) 013106.
10. R. Klein, R. Fliegauf, A. Gottwald, M. Kolbe, W. Paustian, T. Reichel, M. Richter, R. Thornagel, and G. Ulm Calibration of space instruments at the Metrology Light Source AIP Conference Proceedings 1741, 030013 (2016).
11. R. Klein, R. Fliegauf, S. Kroth, W. Paustian, T. Reichel, M. Richter, R. Thornagel Source-based calibration of space instruments using calculable synchrotron radiation *J. Astron. Telesc. Instrum. Syst.* **2**(4), 044002 (2016).
12. R. Klein, S. Kroth, W. Paustian, M. Richter, R. Thornagel PTB's radiometric scales for UV and VUV source calibration based on synchrotron radiation *Metrologia* **55** (2018) 386-391.

Primary and working standards for spectral total reflectance in Mid-IR region in KRISS

Jinwha Gene and Sun Do Lim

Korea Research Institute of Standards and Science, Daejeon, Republic of Korea

Corresponding e-mail address: sdlim@kriss.re.kr

We present a primary standard for spectral total reflectance in Mid-IR region in KRISS, which is based on the 3rd Taylor method with 8°/d geometry. We also introduce a working standard based on a comparison method using a reflectance reference that is calibrated with our primary standard. Some manufacturing techniques and simulation works are presented as well. This measurement capability has been dedicated to supporting a number of ground reference reflectance targets in Mid-IR region for vicarious calibration of satellite sensors.

INTRODUCTION

Recent climate change study has required more accurate satellite-derived land surface temperature (LST) products that are traceable to SI-based unit, so that highly reliable prediction for global warming can be carried out under global networking [1]. The LST products need calibration/validation on a regular basis against some ground reference targets with spectral emittance measured. Having relationship with research partners in Korea Aerospace Research Institute (KARI) on this study since 2015, we have built primary and working standards for spectral total reflectance to provide a number of the ground reference targets with spectral emittance assigned. The reflectance (R) practically represents the emittance (E) in its simplest form as $E = 1 - R$ according to Kirchhoff's law when materials have no transmittance. In this presentation, we are going to introduce our primary and working standards for spectral total reflectance in Mid-IR region, show some measurement results for different samples, and compare them with those measured in NIST.

PRIMARY STANDARD INSTRUMENT

Our primary standard for spectral total reflectance in Mid-IR region is based on 3rd Taylor method with 8°/d geometry. The measurement instrument includes an integrating sphere with a diameter of 15 cm and an MCT detector combined with a collimator on top of

it as shown in Fig.1. The collimator functions as a concentrator used in NIST setup [2], and also defines the field of view of MCT detector in the throughput of the integrating sphere. The integrating sphere has a sample port with a diameter of about 2.5 cm.

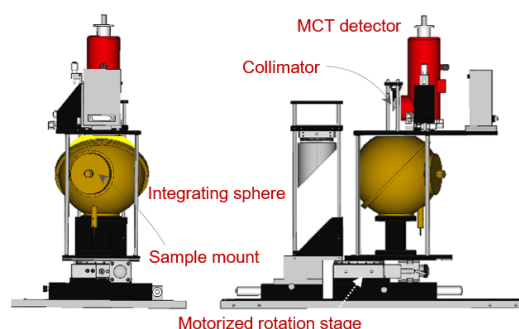


Figure 1. Primary standard instrument

The sample measurements with this instrument are made in a chamber that is integrated with a FTIR spectrometer, allowing operation in either vacuum or purging mode. Measurement on a certain sample was carried out in purging mode in KRISS and NIST by turns, and the comparison of the measurement results is shown in Fig. 2.

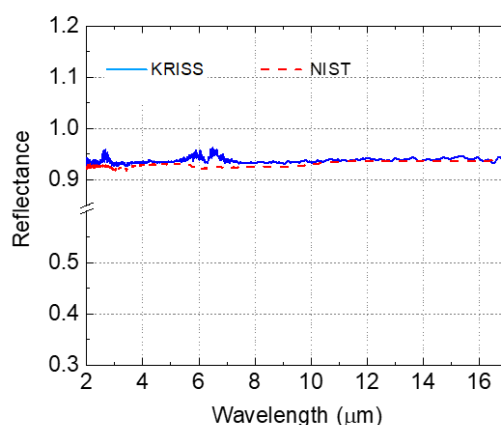


Figure 2. Comparison of KRISS and NIST measurement results

A slight discrepancy between KRISS and NIST were observed, but considering an expanded uncertainty of 3 % in NIST measurement, we believe that it is well

agreed with each other. One more thing noticeable here is that we had some noise-like kinks around 2.7 μm and 6.3 μm , which was we thought due to absorption of water vapour still remained in the chamber. The evaluation of our measurement uncertainty is in progress.

WORKING STANDARD INSTRUMENT

Basic configuration of working standard for spectral total reflectance in Mid-IR region is substantially the same as that of our primary standard, but the only difference is in the design of integrating sphere used. It has two ports for sample and reference as shown in Fig 3. The sample mount is designed to be able to hold various shapes of samples with different sizes.

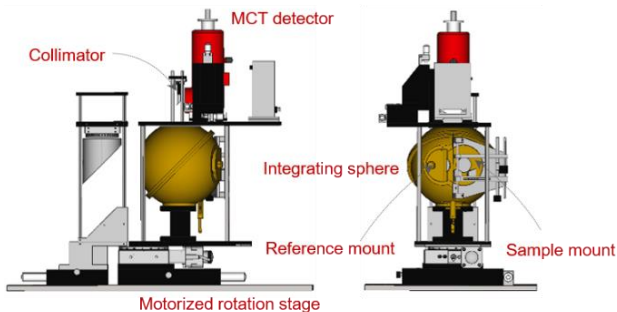


Figure 3. Working standard instrument

This instrument is set in another vacuum chamber that is also integrated with the FTIR spectrometer as shown in Fig. 4

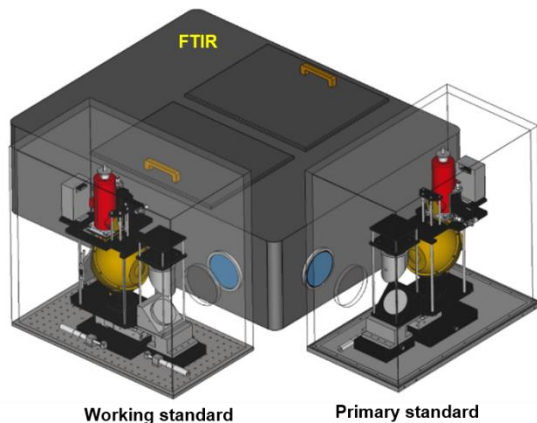


Figure 4. Overall configuration of primary and working standard instruments with FTIR spectrometer

The angular movement of integrating sphere assemblies in primary and working standard instruments and the signal measurement with the

FTIR spectrophotometer are controlled and made by a computer program.

REFERENCE PLATES

Diffuse reference plates with a reflectance of more than 95 % in Mid-IR region were fabricated by our own technique. Figure 5 shows some reference Al plates before being electroplated with gold.



Figure 5. Al plates sprayed with different sizes of Al particles on top of it (#, mesh number)

We differentiated surface roughness of the plates to find the best Lambertian reflection condition. We found some plates after being electroplated with gold had a very good Lambertian reflection with a reflectance of more than 95 % over the wavelength range of interest, which is the best performance to our knowledge among others reported so far including commercialized products.

CONCLUSION

We have built primary and working standards for spectral total reflectance in Mid-IR region in KRISS. Some samples made in KRISS were measured with KRISS primary standard. The measurement results were compared with those measured in NIST, which has a good agreement with each other. We hope that we can provide SI traceable calibration services for the Mid-IR spectral total reflectance with well-defined uncertainties to industries from 2021.

REFERENCES

1. P. Guillevic et al., Land Surface Temperature Product Validation Best Practice Protocol, Version 1.1 (2018), in P. Guillevic et al. (Eds.), Best Practice for Satellite-derived Land Product Validation: Land Product Validation Subgroup of WGCV/CEOS 2.
2. D. B. Chenault, K. A. Snail, and L. M. Hanssen, Improved integrating-sphere throughput with a lens and nonimaging concentrator, Appl. Opt. 34, 7959-7964 (1995)

The European metrology network for climate and ocean observation: a review of Earth observation needs for metrology

Emma Woolliams¹, Nigel Fox¹, Paola Fisticaro², Céline Pascale³ and Christian Monte⁴

¹National Physical Laboratory (NPL), Teddington, UK, ²Laboratoire national de métrologie et d'essais (LNE), Paris, France. ³Federal Institute of Metrology (METAS), Bern, Switzerland. ⁴Physikalisch-Technische Bundesanstalt (PTB), Berlin, Germany.

Corresponding e-mail address: emma.woolliams@npl.co.uk

EURAMET established the European Metrology Network (EMN) for Climate and Ocean Observation to support the observation expert communities to engage with metrologists at national metrology institutes and to coordinate European metrological research in response to community needs. The EMN has carried out a survey of what its stakeholders need from metrology. We present the results of that survey for satellite and related radiometric observations.

METROLOGY IN CLIMATE MEASUREMENT

Observations of essential climate variables (ECVs) and related environmental quantities made by satellites and in situ observational networks are used for a wide range of societal applications. To identify a small climate trend from an observational record that is also sensitive to weather, seasons and geophysical processes, stable, multi-decadal observations are needed, that still allow for changes in the observation instrumentation and procedures. To achieve this, all aspects of data collection and handling must be underpinned by robust quality assurance. The resultant data should also be linked to a common (preferably SI) reference, with robust and transparent uncertainty assessment, so that observational results are interoperable and coherent; measurements by different organisations, different instruments and different techniques should be able to be meaningfully combined and compared.

Metrology can provide a critical role in enabling robust, interoperable and stable observational records and can thus aid users in judging the fitness-for-purpose of such records. Many national metrology institutes (NMIs) worldwide have active research programmes in collaboration with the communities making and using climate observations and provide calibration services to those communities.

The value of metrology in observational systems such as the Global Climate Observing System

(GCOS), and the role of NMIs in supporting the quality assurance of such observations, has been recognised in initiatives such as the Quality Assurance Framework for Earth Observation (QA4EO) established by the Committee on Earth Observation Satellites (CEOS) and in the implementation plans of the World Meteorological Organization's (WMO's), Global Atmosphere Watch and the European Ocean Observing System.

THE EUROPEAN METROLOGY NETWORK FOR CLIMATE AND OCEAN OBSERVATION

The European Association for National Metrology Institutes (EURAMET) has recently created the "European Metrology Network (EMN) for Climate and Ocean Observation" to support the expert communities to engage with and to guide and encourage Europe's metrologists to coordinate their research in response to community needs. The EMN has a scope that covers metrological support for in situ and remote sensing observations of atmosphere, land and ocean ECVs (and related parameters) for climate applications. It also covers the additional economic and ecological applications of Essential Ocean Variable (EOV) observations.

It is the European contribution to a global effort to further develop metrological best practice into such observations through targeted research efforts.

SURVEY OF METROLOGY NEEDS FOR CLIMATE AND OCEAN OBSERVATIONS

The EMN for Climate and Ocean Observation has been carrying out a survey to identify the ways in which metrology can most valuably contribute to the climate and ocean observation communities. The survey has involved the following aspects: (a) a set of online questionnaires that was sent to expert communities and received more than 50 responses, (b) a review of the literature, the strategies of key coordinating organisations and reports of community workshops and (c) a set of webinars, held 12/13

February 2020, with observation experts and metrologists. Here, we present the results of the survey as regards satellite Earth Observation.

METROLOGY IN SATELLITE AND GROUND-BASED EARTH OBSERVATION

The Newrad conference has, since its origin in 1985, “provided a platform for the discussion of developments in optical radiometry among scientists working in laboratory and space radiometry.” (quote from [1], 1996). Arguably it is this joint platform that helped to create the collaborative discipline of Earth Observation Metrology.

In 2008 CEOS formally endorsed QA4EO as a framework [2] around the principle that “All data and derived products must have associated with them a Quality Indicator (QI) based on documented quantitative assessment of its traceability to community-agreed reference standards. This requires all steps in the data and product delivery chain (collection, archiving, processing and dissemination) to be documented with evidence of their traceability.” The framework was introduced alongside practical guidelines for reporting, for assessing uncertainties and for performing comparisons. These guidelines were based on metrology guidelines for comparisons for the Mutual Recognition Arrangement, especially the Consultative Committee for Photometry and Radiometry’s (CCPR) guidelines for comparisons.

This formal recognition of the importance of metrological processes to underpin the long-term stability and interoperability of satellite Earth observation has opened further collaboration between the space agencies and the NMIs, much of which has been presented at Newrad conferences.

Within Europe, the Metrology for Earth Observation and Climate (MetEOC) series of EU-funded projects have developed new metrological techniques and applied them not only to pre-flight and post-launch radiometric calibration, but also to the derivation of ECV products, and to ground-based solar observations for the world standard group and the baseline surface radiation network. Those projects have provided a firm foundation for other work, performed collaboratively with (and often commercially for) the European Space Agency (ESA) and academic partners across Europe.

There have been projects to develop guidelines for ECV records [3], to establish “fiducial reference measurements” (FRM) of SI-traceable ground

truthing observations [4] and for applying metrology to fundamental climate data records [5]. Recently, there has been approval of funding to design, build and launch a satellite that puts NMI traceability (and a cryogenic radiometer) into orbit, implemented through the ESA Earth Watch Programme. The TRUTHS satellite [6] will provide a climate benchmark through highly accurate observations of incoming and reflected solar radiation, and will serve as an inflight calibrator, able to transfer its SI-traceability to other sensors in orbit. The MetEOC projects will also provide SI-traceability to the ESA infrared satellite mission FORUM.

SURVEY RESULTS

At the time of writing the abstract, the survey has not been completed (completion due May 2020). However, preliminary results show that the satellite Earth observation community recognises the value that metrology plays in ensuring long term stability and interoperability of satellite sensor data, but that there are many barriers to the implementation of metrological methods. At present there is no clear framework for systematic provision of metrological traceability prelaunch or in postlaunch calibration through vicarious references. There is a desire for metrologists to support the development of calibration methods and uncertainty analysis determination for a wider variety of sensors – both passive radiometric sensors and active (radar) sensors.

There is also a common request for improved training material and improved coordination of vocabulary.

ACKNOWLEDGEMENTS

Thanks to David Gorman of NPL for establishing a database tool for the survey. The work was supported by the project (18NET04), which has received funding from the EMPIR programme co-financed by the Participating States and from the European Union’s Horizon 2020 research and innovation programme.

REFERENCES

1. B. Wende, Foreword: 5th International Conference on Radiometry, *Metrologia* 32(6), 409, 1996.
2. www.qa4eo.org
3. J. Nightingale, J.P.D. Mittaz, S. Douglas, et al. *Remote Sensing*, 11(8), 986, 2019.
4. www.frm4sts.org, frm4soc.org
5. J. Mittaz, et al. *Metrologia*, 56, 032002, 2019.
6. N. Fox, et al. *Phil. Trans. R. Soc A*, 369, 4028-4063, 2011.

SI Traceability, Uncertainty Analysis and Comparison for RadCalNet

Emma Woolliams, Agnieszka Bialek, Sarah Taylor, Chris MacLellan, Morven Sinclair and Nigel Fox

National Physical Laboratory (NPL), Teddington, United Kingdom

Corresponding e-mail address: emma.woolliams@npl.co.uk

RadCalNet provides nadir-view ground and top-of-atmosphere spectral reflectance values (10 nm steps, 400 nm – 1000 nm / 2500 nm) every 30 minutes from four instrumented reference sites in China, Namibia, USA and France. NPL has been the metrology partner for this initiative and is responsible for ensuring the SI-traceability of the network. In this presentation we describe the metrological processes introduced to ensure SI-traceability to the network.

RADCALNET

The increased use of satellite-derived data in climate and earth monitoring, requires robust and traceable radiometric and spectral calibration of satellite sensors. Vicarious calibration sites play a vital part in ensuring the stability and interoperability of satellite sensor data post-launch for both traditional satellites and the smaller, often commercial satellites which do not have onboard calibration capability.

RadCalNet [1], the Radiometric Calibration Network established through the Committee on Earth Observation Satellites Working Group on Calibration and Validation (CEOS-WGCV), provides a network of instrumented ground reference sites providing users with bottom and top-of-atmosphere (BOA and TOA) reflectance measurements every 30 minutes in 10 nm spectral intervals (for 400 nm to 1000 nm or to 2500 nm) and for nadir view. (For all sites, more detailed spectral information and off-nadir reflectances can be obtained from site owners). Each RadCalNet site provides ground reflectance values that are propagated to TOA through a centralised processing system. RadCalNet has over 300 users.

It is a key aspect of RadCalNet that the sites document their traceability to the International System of Units (SI) and that they provide associated uncertainties for each observation.

RADCALNET WORKING GROUP AND MEMBERSHIP PROCESSES

RadCalNet was established under CEOS-WGCV by the RadCalNet working group (WG). The RadCalNet WG comprises the owners of RadCalNet member

sites (currently AOE, China, CNES, France, University of Arizona, USA and ESA, Europe), the organisation which provides processing of site data to TOA reflectance (NASA, USA), the organisation which operates the RadCalNet data servers and portal (Magellium, France) and NPL as the metrology partner (NPL also operates the Namibian site on behalf of ESA). Additionally, CEOS-WGCV has appointed a “Test site admissions panel” that has the authority to approve sites to join RadCalNet.

New RadCalNet sites must provide 45 days’ data from their site, show that they can provide data operationally (within two weeks of measurement) and provide a questionnaire detailing information about their site (instrumentation, location, climatology) along with a detailed uncertainty statement. These documents are peer reviewed by the RadCalNet WG, which also performs a comparison of the site with others using satellite sensors. Once the documents have been updated, the RadCalNet WG writes a report to the CEOS-WGCV test site admissions panel which formally approves the site.

To support site owners to establish sites, the RadCalNet WG to maintain and monitor the performance of sites and users to understand the data and its limitations, NPL has produced guidance documents on site selection, site instrumentation, uncertainty budgets and comparisons [2] along with document templates and procedures for peer reviewing sites. These guidelines and procedures are based on metrological approaches used by national metrology institutes for the mutual recognition arrangement. NPL also carries out four-monthly comparisons of all sites to ensure ongoing data quality.

RADCALNET REFLECTANCE UNCERTAINTIES

Each site’s uncertainty budget documents the traceability to SI for the field measurements (including laboratory comparison and transfer to field as well) and for any auxiliary information required, e.g. the solar and sky irradiance required to convert measured ground radiance into ground reflectance. Because satellite sensors are not compared with

RadCalNet on a single overpass but through an averaging of multiple overpasses, it is also important to identify which sources of uncertainty have a common (unknown) error for different days and which are due to transient effects that will have different (unknown) errors on different overpasses.

RadCalNet ground reflectances and atmospheric observations, which are provided by site operators with associated uncertainties (that may vary from measurement to measurement), are propagated to TOA through a common RadCalNet processor operated by NASA. Uncertainties associated with TOA reflectances are obtained using look up tables based on ~80k atmospheric, altitude and solar angle conditions. For each condition a 100-sample Monte Carlo run was used to obtain the uncertainty associated with the propagation to TOA.

SITE COMPARISONS

At present, comparisons between the sites are performed using the ESA Multi Spectral Instruments (MSI) on board the Sentinel-2A and -2B satellites as references. These are high quality sensors with onboard calibration capability, which are regularly compared to each other and to other similar sensors (e.g. NASA's Operational Land Imager (OLI) on Landsat 8) over a large variety of vicarious targets.

Every four months NPL performs comparisons between the sites' RadCalNet products and Sentinel-2A/B for every valid matchup. These data (e.g. fig. 1) are provided to the RadCalNet WG for monitoring.

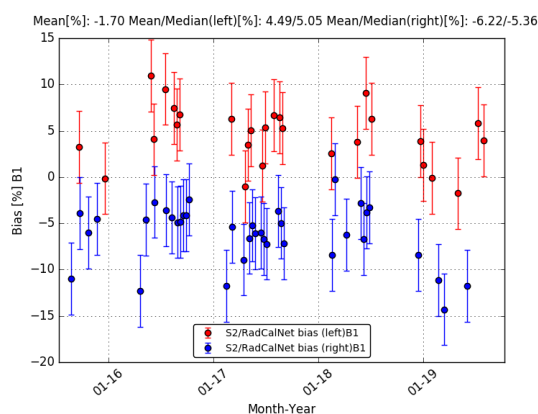


Figure 1 Example comparison results for one of the RadCalNet sites.

Currently comparisons between sites is performed using satellite observations as a reference. During MetEOC-2, the Czech Metrology Institute (CMI) developed an instrument, called MuSTR [2], to act as

a travelling standard for in situ site comparisons. Work is ongoing to develop procedures and analysis methods for such comparisons.

SUPPORTING USERS

RadCalNet provides, at no cost, data for nadir view observations. Most satellites do not observe the sites at nadir view. Satellite sensor spectral response functions are also not represented by data provided in 10 nm spectral steps and satellites do not go over the sites exactly on the half hour. Most sites will provide off-nadir, higher spectral and temporal resolution data as a commercial service, but users need guidance on when RadCalNet data are fit for purpose and what additional uncertainties are to be considered when the RadCalNet conditions are not met.

Figure 1 shows the comparison to Sentinel-2 over one of the RadCalNet sites for one spectral band. There, the red data represent an orbit where the site was imaged on the left-side of the swath, and the blue data where the site was imaged on the right-side. The observed bias from the nadir reflectance values is due to the bi-directional reflectance factors of the surface. NPL is developing site-specific models to understand and quantify such differences.

As a founder member of the RadCalNet WG, NPL has been developing procedures, guidance and protocols for site owners and data users, has performed scientific analysis to develop comparison and uncertainty methods and provides routine quality control on the data provided by RadCalNet.

ACKNOWLEDGMENTS

This work was funded in part by MetEOC-3 (16ENV03) which received funding from the EMPIR programme co-financed by the Participating States and from the European Union's Horizon 2020 research and innovation programme. And by the European Space Agency Technology and Research Programme through the ACTION project.

REFERENCES

1. Bouvet, M. et al, RadCalNet: A radiometric calibration network for Earth observing imagers operating in the visible to shortwave infrared spectral range, Remote Sensing 11(20), 2401. 2019.
2. Guidance documents and site reports all available at www.radcalnet.org
3. Porrovecchio, G, et al. The multi-spectral transfer radiometer as a comparison artefact for the Radiometric Calibration Network. In Proceedings of Newrad. 2017.

Stray-Light Correction Methodology for the Precision Solar Spectroradiometer

Natalia Kouremeti¹, Julian Gröbner¹ and Saulius Nevas²

¹Physikalisch-Meteorologisches Observatorium Davos, World Radiation Center, Davos, Switzerland,

²Physikalisch-Technische Bundesanstalt (PTB), Braunschweig and Berlin, Germany

Corresponding e-mail address: natalia.kouremeti@pmodwrc.ch

A stray-light correction methodology for the Precision Solar Spectroradiometer (PSR) is presented. The correction is based on laboratory-measured line spread functions also taking into account the radiation from the 2nd and 3rd grating orders. The efficiency of the correction is validated on solar and lamp measurement data. The results are compared to those obtained with a PSR equipped with an order-sorting filter and with a Precision Filter Radiometer.

INTRODUCTION

The Precision Solar Spectroradiometer (PSR) is a grating-type array spectroradiometer, developed as a reference instrument for spectral solar irradiance measurements in the spectral range from 300 nm to 1040 nm and for the determination of aerosol optical depth [1]. While previous PSR units were built using an order-sorting filter (OSF) in front of the detector, later instruments were constructed without a physical filter, relying instead on post-processing of the measured spectra using a correction method based on line-spread functions (LSF) and extending the method developed by [2].

STRAY LIGHT CORRECTION METHODOLOGY

The LSFs were measured at PMOD/WRC throughout the full spectral range of the spectroradiometers using a ns-pulsed OPO system. The LSF measurements were performed over 5 to 6 orders of magnitude by varying output power of the laser beam and integration time of the PSR. Figure 1 shows LSF matrices for two PSR units. One instrument is with an OSF in front of the detector while the other one is without it. The 2nd and the 3rd orders of the grating requiring a correction are clearly seen in the matrix shown in the right subfigure.

The measured LSFs of PSR 008 were validated by analogous measurements performed at a similar ns-OPO facility at PTB. The measured LSFs were used to derive a stray-light correction matrix. One problem to be solved was that the wide spectral range

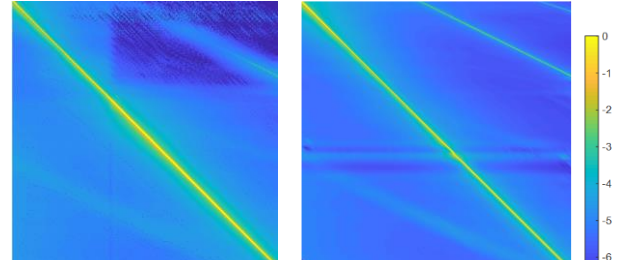


Figure 1. LSF matrices of PSR#004 with OSF (left), and PSR#008, which is without any filter (right). The x and y axis are in pixel space (1024x1024) and cover the spectral range from 300 nm to 1040 nm. The data is shown in logarithmic units.

of the instrument (about 700 nm) is covered by a detector array with 1024 pixels. Since the bandpass is about 2 nm, there are just a few pixels within LSF peaks. To reduce the related discretisation uncertainties, when inverting the LSF matrix, it was necessary first to interpolate the LSFs to a denser pixel grid before building the matrix.

UNCERTAINTY OF THE CORRECTION

The uncertainty of the stray light correction, u_{LSF} , is described by Eq.1,

$$u_{LSF}^2 = \left[\left(\frac{\sigma_S}{S\sqrt{N}} \right)^2 + \left(\frac{\sigma_D}{S\sqrt{Nd}} \right)^2 \right] + \left[\left(1 - \frac{S(ITI)}{S(ITI)} \right)^2 + \left(\frac{3\sigma(Sat)}{Sat\sqrt{3}} \right)^2 \right], \quad (\text{Eq.1})$$

where σ_S and σ_D represent variances of the measured signal (S) and dark counts (D), respectively. The second term of the equation describes the uncertainty contribution resulting from different integration times (IT) and merging of saturated and unsaturated measurements (Sat). Moreover, wavelength shifts also introduce an uncertainty component in the stray light correction results, especially correcting for the 2nd and 3rd dispersion orders. This uncertainty has been determined considering a ± 0.5 nm shift and measurements of a transfer standard lamp (FEL). Figure 2 shows the stray light corrections and the associated uncertainties for the irradiance measurements of an FEL lamp using 3 PSR units without any OSF.

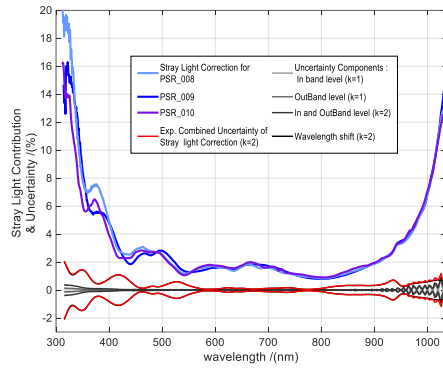


Figure 2. Stray light corrections applied to the new PSR series instruments measuring an FEL lamp and the respective uncertainties of the corrections.

VALIDATION

The efficiency of the PSR stray light correction with respect to the suppression of the radiation from higher dispersion orders has been evaluated using laboratory-based and sun measurement data. Specifically, a UV LED-based source [3] with an emission spectrum in the range 300 nm – 420 nm has been used. The stray light contribution of 0.8% due to the higher grating orders could be corrected by nearly a factor of 10 as shown in Figure 3. Moreover, a comparison of direct solar irradiance spectra measured with the two types of PSRs showed an agreement within $\pm 1\%$ while correcting for up to 40% of the stray light contribution (Figure 4). Similar results were obtained when comparing the solar irradiance at 862 nm and 500 nm measured by

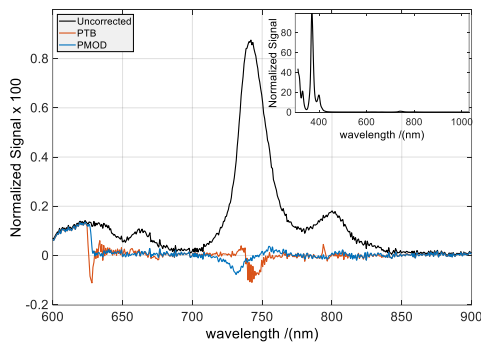


Figure 3. UV-LED source spectrum corrected for straylight contribution (red – PTB data, blue – PMOD data) and uncorrected spectrum (black).

PSR#009 to the respective values measured at these wavelengths by the Precision Filter Radiometer (PFR-N24) forming part of the AOD WMO reference PFR-Triad (see Figure 5). In total, results of 9724 common measurements were compared covering solar zenith angles (SZA) from 40° to 75°. The normalized ratios show negligible SZA dependencies

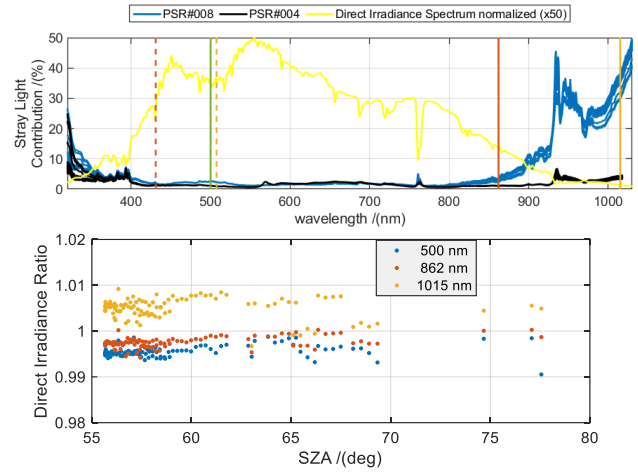


Figure 4. Upper panel: stray light contribution in the direct solar irradiance spectra measured by PSR#004 (black) and PSR#009 (blue). Lower panel: direct solar irradiance ratio PSR #009/#004 at selected wavelengths.

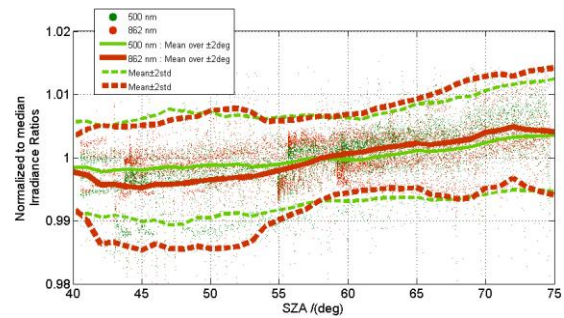


Figure 5. Direct irradiance ratio of PFR-N24 and PSR#009 at 500 nm and 862nm (dots: data points; solid and dashed lines: mean and $\pm 2\sigma$ of the data points over $\pm 3^\circ$ of the SZA, respectively).

(within 1%). As they are similar for both wavelengths, it is an indication that spectral leakages have been compensated within the estimated uncertainty of $\pm 1\%$ ($k=2$).

CONCLUSION

The mathematical suppression of the stray light due to higher grating orders can be realized with an uncertainty of less than 1%. Thus, the approach based on the numerical stray-light correction produces results equivalent to those using an order-sorting filter.

REFERENCES

1. Gröbner, J., and N. Kouremeti, The Precision solar Spectroradiometer (PSR) for direct solar irradiance measurements, *Solar Energy* 185, 199-210, 2019
2. Zong et al., Simple spectral stray light correction method for array spectroradiometers, *Appl. Opt.* 45, 1111-1119, 2006.
3. Sildoja, Meelis-Mait et al, LED-based UV source for monitoring spectroradiometer properties, *Metrologia* 55 S97, 2018.

Traceability of Solar and Lunar Direct Irradiances Measured with Precision Filter Radiometers

Natalia Kouremeti¹, Saulius Nevas², Stelios Kazadzis¹ and Julian Gröbner¹

¹*Physikalisch-Meteorologisches Observatorium Davos, World Radiation Center, Davos, Switzerland,*

²*Physikalisch-Technische Bundesanstalt (PTB), Braunschweig and Berlin, Germany*

Corresponding e-mail address: natalia.kouremeti@pmodwrc.ch

Two Precision Filter Radiometers (PFRs) measuring Solar and Lunar direct irradiances for the retrieval of aerosol optical depth (AOD), have been characterised and calibrated at PTB and PMOD/WRC, respectively. The measured irradiances are used in the classical Langley extrapolation method to assess the precision of the extra-terrestrial Solar and Lunar spectra as well as the accuracy of AOD measurements that can be currently achieved following the SI-traceable methodology.

INTRODUCTION

Atmospheric aerosols are known to impact the climate. They represent also one of the essential climatic variables with the largest uncertainties in the climate change studies. Within the framework of Global Atmospheric Watch (GAW), Aerosol Optical Depth (AOD) is monitored based on direct solar irradiance measurements performed by Precision Filter Radiometers (PFRs). The instrument calibration is carried out at the World aerosol Optical depth Research and Calibration Center (WORCC) in Davos, Switzerland, as mandated by the World Meteorological Organization [1]. The growing interest in night-time observations of AOD, in an effort to close the gap in the annual cycle of the arctic aerosol climatology, led to the development of the Lunar Precision Filter Radiometer. Here we present preliminary characterisations and calibrations of two such instruments.

PFR RELATIVE RESPONSIVITY

The relative spectral responsivities (RR) of sun and lunar PFRs, PFR-S and PFR-L, respectively, have been primarily determined using ns-pulsed OPO systems (EKSPLA NT242) at PTB and at PMOD. The RR measurements of PFR-S at PTB were carried out relative to a calibrated silicon photodiode using a monitor photodiode while at PMOD the reference detector is a pyroelectric radiometer. The OPO wavelengths were measured by a laser spectrum

analyser (LSA) of High Finesse. The PFR signal (V) is provided by a 22-bit data acquisition system (SACRAM) specifically designed for the PFR.

The PFR channels showed a highly nonlinear response under the ns-pulsed OPO irradiation. The nonlinearity was mapped out by changing the laser power and comparing PFR signal readings with those of the linear monitor detector. Channel 4 (368 nm) showed not only nonlinearity but also a hysteresis.

PFR RESPONSIVITY IN SI UNITS

The spectral irradiance responsivity of the PFRs in SI units has been determined at the TULIP setup [2] and at the direct irradiance calibration setup of PMOD/WRC.

The measurements at the TULIP setup were carried out within bandpasses of the channels against a calibrated 3-element silicon trap detector equipped with an aperture. The reference plane of the PFR has been validated against the reference detector introducing displacements along the beam propagation direction. The radiation source in the setup is a quasi-CW laser system generating ca. 200 fs pulses at 80 MHz repetition rate. The spectral bandpass of the fs-laser radiation was limited by a monochromator to 0.8 nm. A homogeneous irradiance field for the measurements is generated by a micro-lens array.

The direct irradiance calibration setup at PMOD/WRC consists of a reference irradiance source (1000W FEL-type lamp) calibrated at PTB and fully motorized XYZ linear translators and rotation stages for azimuth and zenith angles.

The lamp irradiances were measured at 3 distances ranging from 1.5m to 3m and the reference plane was determined by applying the inverse square law. The calibration factors in SI units (Wm^{-2}/V) were calculated as an integral of the TULIP-provided responsivity functions over the measured spectral bandpasses (T). The responsivity functions were extended to wider spectral ranges using the pulsed OPO-based data (TP). For the lamp calibration method, the afore-mentioned responsivities were

converted to relative ones (see Figure 1) and convolved with the spectral irradiance of the reference lamp at the distance of the measurement (L-T, L-TP, and L-P for the PFR-L). The percentage deviation of the calibration factors from the TP ones along with the combined uncertainties are presented

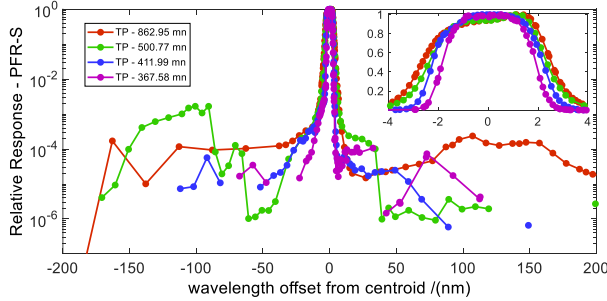


Figure 1: Relative spectral irradiance responsivity of the 4 PFR-S channels measured at PTB. in Table 1.

Table 1: Percentage differences of calibration factors with respect to TP and combined uncertainties in parenthesis.

	862 nm	500nm	412nm	368 nm
T	-0.80(0.50)	-0.79(0.5)	-0.31(0.50)	-0.39(0.70)
TP	0.00 (0.80)	0.00(0.80)	0.00(0.80)	0.00(0.80)
LT	-0.38(1.63)	-1.57(1.63)	-2.72(1.63)	-3.42(1.76)
LTP	-0.29(1.74)	-0.76(1.74)	-2.68(1.74)	-3.29(1.84)

AOD AND EXTRATERRESTIAL SOLAR AND LUNAR SPECTRA

For the evaluation of the calibration accuracy that can be achieved using the publicly available solar extra-terrestrial spectra (ETS), QASUMEFTS [3] and ATLAS [4], we organized a short direct solar irradiance measurement comparison campaign against a PFR-Triad in Davos (48.68°N, 9.85°E, 1600m) in March 2019. In total, measurements during 9 clear days with Langley atmospheric conditions, aerosol loads ranging from 0.01-0.03 AOD at 500 nm, were compared. For a subset of these days (6), a Langley-extrapolation calibration has been performed for the PFR-S. Differences between the ETS convolved with the corresponding RR and the Langley-extrapolated ETS values are shown in Table 2. For TULIP and lamp calibration-based data the agreement at wavelengths below 500 nm is within 1% and 1.5%, respectively. For 862 nm, despite the best agreement of all SI calibrations constants ($1\sigma=0.45\%$) a negative offset of 1% for ATLAS-ETS is identified.

The same validation method has been used for the PFR-L. For this instrument, datasets measured at Izaña [5] and at Ny-Ålesund were tested with the

RIMO lunar ETS irradiance model. For RIMO, we have observed differences of 1.03%, 6.59%, 10.66%, 2.81% at nominal central wavelengths of 862 nm, 500 nm, 412 nm and 675 nm with high standard deviations partly depending on the lunar phase. However, the standard uncertainties of the calibration factors are of the order of 4% due to the 4 orders of magnitude difference in the signal amplification used for laboratory and atmospheric measurements.

In terms of the AOD retrievals using the SI-traceable calibration and the available ETS, the agreement to the reference PFR-Triad is within the accuracy required by the WMO at 412 nm and 500 nm. At 368 nm this is the case only for the calibration factor from the TULIP. Finally, the AOD at 862nm is outside the required limits, with a clear offset of +0.01 in AOD.

Table 2: Percentage differences between ETS and Langley method-obtained extra-terrestrial values at the PFR-S wavelengths.

ETS	ATLAS		QASUMEFTS	
Calibration Factor (CF)	862nm	500nm	412nm	368nm
T	-1.13	0.88	-0.91	-0.70
TP	-2.00	0.47	-0.83	-0.98
L-T	-1.56	1.60	1.03	1.87
L-TP	-1.90	0.86	1.31	1.65
mean	-1.65	0.95	0.15	0.46
std	0.40	0.47	1.18	1.51

These experiments have demonstrated the current measurement accuracies that can be achieved with the PFRs and revealed the major sources of uncertainty that need to be assessed in order to reach the required AOD accuracy of the Langley calibration technique.

REFERENCES

1. Kazadzis, S., et al, The World Optical Depth Research and Calibration Center (WORCC) quality assurance and quality control of GAW-PFR AOD measurements, Geosci. Instrum. Method. Data Syst., 7, 39-53, 2018.
2. Schuster M., et al., Validation of short-pulse-laser-based measurement setup for absolute spectral irradiance responsivity calibration Appl. Opt.53 2815-21, 2014
3. Gröbner, Jet al., The high-resolution extraterrestrial solar spectrum (QASUMEFTS) determined from ground-based solar irradiance measurements, Atmos. Meas. Tech., 10, 3375–3383,2017
4. Thuillier, G. et al., The Solar Spectral Irradiance from 200 to 2400 nm as Measured by the SOLSPEC Spectrometer from the Atlas and Eureka Missions, Sol. Phys., 214, 1–22, 2003
5. Barreto, A., et al., Evaluation of night-time aerosols measurements and lunar irradiance models in the frame of the first multi-instrument nocturnal intercomparison campaign., Atmospheric Environment 202: 190-211, 2019.

New Laser-Driven Light Source (LDLS)-based DSR measurement facility for calibration of reference solar cells

Khaled Mahmoud^{1,2}, Jae-Keun Yoo³, Nasser Al-Qahtani¹, Hong Gyu Lee⁴

¹National Measurement and Calibration Center, Saudi Standards, Metrology and Quality Org. (NMCC/SASO), PO Box 3437 Riyadh 11471, Saudi Arabia,

²National Institute for Standards (NIS), PO Box 136 Giza, Code No 12211, Egypt,

³Division of Physical Metrology, Korea Research Institute of Standards and Science (KRISS), Daejeon, Korea

⁴PIMACS CO., Ltd, Seoul, Korea Republic.

Corresponding e-mail address: k.abdeltah@saso.gov.sa / khaled55eg@yahoo.com

A newly established facility for calibration and characterization of solar cells at NMCC/SASO is presented. This multipurpose instrument can provide a complete set of data for solar photovoltaic (PV) devices including critical spectral and electrical parameters. The system comprises two main parts, first utilizes LDLS-based modulated (AC) source to measure the spectral responsivity of PV detectors and solar cells using the DSR technique, second uses solar simulator to study the IV-curves, measuring the short circuit currents and solar cell efficiencies. The first part will be used to measure the spectral responsivity in the wavelength range from 250 nm to 2000 nm, bias level up to 1.5 kW/m², with which, target measurement uncertainty below 1 % ($k = 2$, in the visible range) can be achieved.

INTRODUCTION

Solar energy has the ability to reduce greenhouse gases, global warming and provide increasing energy efficiency. As a sustainable resource of energy, solar energy is the type of energy that can solve the energy problems in the earth. Saudi Arabia is one of the countries that is reach with solar energy all over the year; this creates an ultimate opportunity to build its own solar power hub to meet its rapidly growing needs of electric power and to become a leading exporter of solar energy [1]. Those objectives motivate the NMCC/SASO (NMI of Saudi Arabia) to build a new facility for solar cell (PV) devices calibration and characterization to meet its challenge as NMI for supporting the emerging solar industry.

Solar energy industry requires the high accuracy testing of energy efficiency of photovoltaic devices, which is directly related to their performance and price. Measurement standards for testing the photovoltaic devices start from the calibration of reference solar cells as specified in the IEC 60904 series. The capability for the primary calibration of

reference solar cells can be useful to study the technical issues in the development of new photovoltaic materials, and has impact to the general metrology of optical detectors. Measurement uncertainty for photovoltaics proved to have a big economic impact, which motivates NMIs to draw careful attention to the calibration and testing of the reference solar cells under specified conditions maintaining the traceability to WPVS.

Measurement of spectral responsivity is of considerable importance in radiometric, photometric, and colorimetric applications where the calibration of optical detectors is a fundamental requirement. For photovoltaic detectors, such as solar cells, in particular, the spectral responsivity is directly related to the energy conversion efficiency, which is one of the most important figures of merit to specify their performances [2].

The widely used scheme for the solar cell standards is the differential spectral responsivity (DSR) technique, which measures the responsivity of a photovoltaic detector under test (DUT) to the AC modulated monochromatic light under the strong broadband DC bias light. The DSR technique has been realized in many standard laboratories as [3-5] with different approaches and similar technique used to analyze the noise in the PV detectors responsivity measurement based on DSR scheme [6].

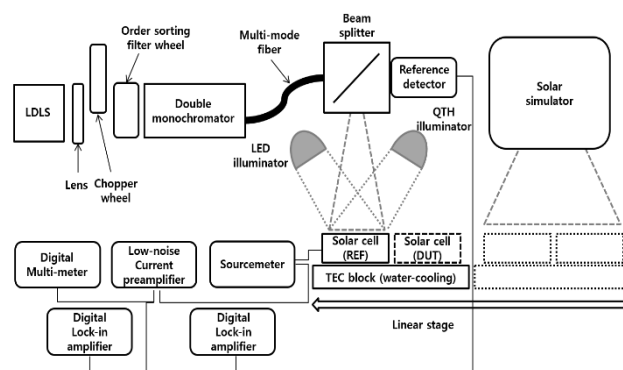


Figure 1. Schematic of the NMCC multifunction PV facility.

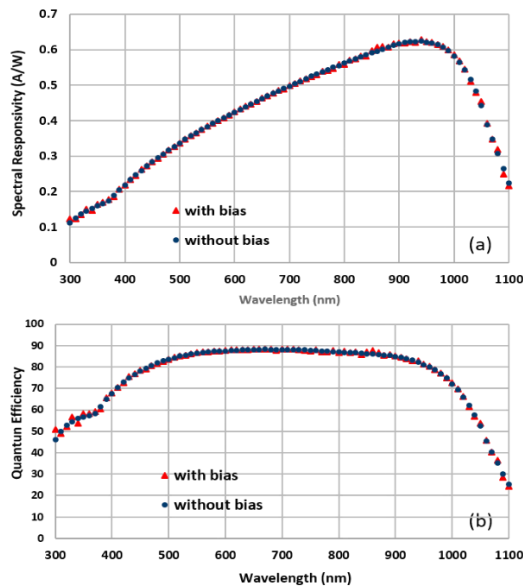


Figure 2. (a) Measurement results of spectral responsivity of reference solar cell using the LDLS-based DSR with bias (red), and without bias (blue) and (b) QE curves

INSTRUMENT

Figure 1 shows the full block diagram of our fully automated facility. Our apparatus, which is a combined multifunction system, comprises two main setups. First one for DSR measurements is based on LDLS-based modulated monochromatic source (ac) and extremely high output power LED-based illuminator + QTH based source as bias sources (dc).

Second Major setup comprises solar simulator with automation software tracing the current-voltage curves for full electrical characterization of solar cells of different sizes up to 152 mm × 152 mm, including the most critical parameters of PV cells, e.g. measurements of short-circuit current i_{sc} , open-circuit voltage V_{oc} , fill factor (FF) and energy conversion efficiency.

The new DSR setup will be used to measure the spectral responsivity in the wavelength range from 250 nm to 2000 nm, bias level up to 1.5 kW/m², modulation frequency range from 0.1 Hz to 100 Hz, with target measurement uncertainty below 1 % ($k = 2$, in the visible range) can be achieved.

Many traditional techniques been developed in standard laboratories to realize the DSR technique for spectral responsivity (SR) measurements. Traditional techniques commonly use incandescent or discharge sources with monochromator, or broadband source with spectrally selective filters (e.g. interference filters). Unfortunately, many drawbacks come with those traditional selections, e.g. low SNR, inherent

instability and noise due to the aging characteristics of the used light source. Those sources have another limitations discussed in [7]. The new facility promises major advantage over traditional one, where it provides much higher monochromatic AC radiation throughput due to the use of high radiance LDLS coupled to multimode optical fiber offering optimum focusing on the DUT at the measurement plane.

PRELIMINARY FINDINGS AND CONCLUSION

Our first results of the spectral responsivity and quantum efficiency (QE) of sample reference solar cell shown in figure 2. The measurements show good agreement between the results of two test schemes (measurement with 14 mA bias light and without bias), which shows a good linearity of the DUT up to the bias level used in this test experiment. This presents a good advantage of using LDLS-based monochromatic radiation, which is expected to ultimately improve the accuracy by introducing much higher SNR with respect to the traditional techniques. This also would allow our lab to study the linearity of the PV detectors over many decades with lower uncertainties (< 1%). Moreover, traceability of calibration can be achieved by developing primary reference standards. The instrument presented here presents other advantages, e.g. better uniformity and stability characteristics and readiness for larger sample (DUT) size which would be shown throughout our current measurements.

The facility is promising to offer potential of applications in variety of metrological, industrial and research fields.

REFERENCES

1. G.W. Crabtree and N.S. Lewis, Physics Today, March 2007 sowie Prof. Eicke Weber, ISE.
2. J. Metzdorf *et al.*, Principle and application of differential spectroradiometry, Metrologia, 28, 247 (1991).
3. IEC 60904-8:1998, Photovoltaic devices Part 8: Measurement of spectral response of a photovoltaic (PV) device, International Electrotechnical Commission.
4. G. Zaid *et al.*, Differential spectral responsivity measurement of photovoltaic detectors with a light-emitting-diode-based integrating sphere source, Applied Optics, 49, 6772 (2010).
5. B. H. Hamadani *et al.*, Versatile light-emitting-diode-based spectral response measurement system for photovoltaic device characterization, Applied Optics, 51, 4469 (2012).
6. Jae-Keun Yoo *et al.*, Noise analysis in differential measurement of detector responsivity, Proceedings of NEWRAD 2014, Espoo, Finland.
7. H. Field, "Solar cell spectral response measurement errors related to spectral band width and chopped light waveform," in Proceedings of IEEE 26th Photovoltaic Specialists Conference (IEEE, 1997), pp. 471–474.

Compact total irradiance monitor flight demonstration

Dave Harber¹, Brian Boyle¹, Zach Castleman¹, Ginger Drake¹, Samuel Van Dreser¹, Karl Heuerman¹, Marc Miller¹, Joel Rutkowski¹, Alan Sims¹, Jacob Sprunck¹, Cameron Straatsma¹, Wengang Zheng¹, Greg Kopp¹, Erik Richard¹, Peter Pilewskie^{1,2}, Nathan Tomlin³, Michelle Stephens³, Christopher Yung³, John Lehman³

¹Laboratory for Atmospheric and Space Physics (LASP), University of Colorado, Boulder, CO, USA,

²Dept. of Atmospheric and Oceanic Sciences, Boulder, CO USA,

³National Institute of Standards and Technology, Boulder, CO USA

Corresponding e-mail address: dave.harber@lasp.colorado.edu

The Compact Total Irradiance Monitor (CTIM) is a CubeSat instrument that will demonstrate next-generation technology for monitoring total solar irradiance. It includes novel silicon-substrate room temperature vertically aligned carbon nanotube (VACNT) bolometers. The CTIM, an eight-channel 6U CubeSat instrument, has a goal of uncertainty $<0.01\%$ and stability $<0.001\%/year$. The underlying technology, including the silicon substrate VACNT bolometers, has been demonstrated and tested in relevant environments in an engineering model of the detector subsystem. We are currently building and testing the flight detector unit and will integrate it with a 6U CubeSat in mid-2020, in preparation for an on-orbit demonstration in 2021.

INTRODUCTION

Long-term measurements of total solar irradiance (TSI) have been performed from space by a 40-year uninterrupted sequence of instruments [1-5]. In order to maintain this long-term TSI record, space-based TSI measurements need to occur indefinitely; thus, it is advantageous to use modern technological advances to develop miniaturized TSI instruments for integration in future CubeSat and SmallSat platforms, making deployment of these sensors into space significantly easier.

The Compact Total Irradiance Monitor (CTIM) is a 6U CubeSat TSI instrument consisting of

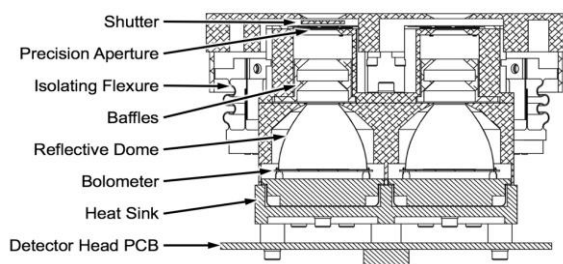


Figure 1: Cross-section of the CTIM detector head showing the optical design and key components.

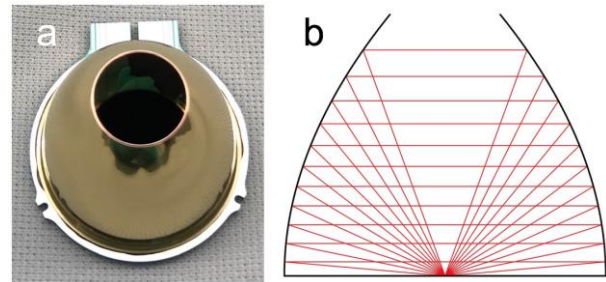


Figure 2: (a) The silicon detector with reflector dome attached. (b) Ray trace of the reflector dome showing that after two bounces off the reflector light scattered by the VACNTs is redirected back.

two four-channel detector heads, each channel being a radiometer which utilizes vertically-aligned carbon nanotube (VACNT) optical absorbers on silicon substrates.

INSTRUMENT DESIGN

The design of the CTIM instrument [6] follows the fundamental design of the SORCE TIM instrument [5]. The first optic solar illumination encounters is a precision 5mm diameter ion-etched silicon aperture, see figure 1. Following a short baffle section, the solar illumination then enters the detector cavity. For CTIM we are using a novel design that incorporates a planar silicon detector with a thermally integrated reflector, see figure 2.

Four of these detectors are integrated onto one detector head, and the CTIM CubeSat has two detector heads for a total of eight channels. Each channel includes a bi-stable shutter to modulate the incoming light with a period of 60-100s. The measurement uncertainty of the CTIM is detailed in Table 1.

Table 1: TSI measurement uncertainty.

Correction	Value	Uncertainty
Aperture Area	100%	0.0022%
Diffraction Loss	0.042%	0.0042%
Detector Reflectance	0.010%	0.0020%
Heater Voltage	100%	0.0014%
Heater Resistance	100%	0.0028%
Heater Linearity	0.050%	0.0028%
Optical/Electrical Non-Equivalence	0.005%	0.0050%
Dark Signal	1.222%	0.0050%
<i>Total</i>		<i>0.0097%</i>

The CTIM design also includes a number of further technology demonstration elements, such as in-situ heater resistance monitoring and wireless detection of the shutter temperature via a miniature thermopile.

CTIM MISSION

The two flight CTIM detector heads are currently being fabricated. Once assembled, the detector heads will undergo end-to-end radiometric testing in the TSI radiometer facility to validate their measurement scale against a SI-traceable detector [7]. These two heads, and the associated electronics, will be integrated in a 6U CubeSat (~120x240x360 mm). Following flight qualification testing, the CTIM CubeSat will be delivered for a launch in 2021 with a mission lasting at least one year. The key mission goals include comparisons of the relative measurements of the eight channels with respect to each other and to the Total and Spectral Solar Irradiance Sensor Total Irradiance Monitor (TSIS-1 TIM) currently in operation on the International Space Station, allowing assessment of accuracy of CTIM relative to the 0.01% goal, and monitoring the measurement noise and long-term measurement stability of CTIM relative also to TSIS-1 TIM to assess performance relative to the stability goal of 0.001%/year.

REFERENCES

1. Lee, R. B. III, Gibson M. A., Wilson R. S., and Thomas S., "Long-term total solar irradiance variability during sunspot cycle 22", J. Geophys. Res., 100, 1667–1675 (1995).
2. Fröhlich, C. and Lean J., "Solar radiative output and its variability: Evidence and Mechanisms", Astron. Astrophys. Rev., 12(4), 273–320 (2004).
3. Fröhlich, C. "Evidence of a long-term trend in total solar irradiance", Astron. Astrophys., 501, L27–L30 (2009).
4. Willson, R. C. and Mordvinov A. V., "Secular total solar irradiance trend during solar cycles 21–23", Geophys. Res. Lett., 30(5), 1199, (2003).
5. Kopp, G. and Lawrence G., "The Total Irradiance Monitor (TIM): Instrument design", Sol. Phys., 230, 1–2 (2005).
6. Harber D., et al. "Compact total irradiance monitor flight demonstration," Proc. SPIE 11131, CubeSats and SmallSats for Remote Sensing III, 111310D (x2019).
7. Kopp, G., Heuerman, K., Harber, D., and Drake, V., "The TSI Radiometer Facility - Absolute Calibrations for Total Solar Irradiance Instruments", SPIE Proc. 6677-09, (2007).

Spectroradiometric Calibration of Bright Stars, Vega and Sirius

John T. Woodward¹, Steven W. Brown¹, Stephen E. Maxwell¹, and Susana Deustua²

¹National Institute of Standards and Technology, Gaithersburg, MD, USA,

²Space Telescope Science Institute, Baltimore, MD, USA

Corresponding e-mail address: john.woodward@nist.gov

We discuss our ground-based approach to making sub 1% spectroradiometric measurements of the top-of-the atmosphere flux from bright stars. We will present results from measurements of Vega and Sirius made from Mount Hopkins, AZ. We present our calibration strategy and discuss the challenges of making high quality radiometric measurements outside of a controlled laboratory environment. We describe the characterization and calibration of our spectrographs that are required for high-accuracy measurements and the development of an uncertainty budget.

INTRODUCTION

The earliest and most widely cited measurements of stellar spectral flux were made on Vega (α -Lyr) by Hayes, Latham, and Hayes at Mt. Hopkins in southern Arizona in the 1970's [1]. Although the details of our calibration differ, the basic strategy is very similar to that used for these measurements.

There are two main parts to our calibration strategy for making top-of-the-atmosphere measurements using a ground-based telescope. The first is to calibrate the telescope+spectrograph by observing a calibration source of known spectral flux located on the ground. This source is calibrated in the field with a reference spectrograph. This allows us to put an absolute spectral responsivity scale on our telescope+spectrograph system. The second is to use that telescope to observe the astronomical target at a variety of air masses as it transits the sky. This allows the use of a Langley analysis which exploits the Beers-Lambert-Bouger Law to calculate the spectral atmospheric extinction and correct ground-based measurements to top-of-the-atmosphere spectral flux.

CALIBRATION

The calibration source is a 50 mm diameter, lamp-illuminated integrating sphere. To calibrate the sphere in the field we use a reference spectrograph with an irradiance head. This in turn is calibrated to an SI-traceable FEL lamp in the lab before and after deployment to the field [2]. Figure 1 shows the

calibration reproducibility over multiple field deployments. In addition, the spectrograph response linearity was characterized using a beam conjoiner system, and a thermal chamber was used to measure effect of temperature on the wavelength solution and responsivity. Stray light response was measured using the NIST Spectral Irradiance and Radiance Calibration using Uniform Sources (SIRCUS) tuneable lasers and Zong stray light correction algorithm [3,4].

OBSERVATION

The observing instrument is a 107 mm refracting telescope, shown in Figure 2, mounted on a computerized German equatorial mount, with an optical fibre at the focus leading to the spectrograph. Prior to the optical fibre, an optical cross with a 90/10 beamsplitting cube allows 90% of the light to be focused directly into the fibre while the other 10% goes to a guide camera that keeps the star centred on the fibre. A camera looking at the reflected light from the fibre tip and beamsplitter is used for the initial centring of the star on the fibre.

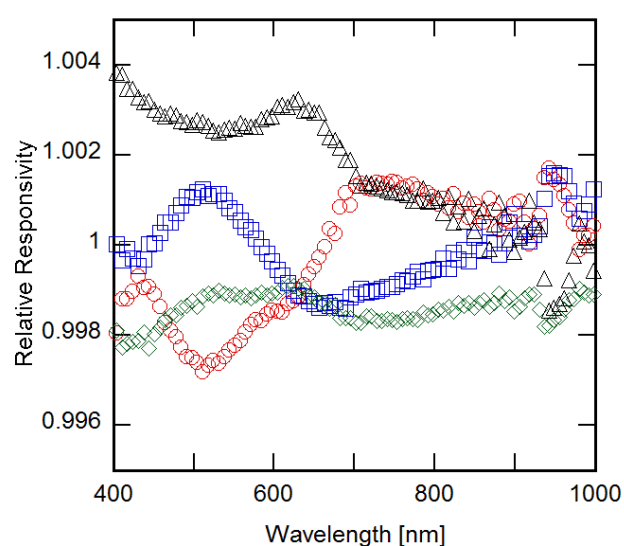


Figure 1. Relative responsivity of calibration spectrometer over multiple deployments. Nov 2012 (blue squares), Jan 2013 (red circles), July 2013 green diamond, and June 2014 (black triangles).



Figure 2 The stellar observation telescope on its mount. On the right side are the red cameras for aligning and guiding on the target star and the orange optical fibre.

The telescope tracks the target as it transits the sky and records spectra once per minute. The autoguiding camera keeps the target centred on the same place on the fibre. The calibration source is located approximately 100 m from the observing telescope and the irradiance is measured by the reference spectrograph placed 0.5 m from the source. The measurement telescope observes the source either immediately before or after making stellar measurements. The inverse square law is used to transfer the reference spectrograph calibration to the telescope with a small correction for the atmospheric extinction along the path from the source to the telescope. We have tested this calibration scheme by verifying the inverse square law in our Telescope Calibration Facility [5].

ANALYSIS

We use a Langley extrapolation to correct our ground based measurements to top-of-the-atmosphere stellar

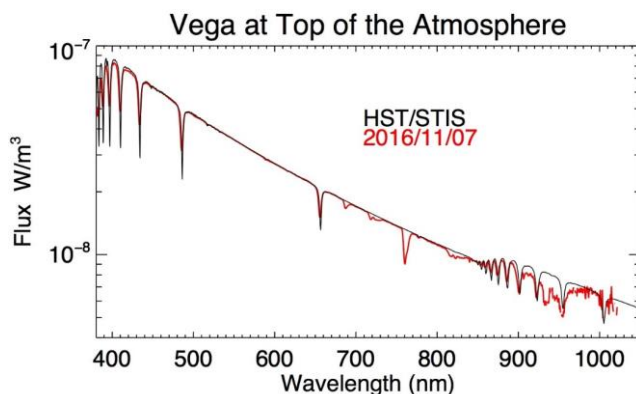


Figure 3 Comparison of the Vega spectral irradiance measured at Mt. Hopkins on Nov. 7, 2016 compared to the HST.

flux. Observations at different zenith angles go through an amount of atmosphere or airmass proportional to the secant of the angle. If the optical properties of the atmosphere stay constant over the course of the observations a valid extrapolation is possible. Even at a mountain top observatory, relatively few nights yield a stable atmosphere, but those that do yield reproducible spectral flux. In Figure 3, we show a comparison to one such night to the model spectrum of Vega in the Hubble Space Telescope CALSPEC data base [6]. This atmosphere model of Vega is a Kurucz at $T_{\text{eff}}=9550$ K [7].

CONCLUSIONS

We are able to transfer an SI traceable irradiance scale in the field using a well characterized spectrograph. This enables SI traceable, top-of-the-atmosphere spectral flux measurements of bright stars, Vega and Sirius.

REFERENCES

1. D.S. Hayes et al., Measurements of the Monochromatic Flux From Vega in the Near-Infrared, *Astrophysical Journal*, 197, 587-592, 1975.
2. H.W. Yoon et al., FASCAL 2: a New NIST Facility for the Calibration of the Spectral Irradiance of Sources, *Metrologia*, 40, S30-S34, 2003.
3. Y.Q. Zong et al., Simple Spectral Stray Light Correction Method for Array Spectroradiometers, *Applied Optics*, 45, 1111, 2006.
4. S.W. Brown et al., Facility for Spectral Irradiance and Radiance Responsivity Calibrations Using Uniform Sources (SIRCUS), *Applied Optics*, 45, 8218-8237, 2006.
5. A.W. Smith et al., Absolute Flux Calibration of Stars: Calibration of the Reference Telescope, *Metrologia*, 46, S219-S223, 2009.
6. Bohlin, R.C. et al., Techniques and Review of Absolute Flux Calibration from the Ultraviolet to the Mid-Infrared, *PASP*, 126, 711, 2014.
7. Bohlin, Hubble Space Telescope CALSPEC Flux Standards: Sirius (and Vega), *Astronomical Journal*, 147, 127, 2014.

JTSIM-DARA Pointing Measurements

Gregor Hülsen¹, Daniel Pfiffner¹, Manfred Gyo¹, and Julian Gröbner¹

¹Physikalisch-Meteorologisches Observatorium Davos, World Radiation Center (PMOD/WRC), Davos, Switzerland

Corresponding e-mail address: gregor.huelssen@pmodwrc.ch

The pointing of the JTSIM-DARA radiometer was measured four times during its construction in the optic laboratory of PMOD/WRC. The final offset of the pointing before shipping relative to the optical axis, defined by a removable alignment cube, is $1.07^\circ/0.67^\circ$ (β/γ -axis) for the four-quadrant sensor and $0.095^\circ/-0.017^\circ$ for the radiometer cavity A.

JTSIM-DARA

Continuous and precise TSI measurements are indispensable to evaluate the influence of short and long-term solar radiative emission variations on the Earth's climate. PMOD/WRC has constructed the JTSIM-DARA (DARA for the Joint Total Solar Irradiance Monitor) absolute radiometer for the Chinese FY-3E mission. JTSIM-DARA is one of PMOD/WRC's contributions to the almost seamless series of spaceborne TSI measurements since 1978. It will be mounted on the FY-3E satellite, which is the 5th flight unit of the Fengyun-3 (FY-3) series. Key aspects of the FY-3 satellite series include collecting atmospheric data for intermediate and long-term weather forecasting and global climate research.



Figure 1. The JTSIM-DARA is composed of a sensor case with 3 radiometer cavities (right) and the control unit.

The JTSIM-DARA instrument (Fig. 1) is a cooperation with CIOMP (Changchun Institute of Optics, Fine Mechanics and Physics of the Chinese Academy of Sciences), and the China Meteorological Administration (CMA). Next to the JTSIM-DARA a solar irradiance absolute radiometer (SIAR) radiometer was designed by CIOMP. The JTSIM-DARA design is based on the Digital Absolute Radiometer (DARA/PROBA-3) and the Compact

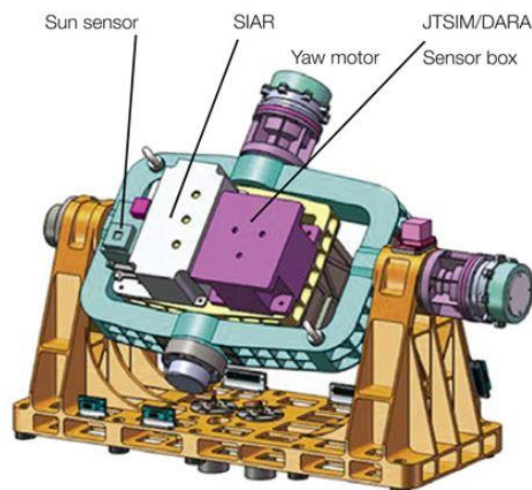


Figure 2. FY-3 sun tracker with the JTSIM radiometers.

Lightweight Absolute Radiometer (CLARA/NorSat-1) instruments.

The two JTSIM radiometers are mounted on the sun tracker (Fig. 2) of the satellite enabling independent pointing toward the sun whereas the other instruments point toward the earth. As two devices are mounted on the sun tracker, the pointing of JTSIM-DARA is a critical parameter of the mission. The instrument is currently integrated into the Chinese FY-3E weather satellite and is made ready for launch in 2020 [1].

MEASUREMENTS

Measurements of the pointing of the three JTSIM-DARA cavities relative to each other were performed on the WSG sun tracker. The pointing relative to a cube alignment mirror was measured at the angular response facility in the optic laboratory of the WRC. This setup (Fig. 3) consists of a 1 kW Xe-Lamp



Figure 3. The angular response setup showing the Xe-Lamp in the back, a WG305 filter and a baffle in the middle and the JTSIM-DARA mounted on the goniometer.

emitting a collimated light beam towards the test device which is mounted on a goniometer about 3 m away from the light source [2]. The variability of the light intensity of a 50 mm³ cube around the optical axis was characterized prior to the measurements. The homogeneity within this entire cube is 3% and

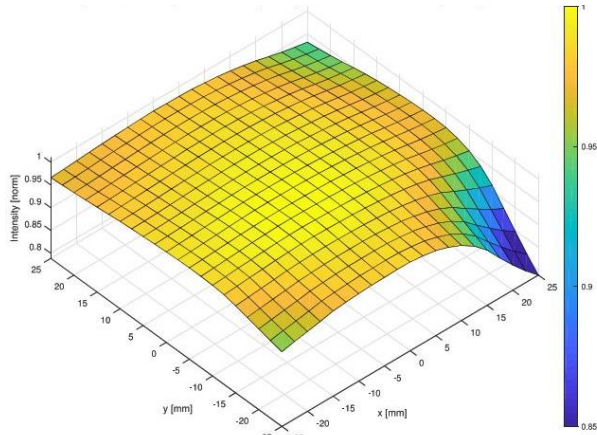


Figure 4. Homogeneity of the light intensity in the plane of rotation.

inside a 10 mm³ below 0.5 % (Fig. 4).

Figure 5 shows the alignment relative to the optical axis using a laser. First JTSIM-DARA was orientated using the removable alignment cube. Thereafter one selected cavity and the four-quadrant sensor (4Q) was moved into the centre. The measurements were performed by rotation around the β -axis of JTSIM-DARA and after a 90° rotation of the device around the γ -axis. The experiment was repeated four times: Before the end assembly (1), before (2) and after (3) the vibration tests and before shipping (4).

RESULTS

Figure 6 and 7 shows results of the pointing measurements of the 4Q and the cavity A. Table 1 the results of the 4 measurements as numbered above.

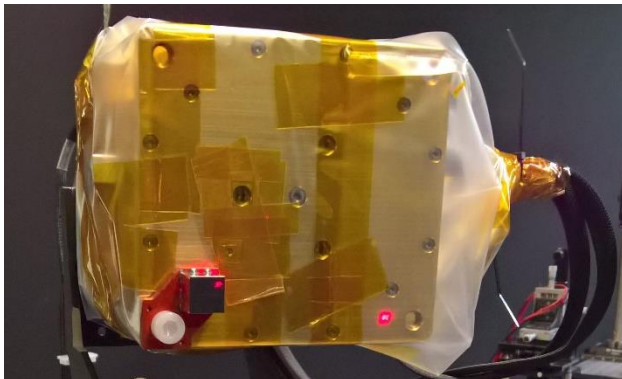


Figure 5. Pointing measurement of the JTSIM-DARA showing the alignment cube in the lower left corner, the 3 holes of the radiometer cavities in the centre and the four-quadrant sensor next to the cube.

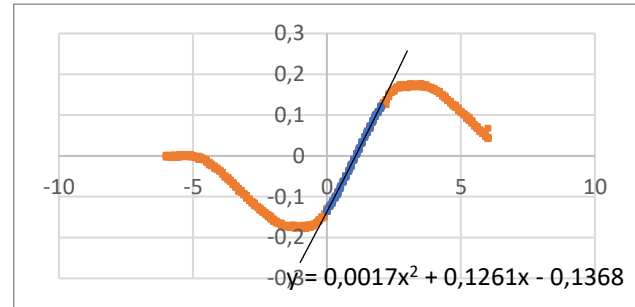


Figure 6. Pointing of the 4Q sensor around the β -axis. Plotted is the 4Q signal vs. the angle of rotation.

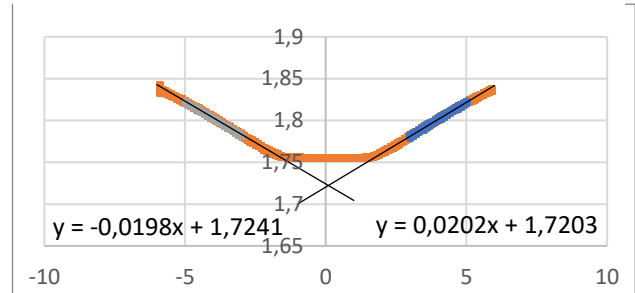


Figure 7. Pointing of the cavity A around the β -axis. Plotted is the intensity of the sensor vs. the angle of rotation.

The assembling has a major influence on the optical axis of the sun sensor and the cavity. The β -angle measurements changed after the vibration test. All other measurements are consistent within the estimated uncertainty of $\pm 0.1^\circ$. The vibration test didn't show any shift on the optical axis defined by the alignment cube.

Table 1. Summary of the offsets for the 4 pointing tests as defined in the text.

Test	β -4Q	β -Cavity A	γ -4Q	γ -Cavity A
1	0.91°	-0.45°	0.76°	0.16°
2	0.98°	0.025°	0.62°	-0.026°
3	0.71°	0.25°	0.67°	-0.00°
4	1.07°	0.095°	0.67°	-0.017°

OUTLOOK

The setup used for the pointing measurements is limited to about 20 Nm load on the goniometer. A new mechanic was constructed to enable loads up to 200 Nm.

REFERENCES

1. http://www.nsmc.org.cn/en/NSMC/Channels/FY_3E.html
2. G. Hülsen et al., Characterization and calibration of ultraviolet broadband radiometers measuring erythemally weighted irradiance, Appl. Optics, 46, 5877- 5886, 2007.

Polarization effects in diffuse reflection measurements at the transition between the UVA and VIS spectral range

Tatjana Quast¹, Irina Santourian¹, Kai-Olaf Hauer¹, and Alfred Schirmacher¹

¹Physikalisch-Technische Bundesanstalt, Braunschweig and Berlin, Germany

Corresponding e-mail address: Tatjana.Quast@ptb.de

Polarization effects play an important role in diffuse reflection measurements. Even for matte, quasi-Lambertian reflection samples, a large degree of polarization can be induced by reflection in certain bidirectional geometries. To study this effect, the Stokes parameters of the reflected light have been determined for several samples at the transition between the visible (VIS) and ultraviolet (UVA) spectral range. As radiation source, a newly designed LED-based sphere radiator has been characterized and applied.

EXPERIMENTAL SETUP

In diffuse reflectance measurements, the main quantity of interest is the spectral radiance factor $\beta(\lambda)$. The gonireflectometer at the Physikalisch Technische Bundesanstalt is a measurement facility dedicated to the determination of β in bidirectional geometries. The sample under test is mounted on a five-axis robot arm. It is illuminated by a broadband light source which can be swivelled around the sample on a large rotation stage. A fixed detection path collects the reflected light. This combination facilitates the determination of β in almost any arbitrary bidirectional geometry [1].

To determine the Stokes parameters of the reflected light and thus its polarization state, a special polarization-analyzer unit is placed in the detection path. It consists of a quarter-wave plate which can be rotated, and a linear polarizer with a fixed transmission axis. Taking measurements at different orientations of the wave plate allows one to calculate the Stokes parameters [2].

As a light source in the VIS and near-infrared spectral range, a sphere radiator with a quartz-tungsten halogen lamp is used. This is an easy-to-operate and reliable light source which produces a spatially homogeneous, unpolarized irradiation. However, it has the limitation that the irradiance and stability quickly decrease towards UVA, where also various materials exhibit higher absorption.

Thus, we developed a new sphere radiator, which uses light-emitting diodes (LEDs) as radiation source, covering wavelengths from about 365 nm to

440 nm. It generates a much higher irradiance compared with the halogen source and considerably improves the signal quality and stability at short wavelengths [3].

POLARIZATION EFFECTS

In reflectometry the control of polarization is essential since almost every reflectometer contains polarization-sensitive components like diffraction gratings. Previous studies have shown that the degree of polarization caused by reflection can be very large even for frequently used matte, quasi-Lambertian samples, depending on the wavelength and geometry [2,4]. All these studies have been performed at wavelengths above 450 nm because the signal-to-noise ratio was too low at shorter wavelengths if the halogen source was used. This obstacle can be overcome if the LED-based sphere radiator is utilized. Measurements of the LED-based sphere radiator which show its unpolarized emission will be presented. Different types of reflection samples were studied and their polarization properties were determined. Exemplary results will be discussed, highlighting the influence of bidirectional geometry and wavelength.

REFERENCES

1. D. Hünerhoff et al, New robot-based gonireflectometer for measuring spectral diffuse reflection, *Metrologia*, 43(2), 2006.
2. T. Quast et al, Polarization properties and microfacet-based modelling of white, grey and coloured matte diffuse reflection standards, *Journal of Physics: Conference Series*, 972(1), 2018.
3. I. Santourian, S. Teichert, K.-O. Hauer, A. Schirmacher, Investigation of the suitability of high-power LEDs for the use as radiation source for PTB's gonireflectometer, *TU Ilmenau, Lux junior 2019*, pp. 43-50, 2019.
4. A. Koo et al, Polarization dependence of bidirectional reflectance from ceramic tiles, *Proceedings of the 13th International Conference on New Developments and Applications in Optical Radiometry*, 2017.

Recommendation for finite intervals in BRDF measurements of glossy samples

Alejandro Ferrero¹, Ana M. Rabal², Joaquín Campos¹, Guillaume Ged², Gaël Obein²

¹*Instituto de Óptica “Daza de Valdés”, Consejo Superior de Investigaciones Científicas, Madrid, Spain;* ²*Conservatoire National des Arts et Métiers, Paris, France*
Corresponding e-mail address: alejandro.ferrero@csic.es

Recommendations on the finite intervals of irradiation and collection solid angles for measuring the bidirectional reflectance distribution function (BRDF) of highly glossy samples, close to their specular direction, are derived from high angular resolution measures. These measures were done with the conoscopic system at the *Conservatoire National des Arts et Métiers*, CNAM, specially designed for measuring gloss. An equation was derived from the data to estimate the systematic relative error due to finite intervals, and it is presented here.

INTRODUCTION

The BRDF of glossy samples has a very high and narrow peak around the specular direction; therefore, a very high angular resolution is required for its measurement, being this resolution determined by the measuring irradiation and collection solid angles. These solid angles are not infinitesimal because finite geometrical intervals cannot be avoided in the measuring systems. The conoscopic system to measure BRDF at the *Conservatoire National des Arts et Métiers*, CNAM [1, 2] allows small solid angles, and, in consequence, angular resolutions high enough for an adequate angular sampling of highly glossy surfaces, with a negligible impact of the finite intervals on the BRDF measurement. From these measures it is possible to estimate by numerical integration the impact of using larger finite intervals on a given sample. This method has been used in this work to propose recommendations on finite intervals (solid angles) to avoid systematic errors in BRDF measurements of samples of different gloss categories.

EXPERIMENTAL DATA

High-angular-resolution BRDF measurements of four samples belonging to four different gloss categories were carried out in CNAM. The name, the FWHM and the visual gloss of each sample are given in Table 1.

Table 1. Samples studied in this work.

Sample name	FWHM	Visual gloss
NCS4	7.91°	30
NCS5	3.70°	50
NCS6	2.59°	75
NCS7	0.84°	95

The measurements are represented in Figure 1. The angular resolution is 0.004°, except for NCS7, which is 0.015°.

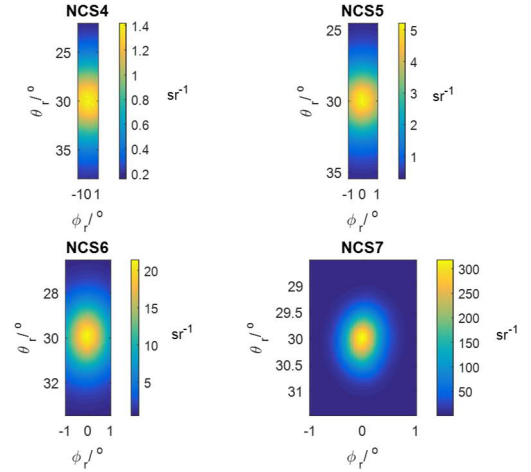


Figure 1. BRDF measurements of the four studied glossy samples around the specular direction. The false colour represents the value of the BRDF at each measurement geometry (see colour bar on the right side).

RESULTS AND DISCUSSION

The BRDF measurements were angularly integrated along a given interval to study the effect of reducing the angular resolution. This effect is equivalent to increase the illumination or collection solid angles widths. Solid angles with full-angle widths (κ) of 0.031°, 0.12°, 0.28°, 0.5°, 0.78°, 1.1°, 1.5°, 2° and 2.5° were selected.

The systematic error of the calculated BRDF by enlarging the solid angle width at the former values, are estimated by comparing them to those measured in the conoscopic system. The relevant angular variable to assess the variation of the BRDF of glossy samples is the aspecular angle (θ_{asp}). The

lower it is, the most relevant is this variable, but its relevancy depends on the FWHM of the sample too. That is why, in a first approach to obtain a general equation for the systematic error, the BRDF was expressed as a function of a normalized angular variable, expressed as $\theta_N = \theta_{asp} / \text{FWHM}$ (Figure 2).

It is observed that the main BRDF change due to the specular peak is found between values of θ_N from 0 to 0.7 for all samples, unlike data in Figure 1, where the variation of BRDF occurs over a different interval of the angular variable for each type of sample.

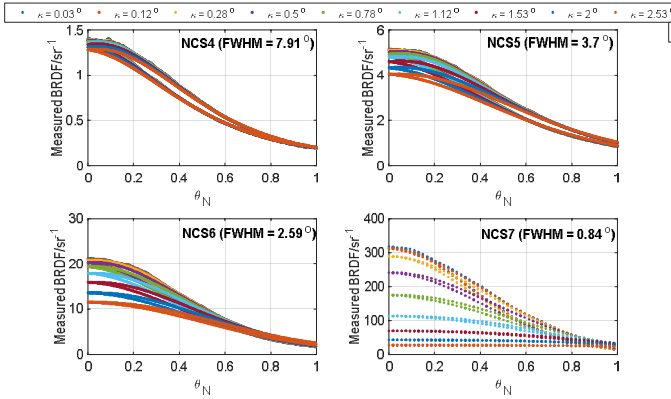


Figure 2. Calculated BRDF values for different solid angle widths, at $\phi_r = 0^\circ$, as a function of the proposed normalized angular variable $\theta_N = \theta_{asp} / \text{FWHM}$. Each plot corresponds to a different sample.

The proposed normalized angular variable θ_N allows the relative angular distribution of relative errors to be normalized. However, the absolute values of these errors are still depending on κ and FWHM. A phenomenological equation can be fitted to estimate the systematic relative as a function of κ , FWHM and θ_N . The relative error positively depends on κ and negatively on FWHM. If this relative error is multiplied by $\kappa^{c2}/\text{FWHM}^{c1}$, with $c1 = c2 = 1.3$, the result of this factor is much more independent of κ and FWHM, as seen in Figure 3.

From this analysis was possible to obtain the following equation to estimate the systematic relative error due to finite intervals:

$$\varepsilon_r = \left(\frac{\kappa}{\text{FWHM}} \right)^{1.3} \times (0.34 - 0.37 \times \theta_N) \quad (1)$$

This equation is only valid from $\theta_N = 0$ to $\theta_N = 0.7$.

CONCLUSIONS

High-angular-resolution BRDF measurements carried out at CNAM were assumed as true values to

numerically evaluate the impact on the measurement in the case of using measuring systems with a lower angular resolution, limited by the illumination or collection solid angles. The analysis has allowed to obtain an equation that estimates the BRDF relative systematic error that would be made when measuring samples of a certain FWHM, with a given angular resolution, and at a specific aspect angle. This should allow for recommendations to be given on solid angle widths for the measurement of the BRDF of glossy samples under different geometrical conditions.

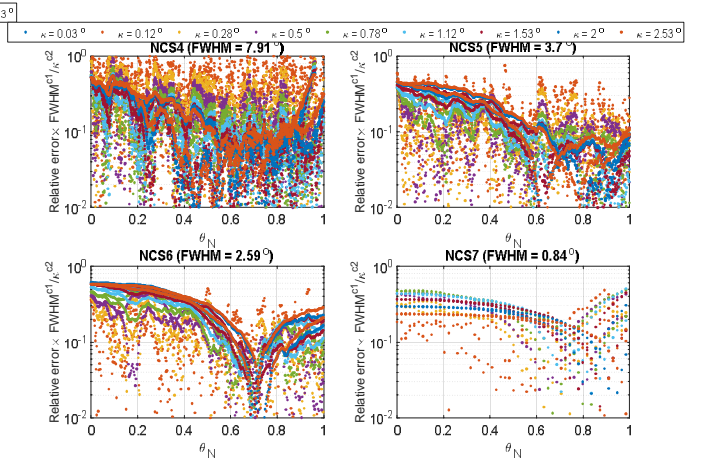


Figure 3. Relative error multiplied by $\text{FWHM}^{c1}/\kappa^{c2}$, with $c1 = 1.2$ and $c2 = 1.425$. The result of this factor is much more independent of κ and FWHM than the relative error.

ACKNOWLEDGMENTS

This work was done within the EMPIR 16NRM08 Project “Bidirectional reflectance definitions” (BiRD). The EMPIR is jointly funded by the EMPIR participating countries within EURAMET and the European Union. Part of the authors (Instituto de Óptica “Daza de Valdés”) are also grateful to Comunidad de Madrid for funding the project S2018/NMT-4326-SINFOTON2-C.

REFERENCES

1. S. Ouarets, T. Leroux, B. Rougie, A. Razet, G. Obein, A high resolution set up devoted to the measurement of the Bidirectional Reflectance Distribution Function around the specular peak, at LNE-CNAM, Proceedings of Metrologie, 2013.
2. G. Obein, S. Ouarets, G. Ged, Evaluation of the shape of the specular peak for high glossy surfaces, in: IS&T/SPIE Electronic Imaging. International Society for Optics and Photonics, pp. 901805–901805, 2014.

A facility for measuring the BSSRDF

Pablo Santafé, Alejandro Ferrero*, Néstor Tejedor, José Luis Velázquez, Joaquín Campos

Instituto de Óptica “Daza de Valdés”, Consejo Superior de Investigaciones Científicas (CSIC), Madrid, Spain

Corresponding e-mail address: alejandro.ferrero@csic.es

This work presents a facility for measuring the Bidirectional Scattering-Surface Reflectance Distribution Function (BSSRDF), a function that describes the scattering in translucent materials. This facility targets an expanded uncertainty of 5 %. As a preliminary result, the half-angle of the collection solid angle was found to be the limiting uncertainty source.

INTRODUCTION

The reflectance of a translucent material cannot be explained only by the reflection at its surface but also by the scattering of the light inside its volume, which makes part of this light to emerge from other non-irradiated positions on the surface. To characterize the reflectance of translucent materials, a distribution function has been proposed that relates the incident radiant flux at a given point on the surface with the radiance at another point. This function, known as BSSRDF, is defined as¹:

$$\text{BSSRDF}(\mathbf{x}_i, \mathbf{r}_i; \mathbf{x}_r, \mathbf{r}_r) = \frac{dL_r(\mathbf{x}_r; \mathbf{r}_r)}{d\Phi_i(\mathbf{x}_i; \mathbf{r}_i)} \quad (1)$$

Fig. 1 shows a schematic representation of the geometrical variables involved in these measurements. The two cones represent incidence (subscript ‘i’) and collection (‘r’) solid angles, respectively.

The BSSRDF, although formally defined, has not been measured with metrological quality to date, and its definition as measurand must be established. As no primary equipment is available for measuring it, no reference exists for the measurement of subsurface scattering or translucency. This work aims to develop a facility for measuring the BSSRDF with expanded uncertainties under 5 %.

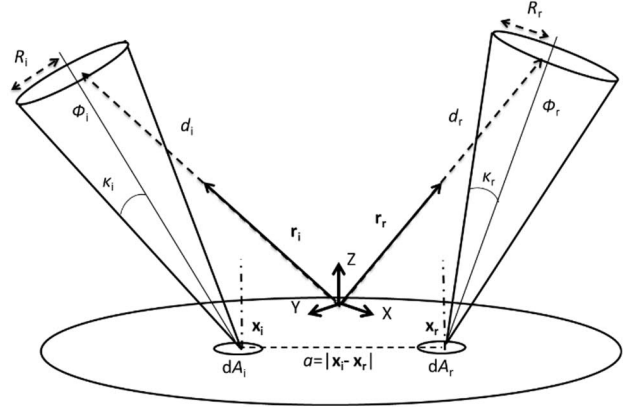


Figure 1. Definition of the geometrical variables involved in the measurement of the BSSRDF.

EXPERIMENTAL SETUP

A BSSRDF measuring system has been developed at CSIC, based on the Spanish goniospectrophotometer (GEFE)². A photograph of the complete experimental device is shown in Fig. 2. The lighting system is located on the right side, which includes a Köhler system, allowing a uniform and directional irradiating spot on the sample, whose size can be modified by a diaphragm placed in front of the first Köhler’s lens. A 1-mm diameter spot on the sample surface was selected for BSSRDF measurements. A 6-axis robotic arm (left) is used to position the sample at any orientation. Finally, the detector is located on a platform which can be moved around the sample on a circular ring. These degrees of freedom are enough to realize almost any incidence and collection bidirectional geometry. For providing spatial resolution, a CCD camera is used as detector, with an objective lens Navitar Zoom 7000 (18:180 mm). This detection system allows spatial resolution of 45 μm on the sample surface.

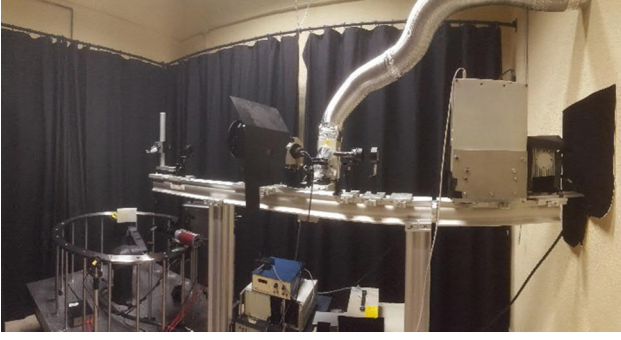


Figure 2. Gonio-spectrophotometer adapted for measuring the BSSRDF.

A measurement equation is derived from Eq. (1):

$$f_{ssr,k} = \frac{1}{A_{fov}\pi \sin^2 \kappa_r \cos \theta_r} \left(\frac{N_{k,r}}{\sum N_{k,i}} \right) \left(\frac{T_i \eta_{e,i}}{T_r \eta_{e,r}} \right) \left(\frac{t_{exp,i}}{t_{exp,r}} \right) \quad (2)$$

where:

$f_{ssr,k}$: BSSRDF at the position of k^{th} pixel of the camera.

N_k : Response of the k^{th} pixel.

A_{fov} : Field of view area of one pixel.

T : Objective lens transmittance.

η_e : External quantum efficiency of the pixel.

t_{exp} : Exposure time.

θ_r : Angle of the collection direction respect to the normal of the sample.

κ_r : Half-angle of the collection solid angle (Fig. 1).

The ratio $T_i \eta_{e,i} / T_r \eta_{e,r}$ represents the ratio of camera responsivities in two different conditions: directional illumination (without sample) and diffuse illumination (with sample out of specular conditions). An experimental procedure for measuring κ_r and the ratio $T_i \eta_{e,i} / T_r \eta_{e,r}$ was developed. This procedure is based on locating a mirror on the sample position and moving it relatively to the camera objective at the measuring conditions, so that the relative responsivity of the camera is obtained for different incidence directions.

Also camera linearity and camera noise were assessed to estimate the BSSRDF uncertainty. The nonlinearity is important when incidence and collected radiant fluxes are evaluated with very different integration times. Specifically, the use of very low integration times should be avoided because smear is produced, the main cause of nonlinearity. So far, the uncertainty of κ_r is the limiting uncertainty source of the BSSRDF

measurement, with an expanded uncertainty of about 5 %.

The detailed uncertainty budget and BSSRDF measurements of specially selected translucent samples will be shown during the conference. These measurements are obtained from images as those shown in Fig. 3, acquired with the presented facility.

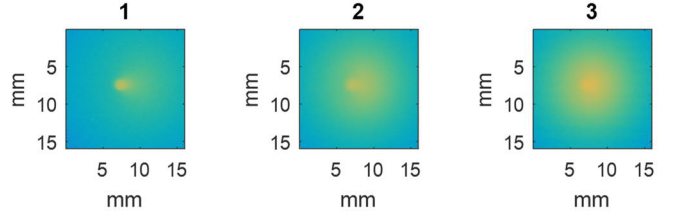


Figure 3. Images of three translucent surfaces irradiated by a 1-mm diameter spot centred on the image. The concentration of scattering particles increases from sample 1 to sample 3.

CONCLUSIONS

A gonio-spectrophotometer was adapted to build a primary facility for measuring the BSSRDF with a target expanded uncertainty of 5 %. Procedures are under development for measuring those variables required to obtain the BSSRDF. So far, the half-angle of the collection solid angle is the limiting uncertainty source.

ACKNOWLEDGMENTS

This work was done within the EMPIR 18SIB03 project “New quantities for the measurement of appearance” (BxDiff) and the project PGC2018-096470-B-I00 BISCAT (MCIU/AEI/FEDER,UE). The EMPIR is jointly funded by the EMPIR participating countries within EURAMET and the European Union. We are grateful to Covestro Deutschland AG for providing with translucent samples.

REFERENCES

1. F. E. Nicodemus et al. Geometrical Considerations and Nomenclature for Reflectance, 1st edition, National Bureau of Standards Department of Commerce, Washington, D.C., 1977.
2. A. M. Rabal et al, Automatic gonio-spectrophotometer for de absolute measurement of the spectral BRDF at in- and out-of-plane and retroreflection geometries, Metrologia, 49, 213-223, 2012.

Improving multiphoton spectroscopy standards through the creation of an accurate, high-throughput spectrometer facility

Charles Stark¹, Meelis Mait-Sildoja¹, Matt Rammo¹, Juri Pahapill¹, Katrin Petritsenko¹, and Aleksander Rebane¹⁻²

¹National Institute of Chemical Physics and Biophysics, Tallinn, Estonia, ²Montana State University, Bozeman, USA.
Corresponding e-mail address: CharStark@gmail.com

We describe a high-throughput, high reproducibility setup for the measurement of femtosecond instantaneous degenerate two-photon absorption cross sections in a broad range of visible to near-IR excitation wavelengths. Preliminary results on some common fluorescent dyes such as Rhodamine 6G are presented and analysed in comparison to previously published data. We also introduce a newly created online 2PA spectra database.

INTRODUCTION

Two-photon absorption (2PA), wherein electronic transitions are activated by the simultaneous absorption of two photons,¹ is a topic of growing interest in optics, with applications ranging from optical power limiting,¹ microfabrication,¹ microscopy and phototherapy,¹ to nanothermometry² and molecular probes of electric fields.³ As a second order process by nature, the probability of 2PA shows quadratic dependence on the excitation power, characterized by chromophore's intrinsic two-photon cross section (σ_{2PA}), which is analogous to the one-photon absorption cross section, but is expressed in the units, $\text{cm}^4 \text{ s photon}^{-1}$. Applications can thus be optimized by knowledge of potentially large 2PA cross sections at specific excitation wavelengths; however, determining σ_{2PA} spectra with sufficient reliability and accuracy has been a difficult task, especially due to the need of characterizing the instantaneous photon flux of the excitation.

As an illustrative example, Figure 1 displays the 2PA spectrum of the laser dye Rhodamine 6G, which has been measured numerous times by several groups,⁴⁻⁹ but with limited reproducibility between measurements. The issues of reproducibility stem from variations between 2PA measurement methods⁹ and a lack of standardization of 2PA equipment, which are generally independently assembled. In addition to this, many 2PA measurements are performed at few wavelengths, due to time or capability constraints of the instrumentation, making comparisons difficult. The several techniques for

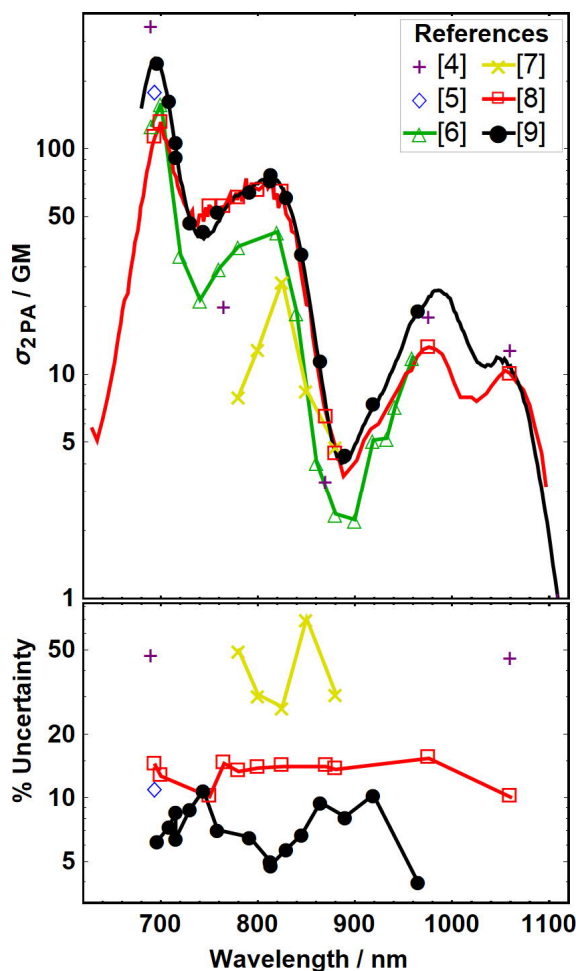


Figure 1. Top: Two-photon cross section measurements of Rhodamine 6G (1 GM = $10^{-50} \text{ cm}^4 \text{ s photon}^{-1}$). Bottom: Reported relative uncertainty ($k = 1$) in cross section measurements. Both plots are on a log scale showing the wide range of reported cross section and relative uncertainties.

measuring 2PA also do not always agree due to other attenuating processes, such as excited state absorption, or concentration dependent effects which can change the behaviour of absorbers.

To address the issues of reproducibility and accuracy, we have developed a high throughput instrument for the automated characterization of two-photon cross section and spectra. This instrument has pulse characterization, coupled with the ability to measure multiple samples, as well as a broad spectral range, so our results may be easily comparable to other systems.

METHODS

Our 2PA setup, depicted in Figure 2, measures the two-photon excited fluorescence of samples. Excitation pulses (1 mJ, <150 fs) are generated by a Yb laser (Pharos-SP, Light Conversion), followed by an optical parametric amplifier (OPA, Orpheus-HE, Light Conversion) and second harmonic generation (SHG), which allow for wavelength tunability from 315-2600 nm. These pulses can be characterized in terms of bandwidth, pulse duration, pulse energy and beam diameter. Power is adjusted using a neutral density filter, providing a quadratic fluorescence response which is recorded via PMT. Collecting emission, rather than direct absorption helps eliminate other nonlinear processes, such as excited state absorption.

The key advantages of this system lie in the automation of many of its functions. It is capable of measuring power dependent spectra over a broad range of wavelengths, with comparisons of up to four samples in a single run. Comparisons can also be made to the corresponding one-photon absorption, which is achieved via SHG using a BBO crystal.

In conjunction with this spectrometer, our research group has also implemented the first online database of two photon absorption spectra (www.kbfi.ee/mpa), providing reference compounds for other facilities to measure 2PA.

INITIAL RESULTS AND FUTURE PLANS

Initial measurements indicate 2PA spectra are highly reproducible, with variations of spectral shape <5%, and of absolute cross section <10%, which we plan to improve shortly. In addition to the emission detection we currently have, we plan to install a nonlinear

transmission detector, which will allow us to determine what circumstances these two techniques agree or disagree. We also have tentative discussions with national metrology institute (AS Metroser) towards establishing a certified and SI-traceable 2PA measurement service.

REFERENCES

1. M. Pawlicki, H. A. Collins, R. G. Denning, & H. L. Anderson, Two-photon absorption and the design of two-photon dyes, *Angew. Chem. Int. Ed.* **48**, 3244-3266, 2009.
2. L. M. Maestro et al. CdSe quantum dots for two-photon fluorescence thermal imaging, *Nano Lett.* **10**, 5109-5115, 2010.
3. A. Rebane et al. Two-photon voltmeter for measuring a molecular electric field, *Angew. Chem. Int. Ed.* **54**, 7582-7586, 2015
4. J.P. Hermann & J. Ducuing, Dispersion of the two-photon cross section in rhodamine dyes. *Opt. Commun.* **6**, 101-105, 1972.
5. P. Sperber & A. Penzkofer, S0-Sn two-photon absorption dynamics of rhodamine dyes. *Opt. Quant. Electron.* **18**, 381-401, 1986.
6. M. A. Albota, C. Xu, W. W. Webb, Two-photon fluorescence excitation cross sections of biomolecular probes from 690 to 960 nm. *Appl. Opt.* **37**, 7352-7356, 1998.
7. G. O. Clay, C.B. Schaffer & D. Kleinfeld, Large two-photon absorptivity of haemoglobin in the infrared range of 780-880 nm. *J. Chem. Phys.* **126**, 025102, 2007
8. N. S. Makarov, M. Drobizhev & A. Rebane, Two-photon absorption standards in the 550-1600 nm excitation wavelength range. *Opt. Express* **16**, 4029-4047, 2008.
9. S. de Reguardati, High-accuracy reference standards for quantitative two-photon absorption spectroscopy. (PhD Thesis, TTÜ Press, 2017)

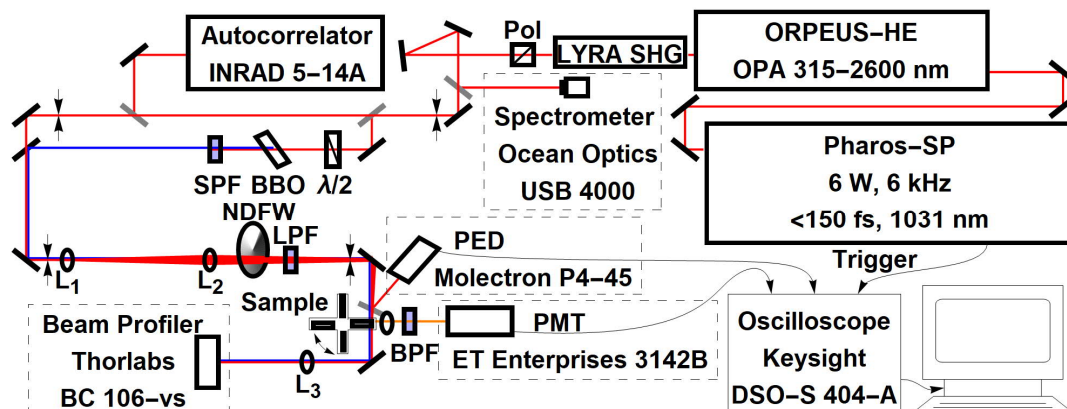


Figure 2. Schematic of the automated femtosecond 2PA spectrometer. Pol – polarizer; FM – flip-mirror; LPF – long-pass filter; SPF – short-pass filter; BPF – band-pass filter; L_n – lenses; $\lambda/2$ – half-wave plate; BBO – barium borate crystal; NDFW – neutral density filter wheel; PED – pyroelectric detector; PMT – photomultiplier tube.

Transmittance Haze Measurement by DIN 5036 Part 3

¹Wen-Chun Liu, ²Hsueh-Ling Yu,

¹Center for Measurement Standards, ITRI, Hsinchu, Taiwan

²Singularity Optics Corp., Hsinchu, Taiwan

Corresponding e-mail address: liuwenchun@itri.org.tw

This paper presents the analysis and results of transmittance haze by using DIN 5036 part 3. From the simulation, diffuse transmittance is strongly dependent on reflectance of the integrating sphere, which also makes transmittance haze deeply affected. The measured data were compared to the data from double compensation method to prove the simulation result.

INTRODUCTION

Transmittance haze inconsistencies exist among various measurement methods. In 1st APMP pilot study, some commonly used methods in Asia-Pacific area, ASTM D1003, ISO14782, BS:2782 Part5, double beam method, and double compensation method were discussed, and the reasons causing non-equivalent transmittance haze among NMIs were also analysed. Because there is no standards specifying the measurement method for such high range, while many products labelled ‘high haze’, the second TCI project (APMP.PR-P3.1) focus on studying in depth the technique of haze measurement including high haze level measurements. In 2019, CIE TC 2-94 was founded by most members that participated in the APMP pilot study. The purpose is to write a CIE Technical Report on measurement methods of total transmittance, diffuse transmittance, and transmittance haze, including their advantages and disadvantages and guidance for determination of measurement uncertainties. The 1st and 2nd pilot study results will be included in TC2-94, and the other commonly used methods, such as DIN 5036 part 3 discussed in this article, will also be analysed in this TC.

PRINCIPLE AND DISCUSSION

Total transmittance (TT) of DIN 5036 Part 3 is shown as step (i) and (ii) in Fig. 1, while diffuse transmittance (DT) is shown as step (i) to (iv)[1]. I_1 to I_4 are the measured values from step (i) to step (iv), respectively. According to the definition of transmittance haze (TH), ratio of DT to TT , TH can be calculated although there is no description about TH measurement in this standard document.

The sphere multiplier M for each measurement step is shown in equation (1) where ρ_0 is the initial reflectance for incident flux, ρ_s is the reflectance for integrating sphere wall, ρ_i is the reflectance for port i and f_i is the fractional area of port i to the sphere internal surface area. Therefore, sphere multiplier M_0 in step (i) equals to M_i in step (ii) and M_s in step (iii) equals to M_d in step (iv) due to the same configuration.

$$M = \frac{\rho_0}{1 - \rho_s(1 - \sum_{i=1}^n f_i) - \sum_{i=1}^n \rho_i f_i} \quad (1)$$

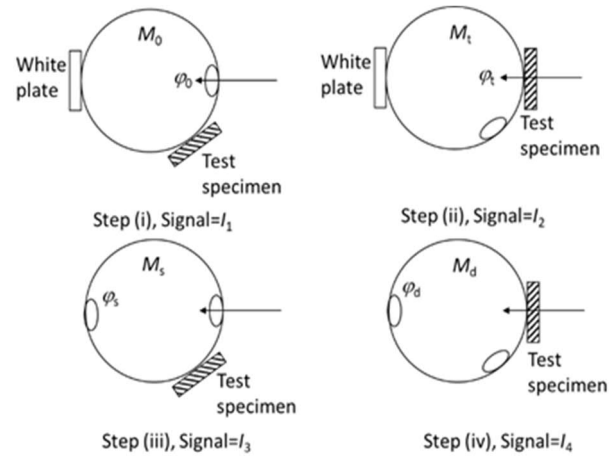


Figure 1 The method specified in DIN 5036 part 3. $TT=I_2/I_1$, $DT=(I_4-TT \cdot I_3)/(I_1-I_3)$, and $TH=DT/TT$.

Because M_0 equals to M_i , TT from DIN 5036 Part 3 can be measured accurately if the structure of the measurement system can be designed properly. However, some discrepancies exist during DT measurement process. The equation of DT can be rewritten as equation (2), where ϕ_d , ϕ_s and ϕ_0 are incident flux in step (iv), (iii), and (i), respectively.

$$DT = \frac{I_4 - TT \times I_3}{I_1 - I_3} = \frac{M_d \times \phi_d - M_s \times TT \times \phi_s}{M_0 \times \phi_0 - M_s \times \phi_s} \quad (2)$$

Equation (2) shows that the sphere multiplier will affect DT . Assume that f_i for all ports is 0.01, TT is 0.95, the reflectance for the test specimen ρ_t is 0.1, ϕ_d , ϕ_s and ϕ_0 are 0.2, 0.01 and 1 respectively, the theoretical DT can be calculated under the same sphere configuration from equation (3), and the value is 0.1905.

$$DT = \frac{M_d \times \phi_d - M_s \times TT \times \phi_s}{M_0 \times \phi_0 - M_s \times \phi_s} \cong \frac{\phi_d - TT \times \phi_s}{\phi_0} = 0.1905 \quad (3)$$

The numerical simulation result of DT by changing the reflectance of sphere (ρ_s) is shown in Fig. 2, which shows that DT is strongly dependent on ρ_s . Except for small ρ_s , DT is usually smaller than its theoretical value of 0.1905. In this case, DT is close to the theoretical value when ρ_s is down to 0.5. However, measured signals would be greatly reduced due to low ρ_s , and usually such low reflectance material is not used for the integrating sphere wall.

Another factor that may have influence on DT is the incident flux φ_s due to the imperfect collimated beam. In this case, assume that ρ_s is 0.9, φ_s is variable, the result in Fig. 3 shows that DT is still smaller than its theoretical value, even though the incident light is a perfectly collimated beam ($\varphi_s = 0$).

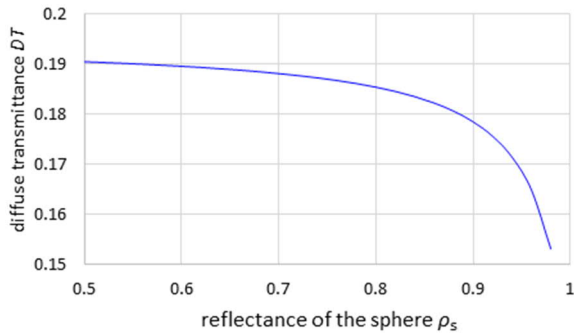


Figure 2 Numerical simulation - reflectance of the sphere ρ_s versus diffuse transmittance DT

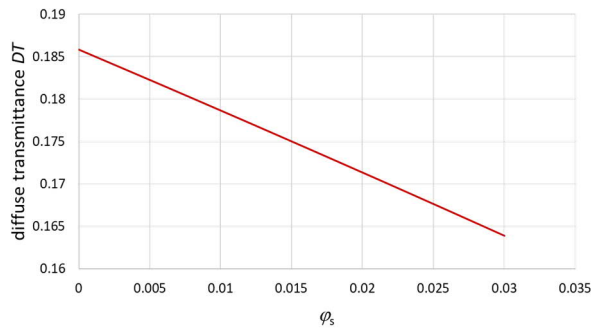


Figure 3 Numerical simulation - incident flux from imperfect collimated beam φ_s versus diffuse transmittance DT

COMPARISON OF DIFFERENT METHODS

To prove the above simulation of DIN 5036 part 3, four transmittance haze plates were used as test specimens. All plates were measured by DIN 5036 part 3 and double compensation method shown in Fig.4, which can be used to measure theoretically accurate TT , DT and TH if the structure of the measurement system can be designed properly under the same configuration in each step.

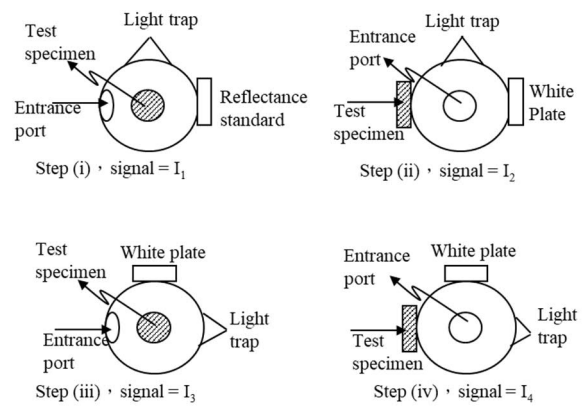


Figure 4 The method of double compensation. $TT=I_2/I_1$, $DT=(I_4-TT \cdot I_3)/(I_1-I_3)$, and $TH=DT/TT$.

Tables 1 to 3 show the DT , TT and TH results from the two methods, respectively. From table 1 and table 2, the DT values from DIN 5036 part 3 are all smaller than the values from double compensation method, and the TT values from the two methods are very close. These results show that the TT can be measured accurately by using DIN 5036 part 3, but DT is smaller than the theoretical value. Due to the definition of transmittance haze (TH), DT/TT , it is known that TH from DIN 5036 part 3 is also smaller than the theoretical value as shown in table 3.

Table 1 DT from two methods

Test Specimen	H20	H40	H70	H90
Method				
DIN 5036 part3	13.50	33.82	62.08	80.04
Double Compensation	14.18	35.85	65.82	84.87

Table 2 TT from two methods

Test Specimen	H20	H40	H70	H90
Method				
DIN 5036 part3	84.95	91.46	90.81	89.99
Double Compensation	84.95	91.43	90.85	89.83

Table 3 TH from two methods

Test Specimen	H20	H40	H70	H90
Method				
DIN 5036 part3	15.88	36.94	68.30	88.84
Double Compensation	16.68	39.18	72.40	94.37

CONCLUSION

TT data can be measured accurately by DIN 5036 part 3, but the obtained DT data are smaller than theoretical values. Therefore, TH data from this method are also smaller than the theoretical values. This is because DT from DIN 5036 is highly dependent on reflectance of the integrating sphere, and higher reflectance causes greater differences from the theoretical values.

REFERENCE

1. Methods of measurement for photometric and spectral radiometric characteristic numbers, DIN 5036 part 3, 1979.

Design and Evaluation of Extremely Low-Reflectance Measurement Device

Ma Yuxuan, Feng Guojin

National Institute of Metrology, China

Corresponding e-mail address: fengguojin@nim.ac.cn

In order to measure extremely low diffuse reflectance of flat samples or cavity samples, a new device has been set up. The biggest difference between normal reflectance measurement systems is that a supercontinuum source is used as the light source to improve the measured signal-to-noise ratio and to expand the scope of measurement results. The measurement condition is just for 0/d right now. Device performance is continuously improving. Currently, the lower limit of the reflectance measurement can reach to 0.00005 in the range of 1100nm-2000nm, and the relative uncertainty is nearly 15% while the reflectance is near to 0.0005($k=2$).

INTRODUCTION

The diffuse reflectance of the material is a key supplementary comparison in CCPR. The accuracy of the measured value and uncertainty of diffuse reflectance measurement directly represents calibration and measurement capabilities in this field. The current international comparison is mainly concentrated in the high reflectance, and comparison about extremely low-reflectance (less than 1%) is still blank. With the development of emerging industries or materials, there are more and more requirements focus on low reflectance measurements not only for higher measurement accuracy but also for more widely spectral range.

Therefore, it is of great significance to improve the measurement method and optimize the measurement device to improve the measurement level of diffuse reflectance and reduce the uncertainty of the measurement result of the diffuse reflectance.

EXPERIMENTAL DEVICE

In order to improve the current level of diffuse reflectance measurement in the ultra-black field, a corresponding measuring device is set up, the principle of the device is shown in Figure 1, it is used to measure the diffuse reflectance under 0/d condition.

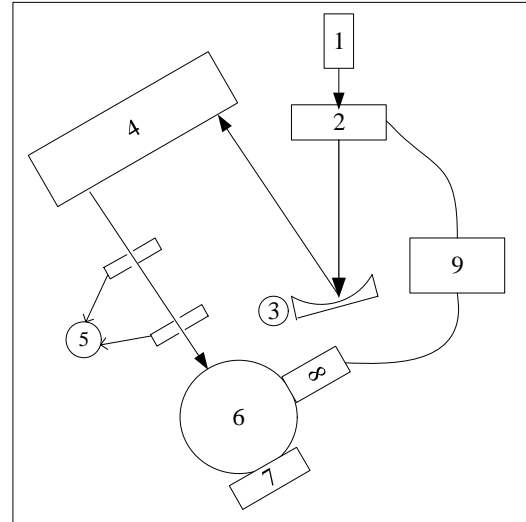


Figure 1. Device Schematic. 1: Supercontinuum Source; 2: Chopper; 3: Concave mirror; 4: Monochromator; 5: Aperture; 6: Integrating Sphere; 7: Sample; 8: Detector; 9: Lock-in Amplifier.

The light source adopts SC-PRO-7 high-power supercontinuum source produced by Anyang Laser, with the spectral range of 400nm-2400nm. Its seed source wavelength is 1064nm, and the maximum light power can reach up to 20W. The monochromator is iHR550 produced by HORIBA Scientific and the scanning range is 250nm-2000nm with 3 gratings and filter wheel. The detector is InSe, also bought by HORIBA Scientific, part number is DSS-PSE020T, spectral rang is 1.0 μ m-4.5 μ m. The Lock-in Amplifier is SR830 produced by Stanford Research Systems.

The light emitted by the supercontinuum source passes through the chopper and the concave mirror, and then enters the monochromator. In the monochromator, the light passes through the filter wheel, the collimator, the diffraction grating, and the focusing lens and reaches the exit slit. The emitted light enters the integrating sphere after passing through the two apertures, and irradiates the sample vertically through the sample window on the integrating sphere coated with PTFE.

PARAMETER SETTINGS

In order to protect the monochromator, the light

source energy was adjusted to 40% of full power, not 100%. The chopper frequency was set to 200Hz to 270Hz to obtain a higher signal from SR830. The entrance slit and exit slit of the monochromator were both set to 2mm, nearly 6nm bandwidth. The grating was selected as 600lp / mm blazed grating, the filter is Lp-1000 which can only pass the wavelength more than 1000nm. In order to obtain greater dynamic range, we connected the detector to SR830 directly, without using the manufacturer's amplifier. The integrating time for each wavelength point is set to 1s.

MEASUREMENT RESULTS

The background signal (using pressed PTFE as sample) and zero signal (no sample) were measured at 1000nm-2000nm range are shown in Figure 2.

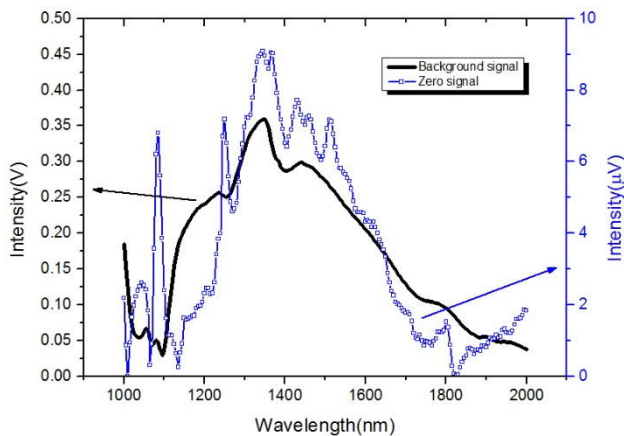


Figure 2. 1000nm-2000nm background and zero signal

From the measured results, due to the similarity between the zero signal (mainly caused by stray light, the background signal from acquisition system and so on) and the background signal, it can be considered that there is a possibility of further reduction for the zero signal of the system.

If we divided “Zero signal” to “Background signal”, the result is shown in Figure 3. It can be known that the device can measure samples with diffuse reflectance as low as 0.00005 in 1100nm to 2000nm. Obviously, if we subtract zero signal before each measurement, lower reflectance may be obtained. The results in the red box in Figure 3 are unreliable abnormal results, which may be caused by the seed source of the pulsed light source. We expect to solve this problem in further experiments.

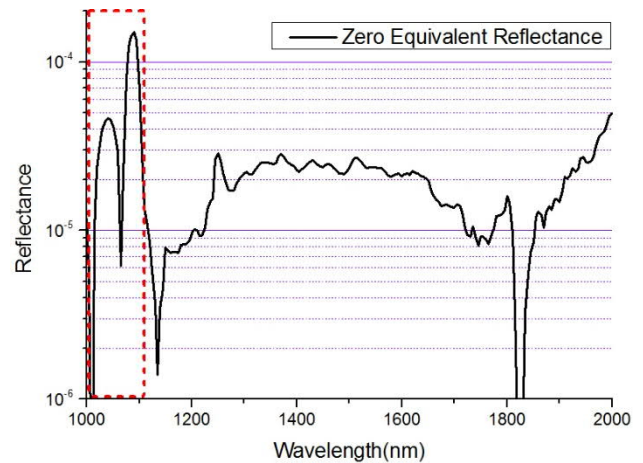


Figure 3. 1000nm-2000nm lower measurement limit

Normally, the measurement sequence is: measure the PTFE (its reflectance value is calibrated in NIM), zero, and the sample, from the measured data, the diffuse reflectance of the sample can be calculated out, shown in Figure 4.

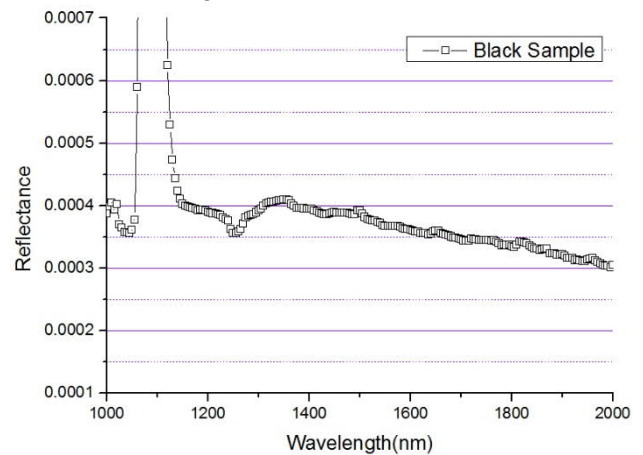


Figure 4. 1000nm-2000nm sample diffuse reflectance

It can be seen from the figure that the diffuse reflectance level of this sample is about 0.0004. The relative uncertainty in our current preliminary estimates is about 15 % ($k=2$).

The final purpose of this device is to achieve the low reflectance measurement in the 500nm-2000nm waveband, however, at this stage only the extremely low diffuse reflectance measurement in the near-infrared region of the 1100nm to 2000nm band achieved preliminary results.

ACKNOWLEDGEMENT

This work was supported by the National Key Research and Development Program of China (Grant No. 2016YFF0200300, "Optical radiation measurement standard: Research on Key Techniques of Extreme Optical Radiation and Material Measurement")

ROSI: the new NIST reference facility for UV-SWIR specular and diffuse reflectance calibrations

Heather J. Patrick and Catherine C. Cooksey

National Institute of Standards and Technology, Gaithersburg, MD 20899 USA,

Corresponding e-mail address: heather.patrick@nist.gov

We report on ROSI, the new NIST reference instrument for specular and bidirectional diffuse reflectance measurements at UV-SWIR (250 nm to 2400 nm) wavelengths. ROSI employs high-brightness tunable light sources and a robotic arm goniometer that have enabled the expansion of diffuse bidirectional reflectance calibrations in the SWIR and research measurements to out-of-plane geometries. We describe the determination of correction factors, uncertainty budget, and validation of ROSI. We will also describe the addition of an integrating sphere for directional/hemispherical reflectance calibrations.

INTRODUCTION

NIST maintains a robust program in reflectance calibrations and research in support of stakeholders from NASA and other government laboratories to manufacturers of optical instruments and components. For many years the NIST reference reflectometer for UV-SWIR wavelengths has been the Spectral Tri-function Automated Reference Reflectometer (STARR) [1]. The new facility, the Robotic Optical Scattering Instrument (ROSI),[2] addresses growing demand for reflectance measurements at expanded geometries, leverages technological advances in light sources, and features the unobstructed sample viewing, reliability and repeatability of a robotic arm goniometer. We describe the operation of ROSI for bidirectional and specular reflectance calibrations

and report on progress towards the addition of directional/hemispherical calibrations to ROSI.

SYSTEM DESCRIPTION

As shown in Figure 1, light from either a broadband supercontinuum fiber laser or a Xenon laser-driven light source (LDLS) is coupled into a monochromator to allow tunable output from 250 nm to 2400 nm. After passing through a diffuser, chopper, and circular aperture (not shown), the output is polarized and imaged to a 1-cm diameter spot incident on the sample plane of the robot goniometer for bidirectional measurements. The 8/di measurement capability (dotted line illumination path) is under development.

In the robot goniometer, light is collected by the UV-SWIR receiver, which consists of a precision aperture followed by a lens that focuses light to one of two detectors that can be translated into position behind the aperture/lens assembly. A silicon photodiode is used for UV-NIR (250 nm to 1100 nm), and an extended InGaAs photodiode on a small integrating sphere is used for SWIR (1000 nm to 2400 nm) wavelengths. The reflectance measurements are absolute: the receiver can be positioned to measure both the incident and reflected flux. The combination of the robotic arm sample holder and the rotation of the receiver arm enables reflectance measurement at nearly any combination of incident and viewing angles.

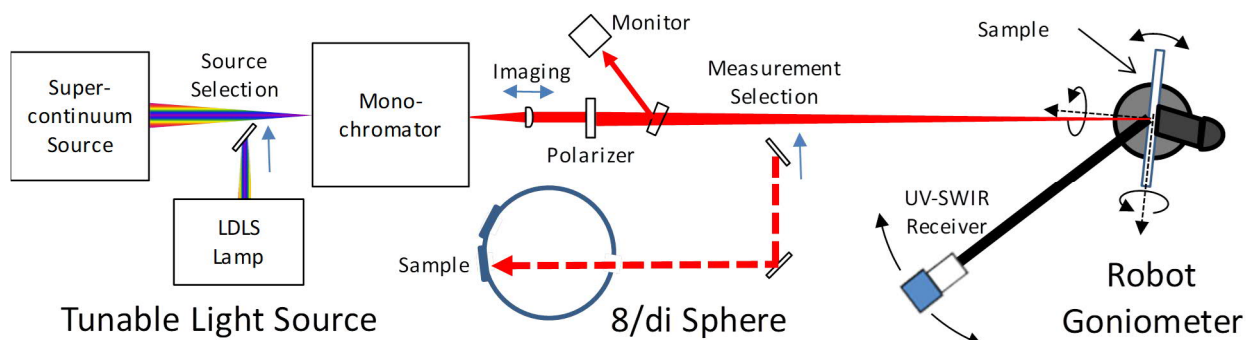


Figure 1: Schematic of the ROSI facility. Commissioning of the tunable light source for wavelengths from 250 nm to 2400 nm, and the Robot Goniometer for bidirectional reflectance calibrations, is complete. The 8/di sphere is operational, with directional/hemispherical calibration capability under development.

VALIDATION AND UNCERTAINTY

As part of the instrument validation for ROSI, we measured a sintered PTFE sample that had been previously measured by the NIST STARR facility and the Physikalisch-Technische Bundesanstalt (PTB) Gonioreflectometer for 0/45 diffuse reflectance factor [3]. The results and residuals are shown in Figure 2. The residuals generally fall within the combined expanded uncertainty for each pair of instruments, validating the quality of measurements obtained on ROSI.

Table 1 shows the components of a typical uncertainty budget for reflectance factor of sintered PTFE. Dominant uncertainty components come from the receiver efficiency uniformity, sample uniformity, illumination centering, and viewing angle. The latter two components are geometrical and arise from our ability to set and maintain alignment of the incident and viewing. Sample uniformity is sample dependent and is evaluated by measurements at different locations on the sample. The receiver efficiency uniformity component is the uncertainty in a correction factor that accounts for differences in efficiency of collecting diffusely scattered

reflected flux compared to collimated incident flux. Details of the instrument characterization, uncertainty budget, and research applications of ROSI will be presented at the conference.

Table 1. Nominal Relative Uncertainty Contributions ($k = 1$) and Expanded Relative Uncertainty ($k = 2$) for 0/45 reflectance factor of a typical sintered PTFE diffuse reflectance standard measured at 550 nm.

Source of Uncertainty	Relative Uncertainty Contribution
Aperture Distance	0.03 %
Aperture Area	<0.01 %
Finite Solid Angle Calculation	0.05 %
Illumination Centering	0.16 %
Detector Gain Ratio	0.06 %
Lock-in Amplifier Sensitivity Ratio	0.02 %
Receiver/Monitor Gain Ratio Stability	0.04 %
Receiver Efficiency Uniformity	0.32 %
Detector Noise	0.01 %
Wavelength	<0.01 %
Sample Uniformity	0.20 %
Incident Angle	<0.01 %
Viewing Angle	0.09 %
	Expanded Relative Uncertainty
	0.86 %

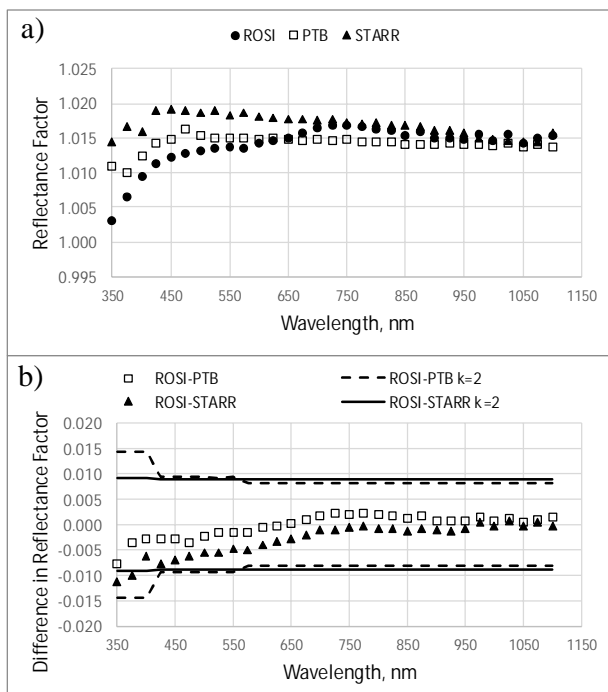


Figure 2a). Reflectance Factor vs. Wavelength for a sintered PTFE sample, denoted PTFE#1 in Ref. 3, as measured by ROSI (solid circles), the NIST STARR facility (solid triangles) and PTB (open squares). STARR and PTB data from Ref. 3. **b)** Residual difference in Reflectance Factor between ROSI and STARR (solid triangles) and ROSI and PTB (open squares) along with the combined $k = 2$ for each instrument pair.

FUTURE WORK

The characterization and validation of an integrating sphere for 8/di reflectance measurements is underway, and when commissioned, will complete the transition of all UV-SWIR reflectance calibration services to ROSI.

REFERENCES

1. J.E. Proctor and P.Y. Barnes, "NIST high accuracy reference reflectometer-spectrophotometer", *J.Res. NIST* 101, 619-627, 1996.
2. H.J. Patrick, C.J. Zarobila, and T.A. Germer, "The NIST Robotic Optical Scatter Instrument (ROSI) and its Application to BRDF Measurements of Diffuse Reflectance Standards for Remote Sensing", in *Proc. SPIE 8866*, edited by J.J. Butler, 886615-1-12, SPIE, Bellingham, 2013.
3. C.C. Cooksey, M.E. Nadal, D.W. Allen, K.-O. Hauer, and A. Hoepe, "Bidirectional reflectance scale comparison between NIST and PTB", *Applied Optics* 54 (13), 4006-4014, 2015.

Fresnel Reflection for Fibre-Coupled Cryogenic Radiometric Measurements

M G WHITE^{1,2}, E BAUMANN^{1,2}, I VAYSHENKER³, M S STEPHENS³, M SMID⁴, J H LEHMAN³

¹Associate of National Institute of Standards and Technology, Boulder, Colorado 80305 USA

²Department of Physics, University of Colorado, Boulder, Colorado 80309, USA

³National Institute of Standards and Technology, Boulder, Colorado, 80305 USA

⁴Czech Metrology Institute, Prague, Czech Republic

Corresponding e-mail address: m.white@boulder.nist.gov

We have measured the temperature dependent Fresnel reflection loss and Rayleigh backscatter of single-mode SMF-28 fibre, polarisation maintaining (PM) single-mode fibre and PM photonic crystal fibre (PCF). We show that the relative effective refractive index of these fibres reduces by 0.11 %, 0.15 % and 0.30 % respectively from room temperature to 5 K. At the same time the Rayleigh backscatter increases 15x for SMF-28 and PM fibres, and 4x for the PM PCF fibres. As a fibre is cooled, the refractive index reduces, which increases the fibre's output power. It is this change we quantify in order to apply a correction to our fibre radiometer measurements. We use an in-situ beam-splitter measurement technique to measure the Fresnel reflection at 1310 nm and 1550 nm and we confirm the results at 1550 nm with optical frequency domain reflectometer measurements.

INTRODUCTION

Optical return loss (ORL) of a fibre encompasses Fresnel reflection from the media boundary interface and Rayleigh back-scatter within the fibre [1]. The temperature dependent effective refractive index n_{eff} of the fibre can be determined from a measurement of each of these parameters as the fibre is cooled.

Recently we reported a fibre-coupled cryogenic primary standard for the calibration of optical fibre power meters [2]. The system used commercial all-fibre beam-splitters and single-mode fibre to direct light from attenuated fibre-coupled laser diode sources to the device under test (DUT) and either of two absolute standard detectors.

The fibre within the cryostat is thermally anchored to a temperature stabilised stage, irradiating a cryogenic detector operating at 7 K. As the fibre from the beam-splitter to the cryogenic detector is cooled, the refractive index reduces. This causes a reduction in the Fresnel reflection R at the media boundary of refractive index $n_1 = 1.47$, propagating to a material of index $n_2 = 1.00$ (vacuum), leading to an increase in fibre output power, Eqn 1. The beam-splitter ratio

$$R = \left| \frac{n_1 - n_2}{n_1 + n_2} \right|^2 = 0.036 \quad (1)$$

between radiometer and DUT is measured at room temperature, and therefore this change in fibre output is required to be measured in order to apply a correction to the room temperature beam-splitter ratio measurement. A measurement of the Fresnel reflection not only enables a correction to the beam-splitter measurement, but also allows us to calculate the temperature dependent effective refractive index n_{eff} . We are interested in quantifying this effect to the best uncertainty possible in order to improve and assure our DUT calibration uncertainty. The work presented here is also applicable to the single-photon detection community where detectors are calibrated for detection efficiency [3].

METHOD

Five fibres were investigated using an in-situ beam-splitter measurement technique, Fig. 1. The results were confirmed at 1550 nm with optical frequency domain reflectometer (OFDR) measurements. The fibres tested included SMF-28 Ultra, PM15-U25D and PM13-U25D (PM single mode fibre), and LMA-PM-10 and PM-1550-01 (PM PCF fibre). The PCF fibre was included in the assessment as it provides the possibility of using one fibre within the cryostat and thus one cryogenic detector, to cover the visible and near infrared wavelength region. This would considerably reduce the complexity around the cryogenic detector. The difficulty of using PCF fibre relates to the evacuation of air within the micro-capillary structure in preparation for cooling.

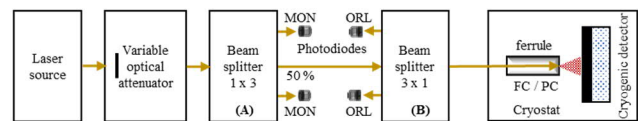


Fig. 1. In-situ beam-splitter setup for the measurement of Fresnel reflection and Rayleigh backscatter. (A) 1 x 3 beam-splitter with monitoring (MON) channels. (B) 3 x 1 beam-splitter connected in reverse to facilitate ORL measurements.

The crosstalk of the beam-splitter is first assessed and then the change in Rayleigh scatter of the fibre measured as it is cooled. This is facilitated by attaching 4 m of fibre to the 4 K cold plate with both ends exiting the cryostat. Light is launched into one end while the other is monitored as the fibre is cooled. This enables the scatter to be calculated. The monitored end is then withdrawn into the cryostat, anchored to the cold plate, and the system cooled. The change in Fresnel reflection is calculated from the measured value of the ORL and Rayleigh backscatter. These measurements were repeated for all five test fibres at 1310 nm and 1550 nm.

A Luna OFDR 4600 swept-wavelength reflectometer, set to a centre wavelength of 1550 nm, was used to record the time of flight along the length of fibre. The change in Rayleigh back-scatter was determined by integrating the signal 10 mm after the source connector to within 10 mm of the plane cut end facet at room temperature, 77 K and 5.2 K. The signal was also integrated 10 mm about the two reflection peaks (Fig.2). By comparing the room and low temperature measurement results, the Fresnel reflection loss change could be determined.

RESULTS

We observed a 15x increase in the Rayleigh backscatter with both techniques for SMF-28 and PM fibres, and a 4x increase for the PM PCF fibres. The results for the five fibres tested are listed in Table 1 below. The effective refractive index n_{eff} is calculated from the measurement of the Fresnel reflection signal. Fig. 2 illustrates a typical OFDR measurement result – in this case a 4 m length of PM PCF fibre with inset showing the distinctive dual reflection peaks of a PM fibre.

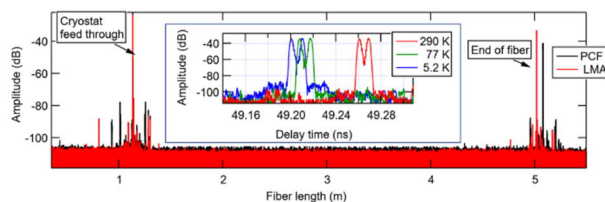


Fig. 2. Fresnel reflection at 1550 nm for plane cut end facet PM PCF fibres; PM-1550-01 and LMA-PM-10 with each fibre connectorised FC / APC at one end only, with modal adaptation of 10 mm fused SMF-28 fibre. Inset: time of flight (ns) for approx. 4 m of PM-1550-01 PM, high index, solid core, PCF fibre at room temperature, 77 K and 5.2 K showing the reflection nodes of the slow and fast axes as the fibre is cooled.

The effective group index of refraction is

calculated to change 0.11 ± 0.01 % for SMF-28 fibre, 0.15 ± 0.01 % for standard PM fibre and 0.30 ± 0.02 % for the PM-1550-01 PCF fibre (holey PM rod structure), Table 1. The signal exiting the fibre end facet increases relatively from 96.40 % to 96.42 %, 96.43 % and 96.46 % for SMF-28 fibre, standard PM fibre and PM PCF fibre respectively, (Eqn 1).

Table 1. Temperature dependent effective refractive index for various fibres at 1310 nm and 1550 nm wavelength.

Fibre Type and Wavelength	Effective Refractive Index n_{eff}		
	293 K	77 K	5 K
1310 nm			
SMF-28 Ultra	1.4676 ³	1.4664 ¹	1.4661 (0.10%) ¹
PM13-U25A	1.4679 ¹	1.4665 ¹	1.4660 (0.13%) ¹
1550 nm			
SMF-28 Ultra	1.4682 ³	1.4670 ^{1, 2}	1.4666 (0.11%) ^{1, 2}
PM15-U25D	1.4684 ²	1.4667 ^{1, 2}	1.4662 (0.15%) ^{1, 2}
LMA-PM-10	1.4664 ²	1.4679 ²	1.4662 (0.014%) ²
PM-1550-01	1.4733 ²	1.4705 ²	1.4688 (0.30%) ^{1, 2}

¹Beam-splitter measurement, ²OFDR measurement, ³from Corning product info SMF-28 ultra-optical fibre. The numbers in parentheses represent the relative change in output power of the fibre.

CONCLUSION

We have developed an in-situ beam-splitter measurement technique to measure the change in output of the optical fibres within our measurement facility as they are cooled. This change is applied as a correction to the room temperature beam-splitter ratio measurement between radiometer and DUT. This work helps assure our calibration uncertainties. The PM PCF results are promising which encourages further work to understand the dynamics of the fibre within a low temperature vacuum environment.

REFERENCES

1. Subcommittee 86B, Fiber optic interconnecting devices and passive components: Basic test and measurement procedures part 3-6: Examination and measurements, return loss, IEC/CEI-61300-3-6:2008, IEC, Geneva, Switzerland 2008.
2. M.G. White, Z.E. Ruiz, C.S. Yung, I. Vayshenker, N.A. Tomlin, M.S. Stephens, and J.H. Lehman, "Cryogenic primary standard for optical fibre power measurement", *Metrologia* **55**(5), 706-715 2018.
3. I. Mueller, R.D. Horansky, J.H. Lehman, S.W. Nam, I. Vayshenker, L. Werner, G. Wuebbeler, and M.G. White, "Verification of calibration methods for determining photon-counting detection efficiency using superconducting nano-wire single photon detectors", *Opt. Express* **25**(18) 21483-21495 2017.

CCPR-K5.2019 Key Comparison of Spectral Diffuse Reflectance

Robin Ångerman¹, Farshid Manoocheri¹, Dmitri Lanevski¹, and Erkki Ikonen^{1,2}

¹ Metrology Research Institute, Aalto University, Espoo, Finland, ²VTT MIKES, Finland

R. Ångerman's email-address: robin.angerman@aalto.fi

The key comparison CCPR-K5.2019 for spectral diffuse reflectance will be performed in the wavelength range of 360 nm to 830 nm using a 0°:d or equivalent geometrical configuration. The key comparison will be carried out in a star pattern among eleven participants using two types of samples. We will present measurement results of the evaluation tests on the quality of the samples at the conference. The samples have negligible fluorescence whose effect is less than 0.1% on the reflectance measurements. The reflectance of the samples is stable and uniform from the surface central area of 30 mm in diameter.

INTRODUCTION

At its meeting in June 2017, the Consultative Committee of Photometry and Radiometry (CCPR) decided that a key comparison of spectral diffuse reflectance would be carried out. Subsequently, CCPR assigned the Metrology Research Institute (MRI) of Aalto University and VTT MIKES metrology in Finland as the pilot laboratory. The effort will result in the key comparison reference values (KCRV) and the unilateral degree of equivalence (DOE) of each national measurement scale, both its deviation from the KCRV and the uncertainty of that deviation at the 95 % level of confidence.

The eleven participants of the CCPR-K5.2019 key comparison will include two National Metrology Institutes (NMIs) from North America, four NMIs from Asia-Pacific and five NMIs from Europe. Each participant will measure 2 pieces of matte ceramic tile samples and 2 pieces of sintered polytetrafluoroethylene (PTFE) samples, here after simply referred to as sintered PTFE samples.

After the receipt of all comparison samples from the suppliers, we have carried out a series of measurements to assess their quality, such as tests for short term stability, uniformity over a central spot of 30 mm in diameter, and the Lambertian behaviour at wavelengths of 360 nm, 580 nm, and 780 nm. Presence of possible UV-induced fluorescence has been checked using a spectrofluorometer at

excitation wavelengths from 350 nm to 360 nm. For the long-term stability test, a set of four samples (two of each type) have been chosen as “Comparison reference standards” for monitoring any drifts in the spectral diffuse reflectance measurements of the gonireflectometer at Aalto and possible changes in the comparison samples throughout the stages of the comparison.

PILOT LABORATORY MEASUREMENT SETUPS

The pilot laboratory measures the average spectral diffuse reflectance using a gonireflectometer. The setup at Aalto [1] is shown in Figure 1. The measurement wavelength is selected using a double-monochromator configuration that has a bandwidth of 5.4 nm. The average spectral diffuse reflectance is determined by integrating the angle-resolved radiance factor over the hemisphere, for a 0°:d equivalent geometry. The setup has a combined standard uncertainty of 0.2%, determined by previous work [1]. Furthermore, the samples are measured on a regular basis against reference standards using a commercial double-beam integrating sphere-based, spectrometer, which has an 8°:d configuration [2].

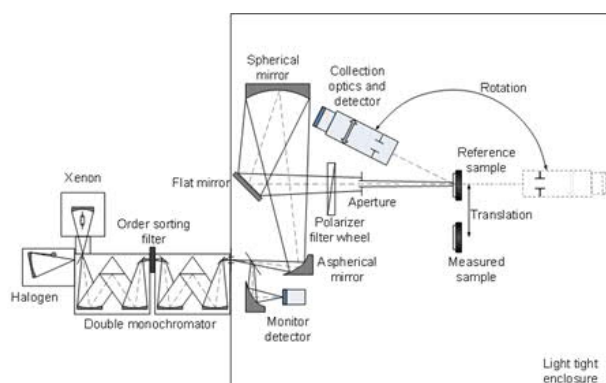


Figure 1. Schematic of the gonireflectometer at Aalto.

In order to determine the presence of possible UV-induced fluorescence at 360 nm wavelength a spectrofluorometer was used. The setup includes a xenon arc lamp, a monochromator, and an imaging spectrophotometer. Several pieces of the comparison samples of each type were irradiated in the 350-

360 nm wavelength range. The spectral radiances of the samples were compared against a few known non-fluorescent PTFE reference samples to determine any effects due to fluorescence as apparent reflectance in the 360-830 nm wavelength range.

REFERENCE MATERIALS AND RESULTS

The sample candidates include twenty-two pieces of matte white ceramic tiles and twenty-two pieces of sintered PTFE samples. Figure 2 shows the two types of reference samples. The samples have been mounted in cap-protected frames/holders. The material dimensions for the ceramic tiles and for the sintered PTFE samples are nominally 50 mm x 50 mm x 10 mm and 50 mm diameter x 10 mm thick, respectively. Figure 3 shows the result of fluorescence measurements for three pieces of matte white ceramic tiles marked as T-i, T-ii, and T-iii and for two PTFE reference samples P-i, and P-ii. Figure 4 shows an example result of a test for the Lambertian behaviour of a reference sample of the matte white ceramic tiles at wavelengths of 360 nm, 580 nm, and 780 nm. The measurements are performed for the bidirectional radiance factor of angles ranging from 85° to -85° in 5° increments.



Figure 2. From left to right, a sintered PTFE puck and a matte white ceramic tile

SUMMARY

The CCPR-K5.2019 Key Comparison measurements have started with MIKES-Aalto as the pilot laboratory according to a technical protocol which follows the guidelines established by CIPM and CCPR [3-5].

The pilot laboratory measures the average spectral diffuse reflectance of two types of samples using a gonireflectometer. The measurement results of the evaluation tests on the quality of the samples indicates that the samples have negligible fluorescence whose effect is less than 0.1% on the reflectance measurements. In the short term, the reflectance of the samples is stable and uniform from

the surface central area of 30 mm in diameter. Measurement results of the sample quality will be fully presented at the conference.

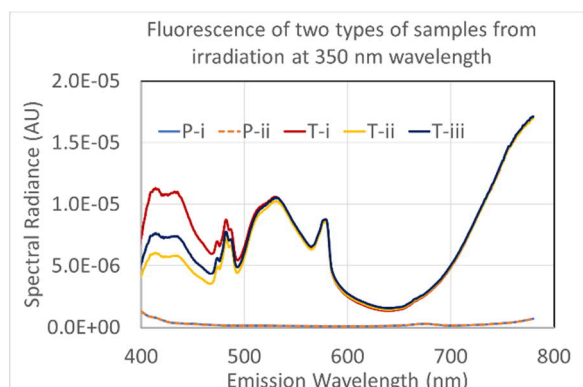


Figure 3. Fluorescence spectral radiance factor for the sintered PTFE samples, P-i, P-ii, and for ceramic tile samples, T-i, T-ii, and T-iii using an excitation wavelength at 350 nm.

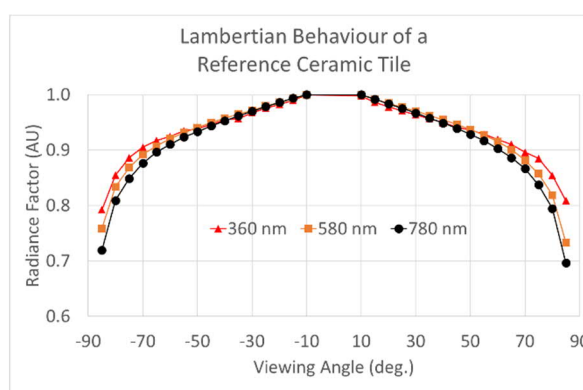


Figure 4. Normalised radiance factor for a matte white ceramic tile measured at wavelengths of 360 nm, 580 nm, and 780 nm. This tile is not circulated to other participants.

REFERENCES

1. S. Nevas, F. Manoocheri, E. Ikonen, Gonireflectometer for measuring spectral diffuse reflectance, Applied Optics, 2004
2. Cary 7000 UV/VIS/NIR spectrophotometer with a DRA-2500 External Diffuse Reflectance Accessory, Agilent Technologies, Inc, www.agilent.com/chem.
3. T.J. Quinn, Guidelines for CIPM key comparisons BIPM, 1999 (modified 2003)
4. CCPR-G4, Guidelines for preparing CCPR Key Comparisons, CCPR Working Group on Key Comparisons, 2013
5. International Committee for Weights and Measures, Mutual Recognition of National Measurement Standards and of Calibration and Measurement Certificates Issued by National Measurement Institutes, Paris: Comité International des Poids et Mesures, 2003

Determining the shape of reflectance reference samples for curved surface reflectors

Dmitri Lanevski¹, Farshid Manoocheri¹, Anna Vaskuri^{1,6}, Jacques Hameury³, Robert Kersting⁴, Christian Monte⁵, Albert Adibekyan⁵, Elena Kononogova⁵ and Erkki Ikonen^{1,2}

¹*Metrology Research Institute, Aalto University, Espoo, Finland, ²VTT MIKES, Espoo, Finland*

³*Laboratoire National de Métrologie et d'Essais (LNE), Trappes, France, ⁴Fraunhofer-Institute for Production Systems and Design Technology (IPK), Berlin, Germany, ⁵Physikalisch-Technische Bundesanstalt (PTB), Berlin, Germany,*

⁶*NIST, Boulder, CO, USA*

Corresponding e-mail address: dmitri.lanevski@aalto.fi

Foils made of different materials are often used as reflective insulators. Many manufacturers aim to accurately measure their optical properties to estimate and improve their performance. However, flat reflectance reference samples used in measurements do not correctly represent reflective insulators and cause discrepancy between different measurement techniques. Current work presents a method for modelling surface shape of appropriate reflectance reference samples that could be produced by additive manufacturing. The method is based on studying the reflection distribution of reflective insulators and is described with an example of aluminium foil. Method's performance is validated using Monte-Carlo simulations.

INTRODUCTION

Precise characterization of reflectivity of reflective insulation products for buildings is important for manufacturers of those products. However, recent intercomparison of reflectivity measurement techniques organized by the standardization working group CEN/TC 89/WG 12 has shown large differences of total hemispherical reflectivity results deviating by 6 % (from 0.92 to 0.98) on the same reflective material. The reasons of these differences are yet to be explained, but one of them ought to be a reflectance reference sample that doesn't represent the measurement object closely enough.

As indicated in the intercomparison, the plane mirrors or diffusing reflectance samples that are usually used for calibration of portable instruments may not be the best calibration targets. They are quite far from actual measurement targets - aluminized or aluminum foils that are usually used as external surfaces of reflective insulators. They usually have non-flat (battered and crumpled) surfaces and their comparison with flat reference standards may introduce some additional variation in reflectivity measurements.

Production of appropriate reference samples seems to be an obvious solution for this problem. Modern additive manufacturing methods allow to produce objects from almost any material with almost any size and shape. The questions that remain are that what should be the sample's surface shape so that it would exhibit reflectance properties similar to the reflective insulation products and what would be a suitable manufacturing method.

Present article tackles these problems by introducing a method to determine a shape of the new reflectance reference sample that could be manufactured by precise additive manufacturing or by some other method.

METHOD

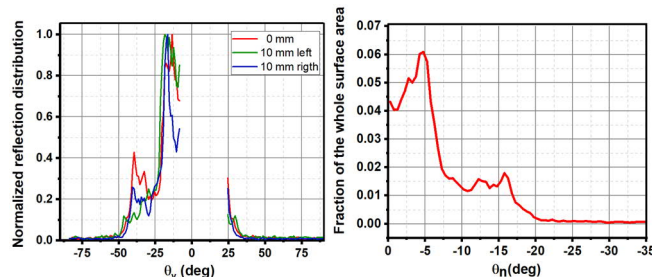


Figure 1. Reflection distribution of mesh-reinforced foil (left) and corresponding distribution of surface normals (right).

To determine the shape of desired reflectance reference sample, a reflection distribution of mesh-reinforced foil insulator was measured by an absolute gonioreflectometer developed at Laboratoire national de métrologie et d'essais (LNE) [1]. From the results, (see Figure 1) a corresponding facets' normals distribution function of crumpled aluminium was derived by averaging measurements and assuming that light reflected specularly from each individual microfacet. Next, an element of the reflectance reference sample surface profile was constructed. It consisted of coaligned linear segments whose slope and length corresponded to a particular facet normal and probability to encounter it defined by normals' distribution function. At the same time, to reduce self-

shadowing effect and avoid microstructures that are impossible to produce, only sharp angles between facets' were allowed. This resulted in the shape depicted in Figure 2 (left):

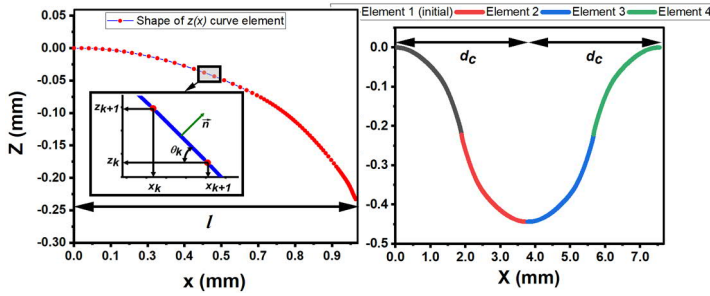


Figure 2. The shape of a single element corresponding to derived distribution of facets' normals (left) and waveform constructed of these elements (right)

Following the same principles, derived elements were flipped and shifted to obtain single period of waveform shown in Figure 2 (right). Finally, multiple periods were stacked together and stretched along Y-axis to form a 3D model (Figure 3) of structured reflectance reference sample with angular reflection distribution of a mesh-reinforced aluminium foil insulator.

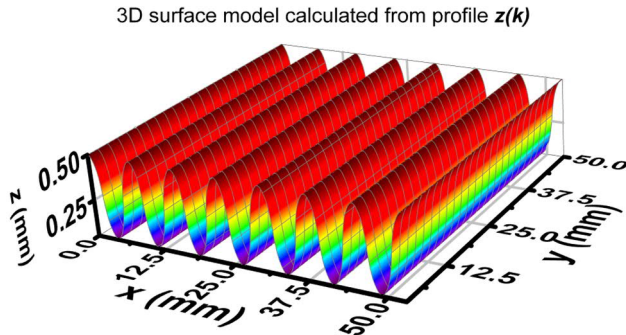


Figure 3. 3D model of structured reflectance reference sample for a mesh-reinforced aluminium foil insulator

The length of the waveform period was estimated from the parameters of LNE's goniometer [1]. It illuminated the measured insulator sample with the beam of 12 mm in diameter. In this case, mean illuminated distance calculated from the average length of chords is $\bar{a}_b = 7.71$ mm. Assuming that there is an equal number of facets with normals pointing to the left and to the right of the sample, $d_c = \bar{a}_b/2 = 3.86$ mm is the characteristic distance within which there should be present enough elements to comprehensively manifest the derived distribution of normals. The amplitude of waveform is defined by profile segments' coalignment method and 3D model dimensions can be chosen freely but should be reasonable for production and exploitation.

RESULTS OF VIRTUAL VALIDATION

To validate the reflection distribution of the modelled reference reflectance sample surface, a Monte-Carlo ray-tracing simulation was performed. Simulation parameters were kept close to the ones used for mesh-reinforced foil measurements. Reflection was modelled by Torrance-Sparrow model [2] with parameters corresponding to bare aluminium. The result of the simulation can be seen in Figure 4.

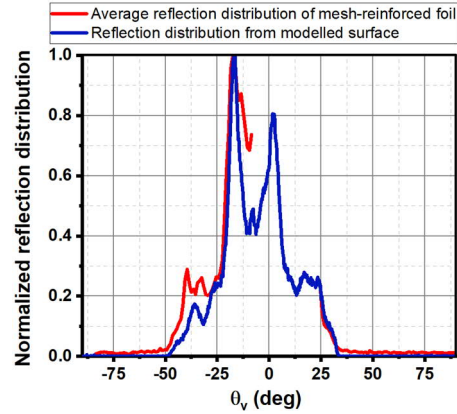


Figure 4. Reflection distribution of modelled surface obtained using Monte-Carlo simulation

The reflection distribution of the modelled surface is fairly close to the original average reflection distribution of the mesh-reinforced foil. The reflection maximum and the dispersion almost coincide and the overall shape is very similar.

The suitability of the modelled 3D surface to serve as a reference sample was also assessed. Virtual illumination beam was moved ± 12 mm along the surface and areas under reflection distribution were compared. Area standard deviation was 4.4%. Decreasing wavelength, i.e. using $d_c = \bar{a}_b/4 = 1.93$ mm decreased standard deviation down to 0.65%.

ACKNOWLEDGEMENTS

This work was funded through the European Metrology Programme for Innovation and Research (EMPIR) Project 16NRM06 'EMIRIM'. The EMPIR initiative is co-funded by the European Union's Horizon 2020 research and innovation programme and the EMPIR Participating States.

REFERENCES

1. Scoarnec V. et al., Development of an absolute reflectometer for reflectance calibration of mirrors in the infrared *Revue française de métrologie* 2014-1 29-38, 2014
2. Sparrow E M, Torrance K E and Birkebak R C, Theory for off-specular reflection from roughened surfaces *J. Opt. Soc. Am.* 57 1105-14, 1967

Advocating a statistical definition for the BRDF

Pierre Chavel¹, Mathieu Hébert¹, Lionel Simonot², Thomas Labardens^{1,3}, Ana-Maria Rabal-Almazor³, and Gael Obein³,

¹ Univ Lyon, UJM-Saint-Etienne, CNRS, Institut d'Optique Graduate School, Laboratoire Hubert Curien 42023, SAINT-ETIENNE, France, ² Université de Poitiers, Institut Pprime CNRS, Chasseneuil Futuroscope, France, ³ LNE-CNAM, La Plaine St Denis, France

Corresponding e-mail address: pierre.chavel@univ-st-etienne.fr

The definition of BRDF as ratio of radiance to irradiance assumes that the geometrical optics framework applies, implicitly meaning that spatial coherence and diffraction of light have no significant effect in the reflection process. However, when pushing the measurement to the limit of small solid angles for illumination and collection, these effects manifest themselves in the form of speckle, an optical phenomenon related to the stochastic nature of scattering objects. We suggest that BRDF should be defined as the statistical average of the former.

ABOUT THE CURRENT DEFINITION

From an optical point of view, there is an issue in the current definition of BRDF [1]. This quantity implicitly assumes spatially incoherent light, which prevents any interference. It also assumes that the limit of illumination of the surface from one single direction, therefore by a plane wave with a zero solid angle, can be reached. But that is precisely the case of maximal spatial coherence, prone to interferences that will occur after scattering by the sample. Similarly, geometrical optics is assumed valid on the light collection side, ignoring diffraction by the

sample. But a minimal collection solid angle corresponds to the most visible diffraction effects, which are however intrinsic to the phenomenon of scattering by small random fluctuations in the surface shape (roughness) and manifest themselves as speckle. Therefore, speckle effects [2] are ignored by that definition, while they are in fact maximized in the limit of the narrowest possible solid angles on the illumination and/or collection side.

THE IMPACT OF COHERENCE

Actually, until recently, the question of coherence was not an issue for BRDF measurement since most devices had a solid angle Ω_i large enough that coherence effects were not observable. Similarly, the rather large collection solid angle Ω_o did not allow to resolve any speckle pattern, but instead averaged the radiance and blurred speckle grains. However, recently, high-resolution BRDF measurement devices have considerably increased the directionality of the incident beam as well as the achievable angular resolution at collection [3]. Consequently, speckle is clearly visible in the measurements (Figure 2).

Notice in addition that speckle patterns depend on wavelength of light. The most contrasted patterns are observed with monochromatic radiations. Some researchers have observed residual speckle in laser-based BRDF measurements [4] and have proposed experimental solutions to reduce it. In case of white light or broad spectral bands, the speckle patterns produced by each wavelength add to each other on an incoherent basis (flux collected). If the detection is not spectrally resolved, the contrast of the speckle patterns decreases or may even disappear, at least far from the specular direction. In the case of ConDOR, however, even though the incident light has $V(\lambda)$ spectrum, the observed speckle has a rather high contrast due to the small solid angles. Because diffraction patterns scale linearly with wavelength and with deviation angle, the speckle blur due to spectral width increases with the angle between the direction of observation \mathbf{o} and the specular direction.

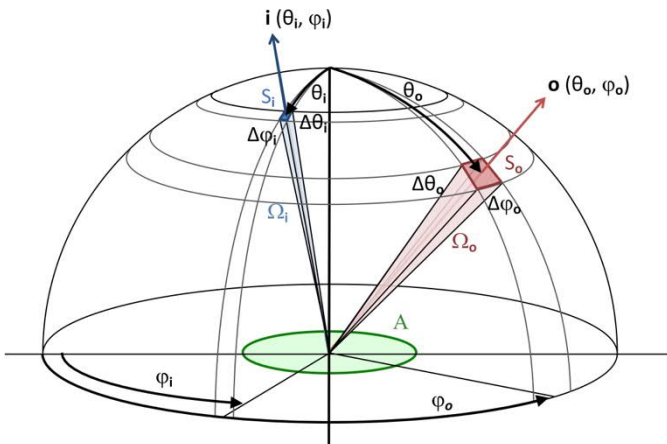


Figure 1. BRDF is the ratio of the radiance of the surface element in a given direction to the irradiance on the sample produced by directional incident radiation. It assumes that the divergence of the incident beam and solid angle of collection both tend to zero.

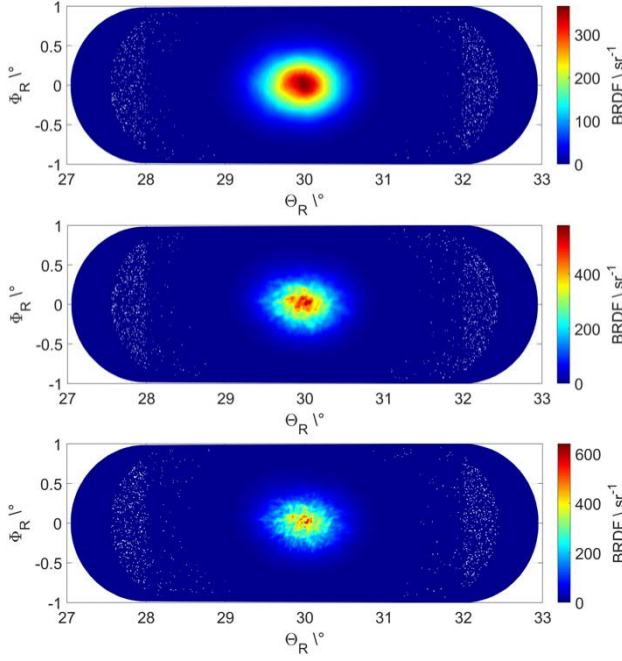


Figure 2. BRDF of a high gloss black sample extracted from NCS gloss scale (gloss_{60°} = 95 GU) around the specular direction. Illumination $\theta_i = 30^\circ$, $\phi_i = 180^\circ$, $V(\lambda)$ spectral range. Angular resolution is 0.315° (top), 0.057° (middle), 0.029° (bottom). Speckle appears when resolution decreases.

Conversely, residual speckle is most conspicuous close to the specular direction.

Enforcing a definition for BRDF that assumes incident light source to be perfectly spatially incoherent, i.e., in which coherence of light is not a parameter (in opposition to wavelength and polarization), would entail considering that speckle is not part of the measured BRDF but rather an experimental error (even though, in certain conditions, this error cannot be removed). To be convinced of this, one may consider a perfectly homogeneous scattering material with uniform appearance: Its BRDF should by definition be the same since the microstructure responsible for scattering is statistically uniform, whereas the speckle patterns varies strongly from one area to another due to the variations of local microstructure.

NEW DEFINITION PROPOSED

The purpose of this paper is not to enumerate practical methods to remove speckle effects but rather to propose a new definition for BRDF representative of the scattering properties of the material "as if" the incident beam was spatially incoherent. Following earlier work by Hoover and Gamiz [5], we suggest that that can be achieved by considering, at each wavelength λ and for given polarization states on

both sides, the expected value of the radiance scattered by the sample over areas whose random structure is statistically similar but independent from each other, in practice over areas which do not overlap with each other:

$$f(\mathbf{i}, \mathbf{o}) = \frac{\langle L(\mathbf{i}, \mathbf{o}) \rangle}{E(\mathbf{i})}$$

where f is the BRDF, L is the radiance in the direction \mathbf{o} and E is the irradiance from direction \mathbf{i} .

The BRDF measurement in each area includes a random fluctuation due to speckle, but the average of all measurements will discard these fluctuations whose expectation is zero. The number of measurements to be averaged depends on the solid angle of illumination: as a smaller solid angle induces a more contrasted speckle, the number of measured areas must be increased, which requires a larger sample. The manufacturers of measuring devices should explicitly state the way to obtain the mathematical expectation of the radiance according to the device's characteristics. If the incident solid angle is large enough to be considered as incoherent, one radiance measurement suffices. The new BRDF definition is then equivalent to the usual one. The user must just be aware of the limitation in terms of angular resolution.

ACKNOWLEDGEMENT

The work reported in this paper was partially funded by project 18SIB03 BxDiff from the EMPIR programme co-financed by the Participating States and from the European Union's Horizon 2020 research and innovation programme.

REFERENCES

- [1] F. Nicodemus, J. Richmond, J. Hsia, I. Ginsberg, T. Limperis, Geometrical considerations and nomenclature for reflectance, US Dept. of Commerce, National Bureau of Standards., US Govt. Print. Off. (1977).
- [2] J.W. Goodman, Speckle Phenomena in Optics: Theory and Applications, ISBN 0 974 7077-9-1, Roberts and Co, Publishers, Englewood (Co), 2007.
- [3] G. Obein, S. Ouarets and G. Ged, "Evaluation of the shape of the specular peak for high glossy surfaces", in Proceedings of the SPIE Proc. SPIE 9018, Measuring, Modeling, and Reproducing Material Appearance, 901805, SPIE, Bellingham, 2014.
- [4] G.T. Georgiev and J.J. Butler "The effect of speckle on BRDF measurements", in Proc. SPIE 5882, Earth Observing Systems X, 588203, SPIE, Bellingham, 2005.
- [5] B.G. Hoover and V.L. Gamiz, Coherence solution for bidirectional reflectance distributions of surfaces with wavelength-scale statistics, J. Opt. Soc. Am. A 23, 314-328, 2006.

A novel optical diffuser with potentially higher spectral flatness in the near infrared region

Hiroshi Shitomi¹ and Shinobu Ito²

¹National Metrology Institute of Japan (NMIJ), AIST, Tsukuba, JAPAN,

² OPTCOM Co., Ltd., Iwata, JAPAN,

Corresponding e-mail address: h-shitomi@aist.go.jp

We have reported a new optical diffuser that has potentially more spectrally neutral than existing optical diffuser in the near infrared region where inherent molecular absorption structure due to water or base material shows strong wavelength dependence that causes big uncertainty. Spectrophotometric comparison has been revealed that the Al₂O₃ optical diffuser processed with plasma powder spraying have relatively flat spectral properties over the entire near infrared region. Basic optical properties of plasma-sprayed Al₂O₃ optical diffuser and its advantage for spectrophotometry has been discussed.

INTRODUCTION

Reflection-type optical diffusers are widely used as a reference material to calibrate various types of spectrophotometers and related instruments. They are also used as key optical components such as the material to finish the surface for an integrating sphere, or an optical target to convert irradiance to radiance. So far, many kinds of optical diffusers are commercially available and their basic reflection properties have been studied in detail.

Recently applications that require accurate spectrophotometry have been extended beyond the visible region where conventional reflection colorimetry is applied. One of the fields that attract attention is the application that makes use of near infrared radiation such as gas analysis, optical communication, remote sensing including LiDAR (Light Detection and Ranging) and non-invasive optical diagnosis. To calibrate a spectrophotometer in the near infrared region for such application, one of the technical issues is that optical diffusers usually show absorption bands mainly due to inherent molecular vibrational structure by water or base material that result in strong wavelength dependence with respect to reflectance and greatly affects the measurement uncertainty.

We have intensively studied a new approach to prepare a material applicable to optical diffuser based on thermal spraying processes, which is one

of the common industrial processes for material coating on metals or ceramics. Main objectives are to improve critical optical properties such as optical durability and mechanical strength. So far, some novel optical diffusers with peculiar optical properties have been developed [1], and among them we have achieved the optical diffuser with more than 50 times UV resistance and around 10 times mechanically stronger surface compared with painted BaSO₄ surface [2]. Further instrumental and process improvement for better optical properties are in progress.

A series of optical characterization for various prototype samples made by thermal spraying has revealed that the optical diffuser made from Al₂O₃ processed with plasma powder spraying shows high spectral flatness especially in the near infrared region compared with existing optical diffusers. In this study, basic infrared optical properties have been examined for plasma-sprayed Al₂O₃ optical diffusers to find out the relationship with material parameters and to discuss their advantage as reflectance standards or material for an integrating sphere used for the measurement in the near infrared region.

EXPERIMENTAL

The plasma-sprayed samples were prepared by use of an apparatus of plasma-sprayed coating for general industrial use such as abrasion-resistant overcoat layer on a metal or a ceramic, as shown in Fig.1. Al₂O₃ powder with reagent grade was

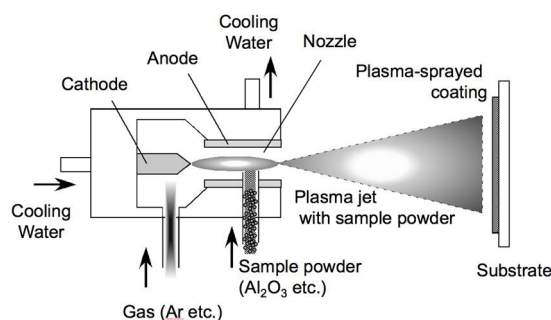


Figure 1. Schematic diagram of the apparatus and the process for plasma powder spraying

installed in the chamber of the plasma-spray apparatus and injected into electrically generated plasma flame based on Ar. The accelerated plasma jet with Al_2O_3 was hit and deposited on 50 mm x 50 mm x 3 mm Al substrate to form diffusing surface. The approximate thickness of the samples onto the substrates was from 0.20 mm to 0.60 mm depending on the spraying condition. The purity of the Al_2O_3 powder used in this study is more than 99.8 %.

For comparison of the reflection properties in the near infrared region, the following optical diffusers used as reflectance standard mainly for colorimetry were prepared.

- Pressed and sintered PTFE (PTFE resin)
- Painted BaSO_4 with polyvinyl alcohol (PVA)
- Pressed BaSO_4
- Matte ceramic tile
- Matte Opal glass

Spectral reflectance of each sample was measured using a calibrated spectrophotometer (Perkin-Elmer Inc., Lambda 900) attached with a 150 mm integrating sphere. The measured wavelength range is from 800 nm to 2500 nm and the measurement geometry is $8^\circ/\text{di}$ and $8^\circ/\text{de}$, respectively.

RESULTS AND DISCUSSION

Fig.2 shows spectral diffuse reflectance of major samples prepared in this study. The measurement geometry is $8^\circ/\text{de}$ geometry. As is clearly observed in Fig.2, plasma-sprayed Al_2O_3 optical diffusers shows spectrally flatten reflection properties over the entire near infrared region (from 800 nm to 2500 nm) with maximum reflectance difference of around 3 %. The spectra of all the other existing optical diffusers show some dips that correspond to the reflection change of 5 % to more than 10 % within

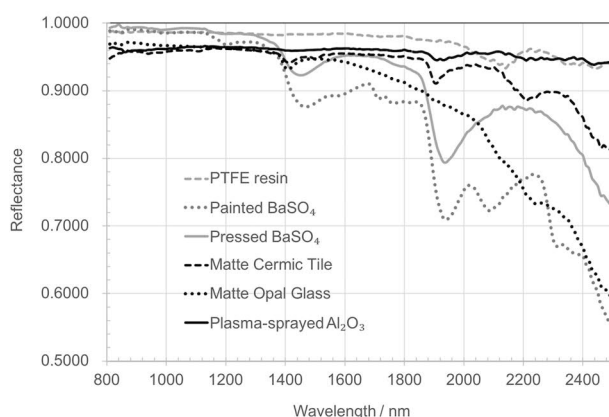


Figure 2. Comparison of spectral diffuse reflectance in $8^\circ/\text{de}$ geometry of the samples used in this study

100 nm bandwidth. For BaSO_4 -based diffusers and the matte ceramic tile, the observed dips would be mainly attributable to the vibrational absorption of water molecule attached within the crack and dent of the diffusing surface. Contribution by crystal water might be another cause. Spectral dips observed for PTFE resin would be attributed to the vibrational absorption by PTFE itself. Matte opal shows much broader spectral dependence that would be caused by translucency increased in proportional to the wavelength.

It can be assumed that the plasma-sprayed Al_2O_3 optical diffuser can also contain water molecule within its surface or as crystal water. However, the spectral analysis in this study showed much less contribution of water for this type of sample, which would be the benefit of plasma-spraying process owing to its high temperature. In addition, controlling the particle size of Al_2O_3 powder during the spraying process is one of the requirements to keep efficiency of the plasma process, which would highly contribute developing relatively uniform and minute surface with less crack and dent.

As was discussed previously [1], when the thickness of the plasma-sprayed Al_2O_3 optical diffusers is not enough, clear wavelength dependence due to the effect of translucency has appeared. The longer the wavelength is, the lower the reflectance becomes. It is found that such translucent effect becomes almost negligible when the coating thickness is beyond 0.40 mm.

CONCLUSION

We have found that the plasma-sprayed Al_2O_3 optical diffuser has better spectral properties especially in terms of spectral flatness in the near infrared region compared with other types of existing optical diffusers. Spectral flatness that would mainly come from the ultra-heating process and uniform surface structure both of which are prominent features of the plasma spraying process.

REFERENCES

1. H. Shitomi *et al.*, Optical properties of Al_2O_3 and $\text{Al}_2\text{O}_3/\text{BaSO}_4$ reflecting diffusers processed with plasma powder spraying, in Proceedings of NEWRAD2011, 138-139, 2011.
2. H. Shitomi *et al.*, Novel BaSO_4 coating for an integrating sphere processed with thermal spraying, in Proceedings of NEWRAD2017, 220-221, 2017

Measurement of far-ultraviolet transmission in hollow-core optical fibers

Dmitry Vorobiev¹, Bartłomiej Winter², Brian Fleming¹, Wesley Gilliam¹, Emily Witt¹, Kristina R. Rusimova², Stephanos Yerolatsitis², Tim A. Birks², and William J. Wadsworth²

¹Laboratory for Atmospheric and Space Physics, Boulder, CO, USA

²Centre for Photonics and Photonic Materials, Department of Physics, University of Bath, Bath, UK

Corresponding e-mail address: dmitry.vorobiev@lasp.colorado.edu

The fabrication of optical fibers for the ultraviolet regime is hindered by the poor transmittance of most optical materials in this spectral range, which is often further degraded by exposure to these highly energetic photons. Hollow-core anti-resonant optical fibers are predicted to achieve much lower losses than those observed in solid core and photonic bandgap fibers. We have measured optical guidance in hollow-core fibers over the spectral range of 120 – 200 nm. These UV hollow-core fibers (UV-HCFs) promise to enable the versatility already afforded by conventional fibers in the visible and infrared regimes.

UV HOLLOW-CORE FIBERS

Hollow-core anti-resonant fibers are made entirely of fused silica and are characterized by a hollow guiding region surrounded by a ring of capillary “resonators”, which are supported by a thick silica cladding (Figure 1). These fibers guide light in spectral regions between high loss locations, which correspond to resonances, m , found at

$$\lambda_m = (2t/m)\sqrt{n^2 - 1}, \quad (1)$$

where t is the capillary wall thickness and n is the refractive index [1].

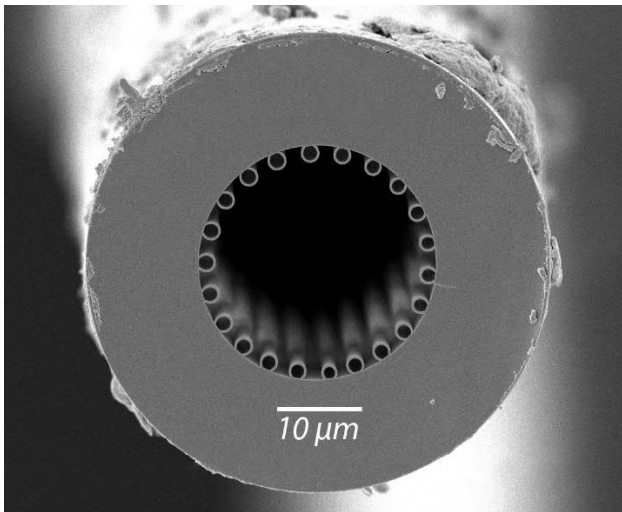


Figure 1. The fibers we fabricated and measured as part of this work are made of fused silica, with a $\sim 25 \mu\text{m}$ diameter guiding region and 22 resonators.

Because the refractive index of silica increases rapidly for $\lambda < 200 \text{ nm}$, the capillaries must be extremely thin. To achieve this thickness, fibers are first fabricated using the stack-and-draw method and then tapered [2] with a draw-down ratio of $\sim 7:1$. The resulting fibers have an OD of $\sim 50 \mu\text{m}$ and a guiding region of $\sim 25 \mu\text{m}$ diameter. This first round of samples had a length of $\sim 20 \text{ cm}$; longer fibers can be made by modifying the tapering rig.

MEASURING FUV FIBER TRANSMISSION

Traditional techniques to measure optical fiber transmission are not easily adopted for the vacuum ultraviolet spectral range, for a number of reasons:

- 1) Conventional fiber launch systems, which employ microscope objectives, cannot be used to couple light into the fibers in a controlled manner. Neither can these fibers be “butt-coupled” to other “source” fibers.
- 2) The relatively short length of the sample fibers used in this experiment makes the cut-back method of determining fiber losses difficult.
- 3) Oxygen strongly absorbs light with $\lambda < 185 \text{ nm}$; this is especially problematic for an experiment employing “free space” optics.

To measure the UV transmission of these fibers, we developed a measurement apparatus (Figure 2) that could be purged with nitrogen, to minimize the transmission losses due to oxygen absorption. In the remainder of this section, we describe our measurement methodology.

First, the sample fiber was cleaved to obtain a clean edge on both ends; the quality of the cleave and the ability of the fiber to guide visible light were verified using a microscope. Next, to remove any air or water vapour from the hollow core and capillaries, the fiber was placed in a vacuum chamber, which was pumped down to $\sim 10^{-5}$ Torr. The chamber was then back-filled with nitrogen and brought up to atmospheric pressure.

Next, the fiber was placed into a v-groove plate on a translation stage, which aligned the output end of the fiber with the entrance slit of an ARC VM-502 UV monochromator. The input end of the fiber was aligned with the output of a deuterium lamp with a MgF_2 window. The lamp output was stopped-down with a 3 mm diameter aperture to produce a $\sim f/25$ outgoing beam; the numerical aperture of these fibers corresponds to a beam of $\sim f/12$; *i.e.* the input beam is well within the fiber's NA. Light from the fiber was dispersed by the monochromator and measured by a photomultiplier tube (PMT) detector. The spectral bandwidth of the outgoing light was $\Delta\lambda \sim 2$ nm.

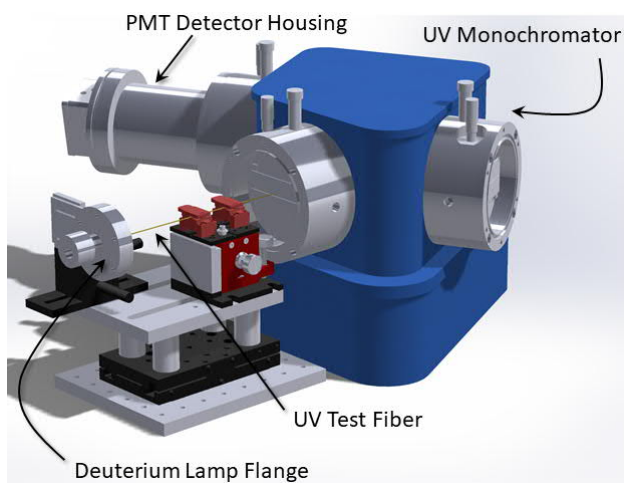


Figure 2. The setup that was used to measure the UV transmission of the hollow-core fibers was designed with an enclosure (not shown here) which allowed us to purge the entire setup with nitrogen.

We took great care to measure any background signal that could be mistaken for light transmitted by the fiber. When the fiber tip was illuminated, it extended ~ 2 mm into the 3 mm aperture. To measure any stray light, we bent the fiber tip out of the aperture and rested it against the aperture plate. In this way, the entire setup was minimally changed, but the fiber tip was moved completely out of the beam.

PERFORMANCE OF UV FIBERS

Due to the complexities associated with working the FUV regime, in this experiment we were unable to perform the cut-back method to quantify the fiber's transmission. Instead, we compared the fiber's throughput to that of a 25 micron pinhole. Using a CCD camera, we measured the divergence of the light beam exiting the pinhole to be $\sim f/60$. Therefore, we are confident that all of the light from the pinhole, and the fiber, was captured by the $f/4$ focusing diffracting

grating of the monochromator and detected by the PMT. The resulting throughput of one of our fibers, normalized to that of a 25 micron diameter pinhole, is shown in Figure 3.

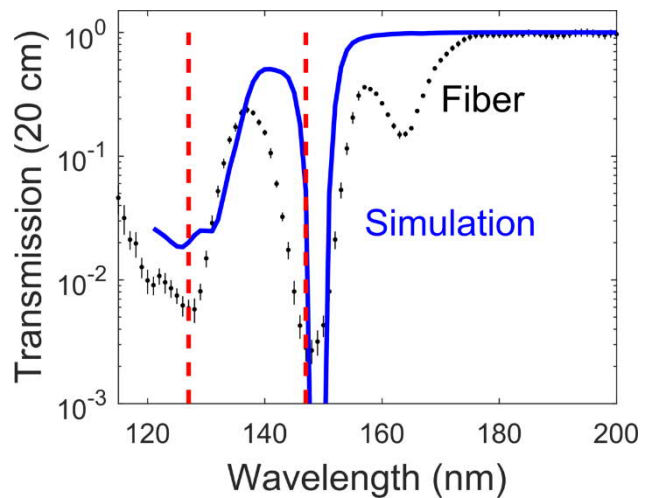


Figure 3. The throughput of the UV hollow-core fiber, with respect to that of a 25 micron diameter pinhole, is shown, along with predictions from a numerical simulation for a fiber with a similar physical structure. The dashed red lines indicate the resonance locations given by Eq. 1.

After the fiber transmission was measured, the shape and thickness of the capillary resonators was determined using scanning electron microscopy. Using the measured structural parameters, we simulated the performance of this fiber using COMSOL Multiphysics. The simulated performance and the measured throughput are similar (Figure 3).

CONCLUSION

We have shown that hollow-core anti-resonant fibers can guide light in the far-UV spectral regime, down to ~ 130 nm, with sufficient throughput to be useful in a wide range of applications. This shatters the current wavelength limit for UV fibers, of ~ 185 nm. Furthermore, the fiber's performance agrees well with results of numerical models and analytic predictions. By tuning the locations of the resonances, it should be possible to fully cover the 100 – 200 nm FUV spectral regime with hollow-core UV fibers.

REFERENCES

1. F. Yu and J. C. Knight, "Negative curvature hollow-core optical fiber," *IEEE J. Sel. Top. Quantum Electron.* 22, 146–155 (2016)
2. S. Leon-Saval, T. Birks, W. Wadsworth, P. S. J. Russell, and M. Mason, "Supercontinuum generation in submicron fibre waveguides," *Optics Express* 12, 2864–2869 (2004).

Improvements to the Ultraviolet Measurement Capabilities of RTS

Catherine C. Cooksey and Thomas Larason

National Institute of Standards and Technology, Gaithersburg, MD, USA

Corresponding e-mail address: catherine.cooksey@nist.gov

We report on recent improvements to performance of NIST's Reference Transmittance Spectrophotometer (RTS) in the ultraviolet (UV) and visible spectral range. The improvements include the installation of a new UV source for increased spectral radiance and a monitor line for reduced signal-to-noise ratio.

INTRODUCTION

The National Institute of Standards and Technology maintains the national scale for regular spectral transmittance through the operation of the Reference Transmittance Spectrophotometer (RTS). The instrument provides the transmittance scale realization and validation for NIST's calibration service for regular spectral transmittance [1] and Standard Reference Materials (SRMs) for spectrophotometry [2,3], respectively, from the ultraviolet to the short-wave infrared (250 nm to 2500 nm).

There has been growing interest in UV measurements, due in part to the wider availability of UV radiation sources, including UV light emitting diodes. RTS originally used a deuterium lamp to provide UV radiation for wavelengths below 350 nm. The deuterium lamp is significantly less stable than the quartz-tungsten-halogen (QTH) incandescent lamp used for longer wavelengths, resulting in UV uncertainties that are an order of magnitude larger in comparison to those in the visible and near-infrared.

LASER-DRIVEN LIGHT SOURCE

To improve performance of RTS in the UV and reduce uncertainties, we procured a high-intensity, laser-driven light source (LDLS) to use in place of the deuterium lamp. The LDLS is a compact, broadband source that uses a continuous wave laser to produce a discharge from a xenon plasma. This discharge provides significantly improved spectral radiance compared to traditional UV lamp sources. Early measurements of the LDLS indicated that signal noise was significant. Consequently, we installed a monitor line.

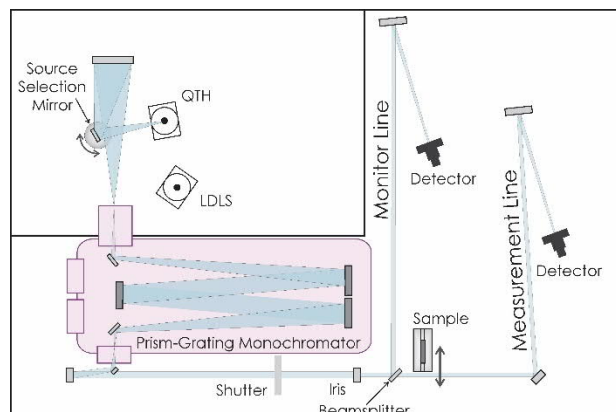


Figure 1. RTS layout, which includes two possible sources, a measurement line, and a monitor line.

SYSTEM LAYOUT

RTS is a custom-built instrument consisting of an illuminator, sample translator, and receiver (Fig. 1). The illuminator generates a nearly monochromatic (3 nm spectral bandwidth), collimated beam. There are two possible radiation sources, a laser-drive light source (LDLS) and a quartz-tungsten-halogen (QTH) incandescent lamp. A rotating mirror selects the appropriate source to be focused onto the entrance slit of a prism-grating monochromator. Upon exiting the monochromator, the beam is collimated by a parabolic mirror.

The sample translator consists of a sample holder mounted on translation stages that have both horizontal and vertical motion. The horizontal motion enables the sample to be moved out of and into the beam path so that both the incident and transmitted flux can be measured. The sample is centered in the beam using both horizontal and vertical motion.

The receiver measures both the incident and transmitted flux. It consists of a shutter, beam splitter, focusing mirrors, and detectors. The shutter is used to collect the dark current. The beam splitter, which is placed ahead of the sample translator, diverts a portion of the beam (30%) to the monitor line where it is focused onto the monitor detector. The remaining portion of the beam is directed through the sample translator to the measurement line where it is focused onto the measurement detector. Both detectors are silicon photodiodes.

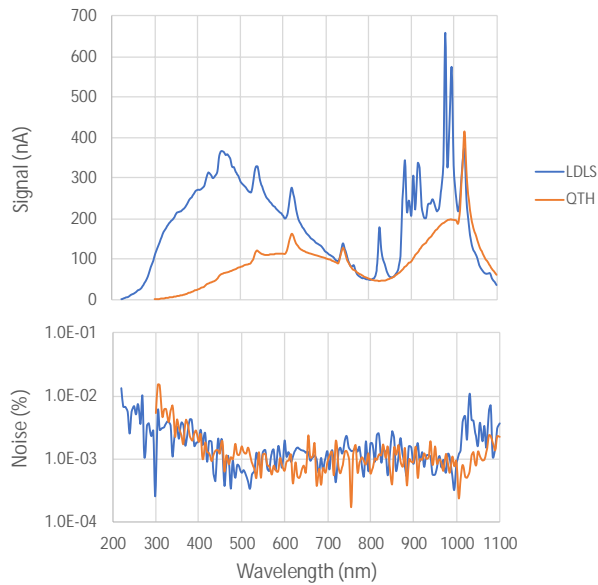


Figure 2. (Top) Signals of the LDLS and QTH sources as measured by the measurement line detector. (Bottom) Noise as a percentage of the signal.

Care was taken to ensure that the conditions for the measurement and monitor lines were nearly equivalent in terms of components and optical dimensions.

INITIAL RESULTS

Fig. 2 shows the signal and noise for the LDLS and QTH sources as measured by the measurement line detector over the spectral of 220 nm to 1100 nm. The LDLS source has 10^2 more signal than the QTH in the UV and most of the visible.

The signal noise is improved by ratioing the signals from the measurement and monitor lines. For both sources, the signal noise (%) is on the order of 10^{-2} for the UV and 10^{-3} for the visible. This represents a significant drop in noise of 2 and 1 orders of magnitude for the LDLS and QTH sources, respectively, for the case with no monitor line (data not shown).

An initial uncertainty budget, which considers contributions from the signals and electronics, was developed for the transmittance measurements. The results for a filter of 0.5 nominal transmittance are provided in Table 1.

The contributions considered in this budget include linearity of the silicon photodiode, accuracy of the digital multimeter, random fluctuations in the voltage measurements, accuracy of the voltage measurements, accuracy of the amplifier gain, and accuracy of the offset voltage for the amplifier.

Table 1. Initial uncertainty budget, which considers contributions from the signals and electronics, for a filter with nominal transmittance of 0.5.

Source	Wavelength (nm)	Rel. Unc. (%) ($k = 1$)
LDLS	300	0.14
	500	0.31
	900	0.17
	1000	0.33
QTH	500	0.013
	900	0.014
	1000	0.059

In general, the largest contributor to the relative uncertainties listed in Table 1 is the random fluctuations in the voltage measurements for the LDLS source; whereas, the largest contributor for the QTH source is the accuracy of the digital multimeter.

FUTURE WORK

Characterization of additional uncertainty components is underway. These components include wavelength accuracy, stability of the signal-to-monitor ratio, out-of-band stray light, and inter-reflections. Also, in progress is validation of transmittance measurements in terms of the measured values.

It is noted that the recent improvements described here do not include any changes to the method for transmittance measurements in the near-infrared and short-wave infrared. These will be implemented in the near future.

REFERENCES

1. D. W. Allen, E. A. Early, B. K. Tsai, C. C. Cooksey, NIST Measurement Services: Regular Spectral Transmittance, NIST Special Publication 250-69, Department of Commerce, Washington, D.C., 2011.
2. R. Mavordineau, R. W. Burke, J. R. Baldwin, M. V. Smith, J. D. Messman, J. D. Travis, J. C. Colbert, Glass filters as a Standard Reference Material for spectrophotometry: Selection, preparation, certification, and use of SRM 930 and SRM 1930, NIST Special Publication 260-116, Department of Commerce, Washington, D.C., 1994.
3. R. Mavordineau, J. R. Baldwin, Metal-on-quartz filters as a Standard Reference Material for spectrophotometry SRM 2031, NIST Special Publication 260-68, Department of Commerce, Washington, D.C., 1980.

Effects of rotation errors on goniometric measurements

Ellie Molloy¹, Peter Saunders¹, Annette Koo¹

¹Measurement Standards Laboratory of New Zealand, Lower Hutt, New Zealand

Corresponding e-mail address: annette.koo@measurement.govt.nz

Goniometric measurements are essential for the determination of many optical quantities. Quantifying the effects of errors in the rotation axes on these quantities is a complex task. In this paper, we show how a measurement model for a four-axis goniometric system can be developed. We then investigate how the uncertainties due to several error sources propagate to the rotation angles and then through to the measurement of bi-directional reflectance.

GONIOMETRIC MEASUREMENTS

Many spectrophotometric and photometric quantities depend critically on the geometry of measurement. The bidirectional reflectance distribution function (BRDF) for materials, for example, is a function of the polar and azimuthal angles of incidence of light, θ_i and ϕ_i , as well as the polar and azimuthal angles of detection of reflected light, θ_d and ϕ_d . Instruments for measurement of BRDF, therefore, must contain four axes to span the parameter space.

Despite the best efforts of the instrument designers, each rotation using these axes will be subject to errors, including:

- displacement of the centres of rotation of the axes;
- misalignment (non-orthogonality) of the axes;
- angular resolution of the axis motors;
- angular accuracy of each axis;
- determining the zero angle of each axis.

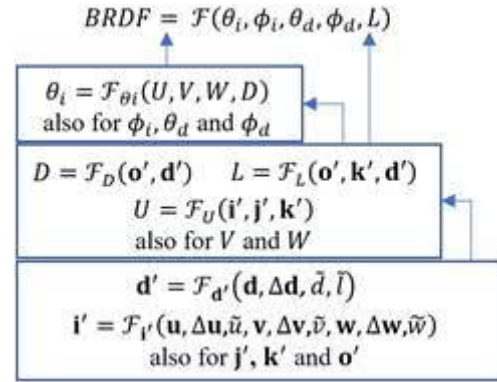
This work describes an approach for assessing the uncertainty of BRDF associated with these errors.

MEASUREMENT MODEL

To capture the effect of various errors on a measured quantity, a measurement model must be constructed. The measurement model expresses the measurand in terms of all input parameters, including the errors (even the errors have been corrected for, and the best estimate is zero, they will carry a standard uncertainty through the equations). The measurement equation should account for the components of the system that define the axes – for example in the MSL system, the z-axis is defined by the incident beam and, therefore, there is no uncertainty in the alignment of this beam, but rather in all other axes relative to it.

If the rotations are controlled in a coordinate system different to that of the measurand, the transformations between coordinate systems are part of the measurement model. For example, at MSL the angle of a detector, D , is set on a slew ring and the sample placed on orthogonal axes rotating about lab x-, y- and z-axes by angles U , V and W . However, BRDF is generally defined in θ_i , ϕ_i , θ_d , ϕ_d space.

The measurement equation(s) therefore consist, in MSL's case, of the following, considering only the parameters relating to the four rotation axes:



Here: L and \tilde{L} are the true and measured distances from the sample to the detector; d is the measured value of D ; \mathbf{d} and $\Delta \mathbf{d}$ define the slope of the detector axis and its displacement from the origin; \mathbf{i}' , \mathbf{j}' , and \mathbf{k}' are rotated basis vectors and \mathbf{o}' is origin rotated by angles \tilde{u} , \tilde{v} and \tilde{w} about the axes defined by the vectors \mathbf{u} , \mathbf{v} and \mathbf{w} displaced by $\Delta \mathbf{u}$, $\Delta \mathbf{v}$ and $\Delta \mathbf{w}$ respectively. The axis vectors and displacements are given by (for example):

$$\Delta \mathbf{w} = [E_{\Delta W_x}, E_{\Delta W_y}, 0] \quad \mathbf{w} = \mathbf{k} - [E_{W_x}, E_{W_y}, 0],$$

where the $E_{\Delta W}$ are displacement errors and the E_W are misalignment errors. These errors are assumed to be distributed with zero mean. The angles of rotation about these axes are given (for example) by:

$$\tilde{w} = w - E_{W_resolution} - E_{W_accuracy} - E_{W_zero}.$$

Here, w is the measured angle to which the axis is set and the E_W are the last three errors identified in the bullet points in the previous section.

The uncertainties associated with the five errors identified have been included in the measurement model and can be propagated through the coordinate systems to the BRDF. The forms of the functions given above can be found in the literature (e.g., [1]

for the transformation from $UVWD$ to $\theta_i \phi_i \theta_d \phi_d$. The position of a point \mathbf{a} (expressed as a vector) after rotation about a displaced and misaligned axis is:

$$\mathbf{a}' = \mathbf{R}(\hat{\mathbf{w}}, \tilde{w})(\mathbf{a} - \Delta\mathbf{w}) + \Delta\mathbf{w},$$

where $\mathbf{R}(\hat{\mathbf{w}}, \tilde{w})$ is the rotation matrix for an angle \tilde{w} about the vector $\hat{\mathbf{w}}$ (\mathbf{w} normalised to unit length). To rotate the basis vectors, each end of the vector (the origin and the tip of the vector) should be rotated and their difference found. If the sample is on a three-axis stage, the rotation about the respective axes are carried out sequentially, and in an order that depends on the specifics of the system being used.

ERROR PROPAGATION

Three methods of error propagation through the measurement equations have been used and compared. Firstly, distributions have been assigned to each of the sources of error and Monte Carlo simulations have been carried out by drawing samples from those distributions and calculating the standard deviation of the results. Secondly, the sensitivity coefficients of the outputs on the error contributions (e.g., $\partial\theta_i/\partial E_{w_x}$) have been evaluated analytically and the GUM [2] methods used to propagate the uncertainties. Thirdly, the GTC [3] Python tool for the automatic propagation of uncertainty, has been used. It was found that all three methods produced the same propagated uncertainties. However, GTC was the most straightforward to use and delivers correlations between quantities (e.g., $u(\theta_i, \phi_i)$) without any additional effort.

Figure 1 shows the standard uncertainty in θ_i , ϕ_i , θ_d and ϕ_d as a function of the ν angle when u is 30° , w is 0° and d is 30° . The standard uncertainty associated with each displacement is 0.02 % of the radius of the system, with each misalignment is 0.06° and with each accuracy is 0.05° . The resolution and zero position errors are negligible.

BRDF AND TOTAL REFLECTANCE

Of more interest is the contribution of rotation errors on the final measurand: the BRDF or the integrated BRDF if, for example, total hemispherical reflectance is required. As a simple example, the uncertainty in BRDF of a Lambertian material measured in $0^\circ:x^\circ$ and in $x^\circ, 180^\circ:45^\circ, 0^\circ$ geometries is shown in Fig. 2.

In the $0^\circ:x^\circ$ data we can see that propagated uncertainties increase with the sensitivity to θ_d (the uncertainty of which is found to be primarily due to the accuracy errors in the \mathbf{v} and \mathbf{d} axes). In the

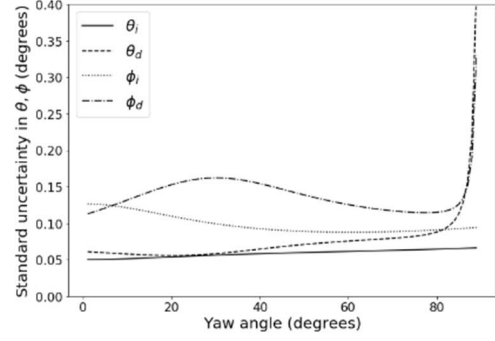


Figure 1. Standard uncertainties of θ_i , ϕ_i , θ_d and ϕ_d as a function of the ν angle when the rotation uncertainties are as given in the text.

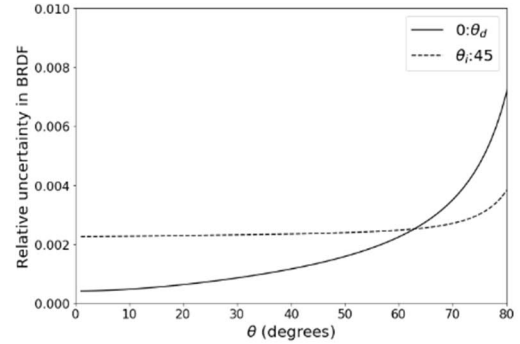


Figure 2. Standard uncertainties in the BRDF of Lambertian material measured in $0^\circ:x^\circ$ and in $x^\circ, 180^\circ:45^\circ, 0^\circ$ geometries.

$x^\circ, 180^\circ:45^\circ, 0^\circ$ data, on the other hand, where θ_d is fixed, the uncertainty is constant across most of the range and is dominated by the uncertainty in L induced by the misalignment of the \mathbf{w} axis under a 180° rotation.

If integrating, then covariances between the BRDF measured at one angle and that measured at another angle must be known for a robust estimate of the uncertainty. In this case, the intrinsic nature of the GTC package becomes invaluable as these are taken account of with no extra effort by the analyst. For example, when calculating the total reflectance of a Lambertian sample, the uncertainty is 0.06 %, dominated again by the uncertainty in L but this time induced by the uncertainty in displacement of the \mathbf{d} axis.

REFERENCES

1. T. Germer and C. Asmail, Goniometric optical scatter instrument for out-of-plane ellipsometry measurements, Rev. Sci. Instrum., 70, 3688, 1999.
2. JCGM, JCGM 100:2008, Evaluation of measurement data – Guide to the expression of uncertainty in measurement, BIPM, 2008.
3. B. D. Hall, Object-oriented software for evaluating measurement uncertainty, Measurement Science and Technology, 24, 055004, 2013.

Production and Characterization of Optics and Coatings with Extremely Low Losses and High Reflectivity

Ramin Lalezari and Howard Champoux

FiveNine Optics, Inc., Boulder CO

Corresponding e-mail address: ramin@fivenineoptics.com, howard@fivenineoptics.com

Low loss optics have been produced for several decades and used in a variety of applications including inertial navigation, gravitational wave detection, precision spectroscopy, atomic clocks and high power and high energy lasers. Ion beam sputtered coatings on super polished substrates allow for the realization of extremely low levels of absorption and scatter (in the range of a few parts per million) in the visible and near infrared portion of the spectrum.

ION BEAM SPUTTERED OPTICAL COATINGS

Ion beam sputtering is a physical vapor deposition where a beam of ions is accelerated electrically to impinge on a target of high purity material causing molecules of the material to be sputtered from the target and deposited on a substrate. The process was developed and patented in the early 1970s by David Wei and Anthony Lauderback [1].

In the 1970s and 1980s the process was used primarily by the manufacturers of ring laser gyroscopes for its ability to produce dielectric mirrors with very low levels of scatter. The very low deposition rates of the early equipment and the cost and difficulty of use of the deposition equipment prevented early broad proliferation of the process. By the mid 1990s the advent of wavelength division multiplexing and the enormous investment in fiber-optics telecommunications industry drove the commercialization of ion beam sputtering and its broader use in the manufacture of optical coatings. The availability of low loss optical coatings have enabled a number of scientific, industrial, and military applications. Gravitational wave detection, development of atomic clocks, the development of laser weapons, and a variety of spectroscopy applications are all enabled by low loss optical coatings and mirrors. Mirror coatings with losses of less than 10 ppm are routinely produced with current ion beam sputtering technology.

SUPER POLISHED SUBSTRATES

Realization of low scatter optical coatings requires substrates with very low roughness in optical spatial frequencies [2]. Polishing techniques and instrumentation for evaluating the substrates were also developed in the 1970s and 1980s by the inertial navigation industries and continue to benefit from materials development in the semiconductor industry. Today substrates with less than 1 angstrom rms roughness for optical spatial frequencies suitable for supporting mirrors with less than 1 ppm of scatter are commercially and broadly available.

DESIGN CONSIDERATIONS AND CHARACTERISTICS OF LOW LOSS MIRRORS AND OPTICS.

Manufacturing technologies and performance characteristics of optics with PPM levels of loss will be presented. Design considerations for applications such as photon pressure power meters, and other large low loss mirrors as well as stress [3], polarization, and laser damage threshold issues will be discussed.

REFERENCES

1. D. Wei and A. Louderback , US Patent # 4,142,958 "Method for Fabricating Multilayer Optical Coatings", 1979
2. J. M. Bennett and L. Mattsson, "Introduction to Surface Roughness and Scattering" (Optical Society of America, Washington DC, 1989)
3. Stoney G, "The tension of metallic films deposited by electrolysis", Proc. Royal Soc. London, A82 (1909) 172

Determining Optical Constants in the VUV Range: Combining Ellipsometry and Angle-Resolved Reflectometry

Alexander Gottwald¹, Hendrik Kaser¹, Johannes Falkenburg², Norbert Esser^{2,3}

¹*Physikalisch-Technische Bundesanstalt, Berlin, Germany*

²*Leibniz Institut für Analytische Wissenschaften e.V. (ISAS), Berlin, Germany*

³*Technische Universität Berlin, Berlin, Germany*

Corresponding e-mail address: alexander.gottwald@ptb.de

The measurement of optical constants of thin films in the vacuum ultraviolet spectral range can be regarded to be challenging. Not only the experimental determination is difficult, but also the dependence of the results on the sample preparation. Thus, available data are scarce and mostly without reliable uncertainties. We present an approach for a sound measurement of n and k by combining two independent methods.

INTRODUCTION

Results from measurements of optical constants (i.e. the refractive index n and the extinction coefficient k) in the vacuum-ultraviolet spectral range (VUV) between 10 nm and 200 nm) can be found in literature, using different methods like e.g. transmission measurements and Kramers-Kronig analysis. Most of these reported values do not come with reliable (i.e.: traceable in the sense of metrology) uncertainties. Moreover, different methods seem to produce deviating results, or the values significantly depend on the individual sample preparation which makes it difficult or even impossible to systematically compare the results. The complexity in creating experimental data arise from the combination of high demanding surface preparation and measurement conditions from ultra-clean vacuum surrounding to the need for a tuneable VUV radiation source what usually requires the use of monochromatized synchrotron radiation.

METHOD

Basically, reflectometry and ellipsometry are both based on the measurement of the radiation reflected from the surface under investigation. They are complementary in the sense that reflectometry measures the change of the amplitude whereas ellipsometry measures the phase shift of the radiation when reflected at a surface. For both methods, the resulting quantities (n , k) must be determined numerically from the measured information.

Our measurements were conducted at PTB's Metrology Light Source. For the reflectometry measurements a goniometer-based vacuum set-up is available [1]. It allows the angle of incidence and reflectance to be independently selected and also to rotate the plane of reflection to account for the polarization. We used the VUV ellipsometer from the Leibniz Institute for Analytical Sciences (ISAS) by which amplitude and phase of the reflected radiation can be determined [2]. From the measured data the results for n and k were obtained pointwise by the Transfer-Matrix-Method and application of the Particle Swarm Optimization to find the best fit. The uncertainty was analyzed by help of a Markov Chain Monte Carlo method.

RESULTS

We developed the method on the example of a TiO₂ thin film (on a Si surface) for which optical constants in the wavelength range from 130 nm to 230 nm were determined [3]. Our focus lay on the comparison of the methods, and validation of the results. We found that the resulting values strongly depend on model parameters like e.g. film thickness. This indicated that a multi-method approach will help to improve the results by independently determining system parameters. Although currently ellipsometry tends to have large uncertainties than reflectometry, it is extremely useful in regions where the values for the reflected amplitudes get very small.

REFERENCES

1. A. Gottwald et al., Determination of B₄C optical constants by angle-dependent reflectance measurement for 40 nm to 80 nm wavelength, *Appl. Opt.* **56**, 5768, 2017
2. M. D. Neumann et al., A synchrotron-radiation-based variable angle ellipsometer for the visible to vacuum ultraviolet spectral range, *Rev. Sci. Instrum.* **85**, 055117, 2014
3. A. Gottwald et al., Validation of thin film TiO₂ optical constants by reflectometry and ellipsometry in the VUV spectral range, *Meas. Sci. Technol.* **30**, 2019

On-Site Measurements of Reflection Characteristics of a Dry Asphalt Road

Shau-Wei Hsu, Cheng-Hsien Chen, Kuei-Neng Wu and Shao-Tang Hung

Center for Measurement Standards, Industrial Technology Research Institute, Hsinchu, Taiwan

Corresponding e-mail address: SWHsu@itri.org.tw

On-site measurements of luminance images as well as illuminance distribution for the studies of reflected properties of a LED lighted dry asphalt road have been performed. The relatively more practical luminance coefficient of this old curved road was obtained from high observation angles. The luminance coefficient can be simply fitted with quadratic equation of angle between the incident and the observation directions.

1. INTRODUCTION

The luminance (L) from a road surface is a function of the illuminance (E) on the road and the reflection characteristics, which depend on the nature of the surface and physical state. Luminance on a point depends on the illuminance incidence angle (ϵ), deviation angle (β), and observation angle (α). The reduced luminance coefficients (r -table) and average luminance coefficient are standardised into different classes for dry and wet conditions [1]. It is convenient for an engineer to simulate the performance of a lighted road.

However, the use of r -tables are limited to some constraint such as low observation angle ($0.5^\circ < \alpha < 2^\circ$), straight road, known material and physical state. The reflection characteristics for an in-service road may not so ideally for the visual experience of a driver. To improve this disadvantage, this work demonstrates on-site measurements of reflected luminance images of a curved road at various observation distance. These luminance images as well as illuminance distribution were analysed and converted to luminance coefficient ($q = L/E$), which is functions of β , ϵ , and α . These results and procedures would get relatively more physical properties for safety road lighting design.

2. EXPERIMENTS

The measurements were carried out on a 2-lane dry asphalt road at southern Taiwan. A LED luminaire was mounted on a lighting pole at roadside. The height of the luminaire and width of lane are 10 m and 3.8 m, respectively. The luminance images of road was measured with a calibrated image luminance measuring device (ILMD) with 10-22 mm focal

length. The distribution of horizontal illuminance was automatically measured with commercial lux-meters on a cart [2-4].

The ILMD was placed at distance of $D+10$ m ($D = 2, 4, 6, 8$ and 10 m) from the lighting pole, and the height of the ILMD is 1.5 m. Typical luminance images are shown in Fig. 1, where the region of interest (ROI, green circles) are selected according to CIE-140 [5]. The notations W and S are the transverse and longitudinal distances of a ROI, respectively.

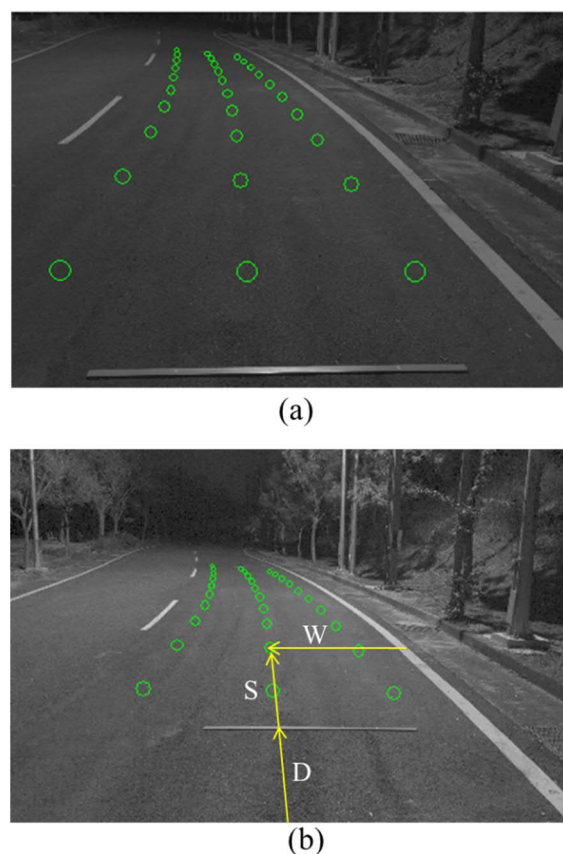
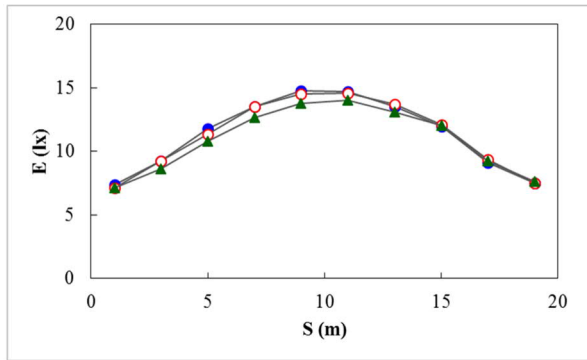


Figure 1. Luminance Images at $D =$ (a) 2 m, and (b) 4 m. The green circles are the ROI for analyzation.

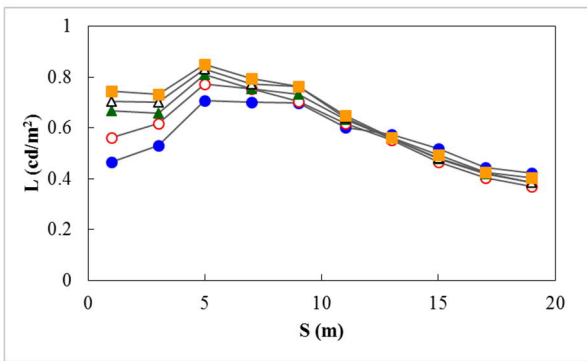
3. RESULTS AND DISCUSSIONS

The horizontal illuminance as a function of S is shown in Fig. 2(a), where the filled circles, empty circles, and filled triangles are corresponding to $W = 0.62, 1.88$, and 3.13 m, respectively. The luminance at $W = 1.88$ m as a function of D is shown in Fig. 2(b), where the filled circles, empty circles, filled triangles,

empty triangles, and filled squares are corresponding to $D = 2, 4, 6, 8$, and 10 m, respectively.

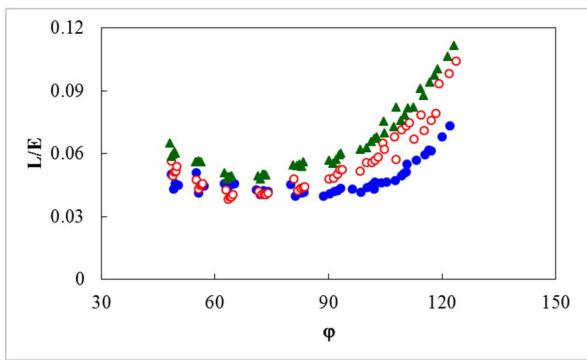


(a)

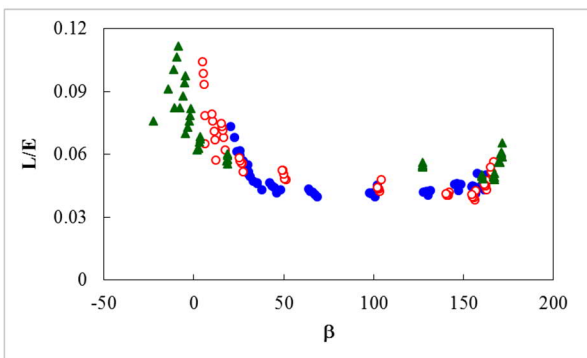


(b)

Figure 2. (a) Horizontal illuminance as a function of S ; (b) luminance at $W = 1.88$ m as a function of D .



(a)



(b)

Figure 3. Luminance coefficient q as functions of ϕ (a), and β (b).

The above data were used to calculate the luminance coefficient q . Furthermore, the angles β , ε , and α can be calculated from D , S , and W with the angular relationships for luminaire, observer and point of observation [5]. The measured angles ε and α are ranged between 2° to 27° , and 10° to 43° , respectively. The angle (ϕ) between the incident and the observation directions was calculated with the following equation:

$$\cos\phi = \cos\varepsilon \cdot \sin\alpha - \cos\beta \cdot \sin\varepsilon \cdot \cos\alpha \quad (1)$$

The luminance coefficient q as a function of ϕ and β is shown in Fig. 3, where the filled circles, empty circles, and filled triangles are corresponding to $W = 0.62, 1.88$, and 3.13 m, respectively. These data can be fitted with the following equation:

$$q = a(\phi - \phi_0)^2 + b(\beta - \beta_0)^2 + q_0 \quad (2)$$

Corresponding parameters are listed in Table 1. It is observed that these parameters is dependent on W , and may be originated from the long-time and uneven wearing by vehicles on this old curved road.

Table 1. Fitted parameters between q and ϕ , β .

$W(m)$	$a(\times 10^{-5})$	$b(\times 10^{-6})$	ϕ_0	β_0	q_0
0.62	1.59	-1.08	59.3	214.1	0.0482
1.88	2.58	-1.16	74.0	91.1	0.0429
3.13	2.43	-0.44	71.3	111.6	0.0507

It is expected that this on-site measuring and analysing method can be applied to other roads with various pavements, physical properties, luminaires, and observation directions. Practical luminance coefficient would be obtained for further design or improvement of illumination of an existing road.

REFERENCES

1. CIE 144: 2001: Road surface and road marking reflection characteristics. Vienna: CIE, 2001.
2. CIE 194: 2011: On site measurement of the photometric properties of road and tunnel lighting. Vienna: CIE, 2011.
3. S.W. Hsu, K.N. Wu and S.T. Hung, Performance of LED road lightings studied by detailed in-field measurements with various devices. Proceedings of CIE2015.
4. S.W. Hsu, Chen, C.S. Chen and Y.D. Jiaan, Measurements of UGR of LED light by a DSLR colorimeter, SPIE Optical Engineering + Applications, 848415, 2012.
5. CIE 140: 2000: Road lighting calculations. Vienna: CIE, 2000.

Temperature and Pressure Dependence of the Reflectivity of Vertically Aligned NanoTube Arrays

Martin Dury¹, Nicole George¹ and Nigel Fox¹

¹ National Physical Laboratory (NPL), Teddington, United Kingdom

Corresponding e-mail address: martin.dury@npl.co.uk

The very high absorptivity of Vertically Aligned NanoTube Arrays (VANTA) coatings makes them desirable for primary radiometry. While their reflectivity is typically measured at ambient temperatures and atmospheric pressures, when applied in cryogenic radiometry they are cooled to very low temperatures and very low pressures. It is therefore essential that the reflectance of VANTA does not increase with decreasing temperature such that the change in cavity reflectance becomes a dominant measurement uncertainty. This paper reports preliminary measurements showing a <13 % increase in reflectivity at 633 nm between room and cryogenic operating temperatures for a VANTA coating applied to a copper substrate. Such a change in coating reflectance approximates to a change in cavity reflectance of 3 ppm for a typical NPL cryogenic radiometer cavity.

INTRODUCTION

The reflectance of VANTA is known to be very low across the spectral range from visible to infrared wavelengths [1–8], and is usually measured at ambient temperatures and at atmospheric pressures. The very high absorptance properties of VANTA therefore make it an attractive material for use in primary radiometry, particularly in cryogenic radiometry [9]. As the detectors in cryogenic radiometers are typically cooled to temperatures within the range from 14 K to 80 K and are operated at pressures of the 10^{-7} mbar level, it is important that the reflectance of VANTA coatings does not increase significantly, leading to it becoming a dominant measurement uncertainty. The target cavity reflectivity for NPL cryogenic radiometers is $\rho < 30$ ppm [10].

NPL is currently developing primary radiometry for the Traceable Radiometry Underpinning Terrestrial- and Helio- Studies (TRUTHS) mission [10]. This mission aims to provide a means of calibrating Earth Observation (EO)

satellites through the measurement of reference targets. For the mission to be a success it is essential that the behaviour of VANTA coatings is well characterised for use in space environments. This paper describes an investigation to simulate the space environment that will be endured by the VANTA coatings used in the detector cavities for the TRUTHS mission, through characterisation of their temperature and pressure dependence on reflectivity.

EXPERIMENTAL SETUP

A variable cryostat was used to measure the temperature and pressure dependence of the reflectance of VANTA. Figure 1 presents a schematic of the experimental setup. The cryostat was modified such that a VANTA coated copper sample plate could be mounted within. A 25 mm diameter integrating sphere was attached in front of the VANTA sample. This admitted light from a HeNe 633 nm laser through the window at the front of the cryostat and through the sphere's front port onto the sample via an additional port at the back. A silicon photodiode mounted to a side port on the sphere monitors the amount of reflected hemispherical radiation. A beamsplitter and additional photodiode outside of the cryostat measured the optical power stability of the laser beam, allowing for the correction in optical input power variations.

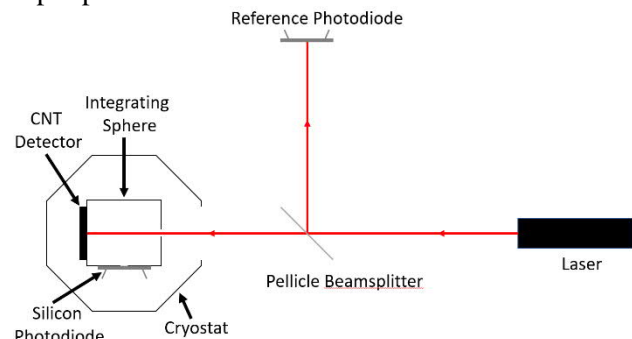


Figure 1 Schematic of the experimental setup.

Variations in the performance of the integrating sphere and the silicon photodiode due to the changes in temperature and pressure were accounted for. To evaluate potential changes in the setup, the

integrating sphere was oriented such that the first reflection of the laser beam was from its internal barium sulphate coating. First the change with pressure was measured: the turbo pump was switched on and the signal from the sphere mounted photodiode was monitored as the pressure dropped to its lowest level at room temperature. The cryostat was then cooled to cryogenic temperatures and the signal from sphere mounted photodiode recorded as cryo-pumping was achieved.

RESULTS

The temperature dependence of the optical setup was measured to be less than $\pm 1.5\%$ over the temperature range of interest. This small percentage has such a negligible effect on the results of this study it is accounted for as a measurement uncertainty.

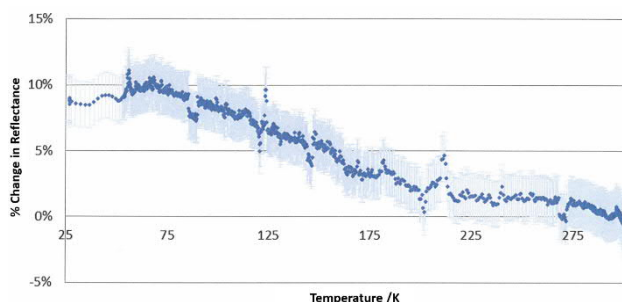


Figure 2 Preliminary data showing temperature dependence of reflectivity of the VANTA sample. Error bars (95% confidence) account for temperature dependence of setup.

Figure 2 shows preliminary data for the temperature dependence of the VANTA sample, which has been corrected for drift in laser power. The data suggest that the reflectivity of VANTA (at 633 nm) increases by $<13\%$ between room and cryogenic operating temperatures.

CONCLUSIONS

The low spectral reflectance of VANTA coatings makes them attractive for use in cryogenic radiometer detecting cavities. Reflectance measurements are typically performed at ambient temperatures and at atmospheric pressures. As cryogenic radiometers operate at near absolute zero temperatures and almost vacuum pressures it is important that the reflectivity of VANTA does not increase significantly when operating under these conditions.

Preliminary measurements of VANTA applied to a copper substrate suggest that the reflectivity of VANTA (at 633 nm) increases by $<13\%$ between room and cryogenic operating temperatures, which

represents a change in cavity reflectance of approximately 3 ppm for a typical NPL cryogenic radiometer cavity. The effect would need to be 30 times greater to become a dominating uncertainty in cryogenic radiometer measurements.

This study is currently limited to a single wavelength. Further work investigating the change in reflectivity at different wavelengths from UV to NIR range and with decreasing pressure are to be reported at NEWRAD 2020.

ACKNOWLEDGEMENTS

The authors wish to acknowledge the work of Rainer Winkler who performed initial NPL investigations into the reflectance properties of VANTA.

REFERENCES

1. Yang ZP, Ci L, Bur JA, Lin SY, Ajayan PM. Experimental observation of an extremely dark material made by a low-density nanotube array. *Nano Lett.* 2008;8(2):446–51.
2. Mizuno K, Ishii J, Kishida H, Hayamizu Y, Yasuda S, Futaba DN, et al. A black body absorber from vertically aligned single-walled carbon nanotubes. *Proc Natl Acad Sci U S A.* 2009;
3. Quijada MA, Hagopian JG, Getty S, Kinzer, Jr. RE, Wollack EJ. Hemispherical reflectance and emittance properties of carbon nanotubes coatings at infrared wavelengths. In: *Cryogenic Optical Systems and Instruments XIII.* 2011.
4. Yang ZP, Hsieh ML, Bur JA, Ci L, Hanssen LM, Wilthan B, et al. Experimental observation of extremely weak optical scattering from an interlocking carbon nanotube array. *Appl Opt.* 2011;
5. Theocharous E, Deshpande R, Dillon AC, Lehman J. Evaluation of a pyroelectric detector with a carbon multiwalled nanotube black coating in the infrared. *Appl Opt.* 2006;
6. Theocharous SP, Theocharous E, Lehman JH. The evaluation of the performance of two pyroelectric detectors with vertically aligned multi-walled carbon nanotube coatings. *Infrared Phys Technol.* 2012;
7. Chunnillall CJ, Lehman JH, Theocharous E, Sanders A. Infrared hemispherical reflectance of carbon nanotube mats and arrays in the 5–50 μm wavelength region. *Carbon.* 2012.
8. Lehman JH, Lee B, Grossman EN. Far infrared thermal detectors for laser radiometry using a carbon nanotube array. *Appl Opt.* 2011;
9. Tomlin NA, Lehman JH. Carbon nanotube electrical-substitution cryogenic radiometer: initial results. *Opt Lett.* 2013;
10. Winkler R. Cryogenic Solar Absolute Radiometer A potential SI standard for Solar Irradiance. University College London; 2012.
11. TRUTHS - NPL [Internet]. [cited 2020 Jan 21]. from: <https://www.npl.co.uk/earth-observation/truths>

Quantum Yield in Induced Junction Silicon Photodiodes at Wavelengths around 400 nm

Lutz Werner¹, Ulrike Linke¹, Ingmar Mueller¹, Toomas Kübarsepp², Trinh Tran³ and Jarle Gran³,

¹Physikalisch-Technische Bundesanstalt, Berlin, Germany, ²Metroserf, Tallinn, Estonia, ³Justervesenet, Kjeller, Norway,
Corresponding e-mail address: lutz.werner@ptb.de

The quantum yield in induced junction photodiodes has been measured. The results show that the quantum yield can be larger than unity at wavelengths longer than 400 nm. This observation has to be considered when applying spectral responsivity models which usually assume a quantum yield of exactly unity.

INTRODUCTION

The quantum yield $y(\lambda)$ is defined as the ratio of the number of generated electron-hole pairs and the number of absorbed photons in a semiconductor photodiode. It is one of the quantities determining the spectral responsivity $R(\lambda)$ of a photodiode which is defined as the ratio of the photocurrent and the incident radiant power generating this photocurrent. Thus, the knowledge of the quantum yield is necessary to model the spectral responsivity.

The quantum yield equals unity if the energy of the absorbed photon is between one and two times the band gap energy E_g . For silicon photodiodes with a band gap energy of 1.12 eV this is the wavelength range from about 550 nm to 1100 nm.

The quantum yield can exceed unity if one of the generated charge carriers, the electron or the hole, has enough energy to create a second electron-hole pair via impact ionisation. For this, the photon energy must exceed $2E_g$. However, because of the requirement of simultaneous energy and momentum conservation in combination with the band structure of silicon, a quantum yield above unity occurs only for photon energies much larger than $2E_g$. The longest wavelength at which a quantum yield above unity has been derived for silicon from experimental data varies between 365 nm and 415 nm [1 - 3].

At high photon energies above 12.4 eV, which corresponds to wavelengths shorter than 100 nm, the quantum yield in silicon seems to be proportional to the energy of the absorbed photon [4].

Models of the quantum yield suffer from free parameters [3, 5] and accurate experimental data and are far away from being applicable at the 100 ppm level. This is crucial for the attempt to establish a new primary detector standard for radiant power

measurements, called predictable quantum efficient detector (PQED) [6, 7], which is based on specially designed silicon photodiodes with predicted spectral responsivity.

In the following, the determination of the quantum yield in silicon is described to identify the wavelength range where the assumption $y(\lambda) = 1$ holds and can be used in the spectral responsivity prediction.

QUANTUM YIELD DETERMINATION

The external quantum efficiency of a semiconductor photodiode is given by

$$Q(\lambda) = (1 - \rho(\lambda))y(\lambda)(1 - \delta(\lambda)) \quad (1)$$

The parameters $\rho(\lambda)$ and $\delta(\lambda)$ describe the external losses due to the reflectance of the photodiode detector and the internal losses due to recombination of charge carriers generated by the incident photons, respectively. Equation (1) can be rearranged for the determination of the quantum yield:

$$y(\lambda) = Q(\lambda)(1 + \rho(\lambda) + \delta(\lambda)) \quad (2)$$

Here, it is assumed $\rho(\lambda) \ll 1$ and $\delta(\lambda) \ll 1$.

$Q(\lambda)$ can be calculated from the measured spectral responsivity $R(\lambda)$ via

$$Q(\lambda) = R(\lambda) / \left(\frac{e\lambda}{hc} \right) \quad (3)$$

where e is the elementary charge, h is the Planck constant, c is the speed of light in vacuum and λ is the vacuum wavelength.

The external losses $\rho(\lambda)$ can be measured or calculated. An experimental determination of the internal losses $\delta(\lambda)$ at wavelengths where the quantum yield $y(\lambda)$ is unknown is difficult as an experimental separation between both is not possible. Thus, $\delta(\lambda)$ must either be calculated or extrapolated from a wavelength region where the quantum yield is known to be equal unity. For both options, a model is required to obtain an estimation of the internal losses with sufficiently low uncertainty.

The PQED [6, 7], constructed from two induced junction silicon photodiodes arranged in a wedge trap configuration, is a good candidate for the experimental determination of the quantum yield.

The windowless photodiodes have a 230 nm thick silicon dioxide layer and were manufactured in the second processing round of the iMera Plus JRP “q-Candela”. The angle between the photodiodes is 11.25° yielding 9 reflections of an incoming laser beam if the PQED is aligned so that the reflected beam and the incident one are colinear.

The external losses of the PQED due to reflectance are small, can be measured and calculated by using the thickness of the silicon dioxide passivation layer on top of the silicon substrate and the optical constants of silicon and silicon dioxide. Also, the internal losses are small being widely studied experimentally and described by a one-dimensional, as well as, by using a more sophisticated three-dimensional theoretical model [8, 9].

MEASUREMENTS AND RESULTS

The spectral responsivity of the PQED described above was measured in the wavelength range from 360 nm to 531 nm for p-polarised laser radiation. The measurements were performed at the laser-based cryogenic radiometer facility of PTB. The facility is equipped with a common Brewster window which means that cryogenic radiometer and PQED under test are irradiated through the same window. Thus, the correction for and the uncertainty contribution from the Brewster window transmittance can be avoided. The detector cavity of the cryogenic radiometer and the PQED are equipped with input apertures with the same diameter of 7 mm and were irradiated at the same position with respect to the laser beam. Thus, the uncertainty contribution arising from the scattered radiation around the laser beam is drastically reduced. A relative standard uncertainty of spectral

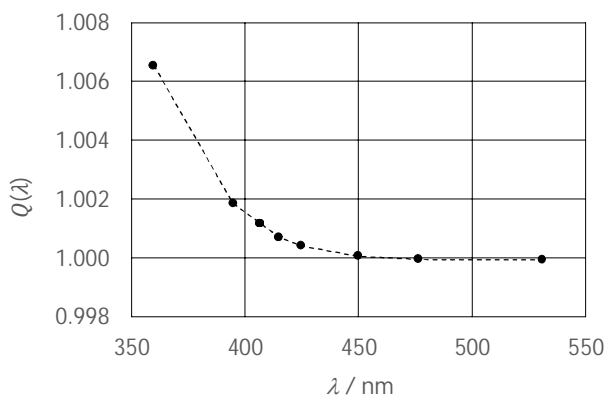


Figure 1. External quantum efficiency of a PQED for p-polarised laser radiation.

responsivity between 25 ppm and 45 ppm has been achieved.

In Fig. 1, the preliminary external quantum efficiency calculated from the measured spectral responsivity according to equation (3) is shown. According to equation (2) $y(\lambda) \geq Q(\lambda)$ and, thus, Fig. (1) indicates that, even without the knowledge of $\rho(\lambda)$ and $\delta(\lambda)$, the quantum yield is significantly larger than unity at wavelengths shorter or equal about 425 nm.

The quantum yield will be derived according to equation (2) and considering both, calculated $\rho(\lambda)$ and modelled $\rho(\lambda)$.

CONCLUSIONS

The results show that the quantum yield can be larger than unity even at wavelengths significant longer than 400 nm. This must be considered when applying spectral responsivity models which usually assume a quantum yield of unity in this wavelength range. Further measurements should be done to investigate the artefact dependence of the quantum yield.

ACKNOWLEDGMENT

The project leading to this study has received funding from the EMPIR programme co-financed by the Participating States and from the European Union’s Horizon 2020 research and innovation programme.

REFERENCES

1. Geist, J., Gardner, J. L., & Wilkinson, F. J. (1990). *Physical Review B*, 42(2), 1262–1267.
2. Durant, N. M., & Fox, N. P. (1993). *Metrologia*, 30(4), 345–350.
3. Kübarsepp, T., Kärhä, P., Ikonen, E., (2000). *Applied Optics*, 39(1), 9–15.
4. Kuschnerus, P., Rabus, H., Richter, M., Scholze, F., Werner, L., & Ulm, G. (1998). *Metrologia*, 35(4).
5. Geist, J., & Wang, C. S. (1983). *Physical Review B*, 27(8), 4841–4847.
6. Sildoja, M., Manoocheri, F., Merimaa, M., Ikonen, E., Müller, I., Werner, L., ... Rastello, M. L. (2013). *Metrologia*, 50(4), 385–394.
7. Müller, I., Johannsen, U., Linke, U., Socaciu-Siebert, L., Smid, M., Porrovecchio, G., Werner, L. (2013). *Metrologia*, 50(4), 385–394.
8. Gran, J., Kübarsepp, T., Sildoja, M., Manoocheri, F., Ikonen, E., & Müller, I. (2012). *Metrologia*, 49(2).
9. C. K. Tang, M. U. Nordsveen and J. Gran, 2018 *International Conference on Numerical Simulation of Optoelectronic Devices (NUSOD)*, Hong Kong, 2018, pp. 1-2.

Systematic errors that depend on diffusivity and absorptance of sample in IEC method for absolute photoluminescence quantum efficiency

Jinhwa Gene¹, Seung-Nam Park¹, Han Pil Kim², and Seongchong Park¹

¹Korea Research Institute of Standards and Science, Daejeon, Republic of Korea,

²Korea Photonics Technology Institute, Gwangju, Republic of Korea

Corresponding e-mail address: seongchong.park@kriss.re.kr

Photoluminescence quantum efficiency is one of the important parameters for lightings and display industries when characterize photoluminescence materials. An IEC paper provides well organized method for absolute photoluminescent quantum efficiency [1]. However, its systematic errors that can occur in specific conditions, in where some of their assumptions are not valid, has not been studied. In this paper, we studied systematic error with Monte-Carlo ray-tracing simulation. From this calculation, we showed that systematic error of the IEC method depends on diffusivity and absorptance of sample under the test. The highest systematic error exhibits 17% with diffuse reflective sample.

INTRODUCTION

The photoluminescent (PL) materials like as quantum dots have been one of important the materials for lightings and display industries. In these fields, PL measurement has been important tool to study bandgap structure of PL materials. However, this qualitative study is not enough for applications to characterize the PL materials. The quantitative PL measurement such as PL quantum efficiency (PLQE) have been started to be crucial for display and lighting applications [2].

For the measurement of PLQE, goniometric method and integrating sphere based method were developed and widely have been used. The goniometric method can measure an angular distribution as well as the total photon flux of PL emission. However, it is very slow compared to the integrating sphere method.

Otherwise, the integrating sphere method is speedy compare to the goniometric method [3]. One of the methods widely used, named as ‘collimated incident light method (CILM)’, has been developed by J. C. Mello et al, and chosen as IEC standard (IEC62607-3-1) [1,4]. This method was designed to compensate the effects where affect on result of PLQE measurement, such as reabsorption of sample

and spectrally non-neutral reflectance of sphere wall. However, it still contains few assumptions that can cause systematic errors, like as specular reflection (zero-diffusivity) of the sample and zero-absorption of the sample in PL emission wavelength ($A_{emit} = 0$).

In this paper, we investigated the CILM in numerical way with a Monte-Carlo ray-tracing simulation tool (software: RayWiz¹). We figured out that maximum systematic error was 17% in particular condition.

SIMULATION METHOD AND RESULTS

Based on the CILM, we conduct simulation using ray-tracing software to evaluate the systematic errors arising from the assumptions mentioned before. In this numerical experiment, we assigned the value of PLQE, then, performed virtual experiment based on CILM. The systematic error was evaluated with comparison between the values of PLQE assigned (η_a) and PLQE virtually measured (η_m). Figure 1 shows 3D image of numerical experimental setup.

The virtual experimental setup has been built complying conditions presented in the IEC paper, such as integrating diameter, port size and positions of baffles. We set the number of excitation rays for simulation set to 2×10^7 .

The integrating sphere is set to exhibit diffusive reflection ($D_s = 1$, Lambertian reflection), and reflectance of the sphere is spectrally neutral. The

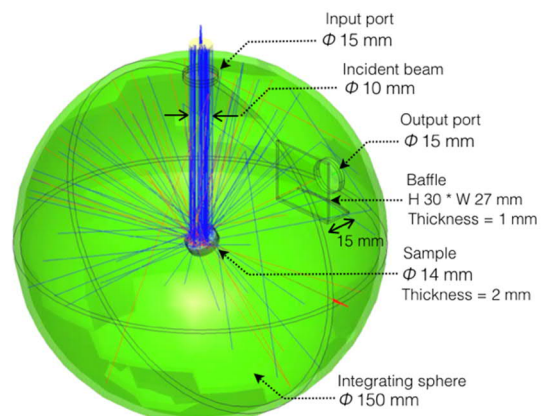


Figure 1. 3D image of numerical experimental setup

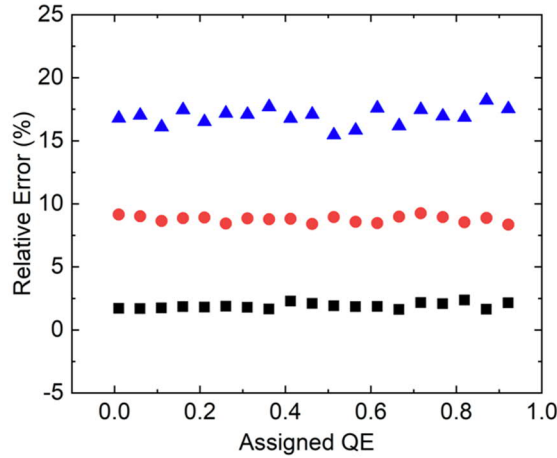


Figure 2. Relative error when $D_s = 1$

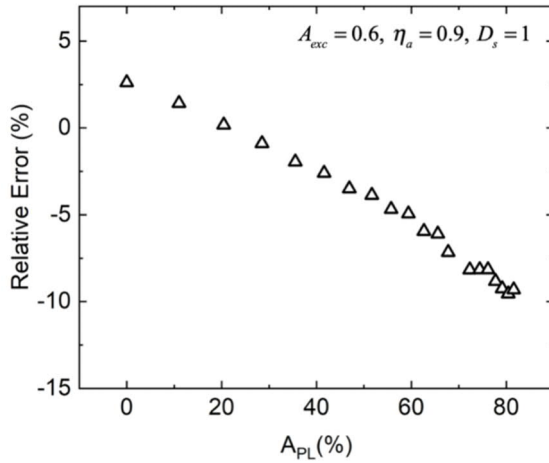


Figure 3. Relative error with respect to A_{PL}

diameter of the sphere inside and sample was set to 150 mm, and 15 mm. The dimensions for simulation are shown in Fig. 1.

Figure 2 shows calculated relative error $\varepsilon = (\eta_m - \eta_a) / \eta_a [\%]$ when the virtual sample is set to exhibit diffusive reflection ($D_s = 1$). Reflectance of the sample at excitation wavelength (A_{exc}) was set to 0.6, and $A_{PL} = 0$. The relative error for each reflectance (0.95, 0.97, 0.99) is evaluated to 17%, 8%, and 2%, respectively.

The relative error in virtual experiment with respect to A_{emit} is shown in figure 3. A_{exc} , η_a is set to 0.6 and 0.9, respectively. These values are arbitrarily chosen, because they do not affect on the result. The largest relative error was evaluated to 10% in minus when $A_{PL} = 0.8$.

CONCLUSION

This work has investigated systematic errors in the IEC standard method for PLQE measurement of PL

materials through numerical experiments using a commercial ray-tracing software. It is found that the underlying assumption of the IEC method causes an error of 17% at most when a diffuse reflective sample is measured using an integrating sphere of 0.95 reflectance. Furthermore, non-zero A_{PL} cause error of 10% in minus when A_{PL} was 0.8.

We also developed a method for compensation of the systematic errors, and presented in a paper [5]. Two more experimental steps with auxiliary light at PL emission wavelength is added for the compensation. We also tested this method with numerical experiments, then, we found that the systematic errors were successfully suppressed with the compensation method.

REFERENCES

1. International standard IEC 62607-3-1 Nanomanufacturing- Key control characteristics Part3-1: Luminescent nanomaterials-Quantum efficiency 1st ed., International Electrotechnical Commission, Geneva, 2014
2. Rohwer, L. S., & Martin, J. E., Measuring the absolute quantum efficiency of luminescent materials, *Journal of Luminescence*, 115(3-4), 77–90, 2005
3. Jaanson, P., Manoocheri, F., & Ikonen, E., Goniometrical measurements of fluorescence quantum efficiency, *Measurement Science and Technology*, 27(2), 025204–9, 2016.
4. de Mello, J. C., Wittmann, H. F., & Friend, R. H., An improved experimental determination of external photoluminescence quantum efficiency, *Advanced Materials*, 9(3), 230–232, 1997.
5. Gene, J., Park, S.-N., Kim, H. P., & Park, S., Systematic errors and their corrections of the IEC standard method for absolute quantum efficiency measurement on photoluminescent materials, *Metrologia*, 57(1), 015003–10, 2020.

Spectroscopic Analysis of Black-Carbon Emissions from Aviation Sources

Li-Lin Tay¹, Meghdad Saffaripour¹, Greg J. Smallwood¹ and Kevin Thomson¹

¹National Research Council Canada, Ottawa, ON, K1A0R6 Canada

Corresponding e-mail address: lilin.tay@nrc-cnrc.gc.ca

Black carbon (BC) emissions from commercial aviation sources are growing concern because of their potential impacts on both human health and climate. BC alters the Earth's radiation budget directly by absorbing and scattering the incoming solar radiation. Optical properties of BC particles depend strongly on their chemical bond structure as well as their size and morphology. To obtain reliable BC mass concentration in the aviation exhaust emission using optical instruments, it is essential that the BC particles used for instrument calibration has similar optical properties to those emitted from the engine being tested. In this paper, Raman spectroscopy, is used to characterize BC particles from various aviation engines. Finding of this analysis is useful in identifying suitable BC sources for the calibration of optical instruments.

THE FIRST SECTION

Black carbon (BC) aerosol, often termed soot, is a dominant form of light absorbing fine particulate matter in the atmosphere. BC emission from combustion processes poses significant health and environmental concerns. Its strong absorption response to the solar radiation implicates the heating of both atmosphere and highly reflective surfaces, such as snow and ice. These effect has important consequences on the climate change. Transportation is considered the largest anthropogenic sources of BC emission in Canada which includes emissions from aviation aircraft. BC aerosol emitted by aircraft strongly absorb solar radiation and have a long lifetime relative to near-surface BC emissions. They also act as vapour condensing nuclei which initiate contrails to further affect the radiative properties of clouds. In addition, aviation-induced cloudiness plays a role in the degradation of air quality in the vicinity of airports. To better understand and assess these undesirable impacts, accurate and quantitative measurement of soot emissions from aircraft engines is crucial. The optical instruments that are commonly used to measure soot mass concentration of aircraft emission have a strong dependence on the optical

properties of the soot particles. The instruments are often calibrated with the laboratory generated surrogated soot particles. In this presentation, we will discuss the use of an optical spectroscopy measurement that is used extensively in the nanocarbon characterization, Raman spectroscopy, to identify a suitable soot calibration sources with the optical properties closely resembles those emitted from aviation engines.

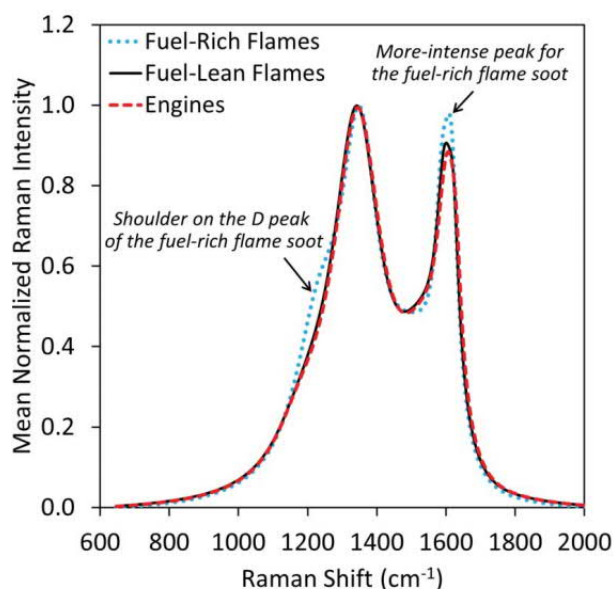


Figure 1. A comparison between the normalized averaged Raman spectra of the soot emitted from the fuel-rich flames, fuel-lean flames and aircraft turbine engines. The two notable features identified by arrows shown signifies differences in BC nanostructure. It is used to guide laboratory soot generation condition to produce BC particles with similar optical properties to those originated from aircraft engines.

REFERENCES

1. M. Saffaripour, L.-L. Tay, K. A. Thomson, G. J. Smallwood and M. Johnson, "Raman spectroscopy and TEM characterization of solid matter emitted from soot generators and aircraft turbine engines", *Aerosol Science and Technology*, **51** (4), 518-531, 2017

Simultaneous Time-Resolved Measurements of Reflected Laser Power, Emittance and Radiance Temperature in Laser Powder Bed Fusion

David C. Deisenroth¹, Leonard Hanssen¹, Steven Grantham¹, Vladimir Khromchenko¹, and Sergey Mekhontsev¹

¹National Institute of Standards and Technology

Gaithersburg, MD, USA

Corresponding e-mail address: hanssen@nist.gov

Currently at NIST there is a significant effort aimed at establishing accurate metrology for the additive manufacturing processes. The purpose of our efforts include generation of reference data sets which could be used to validate multi-physics models. The measurands for comparison with multi-physics models include reflected process laser power, sample reflectance (emittance), and radiance temperature. Reflected power and sample reflectance are measured simultaneously with an integrating hemisphere that includes necessary gas flow provisions. Radiance temperature is measured with classical thermography.

INTRODUCTION

The Additive Manufacturing Metrology Testbed (AMMT) was commissioned in 2017 with a specific goal of supporting laser-based process of layerwise selective melting of the metallic powders [1]–[3].

This process is characterized by the heating laser typically operating at 1070 nm at power levels from 80 to several hundred watts, with spot sizes in the 65 to 120 micron range ($D4\sigma$, representing diameter within which about 95% of the Gaussian laser power profile is contained) and moving at a speed about 1 m/s. The process is defined by a combination of high-power density (on the order of 1 MW/cm²) and laser dwell time of about 100 μ s, resulting in very high spatial and temporal temperature gradients and complex thermo-fluid processes [4]–[6].

The experiments reported here were performed in the National Institute of Standards and Technology (NIST) Additive Manufacturing Metrology Testbed (AMMT). The AMMT is a custom LPBF research platform that was designed to be highly configurable for measurement of all aspects of the LPBF process. The AMMT includes a removable carriage that contains the build-well and a large metrology-well, both of which may be moved laterally within the large build chamber. The laser is an Yb-doped fiber laser with emission wavelength of 1070 nm. Laser power

delivery can be adjusted from 20 W to more than 400 W, with a 4-sigma diameter ($D4\sigma$, representing diameter within which about 95% of the Gaussian laser power profile is contained) spot size that is adjustable from 45 μ m to more than 200 μ m. The laser spot can be scanned with full control of the laser scan path/strategy at 100 kHz and laser power control at 50 kHz, with scan velocity from 0 mm/s to more than 4000 mm/s.

Due to fast growth of these technologies, significant efforts are underway nationwide to perform multi-physics simulation of the process, with an ultimate goal of achieving better understanding and improving production quality and speed [7], [8]. To simplify the task, it is common to start with a single track on a bare metal plate, then proceed with a multiline pad, and then add powder and proceed with a multi-layer builds, as each of these steps bring significant additional complexities.

METROLOGICAL GOALS

The purpose of our efforts include generation of reference data sets, which could be used to validate multi-physics models, which typically have to use multiple assumptions in order to keep the computing requirements within reasonable limits (as even the exascale computers struggle to cope with the first principle models) [9].

Signatures of interest of this process include time-resolved reflected laser power (frequently referred to as ‘laser coupling’), as well as spatially resolved temperature distribution in the process zone. Earlier reported independent efforts resulted in a well-documented laser power reflectometry [10], as well as radiance temperature [11] and reflectance [1] measurement capabilities. This research effort is aimed at prototyping an apparatus for simultaneous, dynamic (time-resolved) measurement of all three process signatures, namely (1) reflected process laser power (@1070 nm, not spatially resolved, directional-hemispherical geometry), (2) sample reflectance (@808 nm, spatially resolved,

hemispherical-directional geometry), and (3) sample radiance temperature (@850 nm, spatially resolved).

The schematic of the apparatus is shown in Fig. 1. The intention of measurements of emissivity and radiance temperature is of course to be able to generate true temperature distribution across the area of interest, but discussion of uncertainty of the true temperature is beyond the scope of this paper.

As shown in Fig. 1, the integrated reflected laser power is detected by radiometers with sintered polytetrafluoroethylene (PTFE) diffusers and a 1070 nm bandpass filters. The radiometers are calibrated by directing the (defocused) heating laser onto a reflectance standard in place of the sample. This is the directional-hemispherical reflectometer operation.

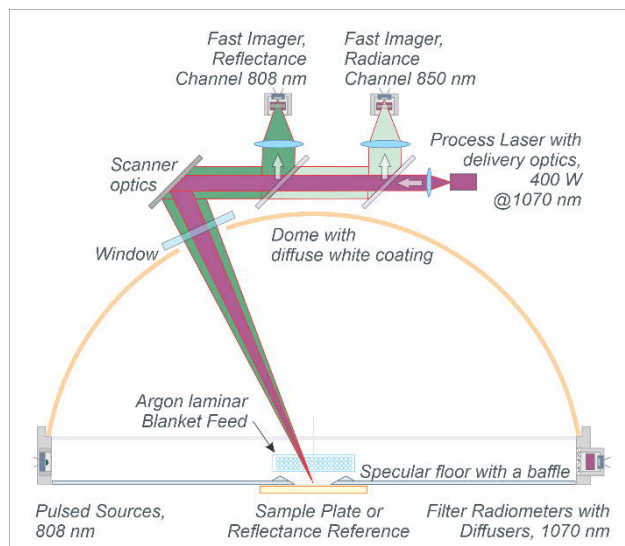


Fig. 1: Schematic of the experimental apparatus

For measurement of emittance, the reflectometer is operated in the hemispherical-directional mode. The probing light is provided by pulsed laser diodes at 808 nm. The narrow waveband of probing light is reflected from the sample and focused into the optics coaxially aligned with the heating laser. The first coaxial beam splitter provides an image of the narrow waveband of the reflected probing light of the laser-metal interaction scene that is then converted to emittance of the scene. A second coaxial beam splitter detects self-emitted light in a narrow waveband about 850 nm, which is then converted to NIST-traceable radiance temperature.

REFERENCES

1. S. Grantham, B. Lane, J. Neira, S. Mekhontsev, M. Vlasea, and L. Hanssen, Optical design and initial

- results from NIST's AMMT/TEMPS facility, in *Laser 3D Manufacturing III*, 9738, 97380S, 2016.
2. B. Lane et al., Design, developments, and results from the NIST additive manufacturing metrology testbed (AMMT), in *Solid Freeform Fabrication Symposium*, Austin, TX, 1145–1160, 2016.
3. H. Yeung, J. Neira, B. Lane, J. Fox, and F. Lopez, Laser path planning and power control strategies for powder bed fusion systems, in *The Solid Freeform Fabrication Symposium*, 113–127, 2016.
4. Bidare, I. Bitharas, R. M. Ward, M. M. Attallah, and A. J. Moore, Fluid and particle dynamics in laser powder bed fusion, *Acta Materialia*, 142, 107–120, 2018.
5. A. Keshavarzkermani et al., An investigation into the effect of process parameters on melt pool geometry, cell spacing, and grain refinement during laser powder bed fusion, *Optics & Laser Technology*, 116, 83–91, 2019.
6. S. Ghosh et al., Single-track melt-pool measurements and microstructures in Inconel 625, *JOM*, 70(6), 1011–1016, 2018.
7. S. A. Khairallah, A. T. Anderson, A. Rubenchik, and W. E. King, Laser powder-bed fusion additive manufacturing: Physics of complex melt flow and formation mechanisms of pores, spatter, and denudation zones, *Acta Materialia*, 108, 36–45, 2016.
8. L. Levine, M. Stoudt, and B. Lane, A Preview of the NIST/TMS Additive Manufacturing Benchmark Test and Conference Series, *JOM* (1989), 70, 2018.
9. M. Mozaffar, E. Ndip-Agbor, S. Lin, G. J. Wagner, K. Ehmann, and J. Cao, Acceleration strategies for explicit finite element analysis of metal powder-based additive manufacturing processes using graphical processing units, *Computational Mechanics*, 64(3), 879–894, 2019.
10. D. C. Deisenroth, S. Mekhontsev, and B. Lane, Measurement of mass loss, absorbed energy, and time-resolved reflected power for laser powder bed fusion, in *SPIE Photonics West*, San Francisco, 2020.
11. I. Zhirnov, S. Mekhontsev, B. Lane, S. Grantham, and N. Bura, Accurate determination of laser spot position during laser powder bed fusion process thermography, *Manufacturing Letters*, 23, 49–52, 2020.

CHARACTERIZATION OF BIDIRECTIONAL TRANSMISSIVE AND REFLECTIVE PROPERTIES OF BLACK SILICON

Georgi T. Georgiev, James J. Butler, Ron Shiri, Christine A. Jhabvala

NASA Goddard Space Flight Center, Greenbelt, MD, USA

Corresponding e-mail address: georgi.t.georgiev@nasa.gov

This paper describes the initial work of characterizing the transmissive and reflective properties of Black Silicon (Si) diffusers. The diffusers are 100mm diameter black silicon samples fabricated at Goddard Space Flight Center (GSFC). The 8° Directional Hemispherical Reflectance (DHR) from 250nm to 20 microns and the Bidirectional Reflectance Distribution Function (BRDF) and Bidirectional Transmissive Distribution Function (BTDF) of a Black Si sample were measured at 632.8nm, 1064nm, and 1550nm using the GSFC Code 618 Radiometric Calibration Laboratory's (RCL)'s optical scatterometer. The diffuser exhibits extremely low specular reflection up to ~1100nm. There is no evidence of retroscatter. The measurements are traceable to those made at the National Institute of Standards and Technology (NIST).

INTRODUCTION

This work was performed at Goddard Space Flight Center's (GSFC) Code 618 Radiometric Calibration Laboratory, a secondary calibration facility with radiometric calibration measurements traceable to those made at the National Institute of Standards and Technology (NIST). The facility's optical scatterometer, [1], was used for BRDF and BTDF measurements at 632.8nm, 1064nm, and 1550nm whereas a Perkin-Elmer Lambda 1050 spectrometer with 150 mm PTFE coated integrating sphere was used for the Directional Hemispherical Reflectance and Transmittance measurements from 250nm to 2500nm. A Bruker 125HR Fourier Transform Infrared (FTIR) spectrometer with 75mm diameter gold coated integrating sphere was used in the range of 2.5microns to 20microns.

EXPERIMENTAL

The Black Si sample was created on a silicon wafer by cryogenic etching [1, 2]. The sample was then mounted in a custom prepared holder used for BRDF, BTDF and directional reflectance and transmittance hemispherical measurements.

RESULTS AND DISCUSSION

The diffuser 8° DHR from 250nm to 2500nm is shown in Fig.1. The Black Si diffuser hemispherical reflectance in UV-VIS-NIR-SWIR can be divided in three distinctive areas. The first is from 250nm to 1micron. In this wavelength range, the reflectance is ~0.5%. The second area is from 1micron to 1.2microns, in which the reflectance grows rapidly from 0.5% to 50%. The third area is from 1.2microns to 2.5microns characterized by reflectance of ~50% to ~52%. The 8° DHR data demonstrate the extreme blackness of the Black Si sample from 250nm up to about 1000nm quantified by the total amount of light that is isotropically reflected. It is worth noting that Black Si possesses the lowest hemispherical reflectance among most often used black materials from 250nm to 1000nm. The 0° Directional Hemispherical Transmittance (DHT) from 250nm to 2.5microns is shown in Fig.2. The directional hemispherical reflectance from 2.5 microns to 20microns is shown in Fig.3.

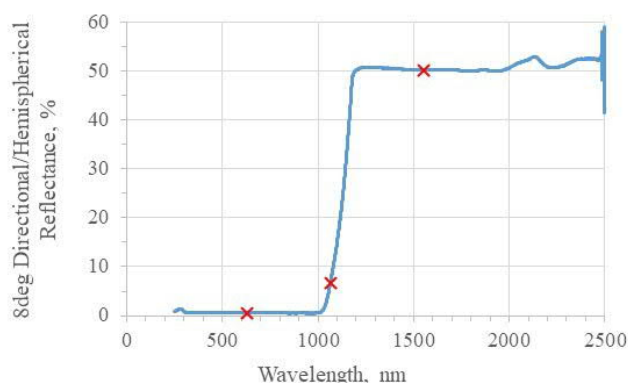


Figure 1. Directional hemispherical reflectance from 250nm to 2.5microns, with 632.8nm, 1064nm, and 1550nm marked

While the directional hemispherical reflectance quantifies the total amount of light that is reflected over all angles, it does not provide sufficient directional information required to characterize diffuse materials. The BRDF and BTDF describes the reflectance and transmittance of a target in a specific direction as a function of illumination and viewing

geometries. BRDF and BTDF were measured on the lack of retroscatter indicates that light illuminating the RCL scatterometer. The BRDF was measured at inside of the coating structure is undergoing multiple 1550nm at angles of incidence 0° , 45° and 60° and internal reflections [3]. viewing angles from -60° to 60° in steps of 5° as shown in Fig.4.

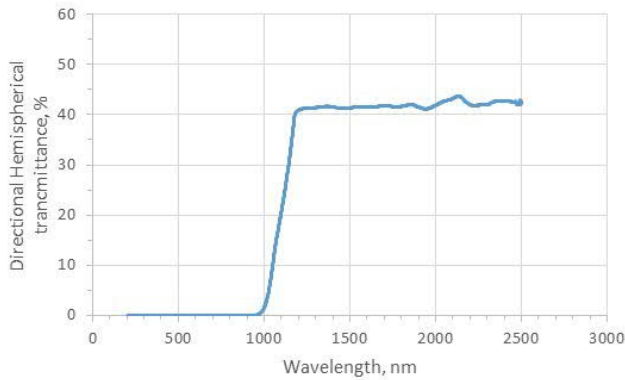


Figure 2. Directional hemispherical transmittance from 250nm to 2.5microns.

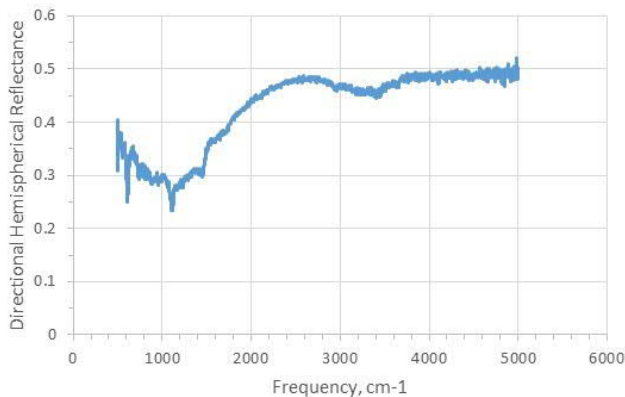


Figure 3. Directional hemispherical reflectance from 500 to 5000cm-1

The BTDF was measured at 1550nm and at the same angles of incidence as the BRDF measurements, 0° , 45° and 60° , and at viewing angles, from -50° to 50° in steps of 5° as measured from the negative normal to the sample surface. These data are shown in Fig.5. The Black Si diffuser exhibits virtually no forward or backward scatter and retroscatter. However, the Black Si sample does not show appreciable reflectance or transmittance peaks with the exception of the specular direction. The FWHM of the specular scatter was 1.5nm when measured in steps of 0.5° . The specular reflectance largely originates from the top surface of the sample, characteristic of a one-bounce surface scattering process. In contrast, the Black Si performs as a very good volume diffuser with multiple reflections within the coating. Interestingly, there is no evidence of retroscatter in the Black Si sample. Retroscatter, if present, would originate from reflectance off the illuminated interior sides of the coating's structure.

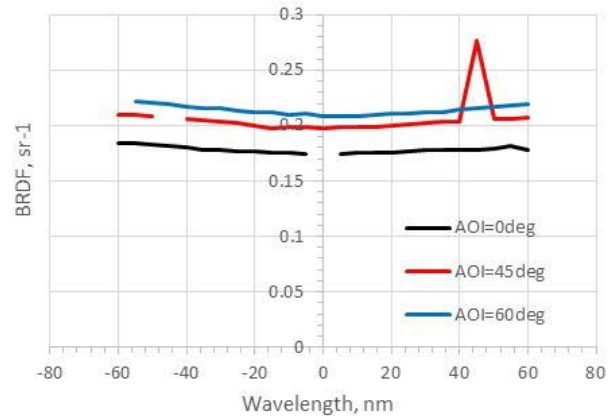


Figure 4. BRDF at 1550nm

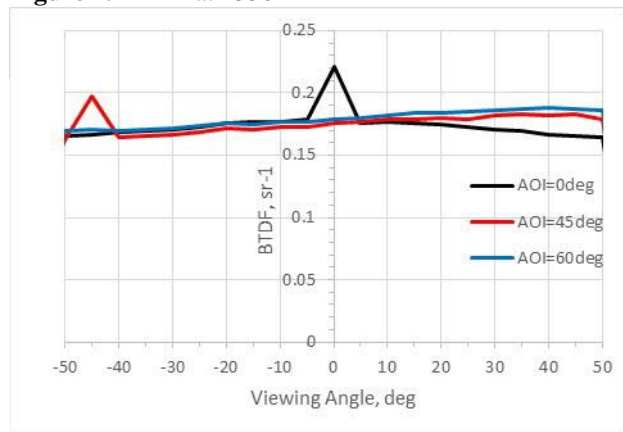


Figure 5. BTDF at 1550nm

The goal of this research was to characterize the diffuse scattering properties of Black Si. It exhibits close to isotropic scattering both in reflectance and transmittance as evident from Figures 4 and 5 and the hemispherical reflectance and transmittance as shown in Figures 1 to 3. The work presented in this paper constitutes only the initial steps in examining the potential of using Black Si as a calibration target for space instruments. Additional engineering and testing is required to ultimately optimize and qualify Black Si formulations for space use. Elements of this environmental validation effort are currently underway.

REFERENCES

- [1] Georgi Georgiev, et al, "The Bidirectional Reflectance of Black Silicon Used in Space and Earth Remote Sensing Applications", Proc. SPIE, Vol. 11151, Edited by Steven Neeck, September 2019.
- [2] Ron Shiri, et al., "Highly absorptive pupil mask fabricated with black silicon", Advanced Telescopes and Instruments, SPIE 1116-51, August 2019.
- [3] Heath D.F., Georgiev G.T., "Characteristics of a new type of Mie scattering volume diffuser and its use as a spectral calibration standard for the solar reflective wavelength region", Proc. SPIE, vol. 8153, 81530V-1-14, 2011.

ARCSTONE: Calibration of Lunar Spectral Reflectance from Space

Constantine Lukashin¹, Trevor Jackson¹, Rand Swanson², Michael Kehoe², Michael Stebbins²,
Hans Courrier², Greg Kopp³, Paul Smith³, Alan Hoskins³, Michael Cooney¹, Warren Davis¹, Noah Ryan¹,
David Taylor¹, Cindy Yong¹, Christine Buleri⁴, Elise Minda⁴, Alexander Halterman⁴, Adam Phenis⁵,
Timothy Christianson⁴, Thomas Stone⁶

¹NASA Langley Research Center, Hampton, Virginia; ²Resonon, Inc., Bozeman, Montana

³LASP Colorado University, Boulder, Colorado; ⁴Quartus Engineering, Inc., San Diego, California;

⁵AMP Optics, LLC., Poway, California; ⁶USGS, Flagstaff, Arizona.

Corresponding e-mail address: constantine.lukashin-1@nasa.gov

EXTENDED ABSTRACT

Improving scientific detection and understanding of long-term trends in complex Earth systems such as climate increasingly depend on assimilating datasets from multiple instruments and platforms over decadal timescales. Calibration accuracy, stability, and inter-consistency among different instruments are key to developing reliable composite data records, but achieving sufficiently low uncertainties for these performance metrics, particularly for space-based instruments, poses a significant challenge. Such instruments commonly carry on-board references for calibration at various wavelengths, but these increase mass and mission complexity, and are subject to degradation in the space environment.

The Moon can be considered a natural solar diffuser which can be observed as a calibration target by most spaceborne Earth-observing instruments. Since the lunar surface reflectance is effectively time-invariant, developing the Moon as a high-accuracy calibration reference enables broad inter-calibration opportunities even between temporally non-overlapping instruments, and provides an exo-atmospheric absolute radiometric standard. The intensity of moonlight reaching a sensor changes with time, governed by the solar illumination of the Moon and the net lunar reflectance as a function of phase angle. To realize a radiometric calibration against the Moon, the Sun-Moon-observer geometry and the solar flux for a particular observation are combined with the lunar reflectance to predict the lunar brightness, for comparison with the sensor's response. This requires development of a lunar irradiance model that provides a continuous predictive capability.

Tools and a methodology for lunar calibration have been developed by the U.S. Geological Survey (USGS) in Flagstaff, AZ, under sponsorship from

NASA's Earth Observing System program. The USGS lunar calibration system was built from a set of Moon images acquired by the ground-based Robotic Lunar Observatory (ROLO) over a period of more than 8 years. These measurements form the basis for an empirically-derived analytic model for the lunar disk-integrated reflectance [1], which can be queried for any geometry of Moon observations within the model's valid range. In operation, the disk reflectance spectrum is generated for a specified set of observation conditions, then interpolated and convolved with the solar spectral irradiance and the sensor's spectral response functions to produce spectral lunar irradiance values in a sensor's bandpasses corresponding to the time and location of its the observation. Utilizing lunar calibrations, top-of-atmosphere radiance measurements from SeaWiFS achieved long-term stability of 0.13% over the 13-year mission lifetime [2]. The USGS system is typically is not used for absolute calibration, however, due to limitations of the current ROLO model's accuracy, which is estimated at 5 – 10% ($k=1$).

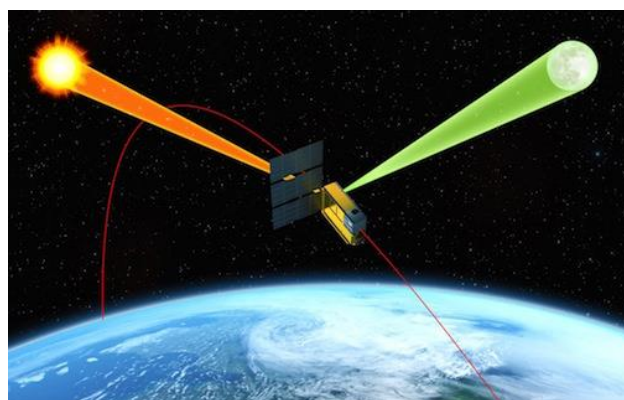


Figure 1: ARCSTONE conceptual mission to calibrate lunar spectral reflectance, flying on a 6U CubeSat (spacecraft bus image courtesy of Blue Canyon Technologies). Calibration of the ARCSTONE instrument itself is achieved on-orbit using the spectral solar irradiance as an absolute reference.

The ARCSTONE mission goal is to develop the Moon as a reliable reference for high-accuracy on-orbit calibration of reflected-solar instruments, including improvements to the absolute accuracy of the lunar spectral irradiance. The ARCSTONE instrument is a compact spectrometer, intended for a CubeSat platform in low Earth orbit. It will measure the lunar spectral reflectance with accuracy $< 0.5\%$ ($k=1$), sufficient to establish an SI-traceable absolute lunar calibration standard referenced to the spectral solar irradiance across the 350 to 2300 nm spectral range with 4 nm spectral sampling.

The ARCSTONE's on-orbit deployment strategy, illustrated in Figure 1, is to sample the Moon with frequency sufficient to adequately characterize the changes in lunar irradiance with time. To achieve the project goal of improving the current ROLO calibration reference, ARCSTONE observations must span both the range of lunar phases and the range of librations with sufficient coverage. The appearance of the Moon from the Earth's surface or low Earth orbit is constrained by its synchronized rotation rate and by the tilt of the lunar orbit. Consequently, at least three years of observations are required to fill out the libration parameter space, defining the duration of ARCSTONE on-orbit operations.

ARCSTONE mission operation requirement is to take lunar measurements every 12 hours when the phase angle (Sun-Moon-ARCSTONE angle) is in the range from zero to ± 135 degrees, providing 3 weeks per month of usable calibration times, expanding the usable range of on-orbit lunar calibrations beyond the current limit of ± 90 degrees phase, or two weeks per month. Lunar measurements will be taken at the highest latitudes of the ARCSTONE orbit, to view the largest range of lunar latitudes. Measurements of the Sun are planned to have at least a weekly cadence to account for solar and sensor variability.

Each lunar measurement sequence will last approximately 5 minutes, and consist of multiple acquisitions of 10 – 15 seconds integration time. Longer integration times are excluded due to orbital effects on the observed lunar irradiance. For a sensor in low Earth orbit, the lunar irradiance can vary up to 0.1% in about 16 seconds due to the changing Moon observer distance and the change in phase angle caused by the moving vantage point. Dark field measurements will be acquired before and after each lunar and solar measurement sequence. These will be obtained through a combination of a closed shutter on the instrument and by viewing deep space.

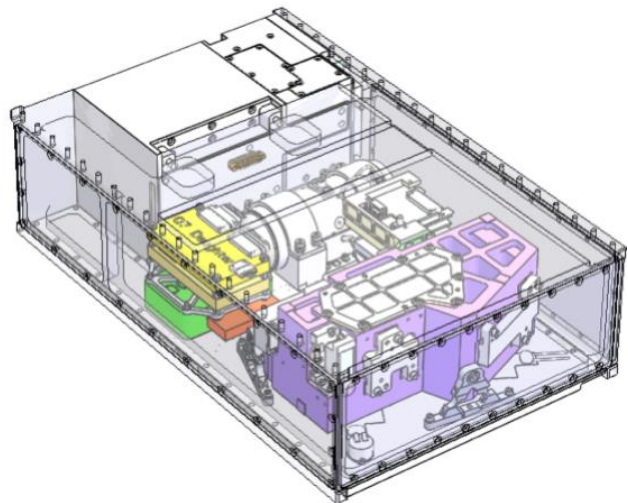


Figure 2: The ARCSTONE instrument integrated in a 6U CubeSat (spacecraft bus CAD courtesy Blue Canyon Technologies). The instrument components include: optical bench (blue), detector and cryocooler assembly (grey), and control electronics (yellow, green, and orange).

The ARCSTONE instrument's purpose is to accurately calibrate spectral lunar reflectance of the entire disc by taking the ratio of solar and lunar measurements. By utilizing identical optics for both solar and lunar measurements, potential impacts from long-term optical degradation are removed. Optical and mechanical designs of the instrument are advanced and a second-generation instrument is being fabricated. The instrument packaging into an intended 6U CubeSat bus is shown in Figure 2.

The ARCSTONE team will present the instrument design, development status, approach to calibration and characterization, and the planned path toward mission implementation.

REFERENCES

1. H.H. Kieffer and T. C. Stone, "The Spectral Irradiance of the Moon," *Astron. J.* 129, 2887-290, 2005.
2. R. E. Eplee Jr. et al., "On-orbit calibration of SeaWiFS," *Applied Optics* 51, 8702 - 8730, 2012.

High Precision Measurement of Terahertz Frequency Based on Frequency Comb

Qing Sun, Zheng Li and Yuqiang Deng

Optics Division, National Institute of Metrology, Beijing, 10029, P. R. China

Corresponding e-mail address: sunqing@nim.ac.cn

A terahertz frequency comb is built by using a commercial femtosecond fiber laser and a fiber-coupled terahertz photoconductive antenna. The absolute frequency of terahertz test source is measured with a measurement uncertainty of 3.2×10^{-11} . A method for terahertz frequency measurement by using unstabilized femtosecond laser is also introduced. Compare to the method by using stabilized femtosecond laser, the system is greatly simplified.

INTRODUCTION

Optical frequency comb is an ultra-precision measuring tool, which has revolutionized the field of optical frequency measurement. Terahertz (THz) electromagnetic wave, lying at the boundary between microwave and the infrared, has emerged as a new method for spectroscopy, imaging, communication and other applications. As frequency is one of the most important physical quantities of EM waves, high precision measurement of THz frequency is also required. The development of a new optical frequency comb to achieve THz frequency measurement has also become a hot topic in recent years [1-3].

In this paper, we demonstrate high precision THz frequency measurement based on frequency comb, by using an stabilized or an unstabilized femtosecond laser, respectively.

PRINCIPLES

A femtosecond laser contains a series of frequency combs with the frequency of $f_{n_opt} = n \cdot f_r + f_0$, where f_r represents the laser pulse repetition frequency and f_0 represents the carrier envelope phase shift. The photoconductive antenna generates broad band THz radiation excited by the femtosecond laser. f_0 is offset during the difference-frequency processes. Thus, the THz frequency comb can be expressed as $f_{m_THz} = m \cdot f_r$.

As shown in Figure 1, the frequency of the measured THz source can be expressed as $f_{THz} = m \cdot f_r \pm f_b$,

where f_b represents the beat frequency of the measured THz source and THz frequency comb. In the equation, both f_r and f_b can be directly measured by using a frequency counter. The only unknown value is m , which must be obtained to determine the frequency of the measured THz source.

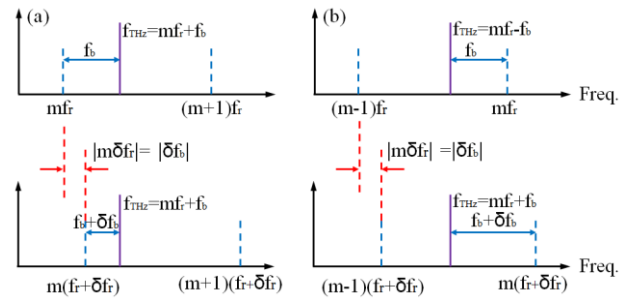


Figure 1. Principle of THz frequency measurement

If interval of the THz frequency comb varies from f_r to $f_r + \delta f_r$, the beat frequency signal will change from f_b to $f_b + \delta f_b$, and $|\delta f_b| = |m \cdot \delta f_r|$. Thus, the following relationship can be obtained:

$$m = \text{int} \left(\left| \frac{\delta f_b}{\delta f_r} \right| \right) \quad (1)$$

The frequency of the measured THz source can be expressed as:

$$f_{THz} = \begin{cases} m \cdot f_r + f_b, & \delta f_b / \delta f_r < 0 \\ m \cdot f_r - f_b, & \delta f_b / \delta f_r > 0 \end{cases} \quad (2)$$

MEASUREMENT USING STABILIZED LASER

The femtosecond laser used was manufactured by Toptica Photonics AG, with the output central wavelength of 1550 nm, the pulse width of 80 fs. The repetition frequency was stabilized using feedback control system. The laser was divided into two beams by a fiber coupler, one beam connected to the fiber-coupled THz photoconductive antenna to generate a THz frequency comb. The other laser beam was detected by a high-speed photodiode, which inputted the pulse signal into the frequency counter to measure repetition frequency. After the output signal from the frequency synthesizer was multiplied six times by the frequency multiplication module, a THz signal with the frequency range of 75–110 GHz was generated.

The THz signal was irradiated on the surface of the photoconductive antenna, focused by silicon lens and then interacted with the THz frequency comb. The beat frequency signal obtained was amplified and inputted into the spectrum analyzer for measurement. Both frequency counters and the frequency synthesizer in the measurement system referred to the rubidium frequency standard.

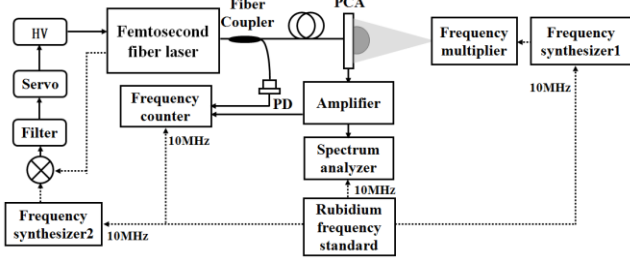


Figure 2. Experimental setup of THz frequency measurement system using stabilized laser

Figure 3 shows the beat signal measured by the spectrum analyzer before and after the repetition frequency change. The absolute frequency of THz test source is obtained according to Equation (2) with a measurement uncertainty of 3.2×10^{-11} .

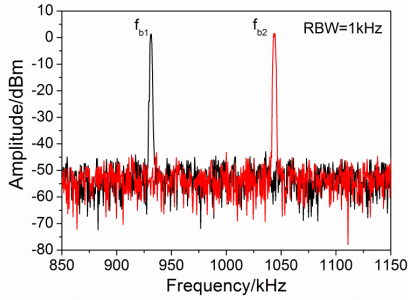


Figure 3. Spectra of f_b with different f_r

MEASUREMENT USING UNSTABILIZED LASER

To simplify the measurement system, we propose a new method. Instead of carrying out complicated stabilization control over repetition frequency of the laser, it was only needed to simultaneously acquire repetition and beat frequencies using two frequency counters as shown in Figure 4.

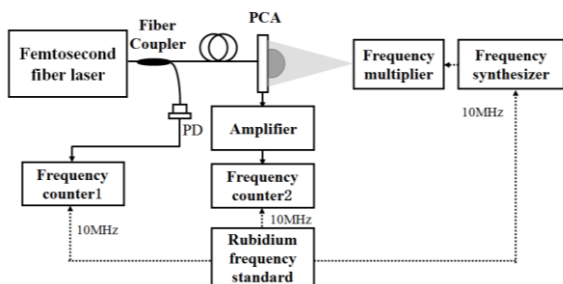


Figure 4. Experimental setup of THz frequency measurement system using unstabilized laser

According to the principle of measurement, the variation of repetition frequency f_r will result in corresponding change in the beat frequency f_b . Figure 5 present the results of measurement of f_r and f_b in a continuous 40-minute period.

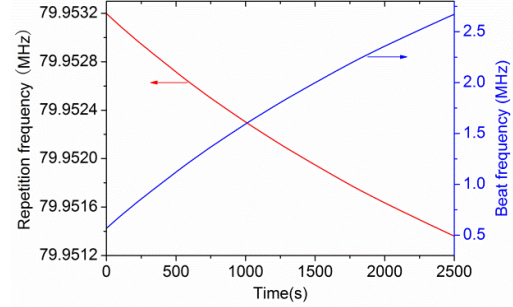


Figure 5. Continuous measurement of f_r and f_b

The value of m was calculated as follows:

$$m = \text{int} \left(\frac{1}{N-M} \sum_{n=1}^{N-M} \left| \frac{f_b(n+M) - f_b(n)}{f_r(n+M) - f_r(n)} \right| \right) \quad (3)$$

Where, N stands for the total number of data and M stands for the selected data interval. The frequency of the measured THz source was calculated as follows:

$$f_{THz} = \frac{1}{N} \sum_{n=1}^N m \cdot f_r(n) \pm f_b(n) \quad (4)$$

Compare to the method by using stabilized femtosecond laser, although the measurement precision dropped from the order of 10^{-11} to the order of 10^{-10} , the measurement system was greatly simplified.

CONCLUSIONS

A THz frequency comb is built by using a commercial femtosecond fiber laser and a fiber-coupled THz photoconductive antenna. The absolute frequency of THz test source is measured with a measurement uncertainty of 3.2×10^{-11} . A method for THz frequency measurement by using an unstabilized femtosecond laser is also introduced.

ACKNOWLEDGEMENTS

This work was supported in part by Basic Research Foundation of the National Key R&D Program of China (Grant No. 2016YFF0200306).

REFERENCES

1. S. Yokoyama, R. Nakamura, et al., *Optics Express* 16, 13052-13061, 2008.
2. T. Yasui, R. Nakamura, et al., *Optics Express*, 17, 17034-17043, 2009
3. Q. Sun, Y. Yang, et al., *Acta Physics Sinica*. 65, 150601, 2016.

REFERENCE LAMP AND DIRECTIONAL RADIATION SOURCE WITH LED SPECTRUM

M. Huriev¹, P. Neyezhmakov²

^{1, 2} NSC “Institute of Metrology”, Kharkiv, Ukraine

mykola.huriev@metrology.kharkov.ua, pavel.neyezhnikov@metrology.kharkov.ua

For assuring the traceability of luminous flux measurements for “white” LEDs, NSC “Institute of Metrology” (Ukraine) has developed prototypes of a reference lamp and a directional radiation source that uses an incandescent lamp with correction filters. The spectrum of the developed sources corresponds to the LED spectrum.

INTRODUCTION

The transition to energy efficient LED light sources causes certain problems with the accuracy of measurements of their luminous flux. These problems are associated with two components: reproducing the luminous flux for LED sources and transferring the unit to the working measuring instruments. The first component is related to the fact that the reproduction of the luminous flux of reference lamps in most measurement standards in the world is carried out using integrating sphere photometers. As a rule, they are spheres with a diameter of 1.5 meters or more (Figure 1).



Figure 1. BaSO₄ coated sphere

The result of measuring the luminous flux of a LED source using a calibrated directional luminous flux from a reference lamp (type A) will contain significant type B uncertainty (up to 5% [1]). This may be due primarily to the difference in the relative spectral sensitivity of the integrating sphere photometer from the visibility function $V(\lambda)$, since the emission spectra of the reference incandescent lamp and the “white” LED source are significantly

different.

The method for reproducing and transferring the luminous flux for LED sources developed at NSC “Institute of Metrology” (NSC IM) allows to eliminate this problem [2].

To test this method, a prototype of a reference lamp of the unit of luminous flux was developed at NSC IM in order to assure the measurement traceability of LED radiation sources. A prototype of a directional radiation source was also developed for calibrating reference integrating sphere photometers.

Both of these prototypes are based on incandescent lamps with correction filters to obtain the spectrum of a standard “white” LED lamp.

REFERENCE INCANDESCENT LAMP WITH LED SPECTRUM

For a halogen lamp, a bulb with correction filters was developed. A cooling system is provided inside the bulb. Figure 2 shows the photo of a lamp prototype.



Figure 2. A prototype of a reference lamp with correction filters developed at NSC “Institute of Metrology”

The relative spectral characteristic of the lamp was measured on a integrating sphere spectrometer.

The integrating sphere spectrometer was calibrated with a reference tungsten halogen lamps of the FEL type with known characteristics. The result of the relative spectral characteristics of the luminous flux is shown in Figure 3.

The results obtained indicate good repeatability of experimental studies with the theoretical model

within the difference between the real spectral transmission of filters from tabulated values and the difficulty of taking into account all parameters in the theoretical model.

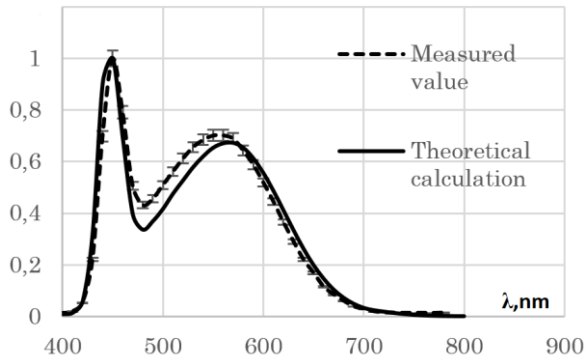


Figure 3. Relative spectral characteristics of the luminous flux of the lamp prototype – theoretical model and measured values

REFERENCE RADIATION SOURCE WITH LED SPECTRUM

For calibrating a reference integrating sphere photometer according to the scheme shown in Figure 4, a prototype of a reference radiation source based on an incandescent lamp with a radiation correction filter for the spectrum of a LED source was developed.

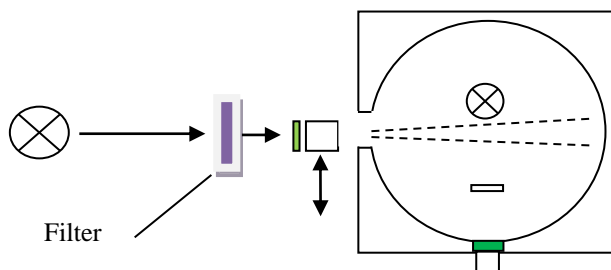


Figure 4. Functional scheme of the installation for reproducing and transferring the unit of luminous flux to LED sources

The results of studies of the relative spectral characteristics of the radiation of directional source by a spectrometer (developed by NSC IM) are presented in Figure 5.

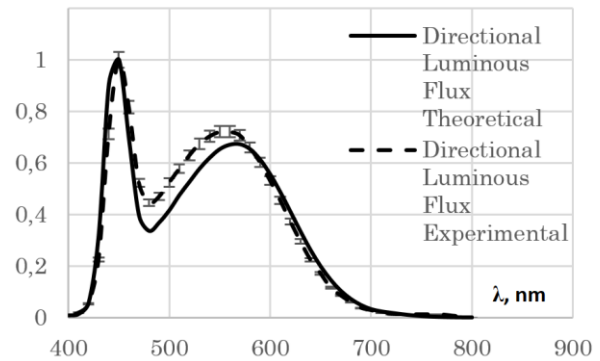


Figure 5. Relative spectral characteristics of the luminous flux of the directional source prototype – theoretical model and measured values

The obtained study results demonstrate a good repeatability.

CONCLUSIONS

The study results of the developed prototypes of the reference lamp and the directional radiation source demonstrate the possibility of realization of theoretical models for LED sources with different emission spectra. Due to the high long-term stability of the reference incandescent lamps compared to LED lamps, the creation of highly stable reference lamps for LED calibrations is possible. Due to the synthesis of the spectrum of the reference lamp prototype, which is close to the spectrum of the standard “white” LED, the difference in the sensitivity of the integrating sphere photometer to LED and the developed prototype does not exceed 0.26% (for a integrating sphere photometer with a difference from $V(\lambda)f' = 6\%$).

REFERENCES

1. Y. Ohno, K. Nara, E. Revtova, W. Zhang, T. Zama, C. Miller, Solid State Lighting Annex 2013/ Interlaboratory Comparison Final Report, International Energy Agency, 89 p (2014). <http://ssl.iea-4e.org>
2. Method of Reproduction of the Luminous Flux of the LED Light Sources by a Integrating sphere photometer: M. Huriev and P. Nyezhamkov 2018 J. Phys.: Conf. Ser.972 012028. <http://iopscience.iop.org/article/10.1088/1742-6596/972/1/012028/meta>

Displacement fiducials for gravitational-wave detectors with sub-percent accuracy using laser power sensors calibrated at NIST

R. Savage¹, D. Bhattacharjee¹, S. Karki¹, Y. Lecoeuche¹, M. Spidell², M. Stephens², and J. Lehman²

¹LIGO Hanford Observatory, Richland, USA, ²National Institute of Standards and Technology, Boulder, USA

Corresponding e-mail address: rsavage@caltech.edu

Gravitational-wave detectors require accurate and precise calibration to maximize scientific benefit. As the sensitivity of these interferometers improve, calibration accuracy better than 1% is needed to optimally extract astrophysical source information. Continuous, differential-length fiducials at the 10^{-18} m level are currently generated via radiation pressure by systems known as *Photon Calibrators*. Recent improvements in methods for transferring laser power sensor calibration from NIST to a reference transfer standard located at the Laser Interferometer Gravitational-wave Observatory (LIGO) Hanford site, then to transfer standards for each detector, and finally to the power sensors of the photon calibrator systems, has enabled differential length calibration at the sub-percent level.

PHOTON CALIBRATORS

Photon Calibrators [1] (Pcals) use auxiliary, power-modulated lasers to induce periodic modulation of the positions of suspended (up to 40 kg) mirrors via radiation pressure. The forces applied to the mirrors, and thus the modulation of the mirror positions, are proportional to the laser power reflecting from the mirror. The accuracy of the calibration fiducials is therefore directly dependent on the accuracy of the reflected laser power measured outside the vacuum envelope and the estimate of the optical losses in propagating from the mirror to the laser power sensor.

CALIBRATION OF PCAL POWER SENSORS

Following a scheme conceived in 2007 in consultation with J. Hadler at NIST, the first step in calibrating the interferometer's power sensors is to calibrate a reference transfer standard that is referred to as the Gold Standard (GS). It consists of a Labsphere 4-inch-diameter integrating sphere with an interior Spectralon shell and an unbiased InGaAs photodetector with an integrated transimpedance amplifier. The GS is sent to NIST annually for calibration.

The next step is to transfer the GS calibration to Working Standards (WS) of similar design, one for each observatory, as shown schematically in Figure 1. This is achieved by measuring the WS to GS responsivity ratios in a laboratory setup at the LIGO Hanford Observatory (LHO). Referencing all of the WSs to a single GS reduces uncertainty in the relative calibration of the detectors in the global gravitational wave (GW) detector network.

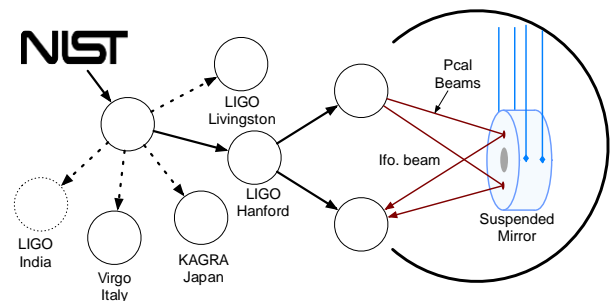


Figure 1 Transfer of laser power calibration from NIST to the GS to a WS maintained at each observatory then to the power sensors located outside the vacuum envelope on the transmitter side (Tx) and the receiver side (Rx). *H* for LIGO Hanford, *L* for LIGO Livingston, *V* for the Virgo observatory in Italy, *K* for the KAGRA observatory in Japan, and *I* for the LIGO India observatory currently under construction in India.

To measure the responsivity ratios, a 1047 nm laser beam is divided on a beamsplitter. One detector is placed in the transmitted beam and one in the reflected beam and sensor outputs are recorded simultaneously. The positions of the two detectors are then swapped using automated pneumatic sliders and additional time series are recorded. The square root of the product of the ratio of the first set time series with that of the second set yields the responsivity ratio, eliminating laser power variations and slow changes in the beamsplitter ratio.

The third step is measurement of the responsivity ratio of the power sensor measuring the light reflected from the interferometer mirror and the WS. This is achieved by placing the WS in one of the two Pcal beams in both the transmitter and receiver modules and recording a set of time series for each beam. These measurements yield the ratio of the laser powers in the two Pcal beams, the optical efficiency

for each beam, and the power sensor to WS responsivity ratios. The measured optical efficiencies, together with in-chamber efficiency measurements made when the vacuum envelope was vented, enable correcting the power sensor calibration to infer the power reflecting from the suspended mirror.

The variation in the responsivity of the power sensors with temperature is measured to be 0.02 to 0.10 % per K. Temperature differences between the NIST laboratory, the Pcal laboratory at LHO, and the various interferometer laboratories where the mirrors are suspended, as large as 4 K, are incorporated in the calibration uncertainty estimate.

Nominally, the Pcal beams are diametrically opposed and equally spaced away from the center of the suspended optic and the interferometer beam is centered. However, in practice the Pcal beams can be mis-located by as much as 2 mm and the interferometer beam is intentionally displaced to optimize interferometer sensitivity. The resulting in unintended rotations of the mirror due to Pcal forces being sensed by the interferometer as length variations is an additional source of uncertainty.

The relative uncertainty introduced by the sources described above are listed in Table 1 for the Y-end mirror at LHO. The overall relative uncertainty in the induced displacement of the mirror is 0.46 %. These results are typical for both interferometer end mirrors and for both LHO and the LIGO Livingston Observatory. Results for other detectors in the global GW network are expected to be similar.

Table 1. Summary of the major factors contributing to relative uncertainty mirror displacement induced by the Pcal system for the LHO Y-end mirror.

Parameter	Rel. Uncertainty (1- σ)
GS responsivity	0.32 %
WS/GS resp. ratio	0.024 %
Rx/WS resp. ratio	0.016 %
Temperature	0.09 %
Optical efficiency	0.044 %
Unintended Rotation	0.31 %
Displacement	0.46 %

RELATIVE AND OVERALL CALIBRATION OF THE GW DETECTOR NETWORK

Referencing the working standards for all of the observatories to the same transfer standard reduces relative calibration uncertainties for the global network. The laser power calibration of the GS carried out by NIST has a 1- σ relative uncertainty of

0.32% (see Table 1). However, in 2009 the EUROMET Comparison [2] reported disagreements between various national metrology institutes as large as 3.5 % for calibration of the same (thermal) power sensors operating at a wavelength and power level close to that used for GW detectors. Pursuant to the EUROMET study and a GW Metrology Workshop hosted by NIST in 2019 [3] some of the discrepancies have been understood and reduced. A bilateral comparison by NIST and PTB in Germany of a LIGO-style power sensor is underway and a broader comparison using one of these sensors is being considered [4].

As shown in Table 1, the dominant sources of uncertainty in the Pcal displacement fiducials are the calibration of the GS and the uncertainty introduced by unintended rotation of the mirror due to calibration forces. A new generation of primary standards under development by NIST [5] may reduce the former and methods to reduce the latter are being investigated.

CONCLUSION/DISCUSSION

Calibration of Pcal power sensors at the various GW observatories using the scheme shown schematically in Figure 1 has enabled generation of differential length fiducials with sub-percent accuracy. Calibrating interferometer output signals over the full frequency range and continuously, over long observing intervals, poses significant additional challenges. Continued development of calibration methods and further improvements in calibration accuracy will be required to ensure that the scientific reward of higher signal-to-noise-ratio GW detections is not limited by calibration uncertainty.

REFERENCES

1. S. Karki, et al., The Advanced LIGO photon calibrators, Rev. Sci. Inst., 87, 114503, 2016.
2. S. Kück, Final report on EUROMET comparison EUROMET.PR-S2 (Project No. 156): Responsivity of detectors for radiant power of lasers, Metrologia, 47, Technical Supplement, 2010.
3. NIST Gravitational Wave Metrology Workshop, Boulder, CO, March 15, 2019, Executive summary by J. H. Lehman: <https://dcc.ligo.org/LIGO-L1900166/public>.
4. M. Spidell, et al., A bilateral comparison of NIST and PTB laser power standards for increased confidence in LIGO's optical power calibration, Proc. NEWRAD 2020.
5. M. Stephens, et al., Towards the Next Generation of Laser Power Measurements, NIST Gravitational Wave Metrology Workshop, Boulder, CO, March 15, 2019, <https://dcc.ligo.org/LIGO-G1900640/public>.

System analysis of ILMD-based LID measurement systems using Monte Carlo simulation

Markus Katona¹, Klaus Trampert¹, Cornelius Neumann¹, Christian Schwanengel²

¹Karlsruhe Institute of Technology, Karlsruhe, Germany, ²TechnoTeam Bildverarbeitungs GmbH, Ilmenau, Germany

Corresponding e-mail address: markus.katona@kit.edu

ILMD- (Imaging Luminance Measuring Device) based LID measuring systems, are an established method for measuring the luminous intensity distribution (LID) of light sources in the far field. The advantage of this system is the high-resolution acquisition of a large angular range with one image. For the uncertainty budget, the mathematical description of the system can be divided into a photometrical and a geometrical component. For the uncertainty analysis, the measurement and calibration process are simulated by Monte Carlo method. Here we present the geometrical system description based on kinematic transformations. An analysis of the geometrical input parameters is shown.

INTRODUCTION

The LID $I(\varphi, \vartheta)$ is the luminous flux Φ per solid angle Ω that is emitted in the direction (φ, ϑ) . To assume the light source (Device under test: DUT) as a point source, the measurement distance is large compared to the DUT dimensions. A common method to measure the LID, is the ILMD measurement system [1]. For this method, a DUT is mounted on a goniophotometer and illuminates a white screen in a large distance (see fig. 1), and the luminance on the screen is measured by an ILMD.

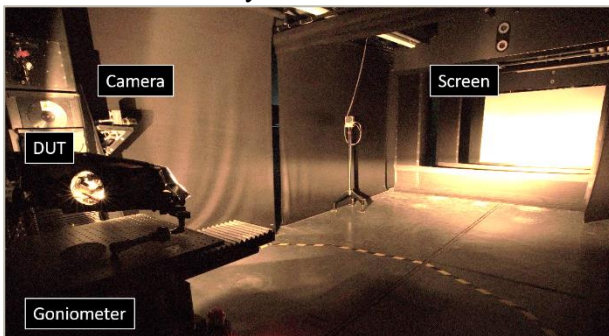


Figure 1: ILMD-based LID measuring system.

Knowing the geometric relation between the system components, the LID in the angular range of the screen can be calculated. If the interesting angular range of the LID of the DUT is larger than the screen, the goniometer rotates the DUT in multiple viewing directions, so that the full range is seen by the screen.

These LID segments are then stitched together with an image-merging algorithm [2]. To determine the uncertainty budget of this system, a Monte Carlo simulation is useful.

SENSITIVITY ANALYSIS

For the sensitivity analysis, according to GUM, a good mathematical description of the system is essential. For the following uncertainty analysis, we separate the LID into its geometric flow and the photometric flux component. We analyse the geometric component and combine a LID with high gradient.

To analyse the geometric flux, we simulate the light path from the DUT to the measuring screen, considering the rotation of the DUT by the goniometer. The geometrical system description is based on kinematic methods from robotics. In case of rotation of the DUT, both static and moving system components have an influence on the measurement uncertainty. Here, for example, geometric deviations between the photometric center of gravity of the DUT and the center of rotation of the goniometer have an impact. Other factors are the skew of the goniometer axes and the distance between the goniometer and the measuring screen.

KINEMATIC SYSTEM SETUP

Kinematics usually describe the motion of robots by representing the relation between moving parts and the position of the robot. Every moving system can be described by a chain of fixed and free translations t and rotations R in homogeneous coordinates [3]. The transformation

$$X_{i+1} = T_i * X_i \quad (1)$$

describes the transfer of position and orientation of the coordinate system X_i to X_{i+1} with the transformation matrix

$$T_i = \begin{pmatrix} R & t \\ 0 & 1 \end{pmatrix} = \begin{pmatrix} R(\theta_x, \theta_y, \theta_z) & t(x, y, z) \\ 0 & 1 \end{pmatrix} \quad (2)$$

By combining multiple transformations, the total transformation matrix can be described as:

$$T_{total} = T_{n-1 \rightarrow n} * \dots * T_{1 \rightarrow 2} * T_{0 \rightarrow 1} \quad (3)$$

To analyse the geometric uncertainty of the ILMD LID measurement system, we define a coordinate

system for every critical system component. The associated chain is shown in fig. 2.

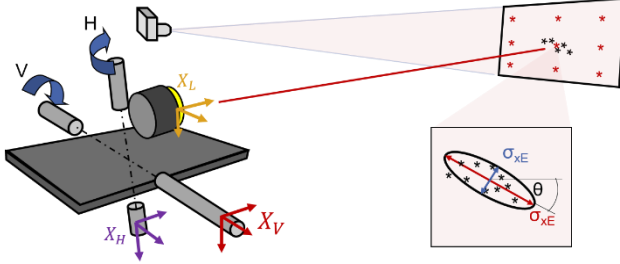


Figure 2: System components and coordinate systems for geometric calibration.

The light source X_L , is somewhere mounted on the goniometer table. The goniometer rotates the light source around the horizontal goniometer-axis X_H that is skewed and shifted to the vertical goniometer-axis X_V . Then the goniometer rotates around the vertical axis that is skewed against the optical axis and is in a measurement distance to the screen X_S . The full transformation matrix for the ILMD LID measurement system is given by

$$T_{total} = T_S * T_{V,pose} * T_{V,act} * T_{H,pose} * T_{H,act} * T_L \quad (4)$$

Note that the transformation of the goniometer-axis coordinate system has a fixed part “pose” that describes an offset and a moving part “act” that describe the goniometer rotation position.

MONTE CARLO SIMULATION

The measurement uncertainty analysis of the system was carried out with a Monte Carlo simulation. The calibration of the geometric relationships was assumed to be ideal. The necessary translation, and rotation parameters of the goniometer, were measured separately. A compact budget of the parameters is shown in tab 1. We assume, for example, that the test object is placed on the goniometer with an uncertainty of 1 mm in each direction, which is described by the translation of T_L . To analyze the geometric uncertainty we now simulate the poses of the test object with known goniometer rotation for nine exemplary directions. They are displayed as a 3x3 point matrix on the measurement screen as shown in Fig. 2. The shown error ellipse shows the result of the MC of the mentioned input parameters with 10.000 iterations. The error ellipse of the point cloud has a large ellipse axis σ_{xE} and a small ellipse axis σ_{yE} (see Fig. 2). These axes form an aperture angle with respect to the goniometer center. Also shown is the distance ratio $\sigma_{dist} = 1 - d/d_0$ of the variation of the measuring distance DUT-screen. The measuring distance is used to convert the illuminance on the screen into luminous intensity to the power of 2.

Table 1: Used input parameter and its uncertainties for Monte Carlo simulation. All empty entrances are zero.

#	t/R	x,y,z [m] $\theta_x, \theta_y, \theta_z$ [°]			Standard deviation [mm] or [°]		
		x	y	z	σ_x	σ_y	σ_z
1	T_L	t			1	1	1
		R			0.01	0.01	0.01
2	$T_{H,act}$	R				0.0043	
3	$T_{H,pose}$	t					0.1
		R					0.05
4	$T_{V,act}$	R			0.0036		
5	$T_{V,pose}$	t		10			2
		R			0.005	0.005	0.005
6	T_S	t			1	1	

RESULTS

The overall result is shown in fig. 3 and tab. 2. This result is a first estimation of the uncertainty of ILMD LID measurement.

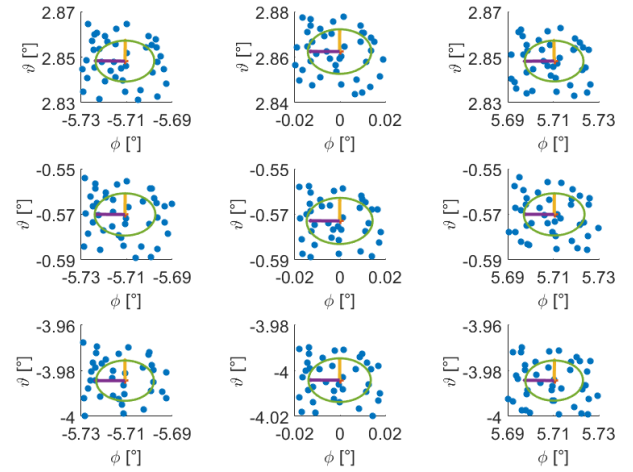


Figure 3: Visualized uncertainty results for every exemplary direction for no goniometer rotation.

These results must now be combined with the LID of the DUT to obtain the angle dependent uncertainty of the LID. The influence of the image merging method still needs to be investigated.

Table 2: Uncertainty results by number

	σ_{dist}	σ_{xE}	σ_{yE}
T_{total}	0.00023	0.01441°	0.01429°

REFERENCES

1. C. Schwanengel 2012 Comparison of Techniques for Measuring Luminous Intensity Distribution Overall and Across Segments (Germany: TechnoTeam Bildverarbeitung GmbH)
2. I. L. Sayanca, K. Trampert and C. Neumann, Indirect Light Intensity Distribution Measurement using Image Merging, AMCTM2017, Glasgow.
3. Lindemann M, Maass R and Sauter G 2015 Robot goniophotometry at PTB Metrologia 52 167–94

Design and development of laser power transfer standard in telecommunication wavelengths under scientific collaboration MOU between NIMT and PTB

Kanokwan Nontapot

National Institute of Metrology (Thailand), Pathumthani, Thailand

Corresponding e-mail address: kanokwan@nimt.or.th

Up to date, fiber optics laser systems are the most efficient way to carry information and very important in the field of telecommunication in Thailand. Typical optical fiber systems composed of laser sources, optical fibers as the transmission mediums, and detectors as receivers, where the most basic measurement necessary is optical power. To maintain quality and standard of information transmission, optical power measurement calibration is very important. The objective of this research was to design and development of InGaAs detectors, to use as an optical power transfer standard in the wavelengths where the optical fiber communication systems are operated. The design and development of the transfer standard under scientific collaboration between the national institute of metrology Thailand (NIMT) and Germany (PTB) will be presented.

INTRODUCTION

At present, the NIMT's reference standard is laser calorimeter (M 601). It has the measurement uncertainty at 0.13-0.22 %. The M 601 reference standard is calibrated with another calorimeter with higher accuracy at the National Metrology Institute of Japan (NMIJ). The M 601 is then used to calibrate the calorimeter M 602, the reference standard for fiber optics laser power meter, with the measurement uncertainty at 0.5-0.6 %. In 2017, cryogenic radiometer, a primary standard for the measurement of the absolute optical radiant power, was installed at NIMT. This instrument can achieve measurement uncertainty below 0.01% [1]. Thus, the objective of this project was to design and characterize single InGaAs photodiode as transfer standard detector in near infrared wavelength, where the optical fiber communication systems are operated. This transfer standard, designed and characterized at PTB, will then be calibrated by the cryogenic radiometer, and it will be used to calibrate the reference standard M601, as shown in Fig. 1.

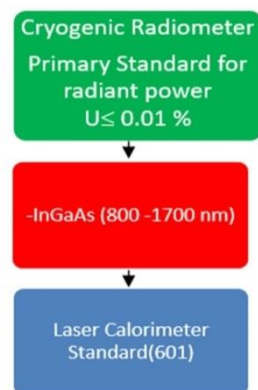
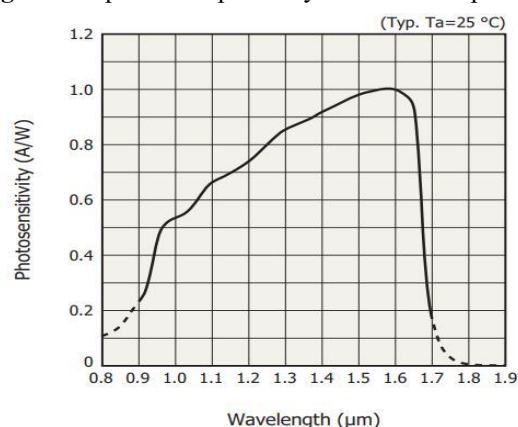


Figure 1. Traceability chain of the transfer standard.

MEASUREMENT METHOD AND SETUP

For metrology purpose such as this project, where high responsivity and linearity is very important, photodiode with the largest sensitive area was chosen. The InGaAs photodiode used in this project, Hamamatsu G8370-10, with diameter of 10 mm, had sensitive area of 78.54 mm². The spectral responsivity of the InGaAs photo diode from the product's data sheet is shown in Fig. 2 [2].

Figure 2. Spectral responsivity of a InGaAs photo diode



(from Hamamatsu data sheet).

The detector was mounted on an aluminum housing designed and fabricated at the PTB. Next to the photodiode in the housing, mounted a temperature sensor (Pt100) to monitor the temperature of the diode during the measurement process.

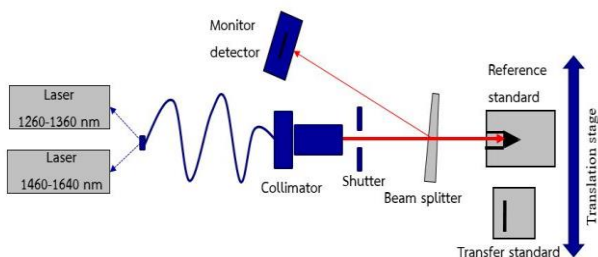


Figure 3. Experimental setup for the measurement of the absolute spectral responsivity of the transfer detector.

The responsivity of a InGaAs photodiode is obtained by measuring the photocurrent generated by the detector I_{photo} and the incident optical power Φ . Schematic diagram of the experimental setup used to measure the responsivity of the detector is depicted in Fig.3. Two tunable diode lasers, with optical power stability of $\pm 0.2\%$ within one hour, with adjustable wavelength from 1260 nm to 1360 nm and from 1460 nm to 1620 nm were used as radiation source. The laser beam is then collimated by a fiber optic collimator. To minimize possible influences on the measurement due to the laser power fluctuation, the beam was monitored by a monitor detector. A beam splitter is used to separate a laser beam into 2 beams, one goes to reference power meter or transfer standard and one goes to a monitor detector. A monitor detector (Ge-diode) is used for the correlative power measurement. A shutter is used to control the on/off of laser beam. Transfer standard (InGaAs) and reference power meter (thermopile sensors, BT14) are mounted on X-and Z- stage for comparison measurement. The laboratory was highly stabilized at $20.5 \pm 0.5^\circ\text{C}$ to minimize the influence from temperature fluctuation. Moreover, the temperature of the InGaAs detectors was measured with the temperature sensor (Pt100) mounted in the housing [3].

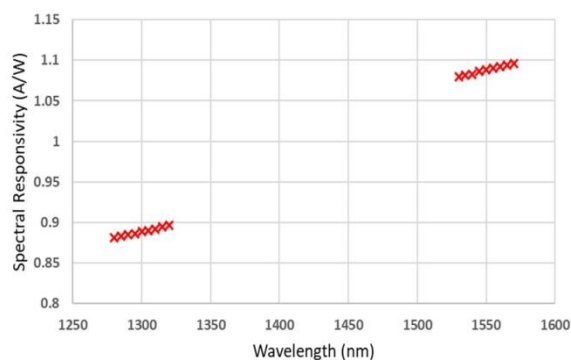


Figure 4. Absolute spectral responsivity of the InGaAs detector measure against reference thermopile detector.

RESULTS

The absolute spectral responsivity of the InGaAs detector, measured by calibration against the PTB reference thermopile detector (BT14) at different laser wavelength available (from 1280-1320 nm and from 1530-1570 nm) is shown in Fig. 4. The measurement uncertainty ($k=2$) is less than 1%.

CONCLUSION

In this paper, the design and development of InGaAs detector to use as a transfer standard for optical fiber communication was presented. The optical characterization of the detectors in this project was determined by measuring the absolute spectral responsivity of the detector. The absolute spectral responsivity of the InGaAs detector measure against reference thermopile detector at PTB was presented and was comparable to the spectral response graph from the manufacture.

The future work is to calibrate the InGaAs detector against the NIMT's cryogenic radiometer, a primary standard for the measurement of the absolute optical radiant power and compare the spectral responsivity results with the results measured at PTB. The calibrated InGaAs detector will then be used to calibrate the Thailand reference standard for optical fiber communication.

ACKNOWLEDGEMENTS

The author would like to thank you Dr. Marco Lopez and Helmuth Hofer from the Laser and Quantum Radiometry working group 4.54, Physikalisch-Technische Bundesanstalt (PTB), Germany, for an opportunity to carry out this measurement in the laser power calibration laboratory at PTB. This research project is under the scientific collaboration between NIMT and PTB.

REFERENCES

1. Martin, J. E., Fox N.P., Key, P. J., A Cryogenic Radiometer for Absolute Radiometric Measurements, *Metrologia*, 21(3), 147-157, 1985.
2. https://www.hamamatsu.com/resources/pdf/ssd/g8370-10_kird1058e.pdf
3. López, M., Hofer, H., Stock, K. D. Bermúdez, J. C., Schirmacher, A., Schneck, F., Kück, S., Spectral reflectance and responsivity of Ge- and InGaAs-photodiodes in the near-infrared: measurement and model, *Appl. Opt*, 46, 7337-7344, 2007.

Global Interlaboratory Comparison of 41 Goniophotometers Measuring Solid- State Lighting Products

Yoshi Ohno¹, Jean Gaudemer², Jun Seok Oh³, and Michael Scholand⁴

¹National Institute of Standards and Technology, USA, ²Laboratoire National de métrologie et d'Essais, France,

³Korea Institute of Lighting and ICT, Korea, ⁴International Energy Agency 4E Solid State Lighting Annex

Corresponding e-mail address: ohno@nist.gov

A global interlaboratory comparison (IC 2017) on measurements of solid-state lighting (SSL) products with goniophotometers was conducted under the International Energy Agency (IEA) 4E SSL Annex, participated by 36 laboratories from 19 countries with a total of 41 goniophotometers. Not only large mirror-type goniophotometers but also near-field type and source-rotating type goniophotometers were included. Three LED luminaires of different types and one narrow-beam LED lamp were used as artefacts for star-type comparisons with two reference laboratories. 16 quantities including electrical, photometric, colorimetric, and goniophotometric quantities were measured and compared. The results revealed the levels of measurement variation for SSL products across the market and a number of specific problems in participants' results.

DESIGN OF THE COMPARISON

Previously, the International Energy Agency's (IEA) Energy Efficient End-use Equipment (4E) Solid-State Lighting (SSL) Annex conducted the first interlaboratory comparison (IC 2013) for measurements of electrical, photometric, and colorimetric quantities of SSL products (LED lamps). This comparison included 55 laboratories [1,2] and provided critical data on the variability of LED lamp measurements, however measurements of luminaires by goniophotometers were not covered.

The IEA 4E SSL Annex organized another global interlaboratory comparison (IC 2017) for measurement of SSL products with goniophotometers. IC 2017 was launched in June 2017 [3] and had 36 participating laboratories from 19 countries for a total of 41 goniophotometers. IC 2017 was designed to investigate the level of agreement in measurements of various quantities for LED luminaires and beam lamps by goniophotometers. It was also designed to investigate the equivalence of non-standard goniophotometers (e.g., near-field type and source-rotating type) to traditional far-field mirror type goniophotometers.

IC 2017 used the international standard CIE S 025 [4] (and equivalent European standard EN 13032-4 [5]) as the test method. Thus, IC 2017 was able to provide information on measurement variations by laboratories that are in compliance with CIE S 025. This comparison was also designed to be in compliance with ISO/IEC 17043 [6] so that it may serve as a proficiency test for SSL testing accreditation schemes around the world.

STRUCTURE OF THE COMPARISON

IC 2017 was led by National Institute of Standards and Technology (NIST, USA) which served as Task Leader. To share the workload of comparison, two laboratories having a large mirror-type goniophotometers served as reference laboratories (called Nucleus Laboratories in IC 2017): Korea Institute of Lighting and ICT (KILT, Korea) and Laboratoire National de métrologie et d'Essais (LNE, France). To establish equivalence of measurements between these two laboratories, a Nucleus Laboratory Comparison was carried out, using two sets of the comparison artefacts and measuring all the quantities (see next section). The details and results of the comparison are available in IC 2017 Nucleus Laboratory Comparison Report [7].

IC 2017 was carried out as a star-type comparison between each participant and one of the two Nucleus Laboratories, which prepared and measured the artefacts, shipped them to participants, and measured them again upon their return. If reproducibility was poor, the measurement of a particular artefact with the participant was repeated. The measurements with participants were made in six rounds, two rounds by KILT and four rounds by LNE. These measurements, and any re-measurements, spanned a time period from November 2017 to September 2019.

TECHNICAL PROTOCOL

Table 1 shows the comparison artefacts used. ART-1 is a MR-16 type narrow-beam LED lamp with a beam angle of $\approx 12^\circ$; ART-2 is a 60cm x 60cm indoor planar

LED luminaire with a broad intensity distribution; ART-3 is a linear LED luminaire including small upward light emission; and ART 4 is a street light LED luminaire having asymmetric intensity distributions, with a low power factor of ≈ 0.7 .

Table 1. Specifications of the comparison artefacts


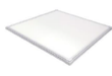


	ART-1	ART-2	ART-3	ART-4
image				
Supply	DC12 V	AC 220 V	AC 220 V	AC 220 V
Power	7.5 W	40 W	20 W	20 W
CCT	2700 K	5500 K	4000 K	4500 K

Table 2 shows the list of measurement quantities. Items 1 to 8 are general quantities used for the proficiency test as well as technical study purposes. Items 9 to 16 are goniophotometric quantities, which are used for technical study purposes. Further details are available in IC 2017 Technical Protocol [8].

Table 2. Measurement quantities used for IC 2017

No.	Quantity	Artefact
1	Total luminous flux (lm)	All
2	Luminous efficacy (lm/W)	All
3	Active power (W)	All
4	RMS current (A)	All
5	Power factor	All
6	Chromaticity coordinates u' , v'	All
7	Correlated Color Temperature	All
8	Color Rendering Index Ra	All
9	Luminous intensity distribution	All
10	Partial luminous flux (15°)	ART-1
11	Center beam intensity	ART-1
12	Beam angle	ART-1
13	Street-side downward flux	ART-4
14	House-side downward flux	ART-4
15	Up light flux	ART-4
16	Color uniformity	ART-1,3

RESULTS

The (relative) differences between each participant and the reference value (result of the Nucleus Laboratory) were calculated for all the 16 quantities, four artefacts (one or two for goniophotometric quantities), and 41 participants, producing nearly 2000 points of comparison in total. Graphs comparing all participants were prepared for all four artefacts together or for each artefact separately, for each measurement quantity, resulting in over 54 graphs of results. In addition, z' scores and E_n numbers (see [6]) for the general quantities were calculated for proficiency test

purposes. The intensity distribution curves were also plotted to compare the participant's and the reference laboratory's results.

Individual Test Reports (ITRs) reporting the results of only each participant have been issued to each participant. The IC 2017 Final Report is to be published in 2020, comparing the results of all participants anonymously.

CONCLUSIONS

This comparison provided valuable data on the agreement of SSL product measurements by goniophotometers. There were numerous problems found in the results, in some cases with very large discrepancies. While total luminous flux showed results as expected, electrical quantities (i.e., active power and RMS current) showed much larger variations than expected. The partial luminous flux quantities showed much larger variations than total luminous flux which implies problems with artefact alignment. Comparison of goniophotometer types (18 mirror-type, 13 near-field-type, 10 source-rotating type) did not show any significant differences overall, though results do vary in individual cases. Further points will be presented and discussed at the conference.

REFERENCES

1. IEA 4E SSL Annex, 2013 Interlaboratory Comparison Final Report, https://ssl.iea-4e.org/files/otherfiles/0000/0067/IC2013_Final_Report_final_10.09.2014a.pdf
2. Y. Ohno, P. Bennich, N. Borg, K. Nara, M. Scholand, 110 labs in world's largest interlaboratory comparison of LED test labs – improving testing competency to support market transformation, ECEEE SUMMER STUDY PROCEEDINGS 8-346-15, 1872 – 1880, 2015.
3. IEA 4E SSL Annex, Launch of IEA 4E SSL Annex 2017 Interlaboratory Comparison of Goniophotometers: http://ssl.iea-4e.org/files/otherfiles/0000/0108/IC_2017_Official_Announcement_-_Final.pdf
4. CIE S 025/E:2015, Test Method for LED lamps, LED luminaires and LED modules
5. EN 2015. EN 13032-4:2015, Part 4 LED lamps, modules, and Luminaires
6. ISO/IEC 2010. ISO/IEC 17043:2010, Conformity Assessment – General Requirements for Proficiency Testing
7. IEA 4E SSL Annex, IC 2017 Nucleus Laboratory Comparison Report (revision), https://ssl.iea-4e.org/files/otherfiles/0000/0131/IC_2017_Nucleus_Lab_Comparison_Report_-_Final_Revised_-_2019-09-30.pdf
8. IEA 4E SSL Annex, IC 2017 Technical Protocol, https://ssl.iea-4e.org/files/otherfiles/0000/0117/IC_2017_Technical_Protocol_v.1.0_final.pdf

Calibrating Gravitational Wave Interferometers: A Review with Astrophysical Implications

J. S. Kissel^{1,2}

(for the The LIGO-VIRGO-KAGRA Collaboration's Calibration Team Members:)

J. Betzwieser,³ D. Bhattacharjee,⁴ V. Bossilkov,⁵ D. Estevez,⁶ E. Goetz,⁷ Y. Inoue,⁸ N. Kanda,^{9,10}
S. Kandhasamy,¹¹ S. Karki,⁴ A. Kontos,¹² G. Mendell,² T. Mistry,¹³ E. Payne,¹⁴ L. Rolland,⁶ R. L. Savage,²
M. Stover,¹⁵ L. Sun,¹⁶ D. Tuyenbayev,¹⁷ A. D. Viets,¹⁸ M. Wade,¹⁵ A. J. Weinstein,¹⁶ and T. Yamamoto¹⁹

¹Corresponding Author: jkissel@ligo.mit.edu

²LIGO Hanford Observatory, Richland, WA 99352, USA

³LIGO Livingston Observatory, Livingston, LA 70754, USA

⁴Missouri University of Science and Technology, Rolla, MO 65401, USA

⁵OzGrav, University of Western Australia, Crawley, Western Australia 6009, Australia

⁶Laboratoire d'Annecy de Physique des Particules (LAPP), Univ. Grenoble Alpes,
Université Savoie Mont Blanc, CNRS/IN2P3, F-74941 Annecy, France

⁷Louisiana State University, Baton Rouge, LA 70803, USA

⁸Department of Physics, Center for High Energy and High Field Physics,
National Central University, Zhongli District, Taoyuan City 32001, Taiwan

⁹Department of Physics, Graduate School of Science, Osaka City University, Sumiyoshi-ku, Osaka City, Osaka 558-8585, Japan

¹⁰Nambu Yoichiro Institute of Theoretical and Experimental Physics (NITEP),
Osaka City University, Sumiyoshi-ku, Osaka City, Osaka 558-8585, Japan

¹¹Inter-University Centre for Astronomy and Astrophysics, Pune 411007, India

¹²Bard College, 30 Campus Rd, Annandale-On-Hudson, NY 12504, USA

¹³The University of Sheffield, Sheffield S10 2TN, UK

¹⁴OzGrav, School of Physics & Astronomy, Monash University, Clayton 3800, Victoria, Australia

¹⁵Kenyon College, Gambier, OH 43022, USA

¹⁶LIGO, California Institute of Technology, Pasadena, CA 91125, USA

¹⁷Institute of Physics, Academia Sinica, Nankang, Taipei 11529, Taiwan

¹⁸Concordia University Wisconsin, 2800 N Lake Shore Dr, Mequon, WI 53097, USA

¹⁹Institute for Cosmic Ray Research (ICRR), KAGRA Observatory,
The University of Tokyo, Kamioka-cho, Hida City, Gifu 506-1205, Japan

I. THE PRESENT

By June 2020, the global network of gravitational wave detectors, run by the LIGO, VIRGO, and KAGRA collaboration, will have just finished their most recent 12 calendar months of data collection at its best sensitivity ever. They will have quintupled the number of detections observed since the last two data collection periods [1]; each detection with typical signal-to-noise ratios of 10 to 20. With that new collection, the detectors cement the field of observational gravitational wave astronomy, *delivering* on its decades-old promise with robust detection of gravitational waves from the collisions of pairs black holes e.g. [2, 3] and of neutron stars, e.g. [4].

At these signal-to-noise ratios, quantitative statements will have been made about the properties of those new events, much like the events found in the first two data collection periods: details about astrophysical progenitors (location, distance, mass, etc.) [5, 6], and the resulting waveforms (polarizations, time-of-arrival compared against Relativity, etc.) [7–10]. With the number of events approaching 100, improved quantitative statements can then be made about the population of events, as in [11], and the surrounding cosmology, e.g. Hubble's constant, as in [12, 13].

These exciting conclusions from gravitational wave astronomy would not be possible without an accurate and precise model of the detector's loop-suppressed output – fundamen-

tally, a digitized sum of photo-currents, d_{err} , resulting from the interferometric laser power output cast on to a few diodes – and its response to the detectors' differential arm length displacement, ΔL_{free} , caused by incident gravitational waves [14, 28]. That model is then used to estimate a near-real-time data stream that corresponds to the estimated strain on the detector, $h = \Delta L_{\text{free}}/L$, where L is the average length of the given detector's arms [15, 17]. Figure 1 shows a simplified diagram of how the model is used to generate h in the LIGO detectors (VIRGO and KAGRA are similar). The creation of this “calibration” model, and the corresponding estimates of uncertainty and systematic error continues to be an exciting challenge in precision engineering as the detectors evolve to achieve better sensitivity.

An example of the network's uncertainty and error during the third observing period is shown in Figure 2. The methods used to create these estimates are described in detail in [16–18]. In the most sensitive regions (20 ;S f;S 500 Hz), the uncertainty and error estimates of the detectors' calibration are dominated by three components. The first dominant component (frequency-independent): the uncertainty in the detectors' absolute displacement reference system – a collection of auxiliary laser systems used to displace the detectors arms differentially via radiation pressure force. The laser power from these so-called “photon calibrators” are captured by their own, NIST-traceable, photo-detector systems, and their output is digitized

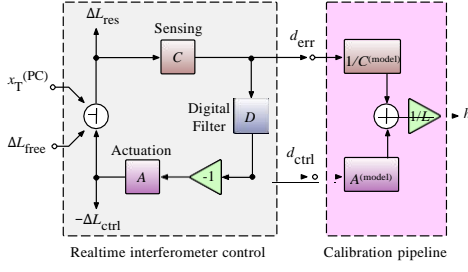


FIG. 1. Simplified diagram of the differential arm length control loop of the detectors. The digital error, d_{err} , and control, d_{ctrl} , signals are converted to an estimate of the strain on the detector in the absence of the control system, $h = \Delta L_{free}/L$. The model for such conversion is referenced to the photon calibrator system, which causes displacement, x_{pc} , equivalent to ΔL_{free}

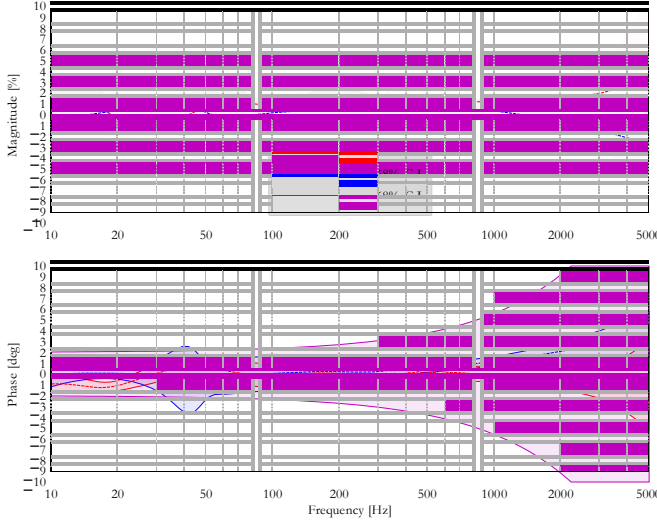


FIG. 2. Example, magnitude (top) and phase (bottom), 68% confidence interval bounds of uncertainty and systematic error of detector output, h , achieved during September 2019 for detector network. LIGO observatories, H1 and L1, and the VIRGO observatory, V1, are shown. Shaded region represents the 68% confidence interval bounds of the combined estimate of (a) statistical uncertainty, (b) systematic error, and (c) uncertainty on that systematic error estimate. Dashed lines are the median of that estimate [18].

and converted to an independent driven displacement estimate, x_{PC} , via their own sophisticated calibration scheme [19, 20]. The second dominant component (frequency-dependent): estimated systematic error (and its associated uncertainty) between the measured detector response and the limited analytic model. The final component (also, frequency dependent): the ability to resolve driven measurements in frequency regions outside the $f \sim 20 - 500$ Hz band where the detector noise increases rapidly, and timing synchronization uncertainty within a given detector limits phase estimates at high frequency (site-to-site timing uncertainty is currently negligible compared to achievable estimates of detector arrival-time for events at $SNR \sim 20$).

The first component – the estimated uncertainty in the displacement created by the absolute reference system – can,

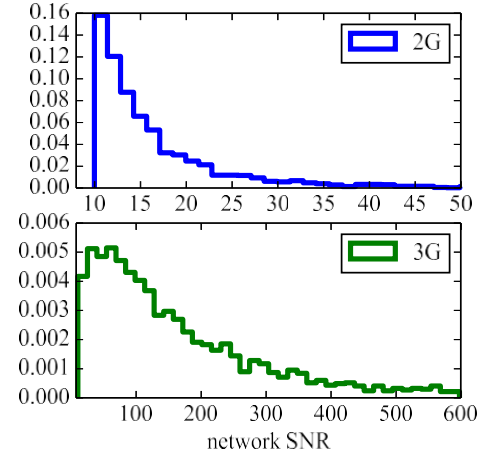


FIG. 3. Estimated distribution of detector network SNR for a theoretical distribution of events detected in a network of detectors at aLIGO target sensitivity (2G), and a network of detectors with a factor of 10 better sensitivity (3G) [27].

and will, continue to improve provided adequate time, person-power, and funding. However, we note that the latter two components are (a) detector configuration dependent, (b) model dependent, (c) time dependent (both that the unknown systematic error evolves in time when the detector configuration is stable due to natural alignment and thermal fluctuations, and also that it relies on amount of time spent understanding model discrepancies before the next detector configuration change), (d) and dependent on the detector sensitivity. Each dependency presents a unique challenge to the authors and their successors, and we anticipate no reduction in that challenge in the future.

II. THE FUTURE

The global network of gravitational wave detectors is constantly improving and expanding. The network’s third observational run began in 2019 with the existing three functional detectors, L1, H1, and V1 with sensitivity improved by almost a factor of 2. The fourth detector, KAGRA or K1, [21], is will have joined the observing run in 2020 [22]. Funding for an upgrade beyond the second generation LIGO design [23] has already been funded and will begin installation just after the current observing run, mid-2020. A decade into the future, the network of 2nd generation (“2G”) detectors be supplemented by an additional, fifth, LIGO-India detector, and may even have the its first of the 3rd generation (“3G”) detectors in which the sensitivity has increased ten-fold [24–26]. In such a 3G network, we expect the network signal-to-noise ratios for events to swell well into the 100s; see Figure 3, [27].

In such an environment, it is imperative that calibration of the detectors is precise, accurate, self-consistent, and coordinated over the many, many promised detections in order to extract the maximum amount of astrophysics and cosmology from the measured population. Extrinsic event parameters like distance and sky-localization will be confused by 1% level if

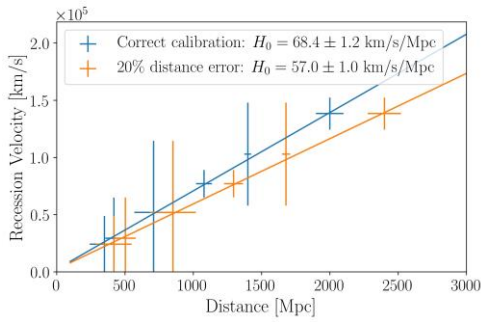


FIG. 4. A toy model of how the estimate of the Hubble constant, H_0 , may be skewed by 20% systematic error in detector network calibration (20% is an exaggerated level of systematic error to demonstrate the effect). Error bars indicate individual events and their uncertainty (with presumed systematic error). The gold solid line indicates the resulting (biased) estimate of H_0 . The blue line indicates an example “true” value of H_0 .

network accuracy and precision remains at the current state-of-the-art. At worst, rare-but-plausible events with SNRs of

500-1000 will no more be beneficial than SNR 100 events unless the level of calibration accuracy and precision is improved. Further, if *collections* of events are skewed by systematic error, then any reports on measurements of cosmological parameters may be skewed; see Figure 4 for example.

Research about how to better marginalize individual event estimates for progenitor astrophysical parameters over detectors’ calibration uncertainty is maturing. Research into the impact of the network’s calibration accuracy and precision as it evolves over time, on populations of events or cosmological statements, is still in its infancy. The photon calibrator systems remain the most promising of references, and all future detectors will remain outfitted with such a system. Projected uncertainties on these systems are already at an incredible 0.5%-level, with a renewed interest in improving them even further. As a supplement, continued development of a smattering of additional techniques also continues [28–30]. Yet, as described above, the absolute reference is not the only uncertainty and systematic error to be tackled: we look forward to the future challenges that await!

-
- [1] B. Abbott, R. Abbott, T. Abbott, S. Abraham, F. Acernese, K. Ackley, C. Adams, R. Adhikari, V. Adya, C. Affeldt, *et al.*, *Physical Review X* **9**, 031040 (2019).
 - [2] B. P. Abbott *et al.* (LIGO Scientific Collaboration and Virgo Collaboration), *Phys. Rev. Lett.* **116**, 061102 (2016).
 - [3] B. P. Abbott, R. Abbott, T. D. Abbott, F. Acernese, K. Ackley, C. Adams, T. Adams, P. Addesso, R. X. Adhikari, and *et al.* (LIGO Scientific Collaboration and Virgo Collaboration), *Phys. Rev. Lett.* **119**, 141101 (2017).
 - [4] B. P. Abbott, R. Abbott, T. D. Abbott, F. Acernese, K. Ackley, C. Adams, T. Adams, P. Addesso, R. X. Adhikari, and *et al.* (LIGO Scientific Collaboration and Virgo Collaboration), *Phys. Rev. Lett.* **119**, 161101 (2017).
 - [5] B. P. Abbott *et al.* (LIGO Scientific Collaboration and Virgo Collaboration), *Phys. Rev. Lett.* **116**, 241102 (2016).
 - [6] B. P. Abbott *et al.* (LIGO Scientific Collaboration and Virgo Collaboration), *Phys. Rev. X* **6**, 041015 (2016).
 - [7] B. P. Abbott *et al.* (LIGO Scientific and Virgo Collaborations), *Phys. Rev. Lett.* **116**, 221101 (2016).
 - [8] N. Yunes, K. Yagi, and F. Pretorius, *Phys. Rev. D* **94**, 084002 (2016).
 - [9] K. Chamberlain and N. Yunes, *arXiv preprint arXiv:1704.08268* (2017), 10.1103/PhysRevD.96.084039.
 - [10] B. P. Abbott, R. Abbott, T. Abbott, F. Acernese, K. Ackley, C. Adams, T. Adams, P. Addesso, R. Adhikari, V. Adya, *et al.*, *The Astrophysical Journal Letters* **848**, L13 (2017).
 - [11] B. P. Abbott *et al.*, *Astrophys. J. Lett.* **833**, L1 (2016).
 - [12] L. S. Collaboration, V. Collaboration, M. Collaboration, D. E. C. G.-E. Collaboration, D. Collaboration, D. Collaboration, L. C. O. Collaboration, V. Collaboration, M. Collaboration, *et al.*, *Nature* **551**, 85 (2017).
 - [13] B. Abbott, R. Abbott, T. Abbott, S. Abraham, F. Acernese, K. Ackley, C. Adams, R. Adhikari, V. Adya, C. Affeldt, *et al.*, *arXiv preprint arXiv:1908.06060* (2019).
 - [14] B. P. Abbott, R. Abbott, T. Abbott, M. Abernathy, F. Acernese, K. Ackley, C. Adams, T. Adams, P. Addesso, R. Adhikari, *et al.*, *Physical review letters* **116**, 131103 (2016).
 - [15] A. Viets, M. Wade, A. Urban, S. Kandhasamy, J. Betzwieser, D. A. Brown, J. Burguet-Castell, C. Cahillane, E. Goetz, K. Izumi, *et al.*, *Classical and Quantum Gravity* **35**, 095015 (2018).
 - [16] C. Cahillane, J. Betzwieser, D. A. Brown, E. Goetz, E. D. Hall, K. Izumi, S. Kandhasamy, S. Karki, J. S. Kissel, G. Mendell, R. L. Savage, D. Tuyenbayev, A. Urban, A. Viets, M. Wade, and A. J. Weinstein, *Phys. Rev. D* **96**, 102001 (2017).
 - [17] F. Acernese, T. Adams, K. Agatsuma, L. Aiello, A. Allocca, M. Aloy, A. Amato, S. Antier, M. Arène, N. Arnaud, *et al.*, *Classical and Quantum Gravity* **35**, 205004 (2018).
 - [18] L. Sun *et al.*, in prep. (2020).
 - [19] S. Karki *et al.*, *Rev. Sci. Instrum.* **87**, 114503 (2016).
 - [20] D. Bhattacharjee, R. L. Savage, S. Karki, *et al.*,
 - [21] Y. Aso, Y. Michimura, K. Somiya, M. Ando, O. Miyakawa, T. Sekiguchi, D. Tatsumi, H. Yamamoto, K. Collaboration, *et al.*, *Physical Review D* **88**, 043007 (2013).
 - [22] B. P. Abbott, R. Abbott, T. Abbott, M. Abernathy, F. Acernese, K. Ackley, C. Adams, T. Adams, P. Addesso, R. Adhikari, *et al.*, *Living Reviews in Relativity* **21**, 3 (2018).
 - [23] J. Miller, L. Barsotti, S. Vitale, P. Fritschel, M. Evans, and D. Sigg, *Physical Review D* **91**, 062005 (2015).
 - [24] B. P. Abbott, R. Abbott, T. Abbott, M. Abernathy, K. Ackley, C. Adams, P. Addesso, R. Adhikari, V. Adya, C. Affeldt, *et al.*, *Classical and Quantum Gravity* **34**, 044001 (2017).
 - [25] S. Hild, S. Chelkowski, A. Freise, J. Franc, N. Morgado, R. Flaminio, and R. DeSalvo, *Classical and Quantum Gravity* **27**, 015003 (2009).
 - [26] S. Hild, M. Abernathy, F. Acernese, P. Amaro-Seoane, N. Andersson, K. Arun, F. Barone, B. Barr, M. Barsuglia, M. Beker, *et al.*, *Classical and Quantum Gravity* **28**, 094013 (2011).
 - [27] S. Vitale, *Physical Review D* **94**, 121501 (2016).
 - [28] B. P. Abbott *et al.* (LIGO Scientific Collaboration), *Phys. Rev. D* **95**, 062003 (2017).
 - [29] D. Estevez, B. Lieunard, F. Marion, B. Mours, L. Rolland, and

- D. Verkindt, [Classical and Quantum Gravity](#) (2018). [arXiv:1804.08249](#) (2018).
- [30] Y. Inoue, S. Haino, N. Kanda, Y. Ogawa, T. Suzuki, T. Tomaru, T. Yamamoto, and T. Yokozawa, [arXiv preprint](#)

Performance Evaluation of a Mid-infrared Spectrometer for Remote Sensing Applications

Jae-Keun Yoo¹, Sun Do Lim¹, Dong-Hoon Lee¹, Seung Kwan Kim², and In-Ho Bae¹

¹Division of Physical Metrology, Korea Research Institute of Standards and Science (KRISS), Daejeon, Korea

²Quantum Technology Institute, Korea Research Institute of Standards and Science (KRISS), Daejeon, Korea

Corresponding e-mail address: inhobae@kriss.re.kr

We report on the development of performance evaluation technologies for mid-infrared (mid-IR) spectrometers. The mid-IR continuous-wave (cw) optical parametric oscillators (OPOs) based on a fan-out grating Mgo:PPLN pumped at 1064 nm and laser diodes were used for wavelength-calibration of mid-IR spectrometer. We used these light sources to evaluate the wavelength resolution, accuracy and optical signal-to-noise ratio (OSNR) of the mid-IR spectrometer.

INTRODUCTION

In recent days, various remote sensing applications such as biomedical sensing, gas sensing, missile tracking, lunar exploration and earth observation have been actively investigated in the mid-IR region [1]. Therefore, it is increasingly important to have accurate mid-IR spectrometer to ensure the meaningful results of such applications.

In this paper, we present the development of performance evaluation technologies for mid-IR spectrometers using cw OPO and laser diodes. The cw OPO is based on the fan-out PPLN crystal pumped at 1064 nm. By changing the poling period of the crystal, we can achieve wavelength-tunable radiation from 2500 nm to 3600 nm. The three laser diodes used in our experiment have 2000 nm and 3800nm, 4000 nm, respectively. By using these wavelength-tunable light sources, we evaluated performance of mid-IR spectrometer from 2000 nm to 4000 nm.

EXPERIMENTAL SETUP

Figure 1 shows the example of the experimental setup for calibration of mid-IR spectrometer. The main light source for the spectrometer calibration were single cw OPO and three diode lasers. To obtain stable mid-IR OPO operating in a single mode, we used modified Pound-Drever-Hall technique [2]. The detailed

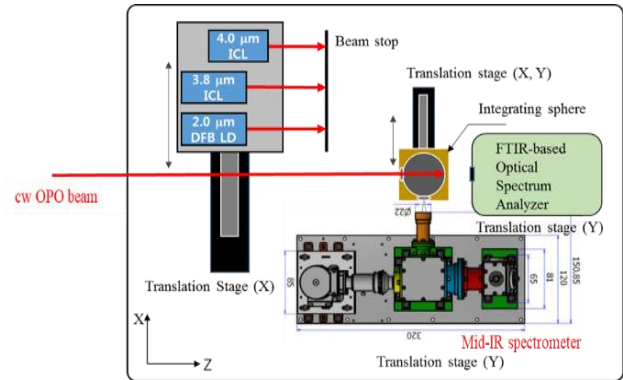


Figure 1. Example of experimental setup.

interpretation of the cw OPO performance is introduced in Ref. [3] (not shown in this paper).

In general, a mid-IR spectrometer can capture surface images of objects, such as a camera with spectral functions. The experimental setup for calibration of mid-IR spectrometer is equipped with a gold-coated integrating sphere to implement the luminance measurement conditions. The mid-IR spectrometer can measure the lambertian light source from the output port of integrating sphere. Laser output from the cw OPO can be delivered in free-space, and the integrating sphere can be mounted on a two-axis automatic linear stage to align the output port of the integrating sphere to the mid-IR spectrometer. The used distributed feedback (DFB) laser diode (LD) and DFB interband cascade laser (ICL) have a center-wavelengths of 2 μm and 3.8 μm , 4.0 μm , respectively. According to the types of the spectrometers, the light sources can be delivered with optical fibre or free-space.

EXPERIMENTAL RESULTS

Now, we present experimental results for the performance evaluation of the mid-IR spectrometer. In our experiment, we evaluated two kinds of spectrometers such as a Fourier transform infrared (FTIR)-based spectrometer (OSA205, THORLABS)

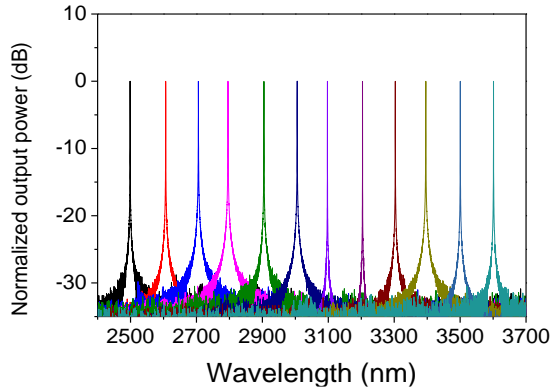


Figure 2. Wavelength spectra of cw OPO.

and a diffraction grating based spectrometer (AQ6376, YOKOGAWA). The combined wavelength spectra of cw OPO recorded by FTIR-based spectrometer is shown in Fig. 2. The poling period of the PPLN crystal moves between 28 μm and 32 μm , the wavelength of the cw OPO output can be tuned from 2500 nm to 3600 nm. Each OPO spectrum was measured in step of 100 nm. From the results, we can clearly confirmed the single mode operation of cw OPO in a wide wavelength tuning range wider than 1 μm . This ensures that the OPO was enough stable to evaluate performance of mid-IR spectrometer.

Fig. 3 shows the laser wavelength of signal and idler of the cw OPO measured using a diffraction grating based spectrometer and FTIR-based spectrometer, respectively. The wavelength of signal measured using the diffraction grating based spectrometer was 1647.7 nm, and the wavelength of idler measured using the FTIR-based spectrometer was 3004.1 nm.

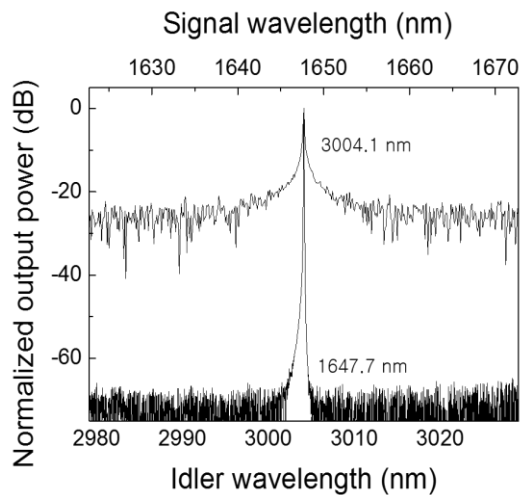


Figure 3. Laser wavelength of signal and idler

The optical signal-to-noise ratio (OSNR) of the FT based spectrometer is about 30 dB at 0.1 nm resolution, and the OSNR measured by the diffraction grating based spectrometer is about 75 dB. Since signal and idler are twin-photons generated from one pump photon and theoretically follow the same physical generating mechanism, we assumed that idler also has OSNR of at least 75 dB. Finally, we conclude that the FTIR-based spectrometer cannot measure the background noise of a signal with OSNR greater than 30 dB.

SUMMARY

Here, we reported on the experimental setup that can evaluate the characteristics of the mid-IR spectrometer. By using the mid-IR lasers, we evaluated OSNR, wavelength resolution and accuracy of the mid-IR spectrometers. We believe that these experimental results will be helpful to evaluate the performance of mid-IR spectrometer.

REFERENCES

1. B. M. Walsh, H. R. Lee, and N. P. Barnes, "Mid infrared lasers for remote sensing applications," *J. Lumin.* 169, 400-405, 2016.
2. K. Schneider, P. Kramper, S. Schiller, and J. Mlynek, "Toward an optical synthesizer: a single-frequency parametric oscillator using periodically poled LiNbO₃," *Opt. Lett.* 22, 1293-1295, 1997.
3. I.-H. Bae, S. D. Lim, J.-K. Yoo, D.-H. Lee, and S. K. Kim, "Development of a Mid-infrared CW Optical Parametric Oscillator Based on Fan-out Grating MgO:PPLN Pumped at 1064 nm," *Current Optics and Photonics*, Vol. 3, No. 1, 33-39, 2019.